Springer Series on Fluorescence 15
Series Editor: Martin Hof

Peter Kapusta
Michael Wahl
Rainer Erdmann *Editors*

Advanced Photon Counting

Applications, Methods, Instrumentation

Springer

15
Springer Series on Fluorescence

Methods and Applications

Series Editor: Martin Hof

Springer Series on Fluorescence

Series Editor: Martin Hof

Recently Published and Forthcoming Volumes

Advanced Photon Counting
Volume Editors: Peter Kapusta, Michael Wahl and Rainer Erdmann
Vol. 15, 2015

Far-Field Optical Nanoscopy
Volume Editors: Philip Tinnefeld, Christian Eggeling and Stefan W. Hell
Vol. 14, 2015

Fluorescent Methods to Study Biological Membranes
Volume Editors: Y. Mély and G. Duportail
Vol. 13, 2013

Fluorescent Proteins II
Application of Fluorescent Protein Technology
Volume Editor: G. Jung
Vol. 12, 2012

Fluorescent Proteins I
From Understanding to Design
Volume Editor: G. Jung
Vol. 11, 2012

Advanced Fluorescence Reporters in Chemistry and Biology III
Applications in Sensing and Imaging
Volume Editor: A.P. Demchenko
Vol. 10, 2011

Advanced Fluorescence Reporters in Chemistry and Biology II
Molecular Constructions, Polymers and Nanoparticles
Volume Editor: A.P. Demchenko
Vol. 9, 2010

Advanced Fluorescence Reporters in Chemistry and Biology I
Fundamentals and Molecular Design
Volume Editor: A.P. Demchenko
Vol. 8, 2010

More information about this series at http://www.springer.com/series/4243

Lanthanide Luminescence
Photophysical, Analytical and Biological Aspects
Volume Editors: P. Hänninen and H. Härmä
Vol. 7, 2011

Standardization and Quality Assurance in Fluorescence Measurements II
Bioanalytical and Biomedical Applications
Volume Editor: Resch-Genger, U.
Vol. 6, 2008

Standardization and Quality Assurance in Fluorescence Measurements I
Techniques
Volume Editor: U. Resch-Genger
Vol. 5, 2008

Fluorescence of Supermolecules, Polymeres, and Nanosystems
Volume Editor: M.N. Berberan-Santos
Vol. 4, 2007

Fluorescence Spectroscopy in Biology
Volume Editor: M. Hof
Vol. 3, 2004

Fluorescence Spectroscopy, Imaging and Probes
Volume Editor: R. Kraayenhof
Vol. 2, 2002

New Trends in Fluorescence Spectroscopy
Volume Editor: B. Valeur
Vol. 1, 2001

Advanced Photon Counting

Applications, Methods, Instrumentation

Volume Editors:
Peter Kapusta
Michael Wahl
Rainer Erdmann

With contributions by

A. Ahlrichs · J.M. Alvarez-Pez · A. Barth · O. Benson · J. Borejdo · G.S. Buller · A. Bülter · A.I. Chizhik · A.M. Chizhik · R.J. Collins · L. Crovetto · T. Dertinger · A. Diaspro · J. Enderlein · C. Eggeling · R. Fudala · S. Galiani · I. Gregor · D. Grosenick · K.S. Grußmayer · I. Gryczynski · K. Gryczynski · Z. Gryczynski · I.C. Hernàndez · D.-P. Herten · K. Ishii · F. Jelezko · N. Karedla · J. Kimball · R.R. Krishnamoorthy · D.C. Lamb · K. Lauritsen · B.P. Maliwal · B. Naydenov · A. Orte · T. Otosu · J.M. Paredes · M. Patting · S. Raut · R.M. Rich · S. Riecke · M.J. Ruedas-Rama · D. Ruhlandt · S. Rüttinger · T. Schönau · B. Sprenger · D.L. Stankowska · T. Tahara · G. Vicidomini · L.V. von Voithenberg · M. Wahl

Springer

Volume Editors
Peter Kapusta
J. Heyrovsky Institute of Physical Chemistry
Academy of Sciences of the Czech Republic
Prague 8
Czech Republic

Michael Wahl
PicoQuant GmbH
Berlin
Germany

Rainer Erdmann
PicoQuant GmbH
Berlin
Germany

ISSN 1617-1306 ISSN 1865-1313 (electronic)
Springer Series on Fluorescence
ISBN 978-3-319-15635-4 ISBN 978-3-319-15636-1 (eBook)
DOI 10.1007/978-3-319-15636-1

Library of Congress Control Number: 2015938183

Springer Cham Heidelberg New York Dordrecht London

Printed on acid-free paper

Springer International Publishing AG Switzerland is part of Springer Science+Business Media (www.springer.com)

Series Editor

Prof. Dr. Martin Hof

Academy of Sciences of the Czech Republic
J. Heyrovsky Institute of Physical Chemistry
Department of Biophysical Chemistry
Dolejskova 3
16223 Prague 8
Czech Republic
martin.hof@jh-inst.cas.cz

Aims and Scope

Fluorescence spectroscopy, fluorescence imaging and fluorescent probes are indispensible tools in numerous fields of modern medicine and science, including molecular biology, biophysics, biochemistry, clinical diagnosis and analytical and environmental chemistry. Applications stretch from spectroscopy and sensor technology to microscopy and imaging, to single molecule detection, to the development of novel fluorescent probes, and to proteomics and genomics. The *Springer Series on Fluorescence* aims at publishing state-of-the-art articles that can serve as invaluable tools for both practitioners and researchers being active in this highly interdisciplinary field. The carefully edited collection of papers in each volume will give continuous inspiration for new research and will point to exciting new trends.

Preface

Get her excited red or green;
let it depend on what she's keen.
Quite soon quite radiant she will be seen;
in colours true of her she'll gleam,
but mind the nanoseconds in between.
For they might tell which way to lean:
perhaps she's other than you had foreseen.
Although, be patient when you try this scheme;
a single flash that lights the scene
is not enough to get her theme.
In fact, her moods are so extreme
that truly random she might seem.
And yet, if patiently you sift her stream
a pattern of true beauty can be seen.
So sum your count and be serene.

In 1926 the physicist Frithiof Wolfers and the chemist Gilbert N. Lewis coined the name photon for the quantum of light discovered about 20 years earlier. Even if it may look a little superficial at first glance, let us note the involvement of chemists here and elsewhere in the evolution of quantum physics. Indeed, the overwhelming success of quantum mechanics as a modern scientific theory is rooted not so much in pure physics but in its inescapably convincing explanatory power for virtually all aspects of physical chemistry and material science. Modelling atoms and molecules as quantum mechanical systems undergoing transitions between quantum states, some of them involving photon absorption and emission, was the key to understanding and eventually even exploiting virtually all previously mysterious spectroscopic effects. In this sense it is not a surprise that the methods addressed in this volume are now used more often in chemistry and related fields than in pure physics. In fact, spectroscopic methods have become indispensible in biochemistry because light as a probe, suitably applied, can be used in living cells without any damage to the specimen and without unduly spoiling the functions or processes

under investigation. Even though classic spectroscopy does not require working with single photons, it turns out very useful that it *can* be done so. This is the case when there are only very few molecules involved in the processes of interest, in particular in the vital processes explored by molecular biology. Even more interesting than classic spectroscopy is the scenario where yet another quantum mechanical property is used: the lifetime of the excited state. It turns out that the average time a molecule spends in this state is so specific to that molecule and its environment that it can be used as a fingerprint of the molecule in addition to its spectrum and/or as a probe for certain environment parameters. Even though the lifetime of an individual excited state is completely unpredictable according to quantum mechanics, the average lifetime is both measurable and meaningful. In practice it can be observed as the duration of luminescence from an ensemble of molecules excited by a short flash of light. Going by the observed phenomenon one speaks of fluorescence or phosphorescence lifetime measurements. In that case the necessary averaging of the individual excited state lifetimes is achieved implicitly because of the simultaneous observation of photons from the entire ensemble. The other interesting scenario is that of averaging the excited state lifetime across multiple cycles of excitation and photon emission observed on just one molecule. Indeed, by virtue of ergodicity, this kind of measurement gives the same results as the ensemble measurement. In this case time-correlated single photon counting (TCSPC) is the method of choice. It allows luminescence lifetime measurements on single molecules and other isolated quantum systems. Combining spectral information and, e.g., fluorescence lifetime one can use this refined "finger print" of the molecules of interest to identify them even in the presence of significant background. It was largely this idea, combined with confocal detection, which finally led to the incredible achievements in single molecule detection, single molecule spectroscopy, and even microscopy by means of TCSPC. Powerful methods such as the exploitation of Förster resonant energy transfer (FRET) as a molecular ruler became routine tools for the investigation of protein folding and interaction when they were made accessible for single molecules along this way.

However, TCSPC is not only useful with single molecules. As we will show in the first chapters of the present volume, it also helps to achieve better time resolution with typical detectors, even in ensemble measurements. These technology related chapters will cover the state of the art of current hardware, hopefully also convincing the reader that despite the inherent statistical nature of the measurement, modern users can rely on incredibly fast instruments and must not be as patient as our little old-fashioned opening poem might suggest. Indeed it is mostly the memory of "oldfashioned" instrumentation that left the impression of slowness attached to TCSPC. This may be illustrated by personal memories held probably not only by the editors: "I recall with nostalgia the long nights spent alone in a dimmed basement lab waiting for collection of at least 1000 counts in the peak by our beautiful TCSPC monster powered by a 45 kHz flashlamp." This is the past. Meanwhile things have changed dramatically, not only because of faster TCSPC electronics but very much also because of faster (and easier to use) lasers, to which a chapter in its own will be dedicated. The remainder of the chapters are covering a

rich eclectic mixture of application topics as well as methodology in experiment and data analysis. Despite of the importance of life science applications we tried to embrace a much wider scope, including, e.g., defect centers in diamond as single photon sources and quantum sensors, as well as optical tomography and super resolution microscopy. Similarly, on the methodology and instrumentation side, we aimed to show the interesting new options arising from the combination of apparently distinct methods such as classic TCSPC and fluorescence lifetime with methods based on intensity fluctuation. Together with the authors, to whom we express our gratitude here, we hope to provide a volume of both an immediate value as a current overview of the field and some longer term value as a collection of reference texts.

Prague, Czech Republic — Peter Kapusta
Berlin, Germany — Michael Wahl
Rainer Erdmann

Contents

Modern TCSPC Electronics: Principles and Acquisition Modes 1
Michael Wahl

Single-Photon Counting Detectors for the Visible Range Between 300 and 1,000 nm 23
Andreas Bülter

Single-Photon Detectors for Infrared Wavelengths in the Range 1–1.7 μm 43
Gerald S. Buller and Robert J. Collins

Modern Pulsed Diode Laser Sources for Time-Correlated Photon Counting 71
Thomas Schönau, Sina Riecke, Andreas Bülter, and Kristian Lauritsen

Advanced FCS: An Introduction to Fluorescence Lifetime Correlation Spectroscopy and Dual-Focus FCS 89
Thomas Dertinger and Steffen Rüttinger

Lifetime-Weighted FCS and 2D FLCS: Advanced Application of Time-Tagged TCSPC 111
Kunihiko Ishii, Takuhiro Otosu, and Tahei Tahara

MFD-PIE and PIE-FI: Ways to Extract More Information with TCSPC 129
Anders Barth, Lena Voith von Voithenberg, and Don C. Lamb

Photon Antibunching in Single Molecule Fluorescence Spectroscopy ... 159
Kristin S. Grußmayer and Dirk-Peter Herten

FLIM Strategies for Intracellular Sensing 191
Maria J. Ruedas-Rama, Jose M. Alvarez-Pez, Luis Crovetto, Jose M. Paredes, and Angel Orte

Multiple-Pulse Pumping with Time-Gated Detection for Enhanced Fluorescence Imaging in Cells and Tissue 225
Rafal Fudala, Ryan M. Rich, Joe Kimball, Ignacy Gryczynski, Sangram Raut, Julian Borejdo, Dorota L. Stankowska, Raghu R. Krishnamoorthy, Karol Gryczynski, Badri P. Maliwal, and Zygmunt Gryczynski

Pattern-Based Linear Unmixing for Efficient and Reliable Analysis of Multicomponent TCSPC Data 241
Ingo Gregor and Matthias Patting

Metal-Induced Energy Transfer 265
Narain Karedla, Daja Ruhlandt, Anna M. Chizhik, Jörg Enderlein, and Alexey I. Chizhik

The Importance of Photon Arrival Times in STED Microscopy 283
Giuseppe Vicidomini, Ivàn Coto Hernàndez, Alberto Diaspro, Silvia Galiani, and Christian Eggeling

Single-Color Centers in Diamond as Single-Photon Sources and Quantum Sensors 303
Boris Naydenov and Fedor Jelezko

Photon Counting and Timing in Quantum Optics Experiments 319
Andreas Ahlrichs, Benjamin Sprenger, and Oliver Benson

Photon Counting in Diffuse Optical Imaging 343
Dirk Grosenick

Index 367

Modern TCSPC Electronics: Principles and Acquisition Modes

Michael Wahl

Abstract Time-correlated single-photon counting (TCSPC) is an extraordinarily versatile and sensitive technique. While it was initially used almost only to measure excited state lifetimes, it can today be used much more flexibly, embracing and combining experimental methods that in the past required separate instrumentation. This has become possible by time-tagged event recording and modern time measurement circuitry. This chapter shows how such technologies operate with regard to electronics, data processing, and applications. Some implementation details will be exemplified by state-of-the-art TCSPC instruments and a recent software package for TCSPC data acquisition and analysis.

Keywords Coincidence correlation · Picosecond timing · Single-photon counting · TCSPC · TDC · Time tagging

Contents

1 Introduction: Fundamentals and History of TCSPC 2
2 Modern Time Measurement Circuits 5
3 Applications Beyond Fluorescence Lifetime 7
4 Time-Tagged TCSPC 9
5 TCSPC Imaging and Multidimensional Techniques 14
6 Real-Time Analysis of Time-Tagged TCSPC Data 16
7 Outlook 18
References 19

M. Wahl (✉)
Instrumentation Division, PicoQuant GmbH, Rudower Chaussee 29, 12489 Berlin, Germany
e-mail: wahl@picoquant.com

P. Kapusta et al. (eds.), *Advanced Photon Counting: Applications, Methods, Instrumentation*, Springer Ser Fluoresc (2015) 15: 1–22, DOI 10.1007/4243_2014_62,

1 Introduction: Fundamentals and History of TCSPC

Time-correlated single-photon counting is an extraordinarily capable and versatile optical measurement technique. By design and definition it uses only single quanta of light and provides information on the temporal structure of such light. It therefore matches the requirements of applications where the light emission of interest is very weak.

Historically the method was first conceived in nuclear physics [1] and then for a long time primarily used to analyze the light emitted as fluorescence during the relaxation of molecules from an optically excited state to a lower energy state [2]. In simple cases this process can be described by just one value: the "fluorescence lifetime," which characterizes the average lifetime of the excited state. The chemical composition, environment, and molecular interaction of the emitter lead to changes of the fluorescence lifetime, which thereby becomes a valuable key to the understanding of important processes at the molecular level of biology and medicine [3].

In order to appreciate the merits of TCSPC, it is very insightful to briefly consider the straightforward alternative of a simple transient recording of the optical flux, for instance, by means of a photodiode and an oscilloscope. By way of the photoelectric effect, the photodiode outputs an electrical current proportional to the incident optical flux. Provided there is a temporal structure in the optical flux, the same temporal structure would (in principle) be observable on the oscilloscope screen.

There are two fundamental limitations to this approach. The first and obvious limitation was already touched upon: when the light levels are low, the quantum nature of light itself will invalidate the concept of optical flux as a continuously measurable quantity. Suppose the light under investigation originated from a single molecule undergoing a radiative transition from an excited state to a lower energy state. By virtue of quantum mechanical indeterminism, there would be a photon emitted at some point in time, but a meaningful interpretation of the photon flux over time within one cycle of excitation and emission would not be possible. The output of the photodiode (if it were actually sensitive enough to respond to single photons) would at best be some small blip at the moment of emission and would not tangibly reflect the temporal structure sought after.

Nevertheless, it is very well possible to perform fluorescence lifetime measurements with analog transient recording if the experiment can be performed with many molecules simultaneously. This typically involves using solutions containing many of the target molecules and their simultaneous excitation by a sufficiently strong light pulse. The many photons subsequently emitted will cause a meaningful optical flux that can be recorded as a function of time. The result for typical fluorescent dyes is an exponential drop over time, characterized by the fluorescence lifetime of that species under the present conditions.

However, there are more issues with analog transient recording. It is well known that both the photodiode (or any other analog optical receiver) and the oscilloscope (or any other comparable transient recorder) have a limited bandwidth and a limited

dynamic range. The upper limit of frequency content such devices can faithfully carry through is typically on the order of some GHz. Translating this to the time domain means that rapid changes on the order of sub-nanoseconds can no longer be faithfully recorded. Considering that many fluorescent molecules of practical interest have fluorescence decay times on the order of less than a nanosecond, analog recording would be very limiting.

All these issues can be resolved with TCSPC as follows. First of all, a detector with single-photon sensitivity must be used (see chapter by Bülter [4] and Buller and Collins [5]). If in the particular experiment there is no inherent limitation due to the number of simultaneous emitters, one deliberately attenuates the light so that the detector is unlikely to receive more than one photon at a time. Then, as opposed to single-shot transient recording, in TCSPC the measurement is conducted over many cycles of excitation and emission. In each cycle the time between excitation and emission is measured and the measurements are collected in a histogram [2]. Figure 1 shows the timing scheme and the basic idea of histogramming time differences. By virtue of ergodicity (which can normally be assumed), the histogram of time differences shows exactly the temporal structure of the fluorescence intensity decay that is obtained in the analog case.

Of course it requires a sufficient number of repetitions to fill the histogram to an extent where the error due to counting statistics becomes negligible. Since the data is acquired just by counting and the number of repetitions can be chosen very large, the dynamic range can be made much larger than in analog recording. Even though the bottom end may be limited by noise (stray light, detector dark counts), it is still possible to achieve a dynamic range as high as 10^6 with TCSPC.

Now, having solved the issues of low light intensity and dynamic range, how does TCSPC solve the issue of detector bandwidth? It may be too bold to claim a complete solution to this issue, but TCSPC does indeed improve the temporal resolution limit imposed by the detector by typically an order of magnitude. This is because in TCSPC, the temporal profile is not extracted directly from the electrical output signal of the detector; instead, the detector only needs to trigger electronic timing circuits. This requires that the output pulses of the detector have a timing-reliable leading edge and sufficient steepness, but it does not require a certain response width. For virtually all types of detectors, it is easier to achieve this leading edge timing-reliability than achieving a corresponding bandwidth in

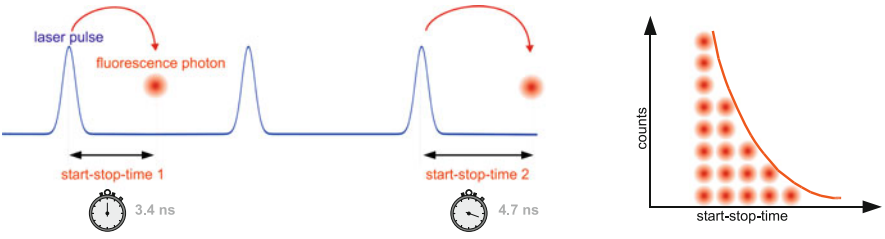

Fig. 1 Basic principle of TCSPC: histogramming of start–stop time differences. Actual timing figures are for example only

analog mode [2, 3, 6]. The technical term used to describe this timing-reliability is the so-called transit time spread. This term is mostly used in the data sheets of photomultiplier tubes (PMT), but the more general terms "timing uncertainty" or "jitter" describe the same phenomenon and can be used for similar types of random timing error introduced by other system components.

One specific issue that arises with some types of detectors, notably PMTs, in single-photon detection mode is that of fluctuating pulse heights. Due to the quantum physical nature of the amplification process in such a device, there can be variations in pulse amplitude (see Bülter [4]). If the timing electronics were triggered just by putting the detector pulses through a voltage comparator, this fluctuation in amplitude would result in a timing error. This is commonly solved by means of a constant fraction discriminator (CFD), which at the same time helps to suppress dark counts originating mostly from thermal effects in the detector [2, 3, 6].

Obviously the time measurement must meet the same requirements of resolution and reliability as the detector. In the 1960s/1970s when TCSPC was beginning to become common practice in fluorescence lifetime measurements, it was not very easy to perform sub-nanosecond timing [2]. The solution at the time was still the so-called time-to-amplitude converter (TAC) invented in the 1940s for the measurement of muon lifetimes [7]. A TAC basically consists of a small capacitor that is charged with a constant current, thereby creating a linearly rising voltage ramp. By starting the charge integration at the moment of excitation and stopping it at the moment of photon detection, a voltage that is proportional to the elapsed time is obtained. The TAC is followed by an analog-to-digital converter (ADC), which converts this voltage to a digital number that assigns the photon count to a corresponding histogram bin. Effectively the TAC and ADC represent a high-resolution stopwatch, which is exactly what classic TCSPC for fluorescence lifetime measurements requires.

Although the combination of a TAC and an ADC meets the requirements for short fluorescence lifetime measurements, it has some limitations that lead to inconvenience, if not even undesirable artifacts in the measurement results. A first limitation is the very principle of a stopwatch. It must always be used in the prescribed order: start first, then stop. In other words, negative times cannot be measured. While this may sound academic, there is a real-world consequence related to this issue. It stems from the fact that TAC and ADC require a certain time to complete a present measurement before they can handle a new run. This constitutes a serious problem when the excitation period is shorter than this dead time of TAC and ADC. With typical modern laser sources, this is mostly the case. At the same time, due to Poisson statistics, one must work with photon rates as low as 1 % of the excitation frequency in order to maintain a reasonable likelihood of receiving only single photons [2, 3, 6]. What follows is that the TAC would permanently start measurements that never complete, because there is no photon in the present cycle. However, as dead time exists even in that case, the next start pulse would be missed. This problem is commonly solved by operating the TAC in reverse start–stop mode, i.e., it is started upon a photon event and stopped on the next laser pulse [2, 6]. By means of cable delay in the detector signal path, one can also stop on the laser pulse that

caused the photon event. While this works reasonably well, it still constitutes an inconvenience in experiment and data handling.

A further limitation of a TAC arises from the temperature dependence of the voltage ramp, leading to the need for temperature control or frequent re-calibration. Another issue is the limited range of the ADC resulting in a limited time range of the stopwatch. In order to cover longer spans, the charge current or the capacitor must be changed. Even when accomplished through software, the need for such adjustments is often unpleasant, especially during the initial setup of an experiment, when the required range and offset are not yet known. Another issue of TAC-/ADC-based TCSPC is the differential nonlinearity (DNL) in the voltage ramp and in the ADC. The DNL becomes particularly pronounced when one tries to make everything fast, usually in an attempt to shorten the dead time. Effectively such nonlinearities lead to nonuniformity of histogram bin widths and consequently to distortions of the recorded decay shapes. This may average out when long decays are observed, but it severely spoils attempts at resolving multi-exponential decays with very short lifetimes. There are technical solutions to such issues based on "dithering," i.e., injecting small voltage shifts on the analog side and subsequent subtraction in the digital domain, thereby averaging out the nonlinearities [6]. However, such solutions go along with an additional reduction of the usable range of the ADC and an increase in timing jitter.

In the next section technical alternatives to picosecond time measurement with TAC and ADC will be demonstrated.

2 Modern Time Measurement Circuits

Precise time measurement is a frequent requirement in science and technology. Classic areas of scientific application are nuclear physics, astronomy, and geodesy. Applications in time-resolved fluorescence spectroscopy became particularly important in the context of the life sciences. In technology and industrial metrology, the key applications are in dynamic testing of integrated circuits and high-speed optical components for data storage and fiber optic telecommunication. Further applications of picosecond timing are found in laser ranging and depth imaging.

The most common application requirement is a repeated time difference measurement in the sense of the stopwatch introduced in the previous section. The difficulty lies in the requirement of picosecond resolution. Even though modern digital circuits can operate at very high clock speeds, as high as some tens of GHz, they are not yet fast enough to directly count picoseconds (1/1 ps = 1 THz). Nevertheless, high-speed digital circuits are the means of choice for modern time measurement circuits, typically called time-to-digital converters (TDCs). This is mainly for three reasons: (1) the option to use crystal clocks, thereby eliminating calibration issues; (2) the option to obtain and process digital results directly; and (3) compatibility with modern production processes for cost-efficient monolithic integration.

There are many variants of TDC implementations, and the literature is vast. Some good reviews exist and may serve as a starting point for further reading [8–10]. The simplest solution for a TDC is a digital counter running at the speed of a fast crystal locked clock. Suitable counter implementations in fast semiconductor technologies such as SiGe can in principle be operated at clock rates as high as 40 GHz, thereby directly providing time resolutions of 25 ps. However, additional difficulties arise from small systematic timing errors on individual bits of the counter or the clock. This leads to differential nonlinearity with its detrimental effects as outlined earlier. It is therefore important to implement the TDC in such a way that the individual tick periods can be tuned to precisely equal duration. At the same time it is worth considering the power consumption of such a circuit. SiGe logic running at maximum clock speeds is quite power consuming. This leads to limitations in integration density due to thermal load. Power consumption can be limited by using lower clock speeds (down to 1 mW per gate at 20 GHz for typical current SiGe designs), obviously compromising time resolution. However, there is a solution that simultaneously solves these issues and even allows the time resolution to be increased beyond the clock period.

The solution is to operate the counter only at a moderate clock speed and to subdivide each clock period by some means of fine counting or interpolation. A direct digital way of subdividing the coarse clock periods is by means of tapped delay lines (Fig. 2).

For very high-resolution TDCs, the delay elements can consist just of regular metal interconnects appropriately designed into the layout of the integrated circuit. The issue of DNL due to nonuniform time steps can be solved by making the delay elements tunable. This is commonly achieved by making them active elements whose supply voltage is variable. A one-time calibration can then be used to minimize the DNL. In order to maintain appropriate delay not only within the individual steps but also in relation to the overall clock and in the presence of temperature changes, it is advantageous to incorporate the entire delay chain in a delay-locked loop (DLL) that controls the overall supply voltage of the delay elements. This is similar to the more widely known concept of a phase-locked loop (PLL).

Deciding for active delay elements is of course a decision that ties the achievable time resolution to the capabilities of the chosen semiconductor technology.

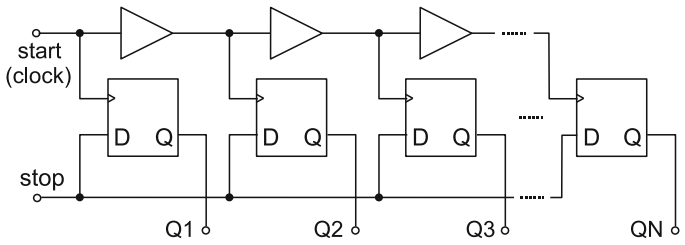

Fig. 2 Example of a tapped delay line circuit for high-resolution TDCs

Fortunately, modern high-speed semiconductor technologies permit very short gate delays. SiGe gates with a propagation delay down to 2 ps have been reported [11]. In practical circuit designs values down to 4 ps are possible, but cost and availability may impose further restrictions so that gate delays of 10. 20 ps are still found in practice. In order to leave some headroom for delay tuning and production tolerances, the TDC is typically designed for a lower target resolution, e.g., 25 ps [12]. Such a TDC does not provide as high a resolution as can be obtained with a TAC, but it has important benefits such as crystal stability, direct and high-speed digital interfacing, virtually unlimited time range, very low DNL, and a very short dead time. Given that the detector's resolution is usually more limiting, this trade-off is very reasonable in many cases.

If a TDC with even higher resolution is required, it is currently still necessary to revert to analog interpolation techniques. There are many such techniques, but the core concept is very similar to that of a TAC. For instance, one can sample a voltage that changes linearly within the clock period. While linear voltage changes are easy to deal with on the data processing side, they can be difficult to create and sample without introducing DNL. An alternative is sinusoidal voltages (synchronous with the clock), which can be made spectrally pure, so that the DNL can be kept very small. Of course the inherent nonlinearity must then be corrected with more involved data processing. In any case, TDCs with analog interpolation can provide resolutions down to a picosecond while maintaining some key benefits of a TDC, namely, crystal stability, unlimited time span, and multi-stop capability.

It is the crystal locking and the unlimited time span of TDCs, together with their easily achievable multi-stop and multichannel capability, that permit an entirely different approach to TCSPC, namely, abandoning the simple stopwatch concept. In the next section we explore some applications where this is of tremendous benefit.

3 Applications Beyond Fluorescence Lifetime

Classic TCSPC basically collects photon arrival times, but with an immediate data reduction to one figure of interest: the delay between excitation and emission. It is then interesting to note that there are several other experimental methods involving photon arrival time measurements such as fluorescence correlation spectroscopy (FCS) and dynamic light scattering (DLS). Both are photon correlation techniques providing information about mobility, size, shape, and flexibility of small particles as well as offering insight to the interactions between the particles and their environments. For FCS it is fair to say that it is at least equally as important in the life sciences as fluorescence lifetime spectroscopy as it facilitates (among other things) extremely sensitive binding assays using minute amounts of material [13, 14]. The basic concept is to observe a small confocal volume containing diffusing molecules and to perform an autocorrelation on the trace of photon density over time. The autocorrelation curve provides information on mobility

(thereby on size and binding) as well as (under controlled volume conditions) information on concentration (see Dertinger and Rüttinger [15]).

Even though for standard FCS the photon arrival times need not be measured at the same high resolution as in fluorescence lifetime measurements, it is clear that a unified instrument could be used for both methods if the raw photon arrival timing was fully available for further processing. Indeed it is common practice to perform FCS and DLS with hardware correlators that also implicitly carry out an early data reduction. While in the past there was good reason to opt for such early data reduction (usually regarding hardware performance), it is now very well possible to try and be much more general. As it turns out, not only can the cost of separate instruments be saved, but combinations of classical TCSPC and FCS can be implemented that open up powerful new dimensions of sensitive detection and analysis.

One of the most impressive results of such a combination of classical TCSPC and FCS is fluorescence lifetime correlation spectroscopy (FLCS). The term was coined several years after the original paper which called the method "time-resolved fluorescence correlation spectroscopy" [16]. At first glance FLCS could be described as a means of filtering photon events by fluorescence lifetime of the decay that produced them. This allows different molecular species to be separated in one single FCS experiment with one single laser and one detector, provided they differ in fluorescence lifetime. This is of extraordinary value as it turns out to be experimentally difficult to obtain the same result by means of differences in excitation/emission wavelength. However, in order to appreciate FLCS fully, it is better to look at its mathematical foundation more closely (see Böhmer et al. [16] and Dertinger and Rüttinger [15]). It can then be seen that the "filtering" is more correctly to be understood as a weighting that lets a given photon contribute more or less to the correlation function according to predetermined lifetime-dependent orthogonal weight vectors. This more general explanation makes it easier to see why FLCS can not only distinguish different molecular species but also species from background and detector afterpulsing [17].

Recently a further generalization of the FLCS principle was proposed by the group of Seidel and termed filtered FCS (fFCS) [18, 19]. It combines the statistical filtering approach developed originally in FLCS with multiparameter fluorescence detection [20].

Further very powerful methods derived from FLCS by Tahara and coworkers termed lifetime-weighted FCS [21] and 2D FLCS [22] are presented in full detail in the chapter by Ishii et al. [23].

While much of this book is focused on the applications of TCSPC for the life sciences, it should not be ignored that the foundation of everything covered here is after all quantum physics. In basic quantum physics research, there are numerous other applications that versatile TCSPC electronics can (and should) target just as well.

The most important technique in this realm is coincidence correlation. For instance, when an experiment is conducted to determine if the observed system actually is a single quantum system, then it is typically done by coincidence correlation of photons received from that system by two separate detectors (see chapter Grußmayer and Herten [24]). If there is really only one single quantum

emitter, then the two detectors should never receive photons at the same time. This applies to single molecules in the life sciences as much as it does to single defect centers in diamonds or single quantum dots. In their simplest form such coincidence correlations can be performed by the classical stopwatch type of TCSPC electronics. However, as the stopwatch concept can always only relate two immediately successive photons, this provides only an approximation of the true correlation function that would consider *all* photons.

Similarly, modern quantum physics research is aimed at hot and advanced topics such as quantum communication, quantum teleportation, and quantum computing, where capturing coincidences frequently involves more than two detectors. In addition, further trigger conditions often need to be captured for heralded photon events or synchronization in quantum communication.

It is time-tagged TCSPC with its removal of early data reduction that enables powerful techniques for the life sciences, such as FLCS, as well as the most versatile approaches for coincidence correlation as required in fundamental quantum physics. The next section is aimed at concepts and hardware designs for time-tagged TCSPC.

4 Time-Tagged TCSPC

Supposing for a moment that a perfect instrument could be designed that captures and maintains all photon timing information required to perform the various methods from fluorescence lifetime measurement, FCS, and all their possible combinations like FLCS, as well as generalized coincidence correlation, what would it have to look like?

It must be considered that such a device would need picosecond resolution in order to capture the fluorescence lifetime as in classic TCSPC. It must also capture intensity variations over time at lower resolution (typically microseconds) in order to perform FCS. The latter forbids classical histogramming unless sequences of many histograms are formed, each with microsecond collection time. This would lead to huge amounts of data and would still not permit photon-by-photon calculations as required for FLCS or full-blown coincidence correlation.

The most general answer to these requirements is a form of data collection called “time tagging” or “list mode” which has been around for quite some time in high energy physics. The resulting raw data is a list of detected photon arrival times on which subsequently any kind of analysis can be performed in order to implement the various analytical methods.

For a perfect instrument we go one step further and include in the list of captured events also the moments of laser excitation (sync events) in order to implement classic TCSPC lifetime measurements. Furthermore, the perfect instrument should provide inputs for more than one detector so that multiple picosecond coincidence correlations and FCS cross-correlations can be performed. The time tags or “time stamps” for all of the recorded input events are derived from a common clock, which now would be like a “picosecond wall clock” instead of a stopwatch. The list

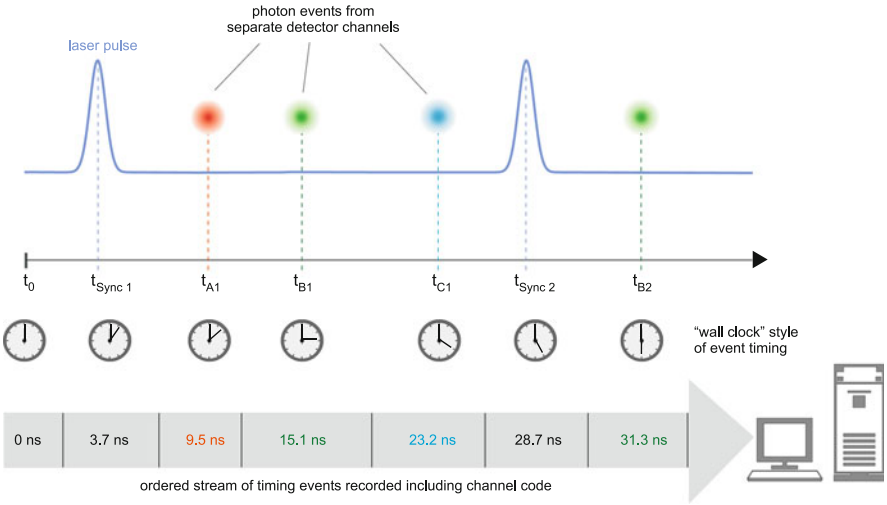

Fig. 3 Concept sketch of an idealized time-tagging TCSPC instrument

of event times would be streamed continuously into a sufficiently fast host computer where the analysis of interest can then be carried out. This could even be done in real time in order to facilitate immediate visualization and experiment control. At the same time the raw data can be stored so that further analysis can be performed any time later. Figure 3 shows a conceptual sketch of the proposed "perfect" time-tagging TCSPC instrument.

Once stopwatches (and in particular the TAC) are no longer involved, one more inconvenience very well known to experimenters can be discarded: the necessity to change cable delays or optical path lengths in order to shift the time differences of interest into the narrow time window of conventional data acquisition. As all time differences obtained from the clock readings in Fig. 3 can now be obtained by plain arithmetics from the raw data, it is straightforward to introduce any arbitrary offset in that calculation, thereby replacing cable delays. The beauty of this concept is that these offsets can be positive as well as negative. Indeed, when using the acquisition scheme of Fig. 3, it is no longer forbidden to calculate (and so effectively measure) even negative time differences.

The only reason why the "perfect instrument" was kept somewhat hypothetical up to this point is that there are some constraints to what can be done with real-world hardware. Of course we use TDCs to realize the instrument. By virtue of high resolution, crystal clock, and inherent multi-stop capability, they nicely meet a large part of the requirements established above. The requirement of handling multiple input channels can be met by building a truly multichannel TDC (one clock plus counter and multiple readout registers) or by running multiple single-channel TDCs from a common clock. The common clock is essential because only then the individual timing records are meaningfully related in subsequent cross-channel data analysis.

The real-world limitations come into play with dead time. When striving for high resolution of, e.g., 1 ps, we must currently accept a TDC dead time of 80 ns, and for 25 ps resolution, we have about 25 ns dead time [12, 25]. However, this limitation is not really only one of the TCSPC electronics. Even if there were no TDC dead time, all real-world photon detectors would also impose a dead time. Even the fastest detector would not be able to produce an electrical output signal where the voltage or current rise and fall infinitely fast between individual events. Fortunately it can be arranged that this is of little impact in relevant applications. By providing strictly independent TDC input channels for all detectors, we can ensure that dead time never acts across channels. Cross-correlations can therefore be done without any limitations all the way down to zero lag time. This is fundamentally different from TCSPC with detector multiplexing [6, 26], where individual channels can blind each other due to shared dead time.

While the conceptual sketch shown in Fig. 3 actually works well for coincidence correlation and FCS, dead time is also an issue when sync signals from fast lasers (some tens of MHz) must be handled. At a (quite common) laser rate of 80 MHz, sync pulses would arrive separated in time by only 12.5 ns. Clearly, with a dead time of 25 or 80 ns, these events would not be continuously captured.

Given that the instrument strives to cover different subsets of applications, each with their own special requirements, it is reasonable to implement different modes of operation. This is quite feasible in practice since much of the functionality of advanced TCSPC instruments is implemented with field-programmable gate arrays (FPGA). This allows reconfiguration at run time at virtually no extra cost.

The first category of applications which needs to be covered is those using only photon detectors and no sync pulses from a laser, i.e., coincidence correlation and FCS. In this case there are no dead time issues, and the instrument can be operated close to the sketch shown in Fig. 3. This mode of operation is called *T2 mode*.[1] In the following some implementation details for this mode of operation shall be examined using a recent instrument as an example [25].

The HydraHarp 400 multichannel TCSPC system uses multiple synchronized TDCs providing a resolution of 1ps with a dead time of 80 ns. This permits a theoretical throughput of 1/80 ns = 12.5 Mcps per channel. In T2 mode all timing inputs of the device are functionally identical. There is no dedication of any input channel to a sync signal from a laser. All inputs can be used to connect photon detectors. The events from all channels are recorded independently and treated equally. In each case an event record is generated that holds information about the channel where it came from and the arrival time of the event with respect to the overall measurement start. The timing is recorded with the highest resolution the hardware supports (1 ps). Each T2 mode event record consists of 32 bits. This number may appear somewhat arbitrary, but it is the best choice given that modern computers operate efficiently with 32 bit data and bus throughput is limited. In the

[1] This naming convention appears a little arbitrary because it has evolved historically. See the related footnote on T3 mode for the original historical meaning.

case of the HydraHarp 400, we use 6 bits for the channel number and 25 bits for the time tag. Obviously, this limited number of time tag bits can cover only a limited time span. However, if the time tag overflows, a special overflow record is inserted in the data stream, so that upon processing of the data stream, a theoretically infinite time span can be covered at full resolution. This concept may be understood like the combination of a clock and a calendar. Even though the clock has an "overrun" every 24 h, we can use it together with a calendar to calculate time spans of any duration, way beyond 24 h.

The event records produced by the TDCs are queued in a FIFO (first in, first out) buffer in the TCSPC hardware, capable of holding up to two million event records. Such a FIFO buffer may be regarded as a "queue" like a waiting line where new customers arrive at largely unpredictable times. The objective is to "serve" them in their original order of arrival and to make sure none gets dropped. The FIFO buffer input is therefore designed to be fast enough to accept records at the full speed of the TDCs. Consequently, even during an intense burst of photons, no events will be dropped in processing. The FIFO buffer output is continuously read by the host PC, thereby making room for freshly arriving events. Even if the average read rate of the host PC is limited, bursts with much higher rates can be recorded for some time. Only if the average input rate over a long period of time exceeds the readout speed of the PC a FIFO buffer overrun can occur. In case of a FIFO buffer overrun, the measurement must be aborted because data integrity cannot be maintained. However, due to the high bandwidth of USB 3.0, a sustained average count rate of 40 Mcps is possible on a modern PC. This is an enormous progress over the first time-tagging TCSPC electronics of the 1990s where sustained throughput was typically less than 1 Mcps.

For maximum throughput, T2 mode data streams are normally written directly to disk, without preview other than count rate and progress display. However, as we will show in Sect. 6, it is also possible to analyze incoming data "on the fly."

The other category of applications that needs to be covered is those requiring photon timing with respect to the excitation moments, e.g., classic fluorescence lifetime measurements or their advanced derivatives as in FLCS. In the case of modern lasers with high repetition rates, there are dead time issues and the instrument cannot be operated exactly like in the idealized sketch of Fig. 3. This is where we must resort to *T3 mode*.[2]

[2] As outlined in the footnote on T2 mode, this nomenclature is somewhat arbitrary and only explicable in historical context. The abbreviation T3 stems from T3R which in turn stands for time-tagged-time-resolved (TTTR). This was essentially an ad hoc term to adequately describe our first implementation of early time-tagged TCSPC by an extension of the classical stopwatch scheme by a lower-resolution time tag [27]. The idea was originally conceived for the purpose of single molecule detection in capillary flow [28] but had not been widely recognized then. Other early implementers of the concept (Becker & Hickl GmbH, unpublished at the time) and related publications [29] referred to it only from a specialized application or implementation perspective, using the terms burst-integrated fluorescence lifetime (BIFL) or FIFO mode. Today it is more common to speak of TTTR or time tagging as the overall method with T2 and T3 modes as its variants. T3 mode was called T3 mode because it is close to the historical T3R scheme.

In T3 mode one timing input is dedicated to a periodic sync signal, typically from a laser. As far as the experimental setup is concerned, this is similar to histogramming in classical TCSPC. The main objective of T3 mode is to allow high sync rates from mode-locked lasers (up to 150 MHz) which could not be handled in T2 mode due to dead time and bus throughput limits. Accommodating the high sync rates in T3 mode is achieved as follows: first, a divider is employed immediately at the sync input. This reduces the sync rate so that the channel dead time is no longer a problem. Given the periodicity of the sync pulses, the events removed by the divider can later be reconstructed in data processing. The remaining problem is now that even with a divider of, e.g., 16, the resulting data rate is still too high for collecting all individual sync events like ordinary T2 mode events. Considering that sync events are not of primary interest, the solution that T3 mode provides is to record them only if they gave rise to a photon event on any of the photon input channels. The event records are then composed of two timing figures: (1) the start–stop timing difference between the photon event and the last sync event and (2) the arrival time of the event pair on the overall experiment time scale (the time tag). In recent TCSPC devices, the latter is obtained by simply counting sync pulses. From the T3 mode event records, it is therefore possible to precisely determine which sync period a photon event belongs to. Since the sync period is also known precisely, this actually allows the arrival time of each photon with respect to the overall experiment time to be reconstructed, which is effectively what was expected of the ideal instrument. Figure 4 shows the event recording scheme of T3 mode.

T3 mode event records of the HydraHarp 400 also consist of 32 bits each. There are 6 bits for the channel number, 15 bits for the start–stop time, and 10 bits for the sync counter (time tag). Like in T2 mode, when the counter overflows, an overflow record is inserted in the data stream, so that upon processing of the data stream, any time span can be recovered, as explained previously with the "clock plus calendar" metaphor. The 15 bits for the start–stop time difference cover a time span of $32{,}768 \times R$, where R is the chosen resolution. At the highest possible resolution of 1 ps, this results in a classic TCSPC time span of 32 ns. If the time difference

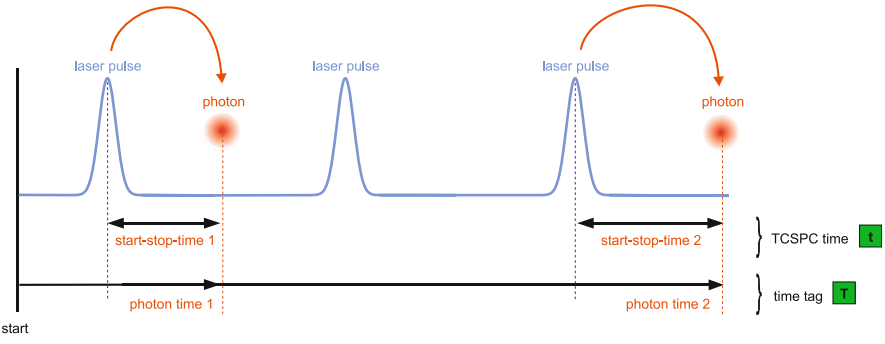

Fig. 4 Concept of time-tagged TCSPC in T3 mode

between the photon and the last sync event is larger, the photon event cannot be recorded. However, by choosing a suitable sync rate and a compatible resolution R, it is always possible to reasonably accommodate all relevant experiment scenarios. R can be chosen as the native resolution of the TDC (1 ps) or any larger resolution resulting from repeated multiplications by two.

Dead time in T3 mode is the same as in T2 mode (80 ns typ. for this particular instrument). Within each photon channel, autocorrelations can be calculated meaningfully only starting from lag times larger than the dead time, which is perfectly sufficient for classic FCS. Across channels, dead time does not affect the correlation so that meaningful results can be obtained at the full resolution, all the way down to zero lag time.

Exactly as in T2 mode, the event records are queued in a FIFO buffer so that no events will be dropped, except those lost in the dead time of the TDC anyhow. As in T2 mode, a sustained average count rate of 40 Mcps is possible. This total transfer rate must be shared by the detector channels; the rate of sync events does not matter. For all practically relevant photon detection applications, this throughput is more than sufficient.

For maximum throughput at data collection time and maximum flexibility at data analysis time, T3 mode data streams are normally written directly to disk. However, as outlined previously, Sect. 6 will show that it is possible to analyze incoming data "on the fly" for preview and immediate experiment optimization.

It should be noted that the HydraHarp 400 was chosen only for example here. There are other recent devices that provide T2 and T3 modes, e.g., with 25 ps resolution and 25 ns dead time in the form of a plug-in card for PCs with PCIe interface [12]. There are also hardware designs where the trade-off between resolution and dead time was pushed further toward shorter dead time, allowing effectively zero dead time at 1 ns resolution [30]. Most of the TAC-based electronics of Becker & Hickl GmbH are also supporting time-tagged TCSPC, although not supporting T2 mode and lacking independent input channels [6].

5 TCSPC Imaging and Multidimensional Techniques

Time-tagged TCSPC with multiple independent detector channels has the potential to be used for many interesting multidimensional techniques. For instance, different color filters can be used in front of multiple detectors to perform wavelength-dependent measurements. Similarly one can use differently oriented polarizers and perform polarization anisotropy measurements. Apart from the "data dimensions" created by additional detectors, other forms of dimensions can be explored by using the temporal patterns of photon arrival at different time scales as outlined in Sect. 3. Finally it is desirable to explore spatial dimensions and employ techniques such as fluorescence lifetime imaging.

When it comes to imaging a first thought is usually to use a camera. However, single-photon sensitivity together with large dynamic range, picosecond timing accuracy, and sufficient spatial resolution is currently hard, if not impossible to

achieve simultaneously with any kind of camera. Reasonable time resolutions can be achieved with time gating [31], but this causes losses of fluorescence photons. It is therefore quite adequate to try and use the well-established techniques of TCSPC with point detectors and simply scan across the area or volume of interest.

In order to capture the spatial origin of photons in the time-tagged scheme introduced in Sect. 4, an extended concept was invented as follows [32]. In addition to the detector inputs, the TCSPC hardware is augmented by a few extra "marker" inputs that can capture external events quite similar to photon events. A scan stage and associated controller that can emit TTL pulses at the beginning and/or end of a frame, a line, and/or a pixel is then chosen. The TTL pulses are fed to the "marker inputs" of the time-tagging electronics where they get captured as part of the stream of photon and laser events. As the scan has a well-defined temporal structure, each recorded photon can be precisely assigned to its pixel or voxel of origin, and thereby images of fluorescence intensity, fluorescence lifetime, polarization, and whatever else could be thought of can be reconstructed.

Since the position markers do not usually require extreme accuracy, the marker inputs do not require picosecond resolution and can be designed to be fairly simple. Typically the T3 mode is employed and the marker events are captured at the resolution of the time tags (usually corresponding to the sync rate). Figure 5 shows the event recording scheme of T3 mode extended for imaging with markers.

Based on this concept it was possible to build a very successful time-resolved confocal microscope for FLIM and single-molecule spectroscopy with sample scanning by a piezo stage [32]. Using the same core technology, it is also possible to upgrade commercial laser scanning microscopes with beam scanning for FLIM [33].

It should be noted that FLIM with time-tagged recording is hugely more flexible than immediate histogramming in the limited onboard memory of the TCSPC

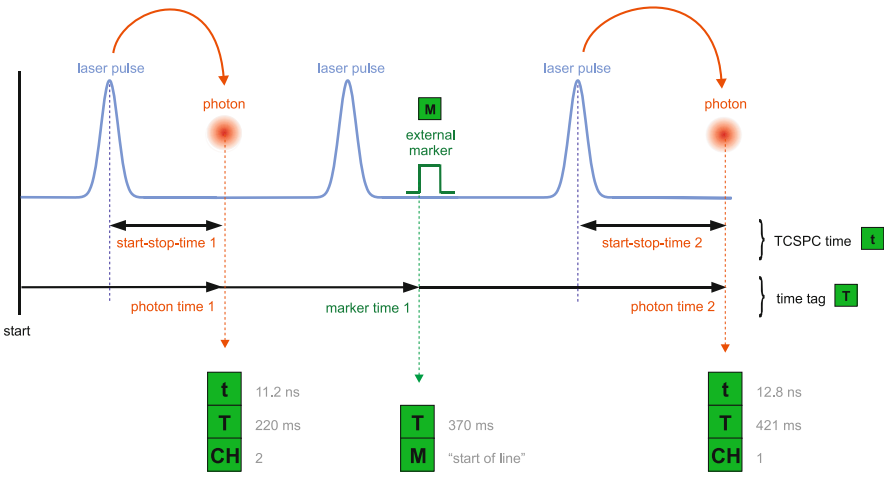

Fig. 5 Concept of time-tagged TCSPC in T3 mode extended with marker signals, e.g., for FLIM. The numbers next to square boxes represent examples

hardware. The latter suffers severe restrictions in image size and/or TCSPC histogram resolution and cannot be used for much more than FLIM or intensity imaging. With time tagging on modern PCs virtually, all memory restrictions are lifted, and with state-of-the-art TCSPC hardware interfacing via USB 3.0, throughput limitations are no longer an issue. Even real-time analysis and preview can be accomplished, as will be shown in the next section.

6 Real-Time Analysis of Time-Tagged TCSPC Data

The ability of an instrument to provide a real-time preview of the measurement results, or at least to give some information on the quality of the data, can be very important when experiments are complicated and lengthy or expensive to perform. Efforts to implement such real-time analysis and preview are therefore part of the R&D activities toward better TCSPC instrumentation in the sense of the "ideal instrument" outlined in Sect. 4. As the time-tagged photon event data is typically collected on PCs with ever-increasing speed, it comes naturally to use the PC's computing power and flexibility for real-time analysis and preview.

When time-tagged data is analyzed (be it in real time or off-line), it is necessary to first of all correct the time tags for overflows of the limited time span each record can carry. This is done by expanding the time tags in computer memory to a sufficiently large number of bits (typically 64) so that overflows can no longer occur. The incoming data stream must be parsed for overflow records, and the expanded time tags are incremented by the rollover constant (typically given by two to the power of time tag bits in the original record) each time such an overflow record is detected. The expanded data is what then can be used to perform application-specific real-time analysis or preview.

One first and obvious type of real-time preview is that of classical TCSPC, i.e., the histogram of start–stop time differences for fluorescence lifetime measurements. The data processing is in this case quite simple and does not require much processing power. When the data is collected in T2 mode, all that is required is the parsing of the data for an excitation (sync) event and then, for all subsequent photon events, calculating the time difference to the sync event, and this difference must be placed in a histogram. When the next sync event is found in the data stream, the process repeats.

If the data is recorded in T3 mode, TCSPC histogramming becomes even simpler, as the differences are readily delivered in the T3 records and overflow correction is not necessary. All that is required then is histogramming. This is in fact how classical TCSPC histogramming is implemented in a very recent TCSPC instrument [12]. While in the past it was common practice to implement TCSPC histogramming in hardware, it is now possible to rely on the speed of modern computers. In particular, when the bus speed is very high, as with PCI express, there is no risk of losing data due to the overhead of real-time processing.

Another relatively simple but useful type of preview is a trace of photon density over time. It is typically used to adjust the optics of a photon counting system for optimum focus, detector alignment, etc. In order to implement this type of real-time

analysis, one must count photon events over fixed intervals of time (typically a few ms each) and display the counts over time as a sliding window on the screen. In order to maintain proper synchronization, it is important to derive the boundaries of the integration bins from the time tags and not from the relatively asynchronous time base of the PC.

A much more challenging type of real-time analysis is required for FCS. Calculating the correlation function is computationally quite expensive. The correlation algorithm must therefore be implemented very efficiently. A first step toward doing so is to exploit the discrete nature of the photon events rather than trying to correlate density functions. In the simplest sense the correlation of a stream of photon event timings may be regarded (and actually be implemented) as histogramming of inter-photon time distances [34, 35]. This is relatively easy in off-line analysis because the data of all photon events are simultaneously available, even if they need to be retrieved from hard disk. In real-time processing of a time-tagged data stream, this is typically not the case because the data is just arriving and overflow correction still needs to be applied. In order to cover a long time span of lag times while keeping the computational load low, a multiple-tau scheme similar to that originally conceived for fast hardware correlators [36] is used. Furthermore, processing speed can significantly be improved if the data is kept in the CPU cache (as much as this is possible). A fast correlation algorithm that optimizes this is implemented in the operating software of PicoQuant's current TCSPC instruments [37].

When cross-correlations of independent detector channels are to be calculated in real time, it is crucial for throughput to receive the data as a single, temporally ordered data stream. This can only be achieved by appropriate hardware design [25]. If the hardware consists of individual streams of photon records arriving, e.g., from separate TCSPC plug-in cards in a PC, then the arrival of data at the software level is massively decorrelated due to unpredictable hardware and software delays influencing the individual streams. It is then necessary to realign the data in software which costs valuable CPU time. If the individual time-tagging electronics capturing the detector channels are not synchronized to the same crystal clock, the entire cross-channel analysis can be severely corrupted by relative clock drift.

An extended set of real-time analysis and preview methods for the instruments discussed in the foregoing sections is provided by a dedicated software package (SymPhoTime 64, PicoQuant). In addition to the methods mentioned so far, it provides preview for FLIM measurements. In order to achieve high throughput in real time, the software avoids full-fledged fitting of decay models. Instead, it employs a fast algorithm inspired by the idea that at least for mono-exponential decays and ideal instrument response, the fluorescence lifetime can be directly extracted from the barycenter of the decay [38, 39]. The implementation is briefly as follows: The arrival time of photons with respect to the excitation time (sync) is averaged within each image pixel. The photon arrival time for barycenter calculation can be taken with respect to the barycenter of the IRF (when available) or (as an approximation) with respect to the 50 %-point of the rising edge of the recorded decay. The advantage is that the time-tagged data does not need to be histogrammed for each pixel. The summation and averaging for the barycenter calculation can be

Table 1 Types of real-time preview and their throughput in a recent software package for collection and analysis of time-tagged TCSPC data in time-resolved fluorescence microscopy applications

Preview analysis type	Throughput limit
TCSPC histogramming (point)	Only TCSPC hardware limits
Intensity time trace (point)	Only TCSPC hardware limits
FCS correlations (point)	~1 Mcps
Fast FLIM (image)	~5 Mcps

updated as the photon records come streaming in and can be renormalized regularly as the averages improve or the display is updated.

For estimates of the real-time performance of the various preview types on a recent computer (Intel Core I7 2700k, 3.5GHz, 32 Gbyte RAM), consider Table 1. It shows the approximate photon rates up to which the preview can be used without disturbing sustained data collection to disk.

The implementation details permitting this kind of throughput in SymPhoTime are too complicated to be presented here in detail, but a few concepts should be outlined: a first key concept is a strict "zero copy" approach. This means that photon record data is never copied in memory. Only pointers to buffer memory are passed between the individual software layers, all the way down to the hardware driver. FIFO ring buffers in PC memory are used to deal with the inevitable unpredictability in the operating system's task switching. A second valuable concept is that of "pseudo-pixels." A pseudo-pixel is a virtual pixel that in the case of actual imaging corresponds to one or more image pixels or, in the case of single point time trace measurements, to one or more data points in a time trace. Each photon record is assigned to such a pseudo-pixel. The benefit is that real-time analysis can be performed by the same routines in each case and in the same way as in off-line analysis. For efficiency in repeated analysis, each pseudo-pixel carries a marker bit that signals whether the pixel has changed, i.e., if there were photons added. This is very valuable in fast scans with LSMs where usually only a few pixels actually change from one frame to the next. In off-line analysis it has the benefit that different types of analysis can be performed in sequence without having to re-parse the entire stream of photon records.

Finally it should of course be mentioned that the software makes use of the multiple processor cores modern CPUs provide. This is achieved by a multi-threaded design. One thread handles time-critical hardware handling, a second thread handles the graphical user interface, and a variable number of further threads are used to perform the processing of multiple pseudo-pixels in real time.

7 Outlook

TDC-based TCSPC electronics are likely to benefit from the ongoing improvements in high-speed integrated circuit technology. Particularly the SiGe technology used in present instruments is currently making rapid progress toward smaller structures,

lower power consumption, and higher speed. For the near future time resolutions down to 10 ps can be expected with SiGe TDCs that will probably consume even less power than now. Similarly, TDCs in CMOS technology are going to improve in throughput so that they may reach performance levels of faster technologies while taking advantage of low-cost production and low-power consumption.

Furthermore, time-tagged TCSPC electronics will benefit from the progress in FPGA technology. This will provide higher throughput and permit more parallel channels. The direct implementation of TDC structures in FPGA (which is already possible now) will quite likely reach levels of performance that can be used for some applications where cost savings are more important than ultimate time resolution and DNL.

At the data analysis side, the trend toward parallelization in microprocessor architectures can be used to speed up real-time processing. Faster PCs with more cores and improved vector processing units will therefore lead to immediate performance gain.

Given the flexibility of time-tagged photon data collection, it can be expected that new ideas for experiments and analysis algorithms will quickly be implemented on such platforms as soon as they emerge.

References

1. Bollinger LM, Thomas GE (1961) Measurement of the time dependence of scintillation intensity by a delayed coincidence method. Rev Sci Instrum 32:1044–1050
2. Connor DVO, Phillips D (1984) Time-correlated single photon counting. Academic Press, London
3. Lakowicz JR (2006) Principles of fluorescence spectroscopy, 3rd edn. Springer Science + Business Media, New York
4. Bülter A (2014) Single-photon counting detectors for the visible range between 300 nm and 1000 nm. In: Kapusta P et al. (eds) Advanced photon counting: applications, methods, instrumentation. Springer series on fluorescence. Springer International Publishing, doi: 10.1007/4243_2014_63
5. Buller GS, Collins RJ (2014) Single-photon detectors for infrared wavelengths in the range 1 to 1.7 μm. In: Kapusta P et al. (eds) Advanced photon counting: applications, methods, instrumentation. Springer series on fluorescence. Springer International Publishing, doi: 10.1007/4243_2014_64
6. Becker W (2005) Advanced time-correlated single photon counting techniques. Springer, Berlin
7. Rossi B, Nereson N (1946) Experimental arrangement for the measurement of small time intervals between the discharges of Geiger-Müller counters. Rev Sci Instrum 17:65–71
8. Kalisz J (2004) Review of methods for time interval measurements with picosecond resolution. Metrologia 41:17–32
9. Roberts GW, Ali-Bakhshian M (2010) A brief introduction to time-to-digital and digital-to-time converters. IEEE Transact Circ Syst II Expr Briefs 57:153–157
10. Henzler S (2010) Time-to-digital converters. Springer, Dordrecht/Heidelberg/London/New York
11. Heinemann B et al. (2010) SiGe HBT technology with fT/fmax of 300 GHz/500 GHz and 2.0 ps CML gate delay. Technical digest, IEEE international electron device meeting (IEDM), San Francisco, 06–08 Dec 2010, pp 688–691

12. Wahl M, Röhlicke T, Rahn HJ, Erdmann R, Kell G, Ahlrichs A, Kernbach M, Schell AW, Benson O (2013) Integrated multichannel photon timing instrument with very short dead time and high throughput. Rev Sci Instrum 084:043102
13. Elson E, Magde D (1974) Fluorescence correlation spectroscopy. I conceptual basis and theory. Biopolymers 13:1–27
14. Thompson NL, Lieto AM, Allen NW (2002) Recent advances in fluorescence correlation spectroscopy. Curr Opin Struc Biol 12:634–641
15. Dertinger T, Rüttinger S (2014) Advanced FCS: an introduction to fluorescence lifetime correlation spectroscopy and dual-focus FCS. In: Kapusta P et al. (eds) Advanced photon counting: applications, methods, instrumentation. Springer series on fluorescence. Springer International Publishing, doi: 10.1007/4243_2014_72
16. Böhmer M, Wahl M, Rahn HJ, Erdmann R, Enderlein J (2002) Time-resolved fluorescence correlation spectroscopy. Chem Phys Lett 353:439–445
17. Enderlein J, Gregor I (2005) Using fluorescence lifetime for discriminating detector after-pulsing in fluorescence-correlation spectroscopy. Rev Sci Instrum 76:033102
18. Felekyan S, Kalinin S, Valeri A, Seidel CAM (2009) Filtered FCS and species cross correlation function. In: Periasamy A, So PTC (eds) Multiphoton microscopy in the biomedical sciences IX; Proceedings of SPIE 7183:71830D:1–71830D:12
19. Felekyan S, Kalinin S, Sanabria H, Valeri A, Seidel CAM (2012) Filtered FCS: species auto- and cross-correlation functions highlight binding and dynamics in biomolecules. Chem Phys Chem 13:1036–1053
20. Eggeling C, Berger S, Brand L, Fries JR, Schaffer J, Volkmer A, Seidel CAM (2001) Data registration and selective single-molecule analysis using multi-parameter fluorescence detection. J Biotechnol 86:163–180
21. Ishii K, Tahara T (2010) Resolving inhomogeneity using lifetime-weighted fluorescence correlation spectroscopy. J Phys Chem B 114:12383–12391
22. Ishii K, Tahara T (2013) Two-dimensional fluorescence lifetime correlation spectroscopy. J Phys Chem B 117:11414–11432
23. Otosu T, Tahara T (2014) Lifetime-weighted FCS and 2D FLCS: advanced application of time-tagged TCSPC. In: Kapusta P et al. (eds) Advanced photon counting: applications, methods, instrumentation. Springer series on fluorescence. Springer International Publishing, doi: 10.1007/4243_2014_65
24. Grußmayer KS, Herten D-P (2014) Photon Antibunching in Single Molecule Fluorescence Spectroscopy. In: Kapusta P et al. (eds) Advanced photon counting: applications, methods, instrumentation. Springer series on fluorescence. Springer International Publishing, doi: 10.1007/4243_2014_71
25. Wahl M, Rahn HJ, Röhlicke T, Kell G, Nettels D, Hillger F, Schuler B, Erdmann R (2008) Scalable time-correlated photon counting system with multiple independent input channels. Rev Sci Instrum 79:123113
26. Birch DSJ, McLoskey D, Sanderson A, Suhling K, Holmes AS (1994) Multiplexed time-correlated single-photon counting. J Fluoresc 04:91–102
27. Wahl M, Erdmann R, Lauritsen K, Rahn HJ (1998) Hardware solution for continuous time-resolved burst detection of single molecules in flow. Proc SPIE 3259:173–178
28. Wilkerson CW Jr, Goodwin PM, Ambrose WP, Martin JC, Keller RA (1993) Detection and lifetime measurement of single molecules in flowing sample streams by laser-induced fluorescence. Appl Phys Lett 062:2030–2033
29. Eggeling C, Fries JR, Brand L, Gunther R, Seidel CAM (1998) Monitoring conformational dynamics of a single molecule by selective fluorescence spectroscopy. Proc Natl Acad Sci U S A 95:1556–1561
30. Wahl M, Röhlicke T, Rahn HJ, Buschmann V, Bertone N, Kell G (2013) High speed multichannel time-correlated single photon counting electronics based on SiGe integrated time-to-digital converters. Proc SPIE 8727:87270W
31. LaVision GmbH (2014) Ultra-fast gated cameras. http://www.lavision.de/en/products/cameras/ultrafast_gated_cameras.php. Accessed 3 April 2014

32. Koberling F, Wahl M, Patting M, Rahn HJ, Kapusta P, Erdmann R (2003) Two channel fluorescence lifetime microscope with two colour laser excitation, single-molecule sensitivity and submicrometer resolution. Proc SPIE 5143:181–192
33. Ortmann U, Dertinger T, Wahl M, Rahn HJ, Patting M, Erdmann R (2004) Compact TCSPC upgrade package for laser scanning microscopes based on 375 to 470 nm picosecond diode lasers. Proc SPIE 5325:179–186
34. Li LQ, Davis LM (1995) Rapid and efficient detection of single chromophore molecules in aqueous solution. Appl Opt 34(18):3208–3217
35. Davis LM, Williams PE, Ball DA, Swift KM, Matayoshi ED (2003) Data reduction methods for application of fluorescence correlation spectroscopy to pharmaceutical drug discovery. Curr Pharm Biotechnol 04:451–462
36. Schätzel K (1985) New concepts in correlator design. In: Institute of Physics conference series, vol 77. Hilger, London, pp 175–184
37. Wahl M, Gregor I, Patting M, Enderlein J (2003) Fast calculation of fluorescence correlation data with asynchronous time-correlated single-photon counting. Opt Express 11:03583–03591
38. Yang H, Xie XS (2002) Probing single molecule dynamics photon by photon. J Chem Phys 117:10965–10979
39. Yang H, Luo G, Karnchanaphanurach P, Louie TM, Rech I, Cova S, Xun L, Xie XS (2003) Protein conformational dynamics probed by single-molecule electron transfer. Science 302(5643):262–266

Single-Photon Counting Detectors for the Visible Range Between 300 and 1,000 nm

Andreas Bülter

Abstract Single-photon counting in the visible spectral range has become a standard method for many applications today, ranging from fluorescence spectroscopy to single-molecule detection and quantum optics. One of the key components for every setup is single-photon sensitive detectors. Unfortunately a detector with "ultimate" features, i.e., high detection efficiency at a large wavelength range, high temporal resolution, and low dark counts, does not exist. For most of the applications, it is therefore necessary to choose a detector based on the most crucial parameters for the targeted application.

This chapter provides an overview about the typically used single-pixel detectors for photon counting in the visible range. It provides information about the key parameters such as detection efficiency, dark counts and timing resolution that principally allow to choose the best suited detector for a targeted application.

Keywords Hybrid-PMT · MCP · PMT · Single photon · SPAD

Contents

1 General Introduction 24
2 Photomultiplier Tubes (PMTs) 25
2.1 General Description 25
2.2 Detection Efficiency 27
2.3 Dark Counts and Afterpulsing 28
2.4 Timing Resolution 29
2.5 Geometrical Factors 30
3 Microchannel Plate Photomultipliers Tubes (MCP-PMT or MCP) 30
3.1 General Description 30
3.2 Detection Efficiency 31

A. Bülter (✉)
Instrumentation Division, PicoQuant GmbH, Rudower Chaussee 29, 12489 Berlin, Germany
e-mail: buelter@picoquant.com

P. Kapusta et al. (eds.), *Advanced Photon Counting: Applications, Methods, Instrumentation*, Springer Ser Fluoresc (2015) 15: 23–42, DOI 10.1007/4243_2014_63,

3.3 Dark Counts and Afterpulsing 32
3.4 Timing Resolution 32
3.5 Geometrical Factors 32
4 Hybrid PMTs 32
4.1 General Description 32
4.2 Detection Efficiency 33
4.3 Dark Counts and Afterpulsing 33
4.4 Timing Resolution 34
4.5 Geometrical Factors 34
5 Single-Photon Avalanche Diodes (SPAD) 35
5.1 General Description 35
5.2 Detection Efficiency 37
5.3 Dark Counts and Afterpulsing 38
5.4 Timing Resolution 38
5.5 Geometrical Factors 40
6 Summary 40
References 41

1 General Introduction

Detectors are core components in every setup based on photon counting. For the spectral range between approx. 300 and 1,000 nm, there are essentially two detector classes available: detectors based on the external photoelectric effect such as photomultiplier tubes, microchannel plate photomultipliers, or hybrid photomultiplier tubes or detectors based on the internal photoelectric effect such as single-photon avalanche diodes. When comparing detectors in order to find the most suited model for the targeted application, there are five key parameters that must be considered:

1. Sensitivity – no detector covers the complete spectral range from 300 to 1,000 nm with a uniform sensitivity. It is therefore necessary to look at the sensitivity of each detector at the targeted detection wavelength (range). The sensitivity is usually expressed as a "quantum efficiency" or "detection efficiency," given in percent. This value essentially corresponds to the probability that a photon is converted into a measurable electrical pulse.
2. Dark counts – dark counts refer to output pulses generated "inside" the detector in the absence of light. Dark counts are emitted at random times and expressed in counts per second (cps). They add a baseline (or offset) to all photon counting measurements and cannot be avoided or removed. It is therefore advisable to choose a detector with a dark count rate much lower than the expected signal rate. Otherwise the effective usable signal count rate might be reduced due to a competition between dark counts and "real" photon counts.
3. Afterpulsing – afterpulsing refers to additional, artificial output signals that are not related to a photon detection event but correlated to a previous detection event. In time-resolved measurements, afterpulses are visible as additional signal peaks at a defined temporal spacing to the main signal. Afterpulses are

generated "inside" the detector and cannot be avoided or removed. Afterpulsing is usually expressed as a percentage that expresses the probability that one detected photon creates an afterpulsing event. In many applications afterpulsing is not a big problem as it can be treated (or ignored) in the data analysis or by using a suited optical setup (e.g., by using two detectors for a cross-correlation analysis). Nonetheless, an afterpulsing probability as low as possible is recommended to minimize the efforts necessary to correct for this effect.

4. Timing resolution – for time-resolved applications, the internal temporal resolution (the "jitter") of the detector is a crucial parameter. The better the timing resolution, i.e., the lower the full width at half maximum (FHWM) of the detector response, the better the overall temporal resolution of the complete setup. Note that this is not the width of the electrical output pulses but the histogram of time differences between photon arrival and electrical output.
5. Size of the active area – this is a geometrical factor that needs to be considered when designing the optical setup. Detectors based on the external photoelectric effect usually have active areas of several mm, whereas detectors based on the internal photoelectric effect only have active areas in the range between 20 and 200 μm. In the latter case, the optical setup must be designed in way that allows to couple the collected light from the sample effectively on the small active area (e.g., by means of optical fibers or using a confocal setup)

In the following sections, the currently commercially available and typically used detector types for the visible range (photomultiplier tubes, microchannel plate photomultiplier tubes, hybrid photomultiplier tubes, and single-photon avalanche diodes) will be described and discussed with respect to these five key parameters. Other detectors which are also suited for photon counting in the visible range such as superconducting nanowires or transition edge sensors are covered in more detail in the next chapter as they are typically used for photon counting in the infrared.

2 Photomultiplier Tubes (PMTs)

2.1 General Description

Photomultiplier tubes (PMTs) are the most established detectors for single-photon counting. The first PMT was already demonstrated in the mid-1930s, after intensive studies of the photoelectric effect and secondary emission multipliers (dynodes) [1].

A PMT is basically a vacuum tube that includes three core components (see Fig. 1):

1. A photocathode in which photons are converted to electrons by the photoelectric effect and emitted into the vacuum. Depending on the material of the photocathode, PMTs can be effective for detection of light at varying wavelengths.

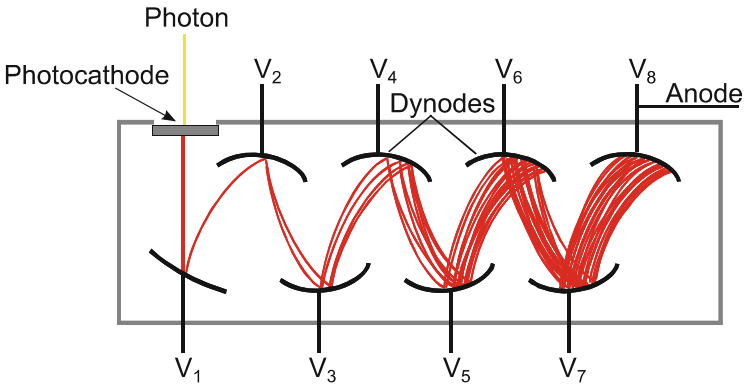

Fig. 1 Basic principle of a photomultiplier tube. Photons are converted to electrons by the photoelectric effect. The electrons are multiplied in a dynode chain and finally collected by an anode to provide an electrical output signal

The most common photocathodes for the visible spectral range are of bialkali, multialkali, GaAs, or GaAsP type.

2. A dynode stage where the electrons are multiplied by means of secondary electron emission. There are a variety of dynode types available, and each type exhibits different gain, time response, uniformity, and secondary electron collection efficiency depending on the structure and the number of stages. Briefly, once an electron is emitted from the photocathode, it is accelerated toward the first positively charged dynode. The electron collides with the dynode and releases further electrons, which are then accelerated toward the next dynode, where they collide and release even more electrons. Each successive dynode in the PMT is charged to a higher positive potential than the preceding one, which thus results in an amplification as the increasing number of electrons collide with later dynodes. The amplification of electrons is very effective and typically leads to multiplication factors in the range of 10^6–10^7.
3. An anode, which collects the multiplied secondary electrons emitted from the last dynode.

The dynode stages typically require operating voltages in the order of 1 kV. This, along with the necessary design of the multiple dynode stages, made PMTs rather large and bulky detectors in the past. In the recent years, however, PMTs have been successfully miniaturized and are now available as small compact units that even include the necessary high-voltage power supply [2, 3]).

Over a certain range of light intensity, PMTs are analog devices, i.e., they output a current, which is proportional to the light level on the photocathode. At high light intensity, the output pulses of individually amplified photoelectrons overlap and can no longer be detected as individual pulses. Due to the varying pulse amplitude and pulse width as well as the underlying Poisson statistics, it is very difficult to define an upper count rate limit where this happens. Only at very low light intensities the PMT

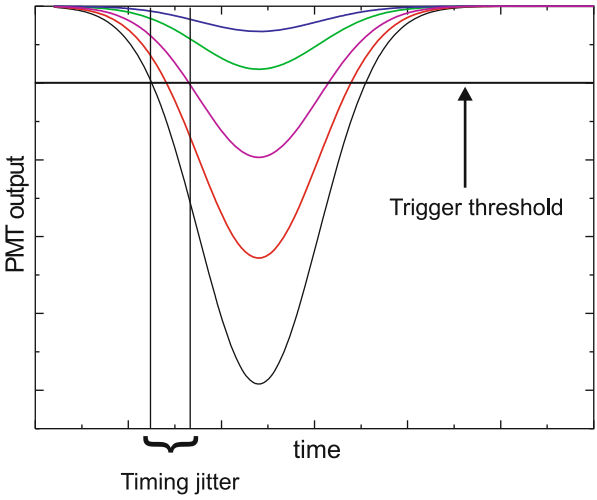

Fig. 2 PMT output pulses show fluctuating pulse amplitudes due to fluctuations in the amplification process of the dynodes. Combined with a simple level trigger threshold, this leads to a timing jitter in time-resolved measurements

outputs individual, well-separated pulses that can be amplified and further processed by photon counting electronics.

The output pulses of a PMT never show a constant amplitude due to fluctuations in the amplification process of the dynodes. These fluctuations will effectively lead to a timing jitter of the order of the pulse rise time in time-resolved measurements, unless the PMT is connected through a constant fraction discriminator to the photon counting electronics (see Fig. 2).

2.2 Detection Efficiency

The detection efficiency of a PMT is determined by the photocathode material (see Fig. 3). Bialkali types are sensitive in the range between approx. 230 and 700 nm. They are most efficient at wavelengths below 500 nm, where they can reach detection efficiencies up to 40 % ("ultra-bialkali"). PMTs based on multialkali photocathodes generally cover larger spectral ranges from approx. 230 to 920 nm but have a lower detection efficiency that reaches values around 15 % between 400 and 700 nm. PMTs based on GaAs and GaAsP photocathodes are sensitive in the spectral range between 300 and 890 nm. Compared to multialkali photocathodes, the GaAsP features a higher detection efficiency reaching up to 40 % at 600 nm.

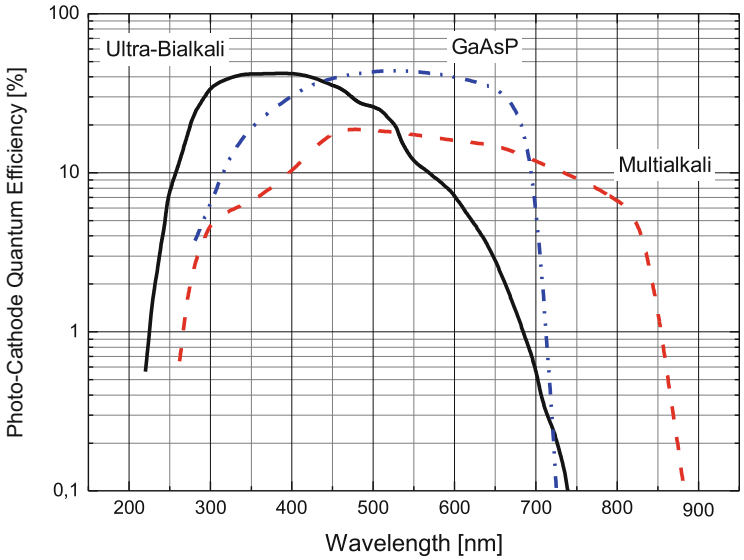

Fig. 3 The detection efficiency of a PMT is determined by the photocathode material. The plot shows typical examples for bialkali [3], multialkali [3], and GaAsP [2] photocathodes

2.3 Dark Counts and Afterpulsing

Dark counts or dark current of a PMT refers to a small amount of current flow even when operated in a completely dark state. The most prominent cause of dark current in a PMT is thermionic emission current from the photocathode or the dynodes [1]. The magnitude of this effect depends on the photocathode material as well as on the temperature. Bialkali photocathodes generally show a much lower thermionic emission than multialkali, GaAs, or GaAsP photocathodes and therefore have correspondingly low dark counts. Typical values are less than 50 cps for bialkali PMTs and can be as high as 10,000 cps for multialkali PMTs. The amount of thermionic emission can be strongly reduced by lowering the operation temperature, which is the reason why especially multialkali, GaAs, or GaAsP PMTs are usually operated in a Peltier-cooled housing. When cooled, the dark counts of these detectors reach values around 1,000 cps, which is small compared to typical count rates in photon counting setups of 10^5 cps.

Afterpulsing in PMTs is visible by additional peaks several nanoseconds after the main pulse (see Fig. 4). This afterpulsing signal is mainly caused by positive ions which are generated by the ionization of residual gases in the PMT [1]. These positive ions return to the photocathode and produce additional photoelectrons, resulting in afterpulsing. The influence of afterpulsing in PMTs can be strongly reduced by a constant, strong illumination (e.g., 48 h at 3×10^6 cps). This strong illumination essentially ionizes most of the residual gases that get trapped at the

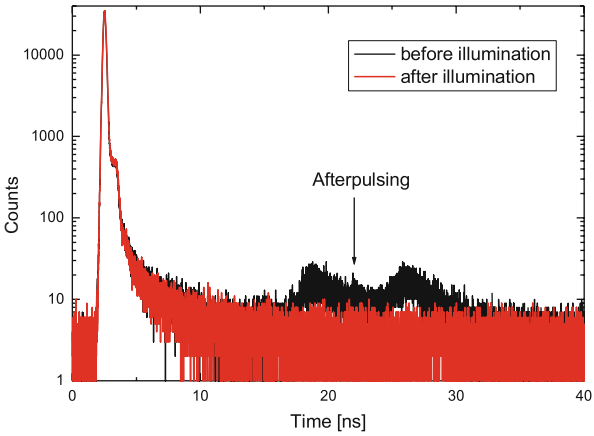

Fig. 4 Afterpulsing in PMTs is visible in the timing response profiles by additional peaks several nanoseconds after the main pulse. The influence of afterpulsing can be strongly reduced by a constant, intense illumination

photocathode. However, once the PMT is switched off, some gases diffuse back into the photomultiplier tube. As a consequence, afterpulsing can again be visible if a PMT has not been used for longer times.

A second common feature of the timing response profile of a PMT is an additional peak a few nanoseconds after the main peak with an amplitude around 2 orders of magnitude lower (see Fig. 4). This peak is caused by elastic scattering of the photoelectrons from the first dynode [1]. It is usually no problem in photon counting experiments due to its low amplitude and because it is independent from the detection wavelength and can therefore be treated in the data analysis procedure.

2.4 Timing Resolution

The timing resolution of a PMT in a photon counting setup is determined by the so-called transit time spread (TTS). The TTS is a measure of the different transit times of the photoelectrons on their way from the photocathode through the dynodes. The major source of the different transit times is the photocathode. As the photoelectrons are emitted at the photocathode at random locations, with random velocities, and in random directions, the time they need to reach the first dynode is slightly different for each photoelectron. This finally leads to different transit times for each photoelectron, which is measurable as the FWHM of the timing response. Modern, compact PMTs based on bialkali or multialkali photocathodes reach TTS values around 140 ps (FWHM) (see Fig. 4), whereas GaAsP PMTs usually have a higher TTS around 200–350 ps (FWHM) [2].

2.5 Geometrical Factors

The active area of a PMT is determined by the size of the photocathode. Typical values are between 5 and 8 mm in diameter. This large active area makes the PMT suitable for more or less all optical setups used in photon counting experiments. PMTs are typically used in setups where the light is collected from a larger volume, such as mm-sized cuvettes in fluorescence spectrometers or tissue surface in diffuse optical imaging (see Grosenick [4]). For similar reasons PMTs are also ideal detectors for confocal scanning microscopes in a non-descanned detection scheme. As the dark count rate is roughly proportional to the active area of the detector, it might be advisable especially for GaAs and GaAsP cathodes to check if PMTs with a smaller active area are available.

3 Microchannel Plate Photomultipliers Tubes (MCP-PMT or MCP)

3.1 General Description

Microchannel plate photomultiplier tubes (MCP) can be considered as a 2-dimensional array of devices that work at similar principles like the PMT [1]. An MCP is assembled from a large number of glass capillaries (channels) with an internal diameter between approx. 6 and 20 μm. The inner wall of these capillaries is coated with a photoemissive material and biased at each end, so that it acts as a continuous dynode. When a primary photoelectron impinges on the inner wall of a channel, secondary electrons are emitted, which again collide with the inner wall to release even more electrons, resulting an exponential multiplication of the electron flux (see Fig. 5). MCPs require rather high operating voltages on the order of 3 kV. Their gain is, however, lower than that of conventional PMTs. MCPs can easily be damaged by overload, which is why the

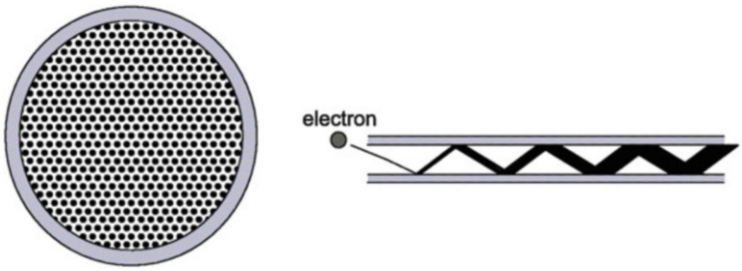

Fig. 5 Schematic structure of an MCP. An MCP is assembled from a large number of glass capillaries (channels), whose inner wall is coated with a photoemissive material and biased at each end, so that it acts as a continuous dynode. Photoelectron impinges on the inner wall of a channel lead to emission of secondary electrons, resulting an exponential multiplication of the electron flux

manufacturers usually suggest to limit the maximum count rate to less than 20,000 cps [5]. It is, however, still possible to use MCPs at higher count rates up to, e.g., 200,000 cps, but it is then recommend to illuminate the full active area of the detector and not to focus the light to a few channels only. Otherwise, since each channel needs a certain time (µs to ms) to be recharged, the count rate the device can deliver is limited by channel saturation.

A second problem is the limited lifetime when used at high count rate, due to degradation of the microchannels under the influence of the flux of electrons. Similar to PMTs, the output pulse of an MCP has fluctuating pulse heights and therefore needs to be connected through a constant fraction discriminator for time-resolved photon counting measurements.

3.2 *Detection Efficiency*

MCPs essentially use the same cathode material as PMTs, i.e., they are available based on standard bialkali, multialkali, GaAs, or GaAsP photocathodes (see Fig. 6). The different cathodes cover spectral ranges from approx. 160 to 910 nm with detection efficiencies reaching 15 % at 400 nm for bialkali and multialkali photocathodes, which is lower than for conventional PMTs. MCPs based on GaAsP photocathodes reach up 40 % efficiency around 500 nm [5, 6].

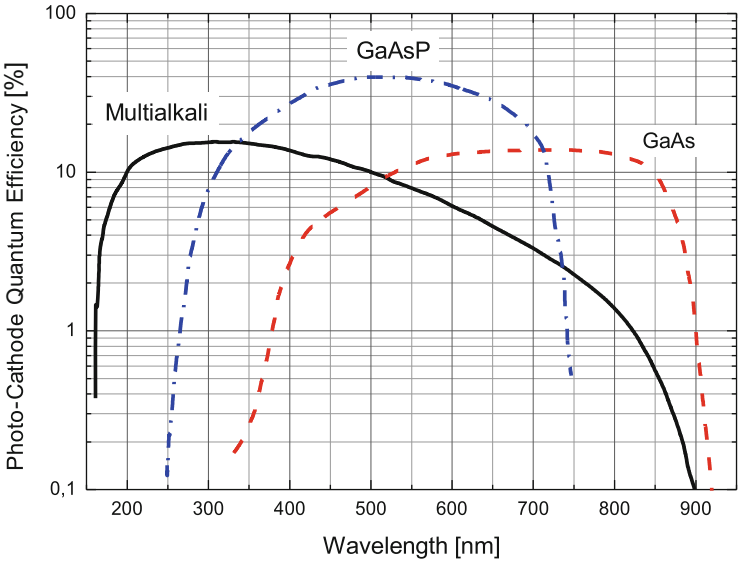

Fig. 6 The detection efficiency of an MCP is determined by the photocathode material. The plot shows typical examples for multialkali [4], GaAsP, and GaAs [5] photocathodes

3.3 Dark Counts and Afterpulsing

The dark counts of MCPs are similar to conventional PMTs. Typical values are less than 50 cps for bialkali MCPs and can be as high as 10,000 cps for multialkali or GaAsP MCPs. When cooled, the dark counts of these detectors usually reach values around 1,000 cps, which is, however, still low compared to typical count rates in photon counting setups of 10^5 cps. Afterpulsing is usually not observed in MCPs.

3.4 Timing Resolution

Due to the small diameter of the glass capillaries of only a few micrometers and the resulting low transit time spread, MCPs have a very good timing resolution that can reach values down to 25 ps (FWHM) for the bialkali or multialkali types and less than 150 ps (FWHM) for the GaAs and down to 60 ps (FWHM) for the GaAsP photocathodes. MCPs are therefore the detectors of choice for applications that require a very high temporal resolution.

3.5 Geometrical Factors

The active area of an MCP is determined by the size of the photocathode. Typical values are around 10 mm in diameter, which is even larger than conventional PMTs. This large active area makes the MCP therefore suitable for more or less all optical setups used in photon counting experiments. Their inherent problem with saturation and damage by overload is, however, limiting their usage. Consequently, MCPs are typically used in setups that allow the precise control of signal intensity, e.g., in fluorescence lifetime spectrometers. In scanning microscopy or other setups that have a strongly fluctuating signal rate, MCPs are usually not chosen.

4 Hybrid PMTs

4.1 General Description

A hybrid PMT is a photomultiplier tube that incorporates a silicon avalanche photodiode in an evacuated electron tube. When light strikes the photocathode, photoelectrons are emitted and then accelerated by a high-intensity electric field of a few kilovolts applied to the photocathode. The photoelectrons are then “bombarded” onto the silicon avalanche photodiode where they create electron-hole pairs according to the energy of the photoelectron (see Fig. 7). These carriers are then further amplified

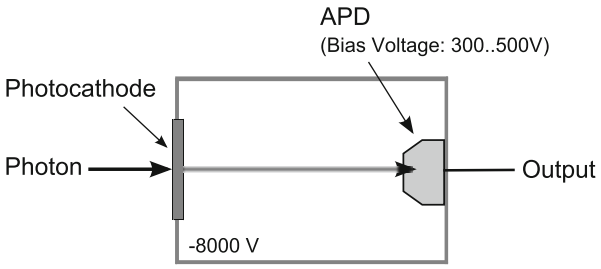

Fig. 7 Schematic of a hybrid PMT. When light hits the photocathode, photoelectrons are emitted and then "bombarded" onto the silicon avalanche photodiode (APD)

by the linear gain of the avalanche diode. The total gain of a hybrid PMT is on the order of 10^5 and thus lower than the gain of PMTs or MCPs but still large enough to be combined with suited preamplifiers for photon counting applications. Similar to PMTs, the output pulse of a hybrid PMT has fluctuating pulse heights and therefore needs to be connected through a constant fraction discriminator for time-resolved photon counting measurements.

Bare hybrid PMTs are not easy to handle as they require an operating voltage of 8 kV and an extremely good shielding and low-noise amplification to deal with the small amplitude of the single-photon pulses [7]. They also require a carefully designed integrated cooling system that controls the temperature of the APD to avoid fluctuations in the gain and dark counts. Nonetheless, complete detector modules based on the hybrid PMT are available today [8] that integrate the necessary high-voltage power supply, temperature stabilization, and preamplification.

4.2 Detection Efficiency

Hybrid PMTs essentially use the same cathode material as PMTs and are currently available based on bialkali, GaAs, or GaAsP photocathodes. The different cathodes cover spectral ranges from approx. 220 to 890 nm with detection efficiencies reaching up 30 % efficiency around 400 nm for the bialkali cathodes and even up to 40 % at 500 nm for the GaAsP cathodes [7, 8] (see Fig. 8).

4.3 Dark Counts and Afterpulsing

The dark counts of hybrid PMTs are similar to conventional PMTs. Typical values range from less than 100 cps for bialkali hybrid PMTs to approx. 1,000 cps for GaAs or GaAsP photocathodes.

One of the most striking features of the hybrid PMT is the virtual absence of afterpulsing. Afterpulsing in single-photon detectors is usually due to two reasons – either, as in PMTs, caused by ionization of residual gas molecules by the electrons traveling through the dynode system or, as in single-photon avalanche diodes,

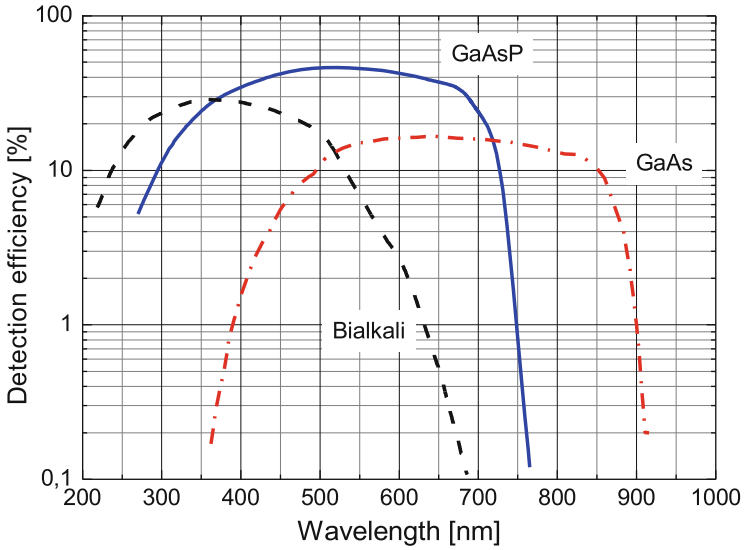

Fig. 8 The detection efficiency of a hybrid PMT is determined by the photocathode material. The plot shows typical examples for multialkali GaAs and GaAsP photocathodes [7, 8]

resulting from trapped carriers of the previous avalanche breakdown. Both causes have no influence in hybrid PMTs because only single electrons are traveling in the vacuum and because the APD works in linear mode, which causes no avalanche breakdown.

4.4 Timing Resolution

The high acceleration of the photoelectrons by the 8 kV acceleration voltage leads to a very low transit time spread. Hybrid PMTs therefore generally feature a very good timing resolution that can be as fast as 50 ps (FWHM) for the bialkali types and $<$120 ps (FWHM) or $<$160 ps (FWHM) for the GaAsP and GaAs photocathode types. Moreover, the timing response of a hybrid PMT is very clean, without significant tails, bumps, or secondary peaks.

4.5 Geometrical Factors

The active area of a hybrid PMT is determined by the size of the photocathode. Typical values are between 3 and 5 mm in diameter. This large active area makes the hybrid PMT suitable for more or less all optical setups used in photon counting experiments. Due to their fast timing response, the good detection efficiency and the

absence of afterpulsing, hybrid PMTs are now becoming the "standard" detector for many photon counting experiments, ranging from classical spectroscopy on bulk material to imaging and correlation spectroscopy in microscopy applications [9].

5 Single-Photon Avalanche Diodes (SPAD)

5.1 General Description

In contrast to photomultiplier tubes, which are based on the external photoelectric effect, i.e., the generation of photoelectrons through a photocathode, avalanche photodiodes are based on the internal photoelectric effect, i.e., the generation of photoelectrons inside the device. An avalanche photodiode is a device formed by a junction between a semiconductor with an excess of holes (p-type) and a semiconductor with an excess of carriers (n-type). Diffusion at the junction leads to a region depleted of free carriers. When a voltage is applied so that the n-type semiconductor is at a higher potential than the p-type semiconductor, the junction is said to be reverse biased, creating an effective voltage gradient in the semiconductor. A drifting electron created, e.g., by the absorption of a single photon, is accelerated along the gradient and can gain enough kinetic energy to knock an electron out of its bound state on collision with an atom. This electron is then again accelerated in the electric field and can also create additional free electrons by collision with atoms, resulting finally in an avalanche of carriers. If the applied electric field across the device is sufficiently high, above the so-called breakdown voltage, single-photon-generated carriers can trigger a self-sustaining avalanche. When operated in this so-called "Geiger" mode, the device is called a single-photon avalanche diode (SPAD) [10].

The avalanche leads to a rise of the current to a macroscopic constant level within less than a nanosecond, which can then be easily detected by suited electronics. If the primary carrier is photogenerated, the leading edge of the avalanche pulse marks the arrival time of the detected photon with picosecond time jitter. The avalanche current will keep flowing as long as the applied voltage is kept above the breakdown voltage. In this stage absorption of additional photons will not lead to any change in the signal output, making the device useless. It is therefore necessary to stop the self-sustained avalanche and reset the detector to be able to detect the next photon. This process of resetting is called "quenching" of the avalanche.

The process of quenching involves detecting of the leading edge of the avalanche, then generating a closely time-correlated electrical pulse that reduces the bias voltage below the breakdown level and finally restoring the voltage to the operating level above the breakdown voltage. There are essentially three principle realizations of quenching circuits for SPADs: passive, active, and gated quenching. The latter is only used for SPADs that are sensitive in the infrared (see Buller and Collins [11]).

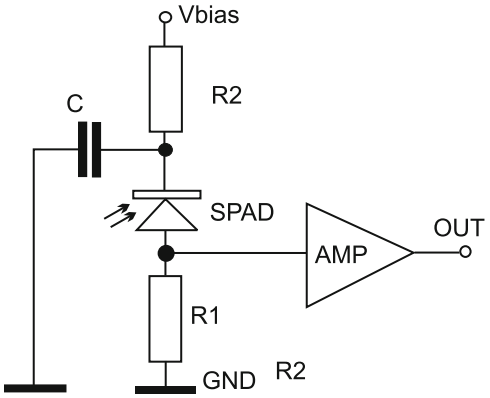

Fig. 9 In passive quenching, a high impedance resistor, connected in series to the SPAD, limits the current flow and effectively quenches the avalanche

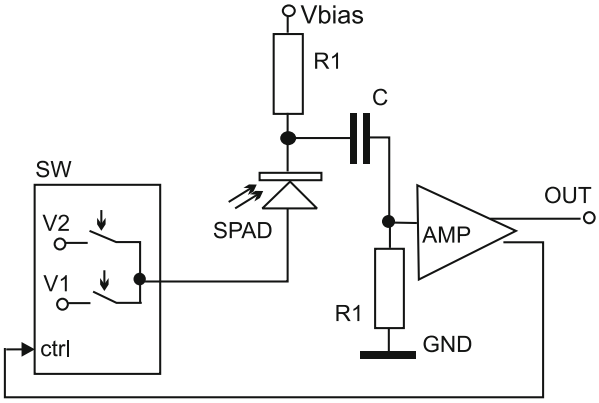

Fig. 10 In active quenching, the operation voltage is actively switched below the breakdown voltage, once the beginning of the avalanche has been detected by a dedicated sensing circuit. The operating voltage is then switched back above the breakdown voltage after a certain (dead) time

In passive quenching a high impedance resistor, connected in series to the SPAD, limits the current flow and effectively leads to the breakdown of the voltage at the diode and thus quenches the avalanche (see Fig. 9) [12]. An additional capacitor is usually included to generate a detectable output pulse. Passive quenching circuits have a slow recovery time (dead time) in the microsecond range in which no further photon detection events can be registered. This long dead time limits the maximum count rate to some hundred kHz. SPADs with passive quenching circuits are therefore usually not employed in current photon counting setups.

In active quenching, the operation voltage is actively switched below the breakdown voltage, once the beginning of the avalanche has been detected by a dedicated sensing circuit (see Fig. 10). This switching must happen within a few nanoseconds in order to avoid damage to the SPAD. The operation voltage is then kept below the breakdown voltage for a certain time in order to remove remaining carriers from the avalanche region. This process typically takes some tens of nanoseconds and

corresponds to the dead time of the SPAD. SPADs with active quenching therefore permit photon detection rates up to several MHz and are thus commonly used in photon counting setups today.

SPADs for the visible range are based on silicon. There are two main types of Si-SPADs architecture available today: thick [13–15] and thin-junction devices [16, 17]. The main difference between these two designs is the thickness of the depletion region in which photon absorption takes place. Thick-junction SPADs usually feature a depletion region of a few tens of µm, whereas thin-junction SPADs only have a few µm thickness.

5.2 *Detection Efficiency*

SPADs based on silicon can generally be used in the spectral range between 400 and 1,100 nm. Their detection efficiency varies not only with detection wavelength but also depends on the type of SPAD. Thin-junction SPADs typically have a lower detection efficiency than thick-junction devices, simply because the depletion region (absorption region) is smaller. Their maximum efficiency typically reaches values around 50 % in the blue/green spectral range around 500 nm falling to approx. 5 % at 1,000 nm. Thick devices on the other hand often reach detection efficiencies of more than 70 % in the red spectral range around 700 nm falling to approx. 15 % at 1,000 nm (see Fig. 11).

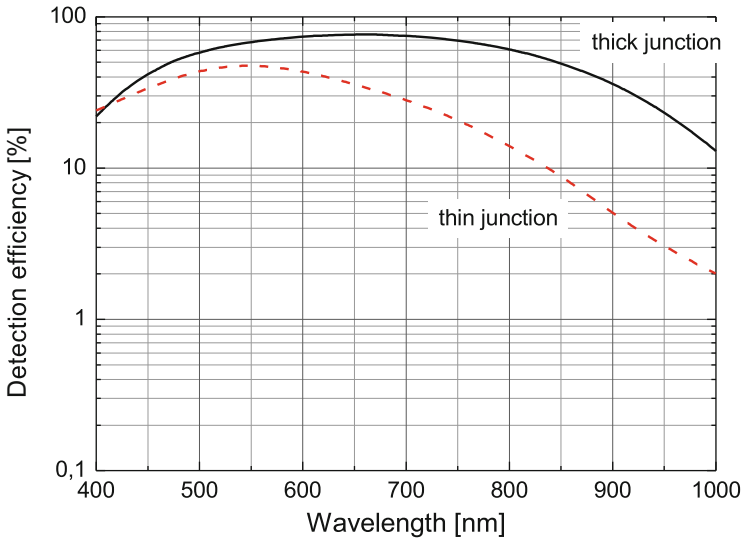

Fig. 11 Typical detection efficiency of a thick-junction SPAD [8] and a thin-junction SPAD [9]

5.3 Dark Counts and Afterpulsing

The dark count rate of an SPAD depends on the size of the active area as well as the chip temperature. Generally speaking, the dark count rate increases with size of the active area and decreases with the chip temperature. Typical values for a cooled device with 100 µm active area are <250 cps, whereas modules with 20 µm active area can reach <5 cps. Thick-junction cooled Si-SPADs usually have dark counts of <250 cps, but as the dark count rate strongly depends on the characteristics of the individual APD, it is also possible to get modules with <20 cps.

Afterpulsing is a common feature of SPADs, caused by impurities and crystal defects which act as "carrier traps." During each avalanche pulse, a few avalanche carriers can be trapped and are subsequently released after increasing the voltage again above the breakdown voltage. The released carriers can then re-trigger the avalanche, thereby generating correlated afterpulses [18]. The overall, measurable afterpulsing probability of a SPAD decreases exponentially after the quenching process. It can therefore be lowered by increasing the dead time of the SPAD, which, however, also reduces the maximum count rate of the device. Typical afterpulsing probabilities for commercially available (actively quenched) Si-SPADs are <1 % at dead times around 50–70 ns.

An often underestimated feature of SPADs is the so-called afterglow or breakdown flash [19]. This term describes the fact that Si-SPADs emit broadband light during the avalanche process. This light is emitted isotropically from the sensor and usually covers a spectral range between approx. 700 and 1,000 nm with varying intensities. Especially in coincidence correlation measurements using a Hanbury-Brown-Twiss (HBT) setup, the afterglow can lead to problems as the light emitted by one SPAD can be detected by the second SPAD. This results in a characteristic double-peak structure in the measurement result. Afterglow cannot be avoided. It is only possible to minimize the influence on the measurement data by, e.g., temporal delay and spectral or spatial filtering.

5.4 Timing Resolution

Thin-junction SPADs have been demonstrated to achieve timing resolutions down to 20 ps [20]. Mainstream commercial solutions feature timing resolutions down to 50 ps for wavelengths >500 nm. At lower detection wavelengths, the timing uncertainty increases and can reach values around 200–300 ps. This increase is caused by the SPAD structure – blue and UV light is not absorbed in the depletion region but near the silicon surface. The generated carriers therefore have to diffuse to the depletion region first to start the avalanche, which increases the timing jitter. The pulse shape of thin-junction SPADs is also very characteristic – it is a narrow peak with a small FHWM, followed by a long "diffusion tail" with much lower amplitude (see Fig. 12). The diffusion tail is due to carriers photogenerated in

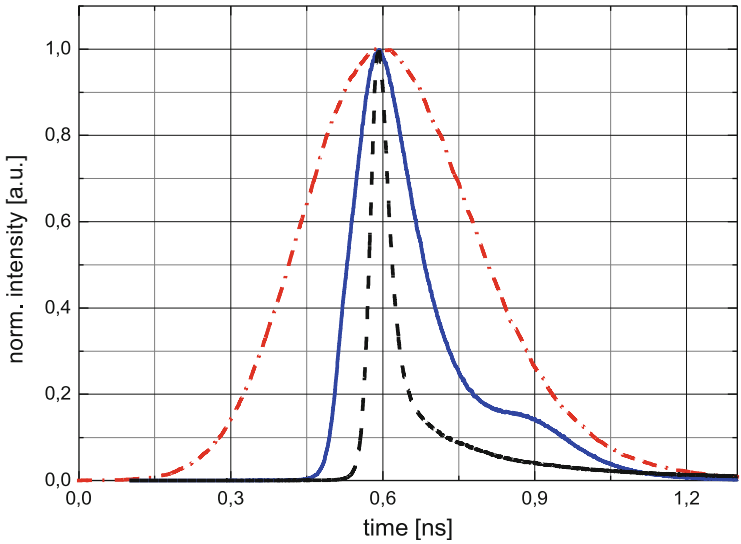

Fig. 12 Thin-junction SPADs have a wavelength-dependent timing response, which can be as fast as 50 ps for wavelengths >500 nm. Thick-junction SPADs do also show a dependence of the pulse profile from the detection wavelength, but the change is less pronounced. The plot shows the pulse profile of a thick-junction SPAD at 670 nm (*red*, *dash-dot*) and the response of thin-junction SPADs at 670 nm (*black*, *dotted*) and at 405 nm (*blue*, *solid*)

neutral regions near the depletion region that walk around by diffusion and eventually reach the edge of the depletion layer, where they are finally accelerated by the electric field. At 1/10th of the maximum, the FWHM of the tail can be as great as 20 times the value of the peak. The timing resolution of thin-junction SPADs is usually not dependent on the signal rate.

Thick-junction devices generally exhibit a timing resolution between 300 and 800 ps. The best timing resolution is obtained in the red spectral range above 600 nm and signal rates below 10^6 cps. At higher signal rates, the temporal response width of the thick-junction SPAD increases and can, in the worst case, reach twice the value at low signal rates. In early commercial products, this rate dependency has to some extent been due to the readout electronics and was reduced in more recent designs [14].

The wavelength-dependent timing resolution of SPADs, the so-called color shift, can be a problem in, e.g., fluorescence lifetime-based applications, where it is often necessary to use reconvolution techniques in the analysis to correct for the finite resolution of the measurement instrument [21]. This resolution includes the influence from the detector and consequently depends on the wavelength due to the color shift of the detector. It would therefore be necessary to characterize the so-called instrument response function (IRF) of a setup at the same wavelength as the fluorescence. This can be realized by, e.g., using samples with ultrafast fluorescence decays in the same spectral range as the analyzed sample instead of the typically employed scattering media recorded at the excitation wavelength.

5.5 *Geometrical Factors*

The active area of an SPAD is much smaller than that of a PMT. Commercial thick-junction SPADs usually have active areas in the order of 150 µm, whereas thin-junction SPADs currently have active areas between 20 and 100 µm. This small active area requires a suited optical setup that allows to focus the collected fluorescence on the active area. Over-illumination of the active area will lead to signal loss and, in case of thick-junction SPADs, also to a decrease of the overall detection efficiency and timing resolution. SPADs are therefore usually used along with confocal microscope setup or in all-fiber setups. For the same reason, they are not suited to be used in fluorescence spectrometers, where the light is collected from a large area.

Due to their high detection efficiency, SPADs are usually used in all single-molecule-based applications such as fluorescence correlation spectroscopy or coincidence correlation (see Dertinger and Rüttinger [22] and Grußmayer and Herten [23]).

6 Summary

There are essentially five different detector types available today for photon counting in the spectral range between approx. 300 and 1,000 nm. Unfortunately there is no detector with "ultimate" combination of features available, i.e., high

Table 1 Overview about typical key parameters of the discussed detector types

	Max. detection efficiency	Timing resolution (FWHM) (ps)	Active sensor area	Max. useful count rate	Dark counts/s
PMT (ultra-bialkali)	42 % @ 380 nm	<150	8 mm	10 MHz	<50
PMT (multialkali)	15 % @ 500 nm	<150	8 mm	10 MHz	<1,500
PMT (GaAsP)	40 % @ 600 nm	250–350	5 mm	10 MHz	< 400
Hybrid PMT (GaAsP)	46 % @ 500 nm	<120	3 mm	2 MHz	<700
Hybrid PMT (GaAs)	18 % @ 650 nm	<160	3 mm	1 MHz	< 1,000
Hybrid PMT (bialkali)	30 % @ 350 nm	<50	6 mm	1 MHz	< 100
MCP-PMT (bialkali)	20 % @ 450 nm	<25	11 mm	20 kHz	<50
MCP-PMT (multialkali)	20 % @ 450 nm	<25	11 mm	20 kHz	<500
MCP-PMT (GaAs)	15 % @ 700 nm	<150	11 mm	20 kHz	<3,000
Si-SPAD (thick junction)	75 % @ 670 nm	300–800	150 µm	1 MHz	<20 to <250
Si-SPAD (thin junction)	50 % @ 520 nm	<50–300	100 µm	10 MHz	<25 to <250

detection efficiency at a large wavelength range, large active area, high temporal resolution, and low dark counts and afterpulsing. It is therefore necessary to choose a detector based on the most crucial parameters for the targeted application. If the experiment is expected to yield very few photons, then the detection efficiency is the most important parameter. In case of time-resolved photon counting applications, the temporal resolution is of course one of the crucial parameters.

Table 1 briefly summarizes the typical main characteristics of the discussed detector types and can be used as a guide to select a suited detector. Note that the table only lists typical values.

References

1. (2007) Photomultiplier tubes – basics and applications, 3rd ed. Hamamatsu. https://www.hamamatsu.com/resources/pdf/etd/PMT_handbook_v3aE.pdf. Accessed 23 April 2014
2. Photosensor modules H7422 series. Hamamatsu. http://www.hamamatsu.com/resources/pdf/etd/m-h7422e.pdf. Accessed 23 April 2014
3. PMA series photomultiplier detector assembly. PicoQuant. http://www.picoquant.com/images/uploads/downloads/pma_series.pdf. Accessed 23 April 2014
4. Grosenick D (2014) Photon counting in diffuse optical imaging. In: Kapusta P et al. (eds) Advanced photon counting: applications, methods, instrumentation. Springer series on fluorescence. Springer International Publishing, doi: 10.1007/4243_2014_74
5. Microchannel plate-photomultiplier tube (MCP-PMTs) R3809U-50 series. Hamamatsu. http://www.hamamatsu.com/resources/pdf/etd/R3809U-50_TPMH1067E09.pdf. Accessed 23 April 2014
6. Microchannel plate-photomultiplier tube (MCP-PMTs) R3809U-61/-63/-64 series. Hamamatsu. http://www.hamamatsu.com/resources/pdf/etd/R3809U-61-63-64_TPMH1295E04.pdf. Accessed 23 April 2014
7. High speed compact HPD (hybrid photo detector) R10467U-40/R11322U-40. Hamamatsu. http://www.hamamatsu.com/resources/pdf/etd/R10467U-40_R11322U-40_TPMH1337E01.pdf. Accessed 23 April 2014
8. PMA hybrid series. PicoQuant. http://www.picoquant.com/images/uploads/downloads/pma_hybrid.pdf. Accessed 23 April 2014
9. Michalet X, Cheng A, Antelman J, Arisaka K, Weiss S, Suyama M (2008) Hybrid photodetector for single-molecule spectroscopy and microscopy. Proc SPIE 6862:68620F
10. Cova S, Ghioni M, Lacaita A, Samori C, Zappa F (1996) Avalanche photodiodes and quenching circuits for single-photon detection. Appl Optics 35:1956–1976
11. Buller GS, Collins RJ (2014) Single-photon detectors for infrared wavelengths in the range 1 to 1.7 μm. In: Kapusta P et al. (eds) Advanced photon counting: applications, methods, instrumentation. Springer series on fluorescence. Springer International Publishing, doi: 10.1007/4243_2014_64
12. Brown RGW, Ridley KD, Rarity JG (1986) Characterization of silicon avalanche photodiodes for photon correlation measurements. 1: passive quenching. Appl Opt 25:4122–41226
13. Dautet H, Deschamps P, Dion B, MacGregor AD, MacSween D, McIntyre RJ, Trottier C, Webb PP (1993) Photon counting techniques with silicon avalanche photodiodes. Appl Opt 32:3894–3900
14. Kell G, Bülter A, Wahl M, Erdmann R (2011) τ-SPAD: a new red sensitive single photon counting module. Proc SPIE 8033:803303
15. τ-SPAD single photon counting module. PicoQuant. http://www.picoquant.com/images/uploads/downloads/tau-spad.pdf. Accessed 23 April 2014

16. Lacaita A, Ghioni M, Cova S (1989) Double epitaxy improves single-photon avalanche diode performance. Electron Lett 25:841–843
17. PDM series photon counting detector modules, MPD. http://www.micro-photon-devices.com/Docs/Datasheet/PDM.pdf. Accessed 23 April 2014
18. Cova S, Ghioni M, Lotito A, Rech I, Zappa F (2004) Evolution and prospects for single-photon avalanche diodes and quenching circuits. J Mod Opt 51:267–1288
19. Kurtsiefer C, Zarda P, Mayer S, Weinfurter H (2001) The breakdown flash of silicon avalanche photodiodes – back door for eavesdropper attacks? J Mod Opt 48:2039–2047
20. Cova S, Lacaita M, Ghioni M, Ripamonti G, Louis TA (1989) 20-ps timing resolution with single-photon avalanche diodes. Rev Sci Inst 60:1104–1110
21. Lakowicz JR (2010) Principles of fluorescence spectroscopy. Springer, Berlin
22. Dertinger T, Rüttinger S (2014) Advanced FCS: an introduction to fluorescence lifetime correlation spectroscopy and dual-focus FCS. In: Kapusta P et al. (eds) Advanced photon counting: applications, methods, instrumentation. Springer series on fluorescence. Springer International Publishing, doi: 10.1007/4243_2014_72
23. Grußmayer KS, Herten D-P (2014) Photon antibunching in single molecule fluorescence spectroscopy. In: Kapusta P et al. (eds) Advanced photon counting: applications, methods, instrumentation. Springer series on fluorescence. Springer International Publishing, doi: 10.1007/4243_2014_71

Single-Photon Detectors for Infrared Wavelengths in the Range 1–1.7 μm

Gerald S. Buller and Robert J. Collins

Abstract The ongoing progress of scientific research in areas such as quantum communications, low-light level laser ranging, and material science (to name but a few) has led to increased interest in the detection of single photons in the wavelength range 1–1.7 μm. Several technologies have been used to detect photons with wavelengths in this range – each with different characteristic parameters that affect their suitability for specific applications. This chapter will provide a review of progress in the development of detectors for use in this spectral region and will highlight some notable results.

Keywords Infrared · Nanowire · Single photon · SPAD · Transition edge sensor

Contents

1 Introduction 44
2 Photomultiplier Tubes (PMTs) 46
3 InGaAs/InP Single-Photon Avalanche Diodes (SPADs) 47
4 Silicon-Germanium (SiGe) Single-Photon Avalanche Diodes (SPADs) 53
5 Quantum Dot-Based Detectors 55
6 Superconducting Transition Edge Sensors 56
7 Superconducting Nanowires 58
8 Upconversion to Higher Photon Energies 61
9 Conclusions 63
References 64

G.S. Buller (✉) and R.J. Collins
Institute of Photonics and Quantum Sciences, School of Engineering and Physical Sciences, Heriot-Watt University, David Brewster Building, Gait 2, Edinburgh EH14 4AS, UK
e-mail: G.S.Buller@hw.ac.uk

P. Kapusta et al. (eds.), *Advanced Photon Counting: Applications, Methods, Instrumentation*, Springer Ser Fluoresc (2015) 15: 43–70, DOI 10.1007/4243_2014_64,

1 Introduction

This chapter will consider the detection of single photons with wavelengths in the range between 1 and 1.7 μm (energies between 1.24 and 0.73 eV). This spectral region of wavelengths is used for a variety of different applications and is of particular interest to the telecommunications industry as the silica-based optical fiber wave guide employed for high bandwidth communications exhibit low loss at wavelengths around 1.3 and 1.55 μm (energies of 0.95 and 0.8 eV). The optical pulses used to transmit telecommunications signals contain multiple photons and typically employ linear-mode operation semiconductor photodiode detectors, where the detector output is linearly proportional to the incident optical signal [1]. These optical fibers are often installed in regions of limited accessibility, and it is important to have a means to characterize the fiber from factory to installation. Optical time-domain reflectometery (OTDR) provides this mechanism by permitting nondestructive measurements of the loss and length of the optical fibers. Although OTDR systems based on multiphoton detectors offer sufficient sensitivity for many applications, approaches operating with single-photon detection technologies offer the prospect of more efficient and cost-effective systems [2].

Single-photon detection is critical to the use of quantum key distribution, a technology which uses quantum mechanics to guarantee verifiably secure communication of a cryptographic key between two parties [3]. A full and detailed discussion of quantum key distribution is beyond the scope of this work, and the curious reader is directed to the excellent work on quantum information edited by Bouwmeester, Ekert, and Zeilinger [3]. To maximize range of transmission, it is important that quantum key distribution systems are compatible with the widely deployed telecommunications optical fiber network, which usually necessitates employing photon sources which emit at wavelengths close to 1.3 or 1.55 μm [4] – hence, high-efficiency single-photon detectors operating at these wavelengths are desirable. The precise operating characteristics of the single-photon detectors play an important role in the rate of the key exchange process, and small changes in the performance of the detectors can affect the final secure information exchange rate to a surprising extent [5].

Applications of single-photon detectors in the 1–1.7 μm wavelength region are not limited to optical fiber-related technologies. For example, low-power, eye-safe photon-counting laser ranging and depth imaging can also benefit from the usage of such detectors. Here, the time-of-flight approach is used to estimate the distance from a source to a remote object by emitting a bright optical pulse and measuring the round-trip time for the photons to be scattered off the object and returned to a single-photon detector. A more detailed discussion of the operation of such systems can be found in the review work of Buller et al. [6]. Operation of such a system, for example, in outdoor environments, leads to challenges such as with atmospheric attenuation [7], unwanted photons from additional sources such as the solar background [6], and, ideally, an extremely low probability of causing injury from stray laser radiation [8]. Low-photon-number pulses at wavelengths around 1.3 μm offer

distinct advantages in these situations as they correspond to a region of the spectrum where there are comparatively few solar-generated photons [9] and offer improved eye-safety thresholds [8].

Additionally, such detectors would be capable of detecting photons with wavelengths that lie in certain atmospheric transmission windows [7], as well as infrared gas absorption features, notably those of the so-called greenhouse gases such as CO_2 and NO_2. In order to provide valuable data for studies of the environment, the measurement and monitoring of the levels of these gases in the atmosphere have fuelled the development of sensitive, high bandwidth detectors for use at these wavelengths [10].

Just as single-photon detection can play a role in monitoring large-scale systems, so it can also be used in the monitoring of microscopic biological systems. Most techniques introduce a fluorophore which bonds to a cell or molecule of interest. These fluorophores commonly emit at a lower wavelength, typically well below 1 μm, which is compatible with single-photon detectors described in the preceding chapter [11]. However, one important example of near-infrared fluorescence is singlet oxygen ($^1O_2$), which fluoresces at a wavelength of 1,270 nm, beyond the detection range of Si-SPAD detectors. Singlet oxygen is an excited state of the oxygen molecule and an important intermediate in many biological and physiological processes [12]. The efficient direct measurement of fluorescence lifetimes of $^1O_2$ at $\lambda \sim 1{,}270$ nm is therefore of interest to the biophotonics field [13].

With so many potential applications for single-photon detection in this spectral region, there is a drive to develop efficient, low-noise single-photon detectors that are sensitive to these wavelengths [14]. As mentioned in the chapter by Bülter [15], many photon detectors will generate spurious events without incident photons, known as dark events or dark counts. The precise cause of these dark counts depends on the type of detector and the exact operating parameters, but one common cause is thermal excitation of carriers [16]. Here we briefly reintroduce the concept of noise-equivalent power (NEP), which is defined as the signal power required to attain a unity signal-to-noise ratio within a one-second integration time [17] and given by:

$$\mathrm{NEP} = \frac{hc}{\lambda\eta}\sqrt{2N_\mathrm{D}} \tag{1}$$

where h is Planck's constant ($6.62606957 \times 10^{-34}$ m^2 kgs^{-1}), c is the speed of light in vacuum (299792458 ms^{-1}), λ is the wavelength of the incident photon, N_D is the dark count rate, and η is the detection efficiency which is the probability that the incident photon generates a measureable current pulse. It can be easily seen that lower values of the NEP are more desirable [17], and relevant examples will be provided throughout this chapter. To provide a reference point for later comparisons, a typical commercially available thick junction silicon SPAD [18], of the type described in the chapter by Bülter [15], has an NEP of approximately 1.7×10^{-17} WHz$^{-½}$ at a wavelength of 550 nm and 4.7×10^{-17} WHz$^{-½}$ at a wavelength of 850 nm [14].

One further important factor in many applications of single-photon detectors is the timing jitter – a measure of the degree of variation in time of the leading edge of the output electrical pulse. There will be a statistical deviation in the individual measurements of timing jitter, and it is often quoted as the full width at half-maximum (FWHM) of a histogram of the distribution, although full width at tenth-maximum (FW10M) and full width at hundredth-maximum (FW100M) are also sometimes used [5].

Another useful aspect of single-photon detector performance is the dead time or "recovery time" which is the time period after an incident photon during which the detector is unable to register further incident photons. The exact cause of the dead time is dependent on the type and configuration of photon detector used and is often primarily due to the additional circuits used to bias, gate, or quench the detector as opposed to the actual detector mechanism itself. The dead time will provide an upper limit on the measurable photon count rate at the detectors.

2 Photomultiplier Tubes (PMTs)

Photomultiplier tubes, or PMTs, were probably the first form of infrared single-photon detector that was widely utilized in a number of applications [19], and PMTs for use in the visible wavelengths were covered in detail in the chapter by Bülter [15]. We will not restate the means by which these devices detect single photons but instead will examine how they may be used in the wavelength band 1–1.7 μm. InGaAs photocathodes have shown promise for detection of photons in this wavelength band, but the commercially available detectors must be cooled to approximately 200 K to reduce the effects of dark counts. While the detection efficiencies of PMTs do not show a strong dependence on the wavelength of the incident photons, they are typically low in comparison to other single-photon detectors [20]. Furthermore, PMTs frequently exhibit long timing jitters of the order of 1 ns, mainly due to the spread in transit times of electrons from photocathode to anode [21]. Most of the dark counts are typically induced by thermionic emission in the photocathode and can be significantly reduced by lowering the operating temperature [22]. However, PMTs also suffer from the deleterious effects of afterpulsing, where multiplication events cause an excited state which later decays, initiating a further avalanche event long after the initial event. The afterpulsing in PMTs is most likely due to ion feedback caused by the ionization of residual gases in the PMT or by luminescence of the dynode material and the glass of the tube [23]. While it cannot be completely eliminated, the effect of afterpulsing depends on the gain of the PMT and may be reduced by decreasing the operating voltage of the PMT and using a preamplifier with a correspondingly higher gain [22].

Figure 1 shows how the quantum efficiency of two PMTs from Hamamatsu Photonics varies with wavelength [20]. The R5509 – 43 PMT has an InP/InGaAsP photocathode, while the photocathode of the R5509 – 73 is InP/InGaAs. Otherwise the two PMTS are identical. It can be seen from Fig. 1 that using the InGaAs

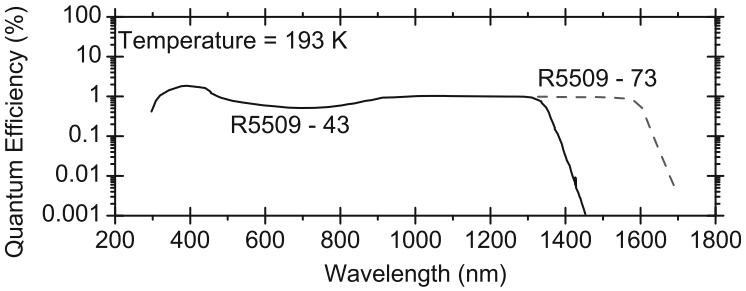

Fig. 1 A plot of the dependence of quantum efficiency on wavelength of two Hamamatsu photomultiplier tubes (PMTs) at a temperature of 193 K. The R5509 – 43 PMT has an InP/InGaAsP photocathode while the photocathode of the R5509 – 73 is InP/InGaAs. Apart from the photocathode, the PMTs are identical (Data courtesy of Hamamatsu Photonics UK Limited [20])

photocathode extends the operating wavelength of the PMT from around 1.4 μm to approximately 1.7 μm with a typical detection efficiency of 1 % and a mean of 0.5 % over the entire 1–1.7 μm range. However, the R5509 – 73 exhibits 1.6×10^5 dark counts per second, ten times the dark count rate of the lower wavelength R5509 – 43 model. The NEP of the R5509 – 43 model at a wavelength of 1.35 μm is 6.7×10^{-15} $\mathrm{WHz}^{-½}$, while that of the R5509 – 73 model at the same wavelength is 8.7×10^{-15} $\mathrm{WHz}^{-½}$. InGaAs is also used in the design of SPAD detectors for the $\lambda \sim 1550$ nm region.

3 InGaAs/InP Single-Photon Avalanche Diodes (SPADs)

At present, the most established approach for near-room temperature single-photon detection at wavelengths in the range 1–1.7 μm InGaAs/InP based single-photon avalanche diodes (SPADs). As has been discussed in the chapter by Bülter [15], a SPAD is an avalanche photodiode (APD) operated in Geiger mode – that is to say the APD is biased above avalanche breakdown and the presence of a single electron (or hole) in the multiplication region can initiate a self-sustaining current. Such devices are digital in operation; the output will be either zero or a well-defined voltage level. The amplitude of the output voltage pulse is independent of the number of incident photons. The operation of SPADs for use at shorter wavelengths was discussed in the chapter by Bülter [15], and some similarities in operating principles apply for detectors used at the wavelengths considered in this chapter. Figure 2 shows a schematic of a cross section through a planar geometry InGaAs/InP SPAD [24]. Here photons are absorbed in a narrow bandgap InGaAs layer causing photogenerated holes to drift into the relatively higher field InP multiplication layer. InGaAs and InP have a large mismatch in their bandgap energies (0.75 and 1.27 eV, respectively, at room temperature), and this leads to a valence band

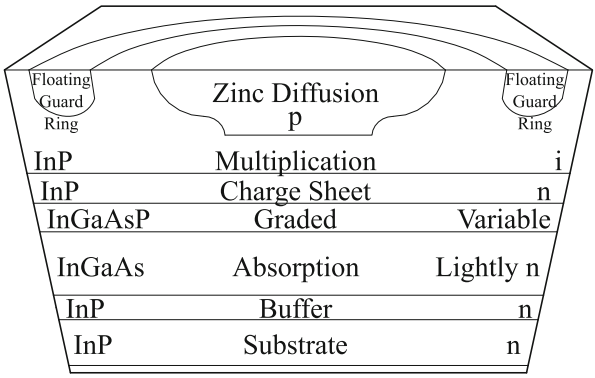

Fig. 2 A schematic of a cross section through a planar InGaAs/InP – single-photon avalanche diode (SPAD). The incident photon enters the device through the p-type zinc diffusion region. A top contact is made to the central Zn-diffused region and a lower contract to the substrate [24]. The guard ring [25] is also formed by Zn diffusion

discontinuity which results in a barrier to hole drift into the multiplication region. This can lead to hole recombination at the interface between the two materials, resulting in reduced detection efficiency. This issue can be addressed by the growth of intermediate bandgap InGaAsP layers (thickness typically 100 nm) between the other two materials to smooth the gradient in valence band energies [26].

Early work was carried out using a linear-mode InGaAs/InP avalanche photodiode biased in Geiger mode and cryogenically cooled to 77 K. This gave an NEP of 1×10^{-16} $\mathrm{WHz}^{-½}$ at a wavelength of 1.55 μm [27] and later improved to NEP of 4×10^{-17} $\mathrm{WHz}^{-½}$ at the same wavelength and temperature using lower dark current devices [28]. A greater understanding of the field-assisted tunneling in the InP has led to the introduction of longer InP multiplication regions and, consequently, improved detection efficiencies [29].

One major drawback of InGaAs/InP SPADs is the comparatively high afterpulsing rate [30]. As discussed previously with photomultipliers, afterpulsing is the generation of additional detector events after an initial avalanche. Afterpulsing in SPADs is caused when an avalanche current causes mid-bandgap trap states in the material to be filled. These traps then release the carriers at a later time, contributing to the overall dark (i.e., non-photogenerated) count rate. These deep-level traps are typically caused by impurities in the materials or dislocations of the crystal lattice [31], and the characteristic trap lifetime increases with reduced temperature. The trap release time is typically long compared to the time between expected photon events or the source repetition frequency, and if this is the case, then the afterpulsing will be manifested as an increase in the background level, reducing the sensitivity of the detector.

There has been a significant quantity of work focused on the study of the afterpulsing phenomenon, and there have been many advances in understanding and reducing the effect [32]. It has been reported that there is evidence that the traps responsible for afterpulsing can be found in the InP layers [24] and focused research into the elimination of these traps will lead to a reduction in dark count rates and a

corresponding improvement in photon-counting rates. In 2012, Itzler et al. showed that there was no physical significance to the detrapping time that could be extracted from the, then canonical, exponential fitting of the decay of the afterpulse probability with time [32]. Instead, they proposed a simpler power law dependence (although also postulated that there may be other mathematical solutions) which suggested that there was a higher density of slower release traps.

The simplest approach to mitigating the effects of afterpulsing is to force the SPAD to be inactive by biasing it below breakdown for a "hold-off" time that is sufficiently long to allow all trapped carriers to be released and swept from the multiplication region without the possibility of triggering afterpulses. However, imposing long hold-off times limits the rate at which photons can be detected, and selection of the duration of the hold-off time is a trade-off between afterpulse suppression and maximum possible count rate. However, it is possible to combine a hold-off time with electrical gating to permit efficient operation [33], as will be described later. There are three main forms of simple quenching applied to detectors: passive, active, and gated. Passive quenching and active quenching have been described in the chapter by Bülter [15], and these techniques have also been used with the detectors described in this section. A passive quenching circuit, shown in schematic form in Fig. 3, is simply a high-impedance load connected in series to the SPAD [35]. Passive quenching circuits can have a slow recovery time in which no further photon detection events can be registered (a dead time), reducing the maximum count rate possible. Although it is possible to reduce both the load resistance and internal capacitance of the diode and thereby minimize the dead time, even at small values of R_L (∼500 kΩ) and internal capacitance (∼1 pF), the dead time can be up to ∼ 1 μs [35].

Due to the comparative simplicity of the approach, passive quenching has been successfully applied to InGaAs/InP SPADs in many applications [36, 37]. Passive quenching with an active reset was used by Liu et al. in 2008 in a demonstration which also varied the hold-off time over the range 0–8 μs [38]. For an excess voltage of 2 V and operating temperature of 230 K, the NEP at a wavelength of

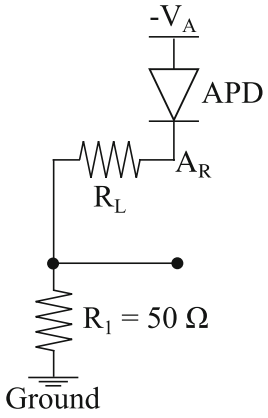

Fig. 3 An example of a circuit used in passive quenching. When the avalanche photodiode (APD) is biased above the breakdown voltage by V_A, an electron–hole pair can generate a self-sustaining avalanche. The avalanche discharges through the high resistance of R_L and the voltage V_A decreases. The point A_R denotes where one end of the FET would be connected when active reset is utilized [34]; see text

1.31 μm was estimated by Liu et al. to be 8×10^{-17} $WHz^{-½}$. Active reset inserts a field-effect transistor (FET – a fast voltage switch) between the ground and the point between the SPAD cathode and ballast resistor R_L marked with A_R in Fig. 3 [34]. The switch's default inactive state is to be open and R_L is selected to be sufficiently large that passive quenching will be guaranteed. Once the avalanche has been quenched, a comparator senses the avalanche pulse and closes the switch for a short duration to recharge the diode and stray capacitance. The switch is closed for a time that is very slightly longer than the time taken by the quenching transition, and the hold-off delay is applied between the completion of the quenching process and the reopening of the switch.

In 2008 Warburton et al. demonstrated a passively quenched room temperature InGaAs/InP SPAD [39] by using a low excess bias approach to minimize avalanche current and permit entirely free-running operation (i.e., without the assistance of electrical gating). At room temperature (295 K), the NEP of this device was 9.70×10^{-15} $WHz^{-½}$ which reduced to 6.57×10^{-17} $WHz^{-½}$ at 170 K, both measured when using a 100 kΩ reverse biasing resistor [39].

Active quenching [40] has been applied to many SPAD systems [41, 42]. In this approach the hold-off time after quenching is determined by the duration of the output pulse from the comparator and is equal to the duration of the avalanche pulse. The dead time associated with this technique is the sum of the avalanche and hold-off durations (approximately twice the duration of the propagation delay in the feedback loop) and can be of the order of a few nanoseconds – permitting photon detection rates of the order of MHz.

In 2009, Zhang et al. demonstrated an approach to active quenching based around an application-specific integrated circuit (ASIC) fabricated using 0.8 μm CMOS [43]. Utilizing this active quenching ASIC approach, they were able to achieve NEPs in the range 2.92×10^{-16} $WHz^{-½}$ to 4.77×10^{-16} $WHz^{-½}$ at a wavelength of 1.55 μm and an operating temperature of 223 K. Operating under the same conditions but using a more conventional external circuit active gating scheme [27], the same detector demonstrated an NEP of between 2.96×10^{-16} $WHz^{-½}$ and 4.26×10^{-16} $WHz^{-½}$ [43].

The effects of afterpulsing can be reduced by electrically gating the detector, only raising the bias voltage above breakdown when an incident photon is expected. This means that between gates, the traps can empty without triggering further avalanche pulses. Some form of gated quenching is used in most applications of InGaAs/InP SPADs. However, the relatively high afterpulse probability and long trap lifetimes mean that only low gating rates are possible using simple gating techniques (i.e., gate periods of 10's of ns duration), typically in the range of 1–100 kHz [44]. Adaptations of this approach have been applied to quantum key distribution since the arrival times of the photons at the detectors can be predicted due to the known length of the transmission medium and the bias voltage level raised and lowered accordingly [45].

Simple gating techniques can have limitations in applications such as time-of-flight-ranging, where the aim is to measure unknown distances, and hence, the arrival time of the returned photon is necessarily difficult to estimate. An approach

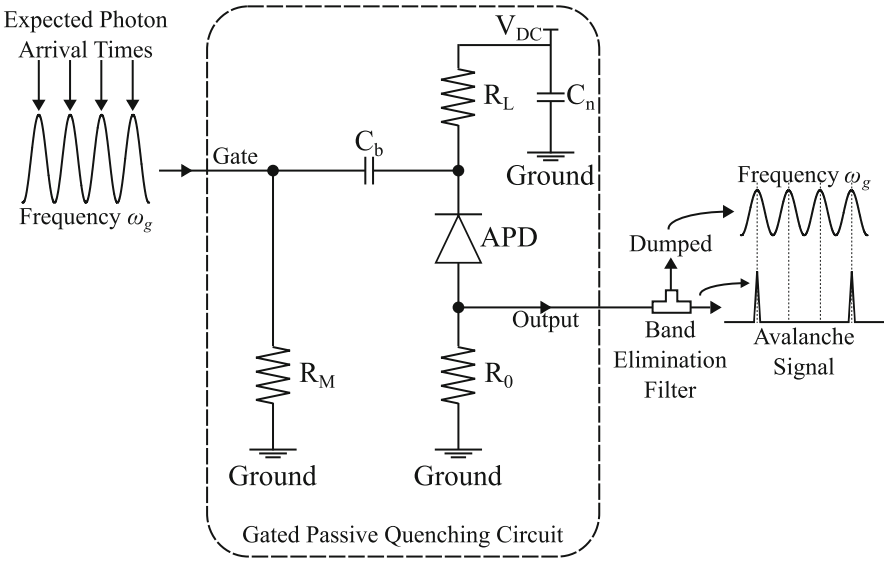

Fig. 4 A schematic of the "sine gating" approach [48]

that has been used successfully is to use a relatively high-frequency gate (i.e., >50 MHz), but a long hold-off time of, typically, milliseconds after each which can yield impressive results [33].

The obvious limitations of some of the early gating techniques motivated researchers to develop new quenching approaches. High-clock-rate single-photon detection relies on the detection of weak avalanches [46]; however, the weak avalanches can be difficult to detect in gated mode due to the capacitive response of the APD to the gating signal [47]. One approach to the removal of the capacitive response is termed "sine gating" which, as the name suggests, applies a sinusoidal electrical gate to the SPAD [48]. An example of the operation of sine gating is shown in Fig. 4. The resistance of the APD, which is considerably greater than R_0, serves to attenuate the gate signal. If an avalanche is not triggered within a gating period, then only the attenuated single frequency input sinusoidal gating signal is output by the circuit. If an avalanche occurs during the gating period, then an output electronic avalanche pulse is mixed with the gating signal. Since the avalanche pulse is composed of many frequencies, it can easily be separated from the single frequency gating signal by using a narrow bandwidth elimination filter centered on the gating frequency ω_g. Selecting an extremely narrow bandwidth elimination filter and perfectly matching the impedance of the circuits mean that it is possible to transfer nearly all of the energy from the avalanche signals and achieve the maximum electrical signal-to-noise ratio [43].

Sinusoidal gating has the advantage that it permits high gating periods of several 100's of MHz (and even as high as the GHz regime [49]) although actual maximum detector count rates are still limited by other detector artifacts and therefore are

lower. In 2011, Liang et al. demonstrated a 1 GHz sinusoidally gated InGaAs/InP SPAD with an NEP of 1.36×10^{-16} WHz$^{-½}$ for a wavelength of 1.55 μm and an operating temperature of 248 K [50]. This detector was then demonstrated at short range in a time-of-flight laser ranging system [51]. Meanwhile in 2012, Walenta et al. demonstrated a 1.25 GHz sinusoidally gated InGaAs/InP SPAD with an NEP of 5.36×10^{-17} WHz$^{-½}$ in a quantum key distribution system [49].

Sine gating relies on filtering the single frequency periodicity of the gating signal to remove the capacitive response of the APD to the gating signal. Another approach, known as "self-differencing," operates by subtracting a delayed copy of an arbitrarily shaped periodic gated signal from the output signal [52] with any avalanche signal being much more evident after the subtraction process. Like sine gating, self-differencing can be employed at high gating signal frequencies of the order of 100's of MHz and beyond. In 2010 Yuan et al. demonstrated a InGaAs SPAD operating at gating repetition frequency of 2 GHz with NEPs of between 1.0×10^{-15} WHz$^{-½}$ and 6.3×10^{-16} WHz$^{-½}$ (depending on the DC bias) at a wavelength of 1.55 μm [46].

Self-differencing circuits may also be used with InGaAs/InP SPADs to produce photon number resolving detectors [53]. The current is measured shortly after the onset of avalanche build-up, and due to the self-differencing approach, it is possible to resolve avalanche currents over ten times lower in amplitude than is normally achievable with conventional gating techniques for Geiger-mode devices. The peak voltage of the output signal varies with input photon number, and it is possible to use a measurement of the amplitude of the output voltage to determine the incident photon number [54].

One further approach to the reduction of afterpulsing in InGaAs/InP SPADs is negative feedback [55]. A thin film resistor is monolithically integrated directly onto the surface of the device, thereby reducing the parasitic effects [56]. In an ideal case this means that the total number of charges in the device during the avalanche process is determined only by the diode depletion capacitance and the excess bias. Fewer charges in the device during avalanche mean that there is a lower probability that a trap state will be filled to later cause an afterpulse.

Some photon-counting applications, such as imaging, can greatly benefit from arrayed SPAD detectors [57, 58]. InGaAs-based single-photon detector arrays have been commercialized by two companies, Princeton Lightwave [57] and Spectrolab [58], who have packaged them into convenient camera systems. In each case, the detector plane consists of a thermoelectrically cooled 32 pixel × 32 pixel Geiger-mode InGaAs/InP SPAD and GaP microlens array, flip-chip bonded to a silicon CMOS integrated readout circuit. The Princeton Lightwave implementation comes in two versions: one which detects photons with wavelengths in the range 0.91–1.14 μm (with absorption in InGaAsP) and one which is sensitive to wavelengths between 0.92 and 1.62 μm (with an InGaAs absorber). The shorter wavelength model exhibits a typical NEP of 1.07×10^{-16} WHz$^{-½}$ for a wavelength of 1.064 μm, while the longer wavelength model exhibits a typical NEP of 1.16×10^{-16} WHz$^{-½}$ for a wavelength of 1.55 μm. Both models have a fill factor

of 75 % and typical dark count rates of 20 kHz and are capable of operating at frame rates of 74, 142 and 186 kHz.

Although the reduction of afterpulsing and dark count rates remains a significant challenge, SPADs based on InGaAs/InP are still the most promising candidate for near-room temperature single-photon detection at wavelengths around 1.55 μm. They have been successfully used in a number of different applications from time-of-flight laser ranging [51] to high-performance demonstrations of quantum key distribution [59].

4 Silicon-Germanium (SiGe) Single-Photon Avalanche Diodes (SPADs)

Ge exhibits good absorption properties at room temperature for wavelengths up to approximately 1.6 μm and has been considered as a material for SPAD detectors. Initially, studies were made of the performance of commercially available linear multiplication germanium avalanche photodiodes operated in Geiger mode. These detectors offered gated single-photon detection efficiencies of around 10 % and timing jitter of less than 100 ps. However, they also exhibited high dark count rates in the high-field narrow-gap Ge multiplication layer and high afterpulsing rates [60]. A typical value of NEP obtained from these measurements for a wavelength of 1.3 μm was 7.5×10^{-16} $WHz^{-½}$ at temperature of 77 K.

Another area of interest was the use of Si multiplication layers used in conjunction with absorbing layers containing Ge. However, the lattice mismatch between Si and Ge makes epitaxial growth of high-quality Ge-on-Si difficult. In the 1980s progress was made in the development of strained-layer silicon/silicon germanium (Si/SiGe) on silicon linear-mode avalanche diodes. An early avalanche photodiode detector structure was a wave guide with the core formed from a strained-layer Ge_xSi_{1-x}/Si superlattice in a sandwich structure between lower refractive index Si cladding layers. Due to interband electron transitions, the absorption of the infrared radiation takes place in the core superlattice region, while the cladding layers collect the photogenerated carriers [61]. The strain in the superlattice resulted in a redshift in the absorption of the material relative to unstrained bulk SiGe so that the detector was able to operate in the wavelength range 1.3–1.55 μm [62].

The first SPAD grown using a similar approach was demonstrated by Loudon et al. in 2002 [63]. These devices were grown with strained SiGe/Si layers and $Si/Si_{0.7}Ge_{0.3}$ multiple quantum-well material as an absorber [64], as shown in Fig. 5. To prevent relaxation of the layer, the overall thickness of the layers containing Ge was limited to only 300 nm, and this led to low levels of absorption at wavelengths of 1,300 nm and above. The devices exhibited an improvement in the maximum detection efficiency of ~0.013 % at a wavelength of 1.21 μm, a 30-fold increase when compared to all-Si control samples. While the efficiency improvement at longer wavelengths was notable, the low detection efficiency can

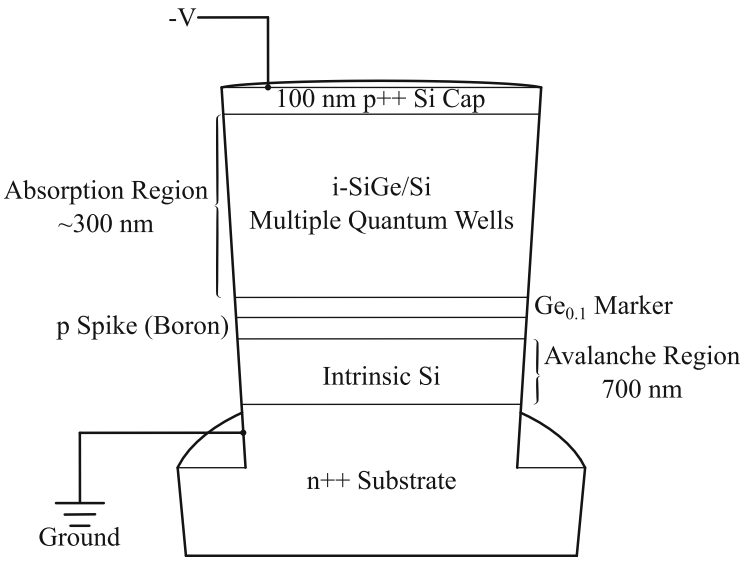

Fig. 5 A cross section through the 120 μm diameter circular mesa structure of a strained silicon-germanium (SiGe) multiple quantum-well layer single-photon avalanche diode (SPAD) [63]. The $Ge_{0.1}$ marker was used as an etch stop during the fabrication process, and the p-type doping spike created a high-field region in the avalanche layer

be primarily traced to the lack of Ge in the absorber layer. This work led to the conclusion that the absorption at $\lambda \sim 1{,}550$ nm needed to be significantly increased and should be composed of thick (i.e., >1 μm) layer of Ge, grown adjacent to the larger gap Si multiplication layer. However, due to the large lattice mismatch of 4.2 %, the direct epitaxial growth of high-quality Ge-on-Si is highly problematic due to the high density of dislocations formed at the hetero-interface. One solution was to grow a thin Ge seed layer (25–100 nm thick) on top of the Si substrate at a low temperature of between 620 and 675 K. This buffer layer will typically have between 10^8 and 10^9 cm^{-2} threading dislocations [65]. Following the buffer layer, a thick layer of Ge is grown at a higher temperature (approximately 920 K) before the thermal annealing over several cycles (at a temperature between 1,270 and 1,370 K). This annealing process can reduce the threading dislocations to around 10^6–10^{-7} cm^{-2} [65]. Following the refinement of the seed layer approach to Ge absorption layer/Si multiplication layer SPADs, there have been several experimental demonstrations of this structure. In 2013, Warburton et al. demonstrated the lowest reported (to date) noise-equivalent power for a thick Ge-on-Si SPAD at 1×10^{-14} $WHz^{-½}$ at a wavelength of 1.31 μm [66]. The structure of this device is shown in Fig. 6. At an operating temperature of 100 K, the dark count rate of this device was approximately 6 mega-counts per second and the detection efficiency 4 %. The paper also reported a low afterpulsing level compared with III–V-based SPADs

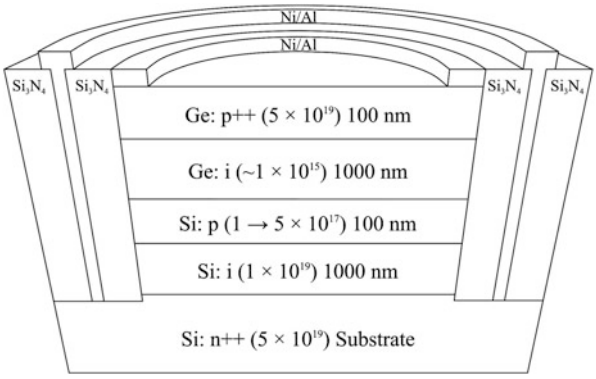

Fig. 6 A cross section through the 25 μm diameter circular mesa structure of a germanium on silicon (Ge-on-Si) single-photon avalanche diode (SPAD) [66]. The Ni/Al layer forms the top contacts and Si3N4 is used for passivation and insulation

5 Quantum Dot-Based Detectors

The avalanche gain process is the primary cause of spurious counts (unwanted "noise") in the avalanche photodiodes [67]. Various methods are under examinations which seek to reduce this contribution. One approach that has shown promise is the use of quantum dots. A quantum dot is a nanometer-dimensioned structure which confines electrons in all three dimensions leading to a quantization of the available energy transitions for carriers similar to that of a single atom [68]. One way that this can be achieved is to form an island of low bandgap semiconductor material surrounded by higher bandgap material. The physics of quantum dots is a wide-ranging field of research, and a detailed analysis is beyond the scope of this chapter. The curious reader is directed to the work edited by Peter Michler [69] for more details.

In 2007 a single-photon detector based on an AlAs/$In_{0.53}Ga_{0.47}As$/AlAs double-barrier resonant tunneling diode containing a layer of self-assembled InAs quantum dots grown on an InP substrate was presented, and this is shown in schematic form in Fig. 7. This device demonstrated an internal efficiency of 6.3 % [71]. This detector sensed a change in the resonant tunneling current through the structure which was caused by a single photoexcited carrier being captured in a quantum dot. The tunneling current in a resonant tunneling device exhibits a strong sensitivity to the energetic alignment of the electrons and the confined level between the double barriers. As the detection mechanism does not rely on an avalanche process, it is believed that the afterpulsing rates of such detectors should consistently be lower than in SPAD detectors.

The detection efficiency and dark count rate of the devices depend on the size and density of the quantum dots [72]. Several different approaches exist for the growth of quantum dots, and the current process of choice for many applications is self-assembly [73].

Self-assembly is a spontaneous formation process that relies on a slight mismatch in the lattice parameters of two different semiconductor materials

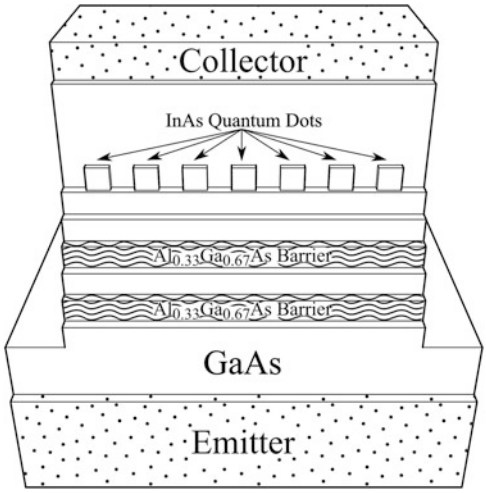

Fig. 7 A staggered cross section through the square mesa structure of an InAs quantum dot single-photon detector [70]. The cross section has been staggered to better illustrate the structure of the device

(heterostructures) with the same crystal axis [74]. Strain is induced by the small mismatch in lattice parameters, and after a critical number of layers have been deposited, nanometer scale islands of semiconductor spontaneously form to relieve the stress. These islands form the quantum dots. The strain energy is reduced by the formation of quantum dots, but the surface energy increases, and the dot formation is the process of an equilibrium forming between these two competing energies. This means that achieving fine control over the exact size and position of the quantum dots is challenging.

Generally, it can be shown that reducing the size and density of the quantum dots typically reduces the dark count rate. Molecular beam epitaxy (MBE) permits some level of control over the density of the dots, for example, by reducing the deposition time (and hence layer thickness), and by altering the physical geometry of the sample during growth, a density gradient can be achieved across the sample surface [75]. Reducing the dot size also lowers the detection efficiency, and the choice of size and density is a balancing act between the desired detection efficiency and dark noise.

6 Superconducting Transition Edge Sensors

All of the single-photon detectors examined so far in this chapter have been based on semiconductor technologies. Other possible technologies can also be utilized for the detection of single photons, such as superconductors. Superconductors are materials which exhibit zero electrical resistance and are therefore able to maintain the flow of an electrical current without a voltage drop [76]. The development and analysis of superconductors is a fascinating topic, and the reader is directed to the review work edited by Bennemann and Ketterson for a more detailed analysis [77].

Since the first superconductor, mercury (Hg), was identified in 1911 [78], there has been a drive to identify further materials which exhibit this useful property. There is one further feature of all the superconductors that have been identified so far in the published literature in that they all require cooling to cryogenic (or near-cryogenic) temperatures – for example, mercury only superconducts at temperatures lower than 4.2 K [79]. The temperature below which a material becomes a superconductor is called the critical temperature and is commonly denoted by T_C. This dependence of superconductivity on temperature can be exploited to produce a single-photon detector. Although photons typically have very low individual energies, the additional heat induced on a correctly configured suitable superconductor can be enough to briefly raise the temperature of the device above T_C and generate a measurable voltage pulse [80]. Naturally, such superconductors need to exhibit a sharply transitioning dependence of superconductivity on temperature.

Transition edge sensors are a form of superconducting single-photon detector based around an extremely sensitive calorimeter [81]. A common transition edge sensor single-photon detector calorimeter design, such as that shown in Fig. 8, features an absorber, which increases in temperature with incident energy of the desired type; a thermometer, which measures this increase in temperature; and a weak link to a thermal heat sink, so that the absorber may slowly cool to the original temperature [82]. To operate a superconducting transition edge sensor, the photon absorber is cooled to a temperature which is below the critical temperature and a bias voltage applied so that the absorber is heated to a temperature where the small heat increase of an incident photon generating a photoelectron will result in a large change in the resistance. The increase in the temperature of the photon absorber results in an increase in the resistance of the device, which leads to a further increase in temperature. The change in resistance is measurable using external circuitry and is used to indicate the detection of single photons.

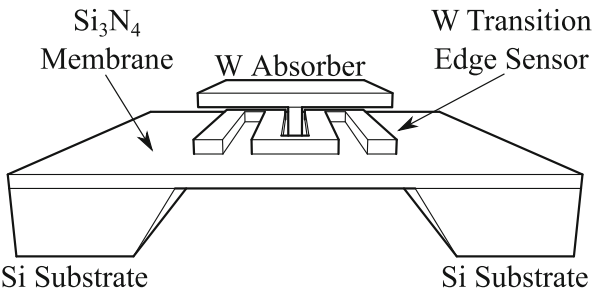

Fig. 8 A schematic of a possible tungsten (W) transition edge sensor (TES) arrangement with both TES and absorber composed of W. The silicon-nitride (Si_3N_4) membrane acts as the weak thermal coupling to the silicon (Si) substrate which serves as the thermal heat sink. The Si substrate is patterned into a waffle-like pattern with angled faces on the vertical holes to provide a weak thermal heat sink. Electrical connections to the TES are not shown (this design is based on that presented by Iyomoto et al. [82])

Single-photon detectors based on transition edge sensors are often manufactured from tungsten as it exhibits the required sharp transition from superconducting to nonsuperconducting with varying temperatures. It is possible to use tungsten patterned onto silicon substrates as both photon absorber and thermometer. An absorbed photon results in an increase in the tungsten's temperature, leading to an increase in the resistance and drop in the Joule power dissipated. There is a relatively weak coupling between the electron and phonon systems at the operating temperatures of such a detector. When the tungsten heats up, only a small amount of the excess heat is lost through thermal conduction to the substrate. The change in current caused by the change in resistance is measured with a superconducting quantum interference device (SQUID) array [83]. SQUIDs are highly sensitive magnetometers based on superconducting loops with Josephson junctions that can be used to measure very weak magnetic fields.

Tungsten-based transition edge sensors can detect a wide spectrum of wavelengths from at least 0.35 to 1.55 μm [80]. They also have low dark count rates, typically around 10 counts per second. The detection efficiency of such detectors in the spectrum of wavelengths considered in this chapter can be as high as 95 % in gated mode operation at a wavelength of 1,556 nm [84] in a resonant cavity configuration. However, they have poor timing attributes with an approximately 1 μs FWHM timing jitter and a thermal recovery time of around 800 ns to 1 μs. As the superconducting transition temperature of the tungsten films is around 100 mK, the devices must be cooled using an adiabatic demagnetization refrigerator [85].

In addition, these detectors are capable of photon number resolving, that is to say that they are capable of indicating (to a certain extent) the number of photons in an incident pulse [84]. The previously described 95 % efficient detector of Lita et al. was capable of resolving up to seven photons in a pulse.

7 Superconducting Nanowires

As the name suggests, these detectors are formed using superconducting nanowires, typically fabricated with a width of approximately 100 nm [86]. The wire is biased with a current which is just below the critical current and maintained at a temperature below the critical temperature. An incident photon generates a localized hot spot which increases the temperature in a small region above the critical temperature. The hot spot develops and grows, constraining the supercurrent in the areas surrounding the hot spot near the edges of the wire. The current density in the edges of the wire has then become so great that it exceeds the critical current density, and a nonsuperconducting stripe is created across the nanowire [87]. This results in the output of a measurable voltage pulse that can be amplified and recorded. This process typically occurs on far shorter timescales than the reset of a semiconductor avalanche diode single-photon detector by present quenching technologies [88].

The first superconducting nanowire-based single-photon detector was demonstrated in 1991 by Gol'tsman et al. [89]. This early device consisted of a series of

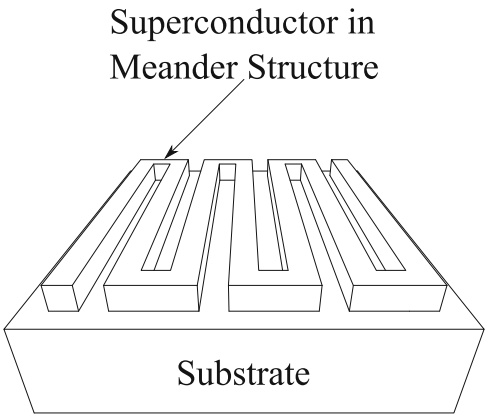

Fig. 9 A schematic of a superconducting nanowire single-photon detector (SNSPD) arranged in a meander line [90]. An incident photon is only detected if it strikes the superconducting nanowire. The width of the superconducting wire cannot be increased indefinitely due to the limitations of the detection mechanism. The meander arrangement ensures that that the area of superconductor is increased without adversely affecting the detection process [86]

ten 0.15 nm thick NbN wires stripes of width 0.7 μm and length 100 μm spaced by 1.3 μm from adjacent wires and connected in parallel on a 0.38 nm thick sapphire substrate and gave a detectivity of 10^{10} W^{-1} cm $Hz^{-½}$. The low detection efficiencies of these early designs could be attributed to the low fill factor of this geometry. The use of individual long straight wires meant that photons had to be directly incident on the relatively narrow wire in order to be registered. While increasing the area of the detector by increasing the width of the wire may seem like an obvious route to take, the small scale of the hot spot formed by an incident photon means that the wire width cannot be increased indefinitely. Therefore, the wire is typically arranged in a large area meander line [90], as shown in Fig. 9, shaping the detector profile to be more consistent with focused optical beams. Furthermore, it has been indicated that thinner films typically offer higher detection efficiencies since the diameter of the hot spot generated by an incident photon is inversely dependent on the thickness so that limitations on the uniformity of the NbN stripe are eased [90].

There has been an ongoing drive to improve the detection efficiency of superconducting nanowire detectors. The interaction length between the incident photons and the detector can be increased by means of an integrated wave guide [91]. This has the effect of increasing the probability that a photon will be absorbed by the nanowire and, hence, the detection efficiency [86]. Additionally, integrated wave guides offer the prospect of more efficient coupling to other wave guide-based optical circuits in, for example, quantum information applications. One of the most commonly used materials for SNSPDs has been NbN [92]; however, other materials are being investigated.

The detection efficiency of a SNSPD depends on the absorption of incident photons in the meander wire (the probability of which increases with the thickness) and the probability that an absorbed photon induces the formation of a resistive state in the nanowire (which increases with decreasing cross-sectional area).

Therefore, a thicker NbN film needs to be patterned with a thinner wire to increase the detection efficiency. The superconducting properties of polycrystalline NbN depend on the crystal phase of the films and are affected by crystal defects which limit the choice of growth substrates, the achievable designs, and the yield of devices. Other superconducting materials, such as WSi, are homogenously disordered and therefore offer the prospect of nanowires that are more robust against structural defects, permitting the fabrication of devices on a wider range of substrates. A further advantage of using WSi with respect to NbN is that WSi has a smaller superconducting band energy leading to higher sensitivity at longer wavelengths. By developing a $W_{0.75}Si_{0.25}$ nanowire detector on a Si substrate [93], a team from the National Institute of Standards and Technology (NIST) has achieved 93 % detection efficiency at a wavelength of 1.55 μm with a dark count rate of 1 s^{-1}, leading to an NEP of 1.9×10^{-19} $WHz^{-½}$.

The detection efficiency of nanowire detectors can also be enhanced by placing the nanowire in an optical resonant cavity [94]. One approach is to form a cavity of this type by using an external mirror and the surface of the substrate on which the detector was grown [95]. In 2006 Rosfjord et al. demonstrated a detection efficiency of 57 % for a 100 nm wide and 4 nm thick NbN wire in cavity formed from the substrate and an external Ti/Au mirror, at a wavelength of 1.55 μm and an operating temperature of 1.8 K [95]. In 2010, Tanner et al. demonstrated an NbTiN SNSPD grown on an SiO_2 buffer layer which formed a cavity with the polished end of the input optical fiber, leading to an NEP of 2.9×10^{-17} $WHz^{-½}$ at a wavelength of 1.31 μm [96]. A detection efficiency of up to 90 % can theoretically be reached for a 20 nm wide and 10 nm thick NbN-based SNSPD at a wavelength of 1.55 μm, as shown by simulations conducted by Marsili et al. [97].

Cavity-enhanced SNSPDs have been successfully utilized in several recent experiments requiring efficient single-photon detection at wavelengths above 1 μm. In 2013 an NbTiN SNSPD in a resonant cavity geometry with an NEP of 3.2×10^{-17} $WHz^{-½}$ at a wavelength of 1.56 μm was employed in a low-optical-power 50 MHz clock rate kilometer range time-of-flight laser ranging system [98]. Also in 2013 a cavity-enhanced NbTiN SNSPD was used to detect $^1O_2$ luminescence at a wavelength of 1270 nm and an NEP of 8.6×10^{-18} $WHz^{-½}$, a 20-fold improvement over the PMTs previously employed [99]. A 10.7 GHz clock rate quantum key distribution system based on a twin element SNSPD was presented by Dauler et al. in 2010 and achieved a sifted bit rate of 4 $Mbits^{-1}$ [100]. The single detector consisted of two nanowire meander elements, each having a detection efficiency of 31 ± 3 % at a wavelength of 1.55 μm, arranged such that each element comprised a half circle of diameter 7 μm.

Increasingly, there has been research into the development of arrayed superconducting nanowire detectors. Arranging the detectors in such a configuration can offer a large active area, improved spatial resolution [101], and "pseudo" photon number resolution that only resolve individual photons if they are incident on separate nanowires.

In 2007 Smirnov et al. reported one of the earliest SNSPD arrays, a 4 pixel NbN detector array arranged in 2×2 grid [102]. Each single detector pixel was a 10×10 μm square containing a 100 nm to 120 nm wide meander wire with a

60–70 % fill factor and a wire thickness of 4 nm. Although the dark count rate and detection efficiency of this device varied with driving current and operating temperature, the best quantum efficiency was 32 % for a wavelength of 1.3 μm, an operating temperature of 1.8 k, and a bias current of ~25 μA. The reported dark count rate was 0.1 s^{-1}, leading to an NEP of 2.1×10^{-19} $WHz^{-½}$.

In 2014 Miki et al. demonstrated a 64 pixel NbTiN superconducting nanowire array. The array was composed of an 8×8 grid of 5×5 μm meander lines arranged with a spacing of 3.4 μm to cover an area of 63×63 μm. Each individual nanowire detector was 5 nm thick and formed into wires 100 nm wide with 100 nm spacing across the 5×5 μm square. It is difficult to quote an NEP for this device as one complete module since each pixel exhibited an individual dependence of detection efficiency on bias current and the dark count rate was not quoted. If we consider a median bias current of 13.5 μA, then it was calculated by Miki et al. that 60 of the 64 pixels themselves had detection efficiency above 90 % before system losses were taken into account.

The low temperature required for operation of these single-photon detectors (typically an absolute maximum in the region 10–20 K and usually far lower of the order of a few Kelvin) means that these detectors require cryogenic cooling to operate. These systems can either be bulky systems operating using liquid cryogens (such as liquid helium) or somewhat more compact systems using cryogen-free refrigerator systems.

8 Upconversion to Higher Photon Energies

One possible way of detecting single photons in the 1–1.7 μm range is to convert them into photons with energies compatible with detectors designed for shorter wavelengths, such as those described in the preceding chapter of this book. This can be achieved by means of a process called parametric upconversion – the conversion of light with one wavelength into light with a shorter wavelength (higher energy) by means of sum frequency generation when incident with a strong pump beam in a crystal of a quadratic nonlinear medium. The conservation of energy and momentum states that the output photon must have an energy which is equal to the sum of the input photon and pump, that is to say:

$$\begin{aligned} E_{\text{Output}} &= E_{\text{Input}} + E_{\text{Pump}}, \\ \text{or } \upsilon_{\text{Output}} &= \upsilon_{\text{Input}} + \upsilon_{\text{Pump}}, \\ \text{or } \frac{1}{\lambda_{\text{Output}}} &= \frac{1}{\lambda_{\text{Input}}} + \frac{1}{\lambda_{\text{Pump}}}, \end{aligned} \tag{2}$$

where E denotes energy, υ frequency, and λ wavelength. A more rigorous mathematical analysis of the process may be found in Chap. 5 of [103].

Such an approach does not have a unity probability of converting the input photons into lower wavelength output photons. The process of upconversion has issues of photons from the pump beam being transmitted through the crystal to the

detector or unconverted input photons passing through the crystal to the detectors. It is possible to spectrally separate these undesired photons from the upconverted photons by the use of narrow wavelength band-pass filters, although physical imperfections mean that the transmission of photons of the converted wavelength will also be reduced. It may be possible to change the wavelength of the pump so that it corresponds to a spectral region where the single-photon detector has low detection efficiency. However, changes to the pump wavelength result in changes to the wavelength output to the single-photon detectors, as outlined in Eq. (2), and these may be sufficient to also move the output photon wavelength into a region where the detectors have low efficiency.

In 2004, Albota and Wong demonstrated the conversion of incident photons with a wavelength of 1,548 μm into photons with a wavelength of 631 nm by means of a periodically poled lithium niobate (PPLN) crystal and a pump of wavelength 1,064 μm delivered from a Nd:YAG laser, as shown in Fig. 10. These shorter wavelength photons were then detected using a silicon SPAD. The silicon absorption edge occurs at a wavelength of 1.1 μm so the upconverted photon must have a shorter wavelength than this limit. The conversion efficiency could be altered by changing the pump power, with higher pump powers typically giving higher conversion efficiencies but also higher background counts from stray pump photons. For a pump power of approximately 22 W, they achieved a detection efficiency of approximately 20 % and a background count rate of around 4.85×10^5 counts per second. The required phase-matching conditions meant that the phase-matching bandwidth was 0.3 nm for the weak input beam, a restriction we shall address later.

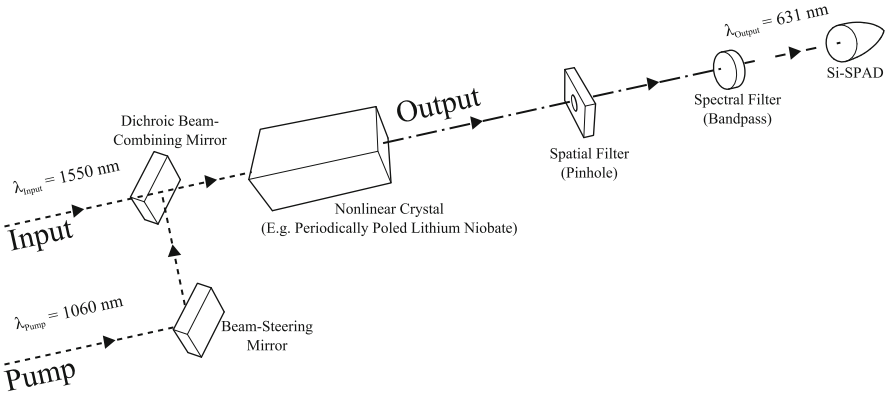

Fig. 10 A possible scheme for upconversion of photons with a wavelength of 1.55 μm into photons with a wavelength of 631 nm which are suitable for detection using silicon single-photon avalanche diodes (Si-SPADs). The Input and Pump are made coaxial by a dichroic beam combining mirror that only reflects the pump wavelength of 1060 nm. Conversion from the higher wavelength to the lower takes place in the nonlinear crystal (e.g. periodically poled lithium niobate). The spatial and spectral filter serve to ensure that only the 631 nm wavelength photons are incident on the Si-SPAD (this scheme is based on that reported by Albota et al. in 2004 [104])

In 2013, Shentu et al. published a system detecting 1.55 μm wavelength light with an overall detection efficiency of 15 % and a noise count rate of 25 s^{-1} for a 58 mW pump or a detection efficiency of 28.6 % and a noise count rate of 100 s^{-1} for a 20 mW pump [105]. This detector was also integrated into an upconversion infrared spectrometer with a quoted NEP of 6.3×10^{-18} $WHz^{-½}$.

The nonlinear conversion process means that upconversion systems typically have a narrow acceptance bandwidth at the input, as mentioned earlier. Although there is some scope for temperature tuning of the crystal, this is a slow process and the accuracy of the wavelength selection depends on the accuracy and stability of the temperature selection. In 2008, Thew et al. demonstrated a tunable upconversion system which offered a tenfold increase in the detectable bandwidth [106]. This system employed a pump composed of a fiber-coupled 980 nm wavelength laser diode with an external cavity formed from a fiber Bragg grating. Physically stretching the fiber resulted in a change in the length of the cavity and hence the pump laser wavelength. Since the accepted input signal wavelength is determined by the pump wavelength and the quasiphase-matching condition of the nonlinear crystal, an alteration in the pump wavelength means that the accepted input signal wavelength also changes. Practical physical limitations of the system meant that Thew et al. were unable to select from a full spectral band of input wavelengths and had to choose from a series of discrete wavebands [106].

9 Conclusions

In this chapter we have provided a summary of the evolution and current status of single-photon detectors for use in the wavelength range 1–1.7 μm. A summary of the main technologies and selected examples of applications have been presented. The impetus of existing applications for efficient and convenient detectors of photon in this wavelength band has driven the development of such detectors. Efficient detection of photons with wavelengths of approximately 1.55 μm is important for applications requiring compatibility with the existing telecommunications optical fiber infrastructure, as well as providing a low loss and low solar background window for free-space optical communication and photon-counting laser ranging and depth imaging.

Perhaps the most promising candidate for room temperature single-photon detectors at these wavelengths at present is InGaAs/InP SPADs. Work in Ge-based devices has shown promise but is currently at a low level of technical maturity compared with InGaAs/InP SPADs. Low-temperature superconducting detectors, particularly nanowires, show exciting potential for numerous application areas were the additional cooling is not a disadvantage. As new single-photon detector technologies are developed and existing approaches are refined, new application areas will be identified that require different operating parameters, further driving the development and refinement of single-photon detectors for use at these wavelengths.

Acknowledgments The authors thank Nick Buttenshaw at Hamamatsu Photonics UK Limited for the information contained in Fig. 1.

References

1. Minoli D (2003) Telecommunication technology handbook, 2nd edn. Artech House, Norwood. ISBN 1-58053-528-3
2. Levine BF, Bethea CG, Campbell JC (1985) Room-temperature 1.3-μm optical time domain reflectometer using a photon counting InGaAs/InP avalanche detector. Appl Phys Lett 46:333–335. doi:10.1063/1.95622
3. Bouwmeester D, Ekert A, Zeilinger A (2000) The physics of quantum information: quantum cryptography, quantum teleportation, quantum computation, 1st edn. Springer, Berlin. ISBN 978-3-642-08607-6
4. Hiskett PA, Rosenberg D, Peterson CG et al (2006) Long-distance quantum key distribution in optical fibre. New J Phys 8:193–197. doi:10.1088/1367-2630/8/9/193
5. Clarke PJ, Collins RJ, Hiskett PA et al (2011) Analysis of detector performance in a gigahertz clock rate quantum key distribution system. New J Phys 13:075008. doi:10.1088/1367-2630/13/7/075008
6. Buller GS, Wallace AM (2007) Ranging and three-dimensional imaging using and point-by-point acquisition. IEEE J Sel Top Quantum Electron 13:1006–1015. doi:10.1109/JSTQE.2007.902850
7. Rothman LS, Jacquemart D, Barbe A et al (2005) The HITRAN 2004 molecular spectroscopic database. J Quant Spectrosc Radiat Transf 96:139–204. doi:10.1016/j.jqsrt.2004.10.008
8. Voke J (1999) Radiation effects on the eye part 1: infrared radiation effects on ocular tissue. Optom Today 39:22–28
9. Willson RC (2003) Secular total solar irradiance trend during solar cycles 21–23. Geophys Res Lett 30:1199. doi:10.1029/2002GL016038
10. Kuenzer C, Dech S (2013) Thermal infrared remote sensing: sensors, methods, applications, 1st edn. Springer, Berlin. ISBN 978-94-007-6638-9
11. Mallidi S, Larson T, Tam J et al (2009) Multiwavelength photoacoustic imaging and plasmon resonance coupling of gold nanoparticles for selective detection of cancer. Nano Lett 9:2825–2831. doi:10.1021/nl802929u
12. Schweitzer C, Schmidt R (2003) Physical mechanisms of generation and deactivation of singlet oxygen. Chem Rev 103:1685–1757. doi:10.1021/cr010371d
13. Jue T, Masuda K (2013) Application of near infrared spectroscopy in biomedicine, 1st edn. Springer, Berlin. ISBN 978-1-4614-6251-4
14. Buller GS, Collins RJ (2010) Single-photon generation and detection. Meas Sci Technol 21:012002. doi:10.1088/0957-0233/21/1/012002
15. Bülter A (2014) Single-photon counting detectors for the visible range between 300 and 1000 nm. In: Kapusta P et al. (eds) Advanced photon counting: applications, methods, instrumentation. Springer series on fluorescence. Springer International Publishing, doi:10.1007/4243_2014_63
16. Kang Y, Lu HX, Lo Y-H et al (2003) Dark count probability and quantum efficiency of avalanche photodiodes for single-photon detection. Appl Phys Lett 83:2955–2957. doi:10.1063/1.1616666
17. Jones R (1959) Phenomenological description of the response and detecting ability of radiation detectors. Proc IRE 47:937–938. doi:10.1109/JRPROC.1959.287047

18. Spinelli A, Davis LM, Dautet H (1996) Actively quenched single-photon avalanche diode for high repetition rate time-gated photon counting. Rev Sci Instrum 67:55–61. doi:10.1063/1.1146551
19. Morton GA (1949) Photomultipliers for scintillation counting. RCA Rev 10:525–553
20. Hammatsu Data Sheet (2005) Low-light-level measurement of NIR: NIR (near infrared: 1.4 μm/1.7 μm) photomultiplier tubes R5509-43/R5509-73 and exclusive coolers
21. Greenblatt M (1958) On the measurement of transit time dispersion in multiplier phototubes. IRE Trans Nucl Sci 5:13–16. doi:10.1109/TNS2.1958.4315600
22. Becker W (2005) Advanced time-correlated single photon counting techniques, 1st edn. Springer, Berlin. ISBN 3-540-62047-1
23. Akgun U, Ayan AS, Aydin G et al (2008) Afterpulse timing and rate investigation of three different Hamamatsu Photomultiplier Tubes. J Instrum 3, T01001. doi:10.1088/1748-0221/3/01/T01001
24. Pellegrini S, Warburton RE, Tan LJJ et al (2006) Design and performance of an InGaAs-InP single-photon avalanche diode detector. IEEE J Quantum Electron 42:397–403. doi:10.1109/JQE.2006.871067
25. Biard J, Shaunfield WN (1967) A model of the avalanche photodiode. IEEE Trans Electron Dev 14:233–238. doi:10.1109/T-ED.1967.15936
26. Antypas GA, Moon RL, James LW et al (1972) III-V quaternary alloys. In: Hilsum C (ed) International symposium on gallium arsenide and related compounds. Institute of Physics, pp 48–54
27. Hiskett PA, Buller GS, Loudon AY et al (2000) Performance and design of InGaAs/InP photodiodes for single-photon counting at 1.55 um. Appl Opt 39:6818–6829. doi:10.1364/AO.39.006818
28. Smith JM, Hiskett PA, Buller GS (2001) Picosecond time-resolved photoluminescence at detection wavelengths greater than 1500 nm. Opt Lett 26:731–733. doi:10.1364/OL.26.000731
29. Xiao Y, Bhat I, Abedin MN (2005) Performance dependences on multiplication layer thickness for InP/InGaAs avalanche photodiodes based on time domain modeling. Proc SPIE 5881, infrared photoelectron imagers detect devices 5881:58810R–58810R–10. doi:10.1117/12.615057
30. Restelli A, Bienfang JC, Migdall AL (2012) Time-domain measurements of afterpulsing in InGaAs/InP SPAD gated with sub-nanosecond pulses. J Mod Opt 59:1465–1471. doi:10.1080/09500340.2012.687463
31. Ben-Michael R, Itzler MA., Nyman B, Entwistle M (2006) Afterpulsing in InGaAs/InP single photon avalanche photodetectors. In: 2006 digest of the LEOS summer topical meetings IEEE, Quebec City, Quebec, Canada, pp 15–16
32. Itzler MA, Jiang X, Entwistle M (2012) Power law temporal dependence of InGaAs/InP SPAD afterpulsing. J Mod Opt 59:1472–1480. doi:10.1080/09500340.2012.698659
33. Tosi A, Della Frera A, Shehata AB, Scarcella C (2012) Fully programmable single-photon detection module for InGaAs/InP single-photon avalanche diodes with clean and sub-nanosecond gating transitions. Rev Sci Instrum 83:013104. doi:10.1063/1.3675579
34. Cova S, Ghioni M, Lacaita A et al (1996) Avalanche photodiodes and quenching circuits for single-photon detection. Appl Opt 35:1956–1976. doi:10.1364/AO.35.001956
35. Cova S, Longoni A, Ripamonti G (1982) Active-quenching and gating circuits for single-photon avalanche diodes (SPADS). IEEE Trans Nucl Sci 29:599–601. doi:10.1109/TNS.1982.4335917
36. Warburton RE, Itzler MA, Buller GS (2009) Improved free-running InGaAs/InP single-photon avalanche diode detectors operating at room temperature. Electron Lett 45:996–997. doi:10.1049/el.2009.1508
37. Acerbi F, Tosi A, Zappa F (2013) Dark count rate dependence on bias voltage during gate-OFF in InGaAs/InP single-photon avalanche diodes. IEEE Photonics Technol Lett 25:1832–1834. doi:10.1109/LPT.2013.2277555

38. Liu M, Hu C, Campbell JC et al (2008) Reduce afterpulsing of single photon avalanche diodes using passive quenching with active reset. IEEE J Quantum Electron 44:430–434. doi:10.1109/JQE.2007.916688
39. Warburton RE, Itzler M, Buller GS (2009) Free-running, room temperature operation of an InGaAs/InP single-photon avalanche diode. Appl Phys Lett 94:071116. doi:10.1063/1.3079668
40. Cova S, Longoni A, Anderoni A (1981) Towards picosecond resolution with single-photon avalanche diodes. Rev Sci Instrum 52:408. doi:10.1063/1.1136594
41. Acerbi F, Frera A, Della TA, Zappa F (2013) Fast active quenching circuit for reducing avalanche charge and afterpulsing in InGaAs/InP single-photon avalanche diode. IEEE J Quantum Electron 49:563–569. doi:10.1109/JQE.2013.2260726
42. Bronzi D, Tisa S, Villa F et al (2013) Fast sensing and quenching of CMOS SPADs for minimal afterpulsing effects. IEEE Photonics Technol Lett 25:776–779. doi:10.1109/LPT.2013.2251621
43. Zhang J, Thew R, Gautier J-D et al (2009) Comprehensive characterization of InGaAs–InP avalanche photodiodes at 1550 nm with an active quenching ASIC. IEEE J Quantum Electron 45:792–799. doi:10.1109/JQE.2009.2013210
44. Ribordy G, Gautier JD, Zbinden H, Gisin N (1998) Performance of InGaAs/InP avalanche photodiodes as gated-mode photon counters. Appl Opt 37:2272–2277. doi:10.1364/AO.37.002272
45. Stucki D, Ribordy G, Stefanov A et al (2001) Photon counting for quantum key distribution with Peltier cooled InGaAs/InP APDs. J Mod Opt 48:1967–1981, doi:10.1080/09500340108240900
46. Yuan ZL, Sharpe AW, Dynes JF et al (2010) Multi-gigahertz operation of photon counting InGaAs avalanche photodiodes. Appl Phys Lett 96:071101. doi:10.1063/1.3309698
47. Tomita A, Nakamura K (2002) Balanced, gated-mode photon detector for quantum-bit discrimination at 1550 nm. Opt Lett 27:1827–1829. doi:10.1364/OL.27.001827
48. Namekata N, Sasamori S, Inoue S (2006) 800 MHz single-photon detection at 1550-nm using an InGaAs/InP avalanche photodiode operated with a sine wave gating. Opt Express 14:10043–10049. doi:10.1364/OE.14.010043
49. Walenta N, Lunghi T, Guinnard O et al (2012) Sine gating detector with simple filtering for low-noise infra-red single photon detection at room temperature. J Appl Phys 112:063106. doi:10.1063/1.4749802
50. Liang Y, Wu E, Chen X et al (2011) Low-timing-jitter single-photon detection using 1-GHz sinusoidally gated InGaAs/InP avalanche photodiode. IEEE Photonics Technol Lett 23:887–889. doi:10.1109/LPT.2011.2141982
51. Ren M, Gu X, Liang Y et al (2011) Laser ranging at 1550 nm with 1-GHz sine-wave gated InGaAs/InP APD single-photon detector. Opt Express 19:13497–13502. doi:10.1364/OE.19.013497
52. Zhang J, Thew R, Barreiro C, Zbinden H (2009) Practical fast gate rate InGaAs/InP single-photon avalanche photodiodes. Appl Phys Lett 95:91103. doi:10.1063/1.3223576
53. Kardynał BE, Yuan ZL, Shields AJ (2008) An avalanche-photodiode-based photon-number-resolving detector. Nat Photonics 2:425–428. doi:10.1038/nphoton.2008.101
54. Chen X, Wu E, Xu L et al (2009) Photon-number resolving performance of the InGaAs/InP avalanche photodiode with short gates. Appl Phys Lett 95:131118. doi:10.1063/1.3242380
55. Zhao K, You S, Cheng J, Lo Y (2008) Self-quenching and self-recovering InGaAs/InAlAs single photon avalanche detector. Appl Phys Lett 93:153504. doi:10.1063/1.3000610
56. Lunghi T, Barreiro C, Guinnard O et al (2012) Free-running single-photon detection based on a negative feedback InGaAs APD. J Mod Opt 59:1481–1488. doi:10.1080/09500340.2012.690050
57. Itzler MA, Entwistle M, Owens M, et al. (2010) Geiger-mode avalanche photodiode focal plane arrays for three-dimensional imaging LADAR. In: Strojnik M, Paez G (eds)

Proceedings of SPIE. 7808, infrared remote sensing and instrumentation XVIII. SPIE, San Diego, p 78080C
58. Yuan P, Sudharsanan R, Bai X, et al (2010) 32 × 32 Geiger-mode LADAR cameras. In: Turner MD, Kamerman GW (eds) Proceedings of SPIE 7684, laser radar technology and applications XV. SPIE, Orlando, p 76840C
59. Korzh B, Walenta N, Houlmann R, Zbinden H (2013) A high-speed multi-protocol quantum key distribution transmitter based on a dual-drive modulator. Opt Express 21:19579–19592. doi:10.1364/OE.21.019579
60. Lacaita A, Francese PA, Zappa F, Cova S (1994) Single-photon detection beyond 1 μm: performance of commercially available germanium photodiodes. Appl Opt 33:6902–6918. doi:10.1364/AO.33.006902
61. Luryi S, Pearsall TP, Temkin H, Bean JC (1986) Waveguide infrared photodetectors on a silicon chip. IEEE Electron Device Lett 7:104–107. doi:10.1109/EDL.1986.26309
62. Lang DV, People R, Bean JC, Sergent AM (1985) Measurement of the band gap of GexSi1−x/Si strained-layer heterostructures. Appl Phys Lett 47:1333. doi:10.1063/1.96271
63. Loudon AY, Hiskett PA, Buller GS et al (2002) Enhancement of the infrared detection efficiency of silicon photon-counting avalanche photodiodes by use of silicon germanium absorbing layers. Opt Lett 27:219–221. doi:10.1364/OL.27.000219
64. Schneider H, Liu HC (2007) Quantum well infrared photodetectors: physics and applications, 1st edn. Springer, Berlin, Germany. ISBN 978-3-540-36323-1
65. Shah VA, Dobbie A, Myronov M, Leadley DR (2011) Effect of layer thickness on structural quality of Ge epilayers grown directly on Si(001). Thin Solid Films 519:7911–7917. doi:10.1016/j.tsf.2011.06.022
66. Warburton RE, Intermite G, Myronov M et al (2013) Ge-on-Si single-photon avalanche diode detectors: design, modeling, fabrication, and characterization at wavelengths 1310 and 1550 nm. IEEE Trans Electron Dev 60:3807–3813. doi:10.1109/TED.2013.2282712
67. Yuan P, Anselm KA, Hu C (1999) A new look at impact ionization-part II: gain and noise in short avalanche photodiodes. IEEE Trans Electron Dev 46:1632–1639. doi:10.1109/16.777151
68. Zrenner A (2000) A close look on single quantum dots. J Chem Phys 112:7790. doi:10.1063/1.481384
69. Michler P (2009) Single semiconductor quantum dots, 1st edn. Springer, Berlin, Germany. ISBN 978-3-540-87446-1
70. Blakesley JC, See P, Shields AJ et al (2005) Efficient single photon detection by quantum dot resonant tunneling diodes. Phys Rev Lett 94:67401. doi:10.1103/PhysRevLett.94.067401
71. Li HW, Kardynal BE, See P et al (2007) Quantum dot resonant tunneling diode for telecommunication wavelength single photon detection. Appl Phys Lett 91:73513–73516. doi:10.1063/1.2768884
72. Hees SS, Kardynal BE, See P et al (2006) Effect of InAs dots on noise of quantum dot resonant tunneling single-photon detectors. Appl Phys Lett 89:153510. doi:10.1063/1.2362997
73. Stranski IN, Krastanow L (1938) Zur theorie der orientierten Ausscheidung von Ionenkristallen aufeinander. Sitzungsberichte der Akad der Wiss Wien 146:797–804
74. Markov I, Stoyanov S (1987) Mechanisms of epitaxial growth. Contemp Phys 28:267–320. doi:10.1080/00107518708219073
75. Leonard D, Pond K, Petroff PM (1994) Critical layer thickness for self-assembled InAs islands on GaAs. Phys Rev B 50:11687–11692. doi:10.1103/PhysRevB.50.11687
76. Hott R, Kleiner R, Wolf T, Zwicknagl G (2005) Superconducting materials – a topical overview. In: Narlikar AV (ed) Frontiers in supercondinting materials, 1st edn. Springer, Berlin, pp 1–69. doi:10.1007/3-540-27294-1_1. ISBN 978-3-540-24513-1
77. Bennemann KH, Ketterson JB (2008) Superconductivity: conventional and unconventional superconductors, 1st edn. Springer, Berlin. ISBN 978-3-540-73252-5

78. Onnes HK (1911) Further experiments with liquid helium C On the change of electrical resistance of pure metals at very low temperatures etc IV The resistance of pure mercury at helium temperatures. Commun from Phys Lab Univ Leiden 120B:2–5
79. Cardwell DA (1991) High-temperature superconducting materials. In: Electronic materials: from silicon to organics, 1st edn. Springer, Berlin, pp 417–430. doi: 10.1007/978-1-4615-3818-9_28, ISBN 978-1-4613-6703-1
80. Cabrera B, Clarke RM, Colling P et al (1998) Detection of single infrared, optical, and ultraviolet photons using superconducting transition edge sensors. Appl Phys Lett 73:735–737. doi:10.1063/1.121984
81. Irwin KD, Nam SW, Cabrera B et al (1995) A quasiparticle-trap-assisted transition-edge sensor for phonon-mediated particle detection. Rev Sci Instrum 66:5322–5326. doi:10.1063/1.1146105
82. Iyomoto N, Bandler SR, Brekosky RP et al (2008) Close-packed arrays of transition-edge x-ray microcalorimeters with high spectral resolution at 5.9 keV. Appl Phys Lett 92:013508
83. Irwin KD, Hilton GC, Wollman DA, Martinis JM (1996) X-ray detection using a superconducting transition-edge sensor microcalorimeter with electrothermal feedback. Appl Phys Lett 69:1945. doi:10.1063/1.117630
84. Lita AE, Miller AJ, Nam SW (2008) Counting near-infrared single-photons with 95 % efficiency. Opt Express 16:3032–3040. doi:10.1364/OE.16.003032
85. Lita AE, Rosenberg D, Nam S et al (2005) Tuning of tungsten thin film superconducting transition temperature for fabrication of photon number resolving detectors. IEEE Trans Applied Supercond 15:3528–3531. doi:10.1109/TASC.2005.849033
86. Natarajan CM, Tanner MG, Hadfield RH (2012) Superconducting nanowire single-photon detectors: physics and applications. Supercond Sci Technol 25:063001. doi:10.1088/0953-2048/25/6/063001
87. Gol'tsman GN, Okunev O, Chulkova G et al (2001) Picosecond superconducting single-photon optical detector. Appl Phys Lett 79:705–707. doi:10.1063/1.1388868
88. Kadin AM, Johnson MW (1996) Nonequilibrium photon-induced hotspot: a new mechanism for photodetection in ultrathin metallic films. Appl Phys Lett 69:3938–3940. doi:10.1063/1.117576
89. Gol'tsman GN, Semenov AD, Gousev YP et al (1991) Sensitive picosecond NbN detector for radiation from millimetre wavelengths to visible light. Supercond Sci Technol 4:453–456. doi:10.1088/0953-2048/4/9/020
90. Verevkin A, Zhang J, Sobolewski R et al (2002) Detection efficiency of large-active area NbN single-photon superconducting detectors in the ultraviolet to near-infrared range. Appl Phys Lett 80:4687–4689. doi:10.1063/1.1487924
91. Ghamsari BG, Majedi AH (2008) Superconductive traveling-wave photodetectors: fundamentals and optical propagation. IEEE J Quantum Electron 44:667–675. doi:10.1109/JQE.2008.922409
92. Il'in KS, Lindgren M, Currie M et al (2000) Picosecond hot-electron energy relaxation in NbN superconducting photodetectors. Appl Phys Lett 76:2752. doi:10.1063/1.126480
93. Marsili F, Verma VB, Stern JA et al (2013) Detecting single infrared photons with 93 % system efficiency. Nat Photonics 7:210–214. doi:10.1038/nphoton.2013.13
94. Gol'tsman G, Minaeva O, Korneev A et al (2007) Middle-infrared to visible-light ultrafast superconducting single-photon detectors. IEEE Trans Appl Supercond 17:246–251. doi:10.1109/TASC.2007.898252
95. Rosfjord KM, Yang JKW, Dauler EA et al (2006) Nanowire single-photon detector with an integrated optical cavity and anti-reflection coating. Opt Express 14:527–534. doi:10.1364/OPEX.14.000527
96. Tanner MG, Natarajan CM, Pottapenjara VK et al (2010) Enhanced telecom wavelength single-photon detection with NbTiN superconducting nanowires on oxidized silicon. Appl Phys Lett 96:221109. doi:10.1063/1.3428960

97. Marsili F, Najafi F, Dauler E, et al. (2012) Cavity-integrated ultra-narrow superconducting nanowire single-photon detector based on a thick niobium nitride film. Quantum electronics and laser science conference, Optical Society of America, San Jose, p QTu3E. doi:10.1364/QELS.2012.QTu3E.3
98. McCarthy A, Krichel N, Gemmell N (2013) Kilometer-range, high resolution depth imaging via 1560 nm wavelength single-photon detection. Opt Express 21:8904–8915. doi:10.1364/OE.21.008904
99. Gemmell NR, McCarthy A, Liu B et al (2013) Singlet oxygen luminescence detection with a fiber-coupled superconducting nanowire single-photon detector. Opt Express 21:5005–5013. doi:10.1364/OE.21.005005
100. Dauler EA, Spellmeyer NW, et al. (2010) High-rate quantum key distribution with high-rate quantum key distribution with superconducting nanowire single photon detectors. Quantum electronics and laser science conference, Optical Society of America, San Jose, p QTHI2. ISBN 978-1-55752-890-2
101. Dauler EA, Robinson BS, Kerman AJ et al (2007) Multi-element superconducting nanowire single-photon detector. IEEE Trans Appl Supercond 17:279–284. doi:10.1109/TASC.2007.897372
102. Smirnov K, Korneev A, Minaeva O et al (2007) Ultrathin NbN film superconducting single-photon detector array. J Phys Conf Ser 61:1081–1085. doi:10.1088/1742-6596/61/1/214
103. Hull R, Parisi J, Osgood RM Jr et al (2005) Spectroscopic properties of rare earths in optical materials, 1st edn. Springer, Berlin, Germany. ISBN 978-3-540-23886-7
104. Albota MA, Wong FNC (2004) Efficient single-photon counting at 1.55 μm by means of frequency upconversion. Opt Lett 29:1449–1451. doi:10.1364/OL.29.001449
105. Shentu G, Pelc J, Wang X (2013) Ultralow noise up-conversion detector and spectrometer for the telecom band. Opt Express 21:1449–1451. doi:10.1364/OE.21.013986
106. Thew RT, Zbinden H, Gisin N (2008) Tunable upconversion photon detector. Appl Phys Lett 93:71103–71104. doi:10.1063/1.2969067

Modern Pulsed Diode Laser Sources for Time-Correlated Photon Counting

Thomas Schönau, Sina Riecke, Andreas Bülter, and Kristian Lauritsen

Abstract Time-correlated single-photon counting applications require pulsed excitation sources at various wavelengths from the UV to the IR that feature a short pulse width (usually picoseconds or femtoseconds) as well as repetition rates in the kilohertz to megahertz range. The repetition rate should ideally be tunable in order to adapt the pulse period to the required measurement window. In the blue, red, and IR spectral range, such pulses with energies of up to 100 pJ can be readily provided by single gain-switched laser diodes which can be housed in compact and robust packages. Laser pulses in the UV or green-yellow spectral range are, however, not directly accessible and require more elaborate setups that are based on power amplification and frequency conversion. An alternative excitation source that has also become popular in the recent years is the supercontinuum laser as it gives direct access to a broad wavelength spectrum that spans from the blue to the IR.

This chapter provides an overview about the fundamental aspects and parameters of pulsed diode lasers as well as a short introduction into pulsed LEDs and supercontinuum lasers that are usually used for time-correlated single-photon counting applications.

Keywords Gain switching · Pulsed diode laser · Pulsed LEDs · Supercontinuum laser

T. Schönau (✉), A. Bülter, and K. Lauritsen
PicoQuant GmbH, Rudower Chaussee 29, 12489 Berlin, Germany
e-mail: schoenau@picoquant.com

S. Riecke
ROFIN-SINAR Laser GmbH, Dieselstrasse 15, 85232 Bergkirchen, Germany

P. Kapusta et al. (eds.), *Advanced Photon Counting: Applications, Methods, Instrumentation*, Springer Ser Fluoresc (2015) 15: 71–88, DOI 10.1007/4243_2014_76,

Contents

1 Introduction 72
2 Diode Lasers 73
2.1 Introduction 73
2.2 Optical Confinement and Resonator Design 73
2.3 Gain Switching 74
2.4 Frequency Conversion 76
3 Sub-nanosecond Pulsed LED 80
4 Supercontinuum Generation 82
5 Summary 85
References 85

1 Introduction

When Theodore Maiman demonstrated the first laser in 1960, the device was famously called "a solution looking for a problem" by his assistant Irnee D'Haenens [1]. Since then, lasers have been developed at a multitude of wavelengths and power levels, and plenty of applications have been found, each requiring specific laser parameters. Often, the improvements of laser sources and applications have gone hand in hand, and the development of tailored light sources is an important direction of industrial and academic research even today.

One important application in the context of photon counting applications is the measurement of the fluorescence lifetime of a sample [2, 3]. In this method, a picosecond pulsed laser is used to excite fluorescence in, e.g., biological samples or semiconductors. In combination with a fast and sensitive single-photon counting system [4], this allows the measurement of the fluorescence decay lifetime, which is typically on the order of a few nanoseconds to some microseconds. For many fluorophores, this lifetime depends on the properties of the molecule's environment, such as pH value or Ca^{2+} concentration [5], and can thus be used to study sample properties or environmental influences.

For optimum fluorescence lifetime measurements, the excitation laser pulse has to be much shorter than the fluorescence decay time, typically below 200 ps, while the pulse intervals have to be much larger. In order to adjust the repetition rate to different lifetimes and to avoid damaging the sample by excessive illumination, variable excitation pulse repetition rates in the megahertz range are preferred [3]. For advanced methods, like pulse-interleaved excitation [5–7], even freely triggerable excitation pulses are needed. Required pulse energies are usually between 1 and 50 pJ.

Since the fluorescence has to be detected in the intervals between the excitation pulses, preferably no light should be emitted by the excitation laser between the two laser pulses. A high extinction ratio of typically above 40 dB (four orders of magnitude between pulse peak and signal level between pulses, already after

approximately one nanosecond later than peak position) is usually required to generate a suitable signal-to-noise ratio using common detectors [8, 9].

Laser pulses meeting these specifications can be readily provided by several laser types. The most common are gain-switched diode lasers, pulsed LEDs, supercontinuum lasers, and Ti:sapphire lasers. A detailed description of Ti:sapphire lasers is, however, beyond the scope of this chapter due to the many different technical realization schemes and resulting parameters of this laser type [10].

2 Diode Lasers

2.1 Introduction

Since the demonstration of the first laser diode consisting of a *p-n* monojunction in 1962 [11], semiconductor optoelectronics have advanced enormously. The first laser diodes had very low efficiency and were limited to pulsed operation at cryogenic temperatures due to heat dissipation problems. Today, modern diode lasers have the smallest size (only a few cubic millimeters including housing), highest efficiency (above 50%), and longest lifetime of all lasers.

In a semiconductor laser, optical gain is generated by recombination of electrons in the conduction band with holes in the valence band. All laser diodes therefore consist of direct bandgap semiconductors in order to enable efficient recombination. Positive gain develops in an active region, where there is a large occupation probability for both the electrons in the conduction band and the holes in the valence band.

The active region of modern laser diodes typically has a quantum well (QW) structure [12] (Fig. 1, left image). It contains very thin layers of a low-bandgap material enclosed by large-bandgap barriers. These quantum wells are able to capture both electrons and holes with good spatial overlap, which increases the laser efficiency. Moreover, the quantum wells are so thin that the momentum of electrons and holes becomes quantized in the direction perpendicular to the quantum well layer. This leads to a change in the density of states, which again increases laser efficiency.

2.2 Optical Confinement and Resonator Design

A functioning laser needs high gain as well as optical feedback and a good overlap between the optical mode and the active medium. In a monolithic laser diode, sufficient reflectivity ($R \approx 30\%$) can simply be provided by the cleaved facets of the semiconductor device which act as resonator mirrors. In modern high-power laser diodes, however, the facet reflectivity is typically optimized using dielectric

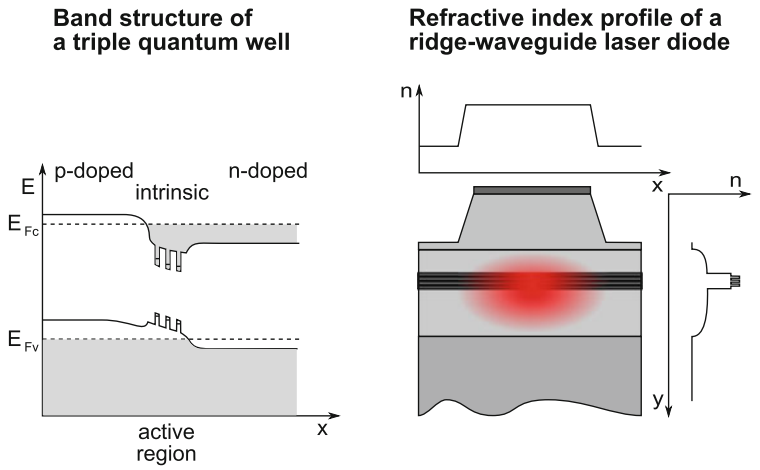

Fig. 1 Triple-quantum-well laser diode. *Left image*: band structure. *Right image*: refractive index profile, lateral confinement is provided by a ridge waveguide

coatings with a high reflectivity at the rear facet and a low reflectivity (down to 1%) at the front facet. Furthermore, the facets are passivated to protect them from optical damage and degradation [13]. This setup with two plane parallel resonator mirrors is called a Fabry-Pérot (FP) resonator [14].

A waveguide which supports only a single lateral mode is usually implemented via a ridge waveguide [14] (Fig. 1, right image). Even though the ridge trenches typically do not cut into the vertical waveguide, they influence the evanescent waves. The presence or absence of a semiconductor material above the waveguide alters the effective refractive index inside the waveguide, leading to lateral confinement. This allows for diffraction-limited beam quality which is required for efficient fiber coupling and small focus sizes. However, the optical mode is not perfectly circular and it exhibits different divergence angles in horizontal and vertical direction. Nevertheless, coupling efficiencies into single-mode optical fibers of 30–50% can be achieved, depending on laser diode type and nominal wavelength.

The continuous-wave output power of ridge waveguide laser diodes is limited to below 1 W. Higher average power level leads to increased risk of damaging the output facet, and also internal heating may degrade the semiconductor material.

2.3 Gain Switching

Time-correlated single-photon applications, especially in the life sciences, usually require pulsed excitation with a duration of less than 200 ps and a pulse energy of around 1–50 pJ. In order to adjust the pulse interval to the required measurement

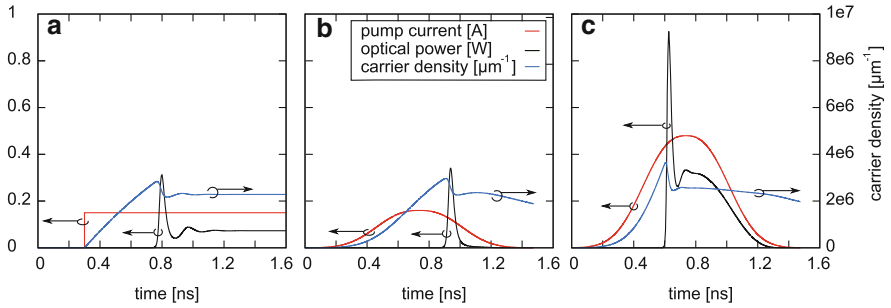

Fig. 2 Simulation of a gain-switched diode laser. In gain switching, the overshoot of the optical power during the first relaxation oscillation is exploited for the generation of short optical pulses. a) constant current supply with sudden onset creating optical relaxation oscillations b) tailored current pulse to create single optical pulse c) laser pulse exhibiting strong after pulse due to high current amplitude

window or for interleaving of excitation pulses at different wavelengths, pulses are required on demand and at variable repetition rates in the kilohertz to megahertz range. Such pulses can be readily generated by gain switching of single ridge waveguide laser diodes.

When a laser diode is disturbed during operation, for example, by a change in pump power, its output power does not transit smoothly to the new steady state. Instead, the laser exhibits relaxation oscillations and damped oscillations of the output power and the inversion density, leading to the new steady-state value [15, 16]. Particularly, pronounced relaxation oscillations appear when the pump power is suddenly switched on (Fig. 2a).

In gain switching, the overshoot of the optical power during the first relaxation oscillation is exploited for the generation of short optical pulses. For this, the pump power is quickly switched off after the first optical relaxation peak has been emitted (Fig. 2b). This yields a single optical pulse whose peak power can be many times higher than the laser's steady-state output power.

If the pump pulse amplitude is increased, the first relaxation oscillation is followed by a characteristic optical afterpulse, as the output power follows the remainder of the pump pulse (Figs. 2c and 3). In order to obtain both a symmetric optical pulse shape and a high peak power, short pump pulses are required [16]. Within the single-pulse regime, an increased pump pulse amplitude not only leads to a higher optical peak power but also to a decreased optical pulse duration [18].

Gain switching is particularly popular for diode lasers, where sub-nanosecond current pulses are required for pumping. In order to implement variable repetition rates between single shot and the upper megahertz range, single-current pulses can be generated by dedicated electrical circuits [15, 16]. Gain switching does not require any special resonator setup, and in principle, any laser diode can be used for gain switching. However, in reality, only carefully designed diodes yield sufficient pulse performance.

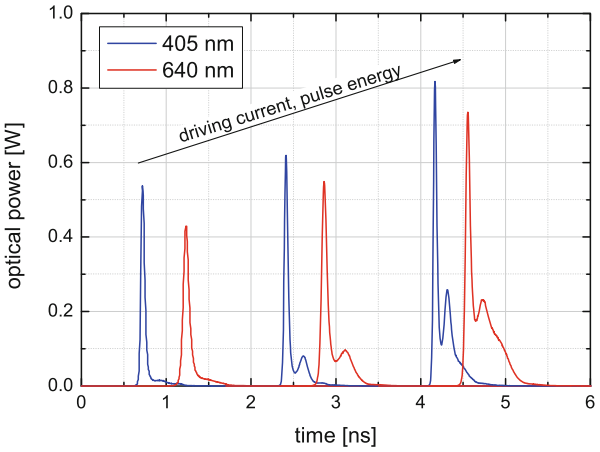

Fig. 3 Measured pulse shapes of typical gain-switched diode lasers [17] as a function of driving current. Pulse width (FWHM) of the first peak, i.e., the first relaxation oscillation at the highest driving current is 48 ps (405 nm) and 76 ps (640 nm). The optical after pulse at high driving currents is clearly visible

Today, gain-switched diode lasers can be provided in a broad wavelength range spanning from 375 up to 2,000 nm [17] with the notable exception of the yellow-green gap between 530 and 630 nm, where still no direct emitting laser diodes are available. These pulsed lasers emit pulses at variable repetition rates between single shot and 80 MHz or even 100 MHz with pulse energies up to a few 10 pJ, which correspond to average power levels of a few milliwatts at repetition rates in the megahertz range. The pulse widths achievable with gain-switched diode lasers are well below 100 ps and can even be as short as 40 ps for selected laser diodes. The spectral width of the laser output is typically in the range of 2–10 nm (FWHM). Due to the principle of gain switching, i.e., "pulses on demand," pulsed diode lasers can be freely triggered by external signals. This special feature makes these lasers especially suited for more complex excitation scenarios in which, for example, several laser wavelengths have to be combined in a single setup and pulsed in a defined sequence. This is useful for, e.g., pulsed-interleaved multicolor Förster resonance energy transfer (FRET) [19] or time-of-flight applications [20]. Even the combination of several interleaved laser wavelengths and burst pulse patterns is possible and is exploited in, e.g., diffuse optical imaging experiments [21]. Consequently, gain-switched diode lasers are the most suited excitation sources for many photon counting-based applications.

2.4 Frequency Conversion

Laser diodes in the green-yellow gap between 530 and 630 nm or below 375 nm are still not available today, although these wavelengths are of high interest for, e.g., spectroscopy of fluorescent proteins [22], NV defect centers in diamond [23], or spectroscopy of natural amino acids [24]. In order to gain access to this wavelength range, different schemes have been devised based on laser diode technology. The

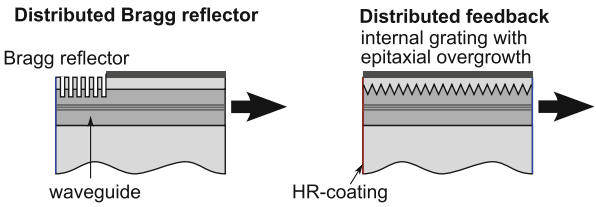

Fig. 4 Spectrally narrow diode lasers are typically implemented via an optical grating providing wavelength-selective feedback according to the Bragg condition

method of choice is harmonic generation or sum-frequency generation in a nonlinear crystal. As a fundamental laser source, this requires high-power infrared picosecond pulses with a narrow spectral line width of no larger than 200 pm and a peak power of at least several watts.

2.4.1 Narrow-Bandwidth Lasers

The generation of spectrally narrowband picosecond pulses is more challenging than the generation of narrowband continuous light. The selection of a single spectral mode is typically implemented via an optical grating providing wavelength-selective feedback according to the Bragg condition [25].

In a distributed Bragg-reflector (DBR) laser [26], the grating is separate from the gain section and acts as a passive resonator mirror (Fig. 4, left). In a distributed feedback (DFB) laser [25], the Bragg grating covers the whole resonator length and consequently needs to be electrically pumped (Fig. 4, right). The Bragg grating therefore needs to be overgrown epitaxially in order to achieve a smooth surface for metalization.

Even when using a DFB or DBR laser for gain switching, the reliable generation of pulses with high peak power and a narrow spectral width requires a careful choice of the operation and diode parameters. For example, a change in device temperature leads to a spectral shift of the material gain spectrum relative to the Bragg wavelength. If these are not well matched, the laser may have a single-mode spectrum under continuous operation, but in gain-switching mode, the high-power relaxation peak comprises multiple longitudinal modes. This is an example of mode competition, which leads to single-mode emission only after several hundred picoseconds. This situation is clearly unsuitable for frequency conversion.

2.4.2 Power Amplification

A standard gain-switched diode laser emits peak power levels of a few hundred milliwatts, which is too low to be used for efficient frequency conversion. It is therefore necessary to further amplify the direct output of a gain-switched diode to a peak power of at least several watts before frequency conversion. This is typically realized in a master oscillator-power amplifier (MOPA) setup [27, 28] (Fig. 5). The general principle of such setups is that a population inversion is created in an

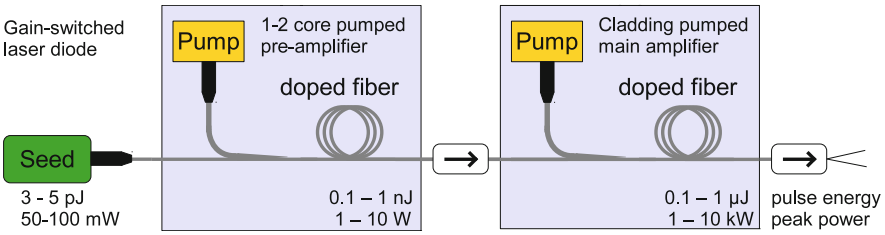

Fig. 5 General scheme of a monolithic multistage fiber amplifier in a master oscillator-power amplifier setup. Given pulse energy and peak power levels correspond to MHz repetition rate range and sub-100 ps amplifier, which is typical for Raman or supercontinuum generation. Doped fiber: type of rare-earth ion dopands define spectral absorption properties (ytterbium ~1 µm, erbium ~1.5 µm, thulium ~2 µm, etc.)

amplifier medium by electrical or optical pumping, and the stored energy is released when the seed pulse passes through the amplifier and stimulates emission at the seed laser wavelength. Many of such setups work at a fixed repetition rate, determined by the layout of the pulsed master oscillator or pulse-picking components. If, however, gain-switched diode lasers are used as a seed, freely triggerable pulsed source can be realized, providing pulses on demand from single shot up to megahertz. Different approaches exist to amplify gain-switched pulses by at least 10 dB. Popular choices for near-infrared wavelengths are semiconductor optical amplifiers (SOA) and rare-earth-doped fiber amplifiers. Each has a characteristic set of advantages.

The main strength of SOAs is their excellent suitability for miniaturization and the possibility to engineer the gain spectrum for amplification of arbitrary wavelengths between 920 and 1,180 nm. Laser chip and SOA can be combined in very compact single housings, making them applicable for, e.g., integration as a seed laser or for direct frequency conversion. The amplified pulse energy is also independent of the repetition rate in the megahertz range, due to a low inversion lifetime [29]. The beam quality emitted by high-power tapered amplifiers is, however, typically not diffraction limited and they are very prone to spurious amplifier lasing if feedback is not carefully suppressed [29, 30].

Rare-earth-doped fiber amplifiers made from single-mode fibers, on the other hand, intrinsically generate diffraction-limited beams. Their long excited state lifetime (e.g., ~0.8 ms for Yb3+ [31]) also supports low repetition rates and CW-pumping schemes without excessive generation of amplified spontaneous emission. Even amplification of bursts with pulses triggered at some 10 MHz and modulated in the medium kilohertz regime can be realized. The availability of various fiber-coupled components, also in polarization-maintaining design, supports an alignment- and maintenance-free setup of the entire laser scheme. The initial temporal pulse shape is generally not changed by the amplification process due to the high saturation energy of doped fiber [32].

In a core-pumped setup, seed and pump wavelengths are combined in a wavelength division multiplexer (WDM) and coupled into the core of the ytterbium-

doped fiber. In such a design, amplified spontaneous emission may be a problem as it adds a CW background noise, covering a much broader optical spectrum. Optimization of the amplifier for given seed power levels and desired amplification factor is therefore needed and leads to typically 3–4 orders of magnitude higher signal power than noise power levels.

In order to achieve higher output powers, cladding-pumped fiber amplifiers can be used. Here, the pump light is not coupled into the fiber core but into the cladding. This enables the use of more powerful pump diodes and also provides for a more gradual absorption of the pump light. Increased core size reduces the power density and consequently minimizes unwanted nonlinear effects and degradation such as photo-darkening [33].

The combination of several amplifier stages even allows the management of amplified spontaneous emission and the efficient usage of the available pump power. With such a multistage setup, infrared picosecond pulses with peak powers above 100 kW have been generated starting from a milliwatt gain-switched diode laser [34].

At a certain pulse energy, however, nonlinear effects start to change the spectral and temporal shape of the laser output. This limits the performance of high-power systems but can also be purposely exploited for Raman gain [35] or supercontinuum generation [36].

2.4.3 Frequency Conversion

Nonlinear frequency conversion strongly depends on the peak power and good spatial and temporal overlap of the fundamental radiation [37, 38]. Among others, second-harmonic generation (SHG), third-harmonic generation (THG), fourth-harmonic generation (FHG), sum/difference frequency generation (SFG/DFG), and Raman conversion are the most common. All processes require an adequate nonlinear medium such as crystals or special optical fibers [39, 40].

Conversion efficiency depends on polarization state and spectral bandwidth of the fundamental wave. Both the fundamental and the second-harmonic wave have to travel through the crystal at the same velocity to maximize the conversion efficiency. This can be achieved in anisotropic crystals by taking advantage of birefringence, where the refractive index is not only a function of wavelength but also depends on the propagation direction through the crystal (critical or noncritical phase matching) [39]. Another method, known as quasi-phase matching, utilizes a crystal engineered to have periodic changes of the sign of the nonlinear susceptibility. Typical examples are PPLN (periodically poled lithium niobate) or PPKTP (periodically poled potassium titanyl phosphate) crystals. This offers some advantages over regular phase matching such as high tolerance for beam pointing angle and the fact that it can be embedded in a waveguide structure. The latter becomes

advantageous for low-peak-power signal conversion as the light remains confined at high power density over the entire crystal length.

Another important aspect is the temporal and spatial cleanup effect of the conversion process on the pulses. For low conversion efficiency, the second-harmonic signal power is proportional to the squared fundamental power. This leads to a certain pulse shortening and suppression of background radiation such as amplified spontaneous emission.

Additionally, only one fundamental polarization is converted, resulting in a highly polarized second-harmonic beam. Any instability of the polarization of the infrared beam, however, translates into significant fluctuations of the second-harmonic power at the output. The use of polarization-maintaining fiber architecture is therefore crucial.

For semiconductor-based amplification and second-harmonic generation of picosecond pulses at 531 nm, pulse energies of 250 pJ have been reached at variable repetition rates [41]. Compact integrations of seed, SOA, and second-harmonic stage into one small module are also already available at 532, 561, and 594 nm [42]. Although these modules were initially mainly designed for continuous operation, gain-switching performance was demonstrated with pulse energies up to 10 pJ [17].

Fiber-based amplification, on the other hand, yields much higher pulse energies in the nanojoule range, but the pulse energy typically decreases at high repetition rates [43].

Using the aforementioned setups and processes, it is possible today to regularly provide ultraviolet (266, 355 nm), green (531 nm), and yellow/orange (560, 590 nm) picosecond pulsed diode lasers with variable repetition rates and average powers that can reach up to 200 mW at 80 MHz repetition rate (depending on wavelength) along with external triggering capabilities based on gain-switched diode seed lasers [17, 44].

3 Sub-nanosecond Pulsed LED

An alternative to using pulsed diode lasers as excitation sources in photon counting experiments is the employment of pulsed LEDs [45]. As LEDs usually do not have a resonant cavity like laser diodes, the effect of relaxation oscillation cannot be used for the generation of picosecond pulses. Instead, the optical output follows almost linearly the carrier density and thus depends on the pulse shape of the electrical pump pulse. The minimal achievable pulse width is therefore physically limited to a few hundred picoseconds. On the other hand, no multiple oscillations, as shown by gain-switched diode lasers, occur at higher power. When changing the pulse energy of a LED, the pulse broadens at most by a factor of two, and the pulse shape remains more or less identical (Fig. 6).

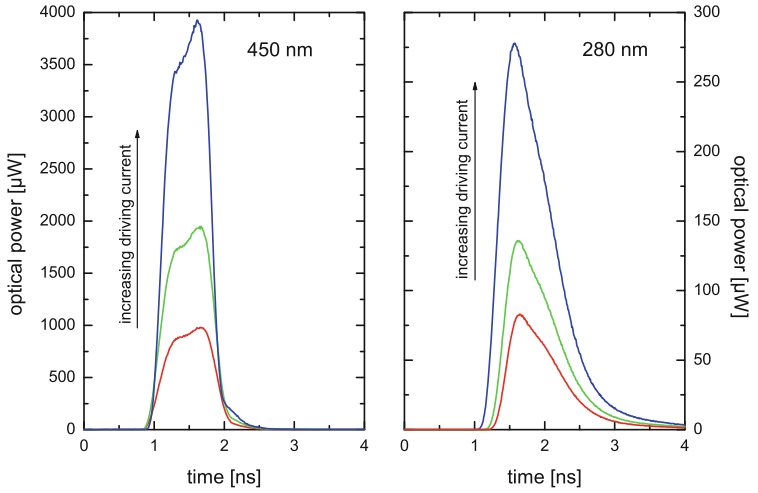

Fig. 6 Pulse shape of two pulsed LEDs at different driving currents. *Left graph* shows a pulsed LED at 450 nm, *right graph* a LED operating at 280 nm [46]. The pulse shape is more or less independent from the driving current

The most important difference between pulsed LEDs and pulsed diode lasers is the fact that the emission of the LEDs is divergent, not coherent, not polarized, and also nonuniform in its intensity distribution. Depending on the LED used, different beam shapes can be seen ranging from near round to elliptical. Fiber coupling into single-mode or multimode optical fibers has therefore only very low efficiency – a notable exception is large-area fibers such as liquid light guides. However, for short-range interactions in, e.g., compact time-resolved fluorescence lifetime spectrometer, pulsed LEDs are very useful excitation sources.

Contrary to diode lasers, LEDs offer direct emission at various wavelengths in the visible up to 600 nm and even in the ultraviolet range down to 245 nm and are therefore the only available compact pulsed light source in this spectral range. Their spectral emission profile is broader than for pulsed diode lasers with typical values between 20 and 50 nm.

Pulsed LEDs can emit picosecond pulses with a full width at half maximum (FWHM) of less than one nanosecond at repetition rates from single shot up to several 10 MHz [46]. The achievable pulse energies of the LEDs depend on the wavelength and are usually in the range around 1–2 pJ, which corresponds to average output powers up to 80 µW at 40 MHz repetition rate. This may seem low but still allows for, e.g., fluorescence lifetime measurements of diluted samples (Fig. 7).

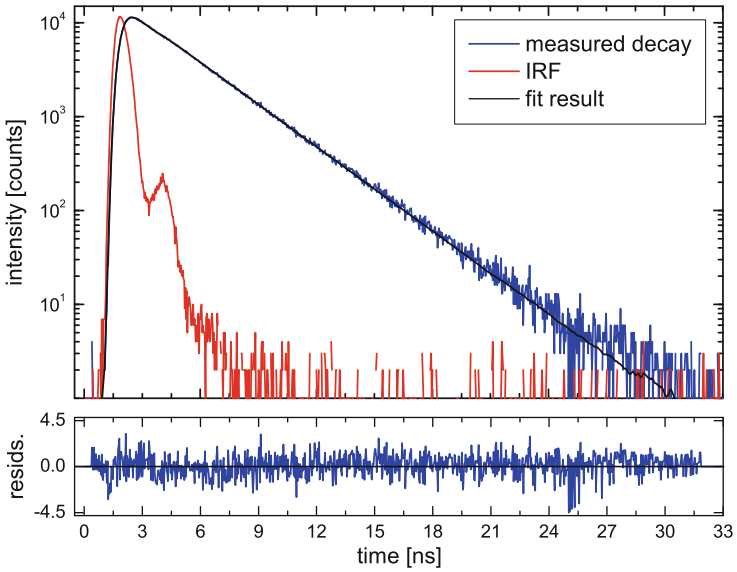

Fig. 7 Fluorescence decay of a 10 μM aqueous NATA (*N*-acetyl-L-tryptophanamide) solution excited with a LED at 280 nm operated at 2.5 MHz [46] using a fluorescence lifetime spectrometer [47]. The example shows the instrument response function (IRF, *red*), the decay (*blue*), and the fitted single exponential curve (*black*). The fitted lifetime is 2.88 ns and the reduced chi-square = 1.065. The quality of the results can be also judged by the residual distribution plotted at the *bottom*

4 Supercontinuum Generation

Visible picosecond pulsed diode lasers and LEDs are suited for many applications in a wide variety of fields. They are, however, not available at every possible wavelength, even when considering frequency conversion techniques. An alternative laser source that spans the entire visible and near-infrared spectral range has made strong advances in the past – the supercontinuum laser.

A supercontinuum can be generated from the interaction of high-peak-power laser radiation interacting with a strongly nonlinear medium. A common approach is based on launching a pulsed laser into a special optical fiber waveguide. In order to enhance the efficiency of the supercontinuum generation, the propagation area of the waveguide needs to be small and the dispersion properties be tailored. This can be achieved with so-called photonic crystal fibers (PCF) [48]. The high peak power of the fundamental laser pulse gives rise to multiple nonlinear effects, e.g., Raman generation, four-wave mixing (FWM), and self-phase modulation (SPM). Since the dispersion properties of the PCF allow a long interaction length without too much temporal broadening, the optical spectrum is broadened towards both sides of the launched fundamental wavelength. A spectrum emitted by a supercontinuum laser

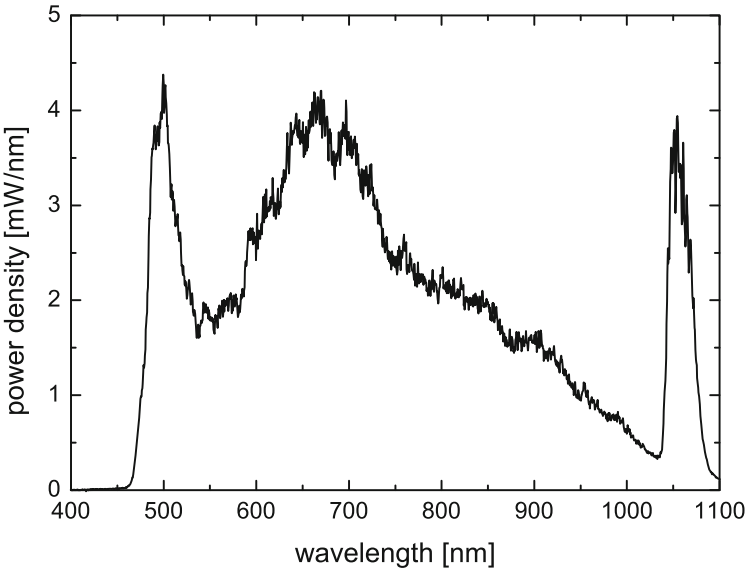

Fig. 8 Example of a supercontinuum spectrum generated from an amplified gain-switched diode laser at 1,064 nm as seed laser [49]

depends on various parameters, such as fiber design and pulse parameters, and can stretch from below 420 nm up to more than 2 μm (Fig. 8) [49–51].

Most supercontinuum lasers are based on a mode-locked fiber cavity as seed laser with subsequent amplification. This has the benefit of having direct access to stable narrowband infrared pulses with pulse widths of a few picoseconds at repetition rates in the megahertz range. On the other hand, the repetition rate cannot be adjusted and therefore requires pulse picking for lower repetition rates and lacks the ability to be synchronized with other sources.

Another approach which yields lower repetition rates in the kilohertz regime is based on Q-switched seed lasers [52]. So-called microchip laser is suitable to deliver several kilowatts of peak power and 4–6 orders of magnitude higher pulse energies than from mode locking of fiber cavities or laser diodes. This eliminates the need for multiple amplification stages to reach a sufficient power level for supercontinuum generation. However, pulse jitter quality and repetition ranges do not favor applications in time-correlated single-photon counting.

A third approach is the use of gain-switched diode lasers as a seed that allows to build a freely triggerable supercontinuum laser in the megahertz range. Similar to mode-locked seed lasers, a multistage amplifier is added before launching the high-peak-power pulses into the PCF for the spectral broadening. For highest convenience, most available sources use rare-earth-doped fiber for amplification. This ensures a high quality of the fundamental mode and, in case of a continuously spliced setup, a highly environmentally stable setup.

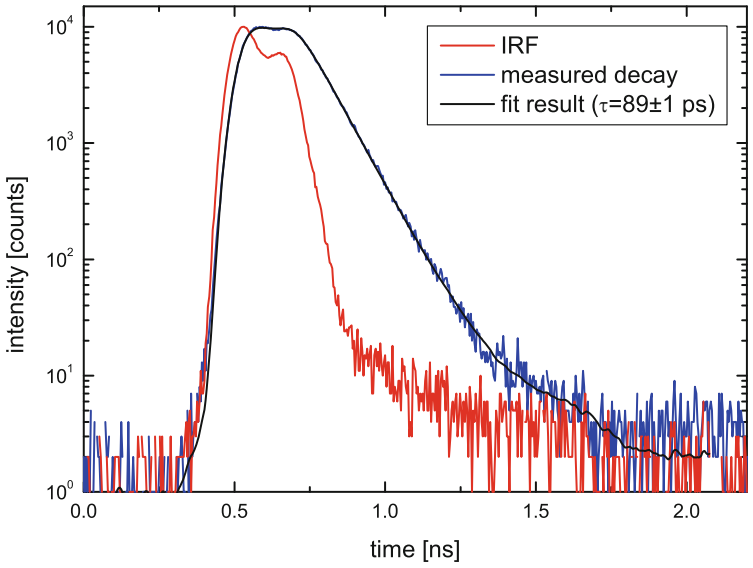

Fig. 9 Fluorescence decay of erythrosin B in water, excited at 532 nm using a supercontinuum laser [49] and a fluorescence lifetime spectrometer [47]. Although the laser pulse shape is slightly distorted as revealed by the instrument response function (*IRF*), it is possible to recover the literature value for the lifetime of erythrosin B of 89 ± 3 ps [53] using numerical reconvolution analysis

Special consideration is needed for subsequent optical filtering of the supercontinuum. Single-photon counting applications require often a high out-of-band rejection in order to achieve the maximum signal-to-noise ratio. Different concepts of filters are based on the use of acoustic optical tunable filters (AOTF), tunable dielectric bandpass filters, or diffraction-based monochromator setups.

Each filter concept features different advantages. For quick scanning or multichannel filtering, the AOTF technology is preferred. Tunable dielectric filters show unmatched extinction ratios for out-of-band suppression and low transmission loss, while monochromators deliver the narrowest linewidth among the other concepts.

Current supercontinuum lasers generate average power densities of the white light, i.e., after the PCF, of a few milliwatt per nanometer with either collimated free space output or directly from a polarization-maintaining single-mode fiber. The pulse width and pulse shapes depend on the pulse width of the seed source and the length of the PCF as the PCF leads to a wavelength-dependent pulse broadening. For gain-switched seed sources, the laser pulses can thus be as broad as 200 ps [49]. Still, such pulses allow to resolve fast processes, e.g., fluorescence lifetimes well below 100 ps using numerical reconvolution analysis (Fig. 9).

5 Summary

Gain-switched diode lasers have become the most commonly used excitation sources for time-correlated single-photon counting applications since they offer moderate pulse energies in the pJ range combined with freely adjustable repetition rates from single shot up to 100 MHz. The lasers are particularly compact and economical, allowing to build multiwavelength laser systems for reasonable cost and with unmatched trigger features. In combination with power amplification and frequency conversion techniques, diode laser-based systems are today available in a broad wavelength range, from the ultraviolet to the infrared.

Pulsed LEDs are an alternative excitation source for applications that do not rely on typical laser properties such as coherence or small divergence. Their output power is also much lower compared to gain-switched diode lasers, but still suitable for many photon counting-based applications.

An alternative laser source that spans the entire visible and near-infrared spectral range is the supercontinuum laser. Different concepts in the design with respect to the seed laser source or the spectral filtering of the supercontinuum are available and allow to select the most suited model with respect to the targeted application.

References

1. Hecht J (2010) Beam: the race to make the laser. Oxford University Press, New York
2. Periasamy A, Clegg RM (eds) (2010) FLIM microscopy in biology and medicine. CRC, Boca Raton
3. Lakowicz JR (2010) Principles of fluorescence spectroscopy. Springer, Berlin
4. Wahl M (2014) Modern TCSPC electronics: principles and acquisition modes. Springer Ser Fluoresc. doi:10.1007/4243_2014_62
5. Carlsson K, Liljeborg A, Andersson RM, Brismar H (2010) Confocal pH imaging of microscopic specimens using fluorescence lifetimes and phase fluorometry: influence of parameter choice on system performance. J Microsc 199:106–114
6. Müller BK, Zaychikov E, Bräuchle C, Lamb DC (2005) Pulsed interleaved excitation. Biophys J 89:3508–3522
7. Rüttinger S, Macdonald R, Krämer B, Koberling F, Roos M, Hildt E (2006) Accurate single-pair Förster resonant energy transfer through combination of pulsed interleaved excitation, time correlated single-photon counting, and fluorescence correlation spectroscopy. J Biomed Opt 11(2):24012
8. Bülter A (2014) Single-photon counting detectors for the visible range between 300 and 1,000 nm. Springer Ser Fluoresc. doi:10.1007/4243_2014_63
9. Buller GS, Collins RJ (2014) Single-photon detectors for infrared wavelengths in the range 1–1.7 μm. Springer Ser Fluoresc. doi:10.1007/4243_2014_64
10. Keller U (2010) Ultrafast solid-state laser oscillators: a success story for the last 20 years with no end in sight. Appl Phys B 100(1):15–28
11. Hall RN, Fenner JD, Kingsley JD, Soltys TJ, Carlson RO (1962) Coherent emission from GaAs junctions. Phys Rev Lett 9(9):366–368

12. Dupuis RD, Dapkus RD, Chen R, Holonyak N Jr, Kirchhoefer SW (1979) Continuous 300 K laser operation of single quantum-well $Al_xGa_{1-x}As$-GaAs heterostructure lasers grown by metalorganic chemical vapour deposition. Appl Phys Lett 34(4):265–267
13. Erbert G, Bärwolff A, Sebastian J, Tomm J (2000) High-power broad-area diode lasers and laser bars, in high-power diode lasers: fundamentals, technologies, applications. Springer, Berlin
14. Unger P (2000) Introduction to power laser diodes in high-power diode lasers: fundamentals, technologies, applications. Springer, Berlin
15. Bimberg D, Ketterer K, Böttcher EH, Schöll E (1986) Gain modulation of unbiased semiconductor lasers: ultrashort light-pulse generation in the 0.8–1.3 μm wavelength range. Int J Electron 60(1):23–45
16. Torphammar P, Eng ST (1980) Picosecond pulse generation in semiconductor laser using resonance oscillation. Electron Lett 16(15):587–589
17. Picosecond pulsed diode lasers from PicoQuant (LDH Series). http://www.picoquant.com/images/uploads/downloads/ldh_series.pdf. Accessed 22 Oct 2014
18. Paulus P, Langenhorst R, Jager D (1988) Generation and optimum control of picosecond optical pulses from gain-switched semiconductor-lasers. IEEE J Quant Electron 24:1519–1523
19. Ernst S, Düser MG, Zarrabi N, Börsch M (2012) Three-color Förster resonance energy transfer within single FOF1-ATP synthases: monitoring elastic deformations of the rotary double motor in real time. J Biomed Opt 17:011004
20. Buller GS, Harkins RD, McCarthy A, Hiskett PA, MacKinnon GR, Smith GR, Sung R, Wallace AM, Lamb RA, Ridley KD, Rarity JG (2005) Multiple wavelength time-of-flight sensor based on time-correlated single-photon counting. Rev Sci Instrum 76:083112
21. Steinkellner O, Wabnitz H, Walter A, Macdonald R (2013) Multiple source positions in time-domain optical brain imaging: a novel approach. Proc SPIE 8799:87990
22. Seefeldt B, Kasper R, Seidel T, Tinnefeld P, Dietz KJ, Heilemann M, Sauer M (2008) Fluorescent proteins for single-molecule fluorescence applications. J Biophotonics 01:074–082
23. Leifgen M, Schröder T, Gädeke F, Riemann R, Métillon V, Neu E, Hepp C, Arend C, Becher C, Lauritsen K, Benson O (2014) Evaluation of nitrogen- and silicon-vacancy defect centres as single photon sources in quantum key distribution. New J Phys 16:023021–028001
24. Ohla S, Beyreiss R, Fritzsche S, Glaser P, Nagl S, Stockhausen K, Schneider C, Belder D (2012) Monitoring on-chip pictet-spengler reactions by integrated analytical separation and label-free time-resolved fluorescence. Chem Eur J 18:1240–1246
25. Morthier G, Vankwinkelberge P (1997) Handbook of distributed feedback laser diodes. Artech House, Boston
26. Achtenhagen M, Amarasinghe NV, Jiang L, Threadgill J, Young P (2009) Spectral properties of high-power distributed Bragg reflector lasers. J Lightwave Technol 27(16):3433–3437
27. Lauritsen K, Riecke S, Langkopf M, Klemme D, Kaleva C, Pallassis C, McNeil S, Erdmann R (2008) Fiber amplified and frequency doubled diode lasers as a highly flexible pulse source at 532 nm. Proc SPIE 6871:68711L–68719L
28. Chestnut DA, Popov SV, Taylor JR, Roberts TD (2006) Second-harmonic generation to the green and yellow using picosecond fiber pump sources and periodically poled waveguides. Appl Phys Lett 88:071113
29. Riecke S, Schwertfeger S, Lauritsen K, Paschke K, Erdmann R, Tränkle G (2010) 23 W peak power picosecond pulses from a single-stage all-semiconductor master oscillator power amplifier. Appl Phys B 98(2):295–299
30. Woll D, Schumacher J, Robertson A, Tremont MA, Wallenstein R, Katz M, Eger D, Englander A (2002) Opt Lett 27(12):1055–1057
31. Pask HM, Carman RJ, Hanna DC, Tropper AC, Mackechnie CJ, Barber PR, Dawes JM (1995) Ytterbium-doped silica fiber lasers: versatile sources for the 1–1.2 m region. IEEE J Sel Top Quant Electron 1(1):2–13

32. Riecke SM, Lauritsen K, Thiem H, Paschke K, Erdmann R (2009) Comparison of an Yb-doped fiber and a semiconductor taper for amplification of picosecond laser pulses. Proc SPIE 7212:72120O
33. Koponen JJ, Söderlund MJ, Hoffman HJ, Tammela SKT (2006) Measuring photodarkening from single-mode ytterbium doped silica fibers. Opt Express 14(24):11539–11544
34. Kanzelmeyer S, Sayinc H, Theeg T, Frede M, Neumann J, Kracht D (2011) All-fiber based amplification of 40 ps pulses from a gain-switched laser diode. Opt Express 19(3):1854–1859
35. Feng Y, Taylor LR, Calia DB (2009) 150 W highly-efficient Raman fiber laser. Opt Express 17 (26):23678–23683
36. Kivistö S, Herda R, Okhotnikov OG (2008) All-fiber supercontinuum source based on a mode-locked ytterbium laser with dispersion compensation by linearly chirped Bragg grating. Opt Express 16(1):265–270
37. Boyd GD, Kleinman DA (1968) Parametric interaction of focused gaussian light beams. J Appl Phys 39:3597
38. Kleinman DA, Ashkin A, Boyd GD (1966) Second-harmonic generation of light by focused laser beams. Phys Rev 145(1):338–379
39. Dmitriev VG, Gurzadyan GG, Nikogosyan DN (1997) Handbook of nonlinear optical crystals, 2nd edn. Springer, Berlin
40. Canagasabey A, Corbari C, Gladyshev AV, Liegeois F, Guillemet S, Hernandez Y, Yashkov MV, Kosolapov A, Dianov EV, Ibsen M, Kazansky PG (2009) High-average-power second-harmonic generation from periodically poled silica fibers. Opt Lett 34(16):2483–2485
41. Riecke SM, Lauritsen K, Erdmann R, Uebernickel M, Paschke K, Erbert G (2010) Pulse-shape improvement during amplification and second-harmonic generation of picosecond pulses at 531 nm. Opt Lett 35:1500–1502
42. 532, 561, 594 nm Compact visible laser module from Qdlaser. http://www.qdlaser.com/?page_id=288. Accessed 22 Oct 2014
43. Schönau T, Riecke SM, Lauritsen K, Erdmann R (2011) Amplification of ps-pulses from freely triggerable gain-switched laser diodes at 1062 nm and second harmonic generation in periodically poled lithium niobate. Proc SPIE 7917:791707
44. Amplified picosecond pulsed diode lasers from PicoQuant (LDH-FA Series). http://www.picoquant.com/images/uploads/downloads/ldh-fa-series.pdf. Accessed 22 Oct 2014
45. Wahl M, Ortmann U, Lauritsen K, Erdmann R (2002) Application of sub-ns pulsed LEDs in fluorescence lifetime spectroscopy. Proc SPIE 4648:171–178
46. Sub-nanosecond pulsed LEDs from PicoQuant (PLS Series). http://www.picoquant.com/images/uploads/downloads/pls_series.pdf. Accessed 22 Oct 2014
47. Fluorescence Lifetime Spectrometer from PicoQuant (FluoTime 300). http://www.picoquant.com/images/uploads/downloads/fluotime300_brochure.pdf. Accessed 22 Oct 2014
48. Dudley JM, Genty G, Coen S (2006) Supercontinuum generation in photonic crystal fiber. Rev Mod Phys 78:1135–1176
49. Supercontinuum laser from Fianium. http://www.fianium.com/supercontinuum.htm. Accessed 22 Oct 2014
50. Supercontinuum laser from NKT Photonics. http://www.nktphotonics.com/supercontinuum_sources. Accessed 22 Oct 2014
51. Supercontinuum laser from PicoQuant (Solea). http://www.picoquant.com/images/uploads/downloads/solea.pdf. Accessed 22 Oct 2014
52. Supercontinuum laser from Leukos. http://www.leukos-systems.com/spip.php?rubrique30. Accessed 22 Oct 2014
53. Boens N, Qin W, Basari N, Hofkens J, Ameloot M, Pouget J, Lefèvre J-P, Valeur B, Gratton E, vandeVen M, Silva ND Jr, Engelborghs Y, Willaert K, Sillen A, Rumbles G, Phillips D, Visser AJWG, van Hoek A, Lakowicz JR, Malak H, Gryczynski I, Szabo AG, Krajcarski DT, Tamai N, Miura A (2007) Fluorescence lifetime standards for time and frequency domain fluorescence spectroscopy. Anal Chem 79:2137–2149

Advanced FCS: An Introduction to Fluorescence Lifetime Correlation Spectroscopy and Dual-Focus FCS

Thomas Dertinger and Steffen Rüttinger

Abstract This chapter focuses on two advanced fluorescence correlation spectroscopy (FCS) methods; fluorescence lifetime correlation spectroscopy (FLCS) and dual-focus FCS (2fFCS). We decided to put our focus on a detailed discussion of these two – and in our eyes well-merited – advanced methods, rather than giving an overview over the broad variety of advanced FCS methods that would consequently lack detail and leave the reader rather uneducated on all these methods. For this reason we had to exclude some candidates that would very well deserve the same amount of attention as the methods that we chose to focus on. Amongst these candidates camera-FCS, Bayes-FCS, and scanning-FCS are to be kept on the radar for sure.

The great benefit of FLCS is that it provides a general tool that allows filtering for sub-populations, afterpulsing-artifacts, background effects, and basically anything that can be distinguished by its fluorescence lifetime. Complementarily, 2fFCS has brought a new level of accuracy to the table that has been previously reached only by complementary methods such as for example pulsed-field gradient NMR.

Keywords 2fFCS • FCS • FLCS • Single-molecule • Spectroscopy

T. Dertinger (✉)
SOFast GmbH, Berlin, Germany
e-mail: t.dertinger@sofast-gmbh.de

S. Rüttinger
PicoQuant Innovations GmbH, Berlin, Germany
e-mail: ruettinger@picoquant.com

P. Kapusta et al. (eds.), *Advanced Photon Counting: Applications, Methods, Instrumentation*, Springer Ser Fluoresc (2015) 15: 89–110, DOI 10.1007/4243_2014_72,

Contents

1 Standard FCS 90
2 Fluorescence Lifetime Correlation Spectroscopy 93
2.1 Method 93
2.2 Applications 95
3 Dual-Focus FCS 100
3.1 Principle 103
3.2 Experimental Setup 104
3.3 Example 106
3.4 Other Implementations 107
References 108

1 Standard FCS

To lay the theoretical basis for FLCS and 2fFCS the general concept of fluorescence correlation spectroscopy (FCS) will be introduced. FCS is based on the evaluation of recorded fluorescence signal fluctuations.

In a typical FCS microscope setup, a laser beam is focused tightly in a so-called focal volume. Confocality in detection is achieved by either a pinhole in the detection path or by two or more photon excitation (see the chapter by Eggeling et al., [1] this volume). Thus, the detection of fluorescence is restricted to a very small volume in the order of femtoliters. A fluorescent probe that for example diffuses into the focal volume will be excited and will therefore emit fluorescence photons that are subsequently recorded by the detector and the detection electronics. If the concentration is low enough, the entering and exiting of fluorescent probes into or out of the detection volume will give rise to fluctuations centered on an average fluorescence signal. The typical optical signal is very weak, as it results from individual molecules and therefore single-photon counting is the method of choice.

It is obvious that the average signal typically increases if the concentration of fluorophores is increased, but at the same time the magnitude of the fluctuations relative to the average signal strength will decrease. Thus, it is intuitively clear that FCS has a maximum concentration regime within it is still applicable before the method breaks down due to the lack of sufficiently strong fluctuations. Typical concentration regimes for FCS measurements comprise picomolar concentrations and reach up to the sub-micromolar concentration regime. More precisely speaking it is not the concentration but the total number of fluorophores which defines these limits. Using modern detection methods allows to adapt also the excitation volume (e.g., STED-FCS, see the chapter by Eggeling et al., [1] this volume) this range can be extended by almost three orders of magnitude towards higher concentrations.

The temporal resolution of FCS can cover processes up to the time the probe needs to diffuse through the focal volume which typically takes place in the millisecond time regime. The lower time limit is simply given by (apart from the electronic and detector capabilities) the quantum nature of a fluorescent molecule, i.e., by the timescale of the fundamental process of excitation and subsequent

emission of a fluorescence photon, that it is the pico to nanosecond regime. FCS therefore covers up to nine orders of magnitude in the temporal domain!

The correlation function in essence comprises information about the probability to detect a photon at some time τ from the same molecule if there has been a photon detected from this molecule at time 0. As many molecular processes are reflected by the photon emission statistics of the molecule, fundamental photo-physical processes can be discovered that otherwise would remain hidden. At the very short timescales antibunching can be observed as a dip in the correlation curve (see the chapter by Grußmayer et al., [2] this volume). This dip has its origin in the fact that once a molecule has emitted a photon, it is unlikely that it will emit another photon just a few picoseconds later, as it might still be in its ground state or if already in the excited state again, it has most likely not undergone spontaneous emission (i.e., fluorescence) yet, as this process usually takes place in the nanosecond time regime. Analogously, within each timescale characteristic processes might be observed that are connected to the molecule's physics such as photo-physical dynamics, like triplet state dynamics, or physical, like rotational diffusion. If the experiment is designed properly it might provide us with an interpretation, e.g., from a change of said photo-physics. Apart from photo-physics the diffusional part of the FCS curve is of interest, as it might be used for binding studies (diffusion coefficient changes as a binding or unbinding event happens), for estimating the hydrodynamic radius of a probe or the viscosity of the surrounding medium.

Correlation is an averaging process that is defined for steady state systems. Therefore, even though the signal of single molecules is crucial to induce the fluctuations, a correlation curve is not providing information about a specific molecule, but only on the ensemble average.

Until very recently recording and processing a correlation function from the picosecond up to the millisecond regime was a very elaborate if not impossible task (as the electronics did not provide the capability to do so). Nowadays it is straightforward to calculate the complete correlation curve using new data acquisition principles [3, 4] (Fig. 1).

Correlation is a very powerful tool as there is only very minor hypothesis necessary to validly perform this process. Firstly, there is the steady state assumption that will in most cases remain valid, particularly if there is only minor photobleaching present. Secondly, the system has been ergodic which means that the particular time when the experiment is performed should not influence the systems behavior/experiments outcome. Other than that, there is no assumption to be made.

Of course in a specific experiment other assumptions might be made about the sample composition etc. but this is merely for subsequent interpretation of the results.

Besides estimating the diffusion coefficient, or photo-physical properties of the probe, the concentration might be extracted from an FCS experiment. Also, many experiments have been conducted on the estimation on reaction rates.

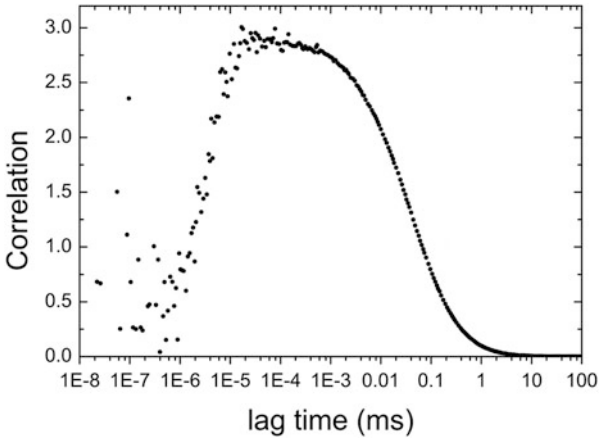

Fig. 1 Correlation curve covering the full temporal spectrum from picoseconds to milliseconds. At very short timescales (nanosecond time regime) the correlation curve increases as the probability increases to detect a photon from the same molecule after a photon has been detected at time zero. In the sub-millisecond time regime (0.1 ms) a prominent decay of the correlation curve can be observed. This decay is due to the fact that the molecule diffuses out of the detection volume on average after approx. 0.1 ms and therefore the probability of detecting a photon at later times is decreasing

Typical challenges for performing an FCS experiment are listed in the following:

- provision of a stable laser source, as fluctuations stemming from varying laser illumination will affect the outcome of the experiment.
- the sample has to be reasonably well defined at the correct concentration regime.
- brightness scales non-linearly, such that bright molecules might outweigh the dim molecules – that is particularly problematic when dealing with aggregates.

There are drawbacks and limitations to the FCS approach mainly in terms of interpretation of a recorded FCS curve. In the following we name the two most common and problematic issues, besides the need for a reasonably bright probe.

- Technical artifacts stemming from uncorrelated noise, afterpulsing of the detectors or so-called bleedthrough do have an often non-negligible impact on the shape of the FCS curve.
- In order to quantitatively evaluate an FCS curve it is crucial to have perfect control and knowledge over the underlying detection volume, more precisely the molecule detection function (MDF), as the MDF acts like an internal ruler for an FCS experiment and furthermore bleaching and optical saturation has to be avoided.

Solving the above-mentioned drawbacks is one of the reasons why FLCS (uncorrelated noise) and 2fFCS (well defined internal ruler) experience increased attention in the community.

2 Fluorescence Lifetime Correlation Spectroscopy

Fluorescence lifetime correlation spectroscopy (FLCS) was first proposed in 2002 [3]. FLCS establishes the fluorescence lifetime analogon to wavelength filtering and enables the separation of components by their different lifetime signatures.

While conventionally the number of detectors has to be equal to the number of fluorescent species in order to resolve them based on their fluorescence emission spectrum, in FLCS a single detector suffices. The filtering in FLCS is done during the downstream data processing (calculation of the respective correlation curve) by separating different species based on their fluorescence lifetime.

2.1 Method

FLCS combines traditional FCS with time-correlated single-photon counting (TCSPC). It therefore relies on pulsed excitation.

The data obtained from a typical FLCS experiment consists of a stream of photon records where each record contains (1) an identifier of the detector; (2) the time elapsed since the start of the experiment with at least microsecond precision; (3) the time elapsed since the prior laser pulse. These pieces of information are recorded for every detected photon and will be assigned to a routing marker, a time-tag and nanosecond delay (ns-delay), respectively.

Separation of species exhibiting differing fluorescence behavior is performed by weighting each detected photon with a statistical weighting function during the calculation of the FLCS correlation function. The weighting function associates weights to the photons particularly having values different than one (as one corresponds to a non-weighted photon), such that in the further processing, these photons have a varying impact on the resulting correlation curves depending on their associated weight. The detailed mathematical treatment can be found in [3, 5] and a recipe for the implementation in software is available in [6].

In the following we will elaborate the mathematical background only cursory in order to establish a basic understanding of the method.

The above-mentioned ns-delay (between the exciting laser pulse and the resulting fluorescence photon) is usually described by the channel number j of the TCSPC board/electronics used for the detection. If for example the interval of two laser pulses is 50 ns (20 MHz repetition rate) and this interval is digitized into 1,000 TCSPC channels the bin-width or TCSPC resolution would be 50 ps.

If all recorded photons are sorted into a histogram according to their channel number j we obtain the fluorescence decay histogram of the sample.

If the sample now contains M different decay components they can be indexed as $k = 1...M$ and the histogram count I_j of the jth channel can be expressed as a linear combination of the individual decay patterns $p_j^{(k)}$

$$I_j = \sum_{k=1}^{M} w^{(k)} p_j^{(k)} \tag{1}$$

where $w^{(k)}$ denotes the number of photons contributed by the respective component k. The decay pattern $p_j^{(k)}$ of component k can be obtained by measuring the fluorescence decay of the individual components separately or by mathematically decomposing the total intensity decay I_j into a sum of mono- or multi-exponential decays if assumptions for the decays of the individual components can be made.

The correlation function used in FLCS:

$$G^{(k)}(\tau) = \frac{\left\langle \sum_j f_j^{(k)} I_j(t) \cdot \sum_j f_j^{(k)} I_j(t+\tau) \right\rangle}{\left\langle \sum_j f_j^{(k)} I_j(t)^2 \right\rangle} \tag{2}$$

strongly resembles the standard auto-correlation function,

$$G(\tau) = \frac{\langle I(t) I(t+\tau) \rangle}{\langle I(t) \rangle^2} \tag{3}$$

but with the addition of the filter functions $f_j^{(k)}$. The filter functions are calculated by inverting a matrix containing the total intensity decay I_j and the individual decay patterns $p_j^{(k)}$. As mentioned above, a detailed derivation of the mathematical formalism is published in [6, 7]. While in FLCS photons with different ns-delays contribute according to the weighting function $f_j^{(k)}$ of the particular component, and in standard FCS every photon contributes equally to the correlation, i.e., in standard FCS $f_j^{(k)}$ equals one. In FLCS a single photon contributes to the correlation of the k-th component with a certain weight depending on the photon's TCSPC channel number j. This enables FLCS to calculate individual correlation functions for the mixture.

The weighting functions can interestingly take values larger than one, and they can even be negative. Nevertheless the sum of all filter functions always equals one for every channel number j.

$$\sum_j f_j^{(k)} = 1 \tag{4}$$

meaning that the number of photons is preserved.

2.2 Applications

2.2.1 Afterpulsing and Background Removal

Since FCS requires to resolve fluctuations in the fluorescence intensity caused by single molecules entering or leaving the confocal volume, highly sensitive detectors are a prerequisite for a successful FCS experiment.

Until the advent of so-called hybrid (Hamamatsu Photonics K.K.) the only type of detector offering the detection efficiency necessary to successfully perform FCS experiments has been the Single Photon counting Avalanche Diode (SPAD).

While having very high detection efficiency, SPADs adversely show an artifact called afterpulsing. After the detection of a photon leading to an electrical avalanche of charge carriers in the diode, there is a certain probability (usually 1–10%) for the SPAD to generate another so-called afterpulse, not caused by the detection of a photon but by the release of charge carriers, that have not been wiped out by the avalanche but have been trapped in the chip. The release of these trapped charge carriers resulting in the afterpulse happens on a μs timescale after the original photon detection event. This of course poses a problem for FCS. Since the two emitted electrical signals (photon detection event and afterpulse) are correlated they will show up in the auto-correlation curve and thus complicate its analysis.

Afterpulses however are not visible in cross-correlation curves since afterpulses of two detectors are naturally not correlated to each other. Therefore in order to omit the afterpulse artifact instead of calculating the auto-correlation of the photon stream of a single detector the cross-correlation between two detectors receiving equal parts of the signal is typically calculated.

This of course makes it necessary to employ two detectors even for auto-correlation experiments.

Although the afterpulses of two detectors are not correlated to each other and therefore do not show up in the cross-correlation curve, they still influence the cross-correlation since they contribute to the uncorrelated background signal (the afterpulses of both detectors are still there, but are processed such that they are not anymore correlated). The uncorrelated background signal in turn causes a reduction in the amplitude of the correlation curve and therefore leads to an apparently higher concentration. This is due to the fact that the correlation curve is normalized with the squared average count-rate no matter whether the recorded counts stem from correlated photons or not.

With FLCS this drawback can be rectified. As mentioned above, the afterpulse is correlated to a photon detection event on a microsecond timescale. On the fluorescence lifetime timescale (ns) however it shows no distinct characteristic but manifests itself only as an increased background in the TCSPC histogram (i.e., as equally distributed counts in all histogram bins). Therefore the "lifetime" patterns of fluorescence signal and afterpulsing are easily distinguishable. This is a quite remarkable finding as it implies that using FLCS not only artifacts caused by afterpulses can be taken care of, but also background counts caused by dark counts

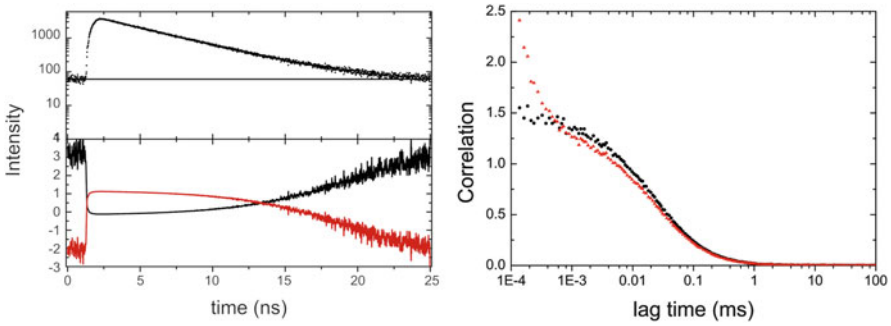

Fig. 2 *Left panel*: TCSPC histogram of Atto-488 in aqueous buffer with the resulting weighting functions for the fluorescence decay (*red*) and uncorrelated background counts (*black*). *Right panel*: Comparison between the standard FCS curve (*red*) and the FLCS curve (*black*). It can be seen that the afterpulsing of the detector, that causes a triplet-like increase of the standard FCS curve in the microsecond time regime is completely eliminated by FLCS. Furthermore the amplitude of the standard FCS curve is slightly lower than the amplitude of the FLCS curve, as the uncorrelated background has been accounted for in FLCS

of the detectors and even room light can be (and in fact is) treated in the exact same way!

Figure 2, left panel, shows in the upper part the TCSPC decay of Atto-488. Two contributions are considered: Fluorescence and afterpulsing/background. The latter manifests as a flat line at the background level. The contribution from fluorescence corresponds to the background-subtracted TCSPC curve depicted in the upper part of the left panel of Fig. 2, and the lower part of the left panel of Fig. 2 depicts the FLCS weighting curves derived from the two mentioned patterns. It is obvious from the left panel of Fig. 2, that where the probability that a detected photon originated from fluorescence (around 3 ns) is high, the filter curve for the fluorescence takes a relatively high value and the filter curve for background takes a relatively low value. The sum of both curves equals one at any time.

In the right panel of Fig. 2 the standard FCS curve is compared to the FLCS-filtered auto-correlation curve. Clearly the afterpulsing artifact responsible for the rising component in the beginning of the FCS curve is absent in the FLCS curve. From the comparison it becomes also evident that regarding the afterpulsing simply ignoring the early part (sub μs) of a standard auto-correlation curve does not overcome the afterpulsing effect. The amplitude of the conventional FCS curve is lower because of the uncorrelated background.

This becomes even more apparent once the distribution of uncorrelated background increases as showcased in the following section.

Rüttinger et al. [8] shows how FLCS is able to not only suppress the afterpulsing artifact in auto-correlation curves but also correctly measure concentrations as low as 2 pM (Fig. 3). Figure 3 left panel also highlights the strong influence uncorrelated background can have on the amplitude of the auto-correlation function. In case the uncorrelated background would not have been corrected for, the error in the concentration estimate would be fourfold.

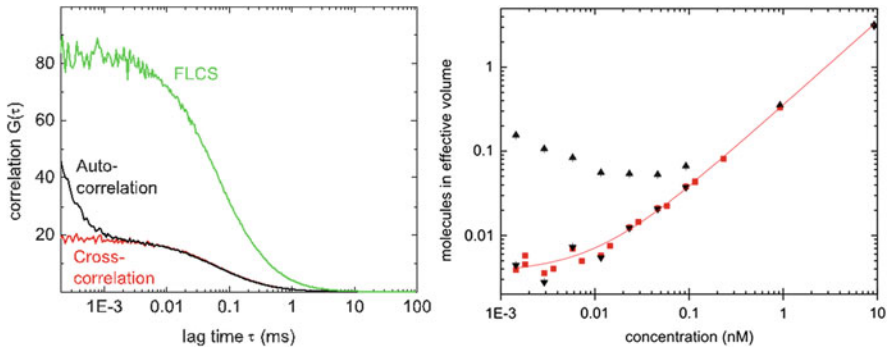

Fig. 3 Atto-655 in aqueous buffer. *Left panel*: Correlation functions for a 10 pM Atto-655 solution. Conventional processing of the photon stream using only one detector results in a strong afterpulsing contribution (*black*). Using two detectors and cross-correlating the incoming photon stream avoids the afterpulsing artifact (*red*), but only the FLCS approach (*blue*) recovers the true amplitude of the FCS curve while suppressing the afterpulsing artifact as well. *Right panel*: Concentration series of Atto-655. Dependence of recovered particle number on prepared concentration. *Red squares*: FLCS result of two independent dilution series. *Black triangles*: conventional two-detector cross-correlation analysis with (*downward pointing triangles*) and without (*upward pointing triangles*) background correction. The *red curve* is a linear fit in this log–log plot

2.2.2 Removal of Scattering (and Afterpulsing, Dark Counts, and Residual Room Light)

Another important source of uncorrelated background is scattered laser light hitting the detectors. Usually this is avoided by choosing appropriate detection filters. However in some cases the Raman scattering band of the solvent falls right into the fluorescence detection window of the reporter molecule. Even though Raman scattering has a very low yield, the excess of solvent molecules compared to the fluorescent molecules within the detection volume compensates easily for the difference in yield. Figure 3 shows an example of a 10 pM Atto-655 solution that is processed by either conventional methods or by FLCS. Decomposing the measured decay curve yields that the measured signal can be attributed to 11% scattered excitation and 45% dark counts, room light, and afterpulses. Only 44% of the photons show the fluorescence pattern.

Figure 4 is nicely suited to detail the steps involved in the calculation of an FCLS correlation curve as shown in Fig. 3. The first step is the collection of TCSPC decay patterns that we expect to be part of the signal during the experiment. For this sample consisting of Atto-655 solved in water we expect five contributions: (1) fluorescence, (2) scattered excitation light, (3) afterpulsing, (4) detector dark counts, and (5) residual room light.

Components (3)–(5) are entirely random events on the typical (nanosecond) TCSPC timescale. They are evenly distributed over all bins of the histogram; their common pattern is a flat line.

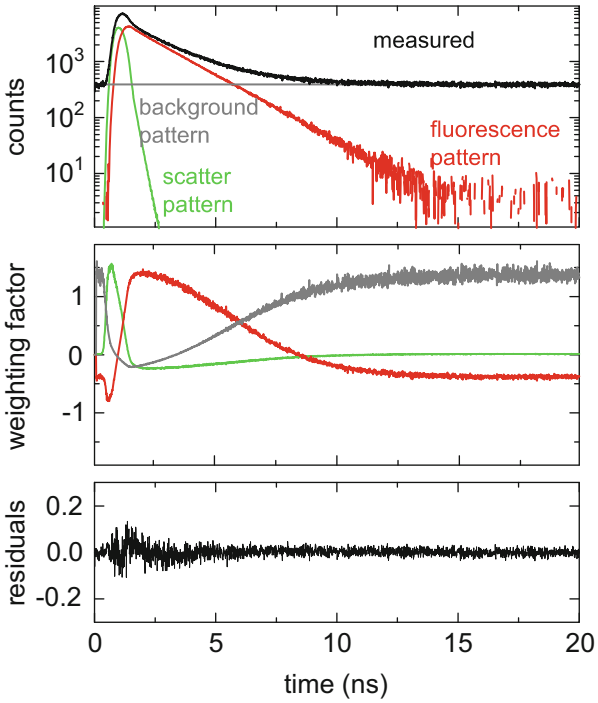

Fig. 4 TCSPC decomposition into patterns and FLCS filter functions for 10 pM Atto-655 solution. Three distinct patterns are identified in the measured TCSPC histogram: pure fluorescence (*red*), scattering (*green*), and the sum of afterpulsing, dark counts, and residual room light (*gray*). The fluorescence pattern is a background-subtracted TCSPC histogram of a 100 nM Atto-655 solution. The scattering pattern was recorded putting a mirror on top of the objective and replacing the detection bandpass filter with an OD3 filter. The third pattern is a horizontal line at the average background level of the TCSPC histogram. The *middle panel* shows the calculated FLCS filters for these signal components. The *bottom panel* shows the weighted residuals of the decomposition

The scattering pattern is well approximated by the background-subtracted histogram of the instrument response function (IRF). One gets the IRF ideally by measuring the fluorescence decay of a sample with a lifetime much smaller than the time resolution of the instrument.

Finally, the pure fluorescence pattern can be obtained by measuring a higher concentrated solution of the same dye. For example, in a decay curve of a 100 nM ATTO-655 solution, the scattering contribution is entirely negligible. Of course, the background level is subtracted again. If the assumptions are correct, the total TCSPC histogram for any ATTO-655 concentration should be a linear combination of three patterns.

As a quick test and a means of improving the patterns, a simple iterative algorithm is used to reconstruct the measured TCSPC histogram. The optimizer varies only the amplitudes and determines the occasional small time shifts of the

normalized patterns. A representative result is shown in Fig. 4. The residuals in the bottom panel indicate that the decomposition is correct, i.e., the reconstructed histogram is virtually the same as the measured.

FLCS filter functions for the identified components are calculated from these patterns and total TCSPC histogram via a matrix pseudo-inversion [5, 6].

Comparison of patterns with the corresponding FLCS filters (middle panel of Fig. 4) clarifies the meaning of weighting. An event has the largest positive weight when the probability of registering it is high, and other events are unlikely at the same time. As an example, detection of a scattered excitation photon is most likely at early times. This is reflected in the filter function for this component by weights greater than one for ns-delays around the onset of the excitation pulse. Slightly later, fluorescence photons start to prevail. The weighting factor provided by the filter for scattering therefore decreases, whereas events with the same ns-delay receive higher weights via the fluorescence filter. A flat TCSPC pattern means ns-delay independent detection probability. However, the shape of the corresponding filter function reflects the time dependent likelihood of other possible (photon) events. It needs to be stressed that the sum of all three weighting factors always equals one at any ns-delay. This means that all events are equivalent, none is discarded, but a single event contribution is specifically distributed between the signal components.

The blue curve depicted in Fig. 3 was obtained using the filter curve for pure Atto-655 fluorescence (red curve in the middle panel of Fig. 4) for the software auto-correlation [4] of all events. This is the FLCS-filtered auto-correlation curve, providing the expected particle number.

2.2.3 Separation of Different Species

Besides proof-of-principle experiments demonstrating the separation of Cy5 and Atto-655 diffusion in a single detector setup [8] FLCS has been used to study metal-fluorophore interactions in solution [9]. Here the fivefold reduction of the fluorescence lifetime of Cy5-DNA-Ag particles as compared to free Cy5-DNA could be exploited to analyze either construct separately, even though the brightness difference of the different constructs was more than tenfold!

2.2.4 Single Detector Cross-Correlation

Besides bleedthrough between different color channels resulting in an artificial, false cross-correlation a major problem of conventional cross-correlation experiments is the inherently differently shaped and sized detection and excitation volumes for the two spectrally different correlation channels. Furthermore the confocal volumes for different wavelengths never fully overlap due to always present chromatic aberrations even of high-end optics used in confocal

microscopes. The offset between the excitation and detection volumes in two color FCS experiments (exc. at 470 and 640 nm) is typically between 50 and 120 nm.

Employing FLCS on the other hand enables the realization of cross-correlation experiments using only one laser for the excitation and reporter fluorophores with similar or identical emission spectra. Therefore the two resulting excitation and detection volumes will be identical.

This has recently been used to resolve protein interactions in live cells [10]. In these experiments the reporter fluorophores are not distinguishable by wavelength but only by fluorescence lifetime.

The field of applications of FLCS is very broad which can be seen for example in recent studies that focused on probing the photoluminescence properties of gold nanoclusters [11] or the determination for accurate nanoparticle sizes [12].

An excellent review that extends beyond the scope of this book chapter on the topic of FLCS can be found in [13]. An extensive review that focuses on the application of FCS and FLCS on lipid bilayers can be found in [14].

3 Dual-Focus FCS

As the popularity of FCS increased, results of an FCS experiment were interpreted more and more quantitatively (rather than qualitatively), as in theory concentration and diffusion coefficients should be readily available by fitting the data appropriately.

However it soon became apparent that this approach had major pitfalls. Some of these pitfalls were due to the models used to extract the quantitative and in particular absolute data, being too simple, i.e. they made too many assumptions that did not necessarily hold true (e.g., assuming an oversimplified shape of the laser focus). On the other hand, providing a more accurate model usually leads to many free fitting parameters that prevent a stable convergence of the fitting procedure.

A closer look on the underlying physics principles reveals why standard FCS might not straightforwardly be used for extracting quantitative values such as the diffusion coefficient.

As for extracting absolute values from an FCS experiment, a description of the so-called molecule detection function (MDF) is necessary. The MDF describes the entirety of detection or excitation probabilities of the measurement system, including the optics, aberrations as well as molecular photo-physical parameters that might influence these probabilities.

In conventional FCS evaluation models the shape of the MDF is a crucial input parameter and conventionally a 2D/3D Gaussian MDF model is applied:

$$\mathrm{MDF}(x,y,z) = \exp\left(-\frac{x^2+y^2}{2\omega_{xy}^2} - \frac{z^2}{2\omega_z^2}\right) \tag{5}$$

wherein x, y, z denote the spatial coordinates, ω_{xy} the variance of the Gaussian probability distribution along the lateral direction (i.e., orthogonally to the optical axis), and ω_z the variance along the axial direction (i.e., along the optical axis). The beauty of this approach is that the resulting formulas for the correlation function can be solved analytically and a closed expression for the correlation function can be found [15]:

$$G(\tau) = 1 + \frac{1}{N}\left(1 + \frac{4D\tau}{\omega_{xy}^2}\right)^{-1}\left(1 + \frac{4D\tau}{\omega_z^2}\right)^{-\frac{1}{2}} \tag{6}$$

wherein $G(\tau)$ is the second-order auto-correlation function for a certain time lag τ, N corresponds to the average number of fluorescent particles within the MDF volume, and D corresponds to the diffusion coefficient of the fluorescent particle. The terms of this expression can be assigned to certain properties of the measurement and persuasively invite to extract the fitted value for, e.g., the diffusion coefficient.

However, as it turned out, photo-physics of the probe, a refractive index mismatch between the immersion objective and the solution the probe is immersed in, optical aberrations, such as astigmatism etc. all affect the apparent shape of the MDF (Fig. 5). That this is not an academic discussion, i.e., the effect is not negligible on the final result, has been shown by [17].

The reason for these deviations has their origin not only in the shape, but also in the size of the MDF, as all the above listed sources for artifacts do increase the size of the apparent MDF. The effect on the measurement is that the assumed shape and size of the MDF, Gaussian model or not, is usually chosen too small and the true shape and size of the MDF cannot be extracted without a considerable number of control measurements. However, as the size and shape of the MDF is used to conclude from a fitted diffusion time to a diffusion coefficient the result might be error prone. In other words, in standard FCS the MDF acts as an internal nanometric ruler. If the ruler however changes its scale in a near uncontrollable manner, it is obviously problematic to conclude on quantitative values.

Most difficult to handle in this regard will be the influence of the photo-physical properties of the probe. Let's consider for example optical saturation of the probe. With optical saturation one refers to the situation where the probe is excited so strong/often, that an increase of excitation intensity will not lead to a proportionally increased number of photons emitted from the probe, as it is not capable to absorb and emit more than a certain number of photons at a time.

In an experiment increasing the excitation power though will usually lead to an increased number of photons. This however is owed to the increased excitation rate of photons at the outer regions of the MDF, where the excitation rate still follows

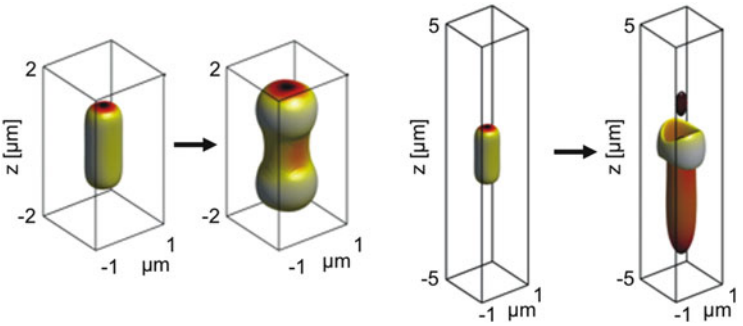

Fig. 5 *Left*: The effect of optical saturation on the underlying MDF of an FCS experiment. On the very left the ideal shape of an MDF is shown that upon saturation changes its shape and size. *Right*: Here the transition from an ideal MDF is shown when there is a refractive index mismatch between objective immersion medium and the measurement solution. The MDF dramatically increases its size and shape. Figure with permission of and adapted from [16]

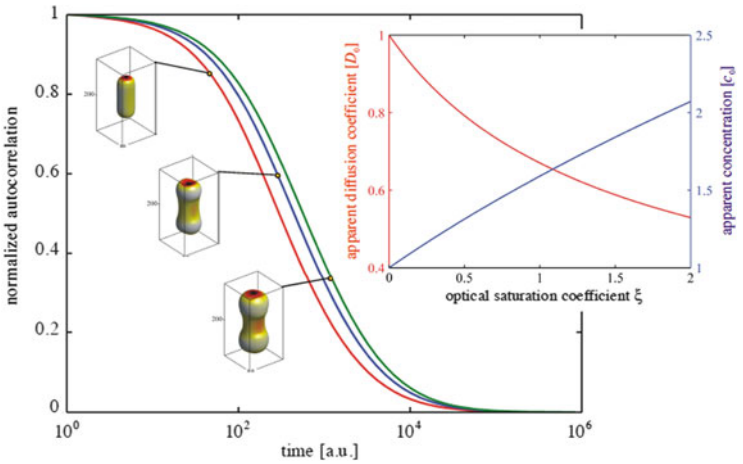

Fig. 6 Effect of optical saturation on the shape of the MDF and the resulting FCS curves. The *inset* shows how the diffusion coefficient obtained from the measured FCS curves deviates from the true diffusion coefficient as optical saturation increases. Figure reprinted with permission of [16]

linearly with the local excitation intensity (non-saturating regime), whereas in the inner region of the MDF the probe might be already saturated and the number of emitted photons remains constant there. The effect of optical saturation is shown in Fig. 6. It can be seen that the volume of the MDF increases dramatically, and the change of shape deviates more and more from an ideally shaped MDF.

This effect is so difficult to handle because there is no straightforward measure for saturation of the probe in an experiment. The experiment therefore should be set up such that optical saturation is not happening, i.e., using low laser power. Often

however the lab practices are the opposite; high excitation power shortens the acquisition time, improves the signal to noise ratio, and is therefore considered favorable.

Analogously to optical saturation, a refractive index mismatch, optical aberrations of the microscope system such astigmatism, etc. influence the outcome of an FCS experiment.

In dual-focus FCS or two-focus FCS (2fFCS), this problem has been solved to a great extent.

3.1 Principle

The basic idea behind 2fFCS is to introduce an external ruler into the experiment – a ruler that is not changing its scale and that leaves the measurement procedure essentially unchanged.

This external ruler is introduced by placing two instead of one MDFs (or laser foci) of the same wavelength next to each other, wherein said two MDFs are shifted only a few hundred nanometers with respect to each other such that the MDFs are still overlapping. The distance between the two MDFs remains widely unchanged by a change of the size and shape of the MDFs as their respective axes along the optical axis of the microscope are unaffected by any aberrations. Therefore this introduced lateral distance is a perfect ruler.

A second ingredient to 2fFCS is a more accurate description of the MDF for the fitting procedure, featuring only two fitting parameters, ensuring proper and stable convergence of the fit procedure. The interested reader might refer to e.g. [18] for further details. Figure 7 shows a comparison between the Gaussian and the new MDF model.

As a result of this approach, it could be shown that diffusion coefficients estimated with 2fFCS are precise within a margin of 2% [18].

For the moment let's take a step back and have a closer look on the external ruler and its realization.

By the introduction of the external ruler, the measurement procedure is modified to a scheme that basically measures how long the probe needs to diffuse from one MDF to the other, rather than measuring the time the probe needs to diffuse through one MDF as in conventional FCS.

As the likelihood to detect the probe in one MDF and subsequently in the other MDF drops dramatically the further the MDFs are placed apart, it becomes obvious, why the MDFs should overlap as otherwise the measurement time becomes undesirably long.

As for the overlapping MDFs the question inevitably arises how the readout of the photons is facilitated so that the detected photons are assigned to the correct MDF as there is no information about the spatial origin in a confocal spot measurement available.

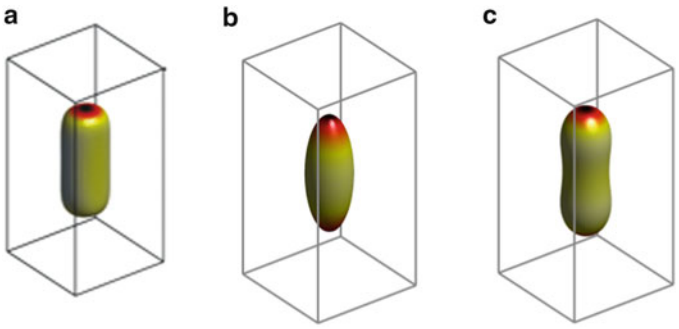

Fig. 7 Comparison between the Gaussian MDF model and the model used for two-focus FCS measurements. (**a**) Ideal MDF, (**b**) Gaussian-shaped MDF, and (**c**) the new MDF model as proposed in [18]

3.2 Experimental Setup

The solution is to use the well-known pulsed-interleaved excitation (PIE) scheme [19], such that the excitation of the probe happens alternatingly in the first MDF or the second MDF. The experimental 2fFCS setup that is best suited for this task is based on a conventional, confocal epi-fluorescence microscope (schematically shown in Fig. 8). Two collimated lasers of the same wavelength are employed, wherein these laser emit linearly polarized laser light and are arranged such that the polarization of the laser light is orthogonal to each other. These two laser beams are combined with a certain time delay with respect to each other via, e.g., a polarization sensitive optical fiber, so that at the output of said fiber, a train of laser light pulses can be observed wherein the polarization of this train of laser light pulses is changing alternatingly with each pulse.

In order to generate now two laterally shifted MDFs from this train of laser light pulses, a so-called Normarski prism [20] is arranged in front of the objective of the microscope. These prisms are conventionally employed in differential interference contrast (DIC) microscopy. The Normarski prism introduces a small angle to the laser light depending on its polarization. This angle is subsequently translated by the objective into two laterally shifted MDFs that light up alternatingly.

The read-out is facilitated by conventional time-resolved confocal detection schemes used for FCS.

Downstream data processing is such that a fluorescence decay histogram (or TCSPC histogram) is generated, which essentially contains the timing of both laser pulses and the detected photons subsequent to such a laser pulse (Fig. 9).

As the time-resolved data stream now contains information on the arrival time of a photon with respect to the laser pulse, it is straightforward to assign the photon to the laser pulse/MDF that caused the emission of this photon. Using this arrangement it is possible to translate the spatial information (in which MDF the photon has

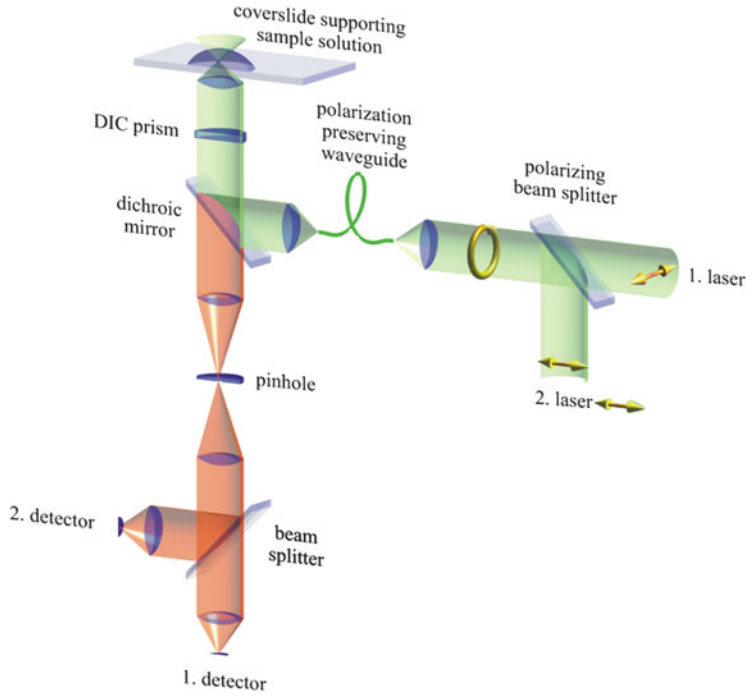

Fig. 8 Schematic microscope setup suited for 2fFCS. Two pulsed-interleaved lasers of identical wavelength, but with orthogonally polarized light beams, are combined by, e.g., a polarizing beamsplitter. Subsequently the light is coupled in a polarization preserving waveguide, therefore essentially creating a single laser source at its output that exhibits alternating polarization. Said laser light is then guided towards a DIC prism that deflects the laser light depending on its polarization at a small, predefined angle. The microscope objective translates this angle into a distance in the sample space, crating two laser foci at a predefined distance. Detection is facilitated with a conventional detection path, but with time-correlated and resolved detection. Figure taken with permission from [16]

been generated) to time domain information, facilitating the assignment of the detected photons to the correct laser pulse/MDF.

In order to extract a diffusion coefficient, two auto-correlation curves are calculated (one for each MDF) and a cross-correlation curve (cross-correlating the photons of the one MDF with the other).

As the distance between the two MDFs is known (it can be for example established by a reference measurement of a substance with a known diffusion coefficient), a global fitting procedure that fits the auto-correlation and cross-correlation curves simultaneously (Fig. 9) will yield very precise information about the diffusion coefficient – almost completely independent of the abovementioned sources of artifacts.

For 2fFCS the detection pinhole of the system has to be larger than in most confocal systems, as it has to accommodate the larger detection volume that results

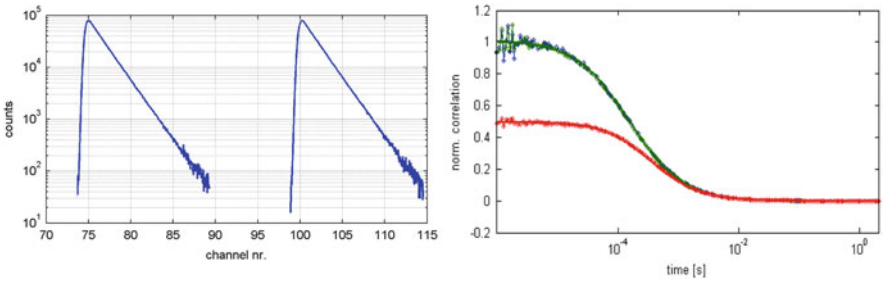

Fig. 9 Downstream processing of the acquired photon stream. *Left panel*: The photons are assigned to the laser pulse that induced their emission by time-correlated single-photon counting in a TCSPC histogram. *Right panel*: Depending on the arrival time with respect to the laser pulse the photons are processed such that for each laser an auto-correlation curve (*blue* and *green line*) and also the cross-correlation curve (*red line*) between the two laser foci is calculated. These three curves are then fitted simultaneously. The fitting procedure involves the more accurate two-parameter MDF model. From the known distance between the laser foci the absolute diffusion coefficient can be extracted from the fit

from the shifted foci. Therefore the signal to noise ratio is slightly worse than in other systems. Furthermore the focusing of the laser is done in a slightly sub-apertured way so that the resulting excitation volumes are slightly larger than in a diffraction limited focusing approach, as the introduced MDF model is suited best for a sub-apertured focusing regime.

3.3 Example

The above-mentioned optical saturation is no longer influencing the apparent value of the diffusion coefficient. In Fig. 10 the well-known dye Cy5 has been investigated. Cy5 shows a strong optical saturation behavior as it exhibits a light driven *cis–trans* isomerization wherein one form is non-fluorescent [22]. Once in the non-fluorescent state, the molecule does not emit any more photons until it relaxes back (typically within microseconds) to the ground state. These non-fluorescent states strongly promote optical saturation. As most probes do exhibit at least one comparably long-lived non-fluorescent state, such as for example a triplet state, optical saturation has to be a concern for almost all probes.

Furthermore and also very importantly, a refractive index mismatch does not affect the outcome of the 2fFCS experiment [18]. In general most optical aberrations will not affect the quality of an 2fFCS experiment with regard to its estimated diffusion coefficient. This is especially important if one considers temperature studies, where the solvent, due to the change in temperature, changes the refractive index. Such temperature studies are often performed such that also the microscope objective is heated/cooled as otherwise the objective being in contact with the measurement chamber (via the immersion liquid) might act as a heating/cooling

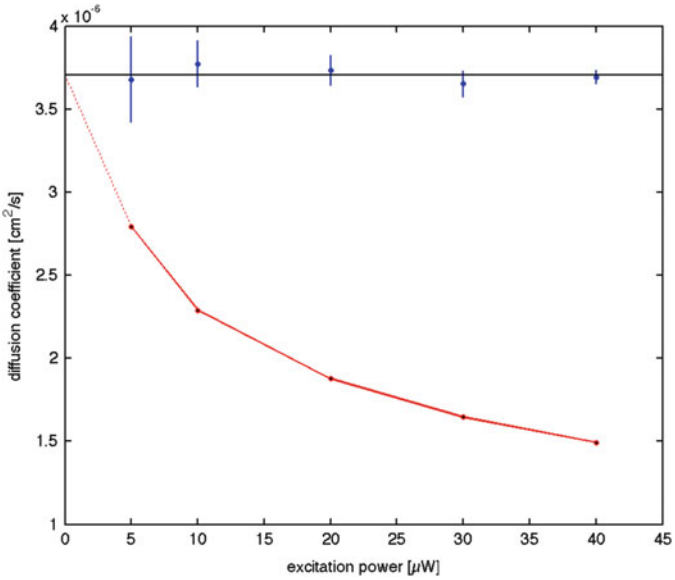

Fig. 10 Comparison between FCS and 2fFCS measurements. The apparent change of the diffusion coefficient under increasing saturating illumination conditions has been investigated. The total laser excitation power per focus is shown on the *x*-axis. Points with error bars are the results of 2fFCS, using ten measurements for each point to determine a standard deviation of the diffusion coefficient. *Solid horizontal line* (*black*) shows the average value of all 2fFCS measurements (*blue*). Lower intensity-dependent curve refers to the results of conventional FCS (*red*), using the extrapolated zero-intensity value as reference. The *dotted line* is an extrapolation of the determined power dependence towards zero power. It can be seen that under saturating conditions the resulting diffusion coefficient remains stable in 2fFCS experiments whereas in the conventional FCS approach the diffusion coefficient apparently becomes slower as saturation increases [21]. Figure adapted with permission from [21]

source itself. Heating or cooling the objective on the other hand might affect the optics of said objective, leading to aberrations that in a conventional FCS experiment might lead to an erroneous estimation of the diffusion coefficient – applying 2fFCS this is no longer the case.

3.4 Other Implementations

It is worth noting that other implementations of 2fFCS have been developed, that specifically aim to avoid equipment that is particularly cost intensive, as for example the need for two pulsed lasers, time-correlated picosecond electronics, or the need for pulsed lasers at all. An appealing alternative in this regard has been demonstrated by the use of electro-optical modulators for rotating the polarization of a single laser source. Here however, a greatly different data evaluation process is

needed and the downstream data processing is quite time consuming [23]. Despite these drawbacks this is most likely the most economic implementation of 2fFCS.

Another example exploits the high rotational speed of a resonant electro-optical modulator that, with 20 MHz, is fast enough for turning the excitation of a pulsed laser within its pulsing period (few nanoseconds). This approach can further be extended to use a cw-laser [24]. Again, this approach as well needs a specific downstream data evaluation process, namely employing the so-called filtered FCS approach [25].

So far the concept of 2fFCS has been analyzed extensively in theory but also in experiment and applied to numerous applications, mainly for estimating the diffusion coefficient of a system, but also for e.g. flow velocity measurements [26]. Recently 2fFCS has been used to study protein adhesion to nanoparticles [27] as well as complex hydrogels [28], to name a few.

2fFCS is the preferred choice for state of the art diffusion measurements. However as the equipment for such a 2fFCS measurement is more advanced and therefore more costly than for conventional FCS setups, the budget of some labs might not allow the setup of a 2fFCS instrument. Furthermore, up to now there is neither commercial nor free/shareware for downstream data processing of the recorded data available that would facilitate adoption of this method much more rapidly (though some labs do provide code upon inquiry).

The interested reader might refer to [16] for a more detailed review of 2fFCS.

References

1. Vicidomini G, Hernández IC, Diaspro A, Galiani S, Eggeling C (2014) The importance of photon arrival times in STED microscopy. Springer Ser Fluoresc. doi:10.1007/4243_2014_73
2. Grußmayer KS, Herten D-P (2014) Photon antibunching in single molecule fluorescence spectroscopy. Springer Ser Fluoresc. doi:10.1007/4243_2014_71
3. Böhmer M, Pampaloni F, Wahl M et al (2001) Time-resolved confocal scanning device for ultrasensitive fluorescence detection. Rev Sci Instrum 72:4145. doi:10.1063/1.1406926
4. Wahl M, Gregor I, Patting M, Enderlein J (2003) Fast calculation of fluorescence correlation data with asynchronous time-correlated single-photon counting. Opt Express 11:3583–3591
5. Gregor I, Enderlein J (2007) Time-resolved methods in biophysics. 3. Fluorescence lifetime correlation spectroscopy. Photochem Photobiol Sci 6:13–18. doi:10.1039/b610310c
6. Kapusta P, Wahl M, Benda A et al (2007) Fluorescence lifetime correlation spectroscopy. J Fluoresc 17:43–48. doi:10.1007/s10895-006-0145-1
7. Enderlein J, Gregor I (2005) Using fluorescence lifetime for discriminating detector afterpulsing in fluorescence-correlation spectroscopy. Rev Sci Instrum 76:033102. doi:10.1063/1.1863399
8. Rüttinger S, Kapusta P, Patting M et al (2010) On the resolution capabilities and limits of fluorescence lifetime correlation spectroscopy (FLCS) measurements. J Fluoresc 20:105–114. doi:10.1007/s10895-009-0528-1
9. Ray K, Zhang J, Lakowicz JR (2008) Fluorescence lifetime correlation spectroscopic study of fluorophore-labeled silver nanoparticles. Anal Chem 80:7313–7318. doi:10.1021/ac8009356

10. Chen J, Irudayaraj J (2010) Fluorescence lifetime cross correlation spectroscopy resolves EGFR and antagonist interaction in live cells. Anal Chem 82:6415–6421. doi:10.1021/ac101236t
11. Yuan CT, Lin CA, Lin TN et al (2013) Probing the photoluminescence properties of gold nanoclusters by fluorescence lifetime correlation spectroscopy. J Chem Phys 139:234311. doi:10.1063/1.4848695
12. Chon B, Briggman K, Hwang J (2014) Single molecule confocal fluorescence lifetime correlation spectroscopy for accurate nanoparticle size determination. Phys Chem Chem Phys. doi:10.1039/c4cp01197j
13. Kapusta P, Macháň R, Benda A, Hof M (2012) Fluorescence lifetime correlation spectroscopy (FLCS): concepts, applications and outlook. Int J Mol Sci 13:12890–12910. doi:10.3390/ijms131012890
14. Basit H, Lopez SG, Keyes TE (2014) Fluorescence correlation and lifetime correlation spectroscopy applied to the study of supported lipid bilayer models of the cell membrane. Methods. doi:10.1016/j.ymeth.2014.02.005
15. Aragón SR (1976) Fluorescence correlation spectroscopy as a probe of molecular dynamics. J Chem Phys 64:1791. doi:10.1063/1.432357
16. Pieper C, Weiß K, Gregor I, Enderlein J (2013) Dual-focus fluorescence correlation spectroscopy. Methods Enzymol 518:175–204. doi:10.1016/B978-0-12-388422-0.00008-X
17. Enderlein J, Gregor I, Patra D et al (2005) Performance of fluorescence correlation spectroscopy for measuring diffusion and concentration. Chemphyschem 6:2324–2336. doi:10.1002/cphc.200500414
18. Dertinger T, Pacheco V, von der Hocht I et al (2007) Two-focus fluorescence correlation spectroscopy: a new tool for accurate and absolute diffusion measurements. Chemphyschem 8:433–443. doi:10.1002/cphc.200600638
19. Müller BK, Zaychikov E, Bräuchle C, Lamb DC (2005) Pulsed interleaved excitation. Biophys J 89:3508–3522. doi:10.1529/biophysj.105.064766
20. Allen RD, David GB, Nomarski G (1969) The zeiss-Nomarski differential interference equipment for transmitted-light microscopy. Z Wiss Mikrosk 69:193–221
21. Loman A, Dertinger T, Koberling F, Enderlein J (2008) Comparison of optical saturation effects in conventional and dual-focus fluorescence correlation spectroscopy. Chem Phys Lett 459:18–21. doi:10.1016/j.cplett.2008.05.018
22. Huang Z, Ji D, Xia A et al (2005) Direct observation of delayed fluorescence from a remarkable back-isomerization in Cy5. J Am Chem Soc 127:8064–8066. doi:10.1021/ja050050+
23. Korlann Y, Dertinger T, Michalet X et al (2008) Measuring diffusion with polarization-modulation dual-focus fluorescence correlation spectroscopy. Opt Express 16:14609–14616
24. Štefl M, Benda A, Gregor I, Hof M (2014) The fast polarization modulation based dual-focus fluorescence correlation spectroscopy. Opt Express 22:885–899
25. Felekyan S, Kalinin S, Sanabria H et al (2012) Filtered FCS: species auto- and cross-correlation functions highlight binding and dynamics in biomolecules. Chemphyschem 13:1036–1053. doi:10.1002/cphc.201100897
26. Arbour TJ, Enderlein J (2010) Application of dual-focus fluorescence correlation spectroscopy to microfluidic flow-velocity measurement. Lab Chip 10:1286–1292. doi:10.1039/b924594d
27. Nienhaus GU, Maffre P, Nienhaus K (2013) Studying the protein corona on nanoparticles by FCS. Methods Enzymol 519:115–137. doi:10.1016/B978-0-12-405539-1.00004-X
28. Lehmann S, Seiffert S, Richtering W (2012) Spatially resolved tracer diffusion in complex responsive hydrogels. J Am Chem Soc 134:15963–15969. doi:10.1021/ja306808j

Lifetime-Weighted FCS and 2D FLCS: Advanced Application of Time-Tagged TCSPC

Kunihiko Ishii, Takuhiro Otosu, and Tahei Tahara

Abstract Time-tagged TCSPC (time-correlated single photon counting) is a special acquisition mode of TCSPC with which one determines not only the excitation-emission delay time of detected photons but also their arrival times measured from the start of the experiment. Time-tagged TCSPC enables us to examine slow fluctuation of fluorescence lifetimes, which is particularly important in the study of heterogeneous or fluctuating systems at the single-molecule level. In this chapter, we describe recent development of new methods using time-tagged TCSPC, aiming at showing their high potential in studying dynamics of complex systems. We depict two closely related methods based on fluorescence correlation spectroscopy (FCS), i.e., lifetime-weighted FCS and two-dimensional fluorescence lifetime correlation spectroscopy (2D FLCS). These methods enable us to quantify fluorescence lifetime fluctuations on the microsecond timescale. Showing examples including the study of a biological macromolecule, we demonstrate the usefulness of these two methods in real applications. In addition, we present another application of time-tagged TCSPC, which analyzes photon interval time for characterizing timing instability of photon detectors.

Keywords Biological macromolecules · Fluorescence correlation spectroscopy · Fluorescence lifetime · Microsecond dynamics · Time-tagged TCSPC

Contents

1 Introduction 112
2 Lifetime-Weighted Fluorescence Correlation Spectroscopy 114
3 Two-Dimensional Fluorescence Lifetime Correlation Spectroscopy (2D FLCS) 116

K. Ishii, T. Otosu, and T. Tahara (✉)
Molecular Spectroscopy Laboratory, RIKEN, 2-1 Hirosawa, Wako, Saitama 351-0198, Japan
e-mail: tahei@riken.jp

P. Kapusta et al. (eds.), *Advanced Photon Counting: Applications, Methods, Instrumentation*, Springer Ser Fluoresc (2015) 15: 111–128, DOI 10.1007/4243_2014_65,

3.1 Constructing Two-Dimensional Correlation Map 116
3.2 Background Subtraction 119
3.3 Inverse Laplace Transform and Decomposition into Multiple Species 120
3.4 Application: DNA Dynamics 123
4 Photon Interval Analysis 125
5 Concluding Remarks 127
References 127

1 Introduction

Time-correlated single photon counting (TCSPC) is a sensitive method for the measurement of fluorescence lifetime with a time resolution of tens to hundreds of picoseconds. A typical TCSPC setup consists of a pulsed excitation source, a photon detector having a short response time, and an electronic circuit which can precisely determine the delay time between the excitation pulse and the photon signal in the unit of TCSPC channel number ("microtime," Fig. 1). After accumulating sufficient number of fluorescence photons, a fluorescence decay curve is built as a histogram of the obtained microtimes. The characteristic fluorescence lifetime of the sample molecule is evaluated from the fluorescence decay curve, typically by fitting analysis using exponential functions.

In ordinary TCSPC experiments, only the microtimes of detected photons are recorded for building the ensemble-averaged histogram, while information of the temporal fluctuation of the microtime in a slower timescale (microseconds to seconds) is discarded. On the other hand, in time-tagged TCSPC [1], one keeps a record of the absolute arrival time of individual photons measured from the start of the experiment ("time tag" or "macrotime," Fig. 1). Combined use of the microtime and macrotime information facilitates simultaneous measurements of fluorescence lifetime and fluorescence intensity fluctuations. Moreover, this acquisition mode of fluorescence photons allows us to analyze the correlation of the microtime and macrotime, which in fact provides information about the fluctuation of fluorescence lifetimes on the microsecond to second timescale. Such fluctuation of the fluorescence lifetime is essential in fluorescence measurements at the single-molecule level, where the fluctuation is caused by conformational dynamics of the molecule. In order to access rich information contained in the fluctuation of fluorescence lifetimes in single-molecule experiments, a reliable, convenient, and versatile method for analyzing time-tagged TCSPC data is critically important.

To date, several methods have been reported to analyze time-tagged TCSPC data. For example, burst-integrated fluorescence lifetime (BIFL) [2] and fluorescence intensity and lifetime distribution analysis (FILDA) [3] are single-molecule-based techniques with which one examines distribution of fluorescence lifetimes by evaluating the mean fluorescence lifetime in short binning windows and analyzing its statistics. These methods can be used to detect distribution of the fluorescence lifetime in static multi-component systems. However, they are not suitable for

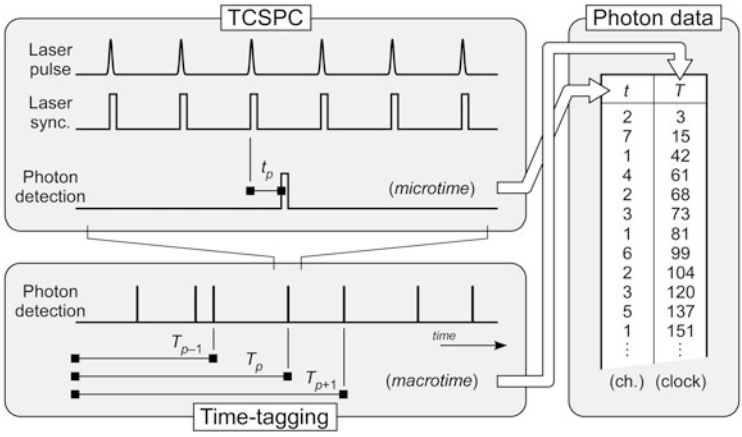

Fig. 1 Schematic description of a time-tagged TCSPC data. For each detected photon, microtime (t) and macrotime (T) are measured with the TCSPC module. Photon data is a combined list of microtimes and macrotimes of detected photons sorted with the macrotime values

dynamic systems that involve rapid lifetime fluctuations, because the time binning limits the time resolution to the bin width.

Fluorescence correlation spectroscopy (FCS) based techniques treat time-tagged TCSPC data with a binning-free (photon-by-photon) manner [4]. Therefore, they allow us to study fluorescence lifetime fluctuations with a time resolution down to tens of nanoseconds. Fluorescence lifetime correlation spectroscopy (FLCS) [5–8] is a useful technique when one has information about the fluorescence decay of each species in advance. In this case, FLCS utilizes the microtime information of each detected photon to infer the source of the photon, i.e., the species from which the photon is emitted. By comparing the observed microtimes with the fluorescence decay curve of each species (reference), FLCS can determine the auto- and cross-correlations of relevant species in a species-selective manner. Nevertheless, FLCS is not applicable in case that we do not have information about the fluorescence lifetime of the component. Therefore, one needs a new "reference-free" method for studying conformational dynamics of macromolecules where unknown intermediate states may appear.

In this chapter, we describe our recent effort to develop reference-free methods to study conformational dynamics of macromolecules using time-tagged TCSPC. Lifetime-weighted FCS [9] is a simple reference-free method to detect inhomogeneity in the sample through fluorescence lifetime fluctuations. This method is used for finding inhomogeneity in the sample and/or for "the first examination" of the timescale of the conformational dynamics of macromolecules. Two-dimensional fluorescence lifetime correlation spectroscopy (2D FLCS) [10–12] is a recently developed versatile reference-free method which analyzes time-tagged TCSPC data by building two-dimensional correlation maps. 2D FLCS is particularly useful for investigating complex dynamics of unknown systems in a visually comprehensible

manner. At last, we describe another type of application of time-tagged TCSPC. It is shown that the photon interval analysis on the time-tagged TCSPC data can solve a long-standing problem of timing instability of photon detectors [13].

2 Lifetime-Weighted Fluorescence Correlation Spectroscopy

Usually, FCS experiments are performed by observing the correlation function of time-dependent fluorescence intensity, $I(T)$ [14]:

$$G_{\mathrm{I}}(\Delta T) = \frac{\langle I(T)I(T+\Delta T)\rangle}{\langle I(T)\rangle^2}, \tag{1}$$

where ΔT is the correlation lag time and angle brackets denote ensemble averaging. This quantity is evaluated photon-by-photon using time-tagged photon data as

$$G_{\mathrm{I}}(\Delta T) = \frac{\sum_{p=1}^{N}\sum_{q=1}^{N}\begin{cases}1 & \Delta T - \Delta\Delta T/2 < T_q - T_p < \Delta T + \Delta\Delta T/2 \\ 0 & \text{otherwise}\end{cases}}{N^2 T_{\max}^{-2}\cdot(T_{\max}-\Delta T)\cdot\Delta\Delta T}. \tag{2}$$

Here, $T_{p(q)}$ is the macrotime of $p(q)$-th photon, N is the total number of detected photons, $\Delta\Delta T$ is an arbitrary window size, and $T_{\max}$ is the measurement time. In this definition, one searches for all possible pairings of photons in the time-tagged TCSPC data which satisfy the condition that the time lag between the pair is ΔT (Fig. 2a). The denominator of Eq. (2) is the normalization factor that is chosen such that $G_{\mathrm{I}}(\Delta T)$ becomes unity when there is no intensity correlation. $G_{\mathrm{I}}(\Delta T)$ characterizes the fluctuations of fluorescence intensity.

If one incorporates the microtime data obtained by time-tagged TCSPC to FCS, one can investigate fluorescence lifetime fluctuations. The simplest way is to replace "1" in the numerator of Eq. (2) with the product of microtimes (t) of photons p and q (Fig. 2a) [9]:

$$G_{\mathrm{L}}(\Delta T) = \frac{\sum_{p=1}^{N}\sum_{q=1}^{N}\begin{cases}t_p t_q & \Delta T - \Delta\Delta T/2 < T_q - T_p < \Delta T + \Delta\Delta T/2 \\ 0 & \text{otherwise}\end{cases}}{\bar{t}^2 N^2 T_{\max}^{-2}\cdot(T_{\max}-\Delta T)\cdot\Delta\Delta T}, \tag{3}$$

where $\bar{t} = \sum_{p=1}^{N} t_p/N$ is the ensemble-averaged mean fluorescence lifetime. Equation (3) is equivalent to

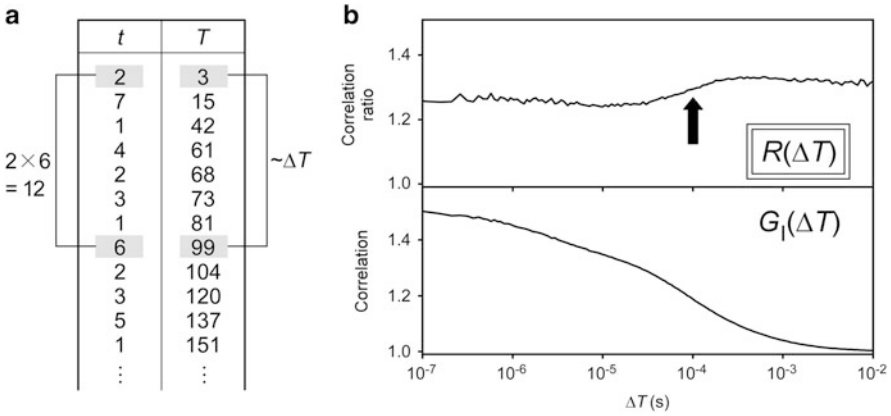

Fig. 2 (**a**) Correlation calculation from time-tagged TCSPC data. Photon pairs with the interval of ΔT are looked up in the photon data and their occurrences are counted. In the lifetime-weighted FCS, the counting is weighted with the product of corresponding microtimes. (**b**) The result of lifetime-weighted FCS measurements of a DNA hairpin. *Top*: correlation ratio defined in Eq. (5). The *arrow* indicates a transition of the correlation ratio. *Bottom*: ordinary fluorescence intensity correlation

$$G_{\mathrm{L}}(\Delta T) = \frac{\langle t(T)I(T)t(T+\Delta T)I(T+\Delta T)\rangle}{\langle t(T)I(T)\rangle^2}, \tag{4}$$

where $t(T)$ is the fluorescence lifetime at the macroscopic time T. The right-hand side of this equation can be interpreted as the correlation function of the "lifetime-weighted" fluorescence intensity. Note that, although it may seem counterintuitive, Eq. (3) is not the correlation function of the fluorescence lifetime itself, i.e., $\langle t(T)t(T+\Delta T)\rangle/\langle t(T)\rangle^2$. The intensity factor $I(T)$ appears in Eq. (4) because the photon-by-photon evaluation of a correlation function is inevitably influenced by the fluctuation of fluorescence intensity. Therefore, more photons are sampled from the time region where the fluorescence intensity is higher.

For separating the lifetime fluctuation from the intensity fluctuation, one can employ the ratio of the lifetime-weighted fluorescence correlation (Eq. (3)) to the ordinary intensity correlation (Eq. (2)) [9],

$$R(\Delta T) = \frac{G_{\mathrm{L}}(\Delta T) - 1}{G_{\mathrm{I}}(\Delta T) - 1}. \tag{5}$$

By canceling the correlation amplitude due to intensity fluctuations as Eq. (5), one can examine the extent and timescale of the fluctuation of the fluorescence lifetime. If the system is homogeneous, $R(\Delta T)$ becomes unity; In contrast, if the system consists of multiple species having different fluorescence lifetimes, $R(\Delta T)$ takes a value deviated from unity. A dynamic process such as conformational dynamics usually induces an interconversion between species having different fluorescence lifetimes, and hence it causes a change of $R(\Delta T)$. Importantly, as long as there is no

variation in the diffusion behavior of the molecules in the sample, $R(\Delta T)$ defined as Eq. (5) is free from the diffusion effect and reports only intramolecular dynamics that causes fluctuations of the fluorescence lifetime. This feature is particularly important when one studies conformational dynamics of macromolecules in the micro to millisecond time region.

Figure 2b shows the $R(\Delta T)$ curve of a single-stranded DNA forming a hairpin structure (*6-FAM*-5′-TTTAACC$(T)_{18}$GGTT-3′-*TAMRA*) [12]. The DNA sample is labeled with two fluorophores that constitute a Förster resonance energy transfer (FRET) pair. The FRET efficiency from the donor (FAM) to the acceptor (TAMRA) increases drastically upon formation of the hairpin structure. Therefore, one can study the formation-dissociation dynamics of the DNA hairpin through monitoring the FRET efficiency. The FRET efficiency, E, is represented by the fluorescence lifetime of the donor, τ_D, as

$$E = 1 - \frac{\tau_D}{{\tau_D}^0}, \tag{6}$$

where ${\tau_D}^0$ is the intrinsic fluorescence lifetime of the donor in the absence of an acceptor. Therefore, the fluctuation of τ_D, which is quantified as $R(\Delta T)$ of the donor fluorescence, can be used to detect dynamics of the DNA hairpin formation. In Fig. 2b, the $R(\Delta T)$ curve of the DNA hairpin clearly shows a transition at $\Delta T \sim 100$ μs. This is a clear evidence of a dynamics on this timescale which changes the fluorescence lifetime of FAM. In other words, a dynamics that changes the DNA structure is unambiguously detected by lifetime-weighted FCS. It is noteworthy that even though the transition is undoubtedly observed in $R(\Delta T)$, the corresponding signature is not apparent in the raw correlation curve ($G_I(\Delta T)$; Fig. 2b) because of coexisting dynamic signals originating from the diffusion and triplet formation.

To summarize, the lifetime-weighted FCS is a simple reference-free application of time-tagged TCSPC data which can be used for detecting inhomogeneity in the sample and the relaxation dynamics of the inhomogeneity through $R(\Delta T)$. This method is advantageous over traditional FCS for detecting the dynamics of biological macromolecules. Nevertheless, the lifetime-weighted FCS does not provide detailed knowledge about the system. Specifically, it does not tell about the number of independent species, the fluorescence lifetime of them, and the species involved in the observed dynamics. The next task is to elucidate these details by carefully examining time-tagged TCSPC data, as described in the next section.

3 Two-Dimensional Fluorescence Lifetime Correlation Spectroscopy (2D FLCS)

3.1 Constructing Two-Dimensional Correlation Map

Time-tagged TCSPC data consists of lists of the microtimes and macrotimes of detected photons (Fig. 1). In order to thoroughly investigate the correlation pattern

contained in the time-tagged data, one should avoid any loss of information in the analytical process. The best way is to individually evaluate the correlation function for all possible combinations of microtime values, $\{t^{(i)}, t^{(j)}\}$ [10–12, 15]. In other words, one should use the following form of a correlation function to fully utilize the microtime information in time-tagged data:

$$M_{ij}(\Delta T) = \left\langle I\left(T; t^{(i)}\right) I\left(T + \Delta T; t^{(j)}\right)\right\rangle = \frac{\sum_{p=1}^{N}\sum_{q=1}^{N}\begin{cases}\delta_{t_p t^{(i)}}\delta_{t_q t^{(j)}} & \Delta T - \Delta\Delta T/2 < T_q - T_p < \Delta T + \Delta\Delta T/2 \\ 0 & \text{otherwise}\end{cases}}{(T_{\max} - \Delta T)\cdot \Delta\Delta T}. \quad (7)$$

$I(T; t^{(i)})$ is the fluorescence intensity detected by ith TCSPC channel at macroscopic time T, and δ_{kl} is the Kronecker delta function. For example, if we set $i = 1$ and $j = 2$, Eq. (7) becomes the (unnormalized) cross-correlation function between the fluorescence intensities detected at the first and the second TCSPC channels. By gathering all $M_{ij}(\Delta T)$ values for various $\{i, j\}$ combinations together, one obtains a two-dimensional matrix of correlation data, $\mathbf{M}(\Delta T)$. Note that if one sums up all the elements of $\mathbf{M}(\Delta T)$, one obtains the ordinary (unnormalized) fluorescence intensity correlation, i.e., $\sum_i \sum_j M_{ij}(\Delta T) = \langle I(T) I(T + \Delta T)\rangle$.

In practice, computation of $\mathbf{M}(\Delta T)$ is done as follows (Fig. 3).

1. An arbitrary timescale of interest and a window size are chosen (ΔT and $\Delta\Delta T$).
2. A two-dimensional array of memory space is prepared for storing $\mathbf{M}(\Delta T)$. The size of this array is the square of the number of TCSPC channels, e.g., 256×256. $\mathbf{M}(\Delta T)$ is initialized by setting zero at all elements of this array.

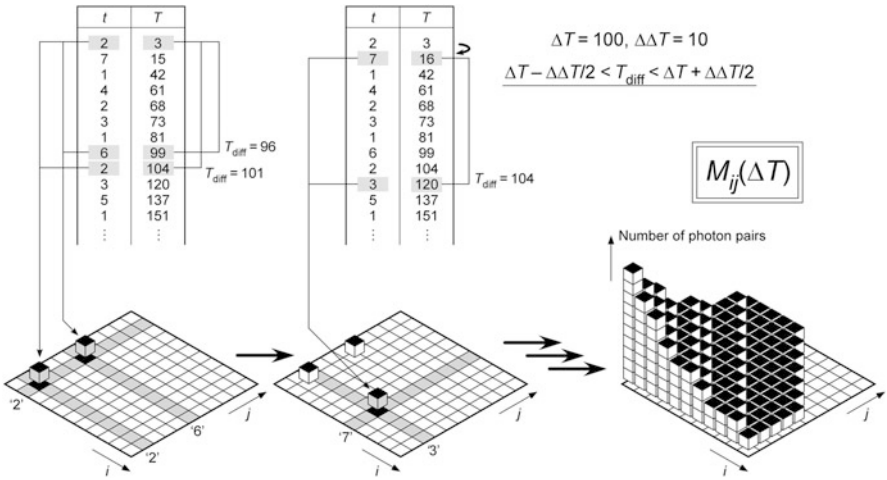

Fig. 3 Schematic illustration of the procedure for building a two-dimensional correlation map. Here, the correlation timescale (ΔT) and the window size ($\Delta\Delta T$) are set at 100 and 10, respectively. The first part (*left*) represents steps 3–7 and the second part (*center*) represents steps 8–9 (see main text)

3. The macrotime and microtime of the first photon in the time-tagged TCSPC data (T_1, t_1) are examined and stored in buffer memory.
4. The macrotime table is scanned to pick up photons that have macrotime values between $T_1 + \Delta T - \Delta\Delta T/2$ and $T_1 + \Delta T + \Delta\Delta T/2$.
5. If a matching photon is found, its microtime is read (t_m).
6. The $\{t_1, t_m\}$ element of $\mathbf{M}(\Delta T)$ is incremented by 1.
7. Steps 4–6 are repeated to find all matching photons.
8. Step 3 is repeated for the second photon. Its macrotime and microtime (T_2, t_2) are examined and stored in buffer memory.
9. Steps 4–7 are repeated for T_2 and t_2.
10. Steps 8 and 9 are repeated for the rest of photons.

Sometimes FCS experiments are performed in the cross-correlation configuration using two independent detectors in order to avoid artifact due to the afterpulsing effect of the detector [16]. In that case, photons examined in step 3 (or step 8) and in step 4 should be those from different detectors.

Roughly speaking, the physical meaning of the obtained two-dimensional matrix $\mathbf{M}(\Delta T)$ can be interpreted as follows.

- Elements of $\mathbf{M}(\Delta T)$ of small $t^{(i)}$, $t^{(j)}$ values mainly reflect the autocorrelation of short lifetime species.
- Elements of $\mathbf{M}(\Delta T)$ of large $t^{(i)}$, $t^{(j)}$ values mainly reflect the autocorrelation of long lifetime species.
- Elements of $\mathbf{M}(\Delta T)$ of small $t^{(i)}$ and large $t^{(j)}$ values mainly reflect the cross-correlation between short lifetime species and long lifetime species.

Importantly, $\mathbf{M}(\Delta T)$ preserves the full information of two-point correlations obtainable from a set of the time-tagged TCSPC data. Therefore, any other analyses of time-tagged TCSPC data can be reinterpreted using $\mathbf{M}(\Delta T)$. Such reinterpretation provides a coherent overview of the existing methods, which can lead us to further development of a new analysis. For example, FLCS developed by Enderlein and coworkers [5–8] can be understood in the framework of $\mathbf{M}(\Delta T)$ as follows. In FLCS, it is assumed that the complete prior knowledge of the fluorescence decay components is available. Then, an observed two-dimensional correlation matrix $\mathbf{M}(\Delta T)$ is expected to be a sum of auto- and cross-correlations of the known decay curves:

$$M_{ij}(\Delta T) = \sum_{k,l} g_{kl}(\Delta T) I_k\left(t^{(i)}\right) I_l\left(t^{(j)}\right). \tag{8}$$

Here, $I_{k(l)}(t)$ is the decay curve of species $k(l)$ and $g_{kl}(\Delta T)$ is the correlation between species k and l at lag time ΔT. FLCS analysis [5–8] is mathematically equivalent to the least mean square fitting of the observed $\mathbf{M}(\Delta T)$ using Eq. (8), i.e., the fitting using combinations of $I_k(t)$ and $I_l(t)$ to determine unknown $g_{kl}(\Delta T)$'s. This interpretation of FLCS using a 2D matrix makes it clear that a new analysis is necessary for more general case where one does not have any prior knowledge of

the fluorescence decay components. In such cases, one should simultaneously determine $I_k(t)$, $I_l(t)$, and $g_{kl}(\Delta T)$ from the observed $\mathbf{M}(\Delta T)$ without any references. In the following, we describe how to achieve this reference-free analysis of $\mathbf{M}(\Delta T)$, which is the core of 2D FLCS [10–12].

3.2 Background Subtraction

First, one needs to note that a correlation signal obtained in FCS is always accompanied with uncorrelated background due to photon pairs emitted by different molecules that coexist in the observation volume. Emissive background signals, such as solvent Raman scattering, also contribute to the uncorrelated background. One can separate the information of the correlated photons from the uncorrelated background by using $\mathbf{M}(\Delta T)$ evaluated at a very long ΔT [10].

After a sufficiently long lag time, the correlation vanishes because of diffusion. Therefore, the $\{i, j\}$-th element of $\mathbf{M}(\Delta T)$ at a long lag time becomes the product of the ith and jth points of the ensemble-averaged fluorescence decay curve:

$$M_{ij}^{\mathrm{unc}} = \bar{I}\left(t^{(i)}\right)\bar{I}\left(t^{(j)}\right). \tag{9}$$

One can obtain the correlated part of $\mathbf{M}(\Delta T)$ by subtracting this uncorrelated part:

$$M_{ij}^{\mathrm{cor}}(\Delta T) = M_{ij}(\Delta T) - M_{ij}^{\mathrm{unc}}. \tag{10}$$

$\mathbf{M}^{\mathrm{cor}}(\Delta T)$ does not contain any contributions from different molecules or uncorrelated backgrounds, because these contributions do not fluctuate in a correlated manner. It means that this separation of the correlated part enables us to treat $\mathbf{M}^{\mathrm{cor}}(\Delta T)$ as if it is built from a strict single-molecule experiment under an ideal condition, i.e., infinitesimally low concentration and no background scattering.

Figure 4 demonstrates the effect of subtraction of uncorrelated background [12]. The sample is a mixture of two fluorescent dyes, Cy3 and TMR (tetramethylrhodamine). Figure 4a shows the fluorescence decay curves of Cy3, TMR, and their mixture. The fluorescence lifetime of Cy3 is 0.18 ns and that of TMR is 2.4 ns. The fluorescence of the mixture solution shows a biexponential decay which corresponds to a sum of the TMR and Cy3 decay curves. Figure 4b is the 2D map of the uncorrelated background, $\mathbf{M}^{\mathrm{unc}}$, and Fig. 4c shows that of the correlated part, $\mathbf{M}^{\mathrm{cor}}(\Delta T)$, at $\Delta T = 10$–100 μs. A clear difference is seen between the shapes of these 2D maps. Namely, the correlated part lacks sharp ridges along the time-zero lines which are, in contrast, obvious in the uncorrelated part. These ridges represent the cross-correlation between the short lifetime component (Cy3) and the long lifetime component (TMR), so that their absence in the correlated part indicates that the cross-correlation between these components is zero. This cross-correlation should naturally be zero, because the sample is just a mixture of two independent

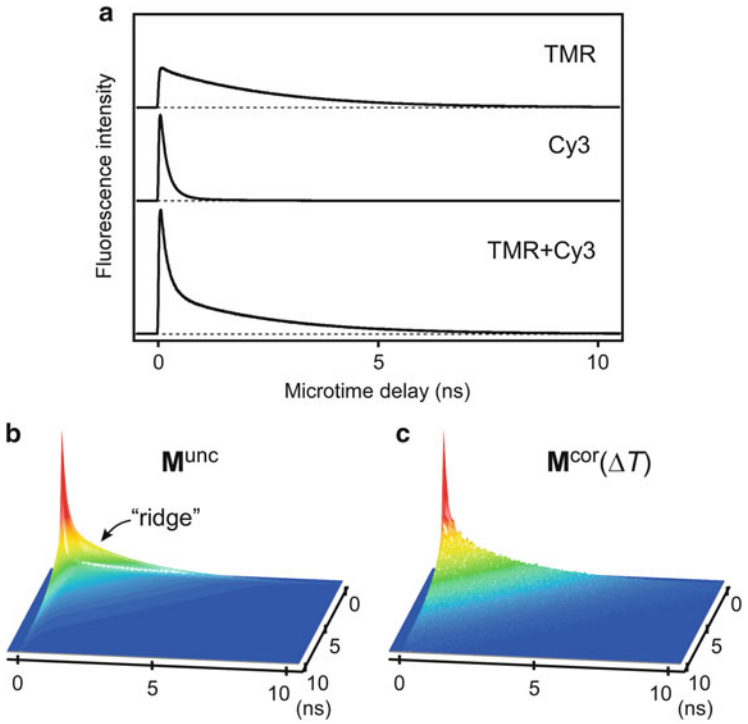

Fig. 4 (**a**) Fluorescence decay curves of two fluorescent dyes (TMR and Cy3) and their mixture measured with the TCSPC method. (**b**, **c**) 2D correlation maps of the uncorrelated part (**b**) and the correlated part at $\Delta T = 10$–100 μs (**c**) built from time-tagged TCSPC data of the mixture solution. Note that ridges are clearly visible in (**b**)

dyes. This consistency proves that the uncorrelated background is properly subtracted in this analysis. Thus, the correlated part can be regarded as an equivalent of the sum of the single-molecule correlation signals of TMR and Cy3.

3.3 Inverse Laplace Transform and Decomposition into Multiple Species

The next step is decomposition of $\mathbf{M}^{\mathrm{cor}}(\Delta T)$ [11, 12]. When a sample consists of multiple species, $\mathbf{M}^{\mathrm{cor}}(\Delta T)$ becomes the sum of contributions from these species. In such cases, one can decompose $\mathbf{M}^{\mathrm{cor}}(\Delta T)$ into each contribution as follows to identify each species and to study their interconversion:

$$M_{ij}^{\mathrm{cor}}(\Delta T) = \sum_{k,l} g_{kl}^{\mathrm{cor}}(\Delta T) I_k\left(t^{(i)}\right) I_l\left(t^{(j)}\right). \tag{11}$$

Here, ${g_{kl}}^{\mathrm{cor}}(\Delta T)$ is the correlated part of the species-specific correlation function between k and l. If no exchange reaction occurs between different species, the corresponding cross-correlation (${g_{kl}}^{\mathrm{cor}}(\Delta T)$, $k \neq l$) becomes zero. On the other hand, if a reaction exchanging two species k and l takes place, ${g_{kl}}^{\mathrm{cor}}(\Delta T)$ starts appearing on the timescale of the reaction.

In practice, however, the decomposition of $\mathbf{M}^{\mathrm{cor}}(\Delta T)$ using Eq. (11) is not easy because the separation of fluorescence decay curves of different species in $\mathbf{M}^{\mathrm{cor}}(\Delta T)$ is not straightforward when reference data (i.e., the functional forms of $I_i(t)$'s) are not available. This complexity is reduced by considering the fluorescence lifetime of each species instead of the fluorescence decay curve. In general, one can represent the fluorescence decay curve of a certain species by using continuously distributed fluorescence lifetime, τ, and corresponding amplitude, $a(\tau)$:

$$I(t) = \int_0^\infty a(\tau) \exp(-t/\tau)\, d\tau. \tag{12}$$

Then, one can rewrite $\mathbf{M}^{\mathrm{cor}}(\Delta T)$ as,

$$\begin{aligned} M_{ij}^{\mathrm{cor}}(\Delta T) &= \sum_{k,l} g_{kl}^{\mathrm{cor}}(\Delta T) \int_0^\infty a_k(\tau') \exp\left(-t^{(i)}/\tau'\right) d\tau' \int_0^\infty a_l(\tau'') \exp\left(-t^{(j)}/\tau''\right) d\tau'' \\ &= \int_0^\infty \int_0^\infty \widetilde{M}_{\tau'\tau''}(\Delta T) \exp\left(-t^{(i)}/\tau'\right) \exp\left(-t^{(j)}/\tau''\right) d\tau' d\tau'', \end{aligned} \tag{13}$$

where we introduced a two-dimensional lifetime correlation map:

$$\widetilde{M}_{\tau'\tau''}(\Delta T) = \sum_{k,l} g_{kl}^{\mathrm{cor}}(\Delta T) a_k(\tau') a_l(\tau''). \tag{14}$$

$a(\tau)$ has well-separated peak(s) when each species has a well-defined fluorescence lifetime. It is also expected that $\widetilde{\mathbf{M}}(\Delta T)$ shows a clear peak pattern in a two-dimensional map which directly represents auto- and cross-correlations of the species in the sample. Therefore, $\widetilde{\mathbf{M}}(\Delta T)$ is much more suitable for intuitively interpreting the whole kinetics on the species basis. The conversion from $I(t)$ to $a(\tau)$ is formally equivalent to inverse Laplace transform (ILT) and the conversion $\mathbf{M}^{\mathrm{cor}}(\Delta T) \rightarrow \widetilde{\mathbf{M}}(\Delta T)$ corresponds to two-dimensional ILT. Usually one needs a special procedure to perform ILT because it is known that ILT is numerically unstable. MEM (maximum entropy method) is sometimes employed for suppressing the numerical instability [17, 18]. As described in detail in a published paper [12], a MEM approach is used for this 2D ILT problem and $\widetilde{\mathbf{M}}(\Delta T)$ is obtained from $\mathbf{M}^{\mathrm{cor}}(\Delta T)$ in 2D FLCS.

The above-described procedure for obtaining $\widetilde{\mathbf{M}}(\Delta T)$ realizes 2D FLCS. The cross-correlation between different species ($g_{kl}^{\mathrm{cor}}(\Delta T)$, $k \neq l$) appears in $\widetilde{\mathbf{M}}(\Delta T)$ map as an off-diagonal peak between two different lifetimes representing the species k and l (Eq. (14)). Therefore, by examining the ΔT-dependence of the intensity of off-diagonal peaks, one can trace the temporal evolution of $g_{kl}^{\mathrm{cor}}(\Delta T)$, which represents the equilibration process between the two species (k and l).

Figure 5 shows an illustrative example of 2D FLCS [11]. Here, in order to exemplify the 2D FLCS analysis using well-defined parameters, a synthetic photon data was generated by kinetic Monte Carlo simulation. We assumed a two-state reaction model between states A and B with the forward rate constant k_{f} and the backward rate constant k_{b}, where $k_{\mathrm{f}} = k_{\mathrm{b}} = (100\ \mu\mathrm{s})^{-1}$. The fluorescence lifetimes of the states A and B were set at 1 and 5 ns, respectively. Figure 5a shows $\mathbf{M}^{\mathrm{cor}}(\Delta T)$ constructed from the simulated photon data for different lag times. One can see that the shape of the 2D correlation pattern changes with ΔT, which are also evident in the slices of the 2D maps at different microtime values (Fig. 5a, bottom). This change reflects the interconversion between A and B which occurs during ΔT. It can

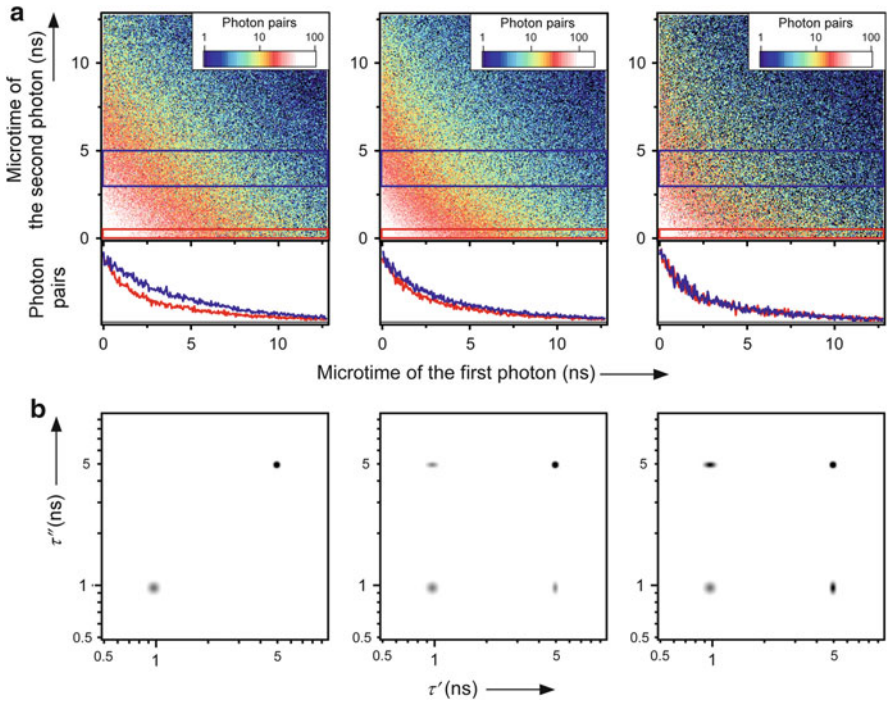

Fig. 5 2D FLCS applied to the synthetic photon data generated by kinetic Monte Carlo simulation. (**a**) The correlated part of the 2D map ($\mathbf{M}^{\mathrm{cor}}(\Delta T)$) at $\Delta T = 0$–10 μs (*left*), 40–60 μs (*center*), and 200–220 μs (*right*). The slices of these maps integrated over the colored rectangle regions are shown in the *bottom* with corresponding colors. (**b**) The converted 2D lifetime maps ($\widetilde{\mathbf{M}}(\Delta T)$) at $\Delta T = 0$–10 μs (*left*), 40–60 μs (*center*), and 200–220 μs (*right*)

be more clearly visualized by using 2D ILT that converts $\mathbf{M}^{\mathrm{cor}}(\Delta T)$ to $\widetilde{\mathbf{M}}(\Delta T)$ (Fig. 5b). In the converted 2D lifetime maps, one can clearly see isolated diagonal peaks, which correspond to the A ($\tau = 1$ ns) and B states ($\tau = 5$ ns). Absence of the cross peaks between these two states at the shortest lag time ($\Delta T = 0$–10 μs) is a clear evidence of independence of these states. Subsequent gradual rise of the cross peaks reflects transformation between the two states, which accords with the adopted reaction model. This result exhibits that, by comparing 2D lifetime maps at different ΔT, one can visualize the equilibration process between different species and determine its time constant in a species-specific manner.

3.4 Application: DNA Dynamics

Next, we show an application of 2D FLCS to the hairpin-forming DNA molecule that was examined in the previous section by lifetime-weighted FCS (Fig. 2) [12]. Here, in order to clarify the dynamics of DNA hairpin observed at $\Delta T \sim 100$ μs, $\mathbf{M}^{\mathrm{cor}}(\Delta T)$ is built for three time regions encompassing this timescale (Fig. 6a). These $\mathbf{M}^{\mathrm{cor}}(\Delta T)$ exhibit ΔT-dependent change. However, in contrast to the previous example, the change of $\mathbf{M}^{\mathrm{cor}}(\Delta T)$ is not very obvious and hence it is difficult to obtain physical insight directly from this 2D map. In this case, the conversion from $\mathbf{M}^{\mathrm{cor}}(\Delta T)$ to $\widetilde{\mathbf{M}}(\Delta T)$ by 2D ILT is very effective (Fig. 6b). In the 2D ILT analysis using MEM, we assumed three independent components that coexist in the sample. For these three components, MEM determined the fluorescence lifetime distribution, $a_k(\tau)$, and the auto- and cross-correlations, ${g_{kl}}^{\mathrm{cor}}(\Delta T)$ (Eqs. (13, 14)). The analysis was simultaneously performed on the three 2D maps shown in Fig. 6a, which enabled us to obtain a common set of $a_k(\tau)$ that is independent of ΔT (global analysis). The obtained $a_k(\tau)$'s ($k = 1$–3) is shown in Fig. 6c. The observed peaks in $\widetilde{\mathbf{M}}(\Delta T)$ in the shortest ΔT (Fig. 6b) correspond to the autocorrelation peaks of these three components. (Note that some components exhibit multi-exponential decays due to fast structural fluctuation, so that cross peaks appear in autocorrelation of these species.) Very importantly, one can find growth of new cross peaks in the second and third panels of Fig. 6b, as indicated by arrows. These cross peaks represent the origin of the ~100 μs dynamics of the DNA hairpin observed by the lifetime-weighted FCS (Fig. 2), and they correspond to the cross-correlation between the second ($k = 2$) and the third ($k = 3$) components in Fig. 6c. Based on the fluorescence decay measurements on control samples, the second and the third components were assigned to the open form and the closed form, respectively, whereas it was found that the first ($k = 1$) component was due to the DNA molecule lacking an active acceptor dye [12]. Therefore, the observed dynamics is attributed to the interconversion between the open form and the closed form. On the other hand, any cross peaks between the first component and others are not observed. It is consistent with that the first component stems from a species without an active acceptor and hence its fluorescence lifetime does not change with the lag time ΔT.

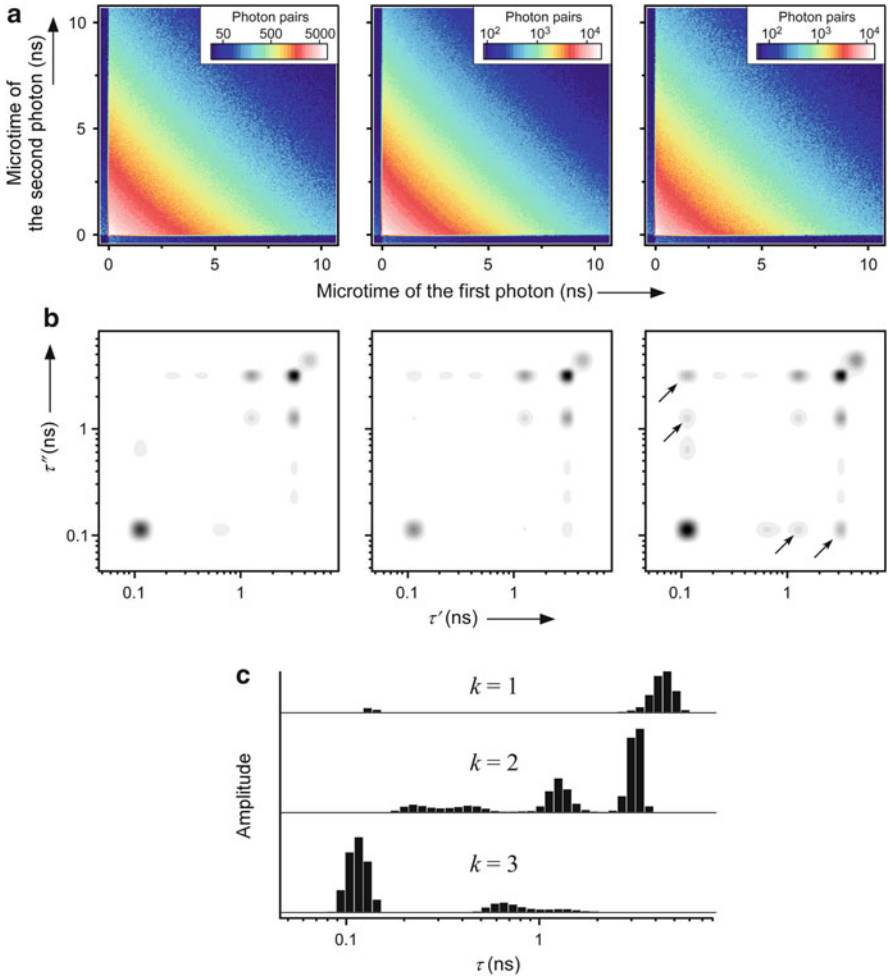

Fig. 6 2D FLCS of a DNA hairpin. (**a**) The correlated part of the 2D map ($\mathbf{M}^{\mathrm{cor}}(\Delta T)$) at $\Delta T = 10$–30 μs (*left*), 30–100 μs (*center*), and 100–200 μs (*right*). (**b**) The converted 2D lifetime map ($\widetilde{\mathbf{M}}(\Delta T)$) at $\Delta T = 10$–30 μs (*left*), 30–100 μs (*center*), and 100–200 μs (*right*). (**c**) Three independent components ($a_k(\tau)$, $k = 1$–3) that are extracted in the analysis. Their auto- and cross-correlations comprises 2D lifetime maps in (**b**)

Figure 7 summarizes the dynamics of the DNA hairpin concluded from this experiment. The dynamics of the hairpin DNA can be described by a two-state model between the open and closed forms, and the acceptor-inactive DNA coexists in the sample. The 2D FLCS was proven to be useful to obtain the species-specific correlation that can separate multiple species such as the open form, the closed form, and even inactive molecules in the sample, without any prior knowledge about each species.

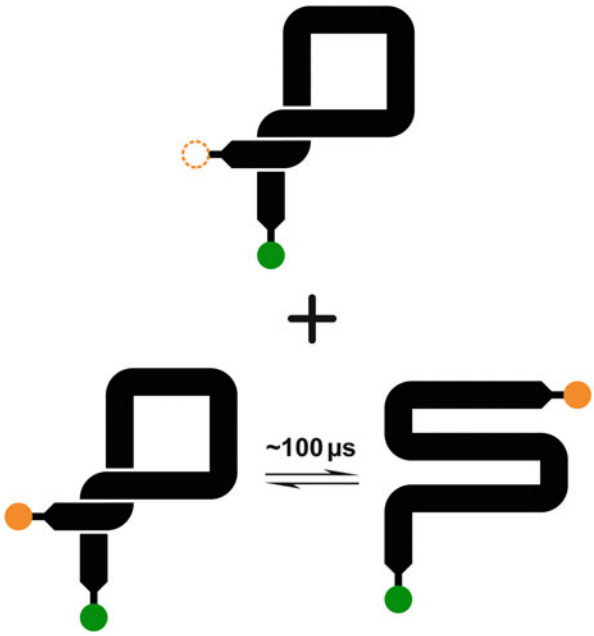

Fig. 7 A schematic picture of the dynamics of a DNA hairpin observed by 2D FLCS. *Green* and *orange circles* represent the donor (FAM) and acceptor (TAMRA) dyes, respectively. The closed form (*bottom left*) and the open form (*bottom right*) are equilibrated in ~100 µs, whereas an acceptor-inactive species (*top*) also exists in the sample solution

4 Photon Interval Analysis

So far, we have discussed how to quantify fluctuations of fluorescence lifetime using time-tagged TCSPC through two newly developed methods, i.e., lifetime-weighted FCS and 2D FLCS. In this section, we turn our attention to another way of using time-tagged TCSPC data, focusing on its local property. Instead of collecting every photon pairs found with a fixed time interval, we consider only photon pairs directly neighboring in the photon table, and examine the relationship between their microtimes and the time interval (Fig. 8a). Photon interval distribution is sometimes investigated by using the Hanbury Brown and Twiss setup [19] to study nanosecond photon correlations [20, 21], utilizing the definite relationship between the photon interval distribution and the intensity correlation function. Here, we present an application of photon interval analysis that incorporates microtime information, and show its usefulness for analyzing the timing instability problem of photon detectors [13].

Single photon avalanche photodiode (SPAD) is a photon detector commonly used in TCSPC experiments, particularly in single-molecule fluorescence lifetime measurements and fluorescence lifetime imaging (FLIM). A well-known drawback of SPADs is the counting-rate dependence of the shape and peak position of the instrument response function (IRF), which hampers accurate determination of the fluorescence lifetime. It has been claimed that this counting-rate dependence arises from the quenching circuit in SPADs [22]. In the following, this problem is analyzed by using the IRF data measured by time-tagged TCSPC, and an efficient calibration method is given [13].

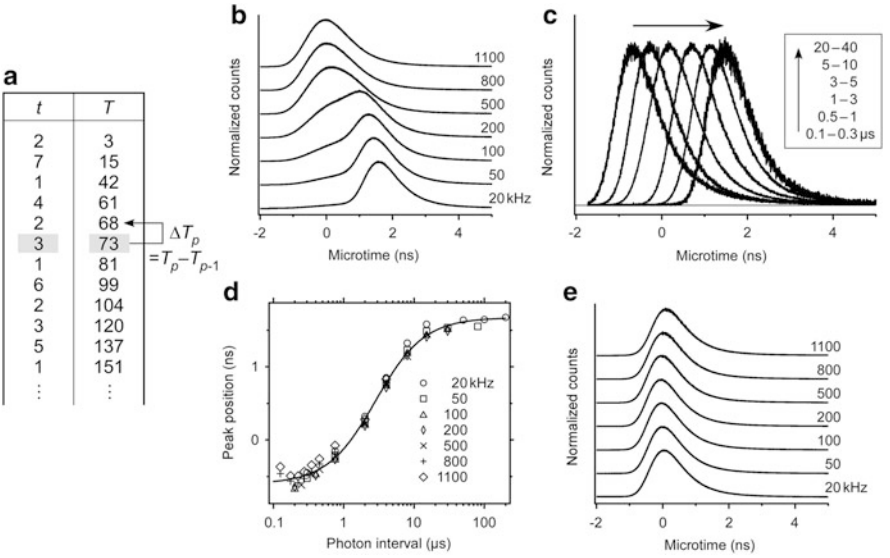

Fig. 8 Photon interval analysis of time-tagged TCSPC data. (**a**) Definition of the photon interval of *p*th photon. (**b**) Counting-rate dependence of the IRF obtained with a SPAD. (**c**) IRF curves reconstructed from photons of selected ΔT values. They demonstrate ΔT-dependence of the IRF. (**d**) ΔT-dependence of the peak position of the IRF measured at various counting rates. (**e**) Counting-rate dependence of the IRF after calibration

Figure 8b shows the counting-rate dependence of the IRF of a SPAD. These curves are obtained by building the microtime histogram of scattered photons of laser pulses with various intensities. The data clearly shows that the time profile of IRF drastically changes with the counting rate. To examine this timing instability in more detail, all the detected photons are classified according to the time interval with respect to the preceding photon using their macrotime information (Fig. 8a):

$$\Delta T_p = T_p - T_{p-1}. \tag{15}$$

ΔT-dependent IRF is evaluated by collecting photons that have common ΔT values (Fig. 8c). The peak position of the IRF shows a monotonous shift with ΔT, whereas the shape is mostly preserved. This implies that the counting-rate dependence observed in Fig. 8b is essentially due to ΔT-dependent timing shift. The ΔT-dependent peak position of IRF was measured at various counting rates and is plotted in Fig. 8d. It is clearly seen that the data measured with different counting rates overlap with each other and follow the same trend. This result leads us to conclude that the time interval, ΔT, rather than the mean counting rate, is the factor that determines the timing instability.

If one analyzes the ΔT-dependence of the mean delay time (Fig. 8d) in more detail, one may further obtain some insight into the underlying physics that causes the timing instability. However, even without going into the detail of the

mechanism, one can use this ΔT-dependence for calibrating the counting-rate dependent timing shift [13]. Actually, the calibration curve is obtainable by fitting the ΔT-dependent peak position of IRF (Fig. 8d) with an appropriate function. We used the Hill equation to fit the observed data (Fig. 8d, solid line). The microtime of any photons detected with the same detector can be calibrated using the same calibration curve. Figure 8e shows the calibrated IRF curves at various counting rates. The effect of the calibration is obvious, i.e., the shape and position of IRF become almost independent of the counting rate. This calibration allows us to obtain the best achievable time resolution in TCSPC experiments, particularly in applications such as FLIM where the counting rate largely fluctuates.

5 Concluding Remarks

In this chapter, we described two methods using time-tagged TCSPC, which have been recently developed to derive as much information as possible from the photon data collected. We note that these methods do not require any modification of the optical (microscopy) setup of a standard TCSPC, because they are purely numerical algorithms. However, these methods can extract information that is usually hidden under seemingly random fluctuations. Even though the structure of time-tagged TCSPC data is rather simple, we believe that the obtainable knowledge from the data has not been fully exploited yet. Therefore, there exist vast possibilities to extend the usage of time-tagged TCSPC for various applications.

References

1. Becker W (2005) Advanced time-correlated single photon counting techniques. Springer series in chemical physics, vol 81. Springer, Heidelberg
2. Eggeling C, Fries JR, Brand L, Günther R, Seidel CAM (1998) Monitoring conformational dynamics of a single molecule by selective fluorescence spectroscopy. Proc Natl Acad Sci U S A 95:1556–1561
3. Palo K, Brand L, Eggeling C, Jaeger S, Kask P, Gall K (2002) Fluorescence intensity and lifetime distribution analysis: toward higher accuracy in fluorescence fluctuation spectroscopy. Biophys J 83:605–618
4. Yang H, Xie XS (2002) Probing single-molecule dynamics photon by photon. J Chem Phys 117:10965–10979
5. Boehmer M, Wahl M, Rahn H-J, Erdmann R, Enderlein J (2002) Time-resolved fluorescence correlation spectroscopy. Chem Phys Lett 353:439–445
6. Gregor I, Enderlein J (2007) Time-resolved methods in biophysics. 3. Fluorescence lifetime correlation spectroscopy. Photochem Photobiol Sci 6:13–18
7. Kapusta P, Wahl M, Benda A, Hof M, Enderlein J (2007) Fluorescence lifetime correlation spectroscopy. J Fluoresc 17:43–48
8. Kapusta P, Macháň R, Benda A, Hof M (2012) Fluorescence lifetime correlation spectroscopy (FLCS): concepts, applications and outlook. Int J Mol Sci 13:12890–12910

9. Ishii K, Tahara T (2010) Resolving inhomogeneity using lifetime-weighted fluorescence correlation spectroscopy. J Phys Chem B 114:12383–12391
10. Ishii K, Tahara T (2012) Extracting decay curves of the correlated fluorescence photons measured in fluorescence correlation spectroscopy. Chem Phys Lett 519–520:130–133
11. Ishii K, Tahara T (2013) Two-dimensional fluorescence lifetime correlation spectroscopy. 1. Principle. J Phys Chem B 117:11414–11422
12. Ishii K, Tahara T (2013) Two-dimensional fluorescence lifetime correlation spectroscopy. 2. Application. J Phys Chem B 117:11423–11432
13. Otosu T, Ishii K, Tahara T (2013) Note: simple calibration of the counting-rate dependence of the timing shift of single photon avalanche diodes by photon interval analysis. Rev Sci Instrum 84:036105
14. Lakowicz JR (2006) Principles of fluorescence spectroscopy, 3rd edn. Springer, New York
15. Yang H, Xie XS (2002) Statistical approaches for probing single-molecule dynamics photon-by-photon. Chem Phys 284:423–437
16. Burstyn HC, Sengers JV (1983) Time dependence of critical concentration fluctuations in a binary liquid. Phys Rev A 27:1071–1085
17. Livesey AK, Brochon JC (1987) Analyzing the distribution of decay constants in pulse-fluorimetry using the maximum entropy method. Biophys J 52:693–706
18. Brochon JC (1994) Maximum entropy method of data analysis in time-resolved spectroscopy. Methods Enzymol 240:262–311
19. Hanbury Brown R, Twiss RQ (1956) Correlation between photons in two coherent beams of light. Nature 177:27–29
20. Berglund AJ, Doherty AC, Mabuchi H (2002) Photon statistics and dynamics of fluorescence resonance energy transfer. Phys Rev Lett 89:068101
21. Nettels D, Gopich IV, Hoffmann A, Schuler B (2007) Ultrafast dynamics of protein collapse from single-molecule photon statistics. Proc Natl Acad Sci U S A 104:2655–2660
22. Rech I, Labanca I, Ghioni M, Cova S (2006) Modified single photon counting modules for optimal timing performance. Rev Sci Instrum 77:033104

MFD-PIE and PIE-FI: Ways to Extract More Information with TCSPC

Anders Barth*, Lena Voith von Voithenberg*, and Don C. Lamb

Abstract Pulsed interleaved excitation (PIE) is the method of fast alternation of pulsed lasers for quasi-simultaneous observation of fluorophores with different spectral properties. PIE was originally introduced to enable artifact-free fluorescence cross-correlation measurements, while first experiments with alternating laser excitation (ALEX) used the dual excitation of donor and acceptor for single-pair Förster resonance energy transfer (spFRET). In this article, we will review the benefit of PIE for spFRET experiments with multiparameter fluorescence detection (MFD). The direct probing of the acceptor fluorophore in PIE increases the robustness of the quantitative MFD analysis and extends it to even more parameters.

Recently, PIE has been combined with commonly used fluorescence fluctuation imaging techniques such as raster image correlation spectroscopy (RICS) and the number and brightness analysis (N&B). We highlight how PIE improves these methods, and how artifacts in the analysis can be avoided. Similar to PIE-FCS, quantitative cross-correlation raster image correlation spectroscopy (ccRICS) is greatly simplified. Additionally, the lifetime information can be used to further increase the contrast and sensitivity of the method with raster lifetime image correlation spectroscopy (RLICS).

*These authors contributed equally to this work.

A. Barth, L. Voith von Voithenberg, and D.C. Lamb (✉)
Department of Chemistry and Center for Nano Science, Ludwig-Maximilians-Universität München, Butenandtstr. 11, 81377 Munich, Germany

Center for Integrated Protein Science Munich, Germany
e-mail: anders.barth@cup.uni-muenchen.de; lena.voithenberg@cup.uni-muenchen.de; d.lamb@lmu.de

P. Kapusta et al. (eds.), *Advanced Photon Counting: Applications, Methods, Instrumentation*, Springer Ser Fluoresc (2015) 15: 129–158, DOI 10.1007/4243_2014_66,

Keywords MFD · PIE · PIE-FI · spFRET

Contents

1 Pulsed Interleaved Excitation 130
1.1 How PIE Works 131
2 Multiparameter Fluorescence Detection with PIE 132
2.1 Primer on Förster Resonance Energy Transfer 133
2.2 Instrumentation 134
2.3 Selection of Bursts 135
2.4 Advanced Parameters 138
2.5 Further Analyses 143
2.6 Increasing the Number of Photons 143
2.7 Summary and Outlook for MFD-PIE 144
3 Pulsed Interleaved Excitation Fluctuation Imaging 145
3.1 Introduction 145
3.2 Basic Theory of Raster Image Correlation Spectroscopy 146
3.3 Comparison of FCS and RICS 148
3.4 What PIE Brings to RICS 149
3.5 Raster Lifetime Image Correlation Spectroscopy 151
3.6 Number and Brightness Analysis with PIE 153
3.7 Summary and Outlook for PIE-FI 154
References 155

1 Pulsed Interleaved Excitation

In the mid-2000s, methods for the quasi-simultaneous excitation of multiple fluorophores have been developed. Alternating laser excitation (ALEX) was first introduced as an alternation of lasers by electro-optical modulators on the microsecond timescale [1, 2]. By use of pulsed lasers, the alternation of excitation is extended to the nanosecond timescale, termed pulsed interleaved excitation (PIE). In combination with time-correlated single photon counting (TCSPC), additional information on fluorescence lifetimes of the fluorophores is available [3–5]. Originally introduced for fluorescence correlation spectroscopy (FCS), PIE can improve the quantitative analysis of almost any multi-color fluorescence method by specifically filtering misguided emission from the more blue-shifted fluorophore into the detection channel of the red-shifted fluorophore (crosstalk or spectral bleed-through) and excitation of the more red-shifted fluorophore by the excitation laser of the blue-shifted fluorophore.

1.1 How PIE Works

In PIE, multiple picosecond pulsed lasers with a typical repetition rate of 1–50 MHz are alternated using an optical or electronic delay (Fig. 1a, b) [6]. The time-delay has to be chosen according to the fluorescence decay of the detected fluorophores

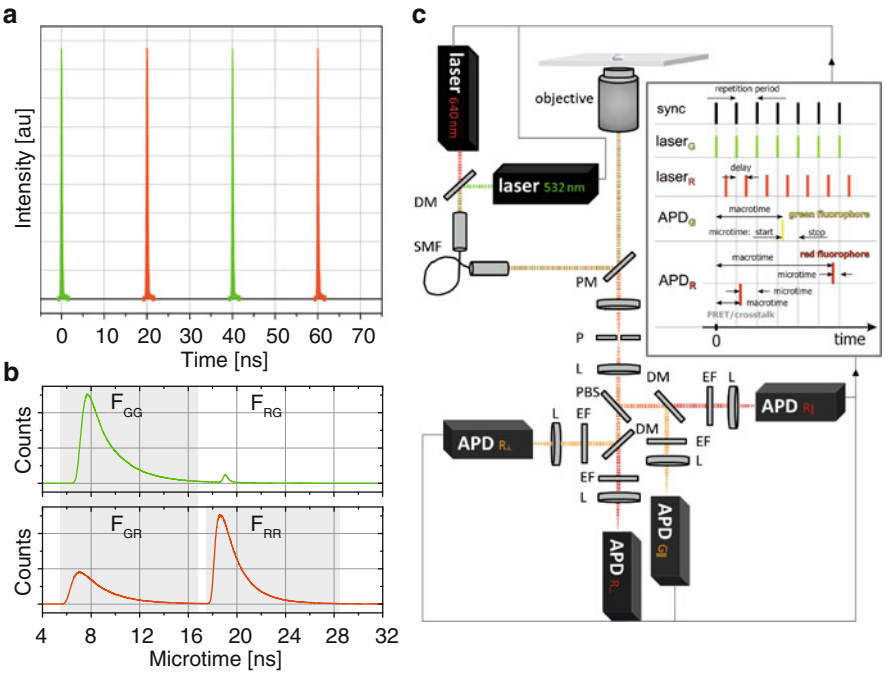

Fig. 1 Schematic illustration of a dual-color confocal microscope with PIE. (**a**) Excitation scheme of pulsed lasers using PIE on a dual-color microscope. A green and a red laser repeatedly excite the sample with picosecond laser pulses, which are alternated on the nanosecond timescale. Pulses are delayed with respect to each other electronically or optically. (**b**) Microtime histograms of four detection channels observable by the use of PIE. F_{GG}: Green detection after green excitation pulse. The microtime histogram shows the fluorescence decay of the green fluorophore. The green fluorophores is not excited by laser light of lower frequency (green detection after red excitation pulse, $F_{RG} = 0$). F_{RR}: Red detection after red excitation pulse shows the fluorescence decay of the red fluorophore. F_{GR}: Fluorescence detected in the red channel after green excitation combines crosstalk of the green sample into the red channel, direct excitation of the red fluorophore by the green laser, and FRET emission of the red fluorophore. (**c**) Schematic of a confocal microscope with polarized dual-color excitation using pulsed lasers. The lasers are combined by a dichroic mirror (*DM*) and focused into the sample by the objective. Fluorescence is collected and focused through a confocal pinhole (*P*). It is then separated by a polarizing beam splitter (*PBS*) into parallel and orthogonal polarized light and split further according to wavelength by dichroic mirrors. An emission filter (*EF*) blocks scattered laser light before the fluorescence is focused onto avalanche photodiodes (*APD*). For each photon, the TCSPC electronic registers the arrival time with respect to the start of the measurement (macrotime), the arrival time after the last laser pulse (microtime), and the detection channel

(Sect. 2.2). In a different approach, Olofsson and Margeat [7] have recently realized PIE with a single white-light laser.

When combining alternating excitation with TCSPC electronics, the emission of different fluorophores can not only be separated spectrally, but also temporally with respect to the excitation source. Each photon is characterized by its detection channel, macrotime (the time relative to the start of the experiment), and microtime (the time between the master clock that controls laser excitation and detection of the photon). For two-color excitation, the result is a total of four PIE channels that can be constructed from the microtime histograms (Fig. 1b). The green channel after green excitation F_{GG} exclusively contains photons originating from the green fluorophore. Likewise, the red channel after red excitation F_{RR} contains only photons from the red fluorophore. The green channel after red excitation F_{RG} is generally empty, since emission filters block fluorescence of longer wavelength and direct excitation of the more blue-shifted fluorophore by the red laser is negligible. In the red channel after green excitation F_{GR}, crosstalk from the green fluorophore, signal from the red fluorophore due to direct excitation by the green laser, and FRET-sensitized acceptor emission are combined. The crucial advantage of PIE is that these contributions to the total red signal are separated from the pure signal of the red fluorophore after red excitation.

2 Multiparameter Fluorescence Detection with PIE

The detection of fluorescence from single molecules requires high sensitivity, low background, and a confined observation volume. In solution-based burst analysis experiments, this is achieved by combining the femtoliter-sized focal volume of a confocal microscope with picomolar concentrations of analytes. High laser powers and detectors with single molecule sensitivity ensure that sufficient signal is detected from individual molecules diffusing through the focus.

Eggeling et al. [8] introduced multiparameter fluorescence detection (MFD) in 2001 with a confocal epi-illuminated microscope, which allowed simultaneous detection of intensity, anisotropy, lifetime, and spectral range of individual molecules. The knowledge about these parameters greatly increases the robustness of the single-pair Förster resonance energy transfer (spFRET) analysis and extends the available parameter space to include additional properties of the fluorophore and molecule of interest. The combination of MFD with PIE (MFD-PIE) further increases the information by direct probing of the acceptor fluorophore [4, 9]. As spFRET experiments are one of the primary applications of MFD-PIE, we will give a short overview of spFRET before discussing details of data collection and analysis.

2.1 Primer on Förster Resonance Energy Transfer

Combining Förster resonance energy transfer (FRET) with single-molecule spectroscopy (single-pair FRET) composes a versatile tool to gain information on conformational states and dynamic transitions of single molecules by observation of the interfluorophore distance. In contrast to ensemble measurements, detailed information about the heterogeneity of the system is accessible, and experimental artifacts such as incomplete labeling can be sorted out on the basis of single molecules.

In FRET, the energy of an excited donor fluorophore is transferred radiation-less to an acceptor fluorophore in close proximity via dipole-dipole interactions. The FRET efficiency is defined as the fraction of donor excitations that result in energy transfer to the acceptor. It can be expressed as the ratio of the rate of energy transfer (k_{FRET}) to the sum of all radiative (k_{f}) and non-radiative (k_{nr}, k_{FRET}, ...) rates that depopulate the excited state of the donor [10]:

$$E = \frac{k_{\mathrm{FRET}}}{k_{\mathrm{FRET}} + k_{\mathrm{f}} + k_{\mathrm{nr}} + \ldots}.$$

The rate of energy transfer, and thus the FRET efficiency, depends on the sixth power of the distance between the fluorophores:

$$E = \frac{1}{1 + \left(\frac{R}{R_0}\right)^6},$$

where the Förster radius R_0 is given by:

$$R_0\ [\mathrm{m}] = \left(\frac{9{,}000 \cdot \ln 10 \cdot \kappa^2 \cdot \phi_{\mathrm{D}(0)} \cdot J}{128 \cdot \pi^5 \cdot n^4 \cdot N_{\mathrm{A}}}\right)^{1/6}.$$

The Förster radius depends on the refractive index of the sample n, the quantum yield of the donor $\phi_{\mathrm{D}(0)}$, the overlap integral J of the donor emission and the acceptor absorption spectra, and the relative orientation of the donor and acceptor dipoles described by κ^2. When the rotation of the dyes is unhindered, complete averaging of the orientation yields a κ^2 value of 2/3rds.

The FRET efficiency can either be calculated from the photon counts after donor excitation, or from the decrease of the fluorescence lifetime of the donor fluorophore caused by the FRET-induced quenching:

$$E = \frac{F_{\mathrm{A}}}{F_{\mathrm{D}} + F_{\mathrm{A}}} = 1 - \frac{\tau_{\mathrm{DA}}}{\tau_{\mathrm{D}(0)}},$$

where $F_{D/A}$ is the number of photons in the donor or acceptor channel, and τ_{DA} and $\tau_{D(0)}$ are the fluorescence lifetimes of the donor in the presence and in the absence of the acceptor, respectively.

A semi-quantitative FRET indicator, or proximity ratio, can be calculated based on the raw photon counts in the donor and the acceptor detection channel after donor excitation:

$$E_{PR} = \frac{F_{DA}}{F_{DD} + F_{DA}}.$$

To obtain accurate FRET efficiencies, the red signal after green excitation has to be corrected for spectral crosstalk of the donor in the acceptor channel (β) and direct excitation of the acceptor by the green laser (α). In addition, the parameter γ, which accounts for relative differences in the detection efficiency and quantum yield of the two fluorophores needs to be determined:

$$\gamma = \frac{\phi_A \eta_A^{\lambda_{emA}}}{\phi_D \eta_D^{\lambda_{emD}}},$$

where $\phi_{D/A}$ is the quantum yield of the donor and acceptor, respectively, and $\eta_A^{\lambda_{emA}}/\eta_D^{\lambda_{emD}}$ is the ratio of the detection efficiencies. The corrected FRET efficiency is thus given by:

$$E = \frac{F_{DA} - \alpha F_{AA} - \beta F_{DD}}{F_{DA} - \alpha F_{AA} - \beta F_{DD} + \gamma F_{DD}}.$$

2.2 Instrumentation

A typical confocal microscope for MFD-PIE experiments combines picosecond pulsed excitation lasers that are synchronized by TCSPC hardware and interleaved by optical or electrical delay (Fig. 1c). The repetition rate of the lasers should be chosen as high as possible to maximize the excitation rate while still allowing the full decay of the fluorescence signal to avoid temporal crosstalk. A repetition rate of the lasers of 27 MHz opens an interval of approximately 18 ns for the photon detection of different fluorophores. With fluorescence lifetimes in the range of 1.5–4 ns for commonly used dyes, this ensures detection of over 99% of the fluorescence decay.

In our setup, the lasers are combined by a single-mode fiber and focused into the sample by a water immersion objective. Fluorescence is collected by the same objective, focused through a pinhole and separated with respect to polarization and wavelength by a polarizing beam splitter and dichroic mirrors, respectively. Emission filters are used to block scattered laser light. Photons are detected using avalanche photodiodes and recorded using TCSPC cards. Thereby, the detection channel, the micro-, and the macrotime are recorded for each photon.

2.3 Selection of Bursts

2.3.1 Burst Search Algorithm

To distinguish bursts of fluorescence from the constant background signal, we employ an all-photon burst search as introduced by Nir et al. [11]. The algorithm uses a sliding time window to estimate the local count rate around every photon. The respective photon belongs to a burst when this value exceeds a given threshold. Bursts with more than a given minimum number of photons are considered for further analysis. The parameters can be tuned as needed. A shorter time window will result in a more accurate detection of the edges of bursts, but leads to an increase in the uncertainty of the estimated local count rate, which may artificially split bursts. If the time window is large, a significant amount of adjacent background signal may be falsely included into the burst. Generally, we use a time window of 500 μs and a minimum photon count of ten, thus requiring a local count rate of at least 20 kHz.

2.3.2 Stoichiometry

The information on stoichiometry obtained by the application of PIE offers the option to distinguish molecules labeled with the donor–acceptor dye pair from singly labeled molecules or molecules that do not have photoactive fluorophores.

The stoichiometry is defined as the ratio of signal after green excitation to the total signal detected during a burst:

$$S_{\mathrm{PR}} = \frac{F_{\mathrm{GG}} + F_{\mathrm{GR}}}{F_{\mathrm{GG}} + F_{\mathrm{GR}} + F_{\mathrm{RR}}}.$$

Although separation of different populations can be achieved using S_{PR}, the corrected stoichiometry can often be helpful in determining correction factors from the single-labeled populations:

$$S = \frac{F_{\mathrm{GR}} - \alpha F_{\mathrm{RR}} - \beta F_{\mathrm{GG}} + \gamma F_{\mathrm{GG}}}{F_{\mathrm{GR}} - \alpha F_{\mathrm{RR}} - \beta F_{\mathrm{GG}} + \gamma F_{\mathrm{GG}} + F_{\mathrm{RR}}}.$$

Donor–acceptor dual-labeled molecules correspond to an intermediate stoichiometry whose value depends on the relative laser powers and absorption probabilities of the fluorophores, while donor-only molecules have a stoichiometry of ~1 and acceptor-only labeled ones a stoichiometry of ~0 [1]. A two-dimensional plot of FRET efficiency and stoichiometry values can therefore aid in the distinction of dual-labeled molecules and avoid the effect of incomplete labeling by the selective choice of dual-colored bursts (Fig. 2).

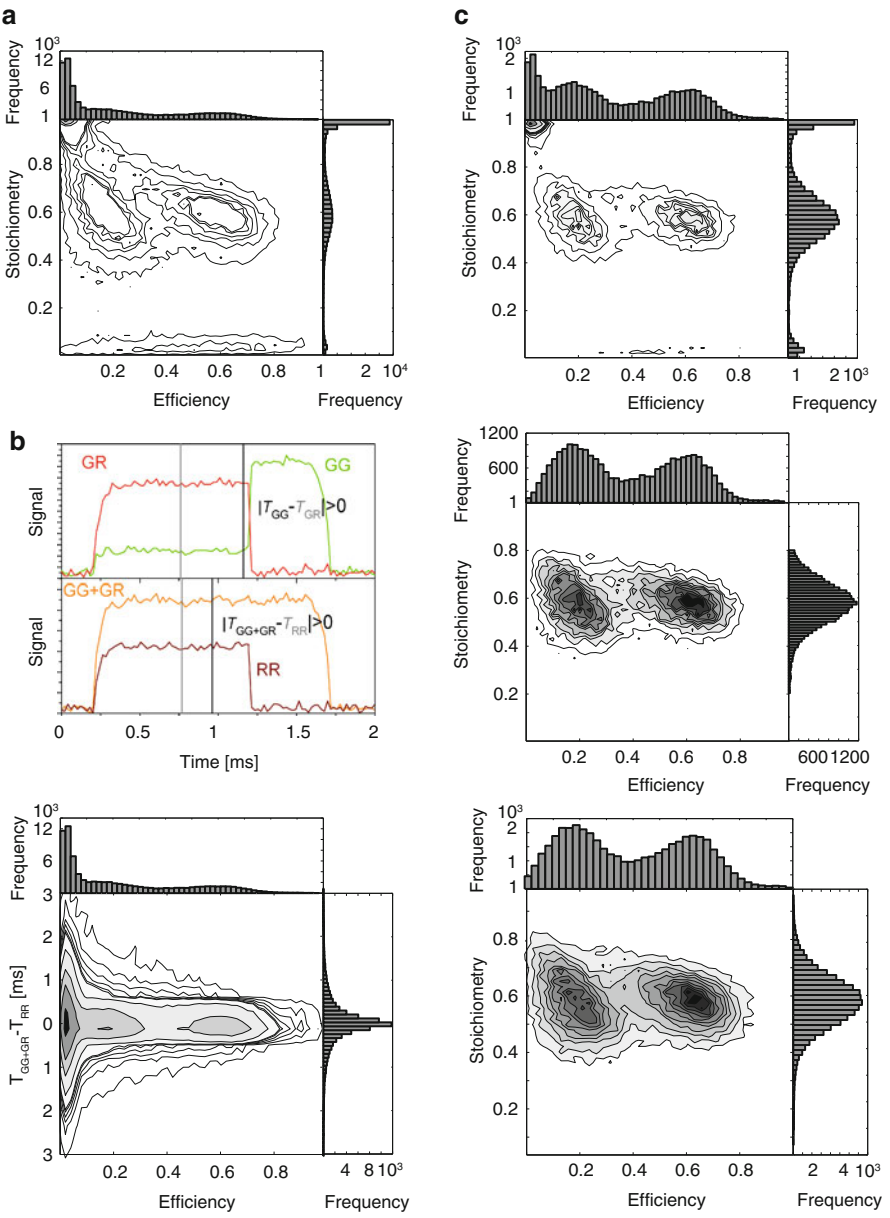

Fig. 2 Selection of double-labeled molecules after an all-photon burst search. Two-dimensional histograms of stoichiometry and $T_{GG+GR} - T_{RR}$ as a function of FRET efficiency for double-labeled DNAs with different FRET efficiencies. (**a**) A histogram of stoichiometry versus FRET efficiency of all bursts after an APBS search shows a population of donor-only ($S \sim 1$), acceptor-only ($S \sim 0$), and dual-labeled molecules (intermediate S). Trailing between donor-only and double-labeled populations is due to photobleaching of the acceptor and multi-molecule events. (**b**) *Upper panel*: Schematic intensity time traces of the fluorescence signal in the green and red detection channels for a burst with photobleaching. Photobleaching events can be detected using

2.3.3 Determination of Correction Factors

One advantage of MFD-PIE is that the correction factors for spectral crosstalk, direct excitation, and detection efficiencies can be extracted from subpopulations in the experiment itself [9]. The correction factor for spectral crosstalk can be calculated from the population labeled with donor-only:

$$\beta = \frac{E_{\mathrm{PR}}^{\mathrm{D_{only}}}}{1 - E_{\mathrm{PR}}^{\mathrm{D_{only}}}}.$$

The acceptor-only subpopulation of a measurement can be used to determine the correction factor for direct excitation α:

$$\alpha = \frac{S_{\mathrm{PR}}^{\mathrm{A_{only}}}}{1 - S_{\mathrm{PR}}^{\mathrm{A_{only}}}}.$$

The parameter for relative detection efficiency γ can be extracted from a linear fit of several FRET populations in a plot of efficiency versus the inverse of the stoichiometry from the slope Σ and the intercept Ω [12]:

$$\gamma = \frac{\Omega - 1}{\Omega + \Sigma - 1}.$$

Alternatively, with the lifetime information available, a comparison of FRET efficiencies determined from photon counts with those determined from the fluorescence lifetime can be used to determine the value for γ (Sect. 2.4.2).

Fig. 2 (continued) the mean macrotime in a burst intensity trace. Distinction of photobleaching of the acceptor from dynamic changes in FRET efficiency is possible using the macrotime information $T_{\mathrm{GG+GR}} - T_{\mathrm{RR}}$ obtained by PIE. *Lower panel*: A histogram of $T_{\mathrm{GG+GR}} - T_{\mathrm{RR}}$ versus FRET efficiency. Bursts can be selected according to the difference of mean macroscopic photon arrival time after donor excitation and mean macroscopic arrival time after acceptor excitation to remove molecules, in which the acceptor photobleached during their residence time in the detection volume. (**c**) Histograms of stoichiometry versus FRET efficiency as in panel a. *Upper panel*: Histogram after selection of molecules with $|T_{\mathrm{GG+GR}} - T_{\mathrm{RR}}| < 0.2$ ms as shown in panel b shows a decrease in trailing between the donor-only and double-labeled populations. *Middle panel*: Histogram after additional burst selection using stoichiometry values from $0.2 < S < 0.8$. *Lower panel*: Histogram of bursts extracted with dual channel burst search (*DCBS*). Only molecules emitting photons in both spectrally different detection channels are chosen by the burst search algorithm

2.3.4 Removal of Artifacts Caused by Bleaching, Blinking, and Multi-Molecule Events

In burst analysis experiments, artifacts can be caused when the acceptor undergoes photobleaching or blinking during the dwell time in the focus, or if multiple molecules reside in the focus simultaneously. When the acceptor molecule is transiently inactive during a burst, both the efficiency and stoichiometry are shifted towards the donor-only population, which is observable as streaking between the populations in the two-dimensional histogram of stoichiometry versus efficiency (Fig. 2a). Likewise, for multi-molecule events, an average value of the involved species is observed. In MFD-PIE, both events can be identified based on the difference in macroscopic photon arrival time after donor excitation and the mean macroscopic arrival time after acceptor excitation: $T_{GG+GR} - T_{RR}$. For molecules in which the acceptor undergoes photobleaching during the time in the detection volume, the mean arrival time after acceptor excitation is reduced compared to the mean arrival after donor excitation (Fig. 2b). By application of a threshold to $|T_{GG+GR} - T_{RR}|$, these molecules can be excluded from further analysis (Fig. 2b, c) [9]. Similarly, the difference in the mean arrival time between the donor and FRET channel ($T_{GG} - T_{GR}$) is sensitive to dynamic interconversion between FRET states. The great advantage of PIE or ALEX is that photobleaching can be filtered independently from conformational dynamics.

2.3.5 Dual Channel Burst Search

In a different approach, burst selection can already be performed early during the process of the burst search using the dual-channel burst search (DCBS) algorithm [11]. By performing all-photon burst searches on the photon streams after donor and acceptor excitation separately, donor-only and acceptor-only molecules can be filtered preemptively. Additionally, in the case of photobleaching, the event is not discarded completely, but the time in which both fluorophores were active is kept for analysis. The criteria for the burst search in the individual channels have to be adjusted according to their brightness. Once the correction factors have been determined, DCBS offers a fast alternative for the selection of bursts. For a comparison of the selection methods, see Fig. 2c.

2.4 Advanced Parameters

Once single-molecule bursts have been selected and the number of photons detected in the different channels from the individual bursts determined, a number of additional parameters can be analyzed from the MFD-PIE data.

2.4.1 Fluorescence Anisotropy

With polarized excitation and detection, it is possible to measure the steady-state anisotropy of a single molecule during a burst (Fig. 3a). Excitation of the fluorophore is most probable when its absorption dipole is collinear with the

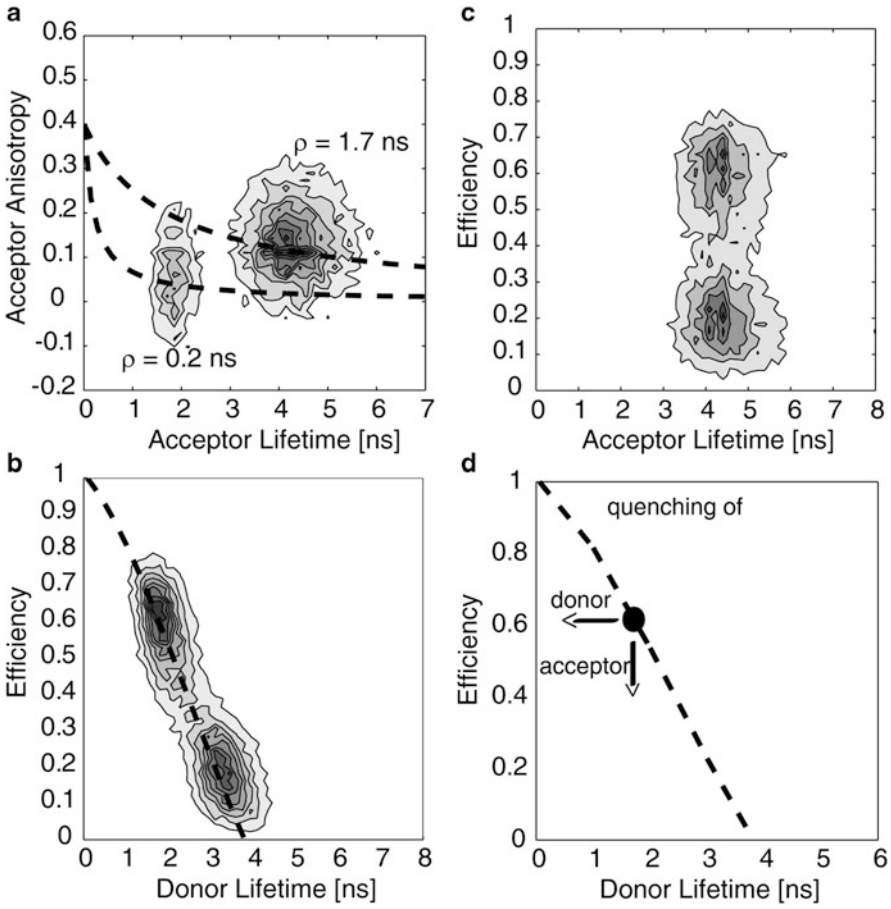

Fig. 3 Two-dimensional histograms including lifetime information derived from MFD-PIE experiments with dual-labeled DNA. (**a**) A histogram of acceptor anisotropy versus acceptor lifetime for a mixture of double-labeled DNA-Atto532-Atto647N and free Atto655 fluorophores. The unbound dye has a different fluorescence lifetime and shows different rotational mobility as described by the Perrin equations with different values for ρ (*dashed lines*). (**b**) A histogram of FRET efficiency versus donor lifetime for double-labeled molecules. The *dashed line* corresponds to the theoretical FRET curve expected for static populations. Two populations of DNA with different FRET efficiencies were found to lie on this curve. (**c**) The histogram of FRET efficiency versus acceptor lifetime after acceptor excitation shows no significant quenching of the acceptor fluorophore. (**d**) A schematic plot describing the effects of donor and acceptor fluorophore quenching on the determined FRET efficiency and donor lifetime. The static FRET curve is shown as a *dashed line*

polarization of the incident light. If the orientation of the fluorophore changes during its lifetime, the degree of polarization of the emitted light is reduced. From the intensities of the signal in the parallel and perpendicular detection channels, the fluorescence anisotropy is calculated by:

$$r = \frac{GF_{\parallel} - F_{\perp}}{(1 - 3k_2)GF_{\parallel} + (2 - 3k_1)F_{\perp}},$$

where G is the correction factor for the different detection efficiencies in the parallel and perpendicular channels, and k_1 and k_2 are correction factors accounting for polarization mixing caused by the objective lens [13]. The fluorescence anisotropy provides information about the rotational mobility and hence the size of the molecule. The relationship of the steady-state anisotropy as a function of fluorescence lifetime, τ, is described by the Perrin equation:

$$r(\tau) = \frac{r_0}{1 + \frac{\tau}{\rho}},$$

where r_0 is the fundamental anisotropy of the fluorophore and ρ is the rotational correlation time.

Figure 3a shows fits to the Perrin equation for free and DNA-bound dye. How appropriate the assumption of $\kappa^2 = 2/3$ is, which is correct for complete averaging of the fluorophore orientations, can be investigated in MFD-PIE experiments by examination of the anisotropy of both the donor and acceptor fluorophores.

Additionally, the time-resolved anisotropy decays available with PIE can be used to extract information about different components that contribute to the mobility of the fluorophores such as the motion of the dye itself and the rotation of the molecule to which it is attached.

2.4.2 Fluorescence Lifetime

By applying pulsed excitation, the fluorescence lifetimes of the donor and the acceptor molecules are accessible (Fig. 3). The lifetime is determined by assuming a single-exponential decay of the fluorescence intensity convoluted with the instrument response function. As the number of photons detected from a single molecule is limited, it is not possible to fit more complex models to the fluorescence lifetime data. The quality of the fit is judged by a maximum likelihood estimator [9, 14], which is known to return the intensity-weighted average of the fluorescence lifetime. In the absence of dynamics, the FRET efficiency is related to the fluorescence lifetime of the donor by:

$$E_{\text{static}} = 1 - \frac{\tau_{\text{D}}}{\tau_{\text{D(0)}}}.$$

Bursts from molecules in a static FRET configuration will always fall on this line, whereas photophysical artifacts or dynamic transitions will show systematic deviations from the "static FRET line" (Fig. 3b, d). Generally, the static FRET line is described by an empirical third-order polynomial due to the flexibility of the linkers used to attach the fluorophore to the molecule of interest [15].

Quenching of Fluorophores

Deviations from the static FRET line will occur when fluorophores are quenched due, for example, to a change in the environment. When quenching of the donor occurs, the fluorescence lifetime of the donor decreases while the intensity derived FRET efficiency remains essentially unchanged, leading to a lateral shift in the two-dimensional plot of E versus τ_D. For acceptor quenching, the lifetime of the donor is unaffected but the FRET efficiency determined from intensity decreases (Fig. 3d). Acceptor quenching is directly observable in MFD-PIE experiments by the decrease in acceptor fluorescence lifetime after direct excitation.

As an illustration, we discuss a MFD-PIE measurement on the RNA-bound form of the spliceosomal subunit U2AF65 (Fig. 4). Clearly, different conformational states are visible. Calculation of the uncorrected FRET efficiency and stoichiometry allows for the selection of dual-labeled molecules (Fig. 4a). Comparison of the fluorescence lifetime of the acceptor for different FRET states indicates quenching of the fluorophore for the lower FRET species due to binding of the RNA (Fig. 4b). These quenching effects of the acceptor fluorophore can be easily identified and corrected for by application of a population-dependent correction factor γ (Fig. 4c), illustrating the advantages of combining PIE with MFD.

Conformational Dynamics

In addition to photophysical effects, deviations from the static FRET line can result from conformational dynamics. Consider a molecule interconverting between multiple FRET states during diffusion through the focus. The FRET efficiency calculated from photon counts will be the time-averaged value of the different FRET efficiencies. However, as only a single average lifetime can be determined for an individual burst, the donor lifetime will be intensity-averaged. The brightness of the donor fluorophore is higher for the low FRET states, biasing the lifetime towards longer values [15]. Hence, deviations from the static FRET curve indicate the presence of dynamic behavior. To extract quantitative information regarding the dynamics, further analysis is required (Sect. 2.5).

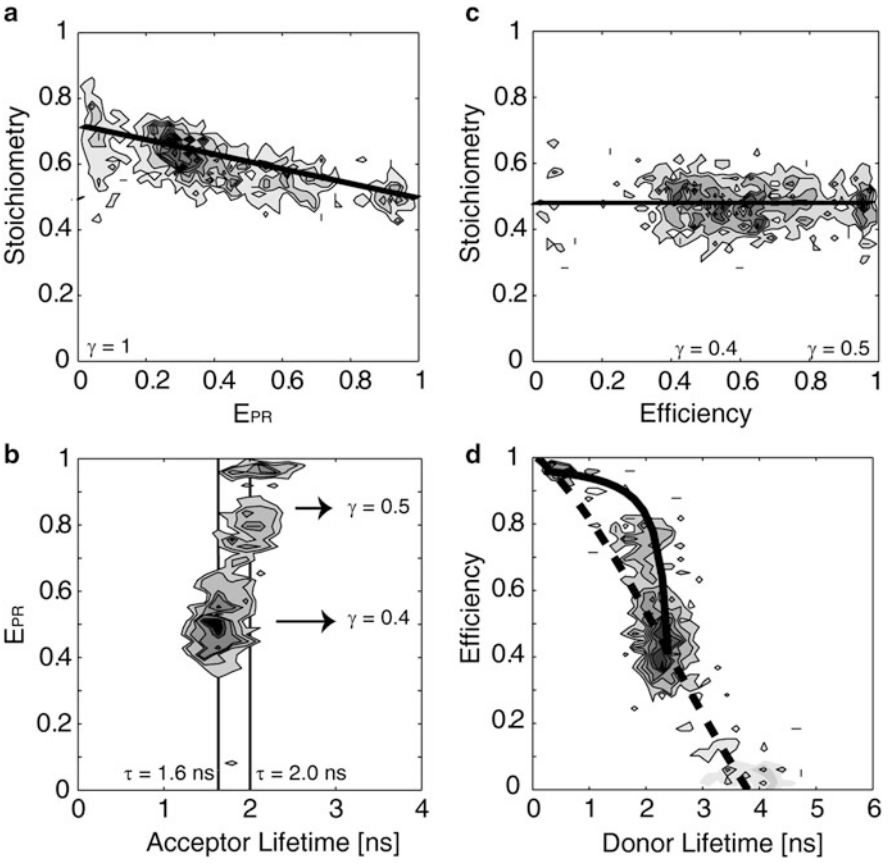

Fig. 4 A MFD-PIE analysis showing acceptor quenching on measurements of the spliceosomal cofactor U2AF65 labeled with Atto532 and Alexa647. (**a**) The histogram of proximity ratios of stoichiometry versus FRET efficiency shows the effect of acceptor quenching for different FRET populations. (**b**) The histogram of FRET efficiency versus acceptor lifetime displays the effects of quenching on the fluorescence lifetime of the acceptor. (**c**) The histogram from panel a after application of the correction factor $\gamma = 0.4$ for the low FRET population and $\gamma = 0.5$ for both populations with higher FRET efficiency. (**d**) A histogram of FRET efficiency versus donor lifetime after application of all correction factors. Conformational dynamics of the protein between two FRET states is observed by the divergence of the data from the static FRET line (*dashed line*). A dynamic description of the conformational motion is possible (*black line*)

The dynamic FRET curve for a two-state FRET system is given by:

$$E_{\mathrm{dyn}} = 1 - \frac{\tau_1 \tau_2}{\tau_{\mathrm{D}(0)}\left(\tau_1 + \tau_2 - \langle\tau\rangle_f\right)},$$

where τ_1 and τ_2 are the respective lifetimes of the FRET states and $\tau_{\mathrm{D}(0)}$ is the fluorescence lifetime of the donor-only population.

When the transitions between the states are much faster than the dwell time in the observation volume, the FRET efficiency is averaged and a single population is visible, which lies on the dynamic FRET curve. When the dynamics occur on a much slower timescale than the passage time of the particle through the detection volume, only two subpopulations with static FRET efficiencies will be detected. However, a single transition occurring during diffusion through the focus is sufficient to shift the burst to the "dynamic FRET line." Hence, even for slow dynamics, a dynamic bridge between the two static populations will be observable provided a significant number of molecules underwent at least one transition during the transit time.

Conformational dynamics can be observed in the discussed RNA-bound U2AF65 sample. After applying the appropriate corrections (Sect. 2.3.3), the efficiency as a function of donor lifetime displays the deviation of bursts from the theoretically predicted static FRET curve (Fig. 4d). The intermediate population between a high FRET and a low FRET state can be described by a dynamic FRET model. As the high and low FRET states as well as the intermediate population are all observable in the FRET efficiency versus donor-lifetime plot, interconversion between the two FRET states must occur on a similar timescale to the passage time through the detection volume.

2.5 *Further Analyses*

The data obtained using MFD-PIE can be further analyzed. The FRET efficiency histogram is broadened both due to biologically relevant heterogeneity of the sample and shot-noise caused by the limited photon counts detected in the experiment. The photon distribution analysis (PDA) offers a detailed quantitative analysis of the width of the distribution of FRET efficiencies [16], making it possible to separate the width of the underlying distance distribution from statistical noise. Dynamic interconversion between different FRET states can also be quantified by PDA [15]. Another approach to quantify the dynamics of fluctuations in FRET efficiency is to use a correlation analysis. Recently, the concept of lifetime-filtered FCS (FLCS, see also Sect. 3.5) [17] has been extended to exploit all information available in MFD (filtered FCS) [18]. With MFD-PIE, it is possible to generate highly specific filters for the observed species based on the different microtime patterns in all available channels, accounting for differences in lifetime, anisotropy, stoichiometry, and FRET efficiency simultaneously. From the resulting species-correlation functions, the kinetics of the system can be accurately quantified.

2.6 *Increasing the Number of Photons*

Ultimately, the number of photons detected from individual molecules in burst analysis measurements limits the analysis. Besides using the best possible detectors

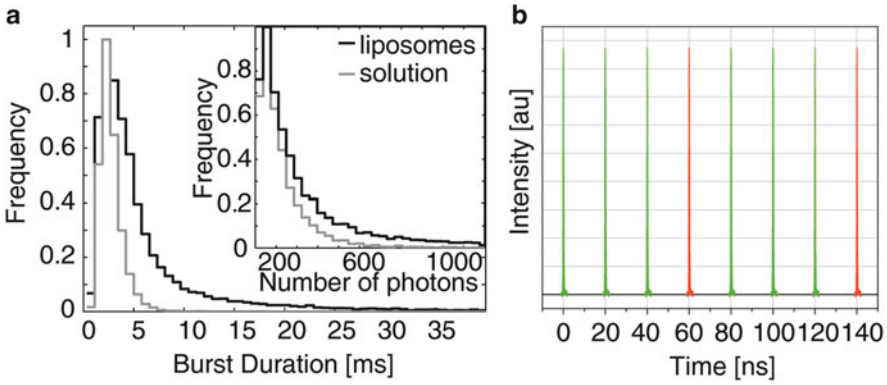

Fig. 5 Advances to increase the number of detected photons. (**a**) Comparison of a MFD-PIE experiment with U2AF65 diffusing freely in solution and encapsulated in 200 nm-sized lipid vesicles. The duration of fluorescence bursts (*outer graph*) and the total number of collected photons (*inset*) increases with the slower diffusion of the liposomes. (**b**) Example of a duty-optimized pulse sequence for a dual-color PIE microscope

and optics, fluorophores with good photophysical properties and relatively high excitation powers, the photon yield can be increased by prolonging the observation time. This can be achieved by various approaches. Immobilization of particles on the surface results in observation times that are only limited by the photostability of the fluorophores. However, surface attachment can influence the properties of the molecule significantly. In solution, the diffusion can be slowed down by increasing the viscosity of the surrounding medium, which may likewise affect the dynamics one wishes to measure. More elegantly, molecules can be encapsulated in lipid vesicles. Provided the molecules do not interact with the lipid bilayer, the effective diffusion of the molecules can be slowed down without influencing their function [19]. This is visualized in Fig. 5a, where the burst duration of molecules diffusing freely in solution is compared to molecules encapsulated in lipid vesicles. A similar approach for increasing the observation time while avoiding attachment of the molecule to the surface is confinement of molecules within aqueous nanodroplets in oil [20].

Since most information for spFRET measurements is contained in the photons after green excitation, the excitation cycle can be tuned to increase the time spent exciting the donor fluorophore. Duty-cycle optimized ALEX has been performed by Zarrabi et al. [21] and can be implemented for pulsed lasers with TCSCP electronics. An example of a duty-cycle optimized excitation scheme for dual-color FRET experiments is shown in Fig. 5b.

2.7 Summary and Outlook for MFD-PIE

The combination of MFD with PIE increases the robustness of the single-pair FRET analysis. Direct probing of the acceptor offers an additional dimension for

separation of single- and dual-labeled species. Fluorophore-related artifacts can be excluded from the analysis by careful analysis of the lifetime and the anisotropy of both dyes. Furthermore, photophysical effects such as photobleaching or blinking can be distinguished from dynamic FRET changes.

When measuring FRET systems with more than two fluorophores, the implementation of ALEX or PIE becomes essential for a complete quantitative description. For a system consisting of a blue, a green, and a red fluorophore, excitation of the blue fluorophore will only yield two independent signal ratios, which is insufficient to disentangle the three FRET efficiencies. Additional excitation of the green fluorophore is needed to extract distance-related FRET efficiencies from the experiment. Studies of multi-color FRET systems based on μsALEX [22–24] have been successful in extracting quantitative distance information. With the additional information available from PIE, we are optimistic that multi-color MFD-PIE will be an excellent tool for quantifying three- or four-color FRET systems [25]. For multi-color FRET experiments, the optimization of the pulse cycle will be of special importance.

3 Pulsed Interleaved Excitation Fluctuation Imaging

3.1 Introduction

In the toolbox of fluorescence fluctuation spectroscopy (FFS) techniques, the most prominent method is FCS [26, 27]. In FCS, intensity fluctuations in the small probe volume of a confocal microscope are analyzed, providing quantitative information about the concentration, diffusion properties, and interaction of analytes. Over the last years, FFS methods have found a broad application in the biophysical sciences. One of the implementations of FFS that is of particular interest for measurements in live cells is image correlation spectroscopy (ICS), which extracts quantitative information from fluctuations in an image. ICS methods include techniques such as spatio-temporal image correlation spectroscopy (STICS) [28], raster image correlation spectroscopy (RICS) [29], and the number and brightness method (N&B) [30]. Unfortunately, the two-color extensions of these methods suffer from spectral crosstalk between the detection channels, which leads to residual cross-correlation. Hence, careful control measurements are necessary and a quantitative analysis challenging.

The combination of PIE with these methods (pulsed interleaved excitation fluctuation imaging, PIE-FI) elegantly eliminates crosstalk from the analysis by interleaving the excitation pulses [31]. In this section, we will discuss the RICS method, which can extract diffusion coefficients and concentrations of fast diffusing molecules from the combined spatio-temporal information available in confocal laser scanning microscopy (CLSM) and how it can be combined with PIE. Additionally, the lifetime information available with PIE can be further exploited to

perform lifetime-weighted RICS (RLICS). The same image data collected for the RICS analysis can also be used for N&B analysis when the appropriate corrections for the dead time of the TCPSC system are applied.

3.2 *Basic Theory of Raster Image Correlation Spectroscopy*

In CLSM, spatial information about the sample is obtained by performing consecutive line scans to build up an image (Fig. 6a). Due to the nature of the scanning,

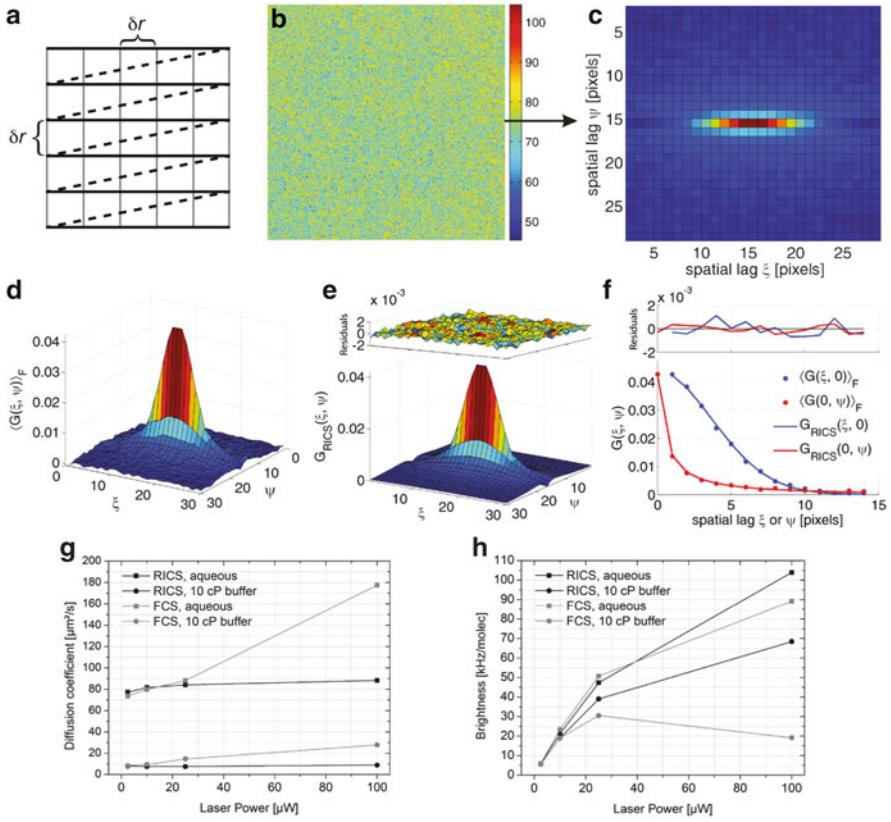

Fig. 6 The basics of RICS. (**a**) The principle of raster scanning: consecutive line scans are performed to create an image of the sample. δr represents the pixel size. (**b**) An average macrotime image of Venus FP freely diffusing in solution. (**c–d**) Average spatial ACF of the data in (**b**) plotted in 2D (**c**) and 3D (**d**). (**e**) Fit of the data in panel (**d**) to the model ACF function. Residuals of the fit are shown in the *upper panel*. (**f**) ξ- and ψ-cross sections of the ACF and fit for visualization. The quality of the fitted residuals is shown in the *upper panel*. (**g–h**) Apparent diffusion coefficient (**g**) and molecular brightness (**h**) of Venus FP as a function of laser power for both RICS and point-FCS measurements

both spatial and temporal information are contained in the rastered image. Pixels within an image series are not only separated in space, but also carry temporal information depending on the pixel dwell time, the line time, and the frame time. Thus, raster scanning covers a large dynamic range for the measurement of diffusion ranging from microseconds to seconds.

RICS is based on the frame-wise spatial correlation function defined as:

$$G_{ij}(\xi,\psi,f) = \frac{\langle I_i(x,y,f) I_j(x+\xi,y+\psi,f)\rangle_{XY}}{\langle I_i(x,y,f)\rangle_{XY}\langle I_j(x,y,f)\rangle_{XY}} - 1,$$

where $I_i(x,y,f)$ is the intensity of the pixel at position x, y in channel i, f is the frame number and ξ and ψ are the spatial lag in x- and y-dimension given in pixels, and angle brackets denote averaging over the whole image. When $i=j$, G_{ii} is the autocorrelation function for channel i; when $i\neq j$, G_{ij} is the cross-correlation function.

The correlation can be interpreted as the probability of detecting the same molecule at spatial lag coordinates ξdr and ψdr and with a temporal lag time $\xi\tau_p + \psi\tau_l$. The decay of the correlation depends on the diffusion properties of the fluorophores as well as the scan parameters.

For a given image series, all frame-wise correlation functions are averaged to improve the signal-to-noise ratio:

$$G_{ij}(\xi,\psi) = \langle G_{ij}(\xi,\psi,f)\rangle_f.$$

The average intensity image of a solution of the fluorescent protein Venus is shown in Fig. 6b. From the image series, the average autocorrelation function is calculated and can be depicted in either two-dimensions (Fig. 6c) or in three-dimensions (Fig. 6d).

A fast Fourier-transform algorithm is used for calculating the correlation functions [32]. Assuming a three-dimensional Gaussian point-spread function (PSF), an analytical form of the ACF for freely diffusing particles can be derived [33]:

$$G_{\mathrm{RICS},D}(\xi,\psi) = \frac{\gamma}{N}\left(1+\frac{4D(\tau_p\xi+\tau_l\psi)}{\omega_r^2}\right)^{-1} \times \left(1+\frac{4D(\tau_p\xi+\tau_l\psi)}{\omega_z^2}\right)^{-\frac{1}{2}} \exp\left(-\frac{\delta r^2(\xi^2+\psi^2)}{\omega_r^2+4D(\tau_p\xi+\tau_l\psi)}\right),$$

where γ is the geometrical factor ($2^{-\frac{3}{2}}$ for a three-dimensional Gaussian PSF) [34], N is the average number of molecules in the PSF, D is the diffusion coefficient, τ_p is the pixel dwell time, τ_l is the line time, ω_r and ω_z are the radial and axial dimensions of the PSF, and δr is the pixel size. Additionally, a blinking term can be added to the model function:

$$G_{\mathrm{RICS}}(\xi,\psi)=\left[1+\frac{F_{\mathrm{b}}}{1-F_{\mathrm{b}}}\exp\left(\frac{\tau_{\mathrm{p}}\xi+\tau_{\mathrm{l}}\psi}{\tau_{\mathrm{b}}}\right)\right]G_{\mathrm{RICS},D}(\xi,\psi),$$

where F_{b} and τ_{b} are the fractional amplitude and the relaxation time of the blinking process. This is particularly necessary when fluorescent protein (FP) labels are used, as is the case for most cellular measurements.

The autocorrelation function for Venus fluorescent protein freely diffusing in solution is shown in a two-dimensional and three-dimensional representation in Fig. 6c, d respectively. The fit to the autocorrelation function is shown in 3D in Fig. 6e where the residuals are displayed in the upper panel. For better visualization, it is often useful to plot the data and the respective fit as one-dimensional slices along the two lag coordinates as depicted in Fig. 6f.

3.3 Comparison of FCS and RICS

FCS and RICS measurements measure the same information: the diffusion coefficient and the concentration of the molecule of interest. In addition, the molecular brightness ε at the center of the PSF [34–36] can be determined by dividing the average count rate by the average particle number in the observation volume N:

$$\varepsilon[\mathrm{kHz}]=\frac{\langle I\rangle[\mathrm{kHz}]}{N}.$$

One significant advantage of RICS is that blinking and photobleaching of fluorescent proteins is reduced due to the short exposition time while scanning, which makes RICS the preferred method to quantify diffusion within cells when the area of interest if fairly homogeneous [37, 38].

To demonstrate the advantages of RICS over point-FCS, the apparent diffusion coefficient and molecular brightness was determined for Venus FP freely diffusing in buffer as a function of laser power. Diffusion coefficients were much more stable when measured with RICS, especially at high laser powers, and even more so when a highly viscous buffer was used to mimic cellular diffusion (Fig. 6g). Additionally, a higher molecular brightness could be achieved with RICS (Fig. 6h). However, as the parameters obtained using RICS are averaged over the sampled region, there are instances where the superior spatial resolution of point-FCS is advantageous. This is the case when the spatial resolution is important or when the distribution of organelles within the cell is highly heterogeneous.

3.4 What PIE Brings to RICS

Multi-color FCS and RICS measurements can elucidate molecular interactions using a cross-correlation analysis [39]. However, a quantitative analysis is difficult since spectral crosstalk affects the amplitude of both the red ACF and the CCF, resulting in a positive cross-correlation amplitude even in the absence of interactions. By interleaving the excitation pulses of the different fluorophores on the nanosecond timescale, a quantitative and straightforward cross-correlation analysis is possible (Fig. 7a–b).

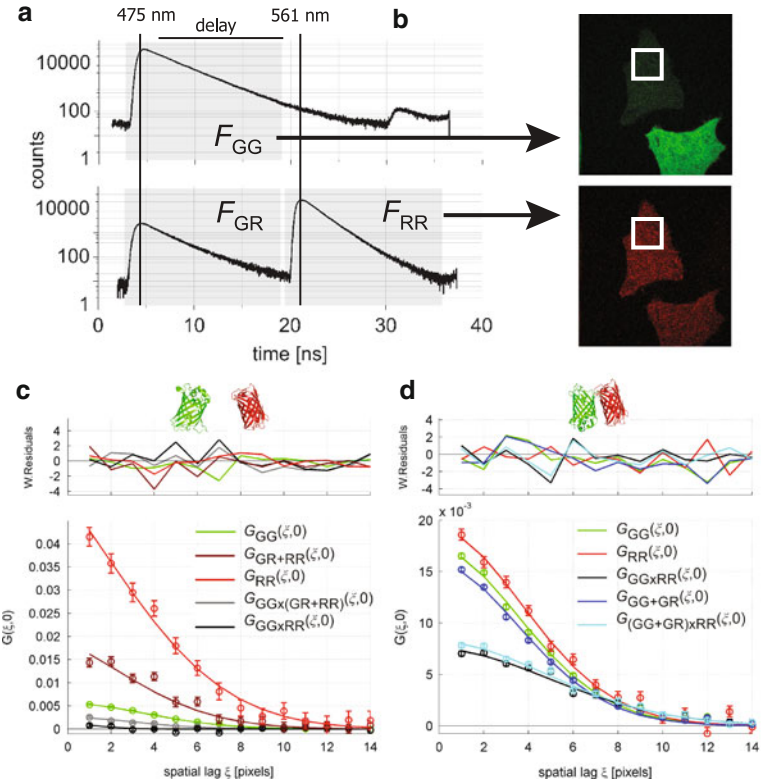

Fig. 7 PIE-RICS. (**a**) Microtime histograms from a measurement of a cell expressing both eGFP and mCherry FPs. The different PIE channels used for the correlation analysis are highlighted in *gray*. (**b**) Images of cells constructed from photons detected in the PIE channels indicated by the *arrows*. (**c-d**) One-dimensional slices through the ACFs and CCFs with respect to the spatial coordinates ξ and ψ determined from the different PIE channels and fits for a cell expressing eGFP and mCherry diffusing independently in the cytosol (**c**) and for a cell expressing a tandem construct of eGFP-mCherry (**d**). The influence of spectral crosstalk and FRET can be observed by the different amplitudes of the various correlation functions observable depending on which photons are correlated

Artifact-free cross-correlation amplitudes can be recovered with PIE even in the presence of significant crosstalk and FRET between the fluorophores. For a cell expressing both eGFP and mCherry diffusing independently in the cytosol (Fig. 7c), a false-positive cross-correlation amplitude is observed when PIE is not used ($F_{\mathrm{GR+RR}}$). The cross-correlation vanishes when crosstalk is excluded from the analysis by using only the PIE channels F_{GG} and F_{RR}. For a tandem construct of eGFP-mCherry (Fig. 7d), a significant cross-correlation amplitude $G_{\mathrm{GG\times RR}}$ is observed, confirming the co-diffusion of both proteins. However, in the absence of PIE, a quantitative analysis is difficult because the amplitude is dependent on both the FRET efficiency and the degree of labeling. Provided there is no significant direct excitation of the red fluorophore with green excitation (i.e. direct excitation), PIE can be used to perform quantitative correlation experiments in the presence of FRET (even with PIE, it is not possible to distinguish FRET from direct excitation). When all photons originating from the green fluorophore after green excitation are combined ($F_{\mathrm{GG+GR}}$), the FRET-related decrease in brightness of the green fluorophore is compensated by the increase of brightness of the red fluorophore in the F_{GR} PIE channel. In this case, the amplitude of the cross-correlation function is what it would have been in the absence of FRET:

$$G_{(\mathrm{GG+GR})\times\mathrm{RR}}(0,0)=\frac{N_{\mathrm{GR}}}{N_{\mathrm{G_T}}N_{\mathrm{R_T}}},$$

where $N_{\mathrm{G_T}}$, $N_{\mathrm{R_T}}$, and N_{GR} are the total number of green, red, and double-labeled molecules in the confocal volume, respectively.

When there is significant amount of crosstalk from the green fluorophore into the red detection channel, the amplitude of the red ACF is distorted. In essence, there are two species in the red channel with different molecular brightnesses contributing to the correlation function. With PIE, crosstalk can be completely avoided by only using the F_{RR} PIE channel, thus recovering the artifact-free amplitude:

$$G_{\mathrm{RR}}(0,0)=\frac{1}{N_{\mathrm{R_T}}}.$$

The influence of crosstalk on the amplitude of the red autocorrelation function can be observed in cellular experiments where eGFP and mCherry are simultaneously expressed (Fig. 7c). The amplitude of the red ACF increases significantly when crosstalk is removed, allowing the correct concentration of mCherry to be determined.

Similar problems arise for the amplitude of the green ACF when the system undergoes FRET. As the labeling efficiency of photoactive acceptor molecules is never 100%, two species contribute to the autocorrelation function in the green channel, the donor-only molecules, and donor molecules that undergo FRET. Assuming that the FRET-lowered brightness in the F_{GG} channel is compensated by the FRET-increased brightness in the F_{GR} channel, addition of the two detection channels after green excitation leads to identical brightnesses for the donor-only

and FRETing species. Hence, an accurate concentration of the green fluorophore can be obtained directly from the F_{GG+GR} channel:

$$G_{GG+GR}(0,0) = \frac{1}{N_{G_T}}.$$

For the tandem construct of eGFP-mCherry, a clear deviation of the amplitude of G_{GG} from the amplitude of the artifact-free correlation function G_{GG+GR} is observed because of FRET (Fig. 7d).

By rearranging the above equations, it becomes possible using PIE to straightforwardly quantify molecular interactions from the amplitudes of the various correlation functions:

$$N_{GR} = \frac{G_{(GG+GR)\times RR}(0,0)}{G_{GG+GR}(0,0)G_{RR}(0,0)}.$$

3.5 *Raster Lifetime Image Correlation Spectroscopy*

To take advantage of the fluorescence lifetime information offered with PIE, we combined fluorescence lifetime correlation spectroscopy (FLCS) with RICS [17]. In FLCS, filters based on the contributions of different species to the fluorescence decay histogram are generated from the microtime patterns of the individual species. These filters can be interpreted as a measure for the probability that a photon detected at a specific microtime belongs to the respective species. By weighting the individual photons based on their microscopic arrival times, the correlation functions of the different contributions can be separated. In raster lifetime image correlation spectroscopy (RLICS), the same principle holds. Each photon in a pixel of the macrotime image is weighted, based on its microscopic arrival time, by the respective filter value. The weighted pixel intensity is then used to calculate species-correlation functions. Since this procedure can generate weighted pixel intensities close to zero, or even equal to zero, which would distort the amplitude of the ACF, the pixel intensities are scaled prior to calculation of the correlation function:

$$I(x,y,f)_{\text{scaled}} = I(x,y,f) + \min(I),$$

where $\min(I)$ is the lowest pixel intensity in the image series. Then, the autocorrelation function is determined and rescaled to its original amplitude [40],

$$G(\xi,\psi) = \left(\frac{\langle I\rangle_{XYF} + \min(I)}{\langle I\rangle_{XYF}}\right)^2 G_{\text{scaled}}(\xi,\psi),$$

where I_{XYF} is the mean pixel intensity of the whole image series.

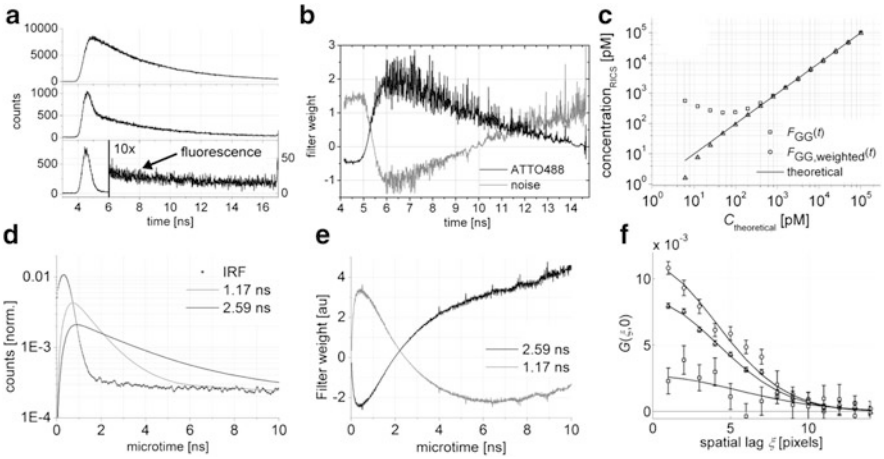

Fig. 8 RLICS. (**a**) Microtime histograms of Atto488 in solution at concentrations of 100 nM (*top*), 0.195 nM (*middle*) and 0.006 nM (*bottom*). (**b**) Lifetime-weighting filters calculated from a pure sample of Atto488 and for scattered laser light. (**c**) Measured concentration determined from the amplitude of the RICS ACF versus the theoretical concentration for a dilution series determined with and without lifetime filtering. (**d**) Microtime patterns of the instrument response function (*IRF*) and calculated fluorescence decays of unquenched (2.59 ns) and FRET-quenched (1.17 ns) eGFP convoluted with the IRF. (**e**) Lifetime-weighting filters for the donor-only and the FRET-quenched species. (**f**) $G_{GG\times RR}(\xi,0)$ correlation functions without filters (*triangles*), filtered for the FRET species (*circles*), and filtered for the non-FRET species (*squares*)

RLICS can be used to enhance the capabilities of RICS in multiple ways. One possibility is to use RLICS to increase the sensitivity of concentration measurements at low concentrations, where laser and Raman scattering distort the amplitude of the ACF. Another possibility is to use the lifetime information to produce a species-ACF and species-CCF (as in filtered-FCS [18]), making it possible to analyze multiple species with different lifetimes simultaneously and to quantify their interactions.

To demonstrate the capabilities of RLICS, we measured a dilution series of Atto488 in water, ranging from 100 nM to 6.1 pM. With decreasing concentration, the contribution of uncorrelated noise (Raman scattering, laser reflections, detector dark counts, background light) or correlated noise (detector afterpulsing) to the microtime histogram increases (Fig. 8a). The contribution of uncorrelated noise systematically lowers the amplitude of the ACF, leading to distortion of the determined concentration below 1 nM. By constructing lifetime-weighting filters based on the microtime patterns of the noise and the fluorescence decay (Fig. 8b), the noise contribution can be filtered out. The range in which accurate concentrations can be determined is hereby extended to picomolar concentrations (Fig. 8c). The deviation at low concentration is most likely related to dilution artifacts.

The ability to separate species based on their lifetime with RLICS is demonstrated by in cellulo measurements on an eGFP-mCherry tandem construct. The fluorescence lifetime of eGFP in the absence of FRET was determined to be 2.59 ns,

while the FRET-quenched eGFP in the heterodimer shows a lifetime of 1.17 ns. Lifetime-weighted filters were constructed based on the calculated fluorescence decays of the two species (Fig. 8d–e). The cross-correlation function $G_{\mathrm{GG}\times\mathrm{RR}}(\xi,\psi)$ was calculated from the weighted macrotime images. When the F_{GG} PIE channel is weighted for the FRET-quenched species, the cross-correlation amplitude between the FRET-quenched species and direct excitation of mCherry increases compared to the amplitude when no weighting was performed. Likewise, the cross-correlation amplitude decreases when F_{GG} is weighted for the lifetime of the unquenched eGFP. However, the cross-correlation amplitude did not decrease to zero, indicating that the filters were not perfect. This is due, at least in part, to the fact that the filters were only approximated. The fluorescence decay of eGFP is multiexponential and a single-exponential filter is not sufficient. In addition, it may be that the difference in fluorescence lifetime of a factor of two between the two species is not sufficient to completely separate the contributions of the different correlation functions for the given data quality. However, the proper trend is observed demonstrating that a species-correlation analysis is possible with RLICS.

3.6 Number and Brightness Analysis with PIE

The number and brightness analysis (N&B) is a complementary method to analyze the intensity fluctuations in an image series. It is based on the moment analysis of intensity fluctuations of a single pixel through time. With N&B, it is possible to extract the average number of molecules $n(x,y)$ and their brightness $\varepsilon(x,y)$ in each pixel (x,y) [30]:

$$n(x,y) = \frac{\langle k(x,y,f)\rangle_f^{\,2}}{\sigma^2(x,y) - \langle k(x,y,f)\rangle_f},$$

$$\varepsilon(x,y) = \frac{\sigma^2(x,y) - \langle k(x,y,f)\rangle_f}{\langle k(x,y,f)\rangle_f}.$$

Here, $\langle k\rangle$ is the mean number of counts and σ^2 is the variance of the pixel intensity over the whole image series.

For a proper N&B analysis, the temporal pixel variance has to be accurately determined. In this case, the use of TCSPC electronics for PIE is a disadvantage. The relatively high dead time of the electronics leads to photon loss at high count rates and thus an underestimation of the variance even at low count rates [41]. Fortunately, dead-time correction can be applied to recover correct pixel intensities [42]:

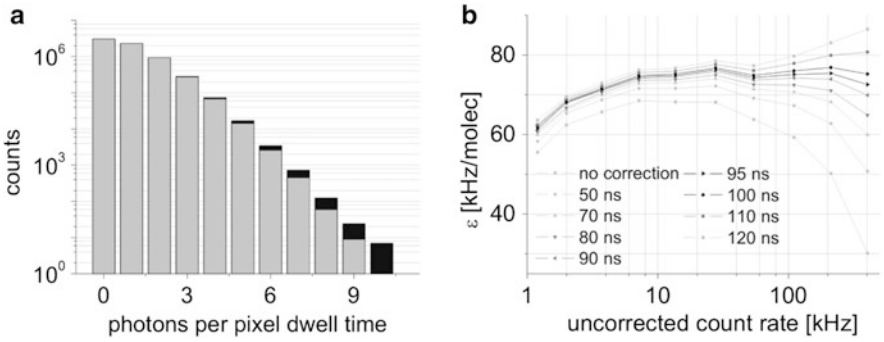

Fig. 9 N&B analysis using TCSPC detection. (**a**) Photon counting histograms of pixel counts for Atto488 in solution before (*gray*) and after (*black*) dead-time correction at an average count rate of ~75 kHz. (**b**) The determined brightness of Atto488 in solution at different concentrations without correction and corrected assuming different dead times of the detection electronics. The correction for a dead time of 100 ns yields the best results for intensities above ~3 kHz, as expected for our electronics

$$I_C(x,y,f) = \frac{I_M(x,y,f)}{1 - I_M(x,y,f)\frac{\tau_{dead}}{\tau_p}},$$

where $I_C(x,y,f)$ is the corrected pixel count and $I_M(x,y,f)$ is the measured pixel count, τ_{dead} is the dead time of the detector and electronics, and τ_p is the pixel dwell time. The effect of a 100 ns dead time, as determined for our TCSPC setup, on the distribution of pixel counts at a count rate of ~75 kHz is shown in Fig. 9a. When correcting for the 100 ns dead time of our electronics, a constant molecular brightness for Atto488 freely diffusing in solution is observed independent of concentration (Fig. 9b). The deviation at low concentrations is related to dilution artifacts as noted before.

Recent technological developments succeeded in further lowering the dead time of TCSPC systems. With TCSPC cards available with dead times of 25 ns or less, the limiting factor becomes the dead time of the detectors rather than the TCSPC electronics [43].

3.7 Summary and Outlook for PIE-FI

We showed that PIE significantly enhances the capabilities of RICS and enables straightforward quantitative cross-correlation analysis even when the system undergoes FRET. The combination of RICS with FLCS adds a new dimension to RICS by including the lifetime information into the analysis. Additionally, the lifetime information that comes with PIE-FI can be used for simultaneous fluorescence lifetime imaging (FLIM). The two-color cross-correlation analysis presented here is easily extended to multi-color imaging as well. This is possible even when

the emission spectra are highly overlapping, as is usually the case due to the limited choice of fluorescent proteins available. Lastly, it has to be stressed that any raster-scanning microscope, even commercial systems, is easily upgraded to perform PIE-FI, as long as the scanning and detection modules can be synchronized [6]. Software to analyze PIE-MFD and PIE-FI data is available upon request.

Acknowledgments We thank Dr. Jelle Hendrix for the data on PIE-FI and Carolina Sanchéz Rico, Dr. Lisa Warner, and Prof. Dr. Michael Sattler for providing the U2AF65 protein. We gratefully acknowledge the financial support of the Deutsche Forschungsgemeinschaft through the Excellence Cluster Nanosystems Initiative Munich (NIM) and the Collaborate Research Center (SFB1035) and the Ludwig-Maximilians-University Munich (LMUinnovativ BioImaging Network).

References

1. Kapanidis AN, Lee NK, Laurence TA et al (2004) Fluorescence-aided molecule sorting: analysis of structure and interactions by alternating-laser excitation of single molecules. Proc Natl Acad Sci U S A 101:8936–8941
2. Kapanidis AN, Laurence TA, Lee NK et al (2005) Alternating-laser excitation of single molecules. Acc Chem Res 38:523–533
3. Laurence TA, Kong X, Jäger M, Weiss S (2005) Probing structural heterogeneities and fluctuations of nucleic acids and denatured proteins. Proc Natl Acad Sci U S A 102:17348–17353
4. Müller BK, Zaychikov E, Bräuchle C, Lamb DC (2005) Pulsed interleaved excitation. Biophys J 89:3508–3522
5. Lamb DC, Müller BK, Bräuchle C (2005) Enhancing the sensitivity of fluorescence correlation spectroscopy by using time-correlated single photon counting. Curr Pharm Biotechnol 6:405–414
6. Hendrix J, Lamb DC (2013) Implementation and application of pulsed interleaved excitation for dual-color FCS and RICS. In: Engelborghs Y, Visser AJWG (eds) Fluorescence spectroscopy and microscopy. Humana, Totowa, pp 653–682
7. Olofsson L, Margeat E (2013) Pulsed interleaved excitation fluorescence spectroscopy with a supercontinuum source. Opt Express 21:3370–3378
8. Eggeling C, Berger S, Brand L, Fries JR (2001) Data registration and selective single-molecule analysis using multi-parameter fluorescence detection. J Biotechnol 86(3):163–180
9. Kudryavtsev V, Sikor M, Kalinin S et al (2012) Combining MFD and PIE for accurate single-pair Förster resonance energy transfer measurements. ChemPhysChem 13:1060–1078
10. Förster T (1948) Zwischenmolekulare energiewanderung und fluoreszenz. Ann Phys 437:55–75
11. Nir E, Michalet X, Hamadani KM et al (2006) Shot-noise limited single-molecule FRET histograms: comparison between theory and experiments. J Phys Chem B 110:22103–22124
12. Lee NK, Kapanidis AN, Wang Y et al (2005) Accurate FRET measurements within single diffusing biomolecules using alternating-laser excitation. Biophys J 88:2939–2953
13. Koshioka M, Sasaki K, Masuhara H (1995) Time-dependent fluorescence depolarization analysis in three-dimensional microspectroscopy. Appl Spectrosc 1–5
14. Maus M, Cotlet M, Hofkens J et al (2001) An experimental comparison of the maximum likelihood estimation and nonlinear least-squares fluorescence lifetime analysis of single molecules. Anal Chem 73:2078–2086

15. Kalinin S, Valeri A, Antonik M et al (2010) Detection of structural dynamics by FRET: a photon distribution and fluorescence lifetime analysis of systems with multiple states. J Phys Chem B 114:7983–7995
16. Antonik M, Felekyan S, Gaiduk A, Seidel CAM (2006) Separating structural heterogeneities from stochastic variations in fluorescence resonance energy transfer distributions via photon distribution analysis. J Phys Chem B 110:6970–6978
17. Böhmer M, Wahl M, Rahn HJ et al (2002) Time-resolved fluorescence correlation spectroscopy. Chem Phys Lett 353:439–445
18. Felekyan S, Kalinin S, Sanabria H et al (2012) Filtered FCS: species auto- and cross-correlation functions highlight binding and dynamics in biomolecules. ChemPhysChem 13:1036–1053
19. Goldner LS, Jofre AM, Tang J (2010) Droplet confinement and fluorescence measurement of single molecules. Methods Enzymol 472:61–88
20. Milas P, Rahmanseresht S, Ben D Gamari, Goldner LS (2013) Single molecule sensitive fret in Attoliter droplets. arXiv: 1312.0854 [physic.bio-ph]
21. Zarrabi N, Ernst S, Dueser MG et al (2009) Simultaneous monitoring of the two coupled motors of a single FoF1-ATP synthase by three-color FRET using duty cycle-optimized triple-ALEX. arXiv: 0902.1292 [q-bio.BM]
22. Lee NK, Kapanidis AN, Koh HR et al (2007) Three-color alternating-laser excitation of single molecules: monitoring multiple interactions and distances. Biophys J 92:303–312
23. Lee J, Lee S, Ragunathan K et al (2010) Single-molecule four-color FRET. Angew Chem Int Ed Engl 49:9922–9925
24. Stein IH, Steinhauer C, Tinnefeld P (2011) Single-molecule four-color fret visualizes energy-transfer paths on DNA origami. J Am Chem Soc 133:4193–4195
25. Milles S, Koehler C, Gambin Y et al (2012) Intramolecular three-colour single pair FRET of intrinsically disordered proteins with increased dynamic range. Mol Biosyst 8:2531
26. Elson EL, Magde D (1974) Fluorescence correlation spectroscopy I. Conceptual basis and theory. Biopolymers 13:1–27
27. Rigler R, Mets Ü, Widengren J, Kask P (1993) Fluorescence correlation spectroscopy with high count rate and low background: analysis of translational diffusion. Eur Biophys J 22:169–175
28. Hebert B, Costantino S, Wiseman PW (2005) Spatiotemporal image correlation spectroscopy (STICS) theory, verification, and application to protein velocity mapping in living CHO cells. Biophys J 88:3601–3614
29. Digman MA, Brown CM, Sengupta P et al (2005) Measuring fast dynamics in solutions and cells with a laser scanning microscope. Biophys J 89:1317–1327
30. Digman MA, Dalal R, Horwitz AF, Gratton E (2008) Mapping the number of molecules and brightness in the laser scanning microscope. Biophys J 94:2320–2332
31. Hendrix J, Schrimpf W, Höller M, Lamb DC (2013) Pulsed interleaved excitation fluctuation imaging. Biophys J 105:848–861
32. Petersen NO, Höddelius PL, Wiseman PW, Seger O (1993) Quantitation of membrane receptor distributions by image correlation spectroscopy: concept and application. Biophys J 65:1135–1146
33. Digman MA, Wiseman PW, Horwitz AR, Gratton E (2009) Detecting protein complexes in living cells from laser scanning confocal image sequences by the cross correlation raster image spectroscopy method. Biophys J 96:707–716
34. Thompson NL (1999) Fluorescence correlation spectroscopy. Topics in fluorescence spectroscopy 1:337–378
35. Ivanchenko S, Lamb DC (2011) Fluorescence correlation spectroscopy: principles and developments. Supramolecular Struct Funct 10:1–30
36. Hendrix J, Lamb DC (2013) Pulsed interleaved excitation: principles and applications. Methods Enzymol 518:205–243

37. Schwille P, Kummer S, Heikal AA et al (2000) Fluorescence correlation spectroscopy reveals fast optical excitation-driven intramolecular dynamics of yellow fluorescent proteins. Proc Natl Acad Sci U S A 97:151–156
38. Hendrix J, Flors C, Dedecker P et al (2008) Dark states in monomeric red fluorescent proteins studied by fluorescence correlation and single molecule spectroscopy. Biophys J 94:4103–4113
39. Digman MA, Gratton E (2009) Fluorescence correlation spectroscopy and fluorescence cross-correlation spectroscopy. WIREs Syst Biol Med 1:273–282
40. Schwille P, Korlach J, Webb WW (1999) Fluorescence correlation spectroscopy with single-molecule sensitivity on cell and model membranes. Cytometry 36:176–182
41. Hillesheim LN, Müller JD (2003) The photon counting histogram in fluorescence fluctuation spectroscopy with non-ideal photodetectors. Biophys J 85:1948–1958
42. Becker W (2005) Advanced time-correlated single photon counting techniques. Springer, Heidelberg
43. Wahl M, Röhlicke T, Rahn H-J et al (2013) Integrated multichannel photon timing instrument with very short dead time and high throughput. Rev Sci Instrum 84:043102

Photon Antibunching in Single Molecule Fluorescence Spectroscopy

Kristin S. Grußmayer and Dirk-Peter Herten

Abstract Single molecule fluorescence spectroscopy (SMFS) opened an important pathway for studying properties of individual quantum systems under ambient conditions. One such fundamental characteristic is based on the fact that single emitters can only emit single photons. This leads to the phenomenon of antibunching, that is, the probability for detecting multiple photons approaches zero for decreasing detection time windows shorter than the excited state lifetime. In the last decade photon antibunching has regained interest by many researchers in the field of SMFS for two main reasons. First, the observation of antibunching by measuring photon correlations could easily be transferred to become the only direct proof that a single fluorescing molecule is observed. This is crucial for quantum information processing, quantum cryptography, and metrology. Second, its characteristic photon statistics could be exploited for estimating the number of independently emitting molecules with a confocal fluorescence microscope. Recent applications aim at understanding mechanisms of energy transfer in multichromophoric molecules and photo-systems and at quantifying copy numbers in protein complexes. This chapter highlights different methods to measure photon antibunching in SMFS experiments. Aside from technical aspects we will consider the fundamental theories that are used for data analysis. Each methodological approach is then followed by a section illustrating the respective applications of photon antibunching.

Keywords Coincidence analysis · Counting by photon statistics · Hanbury Brown and Twiss interferometer · Photon correlations · Time-correlated single photon counting

K.S. Grußmayer and D.-P. Herten (✉)
CellNetworks Cluster and Institute for Physical Chemistry, Heidelberg University,
Im Neuenheimer Feld 267, 69120 Heidelberg, Germany
e-mail: dirk.herten@bioquant.uni-heidelberg.de

P. Kapusta et al. (eds.), *Advanced Photon Counting: Applications, Methods, Instrumentation*, Springer Ser Fluoresc (2015) 15: 159–190, DOI 10.1007/4243_2014_71,

Contents

1 Introduction 160
2 Photon Antibunching as Proof for Single Molecule Fluorescence 162
3 Photon Antibunching Measurements with Continuous Wave Laser Excitation 162
3.1 Early Applications of Photon Antibunching in SMFS 165
3.2 Counting of Independent Fluorescence Emitters Using CW Excitation 167
4 Photon Antibunching Measurements with Pulsed Laser Excitation 169
4.1 Counting Independent Emitters in Experiments 173
5 Measuring Extended Photon Statistics with Pulsed Laser Excitation 174
5.1 Theory and First Experimental Realization 176
5.2 Experimental Characterization of CoPS with Application to DNA Origami and Fluorescent Markers 181
6 Conclusion 187
References 187

1 Introduction

The particle-wave dualism raised by modern quantum mechanics offers two fundamentally different perspectives on describing light and its interactions with matter [1]. The perspective taken by the observer determines which properties become relevant and thereby the effects that can be observed. Usually, the wave nature of light is used to describe phenomena such as interference and polarization. In contrast, when light is sensed as a stream of individual particles, i.e., photons, another interesting phenomenon arises in their temporal distribution which depends on the fundamental nature of the light source. Coherent light sources such as perfect single-mode lasers have constant beam intensity. The naive observer would expect to encounter a series of individual photons with regular time intervals between them when the photon stream is sampled at high time resolution. However, even for shorter and shorter time intervals the occurrence of one or multiple photons is arbitrary. In other words, the incident light beam displays random, statistical fluctuations in its photon flux and it can be shown that the photon number distribution follows Poisson statistics. Other classical light sources with time-varying intensity such as that of a discharge lamp will have super-poissonian photon number distributions, meaning that the variance in photon numbers is higher than for a Poisson distribution with the same mean [2]. The reason why any of the above light sources emit photons with irregular spacing in time is simply because they consist of multiple equivalent but independent emitters. Because emission from an electronically excited state of each of the independent emitters is stochastic in nature, we observe this statistical distribution of photons in time. This was proven experimentally for the first time by Hanbury Brown and Twiss already in 1956 [3] and is known as the HBT-effect, although the original experiment was controversially discussed for some time thereafter [4]. Hanbury Brown and Twiss investigated the coherence of a light beam by measuring the second-order correlation function, i.e., the intensity autocorrelation function $G^{(2)}(\tau)$. It is interesting to know

that this important finding was a side effect of their search for a method to determine the diameter of stars [5]. Temporally coherent light sources with constant intensity show a flat autocorrelation function with $G^{(2)}(\tau) = 1$. It can be easily shown that classical light sources with variations in intensity over time have $G^{(2)}(0) \geq 1$. This means that it is more likely to detect subsequent photons at short time intervals than at longer ones, indicating that photons occur in bunches [2].

This chapter is interested just in the opposite which is the so-called photon antibunching, a purely quantum mechanical effect. As we will discuss below, this phenomenon enables us to determine the number of emitters contributing to a ray of light. Antibunching means that there is always a finite temporal separation between photons. This effect will never occur if multiple independent emitters contribute. The emitters must either be entangled, which is studied in quantum optics, or there is only a single emitter present, which is what we assume for the remainder of this article. The consequence of photon antibunching is that for short inter-photon time intervals the temporal intensity autocorrelation approaches zero since it is proportional to the probability for detecting two photons within said time interval. Simplified, a singular two-state quantum system undergoing a transition like the spontaneous emission of fluorescence can never emit two photons at the same time. Thus, regular fluorophores emit light as a series of individual entities. The first experimental proof of such behavior has been given by Kimble et al. in 1977 [6] and was previously predicted by Kimble and Mandel [7] and independently by Walls and Carmichael [8] just the year before.

As mentioned above, it is frequently discussed in this context that photons emitted by a single fluorescent dye molecule come more equally spaced than, e.g., photons emitted by a coherent or even a thermal light source. The regularity of that inter-photon spacing can be statistically characterized and one usually finds that such singular quantum systems give rise to a photon number distribution narrower than a Poisson distribution. Although these effects frequently coincide it has been shown that photon antibunching can occur without obeying a sub-poissonian photon number distribution [9].

Over the last decade photon antibunching has been rediscovered by many researchers in the field of single molecule fluorescence spectroscopy (SMFS) for two main reasons. First, the HBT-type experiment could easily be transferred to become the only direct proof that a single molecule is observed using fluorescence microscopy [10] and, second, it could be further developed for estimating the number of independently emitting molecules with a confocal fluorescence microscope [11–14]. Photon antibunching is nowadays frequently applied in SMFS [15, 16]. Recent topics are studies of energy transfer in multichromophoric molecules [11, 14, 17, 18] and photo-systems [19, 20] as well as quantification of proteins in biology [21, 22].

In line with this and more recent developments, this article will explain the different methods to measure photon antibunching in SMFS experiments in the order of their appearance. Aside from technical aspects the fundamental theories will be explained that are used for data analysis. Each methodological approach is then followed by section covering its applications in SMFS.

2 Photon Antibunching as Proof for Single Molecule Fluorescence

As briefly outlined before, single fluorophores and ensembles of multiple independent emitters display significant differences in their characteristic fluorescence emission. These differences may be exploited to identify isolated independent emitters. Single molecules have a defined absorption and emission dipole moment, thus polarization dependent excitation and detection of fluorescence gives valuable insights. Also, spectral fluctuations do not occur in ensemble measurements. The observation of discrete events in the intensity transient on the millisecond to seconds timescale, such as blinking and single-step photobleaching, is as well an indicator for single emitters. Yet another striking characteristic of the temporal distribution of photons from a single fluorophore is that, on the shorter nanosecond timescale, they arrive with almost regular gaps between them leading to the mentioned sub-poissonian distribution. This can be readily explained in the simplified picture of an isolated two-state quantum system. A single molecule that is prepared in the ground state can be excited by, e.g., laser light. It then resides in the excited state, on average for the excited state lifetime, until it returns to the ground state by emission of a photon. Subsequently, the molecule may undergo the next excitation–emission cycle. It is evident that photons can only be emitted one at a time within this process. In other words, the probability to observe a photon after the detection of a previous one vanishes as the time interval between the photon-pair approaches zero. This purely quantum mechanical phenomenon is called photon antibunching. It was first explored in SMFS using continuous wave (CW) excitation which is covered in the following section before we turn to more efficient pulsed detection schemes that were developed thereafter.

3 Photon Antibunching Measurements with Continuous Wave Laser Excitation

Photon antibunching can be detected by measuring photon correlations, i.e., the conditional probability of detecting a photon at time $t + \tau$ after the detection of first photon at time t. This is traditionally investigated using CW-laser excitation in a confocal microscope with the detected light split onto two single photon sensitive detectors (see Fig. 1). Time-correlated single photon-counting (TCSPC) electronics or fast photon-counting cards are used to measure the time between successively detected photons at the two detectors. This detection scheme is referred to as HBT-interferometer.

A typical configuration to determine photon antibunching in a fluorescence signal, i.e., to measure the intensity autocorrelation function at short (ns) lag times, uses a regular confocal microscope scheme for excitation of the sample (see Fig. 1). A CW-laser is focused to a diffraction limited spot and the fluorescence

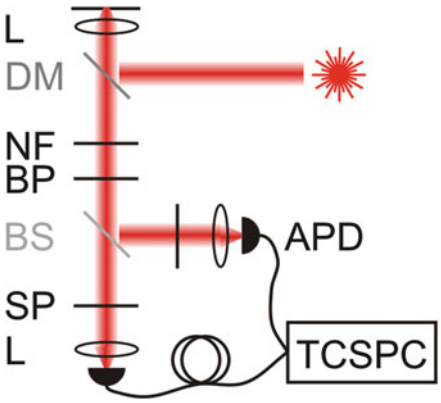

Fig. 1 Microscope setup used for photon antibunching measurements with continuous wave laser excitation. Confocal microscope with CW excitation and HBT-interferometer detection scheme; fluorescence photons are split 50:50 towards two avalanche photon diodes (APDs) by a non-polarizing beam splitter (BS). Time-correlated single photon-counting (TCSPC) with one "start"- and one "stop"-channel allows the determination of the histogram of inter-photon arrival times. *DM* dichroic mirror, *BP* bandpass filter, *SP* shortpass filter, *L* lens

from the sample is collected by the same objective as used for illumination. The laser light is separated from fluorescence photons by a dichroic mirror (DM). A notch filter (NF) or a longpass filter is used to further suppress photons at the wavelength of the laser. Additionally, a bandpass filter (BP) may be used to further narrow the detection wavelength range if the probe is of sufficient brightness. The detection path is then equally divided by a 50:50 non-polarizing beamsplitter to form a classical HBT-interferometer with two single photon sensitive detectors [23, 24], e.g., avalanche photo diodes or photo multiplier tubes [4]. In some experiments, a dichroic mirror is used instead of a beamsplitter to divide the photon detection channels spectrally. Two detectors are needed because the dead time of the detectors (~50 ns) is larger than the typical fluorescence lifetime of small organic fluorophores that sets the timescale of the experiments. Formerly and still widely applied, the time lag between two subsequently detected photons was measured by using one of the detectors as "start"-signal and the second as "stop"-signal for a TCSPC board. Signals from one of the detectors are commonly delayed to enable the detection of "negative" photon-pair delay times. In this case, the first photon is detected in the "stop"-channel rather than in the "start"-channel. Nowadays, arrival times of individual photons can directly be measured either by TCSPC with picoseconds or by fast photon-counting cards with multiple input channels with nanoseconds time resolution [25]. Typically, many photons ($\sim 10^5$) need to be recorded until the histogram of the inter-photon arrival time delay is built up with sufficient statistics. Photon antibunching is reflected by a vanishing probability to detect photon pairs when the lag time approaches zero. Since APDs operated in the Geiger mode are likely to emit an infrared photon for every photon they detect, it is advisable to use either shortpass filters (SP) or adequate BP filters

in front of each detector. This prevents a premature false "stop" signal due to such an infrared photon traveling to the other detector before the real second photon of the pair arrives [15]. The result of the HBT-interferometer observations is a histogram of inter-photon arrival time delays. This measurement constitutes a good approximation of the intensity autocorrelation function $G^{(2)}(\tau)$ [see Eq. (1)] in case of overall low photon detection probabilities [10]. As described above, photon antibunching manifests as a dip in the second-order correlation function at short lag times. In an ideal experiment $G^{(2)}(0) = 0$ holds for single molecules. The magnitude of the dip is diminished the more molecules there are in the confocal volume and the higher the number of background photons.

The normalized photon correlations can be expressed as follows:

$$G^{(2)}(\tau) = \frac{\langle n_1(t) n_2(t+\tau)\rangle}{\langle n_1(t)\rangle \langle n_2(t+\tau)\rangle} = \frac{\langle I_1(t) I_2(t+\tau)\rangle}{\langle I_1(t)\rangle \langle I_2(t+\tau)\rangle} = \frac{\langle I(t) I(t+\tau)\rangle}{\langle I(t)\rangle^2} \quad (1)$$

Here, n_m is the number of photon counts observed at detector m. The number of registered counts is proportional to the intensity I_m. We assume that the average intensity is not time dependent and treat both APDs as equal detectors. Furthermore, we consider the case of N identical, uncorrelated emitters, with the emission intensity i independent of the position in the laser focus and we neglect background photons.

$$\langle I(t)\rangle = N\langle i\rangle \quad (2)$$

$$\langle I(t) I(t+\tau)\rangle = \left\langle \sum_{j=1}^{N} i_j(t) \sum_{k=1}^{N} i_k(t+\tau) \right\rangle = \left(N^2 - N\right)\langle i\rangle^2 + N\langle i(t) i(t+\tau)\rangle \quad (3)$$

Taken together, the normalized second-order correlation function is described by the number of molecules N and by the conditional probability of a molecule emitting a photon at time t (preparing the emitter in the ground state g), being re-excited and emitting a second photon at time $t+\tau$.

$$G^{(2)}(\tau) = \frac{N(N-1)}{N^2} + \frac{1}{N}\frac{\langle p(t) p(t+\tau)\rangle}{\langle p(t)\rangle^2} \quad (4)$$

For the simplified picture of an immobile two-state emitter, this conditional probability can be calculated considering the rate equations for excitation and emission and the initial conditions. More detailed derivations of the intensity correlation function for the general case of diffusing molecules with more than two states can be found, e.g., in [10, 21, 26]. For short timescales, the initial rise of $G^{(2)}(\tau)$ due to photon antibunching [Eq. (5)] is recovered.

$$G^{(2)}(\tau) = 1 - \frac{1}{N} e^{-\left|\frac{\tau}{T}\right|} \quad (5)$$

$$T = \frac{1}{k_{ex} + k_s} \tag{6}$$

The width of the antibunching dip depends on the excitation pump rate k_{ex} and on the rate of spontaneous emission k_s. Fitting the experimentally obtained histogram of inter-photon arrival time delays with Eq. (5) estimates these photophysical parameters and the number of molecules in the confocal volume. In practice, the contrast of the antibunching dip is lowered by uncorrelated coincidences with background photons. To achieve good antibunching measurements, the microscope detection efficiency should be optimized to avoid loss of signal photons; substrates should be of high purity and appropriate filters should be used to suppress Rayleigh scattered laser light and Raman scattered light from the sample.

3.1 Early Applications of Photon Antibunching in SMFS

Photon antibunching of fluorescent molecules was first observed at low temperatures for single dye molecules trapped in a solid by [10]. The researchers investigated pentacene in a crystal host of *p*-terphenyl. Crystal platelets were mounted in an optical cryostat at $T = 1.5$ K in the focus of a CW-laser with $\lambda = 593.4$ nm. Fluorescence was separated by a LP filter and the histogram of inter-photon arrival time delays was measured with a HBT array with two photomultipliers as "start"- and "stop"-channels over the timespan of ~1 h. The antibunching dip for short lag times as an indicator for single molecules can be seen in Fig. 2. The background due to Raman scattering of the embedding *p*-terphenyl molecules leads to an increased deviation of $N(\tau)$ (unnormalized $G^{(2)}(\tau)$) from zero in Fig. 2a–c with increasing laser power. Correspondingly, the width of the antibunching dip is decreasing. For the highest laser power (Fig. 2c), the correlation function shows Rabi oscillations which are damped out for the other measurements.

Initial photon antibunching measurements with CW excitation of fluorescent molecules at room temperature were conducted on a surface in air [27], in solution [28, 29], in a crystalline host [30], and in a thin polymer film [31]. Figure 3 displays a histogram of the inter-photon arrival time delays for (a) an ensemble of Rhodamine 6G (R6G) molecules and (b) single R6G molecules immobilized on a silica surface exposed to air. Patrick Ambrose et al. [27] accumulated coincidence measurements from many points on the surfaces to obtain enough events for reconstructing the photon correlations. This experiment also used a HBT array with two APDs as "start"- and "stop"-channels. Even though excitation with 514.5 nm CW-laser light was modulated by an AOTF to prevent exposure during the detector dead time, studies with single molecules were not possible due to premature photobleaching. The antibunching dip at a lag time of zero indicates that mostly single molecules contributed to the histogram in (b) and is lacking in the measurements of an ensemble of ~200 molecules in (a). The overall shape of the

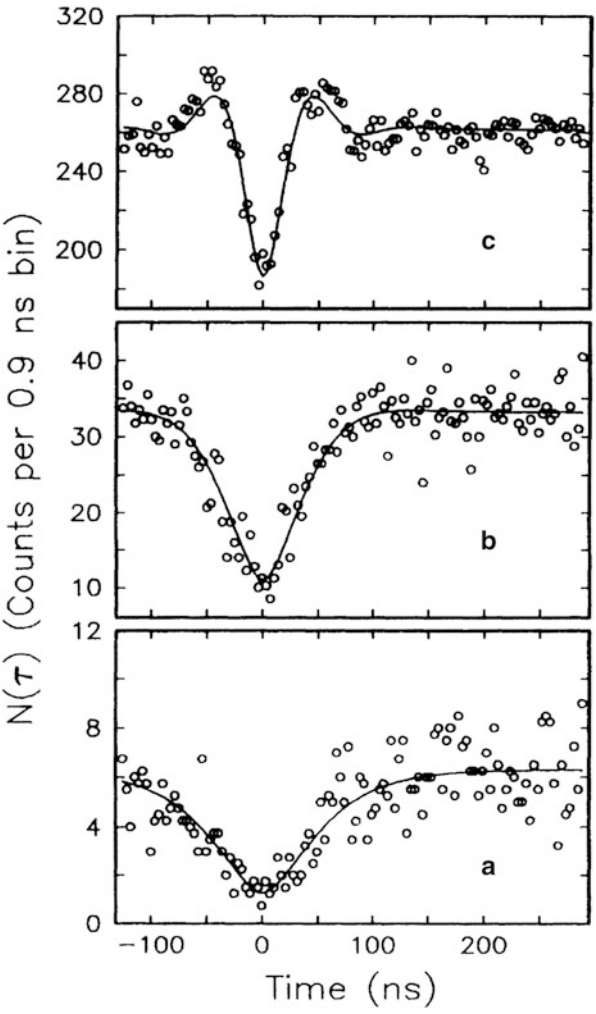

Fig. 2 Histogram of interphoton arrival time delays for a single pentacene molecule embedded in a crystal of *p*-terphenyl: The antibunching dip can be seen for lag times approaching zero. Laser excitation at $\lambda = 593.4$ nm with increasing laser power corresponding to Rabi frequencies Ω of (**a**) 11.2 MHz, (**b**) 26.2 MHz, and (**c**) 68.9 MHz. The *solid lines* are fits to the data with $\Omega =$ (**a**) 1–10 MHz, (**b**) 25.5 MHz, and (**c**) 71.3 MHz. Reprinted with permission from Basché et al. [10]. Copyright 1992 by The American Physical Society

shown histograms can be explained by the autocorrelation of the modulated laser excitation. The dip in (b) is consistent with a model for single molecules using the photophysical parameters of R6G obtained in other experiments.

A serious limitation of CW excitation is that antibunching measurements generally cannot be performed with single organic molecules under ambient conditions due to the limited amount of fluorescence photons available from a single molecule before photodestruction. Photobleaching of single molecules is inhibited, e.g., at low temperature or when they are protected from reactive oxygen species in a solid or a polymer matrix [27, 28]. More recently, a system of reducing and oxidizing agents in combination with enzymatic oxygen scavenging was shown to significantly prolong the lifespan of organic dyes in aqueous buffer [32].

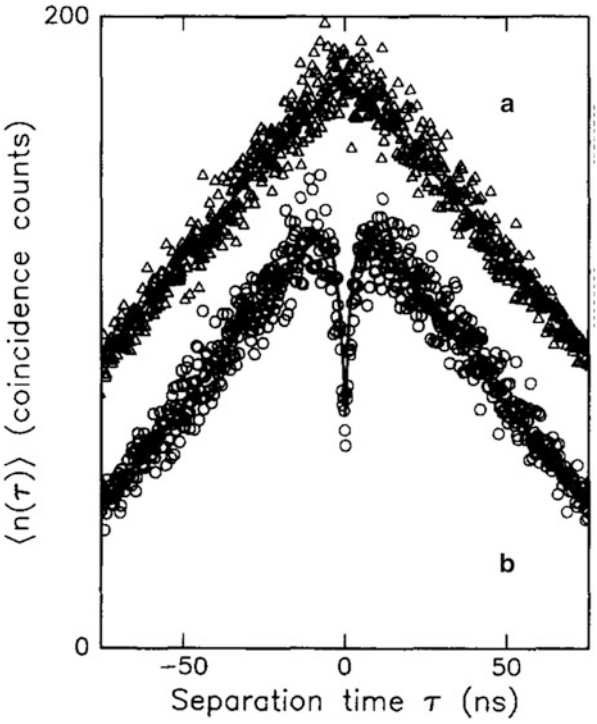

Fig. 3 Histogram of inter-photon arrival time delays of Rhodamine 6G on borosilicate glass. A field of view of $10 \times 10\ \mu m^2$ was imaged with a pixel dwell time of 20 ms using modulated laser excitation at $\lambda = 514.5$ nm; peak intensity and coverage in (*a*) 30 W/cm^2 and ~10^{11} R6G/cm^2 and (*b*) 60×10^3 W/cm^2 and ~10^8 R6G/cm^2. (*a*) Coincidences accumulated directly from a scan of a surface, (*b*) coincidences accumulated from ~300 individual molecules on six different surfaces. Reprinted with permission from Patrick Ambrose et al. [27]. Copyright 1997 by Elsevier

Photon antibunching measurements were also used to prove single photon emission of single bleaching resistant quantum dots [33–35] and nitrogen-vacancy centers in diamond [36, 37]. These two types of emitters along with regular organic fluorophores in a matrix play an important role in fabricating single photon turnstile devices that deliver photons on demand. Different approaches use, e.g., optical [38–41], electrical [42, 43], or electron beam excitation [44] to trigger the emission of single photons. The generation of pure single photon states is important for quantum information processing [45–47], secure communication through quantum cryptography [48, 49], and for quantum metrology [50].

3.2 *Counting of Independent Fluorescence Emitters Using CW Excitation*

Most of the above mentioned experiments use the antibunching signature to confirm the existence of single emitters. They also model the photon correlation function with the expression for $G^{(2)}(\tau)$ in Eq. (5) to learn about the photophysical rate constants accessible through the fit. Since the dip amplitude is antiproportional to the number of independent emitters N, antibunching measurements can also be

used to count the number of constituents in a molecular complex. For example, Hui et al. [51] quantified the number of color centers in nanodiamonds and found that the concentration of nitrogen-vacancy centers could be increased even further to enhance the brightness of the particles. Hollars et al. [11] investigated how the chain conformation affects the photophysical properties of multichromophoric conjugated polymers. They determined the average number of independent emitters to be close to two ($N = 2.4$) when single molecules of poly[2-methoxy,5-(2-ethyl-hexyloxy)-*p*-phenylene-vinylene] (MEH-PPV) were spincast on glass from a toluene solution. In contrast, processing in chloroform leads to many active emitters in a single chain and no dip is apparent in the antibunching histogram. This means that efficient intra-molecular energy transfer to only two or three chromophoric units takes place in the former experiment. Together with other spectroscopic measurements, Hollars et al. concluded that MEH-PPV adopts a tightly folded structure promoting chromophore interaction in toluene, whereas the polymer chain is more relaxed in the polar solvent chloroform. Kumar et al. [18] soon after demonstrated the presence of single emissive sites in single, z-oriented cyano-substituted polyphenylene vinylene (CN-PPV) chains with many chromophoric units when processed in toluene. These measurements were possible because of the much increased photostability of CN-PPV over MEH-PPV. Biological multichromophoric systems were also investigated by photon correlation measurements. B-Phycoerythrin (B-PE), a highly fluorescent phycobiliprotein found in the light harvesting structures of red algae and cyanobacteria, contains 34 bilin chromophores. Wu et al. [20] imaged many single B-PE molecules in solution and found that they behave as a single quantum system. With nearest-neighbor bilin distances ranging from 1.9 to 3.5 nm in the crystal structure of B-PE, efficient intra-molecular energy transfer explains the observations [52].

All of the initial photon antibunching experiments were performed with continuous wave laser excitations using the "start"–"stop" channel recordings described above. However, a severe limitation of CW excitation is that under ambient conditions the photon statistics from single (probe) molecules are generally not sufficient to build a proper histogram of inter-photon arrival time delays before photobleaching. Unless photobleaching is prevented by, e.g., measurements at cryo-temperatures [10] or by using ultra-stable chromophores such as quantum dots [33, 34, 39], thus, antibunching can only be characterized by measuring photon statistics from many molecules. Therefore, CW antibunching experiments yield average properties of an ensemble of molecules. The main reason for insufficient statistics is that photon emission upon CW excitation occurs randomly and this leads to a loss of photons that cannot be detected due to the dead time of the detectors. As well, the two-detector arrangement requires an arbitrary, but fixed assignment of "start"- and "stop"-channels. In addition to missing coincident events where both photons of a pair are directed towards the same APD (50%), events where the first photon arrives at the "stop"-channel outside of the electronically imposed delay window mentioned above are not registered. Also, if the "start"-channel is triggered, any further photons directed towards it will be ignored

until the electronics is reset, which leads to a loss of genuine photon pairs. Modern time tagged electronics alleviate these problems [25].

4 Photon Antibunching Measurements with Pulsed Laser Excitation

In the previous section, we introduced the measurement of photon antibunching under CW-laser illumination. More effective measurements of photon pairs in terms of photon statistics can be made with pulsed excitation sources. Typically, picoseconds laser pulse widths ($\leq$100 ps) are chosen to excite the molecules only once within a single laser pulse [53]. Instead of random photon emission events, photons then arrive within predefined excitation cycles delayed by the fluorescence lifetime. If the laser repetition rate is sufficiently low, no photons are missed during the dead time of the detector and TCSPC electronics. Also, molecules undergo less excitation–emission cycles per time interval which leads to prolonged photochemical stability. Photon antibunching experiments with pulsed laser excitation may be performed with the same setup as described for continuous wave except for the excitation (see Fig. 4a). Common setups use inverse TCSPC where the "start" signal is provided by the detectors while the "stop" signal comes from the laser sync, i.e., the timing of the laser pulses, as a reference. For each photon, the arrival time after the beginning of data acquisition (macrotime) is recorded with nanosecond resolution and the time between photon detection and the next laser pulse (microtime) with picosecond resolution along with an ID identifying the detector. In case of routed TCSPC electronics, the TCSPC card introduces a detection dead time between channels (~100 ns) because the router just serves to identify the input channels which are processed by the same TCSPC unit. To prevent missing multiple closely spaced detection events (mDE) at two APDs in one laser cycle, a signal delay is introduced for one of the detectors. This TCSPC scheme leads to even fewer missed events as compared to measurements with pulsed laser excitation and assignment of the two detectors to fixed "start"- and "stop"-channels.

As explained above, molecules undergo less excitation cycles per time interval and remain fluorescent for longer times with pulsed laser excitation. This finally enables collecting sufficient statistics for antibunching measurements of single molecules [12, 38]. It was first demonstrated by Lounis and Moerner [38] who used a single molecule as a source for single photons. They measured with a HBT array and conventional "start"–"stop" TCSPC electronics. Instead of the continuous distribution of inter-photon arrival time delays obtained with CW excitation, the histogram now displays peaks that are equally spaced according to the laser repetition rate with a shape reflecting the fluorescence lifetime of the fluorophore (see Fig. 4b). The peak around lag time zero corresponds to photon pairs registered within the same excitation cycle whereas the satellite peaks stem from photon pairs originating from different laser cycles. The single molecule antibunching signature

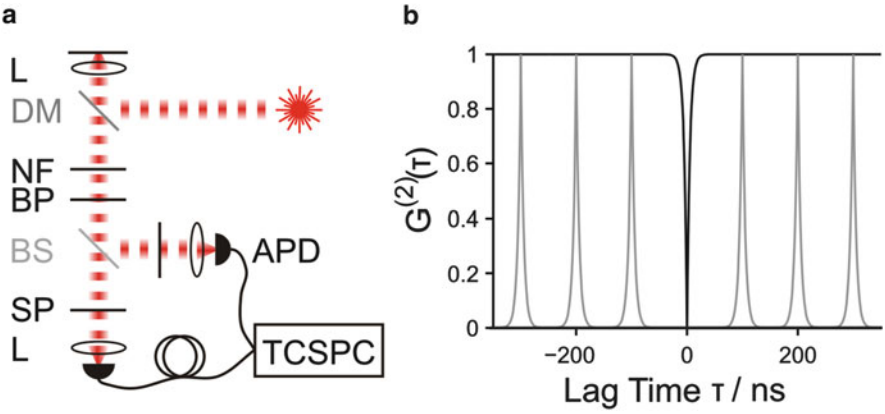

Fig. 4 Microscope setup used for photon antibunching measurements with pulsed laser excitation and modeled inter-photon time histogram. (**a**) Confocal microscope with pulsed excitation and HBT-interferometer detection scheme; fluorescence photons are split 50:50 towards two avalanche photon diodes (APDs) by a non-polarizing beam splitter (BS). Time-correlated single photon-counting (TCSPC) with one "start"- and one "stop"-channel allows the determination of the histogram of inter-photon arrival times. *DM* dichroic mirror, *BP* bandpass filter, *SP* shortpass filter, *L* lens. (**b**) Modeled inter-photon time histogram. The *black line* indicates photon correlations for a single molecule with continuous wave laser excitation. The *gray line* represents pulsed laser excitation with a repetition rate of 10 MHz. The excitation at defined points in time (every 100 ns) is reflected by distinct peaks with a width influenced by the fluorescence lifetime

still corresponds to vanishing photon correlations at and around a lag time of zero, i.e., the central peak is suppressed.

In measurements with inverse TCSPC, photon antibunching can be quantified through data post-processing by either calculating the inter-photon arrival time delay histogram or by using a cross-correlation algorithm with the signals from the two detectors. In addition to the coincidence ratio, i.e., the ratio of coincidence counts in the central peak N_c over the mean count in the lateral peaks $\overline{N}_l$ as a measure for antibunching, several photophysical parameters such as fluorescence intensity and fluorescence lifetime can be monitored simultaneously for single molecules and even transients thereof may be recorded [12, 13]. Indeed, picosecond time resolution is not necessary to determine the number of independently emitting fluorophores. The macrotime suffices to determine in which laser cycle the photon was detected. In turn, the photon pairs can be sorted into the discrete peaks of the inter-photon arrival time histogram, disregarding the spread of the peaks due to the uncertainty of photon emission around the fluorescence lifetime (see below and [13]).

Further refined single photon-counting electronics provide fully independent input channels with picosecond resolution eliminating the dead time between channels. This allows a direct computation of the intensity autocorrelation function

down to picosecond lag times. However, a dead time on the order of 100 ns due to detector and electronics remains for the respective channels [54–57].

A possible problem for antibunching measurements leading to erroneous events when recording all photons from the detectors lies in the so-called APD afterpulsing. For APDs, there is a certain probability of generating an additional secondary signal output after detection of a photon without detecting another photon. This is due to the signal amplification process inherent to APDs; the likelihood of such events depends on the photodiode material and decays rapidly with time [23, 24]. Afterpulsing can be effectively eliminated by using photon pairs from different detectors and appropriate delays between the detectors.

As for measurements with CW-laser excitation, pulsed laser excitation antibunching experiments can be used to estimate the number of independent emitters. The relationship between the coincidence ratio $N_c/\overline{N}_1$ and the number of molecules in the focus can be readily derived, e.g., by combinatorics. Again, we take into account N identical, uncorrelated fluorescent molecules, with the emission independent of the position in the laser focus and neglect background photons. For an ideal 50:50 beamsplitter and a setup with an overall photon detection probability of p, the likelihood to detect one photon at one of the detectors is $0.5p$. In any laser cycle two photons can be detected when molecules i and j emit at the same time, except for the case $i = j$ which describes the same single molecule. The probability to obtain a photon pair at the two APDs from the same laser pulse P_c is described by all possible combinations of photon detections from different molecules.

$$P_c = \sum_{i=1}^{N} \sum_{j=1, j\neq i}^{N} (0.5p)^2 \tag{7}$$

The probability to detect consecutive photon pairs in different laser cycles can be calculated similarly, allowing for $i = j$.

$$\overline{P}_1 = \sum_{i=1}^{N} \sum_{j=1}^{N} (0.5p)^2 \tag{8}$$

The coincidence ratio is then simply the ratio of the two probabilities [Eq. (9)]. For a single molecule $N_c/\overline{N}_1 = 0$, for two molecules $N_c/\overline{N}_1 = 0.5$ and for three molecules $N_c/\overline{N}_1 = 0.67$. Again, corrections have to be applied to account for uncorrelated coincidences with background photons when reliable fluorophore number estimates are to be made.

$$\frac{N_c}{\overline{N}_1} = \frac{P_c}{\overline{P}_1} = \frac{N(N-1)0.25p^2}{N^2 0.25p^2} = 1 - \frac{1}{N} \tag{9}$$

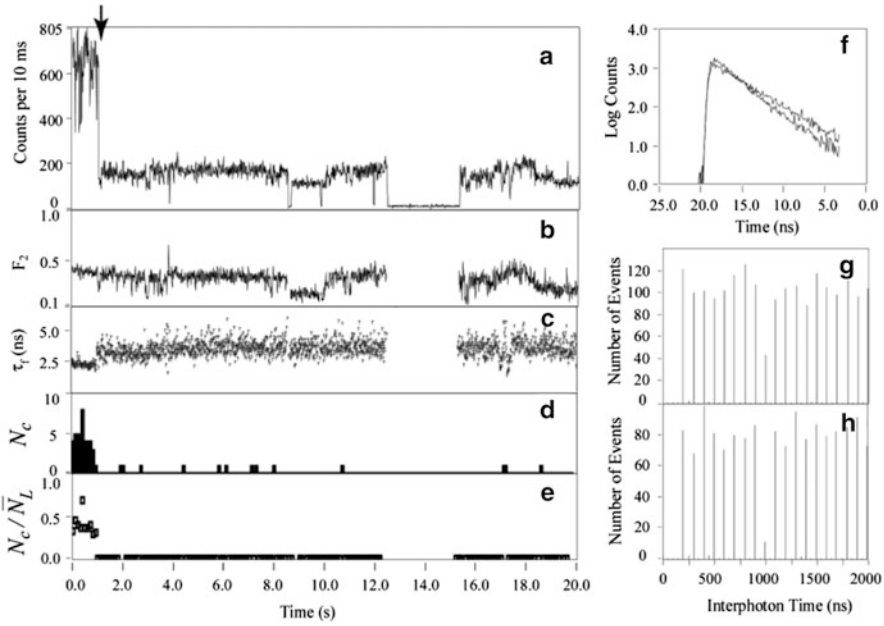

Fig. 5 Multiparameter fluorescence acquisition for a Cy5-DNA-Cy5 construct. (**a**) Total intensity, (**b**) fractional intensity F_2, (**c**) fluorescence lifetime τ_f, (**d**) coincidence counts N_c, (**e**) coincidence ratio $N_c/\overline{N}_1$ of a single probe excited with a 10 MHz 635 nm laser at 4 kW/cm^2, (**f**) the fluorescence decay before and after photobleaching indicated by the *arrow* in (**a**), (**g**), and (**h**) are the respective inter-photon arrival time delay histograms with a resolution of the recorded macrotime corresponding to a coincidence ratio of 0.39 ± 0.06 and later 0.14 ± 0.04. Reprinted with permission from Weston et al. [13]. Copyright 2002 American Chemical Society

A single TCSPC card can be used to record the absolute arrival time in terms of the time after the beginning of the experiment (macrotime, ns time resolution) and the time between photon detection and the subsequent laser pulse (microtime, picoseconds time resolution) as well as the channel number [13]. This is achieved using the two channels connected to the APDs as "start"- and the laser sync as "stop" signals and was synchronized with image acquisition. These electronics make antibunching measurements even more efficient because the artificial "start"–"stop"-channel assignment to APDs can be omitted. We have shown that from a stream of photon transients the total fluorescence intensities, the fractional intensity F_2 at one of the APDs, the fluorescence lifetime, the number of coincident counts in the central peak, and the coincidence ratio can be recovered. We then used this multiparameter approach to investigate DNA samples with two Cy5 fluorophores at single molecule densities on a glass coverslip. The HBT array used a dichroic mirror to split the emission at $\lambda \approx 570$ nm (~50:50). The fractional intensity measurement enabled the observation of spectral fluctuations of the fluorophores. Figure 5 shows an example transient with initially two Cy5 dyes that subsequently photobleach. The decrease in the coincidence ratio from 0.39 ± 0.06 to 0.14 ± 0.04 at ~1 s unequivocally proves that the stepwise decrease

in the intensity is not just a fluctuation in the emission intensity of a single Cy5 molecule, but a decrease in fluorophore number from two to one. The pre- and postbleach photon pair arrival time delay histograms are shown in Fig. 5g, h, respectively. The fractional intensity and the fluorescence lifetime fluctuate throughout the transient as commonly observed. Any variation of the fractional intensity away from 0.5 as well as unequal detection probabilities of the two APDs and background coincidences leads to deviations from the $1 - 1/N$ dependency of the coincidence ratio.

Variations in coincidence measurements were investigated in a similar manner using DNA-hairpin probes with one, two, or three fluorescent dyes [58]. These experiments demonstrate the potential of photon antibunching methods to investigate molecular complexes and processes in life science on the single molecule level.

4.1 Counting Independent Emitters in Experiments

Later, Fore and coworkers [22] applied photon antibunching to determine the number of apolipoprotein A-I (apo A-I) molecules that are bound to high density lipoprotein (HDL) particles. Apo A-I plays a central role in the structure and metabolism of HDL particles which in turn carry out cholesterol transport. In their study they reconstituted HDL particles with a single cysteine mutant of apo A-I that was site specifically labeled with one Alexa647 dye and lipid vesicles. Photon correlations were recorded for diffusing particles using a HBT array with APDs and recording the arrival time of each photon. They concluded that there are two apo A-I per rHDL particles and validated biochemical experiments with their investigations in this more natural environment. Fore et al. [22] also obtained number estimates with the photon-counting histogram (PCH) method that analyzes fluctuations in fluorescence intensity [59]. PCH confirmed the photon antibunching measurements but requires a singly labeled control sample to work.

When photon statistics are used to count the number of monomers in a complex, care has to be taken to avoid energy transfer between the fluorophores that are used for labeling. For example, Sánchez-Mosteiro et al. [19] found that DsRed tetramers appear mostly as single emitters which may be explained by efficient energy transfer of the chromophores in nanometer proximity. Another extensive study of well known diffusing molecules revealed fluorophore numbers as presumed only for some of the systems under investigation [21]. Antibunching measurements with single dyes, fluorescent proteins (EGFP), and dye labeled oligomer hybridization probes returned one, two, or three labels per complex according to expectations. In contrast, EGFP-tagged ligand gated ion channels $P2X_1$ (homotrimer) and α1 glycine receptor (homopentamer) appeared on average as complexes of 2.51 ± 0.09 and 2.06 ± 0.06 monomers. In addition to excitonic coupling among adjacent EGFP labels, incomplete fluorescent protein maturation and instability of the oligomeric complexes could be reasons for lower number estimates.

Photon antibunching measurements can distinguish between active, independent emitters, and molecules that are present in a complex but do not directly contribute to fluorescence emission as already mentioned earlier. This ability of coincidence analysis is widely used to investigate energy transfer in single molecules of engineered multichromophoric systems [60–66] and in model systems of conjugated polymers [15, 17].

5 Measuring Extended Photon Statistics with Pulsed Laser Excitation

As discussed above, the degree of antibunching can be used to estimate the number of active, independent emitters. In previously mentioned experiments, the occurrence of photon pairs and their temporal distribution were measured using two detectors in a HBT array with continuous wave or pulsed laser excitation. However, as the number of emitters increases the amplitude of the intensity autocorrelation function at zero lag time (CW-laser) or the central peak (pulsed laser), which are the respective measures for antibunching, quickly approach the value at large lag times (CW-laser) or that of the lateral peaks (pulsed laser) which is the limiting case for an infinite number of emitters. The theoretical signature for N emitters in a HBT-type interferometer is proportional to $1 - 1/N$ (see Fig. 6a). In practice, this function quickly saturates already for three or four emitters making its use for estimating the number of molecules very limiting.

Over the past years we could both theoretically and experimentally show that this limit can be overcome when also photon triples and quadruples are taken into

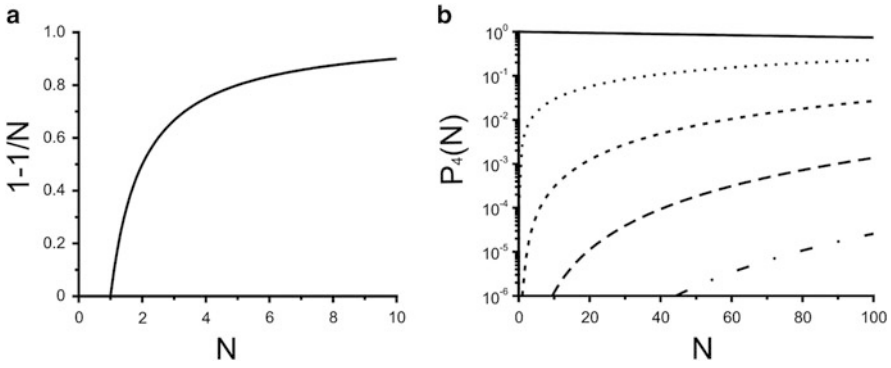

Fig. 6 Observable photon statistics for two and four detector pulsed laser antibunching measurements. (**a**) The theoretically expected coincidence ratio $N_c/\overline{N_1}$ in dependence of the number of emitters N for an ideal two-detector setup. (**b**) The probability distributions $P_4(N; p; i)$ for i simultaneous multiple detection events (mDE) ($i = 0$ *solid*, 1 *dotted*, 2 *dashed*, 3 *long dashed*, 4 *dashed/dotted*) in dependence of the number of emitters N for an ideal four detector setup. Adapted from Ta et al. [67]

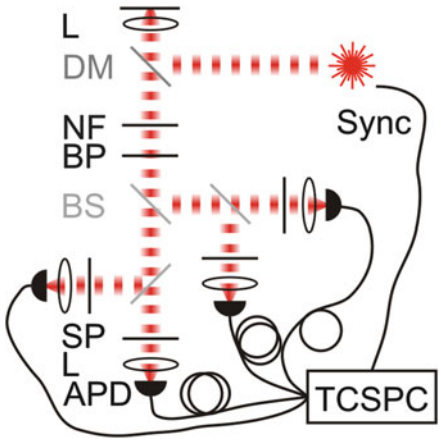

Fig. 7 Microscope setup used for photon antibunching measurements with pulsed laser excitation with an extended HBT-like interferometer. Confocal microscope with pulsed laser excitation; fluorescence photons are split 50:50 twice towards four avalanche photon diodes (APDs) by a non-polarizing beam splitter. TCSPC with four synchronized, independent channels registers the absolute arrival time of the photons at each APD. *DM* dichroic mirror, *BP* bandpass filter, *SP* shortpass filter, *L* lens

account. The measurement of three or four coincident photons can easily be achieved by splitting the emitted fluorescence onto four equivalent detectors using the pulsed excitation scheme [56, 67]. The experiments are realized similar as with pulsed laser excitation only that the HBT-interferometer is extended with three 50:50 beamsplitters (see Fig. 7). Again, a laser with picosecond pulse width is used to prevent multiple excitations of single molecules. The laser repetition rate is kept low such that all molecules that are excited return to the ground state and that the TCSPC system is ready to register new photons in the following excitation cycle. This scheme guarantees that each fluorescent label in the laser focus emits at most one photon per excitation cycle. By using state of the art TCSPC electronics with four synchronized, independent channels, the train of photons with the absolute arrival time is registered for each detector independently. The four detector setup now allows computation of the four channel correlation function and the determination of up to four multiple detection events (mDE), i.e., the number of photons detected in one laser cycle. Still, events may be missed if a photon reaches an APD during the signal processing dead time; in general, only one photon may be detected per APD and laser cycle. It should be noted that the detection efficiency of the four detector setup for coincident photon pairs in one laser cycle is 1.5 times higher than for the two-detector setup (see below). To determine the frequency of mDE for counting emitters by their photon statistics and disregarding the fluorescence lifetime information, again only the macrotime is required. In fact, simple and cost effective photon counter cards are sufficient that only determine the number of photons detected in a laser cycle.

5.1 Theory and First Experimental Realization

The extended HBT-type interferometer no longer measures inter-photon arrival times to do photon-pair correlation but the statistics of photons simultaneously registered by different detectors (mDE – multiple detection events) to expand the counting range of photon antibunching experiments [67]. The experimental conditions are similar as for conventional coincidence analysis with pulsed laser excitation. The occurrence of mDE thus carries the information that more than one emitter is present.

For statistical analysis we model the full mDE probability $P_m(N, p; i)$. Again, we assume an idealized experiment with 50:50 beamsplitters and consider N independently emitting fluorophores. Furthermore, we presume the average photon detection probability per laser pulse and label p of the microscope setup [short: detection probability p, see Eq. (11)] to be the same for all emitters. m denotes the number of detectors (here, $m = 4$) and i is the number of mDE. The model considers the stochastic processes of excitation, emission, and detection of photons including the geometry of the detection path. It is important to note that we take into account the detection dead time, i.e., per laser cycle only one photon is detected in one channel although multiple photons may be approaching the same detector. The mDE probability can be constructed from a multinomial distribution. The first part of the recursive formula described in Eq. (10) is the probability for i detection events and the second part is the sum of all probabilities for less than $\leq i$ detection events.

The number of independent emitters N and their detection probability p is then estimated by non-linear regression of the model $P_m(n, p; i)$ to the mDE data accumulated for a certain number of laser cycles with a standard Levenberg–Marquardt algorithm. It is worth mentioning that only four of the mDE probability distributions of the four detector model are independent from one another. However, it is more convenient to assume that all five probability distributions (12)–(16) are independent which can be justified by the small covariance values $<10^{-3}$.

$$P_m(n,\ p; i) = \binom{m}{i}\left[\left(1 - \left(\frac{m-i}{m}\right)p\right)^n - \sum_{k>0}^{i-1}\frac{\binom{i}{k}}{\binom{m}{k}}P_m(n,\ p; k)\right] \tag{10}$$

$$p = \frac{I_{\text{laser}}}{f_{\text{rep}}h\nu}\sigma_{\text{abs}}Q_{\text{f}}\eta_{\text{det}} = \frac{\varepsilon_{\text{MB}}}{f_{\text{rep}}} \tag{11}$$

The detection probability p depends on the photon flux, i.e., the average laser intensity I_{laser} divided by the photon energy $h\nu$, the laser repetition frequency f_{rep}, the absorption cross-section σ_{abs}, and the overall detection efficiency of the microscope setup η_{det}. The molecular brightness ε_{MB} is calculated by multiplication of the detection probability p with the laser repetition frequency. The probability to

observe i simultaneous photons for the $m = 4$ four detector setup can be expressed explicitly by Eqs. (12)–(16):

$$P_4(n,\ p;\ i=0) = \ (1-p)^n \tag{12}$$

$$P_4(n,\ p;\ i=1) = \ 4\left(1-\frac{3}{4}p\right)^n - 4(1-p)^n \tag{13}$$

$$P_4(n,\ p;\ i=2) = \ 6\left(1-\frac{1}{2}p\right)^n - 12\left(1-\frac{3}{4}p\right)^n + 6(1-p)^n \tag{14}$$

$$P_4(n,p;i=3) = 4\left(1-\frac{1}{4}p\right)^n - 12\left(1-\frac{1}{2}p\right)^n + 12\left(1-\frac{3}{4}p\right)^n - 4(1-p)^n \tag{15}$$

$$P_4(n,p;i=4) = 1-4\left(1-\frac{1}{4}p\right)^n + 6\left(1-\frac{1}{2}p\right)^n - 4\left(1-\frac{3}{4}p\right)^n - (1-p)^n \tag{16}$$

The mDE probability $P_4(N, p; i)$ is shown in Fig. 6b for detection probabilities that are typical in experiments with organic dyes. The expressions above can be approximated for small $Np \ll 1$ by Eq. (17).

$$P_4(N,\ p; 1 \leq i\ \leq 4) \tilde{} \prod_{k=0}^{i-1}(N-k)\ p^i \tag{17}$$

Significant three and four photon detections only occur only for higher numbers of bright fluorophores. The four detector setup collects the same number of one photon detection events as a two-detector setup in the approximation for small Np, given that the fluorophores and the setup detection efficiency η remain unchanged. Yet, the four detector setup collects 1.5 times more two photon detection events $P_4(N, p; i = 2) = 1.5\ P_2(N, p; i = 2)$. Moreover, the maximum photon count rate of four independent detection channels is twice that of two channels. Four channels enable us to collect photons from a higher number of fluorophores without saturating the APDs and data acquisition cards in a short time.

This new approach, which we termed counting by photon statistics (CoPS), is only of advantage if it can estimate a low number of molecules with higher precision or if the range of number estimation is significantly extended as compared to previously described methods with two detectors. Therefore, we were first interested in its limits which we tested with Monte-Carlo simulations [67]. We simulated the number of multiple photon detection events on a parameter set of $p = 2.5 \times 10^{-3}$ and $N = 1$–50. It is noteworthy that the value of p was estimated from real data to be as close to the experiment as possible. The target APD of each photon from every fluorophore is determined by generating a random number.

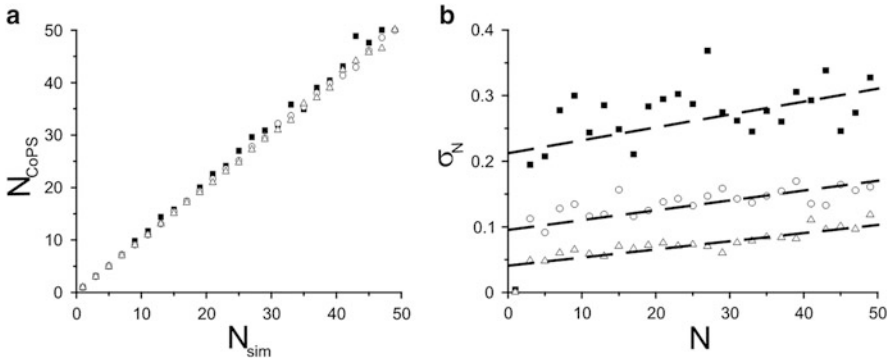

Fig. 8 Simulations of multiple-photon-detection events for different number of average detected photons per molecule with subsequent CoPS estimation. $n_{tot} = 10{,}000$ *black squares*; 20,000 *open circles*; 40,000 *open triangles*. (**a**) The number of estimated independent emitters N_{CoPS} versus the number of simulated emitters N_{sim}. (**b**) The corresponding relative standard deviation in dependence of the number of simulated emitters. Adapted from Ta et al. [67]

Multiple-photon-detection events are recorded and summarized until a certain number of average photons n_{tot} per molecule are acquired. We varied $n_{tot} = 1\text{–}4 \times 10^4$, corresponding to $4\text{–}16 \times 10^6$ laser cycles, which roughly reflects single molecule experiments under standard conditions. However, with the use of stabilizing buffer systems such as ROXS [32], photon yields from single molecules before photobleaching can be even higher.

As can be seen in Fig. 8a, the estimated number of emitters N_{CoPS} increases linearly with the simulated number of emitters N_{sim} and there are no significant differences among the three simulated photon yields. However, the higher number of accumulated photons leads to a decrease in the relative standard deviation of the number estimations from 20–30% to 10–15% down to 5–8% for $n_{tot} = 1\text{–}4 \times 10^4$, respectively (see Fig. 8b). These simulations put into perspective that counting the number of independent emitters by analysis of photon statistics with four detectors is feasible even in larger molecular assemblies. Encouraged by these results, we set out to test the CoPS approach in experiments.

For our first experiments, we chose a double-stranded DNA probe labeled with up to five fluorescent Atto647N dyes. The probe is formed by a long fluorophore- and biotin-labeled single strand consisting of four repeats (termed REP4) and by short fluorophore-labeled oligonucleotides (termed REP′), up to four of which may hybridize to REP4. High affinity biotin–streptavidin binding is used to immobilize the hybridization probe at a single molecule density on a glass surface that is coated with bovine serum albumin (BSA) doped with biotinylated BSA (see Fig. 9a). To enhance photostability and brightness of the dyes we used a photostabilizing ROXS buffer and enzymatic oxygen depletion during the experiment, for details see [56]. For calibration of CoPS number estimates against bleaching step analysis (BS), we selected individual probe molecules and recorded the intensity transient until complete photobleaching to background photon level (8 kW/cm^2 laser

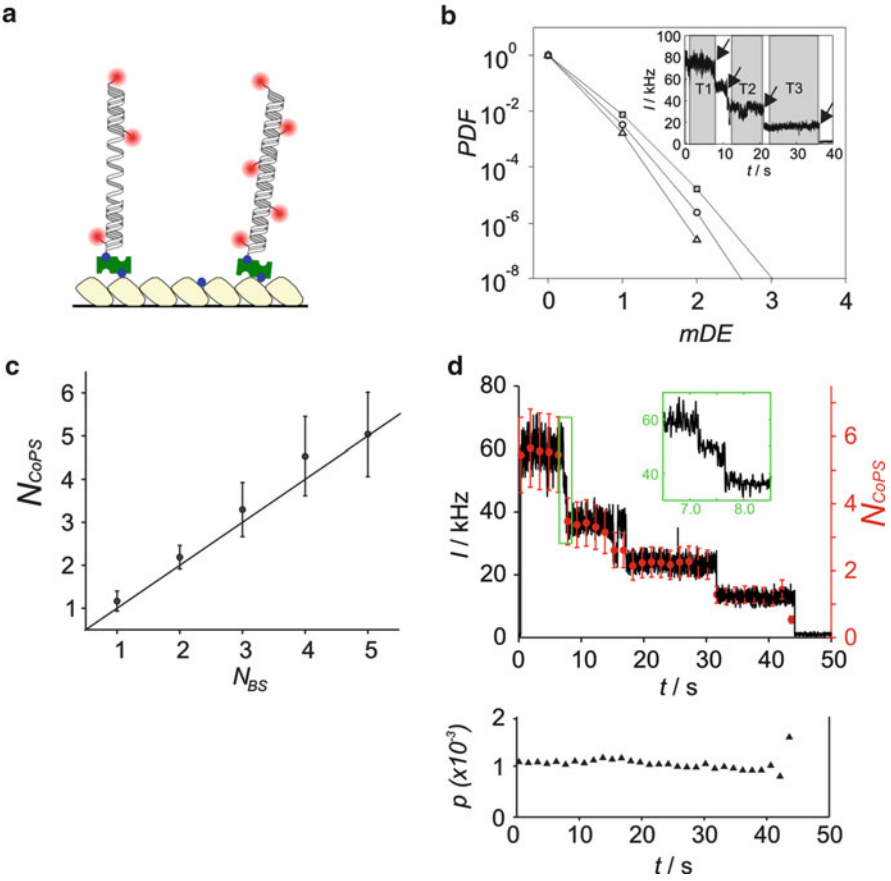

Fig. 9 Counting by photon statistics (CoPS) of up to five fluorophores on a DNA sample. Measurements with 8 kW/cm^2 laser excitation at 635 nm and a repetition rate of 10 MHz. (**a**) DNA hybridization probe with one labeled strand with four repeats (termed REP4) and up to four complementary, short fluorophore-labeled oligonucleotides (termed REP′) immobilized on a BSA coated glass surface via biotin (*blue*)–streptavidin (*green*) binding, (**b**) normalized mDE for a typical fluorescent transient accumulated from the intensity levels indicated in the inset, T1 *squares*; T2 *circles*; T3 *triangles* (**c**) estimated label numbers N_{CoPS} plotted against the number of bleaching steps N_{BS} from experiments with 188 independent time intervals between bleaching steps of imaged DNA hybridization probes, (**d**) time-resolved CoPS number estimates using a sliding analysis window of 1.5 s follow the intensity decay of the fluorescence transient with almost constant estimated detection probability p. Adapted from Ta et al. [56]

excitation at 635 nm and with a repetition rate of 10 MHz). A new photon-counting system was used for data acquisition with the extended four APD HBT array [54–57].

For each fluorescence transient, we manually selected intensity levels with subsequent bleaching steps and accumulated the mDE (see Fig. 9b). To account for realistic experimental conditions, mDE due to random coincidences of

background photons with signal photons have to be considered. Since the detection probability of background photons from scattering in the sample and electronic noise is on the order of $p_b = 0.1\text{–}5 \times 10^{-4}$, the occurrence of more than one background photon can be neglected. Background photons in the photon probability distribution are thus modeled as an additional dim fluorophore with a fixed detection probability p_b that is estimated from experimental data [56]. Equation (10) is then modified to give Eq. (18).

$$P_{m,b}(N,p;i) = \binom{m}{i}\left[\left(1-\left(\frac{m-i}{m}\right)p\right)^{N}\left(1-\left(\frac{m-i}{m}\right)p_b\right) - \sum_{k\geq 0}^{i-1}\frac{\binom{i}{k}}{\binom{m}{k}}P_m(N,p;k)\right] \tag{18}$$

We tested the reliability of the method by correlating the label number estimates N_{CoPS} for 188 respective regions of constant intensity with the number of following bleaching steps N_{BS}. Figure 9c shows that CoPS slightly overestimates the label numbers as compared to bleaching step analysis. Possible reasons are that the background photons were underestimated or that bleaching step analysis slightly underestimates the label numbers by missing rapid bleaching events. The relative standard deviation of N_{CoPS} is on the order of 20% which is consistent with the simulations shown above. Time-resolved CoPS analysis returns number estimates that correlate with the stepwise decrease in intensity even when analysis periods are shortened to 1.5 s (see Fig. 9d). The respective estimated detection probability remains relatively constant throughout the whole transient. The average count rate per label in these experiments was ~13 kHz corresponding to a detection probability $p \approx 1.3 \times 10^{-3}$.

Both, the simulations as well as experimental validation have shown that quantification of fluorescent samples with CoPS is feasible and thus becomes interesting for applications in the life sciences. The formation of molecular clusters of higher order is an important mechanistic component in many hierarchically organized processes. Especially in cells, biological functions are often regulated by the assembly of single proteins into homo- or heterooligomers of defined protein numbers [68]. Malfunctions that lead to diseases can be caused by unwanted or uncontrolled aggregation [69]. To approach this research area we first wanted to experimentally validate counting of higher fluorophore numbers and determine the precision of the method which is described in the next section. We also applied CoPS for the investigation of the label number of different fluorescent markers that are frequently used to label proteins in cells.

5.2 *Experimental Characterization of CoPS with Application to DNA Origami and Fluorescent Markers*

We used DNA Origami [70] with 6–36 Atto647N dyes to experimentally characterize CoPS with higher fluorescent label numbers. Figure 10a shows a scheme of the rectangular 70 × 100 nm sub-optical resolution folded DNA constructs. Dyes and other small tags can be incorporated at defined positions via modification of respective DNA strands. We immobilized and imaged the single DNA Origami structures much as described before on BSA coated glass cover slides via biotin–streptavidin binding in ROXS buffer (for details see [71]). At these higher label numbers we could no longer use bleaching step analysis as a comparison for number estimations. Individual bleaching steps cannot be resolved especially at the beginning intensity transient which almost resembles an exponential decay as for an ensemble of molecules (Fig. 10b). In contrast, CoPS estimates the label numbers by analyzing the photon statistics of just a few million laser cycles and they follow the intensity transient. We refined the CoPS algorithm to achieve more robust label number estimates in a defined analysis period by iterative random resampling of 75% of the laser cycles and fitting of the respective mDE probabilities. After one hundred of these bootstrapping repeats, the estimated number N_{CoPS} and the corresponding error for a single measurement are given by the median of the results and the quartiles of the number estimate distribution.

Next, large numbers of fluorescence transients for four different DNA Origami samples were accumulated. To assess the quality of CoPS number estimation, its variance and bias as compared with the nominal label number under varying experimental and analysis parameters was investigated. For one, the excitation power (2, 5, 7 and 10 μW) was varied to see how this influences the estimates. The CoPS estimate, i.e., the median of the bootstrapping distribution for the first analysis period of each intensity transient, enters the probability distribution function (PDF). The data showed that the estimation is essentially independent of the applied laser power as long as it exceeds a certain minimal laser power (here: more than 2 μW for the chosen label and conditions). The combined PDFs for measurements with 5, 7, and 10 μW are skewed to the right and can be modeled with a log-normal distribution (see Fig. 10c). It should be noted that the PDF shape is a convolution of CoPS intrinsic estimation variance and the label number variation of DNA Origami. CoPS estimates from simulated data also have a right skewed PDF. The mode of the fitted log-normal distribution estimates the nominal label number well for 6, 12, and 18 labels (see Table 1). Both the median and sigma, defined by half the central 68% of the data about the median, from the fit are very similar to the parameters calculated directly from the data. We chose the descriptive statistics approach to determine the relative median μ_{rel} and relative sigma σ_{rel} to quantify the bias and precision [see Eqs. (19 and 20)].

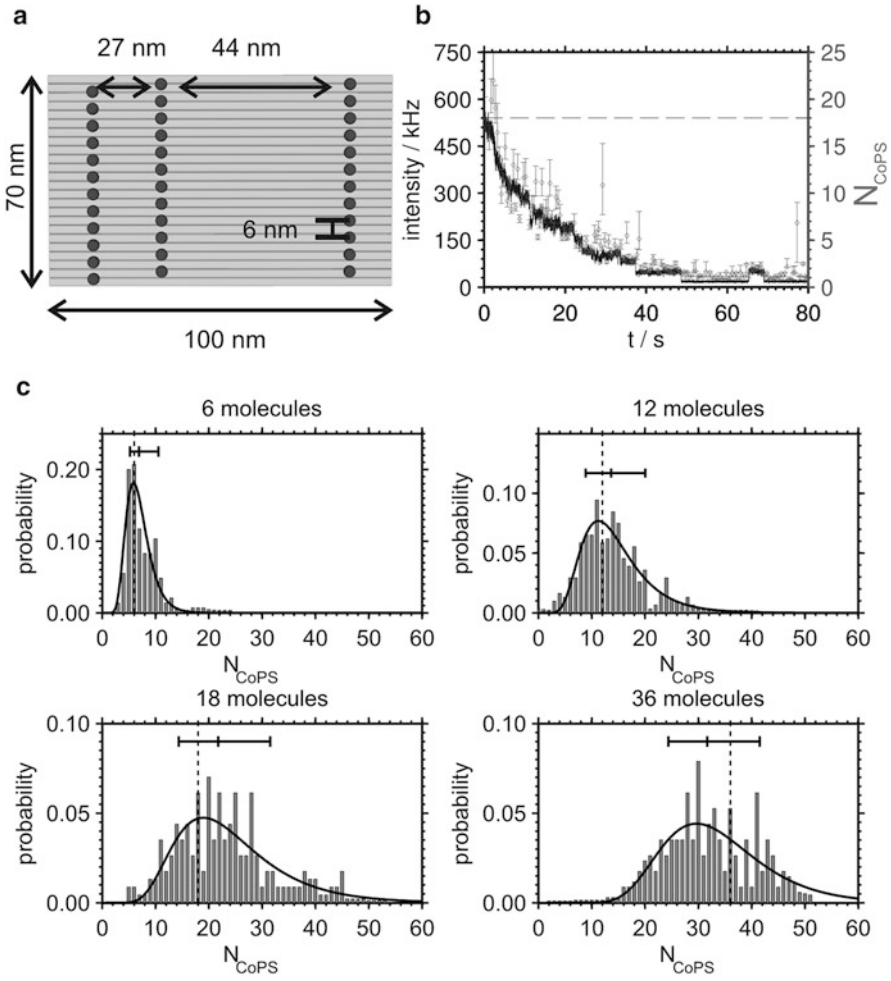

Fig. 10 Counting fluorescent labels on DNA Origami by CoPS. (**a**) Scheme of rectangular DNA Origami structure labeled with 36 Atto647N dyes (indicated by *dots*), (**b**) time-resolved CoPS number estimates (*gray*) using a sliding analysis window of $t_{acq} = 500$ ms ($=10^7$ laser cycles) follow the intensity decay of the fluorescence transient (*black*) of DNA Origami nominally labeled with 18 Atto647N dyes. Error bars as derived by bootstrapping. The *dashed line* indicates the nominal label number 18, (**c**) Probability density function (PDF) of the estimated label numbers of DNA Origami with nominally 6, 12, 18, or 36 Atto647N dyes. Accumulated emitter number estimates of the first 250 ms ($= 5 \times 10^6$ laser cycles) from each transient of experiments with 5, 7, and 10 μW with a total of 520, 1,199, 439, and 346 histogram entries. Log-normal PDF models the data (*black*), *dashed horizontal line* indicates the nominal label number, *box plot* indicates the median and the central 68% of the label number estimates. Adapted from Kurz et al. [71]

Table 1 Comparison of log-normal parameter estimation with descriptive statistics calculations of the data shown in Fig. 10

	From log-normal distribution			Descriptive statistics	
N_{Origami}	Mode	μ	σ	μ	σ
6	6	7	3	7	2
12	10	13	6	14	6
18	19	22	8	22	9
36	26	30	10	32	9

Mode, median μ, and standard deviation σ calculated from the parameters of the log-normal distribution and median μ and sigma σ (half the central 68% of the data about the median) calculated directly from the data. Adapted from Kurz et al. [71]

$$\mu_{\text{rel}} = \frac{N_{\text{CoPS,median}} - N_{\text{Origami}}}{N_{\text{Origami}}} \tag{19}$$

$$\sigma_{\text{rel}} = \frac{N_{\text{CoPS},Q(0.84)} - N_{\text{CoPS},Q(0.16)}}{2N_{\text{Origami}}} \tag{20}$$

Variation of the analysis period t_{acq}, i.e., the number of laser cycles to accumulate mDE, showed that the relative median initially increases and saturates at values of 10–20% for $t_{\text{acq}} \geq 3 \times 10^6$ laser cycles. The corresponding relative sigma is about 50% and slightly decreases with increasing t_{acq}. Only the estimates for DNA Origami with 36 nominal labels deviate and are shifted to lower numbers also apparent in Fig. 10c. We interpret this inconsistent behavior as incorrect CoPS number estimation since the DNA Origami technique has been shown to deliver reliable samples [70, 72]. Experiments with a DNA sample with four nominal Atto647N labels covalently attached at one DNA strand confirmed the experiments varying the time to accumulate mDE. They displayed less variance in the label number estimates and a more pronounced decay of relative sigma with increasing analysis period and laser power from ~30% to less than 20%. Altogether, we could show that reliable CoPS number estimates can be made at least in the number range of 1–20 in as little as ~150 ms at laser repetition rates of 20 MHz. Still the method gives number estimates above 20 emitters, however, with a potential bias and loss in precision.

The previous experiments were all carried out with ATTO647N because of its exceptional brightness and photostability in ROXS buffer. Yet, it is of advantage to have a range of different fluorophores to choose from. It is then possible to select the dye for a specific counting application according to, e.g., excitation and emission wavelength, fluorescence lifetime or hydrophobicity. Prerequisites for potential candidates are high extinction coefficients and quantum yields, and they should be photostable, which is more likely for dyes emitting in the red region than for their pendants at the blue end of the visible spectrum. Nevertheless, we envision that also dyes emitting in the green and yellow wavelength regime are as well suitable candidates for CoPS. Some have high extinction coefficients and photostabilities reaching those of fluorophores in the far-red, e.g., Cy3B. CoPS or

any photon antibunching based counting method should be applicable independent of the excitation/emission wavelengths if brightness is sufficient to generate mDE and fluorescence photostability is high.

To this end, more fluorophores in the red emission range were examined to see if the applicability of CoPS can be extended [73, 74]. Namely, Atto633, Cy5, AlexaFluor647 (further referred to as Alexa647), and AbberiorStar635 were included in our study to compare them with Atto647N. For ease of use we reverted to the DNA hybridization probe that was employed for our initial experiments. Both the distribution of CoPS label number estimates, the estimated CoPS detection probability and the photostability of the dyes were investigated at two different excitation powers, 5 and 10 μW, at 635 nm laser excitation with 20 MHz repetition rate. All dyes are bright enough for CoPS estimation with $p_{\text{median}} \geq 1.8 \times 10^{-3}$, surpassing the detection probabilities of the initial experiments. Detection probabilities among the different dyes scaled according to the brightness as calculated from fluorescence parameters and increased accordingly upon doubling the excitation power. The photostabilities of the dyes in ROXS buffer as determined by bleaching step analysis rise in the order of Alexa647 < Cy5 < Atto633 < AbberiorStar ≤ Atto647N (for details see [74]). Photostability may be limiting only in the case of Alexa647 at higher excitation power. The estimated photostability time constant from monoexponential fitting is at least one order of magnitude higher than the analysis period of 125 ms for all other measurements. This is also reflected in the stable median of the label number distribution irrespective of the laser excitation power. Representative fluorescence transients in Fig. 11 demonstrate that CoPS can dynamically follow the number of independent active emitters for all tested dyes.

In our latest study, we addressed the label number distributions of different fluorescent markers. To date, a number of different fluorescent labeling systems exist to visualize the protein of interest [75–80]. For any quantitative determination of protein numbers in a molecular complex, it is essential to precisely know the label stoichiometry. Also, super-resolution methods raise demands for defined label stoichiometries in addition to small marker size and high marker densities [81]. We labeled conventional anti-GFP antibodies and their much smaller single domain counterparts – nanobodies [82, 83] – by random covalent coupling of NHS-ester activated dyes to free amino groups in the protein. Immunofluorescence is still the most widely used technique to visualize endogenous proteins in cells. We also investigated NHS-ester dye conjugated streptavidin, which is frequently used as a marker for biotin-tagged compounds. Lastly, we added SNAP-tag that can be genetically fused to the protein of interest and provides an elegant way for introducing up to one organic dye via modified SNAP-tag substrates.

All markers were labeled, purified from free remaining dye, and immobilized on a BSA coated glass surface doped with their binding target. SNAP-tag fused to six histidine amino acids was attached to the surface via an anti-His_6 antibody (see schemes in Fig. 12a–d). As dyes we chose Atto647N for its exceptional spectroscopic properties (light gray bars) and Alexa647 (dark gray bars) because of its widespread use in biology. As expected, SNAP-tag conjugates have mostly one label. We attribute differing number estimates to CoPS estimation uncertainty or to

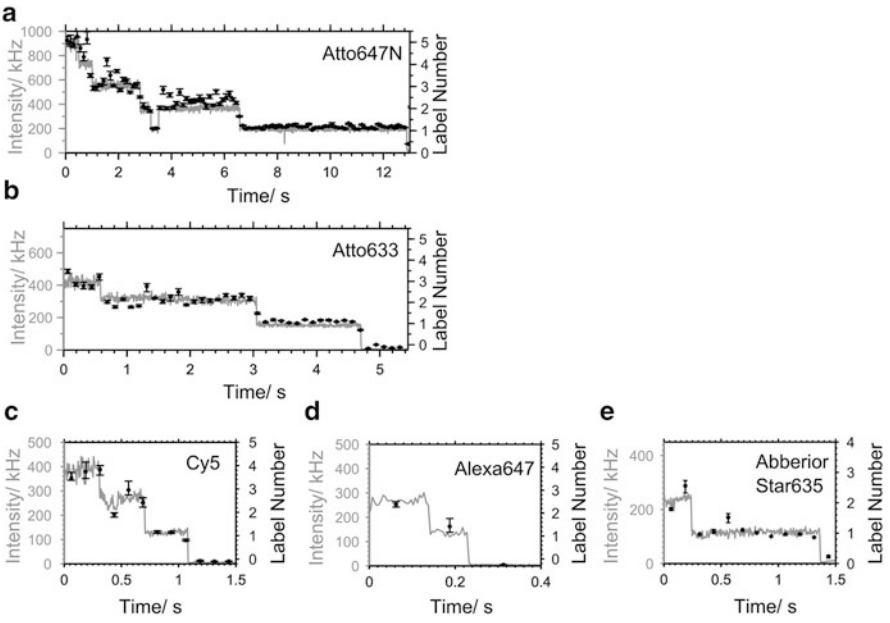

Fig. 11 Dynamic CoPS analysis for dyes in the red wavelength region. Estimated label numbers with a time resolution of 125 ms ($= 2.5 \times 10^6$ laser cycles) coincide with intensity bleaching steps in fluorescent transients of DNA hybridization probes. Label number with error bars derived from bootstrapping in *black*; intensity at 10 mW excitation with a 20 MHz pulsed $\lambda = 635$ nm laser in *gray*, FOV scan: 5 mW. (**a**) Atto637N, (**b**) Atto633, (**c**) Cy5, (**d**) Alexa647, (**e**) AbberiorStar635. Adapted from Grußmayer et al. [74]

the unlikely binding of two SNAP proteins to one anti-His_6 antibody. The label number distribution of the antibodies and streptavidin display a broader shape and can be shifted to higher numbers with increasing amount of dye in the labeling reaction (3:1 versus 10:1 dye to protein ratio for antibodies, data for 3:1 Atto647N labeled antibody not shown). Number estimates of labeled nanobodies peak at one and resemble the distributions observed for SNAP-tag. This was surprising since we used up to 40:1 dye excess during labeling reactions. Possible reasons for this finding are the low availability of the four lysines and the amino function at the N-terminus of the small protein for reaction with NHS-ester activated dyes. Alternatively, binding to the eGFP-target may be impaired for nanobodies bearing more labels.

It should be noted that we observed diverse photophysics for all labeled proteins although the same stabilizing buffer conditions were used as in experiments with DNA probes (for details see [74]). The effects of slightly reduced photostability and fast blinking did not significantly influence the number estimates. Our experiments provide the number distribution of active, independent emitters for different fluorescent markers bound to their target. We cannot exclude energy transfer and subsequent singlet–singlet annihilation between dyes if they are close together.

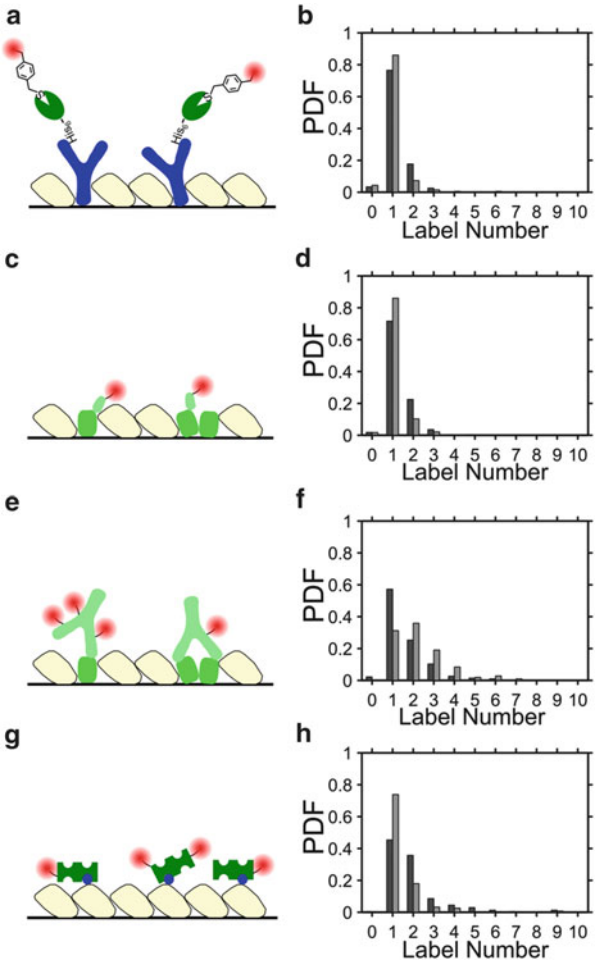

Fig. 12 Label number distributions of fluorescent markers. Labeling scheme with corresponding probability distribution function of CoPS label number estimates (*light gray*: Atto647N label, *dark gray*: Alexa647 label). Measurements with 5 µW laser excitation with a 640 nm laser at 20 MHz repetition rate, CoPS analysis period $t_{acq} = 125$ ms ($= 2.5 \times 10^6$ laser cycles). (**a**, **b**) BG-dye (*red*)-labeled SNAP-tag (*dark green*) immobilized by anti-His_6 antibodies (*blue*) on a BSA passivated glass surface, (**c**, **d**) labeled anti-GFP nanobody (*green–red*) immobilized by eGFP (*green*), (**e**, **f**) labeled anti-GFP antibody (*green–red*, dye to protein ratio 10:1 (Atto647N) and 3:1 (Alexa647)) immobilized by eGFP (*green*), (**g**, **h**) labeled streptavidin (*dark green–red*, dye to protein ratio 6:1) immobilized by BSA-biotin (*light yellow–blue*). Adapted from Grußmayer et al. [74]

CoPS, like any other fluorescence-based method, only evaluates the fraction of markers that are labeled. Incomplete labeling and occasional photobleaching cannot be completely prevented. For quantitative measurements of protein complexes, both the label number distribution of the marker and the marker-target binding efficiencies need to be taken into account.

The experiments clearly show that photon antibunching is suited for developing novel quantitative methods as required in biology and the material sciences. Beyond this, a single CoPS-measurement takes only 125 ms which puts time-resolved studies of photophysical dynamics into perspective.

6 Conclusion

Taken together the experiments described above show a variety of applications of the photon antibunching principle in material as well as in life sciences. Photon antibunching is by far not limited to a proof of single emitters, but the rich information of photon statistics captured by extended HBT-type interferometers opens a new perspective on quantitative fluorescence microscopy. Furthermore, it was recently shown on semi-conductor quantum dots that antibunching can, in principle, also be used to improve resolution in optical microscopy because the spatial distribution of the point-spread functions is also reflected in the spatial distribution of photon emission statistics [84, 85]. Developments in this area are still ongoing, promising potential for novel applications. Especially the new photon number resolving detectors [86] will provide new opportunities in the field of single molecule detection and its applications not only in material and life sciences but also in the field of quantum optics.

References

1. Paul H (2004) Introduction to quantum optics: from light quanta to quantum teleportation. Cambridge University Press, Cambridge
2. Fox M (2006) Quantum optics: an introduction. Oxford University Press, Oxford
3. Hanbury Brown R, Twiss RQ (1956) Correlation between photons in two coherent beams of light. Nature 177:27–29
4. Hanbury Brown R, Twiss RQ (1956) The question of correlation between photons in coherent light rays. Nature 178:1447–1448
5. Hanbury Brown R, Twiss RQ (1956) A test of a new type of stellar interferometer on Sirius. Nature 178:1046–1048
6. Kimble HJ, Dagenais M, Mandel L (1977) Photon antibunching in resonance fluorescence. Phys Rev Lett 39:691–695
7. Kimble H, Mandel L (1976) Theory of resonance fluorescence. Phys Rev A 13:2123–2144
8. Carmichael HJ, Walls DF (1976) A quantum-mechanical master equation treatment of the dynamical Stark effect. J Phys B At Mol Phys 9:1199
9. Singh S (1983) Antibunching, sub-poissonian photon statistics and finite bandwidth effects in resonance fluorescence. Opt Commun 44:254–258
10. Basché T, Moerner WE, Orrit M, Talon H (1992) Photon antibunching in the fluorescence of a single dye molecule trapped in a solid. Phys Rev Lett 69:1516–1519
11. Hollars CW, Lane SM, Huser T (2003) Controlled non-classical photon emission from single conjugated polymer molecules. Chem Phys Lett 370:393–398
12. Tinnefeld P (2001) Time-varying photon probability distribution of individual molecules at room temperature. Chem Phys Lett 345:252–258. doi:10.1016/S0009-2614(01)00883-1
13. Weston KD, Dyck M, Tinnefeld P et al (2002) Measuring the number of independent emitters in single-molecule fluorescence images and trajectories using coincident photons. Anal Chem 74:5342–5349. doi:10.1021/ac025730z
14. De Schryver FC, Vosch T, Cotlet M et al (2005) Energy dissipation in multichromophoric single dendrimers. Acc Chem Res 38:514–522
15. Fore S, Laurence TA, Hollars C, Huser T (2007) Counting constituents in molecular complexes by fluorescence photon antibunching. IEEE J Sel Top Quantum Electron 13:996–1005

16. Brunel C, Tamarat P, Lounis B, Orrit M (2001) Triggered Emission of Single Photons by a Single Molecule. Single molecule spectroscopy. Springer, Heidelberg, pp 99–113
17. Thiessen A, Vogelsang J, Adachi T et al (2013) Unraveling the chromophoric disorder of poly (3-hexylthiophene). Proc Natl Acad Sci U S A 110(38):E3550–E3556
18. Kumar P, Lee T-H, Mehta A et al (2004) Photon antibunching from oriented semiconducting polymer nanostructures. J Am Chem Soc 126:3376–3377
19. Sánchez-Mosteiro G, Koopman M, van Dijk EMHP et al (2004) Photon antibunching proves emission from a single subunit in the autofluorescent protein DsRed. Chemphyschem 5:1782–1785
20. Wu M, Goodwin PM, Patrick Ambrose W, Keller RA (1996) Photochemistry and fluorescence emission dynamics of single molecules in solution: B-phycoerythrin. J Phys Chem 100:17406–17409
21. Sýkora J, Kaiser K, Gregor I et al (2007) Exploring fluorescence antibunching in solution to determine the stoichiometry of molecular complexes. Anal Chem 79:4040–4049
22. Ly S, Petrlova J, Huser T et al (2011) Stoichiometry of reconstituted high-density lipoproteins in the hydrated state determined by photon antibunching. Biophys J 101:970–975
23. Bülter A (2014) Single-photon counting detectors for the visible range between 300 and 1,000 nm. Springer Ser Fluoresc. doi:10.1007/4243_2014_63
24. Buller GS, Collins RJ (2014) Single-photon detectors for infrared wavelengths in the range 1–1.7 μm. Springer Ser Fluoresc. doi:10.1007/4243_2014_64
25. Wahl M (2014) Modern TCSPC electronics: principles and acquisition modes. Springer Ser Fluoresc. doi:10.1007/4243_2014_62
26. Kitson SC, Jonsson P, Rarity JG, Tapster PR (1998) Intensity fluctuation spectroscopy of small numbers of dye molecules in a microcavity. Phys Rev A 58:620
27. Patrick Ambrose W, Goodwin PM, Enderlein J et al (1997) Fluorescence photon antibunching from single molecules on a surface. Chem Phys Lett 269:365–370
28. Kask P, Piksarv P, Mets Ü (1985) Fluorescence correlation spectroscopy in the nanosecond time range: photon antibunching in dye fluorescence. Eur Biophys J 12:163–166
29. Mets Ü, Widengren J, Rigler R (1997) Application of the antibunching in dye fluorescence: measuring the excitation rates in solution. Chem Phys 218:191–198
30. Fleury L, Segura J, Zumofen G et al (2000) Nonclassical photon statistics in single-molecule fluorescence at room temperature. Phys Rev Lett 84:1148–1151
31. Treussart F, Clouqueur A, Grossman C, Roch J-F (2001) Photon antibunching in the fluorescence of a single dye molecule embedded in a thin polymer film. Opt Lett 26:1504–1506
32. Vogelsang J, Kasper R, Steinhauer C et al (2008) A reducing and oxidizing system minimizes photobleaching and blinking of fluorescent dyes. Angew Chem Int Ed 47:5465–5469. doi:10.1002/anie.200801518
33. Michler P, Imamoglu A, Mason MD et al (2000) Quantum correlation among photons from a single quantum dot at room temperature. Nature 406:968–970
34. Lounis B, Bechtel HA, Gerion D et al (2000) Photon antibunching in single CdSe/ZnS quantum dot fluorescence. Chem Phys Lett 329:399–404
35. Messin G, Hermier JP, Giacobino E et al (2001) Bunching and antibunching in the fluorescence of semiconductor nanocrystals. Opt Lett 26:1891–1893
36. Brouri R, Beveratos A, Poizat J-P, Grangier P (2000) Photon antibunching in the fluorescence of individual color centers in diamond. Opt Lett 25:1294–1296
37. Kurtsiefer C, Mayer S, Zarda P, Weinfurter H (2000) Stable solid-state source of single photons. Phys Rev Lett 85:290–293
38. Lounis B, Moerner WE (2000) Single photons on demand from a single molecule at room temperature. Nature 407:491–493
39. Michler P, Kiraz A, Becher C et al (2000) A quantum dot single-photon turnstile device. Science 290:2282–2285
40. Babinec TM, Hausmann BJM, Khan M et al (2010) A diamond nanowire single-photon source. Nat Nanotechnol 5:195–199

41. Claudon J, Bleuse J, Malik NS et al (2010) A highly efficient single-photon source based on a quantum dot in a photonic nanowire. Nat Photonics 4:174–177
42. Nothaft M, Höhla S, Jelezko F et al (2012) Electrically driven photon antibunching from a single molecule at room temperature. Nat Commun 3:626–628
43. Mizuochi N, Makino T, Kato H et al (2012) Electrically driven single-photon source at room temperature in diamond. Nat Photonics 6:299–303
44. Tizei LHG, Kociak M (2013) Spatially resolved quantum nano-optics of single photons using an electron microscope. Phys Rev Lett 110(15):153604. arXiv.org cond-mat.m
45. Nielsen M, Chuang I (2004) Quantum computation and quantum information (Cambridge series on information and the natural sciences). Cambridge University Press, Cambridge
46. Rarity JG, Owens PCM, Tapster PR (1994) Quantum random-number generation and key sharing. J Mod Opt 41:2435–2444
47. Feynman RP (1982) Simulating physics with computers. Int J Theor Phys 21:467–488
48. Beveratos A, Brouri R, Gacoin T et al (2002) Single photon quantum cryptography. Phys Rev Lett 89:187901
49. Waks E, Inoue K, Santori C et al (2002) Secure communication: quantum cryptography with a photon turnstile. Nature 420:762
50. Giovannetti V, Lloyd S, Maccone L (2011) Advances in quantum metrology. Nat Photonics 5:222–229
51. Hui YY, Chang Y-R, Lim T-S et al (2009) Quantifying the number of color centers in single fluorescent nanodiamonds by photon correlation spectroscopy and Monte Carlo simulation. Appl Phys Lett 94:13104
52. Ficner R, Lobeck K, Schmidt G, Huber R (1992) Isolation, crystallization, crystal structure analysis and refinement of B-phycoerythrin from the red alga *Porphyridium sordidum* at 2.2 Å resolution. J Mol Biol 228:935–950
53. Lauritsen K, Riecke S, Bülter A, Schönau T (2014) Modern pulsed diode laser sources for time-correlated photon counting. Springer Ser Fluoresc. doi:10.1007/4243_2014_76
54. Wahl M, Rahn H-J, Gregor I et al (2007) Dead-time optimized time-correlated photon counting instrument with synchronized, independent timing channels. Rev Sci Instrum 78:33106
55. Wahl M, Rahn H-J, Röhlicke T et al (2008) Scalable time-correlated photon counting system with multiple independent input channels. Rev Sci Instrum 79:123113
56. Ta H, Kiel A, Wahl M, Herten D-P (2010) Experimental approach to extend the range for counting fluorescent molecules based on photon-antibunching. Phys Chem Chem Phys 12:10295–10300. doi:10.1039/c0cp00363h
57. Koberling F, Kraemer B, Buschmann V et al (2009) Recent advances in photon coincidence measurements for photon antibunching and full correlation analysis. SPIE BiOS Biomed Opt 71850Q–71850Q-8
58. Fore S, Laurence TA, Yeh Y et al (2005) Distribution analysis of the photon correlation spectroscopy of discrete numbers of dye molecules conjugated to DNA. IEEE J Sel Top Quantum Electron 11:873–880
59. Chen Y, Müller JD, So PT, Gratton E (1999) The photon counting histogram in fluorescence fluctuation spectroscopy. Biophys J 77:553–567. doi:10.1016/S0006-3495(99)76912-2
60. Tinnefeld P, Weston KD, Vosch T et al (2002) Antibunching in the emission of a single tetrachromophoric dendritic system. J Am Chem Soc 124:14310–14311
61. Tinnefeld P, Hofkens J, Herten D-P et al (2004) Higher-excited-state photophysical pathways in multichromophoric systems revealed by single-molecule fluorescence spectroscopy. Chemphyschem 5:1786–1790. doi:10.1002/cphc.200400325
62. Hübner C, Zumofen G, Renn A et al (2003) Photon antibunching and collective effects in the fluorescence of single bichromophoric molecules. Phys Rev Lett 91:93903
63. Berglund AJ, Doherty AC, Mabuchi H (2002) Photon statistics and dynamics of fluorescence resonance energy transfer. Phys Rev Lett 89:68101

64. Vosch T, Cotlet M, Hofkens J et al (2003) Probing Förster type energy pathways in a first generation rigid dendrimer bearing two perylene imide chromophores. J Phys Chem A 107:6920–6931
65. Fückel B, Hinze G, Nolde F et al (2010) Quantification of the singlet–singlet annihilation times of individual bichromophoric molecules by photon coincidence measurements. J Phys Chem A 114:7671–7676
66. Hofkens J, Cotlet M, Vosch T et al (2003) Revealing competitive Forster-type resonance energy-transfer pathways in single bichromophoric molecules. Proc Natl Acad Sci U S A 100:13146–13151
67. Ta H, Wolfrum J, Herten D-P (2009) An extended scheme for counting fluorescent molecules by photon-antibunching. Laser Phys 20:119–124
68. Matthews JM, Sunde M (2012) Dimers, oligomers, everywhere. Adv Exp Med Biol 747:1–18
69. Chiti F, Dobson CM (2006) Protein misfolding, functional amyloid, and human disease. Annu Rev Biochem 75:333–366
70. Rothemund PWK (2006) Folding DNA to create nanoscale shapes and patterns. Nature 440:297–302
71. Kurz A, Schmied JJ, Grußmayer KS et al (2013) Counting fluorescent dye molecules on DNA Origami by means of photon statistics. Small 9(23):4061–4068
72. Schmied JJ, Gietl A, Holzmeister P et al (2012) Fluorescence and super-resolution standards based on DNA Origami. Nat Methods 9:1133–1134
73. Kurz A, Schwering M, Herten D-P (2012) Quantification of fluorescent samples by photon-antibunching. Proceedings of SPIE 8228, Single Mol. Spectrosc. Superresolution Imaging V. 82280K. doi:10.1117/12.909099
74. Grußmayer KS, Kurz A, Herten D-P (2014) Single-molecule studies on the label number distribution of fluorescent markers. Chemphyschem 15:734–742
75. Shaner NC, Steinbach PA, Tsien RY (2005) A guide to choosing fluorescent proteins. Nat Methods 2:905–909
76. Giepmans BNG, Adams SR, Ellisman MH, Tsien RY (2006) The fluorescent toolbox for assessing protein location and function. Science 312:217–224. doi:10.1126/science.1124618
77. Wombacher R, Cornish VW (2011) Chemical tags: applications in live cell fluorescence imaging. J Biophotonics 4:391–402
78. Johnsson N, Johnsson K (2007) Chemical tools for biomolecular imaging. ACS Chem Biol 2:31–38
79. Boyce M, Bertozzi CR (2011) Bringing chemistry to life. Nat Methods 8:638–642
80. Szent-Gyorgyi C, Schmidt BA, Creeger Y et al (2007) Fluorogen-activating single-chain antibodies for imaging cell surface proteins. Nat Biotechnol 26:235–240
81. Van de Linde S, Heilemann M, Sauer M (2012) Live-cell super-resolution imaging with synthetic fluorophores. Annu Rev Phys Chem 63:519–540
82. Kirchhofer A, Helma J, Schmidthals K et al (2009) Modulation of protein properties in living cells using nanobodies. Nat Struct Mol Biol 17:133–138
83. Ries J, Kaplan C, Platonova E et al (2012) A simple, versatile method for GFP-based super-resolution microscopy via nanobodies. Nat Methods 9:582–584
84. Schwartz O, Levitt JM, Tenne R et al (2013) Superresolution microscopy with quantum emitters. Nano Lett 13:5832–5836
85. Schwartz O, Oron D (2012) Improved resolution in fluorescence microscopy using quantum correlations. Phys Rev A 85:33812
86. Thomas O, Yuan ZL, Shields AJ (2012) Practical photon number detection with electric field-modulated silicon avalanche photodiodes. Nat Commun 2:1–5

FLIM Strategies for Intracellular Sensing

Fluorescence Lifetime Imaging as a Tool to Quantify Analytes of Interest

Maria J. Ruedas-Rama, Jose M. Alvarez-Pez, Luis Crovetto, Jose M. Paredes, and Angel Orte

Abstract Since the very early years of microscopy development, scientists have pursued the ability to observe live cellular activity in order to probe the processes occurring inside cells in real time. Fluorescence microscopy has become an extraordinary tool for unraveling the myriad cellular processes and interactions that are relevant to understanding cell physiology. The intracellular sensing of certain analytes is of crucial importance to understanding some of these processes, such as the relation between cellular pH and metabolic states or the roles of specific ions in signaling pathways. However, the acquisition of quantitative information from the interiors of cells is not a trivial challenge. Ratiometric, intensity-based fluorescence microscopy approaches are commonly used, but they suffer from many systematic difficulties that make them unsuitable for quantitative sensing. Fluorescence lifetime imaging microscopy (FLIM) detects the time duration of fluorescence emission, taking advantage of the multidimensional nature of photon emission. FLIM-based intracellular sensing approaches, especially in the time domain in single-photon timing (SPT) mode, overcome many of the limitations of fluorescence-intensity methods. Herein, we review strategies for the FLIM-based intracellular sensing of local pH, ion concentration, and biomolecular interactions. In the first section, we demonstrate how in-depth knowledge of the photophysics of dyes can be useful in the development of FLIM sensors. Then, we review the growing field of nanoparticle-based FLIM sensors. Finally, the expanding detection capabilities of FRET and the use of FLIM for the larger-scale analysis of tissues are discussed.

M.J. Ruedas-Rama, J.M. Alvarez-Pez, L. Crovetto, and A. Orte (✉)
Faculty of Pharmacy, Department of Physical Chemistry, University of Granada, Campus Cartuja, 18071 Granada, Spain
e-mail: angelort@ugr.es

J.M. Paredes
Biophysics Institute, CNR, Fondazione Bruno Kessler, Via Sommarive 18, 38123 Povo (TN), Italy

P. Kapusta et al. (eds.), *Advanced Photon Counting: Applications, Methods, Instrumentation*, Springer Ser Fluoresc (2015) 15: 191–224, DOI 10.1007/4243_2014_67,

Keywords Fluorescent proteins · FRET · Lifetime imaging · Noninvasive tissue imaging · Quantum dots · Xanthene dyes

Contents

1 Intracellular FLIM in the Time Domain: Advantages and Overall Strategies 192
2 Intracellular FLIM Phosphate Sensing Based on an Excited-State Proton-Transfer Reaction 197
3 Intracellular FLIM Nanoparticle Sensors 201
4 Sensing via FLIM-FRET 205
5 FLIM Sensing in Tissues 208
6 Conclusions and Outlook 211
References 214

1 Intracellular FLIM in the Time Domain: Advantages and Overall Strategies

The quantification of the intracellular levels of biologically relevant analytes has posed a challenge in many branches of research over the years. Understanding how cells function in important biological processes, such as metabolism, DNA replication, cell differentiation, cellular tropism, protein synthesis, or membrane response, and the determination of structural information are active areas of research. Furthermore, some of these processes may be strongly affected by certain diseases. For instance, in neurodegenerative diseases, such as Alzheimer's and Parkinson's, neuronal toxicity is significantly enhanced by small proteinaceous aggregates at the cellular level [1]. Likewise, cancer tissues display important metabolic alterations that cause distinctive changes in the concentrations of certain metabolites [2]. Hence, the comprehension of diseases at the cellular level and their effects on normal cell functioning is an exciting field that promises to provide novel therapeutic tools for many of the major scientific challenges of our time.

Since the very early years of microscopy development [3], scientists have pursued the ability to observe the processes occurring inside cells. The seminal work by Heimstädt and Lehmann reported the use of UV light to observe autofluorescence from bacteria and tissues with improved resolution compared with conventional optical microscopy [4]. Not long after this milestone, the addition of fluorophores to the studied samples initiated the development of staining techniques for tissues [5, 6], facilitated by the use of optical filters. However, it was in the early 1940s that the development of immunofluorescence [7], i.e., antibodies containing extrinsic fluorophores, greatly enhanced the visualization of specific and targeted portions of the cell and created the field of intracellular sensing. From these early days to the present era of super-resolution microscopy [8–10], fluorescence microscopy has offered an inestimably valuable means of interrogating and investigating the dynamic cell interior.

Intracellular fluorescence sensing can be achieved by detecting changes in any one of the various aspects of the fluorescence emission of photons. For example, the presence of certain analytes may cause a change in the fluorescence intensity, and many fluorophore sensors have been developed on these grounds. However, the use of fluorescence intensity as the analytical signal inside the cell is rather unreliable because it is not possible to control the local probe concentration, which can vary because of diffusion and photobleaching. This means that the signal intensity can only be employed to gather spatial information (localization) and cannot be used for quantification. For quantifying intracellular analytes, the most widely accepted approach is based on ratiometric methods, which make use of the fluorescence-intensity ratio at two (or more) different (excitation or emission) wavelengths. These approaches provide concentration-independent signals. There are many well-established ratiometric intracellular sensing methods, such as Ca^{2+} and pH sensors [11]. However, ratiometric methods also suffer from many complications that can lead to questionable data. A very clear example is 2′,7′-bis-(2-carboxyethyl)-5-(and-6)-carboxyfluorescein (BCECF), an extensively used intracellular pH sensor [12]. The measurement of pH using BCECF requires two different excitation sources because it involves the fluorescence ratio of signals at two different excitation wavelengths [11]. Moreover, the pK_a value of BCECF, which defines its pH response, is highly dependent on the total ionic strength of the medium [13]. As a result, the cellular environment can cause systematic errors in the calibration curves, making it crucial to apply corrections that are usually pH-dependent [14] and preventing reliable pH determination. However, because BCECF is a relatively affordable, commercial solution, it remains in widespread use for intracellular pH determination. In addition, ratiometric methods suffer from an even more important systematic complication, which primarily originates from the presence of cell autofluorescence. This autofluorescence can affect one spectral region more strongly than others, dramatically altering the signal ratio and leading to systematic errors in the measurements (Fig. 1). Therefore, the development of more reliable and robust intracellular sensing methods has been a very active research field in recent years.

A powerful alternative to ratiometric fluorescence methods is the use of fluorescence lifetimes for sensing. The fluorescence emission from molecules that have been excited by a finite light pulse exhibits exponential decay kinetics, with a lifetime typically on the order of a few nanoseconds. The fluorescence lifetime can be experimentally measured in the frequency domain [15] or in the time domain using the single-photon timing (SPT) methodology, to which this book is entirely dedicated. Fluorescence lifetime imaging microscopy (FLIM) can be accomplished by appropriately modifying a fluorescence microscope. FLIM can be performed in the frequency domain, or in the time domain, using a gated-image intensifier or via SPT [16, 17]; the latter method makes use of all photons that reach the detectors. FLIM microscopy in SPT mode involves raster scanning the sample and collecting a single fluorescence decay trace in each pixel of the image. The excitation laser is focused at various positions on the sample in confocal mode, the pulsed laser is directed into the specimen, and the collected fluorescence is detected using point

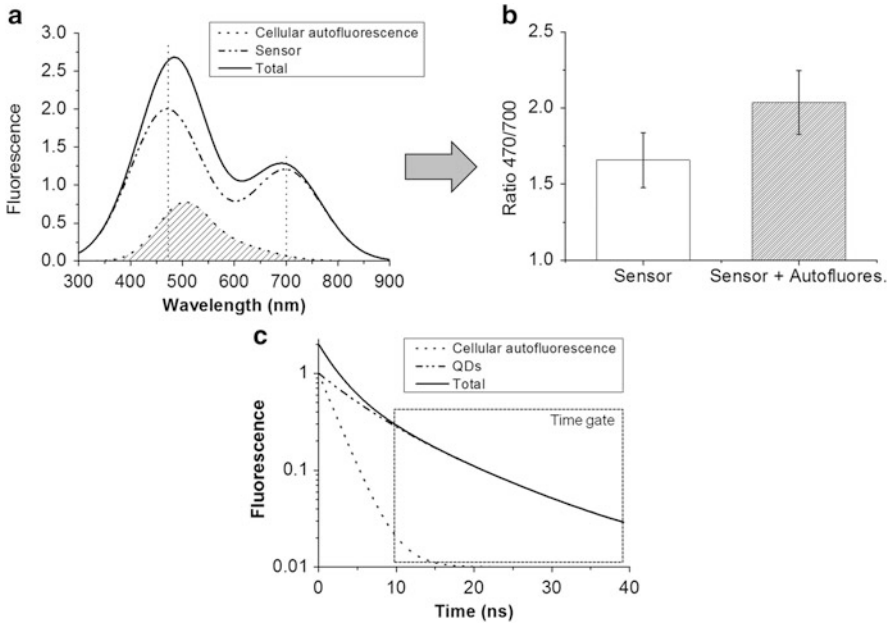

Fig. 1 (**a**) The ratiometric signal of a fluorescence sensor (*dash-dotted line*) can be dramatically altered by the presence of cellular autofluorescence (*shaded*). The sum (*solid line*) of both signals, from the sensor and the cell autofluorescence, corresponds to a different sensing ratio than does the signal from the sensor only (**b**). (**c**) The exponential decay of long-lived quantum dots (QDs) (*dash-dotted line*) differs from that of the cell autofluorescence (*dotted line*). A time gate can be set for the overall decay (*solid line*) to probe only the QD fluorescence

detectors (such as avalanche photodiodes). Specialized hardware is used to correlate the arrival time of each individual photon in SPT mode (including constant fraction discriminators, time-to-amplitude converters, delay lines, analog-to-digital converters, etc.). Multi-wavelength FLIM [18] can be accomplished by using different detection channels, which detect photons according to their spectral distribution through the use of appropriate filters or wavelength-selection gratings. Then, each individual detected photon must be tagged with multiple pieces of information: the photon arrival time at the detector, the *x*–*y* position in the scanned image, and the number of detection channels for multi-wavelength FLIM [18]. This setup requires large and fast histogram memory to sort all the information carried by each photon. Hence, the FLIM technique is inherently multidimensional because an FLIM image comprises both intensity (total number of photons) and lifetime information (Fig. 2). The primary advantage of FLIM is that the fluorophore's lifetime does not depend on the local probe concentration or the power of the excitation source [19]. Another advantage of the FLIM technique is that it allows time gates to be set to discriminate among photons that arrive at different times after the excitation pulse. This capability is particularly advantageous for discriminating photons emitted via cell autofluorescence from those emitted by fluorescent dyes,

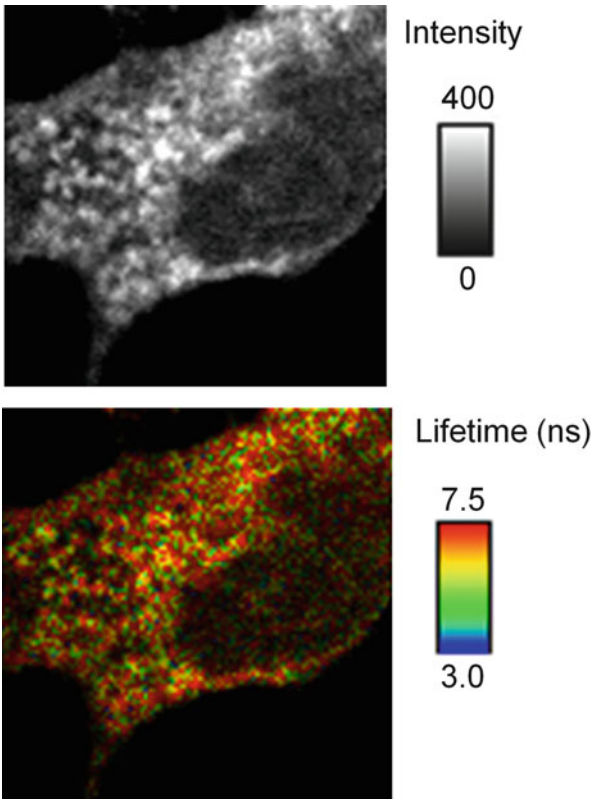

Fig. 2 Example of a multidimensional FLIM image. The image comprises both total intensity information (*upper panel*) and lifetime information (*bottom panel*)

which have a different, longer lifetime (Fig. 1c) [20, 21]. Thus, this discrimination serves as a filtering tool to obtain exclusively the signal from the fluorescence sensor and avoid interference from the cell.

Although the FLIM methodology offers distinct advantages for quantitative biological imaging [22], it is somewhat underused in comparison with ratiometric fluorescence imaging for intracellular sensing. Some studies that have employed FLIM for intracellular sensing have used genetically encoded fluorescent proteins as the sensors. For instance, Tantama and colleagues have designed an intracellular pH sensor termed "pHRed" via the mutagenesis of the red fluorescent protein mKeima [23]. The intracellular pH of live Neuro2A cells expressing pHRed was manipulated to perform an intracellular calibration. The sensor demonstrated a good pH-responsive fluorescence lifetime that changed by approximately 0.4 ns over physiological pH values, and this response proved to be useful for intracellular pH determination using two-photon excitation FLIM. Organic fluorophores can also be directly employed as intracellular FLIM sensors. Intracellular calcium is an important analyte that is involved in many cellular processes. Sagolla and colleagues have employed Oregon Green Bapta-1 for the intracellular determination of Ca^{2+} ions using FLIM [24]. Intracellular pH sensing via time-domain FLIM has

also been achieved using organic fluorophores, such as SNAFL-1 [25] or BCECF [26], although a greater number of studies have focused on frequency-domain FLIM [27, 28]. FLIM also allows the measurement of other properties beyond ion concentration; for instance, Kuimova and colleagues have developed a versatile sensor for the measurement of intracellular microviscosity based on the fluorescence lifetime of a meso-modified BODIPY fluorophore [29]. The fluorescence lifetime of the dye changed as a function of the medium viscosity in methanol/glycerol solutions. The authors then used the fluorescence lifetimes obtained from the intracellular FLIM images of SK-OV-3 cells incubated with the fluorophore to determine the intracellular viscosity by interpolating from a calibration performed in solution. However, although this approach may seem satisfactory, to provide an accurate estimation, the fluorescence lifetime of the dye must remain unaltered by other elements inside the cell that may cause additional quenching relaxation, and the contribution to the overall fluorescence decay of the intracellular autofluorescence should be taken into account. Otherwise, the FLIM readout may exhibit systematic errors, making the calibration plot useless. In fact, the authors found a difference of more than 40% between the intracellular viscosity estimated via FLIM and that estimated via fluorescence anisotropy. This difference may have arisen from the effects mentioned above. This approach has also been employed to measure the microviscosity inside bacteria [30]. A similar concept has been employed by van Manen and colleagues, who developed a method of determining the intracellular refractive index using the lifetime of a green fluorescent protein (GFP) [31]. Other approaches have used FLIM to increase contrast and localize various structures within live cells. For instance, Pyronin Y is a FLIM biosensor that allows the imaging of double-stranded RNA [32], and the dye *o*-BMVC has been employed to image G-quadruplexes in live cells [33]. Other processes can be followed inside living cells by means of FLIM, such as the active transport of important substances. As an example, Bochaway and colleagues have used two-photon excitation for FLIM microscopy to follow the cellular-uptake kinetics of the neurotransmitter serotonin and 5-hydroxytriptophan [34]. The fluorescence lifetime of NADH has been reported as the basis of a noninvasive FLIM method for the detection of cell apoptosis [35]. The levels of O_2 in cells and tissues have also been probed using the quenching of long-lifetime fluorescence and phosphorescence, typically through time-gated FLIM [36–39].

Aside from the few examples just mentioned, in this chapter, we will focus on the use of FLIM for intracellular sensing from various perspectives. In the first section, we will demonstrate how in-depth knowledge of the photophysics of dyes can be useful for the development of FLIM sensors. Then, we will review the growing field of intracellular FLIM nanosensors (nanoparticle-based sensors). Later, the expanding sensing capabilities of FRET and the use of FLIM for the larger-scale study of tissues will be discussed.

2 Intracellular FLIM Phosphate Sensing Based on an Excited-State Proton-Transfer Reaction

The recognition and sensing of phosphate ions is a popular research topic. Phosphate anions play important roles in signal transduction and energy storage in biological systems. Phosphate is also involved in bone mineralization. Inside the osteoblast, phosphate functions as an important constituent of bone minerals and as an important signaling molecule. An increase in intracellular phosphate triggers a series of cellular and molecular changes that prepare the cell and the extracellular matrix to enter a mineralization-competent state [40]. In this section, we describe, as an example, the development of a FLIM methodology for quantifying the total intracellular phosphate concentration. This FLIM methodology is based on a specific excited-state proton-transfer (ESPT) reaction that xanthene derivatives undergo and that is promoted by phosphate ions (at near-physiological pH, the prototropic phosphate species that are present are $H_2PO_4^-$ and HPO_4^{2-}). These ESPT reactions in xanthenic fluorophores provide a unique basis for the real-time sensing of the concentrations of phosphate anions inside living cells through the use of FLIM.

Since the pioneering works of Förster [41] and Weller [42], the study of ESPT reactions has been reviewed multiple times. However, most of these reviews have focused on photoacids (or photobases) to describe dyes that may undergo reversible ESPT processes in aqueous solution [43, 44], and very few have considered the need for a suitable proton donor/acceptor for the reaction to progress. The phosphate-mediated ESPT reaction of fluorescein has been demonstrated in two pioneering papers. It was shown that at near-neutral pH and in the presence of 1 M phosphate buffer, which acts as a suitable proton donor and acceptor, the proton-transfer reaction between two prototropic forms (monoanion and dianion) of fluorescein proceeds very efficiently in the excited state, and their fluorescence decays become coupled. However, at low buffer concentrations (5 mM phosphate buffer or less), the excited monoanion and dianion are not coupled via ESPT and thus decay independently of each other [45, 46]. The study of ESPT reactions between the mono- and dianion of fluorescein is challenging because the pK_a values in the excited and ground states are very similar and because of the strong spectral overlap of the absorption and emission spectra of the two anionic forms. Therefore, the full characterization of the ESPT reaction requires the use of advanced methods of analysis. The method of choice is Global Compartment Analysis (GCA), which allows the determination of the rate constants of the full ESPT kinetic scheme (Fig. 3) and the associated absorption and emission spectral parameters [47] and permits the establishment of a rational design for the experimental conditions to ensure full characterization of the kinetic system [48]. Once the entire set of rate constants is known, the model equations permit the prediction of the two fluorescence decay times as a function of the pH and total buffer concentration and the comparison of these predicted values with the experimental values. Indeed, the two fluorescence decay times that arise from the phosphate-mediated ESPT reaction are

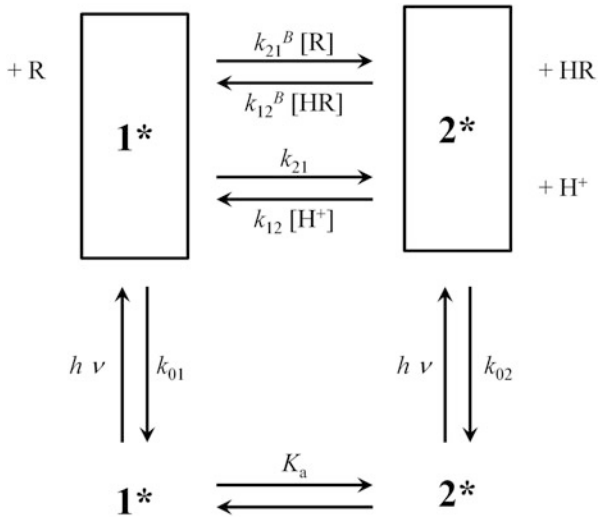

Fig. 3 The kinetic scheme of the buffer-mediated ESPT reaction. Species **1** and **2** are the mono- and dianionic forms, respectively, of fluorescein at near-physiological pH. Photoexcitation creates the excited-state species **1*** and **2***, which can decay via fluorescence (F) and non-radiative (NR) processes. The composite rate constants for these processes are denoted by k_{01} ($=k_{F1}+k_{NR1}$) and k_{02} ($=k_{F2}+k_{NR2}$). k_{12} and k_{21} represent the excited-state deprotonation and protonation rate constants, respectively. At near-neutral pH, $[H^+]$ is so small that the protonation rate k_{12} is usually neglected. The buffer acid and base species are denoted by HR and R, respectively, and may act as suitable proton donors/acceptors for the buffer-mediated excited-state protonation ($k_{12}{}^{B}$) and deprotonation ($k_{21}{}^{B}$)

sensitive to the total phosphate concentration at a given pH [47, 48]. The ESPT reaction described for fluorescein is also characteristic of other fluorescein derivatives, such as BCECF and Oregon Green 488 [13, 49, 50]. Nevertheless, at near-neutral pH, only phosphate buffer is capable of accelerating the ESPT reaction sufficiently to make it competitive with the fluorescence emission. In turn, other buffers, such as Tris or HEPES, do not promote the ESPT reaction at typical experimental concentrations [51, 52]. This feature of phosphate buffer serves as the basis for fluorescence-lifetime-based phosphate quantification.

Nevertheless, the fluorescence decays of fluorescein and its aforementioned derivatives in the presence of the ESPT reaction are bi-exponential. This feature is not desirable for the design of a FLIM sensor because it complicates the analysis and interpretation of the results. A good sensor dye for FLIM should exhibit monoexponential fluorescence decay with a decay time that is dependent on the experimental parameter of interest. In this regard, the works by Urano and colleagues that describe the synthesis of new fluorescein derivatives, called Tokyo Green (TG) dyes, are of considerable importance. In this family of dyes, methyl or methoxy groups are introduced into the benzene moiety (one of them replacing the carboxylic group and the other at position 4 or 5) [53]. Among TG derivatives, 9-[1-(2-methoxy-5-methylphenyl)]-6-hydroxy-3H-xanthen-3-one (2-OMe-5-Me

TG) and 9-[1-(2-methyl-4-methoxyphenyl)]-6-hydroxy-3H-xanthen-3-one (2-Me-4-OMe TG) are the most interesting for the purposes discussed here because their anionic forms are fluorescent states with high quantum yields and lifetimes of approximately 4 ns, whereas the neutral forms are only slightly fluorescent, with low quantum yields and short lifetimes of less than one nanosecond [54, 55]. More interestingly, these two dyes undergo a characteristic ESPT reaction in which the fluorescence from the prototropic forms exhibits a phosphate-sensitive decay time on the order of nanoseconds, whereas the other decay times are on the order of sub-nanoseconds [54, 55]. In fact, the "on/off" character of 2-Me-4-OMe TG has allowed its phosphate-buffer-mediated proton-transfer reaction in the ground state to be studied by means of both fluorescence correlation spectroscopy (FCS) and fluorescence lifetime correlation spectroscopy (FLCS). Interestingly, the rate constants thus obtained were similar to those previously determined for the phosphate-buffer-mediated ESPT reaction of the same dye using bulk fluorescence techniques [51]. These results support the uniformity of the process in the ground and excited states and the need for an adequate buffer species to promote the excited-state reactions [52]. Thus, it was concluded that the ESPT reaction is only promoted when a sufficiently high concentration of a suitable buffer makes the reaction occur sufficiently rapidly to compete with radiative decay; thus, the proton transfer can occur within the lifetime of the excited state. 2-Me-4-OMe TG exhibits a long, phosphate-dependent decay time at both the ensemble and single-molecule levels. These decay times are extraordinarily well predicted by the theoretical equations of the kinetic model and the rate constants estimated using GCA [55]. The correspondence of the simulated curve with the decay times obtained using two different fluorescence methodologies and the sensitivity to the phosphate-buffer concentration establish 2-Me-4-OMe TG as an appropriate dye for probing the concentration of phosphate anions at physiological pH.

In this context, 2-Me-4-OMe TG has been employed to develop a FLIM-based intracellular phosphate sensor using the ESPT reaction as the sensing mechanism [56]. The dye was tested in cells permeabilized with α-toxin, which generates 1.5-nm membrane pores that permit the diffusion of low-molecular-weight compounds, including both 2-Me-4-OMe TG and phosphate anions, without the loss of cytosolic proteins or high-molecular-weight compounds [57]. Two cell lines were used: wild-type Chinese hamster ovary (CHO-k1) cells that lacked a phosphate-transport system and MC3T3-E1 preosteoblast cells, a well-established model for osteoblast differentiation [58]. The decay time of 2-Me-4-OMe TG recovered from the FLIM images was sensitive to the total phosphate concentration in the permeabilized cells (Fig. 4a). Interestingly, the dependence of this decay time could also be predicted using the ESPT rate constants obtained via GCA (solid line in Fig. 4a). The theoretical and experimental values displayed excellent agreement, which allowed the phosphate concentration inside the cell to be calculated with remarkable accuracy. Similar results were obtained for both types of permeabilized cells (CHO-k1 and MC3T3-E1 preosteoblast). This finding indicates that the decay time of 2-Me-4-OMe TG dye is sensitive to the presence of phosphate inside the cell regardless of the cell type.

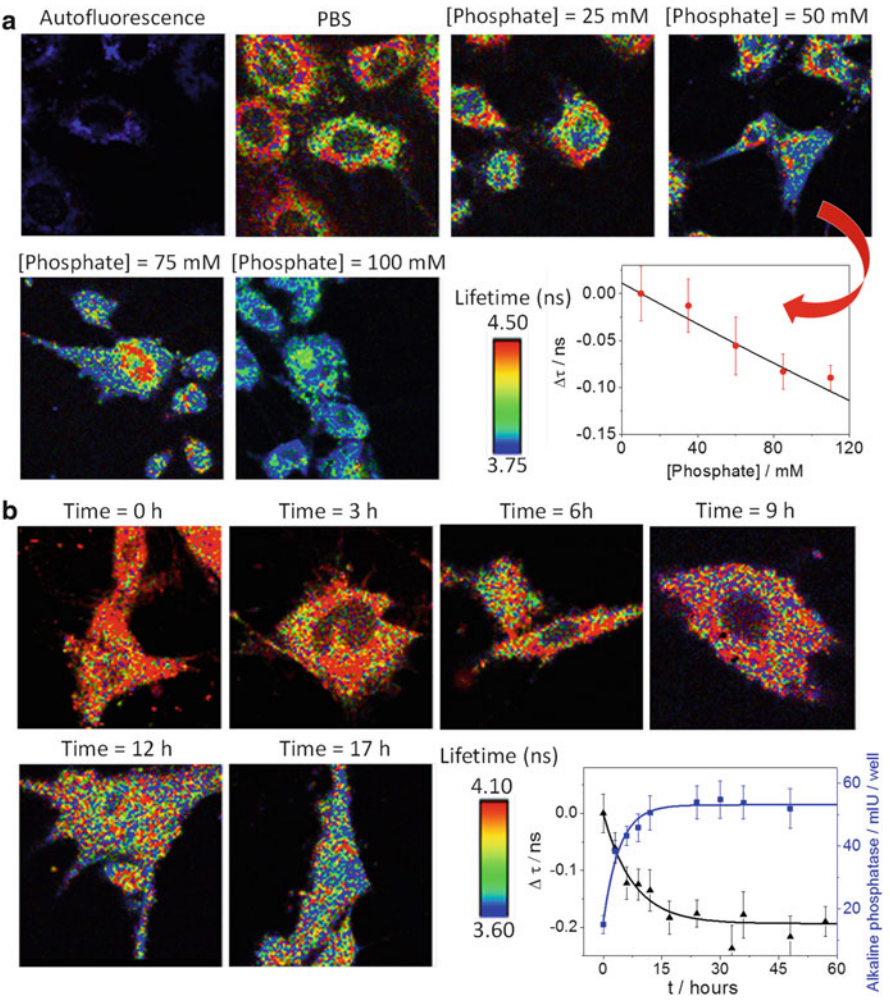

Fig. 4 (**a**) FLIM images of 2-Me-4-OMe TG dye in osteoblast cells treated with α-toxin in PBS medium at various phosphate concentrations. The plot illustrates the decrease in τ determined from the FLIM images. (**b**) FLIM images of 2-Me-4-OMe TG dye in MC3T3-E1 preosteoblast cells in PBS medium at various differentiation times. The plot illustrates the changes in the decay times determined from the images (*black*) and the extracellular levels of alkaline phosphatase (*blue*) during the differentiation of MC3T3-E1 cells. Reprinted and adapted with permission from Paredes et al. [56]. Copyright © 2013 American Chemical Society

Once it had been demonstrated that 2-Me-4-OMe TG could be used to quantify the intracellular concentration of phosphate, this FLIM sensor was employed to detect active phosphate transport in a biologically relevant process. The time evolution of intracellular phosphate intake from the extracellular medium was examined using the MC3T3-E1 cell line, in which the expression of specific phosphate transporters is induced at the onset of the differentiation process

[59]. The FLIM images of 2-Me-4-OMe TG in the MC3T3-E1 cells at several stages of differentiation (Fig. 4b) demonstrated a clear decrease in the decay time of the fluorophore as the cellular differentiation of the preosteoblast line proceeded [56]. These results reflect the active transport of phosphate anions through the cellular membrane of the osteoblasts and the subsequent phosphate accumulation inside the cell. The recovered decay times allowed the apparent first-order kinetic rate constant of the active phosphate intake process to be determined to be $(3.1 \pm 0.7) \times 10^{-5}$ s^{-1}. The increase in the intracellular concentration of phosphate anions was corroborated by the correlated enhancement of the extracellular levels of the membrane-bound enzyme alkaline phosphatase (circles in Fig. 4b), an enzyme that peaks during the differentiation of MC3T3-E1 cells [40, 58]. Moreover, when the same methodology was applied using non-permeabilized CHO-k1 cells, which lack a phosphate-transport system, the FLIM images of 2-Me-4-OMe TG demonstrated that the decay time of the dye was unaffected, as indicated by a constant and negligible intracellular phosphate concentration [56].

Following the development of this ESPT-based FLIM sensor, further studies are underway to increase the sensitivity of the method. In a recent study, 9-alkyl xanthenones with different aliphatic pendant groups have been prepared [60]. Remarkably, they retained fluorescent properties similar to those of fluorescein, including the characteristic phosphate-mediated ESPT reaction. This work demonstrated that the presence of an aryl group at the xanthenic C-9 is not required for high fluorescence quantum yields, broadening the possibilities for the development of novel fluorescent sensors with FLIM capabilities. As an example, 6-hydroxy-9-isopropyl-3H-xanthen-3-one has been investigated in living cells and found to exhibit good permeability and efficient accumulation inside the cytosol [60].

3 Intracellular FLIM Nanoparticle Sensors

Over the past decade, a major focus of research has been the development of nanosensors based on fluorescent nanoparticles (NPs). Usually, fluorescent NPs exhibit unique chemical and optical properties, such as brighter fluorescence, higher photostability, and higher biocompatibility compared to classical, organic fluorescent dyes. Moreover, their high surface-to-volume ratio provides a versatile synthetic platform for the implementation of various sensing schemes. Nevertheless, the use of FLIM with fluorescent NPs has not yet been thoroughly exploited. There exist only a few reports of the use of carbon NPs with FLIM techniques; these studies have mainly used FLIM to generate contrast for the detection of particles in intracellular media [61, 62] rather than for actual sensing purposes. In another study, FLIM has been employed for the detection of the intracellular interaction between gold NPs and the dye DAPI. These interactions were detected via the decrease in the fluorescence lifetime of DAPI caused by energy transfer [63]. Recently, FLIM has also been combined with polymer NPs acting as a

fluorescent polymeric thermometer. By examining the temperature-sensitive fluorescence lifetime of these polymeric NPs, the intracellular temperature was mapped. This approach also allowed the relations between the temperature and certain organelle functions to be studied [64].

Among all fluorescent NPs, semiconductor quantum dots (QDs) may exhibit the most unique photoluminescence-lifetime properties compared to organic fluorophores. In general, organic dyes exhibit monoexponential decay kinetics, which makes their identification based on fluorescence lifetimes rather straightforward. However, their fluorescence lifetimes are typically between 1 and 5 ns, which is too short for their effective temporal discrimination from short-lived fluorescence interference and scattered excitation light [65]. Although QDs exhibit multiexponential fluorescence decay [66], the average lifetime of QDs is significantly longer than the autofluorescence-decay time scale of cells (1–2 ns) and the fluorescence lifetimes of most conventional dyes but is sufficient to maintain a high-rate photon stream [65]. Therefore, these features mean that QDs are ideal intracellular probes for use in FLIM and have considerable potential for spectrally multiplexed, time-gated cellular detection with enhanced selectivity and sensitivity. In 2001, Dahan et al. reported the first use of FLIM with QD nanoparticles for the imaging of fixed cells [67]. They demonstrated that QDs could enhance the contrast and sensitivity of fluorescence biological imaging through the significant and selective reduction of the contribution of autofluorescence to the overall image. In another study, FLIM was employed with QDs for the detection of DNA hybridization events in DNA microarray spots [68]. Later, some examples of the use of FLIM to detect energy transfer from QDs to energy acceptors were reported, such as the use of hybrid NPs of valerite coated with QDs with TdTomato proteins bonded on the surface [69] or Tat-conjugated PEGylated QDs and a phthalocyanine photosensitizer [70]. However, for all these systems, the detection of the target molecules was reported, but not their quantification.

The primary advantages of the combination of FLIM with QDs emerge when these NPs are employed for intracellular sensing purposes. For instance, mercaptopropionic-acid-capped QD nanoparticles (QD-MPAs) exhibit long decay times that are easily distinguishable from intrinsic cell autofluorescence. This feature could improve the sensitivity and selectivity of sensing applications. Thus, QD-MPAs can serve as a suitable lifetime-based pH sensor in time-resolved fluorimetry [71] because their average photoluminescence lifetime is enhanced as the pH of the environment increases because of changes in the protonation degree of the carboxylic acid on the QD surfaces [72]. This pH sensitivity was first measured using QD-MPAs in buffered solutions and solutions that mimicked the intracellular environment at various pH values [71, 73]. Moreover, the quantification of the pH value was also achieved by analyzing FLIM images of QD-MPAs suspended in buffered solutions and deposited on the surface of a glass microscope slide [20]. Analysis of the FLIM images indicated that the QD-MPAs exhibited multiexponential decay kinetics, and the calibration plot obtained from these buffered suspensions was in good agreement with the one obtained previously in bulk aqueous solutions [71]. As a preliminary step before using the nanosensors for

FLIM inside cells, an appropriate calibration must be performed using solutions that mimic the cellular cytoplasm, including by the presence of salts, proteins, and other crowding agents, as the intracellular environment may alter the response of the nanosensors [20]. For instance, the FLIM calibration of the QD-MPA pH nanosensors resulted in the frequency histograms presented in Fig. 5a. The arithmetic mean of the average lifetimes in the pixels of interest provided the calibration plot, with a linear response range from pH 6 to 7.5 (Fig. 5a). The average lifetime of the nanosensors increased from 8.7 ± 0.3 ns (at pH < 5) to 15.4 ± 0.2 ns (at pH > 9), representing a much higher sensitivity than other types of fluorescent dyes used in FLIM [74, 29], including other fluorescent pH probes [23, 26], for which the changes in lifetime are sometimes as small as one-hundredth of a nanosecond. These QD-MPA nanosensors were employed to detect changes in the intracellular pH of various types of cells [20]. MC3T3-E1 and CHO-k1 cells were incubated with QD-MPA solutions, and the cells internalized the nanoparticles via cellular endocytosis. In the absence of QDs, the cells displayed minimal emission and an even distribution of autofluorescence lifetimes across the entire cell, with lifetimes ranging from 1.5 to 2.4 ns. The FLIM images of the cells after the uptake of the QD-MPAs exhibited a strong contrast between the QD lifetimes and those attributable to autofluorescence. The facile discrimination between the signal from the sensor and the intrinsic fluorescence of the cells is one of the greatest advantages of the combination of QDs with FLIM because it enhances the signal-to-background ratio. The usefulness of QD-MPA nanoparticles for intracellular pH sensing was evaluated by changing the pH of the cell medium from 4.7 to 8.2 by exposing the cells to the ionophore nigericin, which equilibrates the concentrations of H^+ and K^+ along the cellular membrane and causes the intracellular pH to become approximately equal to the extracellular value. Figure 5b illustrates the changes in the fluorescence lifetimes of the QD-MPAs in the cytoplasm of CHO-k1 cells treated with nigericin in buffered extracellular media at various pH values. The fluorescence decays of the QD-MPAs in the cellular cytoplasm still displayed multiexponential kinetics, and the PL lifetime distributions obtained from the pixels in which QD emission was detected demonstrated an excellent pH response (Fig. 5b). Therefore, this system permits the quantification of intracellular pH and should allow the monitoring of changes in pH within the cellular cytoplasm during important cellular processes.

Interestingly, it might be possible to extend this FLIM methodology, in which sensitive QD-based nanosensors are used intracellularly, to the determination of a wide range of molecules with high biological impact inside cells by applying appropriate modifications and tailoring the design of the nanosensor.

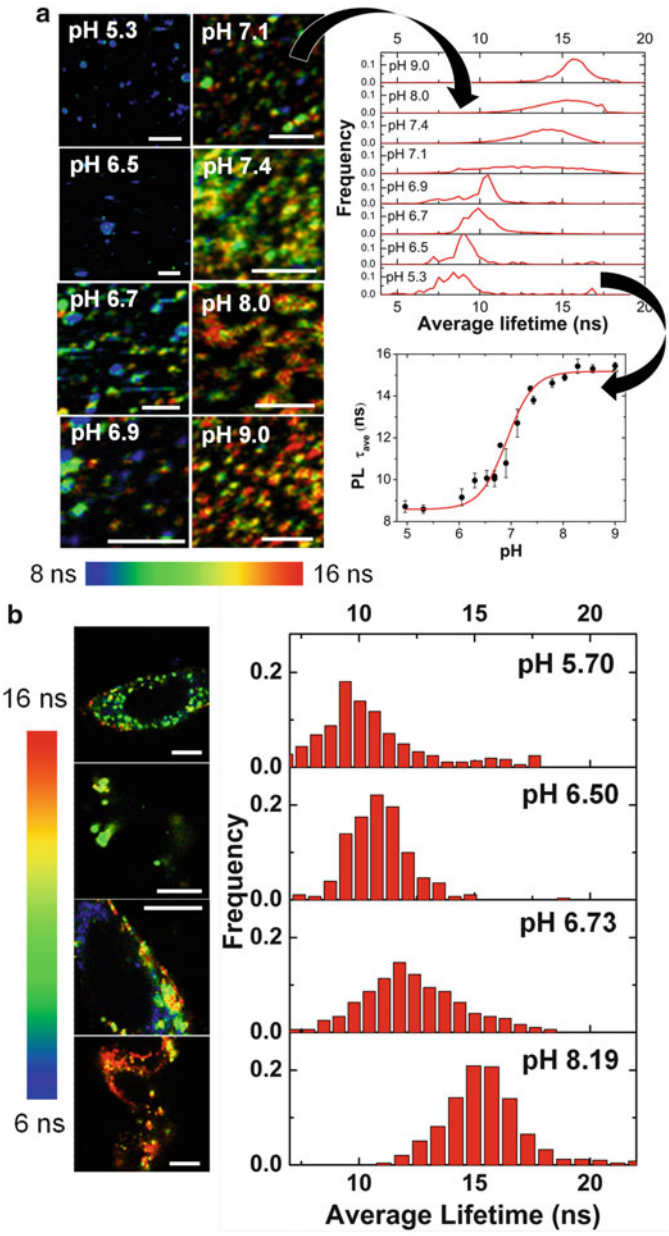

Fig. 5 (**a**) FLIM images, examples of photoluminescence-lifetime histograms, and pH response plot obtained from FLIM images of QD-MPAs suspended in solutions mimicking the intracellular environment at various pH values. (**b**) FLIM images and recovered lifetime histograms of QD-MPAs in the cytoplasm of CHO-k1 cells after incubation with nigericin in buffers at various pH values. The scale bars (*white lines*) represent 10 μm. Reprinted and adapted with permission from Orte et al. [20]. Copyright © 2013 American Chemical Society

4 Sensing via FLIM-FRET

One of the most commonly employed methods of probing bimolecular interactions at the cellular level is Fluorescence Resonance Energy Transfer (FRET). In this phenomenon, the excitation energy of a donor fluorophore is transferred non-radiatively to an acceptor molecule through Coulombic dipole-dipole coupling. As a consequence, the donor fluorophore undergoes a decrease in fluorescence-emission intensity, quantum yield, and fluorescence lifetime, and provided the acceptor is a fluorophore, the excited acceptor may subsequently relax by emitting fluorescence. The efficiency of this energy transfer is highly, although not solely, dependent on the separation distance between the donor and acceptor dyes. This phenomenon, first described by Theodore Förster and later demonstrated experimentally by Wilchek [75] and Stryer and Haugland [76, 77], has been largely employed to study distance-dependent biomolecular interactions, conformational dynamics, and structural information. The use of FRET has also undergone an interesting renaissance with the development of single-molecule fluorescence methodologies, which permit the FRET process to be visualized in individual molecules [78–81].

As mentioned above, the fluorescence lifetime of the donor dye decreases when effective FRET occurs. Indeed, the donor lifetime in the absence of the acceptor (τ_D) is given by Eq. (1).

$$\tau_D = 1/(k_F + k_{NR}), \tag{1}$$

where k_F is the rate constant of fluorescence emission and k_{NR} is the sum of all rate constants of the non-radiative deactivation processes. However, when there is effective FRET in the presence of an energy acceptor, the donor fluorescence lifetime (τ_{DA}) is given by Eq. (2).

$$\tau_{DA} = 1/(k_F + k_{NR} + k_{FRET}), \tag{2}$$

where k_{FRET} is the rate constant of the FRET process. Therefore, the fluorescence lifetime is reduced depending on the relative value of k_{FRET}. In fact, the efficiency of the energy transfer (E) can be obtained using Eq. (3).

$$E = 1 - \tau_{DA}/\tau_D. \tag{3}$$

Therefore, the reduced fluorescence lifetime of the donor dye can provide a basis for the development of FLIM strategies. In this section, we review intracellular sensing strategies based on FRET.

Perhaps the most exploited capability of FRET in intracellular FLIM lies in the detection of biomolecular interactions, such as protein–protein or protein–nucleic-acid interactions. Experiments of this type have yielded major breakthroughs in the understanding of many cellular processes, both structurally and physiologically.

The literature is broad, with many excellent studies employing FLIM-FRET to understand molecular interactions at the cellular level. Excellent reviews [16, 22, 82–84] and descriptions of experimental protocols [85, 86] have also previously summarized some of the most important works in the field. However, strictly speaking, these studies are not related to the topic of sensing itself, so we will mention only a few interesting examples as a preview of the capabilities of FLIM-FRET in the time-domain. Some of these research programs have studied the homo- or hetero-oligomerization of important receptors, transcription factors, or kinases that regulate cell signaling pathways [85–91]; the structural interactions of membrane proteins [92–94], membrane lipids [95], and actin-like proteins in bacteria [96]; viral infectivity factors [97, 98]; and protein aggregation [99, 100]. As an example, in an interesting study, Jose and colleagues investigated the structural arrangement of the active zones of presynaptic plasma membranes to better understand the membrane trafficking of neurotransmitter release [93]. In another work related to neurodegenerative diseases, Berezovska and colleagues described the intracellular interaction between the amyloid precursor protein (APP) and preselin, a protein involved in the functioning of γ-secretase, through which the β-amyloid peptide is cleaved from APP [99]. Importantly, mutations of the preselin gene are related to early onset autosomal dominant Alzheimer's disease. FLIM images revealed the close proximity of APP and preselin, especially in regions near the cell membrane, and demonstrated that this interaction is not prevented by mutations of preselin or by the presence of γ-secretase inhibitors. The effect of prion aggregation on the membranes of neuroblastoma cells was also studied by Tavares and colleagues [101] using FLIM-FRET to investigate prion domains fused to fluorescent donor and acceptor proteins. The authors found supporting evidence for the initial aggregation of prions in the cell membrane, which could trigger the infectivity of prion diseases.

With regard to intracellular sensing, fused donor–acceptor fluorescent proteins (FPs) represent a well-known family of FLIM-FRET sensors. Genetically encoded proteins that include two FP domains, one acting as the energy donor and the other as the acceptor, represent a clear example of systems in which intramolecular FRET is easily discernible. The sensed analyte should cause a change in the FRET process, such as a change in the donor–acceptor distance or a change in the fluorescence emission of one of the domains. For example, Esposito and colleagues have designed a family of fluorescent proteins that exhibit FRET for the determination of intracellular pH using FLIM [102]. As another example, Clomeleon is a chloride-ion sensor that is composed of a cyan fluorescent protein (CFP) domain and a yellow fluorescent protein (YFP) subunit. The differential effect of Cl^- ions on the two FP chromophores modulates the FRET efficiency. Jose and colleagues have employed this sensor in FLIM microscopy to study various stages of neuronal development [103]. Another typical example of genetically encoded sensors is Cameleon Ca^{2+} sensors, which are composed of a fused FRET pair of fluorescent proteins and a Ca^{2+} binding domain. Ca^{2+} binding induces a conformational change and causes changes in the efficiency of FRET from the donor to the acceptor [11, 104]. Laine and colleagues have recently tested the performance of some of

these Ca^{2+} sensors in FLIM-FRET, analyzing issues related to the donor fluorophore [105]. Novel FRET-based genetically encoded chloride [106, 107] and calcium probes [108] are being designed every year. For instance, the SuperClomeleon probe is an improved Cl^- FRET-based sensor that was designed using cell-free, automated protein-engineering techniques [107]. The introduction of controlled mutations led to improvements in the fluorescence properties and halide affinity of the sensor. However, all these novel FRET biosensors have been tested primarily in ratiometric fluorescence-intensity microscopy; it will therefore be interesting to test their performance in FLIM-FRET applications.

A common strategy for the design of FRET-based biosensors, such as those discussed above, employs a linker that undergoes a conformational change upon binding of the target analyte. Using this approach, Caron and colleagues have developed a FRET biosensor for time-domain FLIM-FRET to probe the subcellular localization and conformational changes of transglutaminase type 2, an enzyme that becomes hyperactive in Huntington's disease [109], inside live cells [110]. Similarly, Harvey and colleagues have developed a genetically encoded, FLIM-FRET-based sensor for ERK activity (the extracellular signal-regulated kinase activity reporter, EKAR) [111]. ERK activation in HEK293 cells upon epidermal-growth-factor stimulation was found to cause changes in the fluorescence lifetime of the sensor. This technique has also been used in dendrites and in the nuclei of hippocampal pyramidal neurons in brain slices after theta-burst stimuli or trains of back-propagating action potentials. Nevertheless, a drawback of this sensor is its very low sensitivity; the maximum change in the fluorescence lifetime is approximately 0.06 ns. Other biosensors make use of two different chains, one fused to the donor FP and the other to the acceptor FP. Based on this concept, Oliveira and Yasuda have recently improved the biosensors that are available for the detection of Ras GTPase [112, 113]. In the design of FRET-based biosensors, the use of a nonfluorescent acceptor may constitute an advantage for FLIM-FRET because contributions from the acceptor emission caused by direct excitation are eliminated. This possibility has been explored by Ganesan and colleagues, who have reported the detection of intracellular ubiquitination using a GFP-labeled ubiquitination substrate and ubiquitin fused to a nonfluorescent variant of YFP [114]. Murakoshi and colleagues have also improved and applied non-radiative YFP variants to probe filamentous actin monomers in spines and dendrites using FLIM-FRET [115].

The use of fused donor–acceptor fluorescent-protein constructs is one of the most common strategies for testing and proving the performance of novel FLIM instruments and technical advances. CFP–YFP fusion constructs have been frequently employed to improve FLIM systems in SPT mode, without the necessity of time gating [116–118], for multi-wavelength FLIM systems [18, 116, 119] and two-photon FLIM-FRET instruments [120]. The decrease in donor lifetime caused by energy transfer provides a simple means of validating the capabilities of a FLIM instrument.

Although the localization and probing of biomolecular interactions via FLIM-FRET is quite well established, few examples of actual quantitative intracellular sensors exist. Improved analysis methods may assist in harnessing FLIM-FRET

capabilities for quantitative sensing. For instance, global analysis approaches [121, 122] increase the statistical significance of single-pixel decay fittings, although some methodological precautions must be taken into account [123]. The development of faster, less computation-intensive algorithms for analysis is also improving the applications of global analysis [124]. One example is the use of the acceptor's rise time as complementary information in global analysis to permit more accurate determination of the FRET efficiency [125]. With these developments and others that will be discussed in the final section of this chapter, FLIM-FRET approaches to quantitative intracellular sensing should undergo fascinating development in the near future.

5 FLIM Sensing in Tissues

The FLIM technique has also been used to characterize the physical and chemical changes that occur in tissues. Light-based diagnostic systems are of interest because they are minimally invasive and can be easily applied to any part of the human body that can be reached by light, directly or by means of an endoscope [126]. The nondestructive and noninvasive character of this technique permits continuous, long-term probing of specimens [127]. The underlying physical basis for this fluorescence approach is the influence of both the chemical composition and cellular structure of tissues on fluorescence decay times, and it offers the additional advantages of high specificity and minimal sensitivity to fluorescence-intensity artifacts [128]. It may be implemented in scanning confocal or multiphoton microscopes as well as in wide-field microscopes and endoscopes. In general, studies of basic physiological processes and cancer diagnoses have been the focus of major efforts using the FLIM methodology, including the search for cancer biomarkers, the evaluation of the histological architecture of cancer tissue, and the differentiation of tumor tissue from normal tissue.

Most FLIM studies in tissues have been performed by measuring the autofluorescence signal of the intrinsic fluorophores present in biological tissues, such as tryptophan, tyrosine, phenylalanine, collagen, elastine, and NAD(P)H, because these substances reflect the redox status of tissues [129, 130]. Thus, FLIM images of tissue autofluorescence reveal the intrinsic contrast among different types and states of cells within the tissue, thereby providing noninvasive functional/diagnostic imaging modalities. Indeed, alterations in cell metabolism result in abnormal concentrations of NAD(P)H, and therefore, images of NAD(P)H autofluorescence can be used to differentiate cancerous from noncancerous tissues. As an example, time-resolved fluorescence studies of human lung cancer cells and bronchiolar epithelial cells have consistently demonstrated that the average lifetime of NADH is lower in metastatic cells than in non-metastatic cells. Nevertheless, the resolution of free and bound NAD(P)H represents a challenge for the FLIM methodology because the decay times are on the sub-nanosecond timescale [131, 132]. Autofluorescence at excitation wavelengths above 400 nm can produce

FLIM contrast from unstained bulk tissues [133]. Papour et al. have reported an autofluorescence lifetime wide-field imaging system that generated high contrast between the structures of normal and malignant brain-tissue samples with rapid imaging rates and processing times [134]. Using tryptophan fluorescence as a reference, the ratio of the NADH signal to the tryptophan signal has been used to differentiate normal cells from cancer cells by means of a two-photon autofluorescence lifetime imaging system that excites the two fluorophores simultaneously [135]. FLIM has also been used to analyze various fluorescent hair components. Ehlers and colleagues have used multiphoton imaging to generate 4D images from the fluorescent structures of hair with submicron spatial resolution and temporal resolution in the picosecond range. This technique allows the intrinsic and artificial components of hair to be analyzed without destroying the sample [136]. Recently, Nie et al. have developed a FLIM instrument that is capable of providing multidimensional information—in space, spectrum, and time—of intrinsic and extrinsic fluorophores; this instrument is valuable for use in biological tissue research and as an optical biopsy tool [137]. Multiphoton laser tomography combined with FLIM from intrinsic fluorophores can facilitate the characterization of melanoma from both a morphological and a quantitative point of view, enabling improvements in diagnostic accuracy (Fig. 6) [138].

The measurement of autofluorescence is not the only strategy for FLIM studies in tissues. Extrinsic fluorophores have also been employed as fluorescent markers to increase the specificity for tumor detection. In this case, information is obtained from the changes in the fluorescent properties of the marker when it interacts with various components of the tissues or from its selective location in certain components of the tissues [139]. Genetically encoded fluorescent indicators, such as the circularly permuted YFP (cpYFP) integrated into a domain of the H_2O_2 sensing protein OxyR [140, 141], have been developed to detect reactive oxygen species, allowing the monitoring of dynamic events in cells and organisms. Much attention has also been directed toward photosensitizers developed to treat tumors through photodynamic therapy [142], as these substances accumulate in cancerous tissues with high selectivity. As an example, Protorphyrin IX has been used to differentiate benign lesions from basal-cell carcinomas [143]. Because the FLIM of skin autofluorescence can also provide useful contrast between malignant skin carcinomas and surrounding unaffected skin [144], the combination of FLIM using extrinsic and intrinsic fluorescence could offer a superior method of tumor detection.

FLIM sensing strategies have proven to be useful in monitoring physiological processes in tissues. For instance, the chloride efflux in olfactory dendrites associated with signal transduction has been measured using FLIM with multiphoton excitation [145]. The authors employed the dynamic quenching of 6-methoxyquinolyl acetoethyl ester caused by chloride ions to probe the chloride concentration in the olfactory epithelium. The uptake of Cu^{2+} ions by plant tissues has also been studied through FLIM imaging by measuring the dynamic quenching of GFP fluorescence caused by the cation [146].

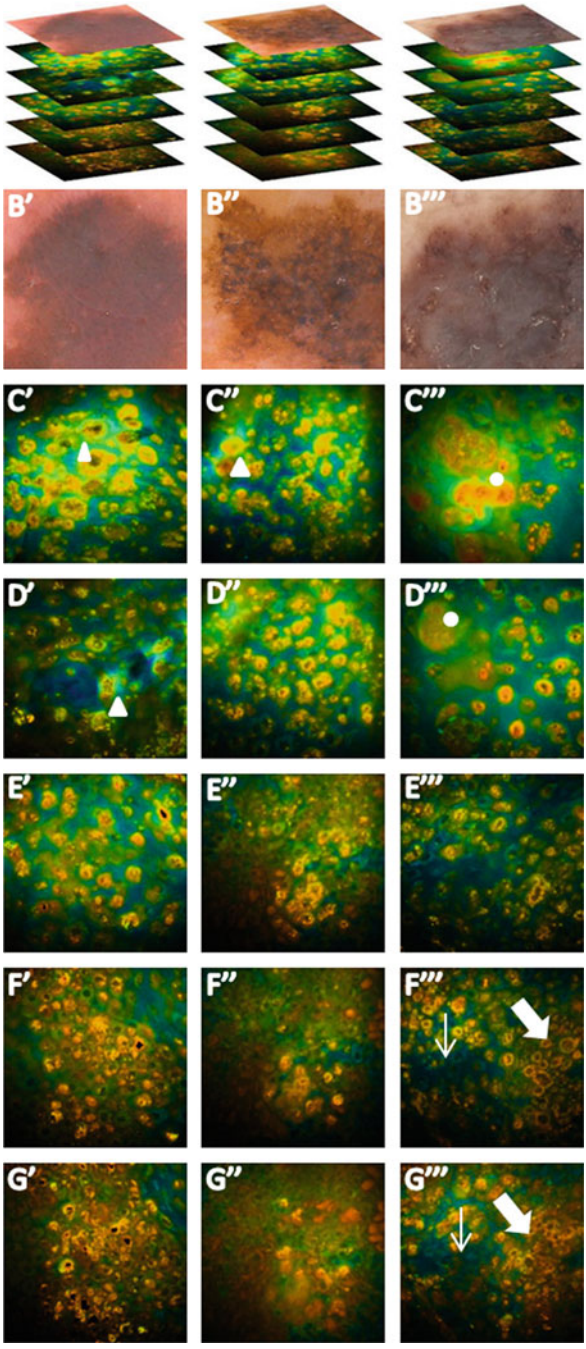

Fig. 6 FLIM imaging of melanoma at various depths, showing irregularly distributed, atypical short-lifetime cells (ASLCs) in the upper melanoma layers. The ASLCs are more prolific and more aggregated in the deeper melanoma layers. Reprinted from Seidenari et al. [138] under the terms of the Creative Commons Attribution License. Copyright © 2013 Seidenari et al.

The primary requirement for FLIM in live tissue is rapid acquisition, in the range of tens or hundreds of milliseconds. As the key technological components become simpler, a number of different commercially available implementations adapted for specific applications will emerge, and time-resolved fluorescence imaging will become much more widespread.

6 Conclusions and Outlook

FLIM microscopy is increasing in importance for biological applications and intracellular sensing. Although FLIM requires specialized instrumentation and trained operators, the advantages that FLIM offers for sensing compensate for its increased complexity. In this chapter, we have provided a brief introduction to certain examples of intracellular FLIM sensing, such as the use of fluorescein derivatives to develop phosphate sensors based on ESPT reactions, the use of intracellular pH-sensitive quantum dots, the advantages of FLIM-FRET over conventional ratiometric FRET, and the use of FLIM in tissue diagnostics. Nevertheless, significant room remains for novel developments that may further enhance the importance of FLIM in the biological and biomedical research fields (Fig. 7). For instance, many technical improvements may be obtained through the development of faster excitation laser sources [147] and detectors with narrower instrument response profiles but good sensitivity across the visible spectrum [148] and less temporal drift in the count rate [149]. One of the drawbacks of time-domain FLIM is the image acquisition time. To collect a sufficient number of photons per pixel to constitute adequate statistics for fitting, the dwell time and the total scanning time

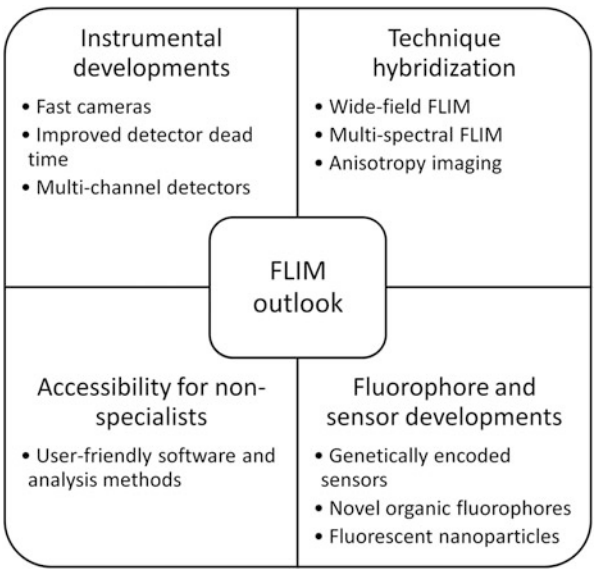

Fig. 7 Potential fields of development for quantitative intracellular FLIM sensing

must be sufficiently long. Through the maximum-likelihood estimator, the parameters of a single-exponential decay can be accurately determined using approximately 100 photons [150, 151], although many more photons are required for double- or triple-exponential decays. This means that the collection of a FLIM image may take up to several minutes. An interesting approach that permits the acquisition time to be decreased is wide-field FLIM microscopy, in which a CCD camera is employed for collection across the full field of view. However, in this case, the response time of the detector is an even more critical issue. These multidimensional camera detectors must be sufficiently fast to process spatial and temporal information at very high rates, and engineering efforts in this direction are currently ongoing. Multi-channel devices with 1-ns time resolution are already available [152] and are capable of collecting photons from single molecules and extracting lifetime information in a wide-field configuration [153, 154]. The combination of spectral imaging and FLIM (multispectral FLIM) is also an interesting approach to expanding the multi-dimensionality of microscopy and obtaining as much knowledge as possible regarding cellular systems. For instance, a detection unit for correlated fluorescence lifetime imaging and spectral imaging (SLiM) has been developed based on a novel combination of a spectrograph and a multichannel photomultiplier head [155]. Using a supercontinuum excitation source, Owen and colleagues have developed a hyperspectral FLIM technique that rapidly extracts lifetimes and spectral excitation and emission information [156]. A number of other instrumental and technical improvements [157, 158], such as the optimization of the detector dead time, may further broaden the applications of intracellular FLIM sensing.

Another area for potential improvement is the development of novel data-analysis methods and fast computing algorithms [159, 160, 124, 161] as well as alternative fitting-free methods of analyzing FLIM images, such as the moments method [162] and the phasor approach [163]. The phasor method transforms the histogram of the time delays of each pixel into a pair of sine–cosine polar coordinates (phasor). Each pixel is then plotted in 2D phasor space (phasor plot). The phasor plot assists in the identification of clusters of pixels with a certain lifetime, the mapping of regions in which two or more fluorophores are emitting, and even the determination of the relative concentrations of these fluorophores [163]. Phasor analysis does not require data fitting and therefore avoids the necessity of assuming a particular fluorescence-decay model. The phasor approach has been successfully applied for the identification of various cellular metabolic states using cell autofluorescence [164, 165] and for the measurement of intracellular pH using fluorescent proteins [166]. Interestingly, the phasor approach is also useful for FRET-based biosensors, as demonstrated by Hinde et al. [167] (Fig. 8), as the method allows the discrimination of mixtures of fluorophores based on changes in the FRET lifetime. By merging the phasor approach for FLIM-FRET and the cross-pair correlation function, Hinde and colleagues were able to characterize the localized activity and dynamic intracellular mobility of the GTPases RhoA and Rac1 [167, 168].

The potential technical advances in the FLIM field are far from exhausted. Once the potential sources of error have been clearly identified and the analysis methods

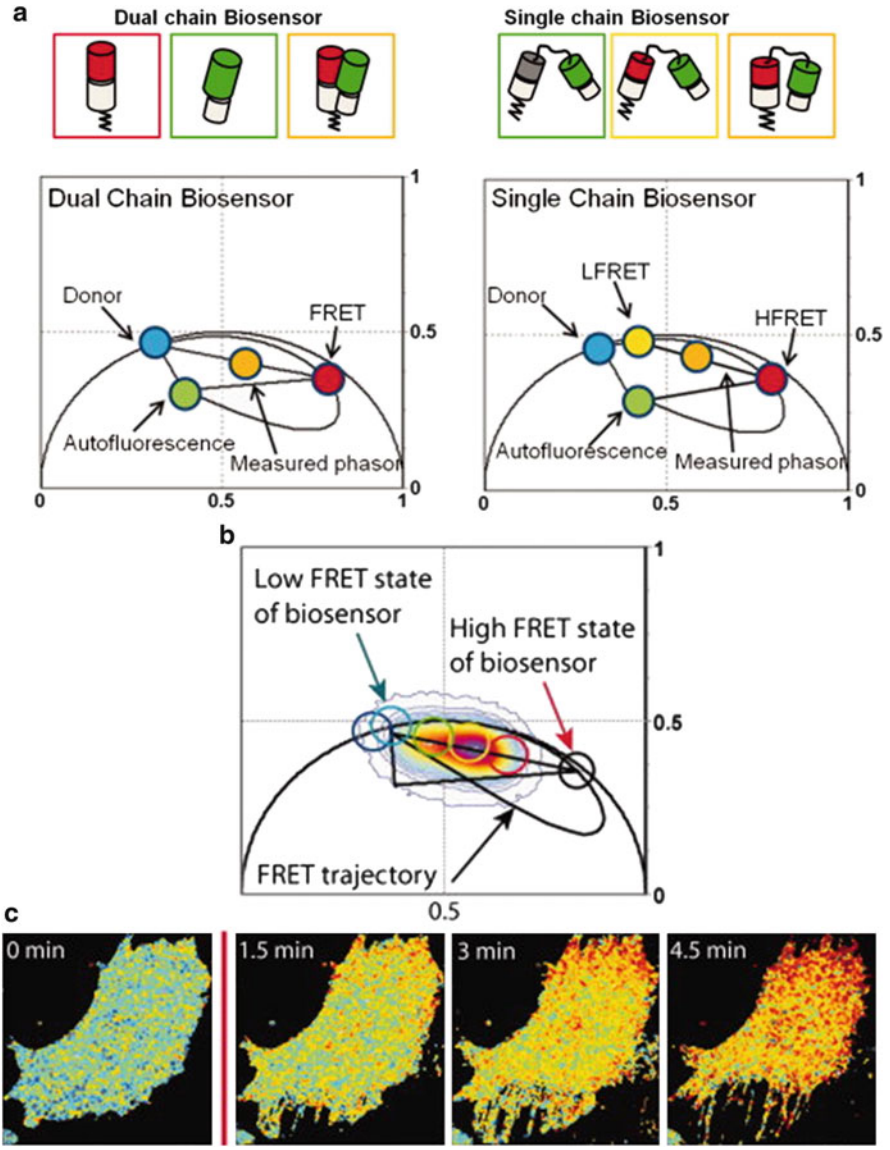

Fig. 8 (**a**) Analysis of the FRET signal from a dual-chain biosensor and a single-chain biosensor in phasor plots. (**b**) and (**c**) Phasor plot and FLIM images of a COS7 cell transfected with (RBD-Citrine)-1L-(ECFP-RhoA), a RhoA GTPase, single-chain biosensor, after stimulation with lysophosphatidic acid. Copyright © 2011 Wiley. Used with permission from Hinde et al. [167]

have been made more accessible to the non-specialist, research groups in biological fields will begin to show increasing interest in FLIM experiments. High-impact results obtained using this approach are foreseeable and will enhance the interest of

other groups in exploring alternative methods for use in their investigations. Hence, FLIM microscopy represents an invaluable tool that is capable of providing significant breakthroughs for many scientific challenges.

Acknowledgments AO acknowledges the support received through grant P10-FQM-6154 from the Conserjeria de Innovacion, Ciencia y Empresa (Junta de Andalucia). JMP thanks the RESTATE Programme co-funded by the European Union under the FP7 COFUND Marie Curie Action - Grant agreement no. 267224.

References

1. Cremades N, Cohen SIA, Deas E, Abramov AY, Chen AY, Orte A, Sandal M, Clarke RW, Dunne P, Aprile FA, Bertoncini CW, Wood NW, Knowles TPJ, Dobson CM, Klenerman D (2012) Direct observation of the interconversion of normal and toxic forms of α-synuclein. Cell 149(5):1048–1059
2. Vazquez A, Liu J, Zhou Y, Oltvai ZN (2010) Catabolic efficiency of aerobic glycolysis: the Warburg effect revisited. BMC Syst Biol 4:58
3. Rusk N (2009) Milestone 4 (1911, 1929, 1967). First fluorescence microscope, first epifluorescence microscope, the dichroic mirror. In: Evanko D, Heinrichs A, Karlsson Rosenthal C (eds) Nature milestones in light microscopy. Macmillan
4. Heimstädt O (1911) Das Fluoreszenzmikroskop. Z Wiss Mikrosk 28:330–337
5. Prowazek S (1914) Zur Kenntuis der Giemsafärbung vom Standpunkte der Cytologie. Z Wiss Mikrosk Mikrosk Tech 31:1–16
6. Ellinger P, Hirt A (1929) Mikroskopische Beobachtungen an lebenden Organen mit Demonstrationen (Intravitalmikroskopie). Arch Exp Pathol Phar 147:63
7. Coons AH, Creech HJ, Jones RN (1974) Immunological properties of an antibody containing a fluorescent group. Proc Soc Exp Biol Med 47:200–202
8. Betzig E, Patterson GH, Sougrat R, Lindwasser OW, Olenych S, Bonifacino JS, Davidson MW, Lippincott-Schwartz J, Hess HF (2006) Imaging intracellular fluorescent proteins at nanometer resolution. Science 313(5793):1642–1645. doi:10.1126/science.1127344
9. Hess ST, Girirajan TPK, Mason MD (2006) Ultra-high resolution imaging by fluorescence photoactivation localization microscopy. Biophys J 91(11):4258–4272
10. Rust MJ, Bates M, Zhuang X (2006) Sub-diffraction-limit imaging by stochastic optical reconstruction microscopy (STORM). Nat Methods 3(10):793–796
11. The Molecular Probes® (2010) Handbook—a guide to fluorescent probes and labeling technologies, 11th edn. Life Technologies Corporation. http://www.lifetechnologies.com/es/en/home/references/molecular-probes-the-handbook.html. Accessed October 2014
12. Han J, Burgess K (2009) Fluorescent indicators for intracellular pH. Chem Rev 110(5):2709–2728. doi:10.1021/cr900249z
13. Boens N, Qin W, Basaric N, Orte A, Talavera EM, Alvarez-Pez JM (2006) Photophysics of the fluorescent pH indicator BCECF. J Phys Chem A 110(30):9334–9343. doi:10.1021/jp0615712
14. Boyarsky G, Hanssen C, Clyne LA (1996) Inadequacy of high K+/nigericin for calibrating BCECF. II. Intracellular pH dependence of the correction. Am J Physiol 271(4):C1146–C1156
15. Lakowicz JR, Szmacinski H, Nowaczyk K, Berndt KW, Johnson M (1992) Fluorescence lifetime imaging. Anal Biochem 202(2):316–330. doi:http://dx.doi.org/10.1016/0003-2697(92)90112-K

16. van Munster E, Gadella TJ (2005) Fluorescence lifetime imaging microscopy (FLIM). In: Rietdorf J (ed) Microscopy techniques, vol 95. Advances in biochemical engineering. Springer, Heidelberg, pp 143–175. doi:10.1007/b102213
17. Lakowicz JR (2006) Principles of fluorescence spectroscopy, 3rd edn. Springer
18. Becker W, Bergmann A, Biskup C, Zimmer T, Klöcker N, Benndorf K (2002) Multi-wavelength TCSPC lifetime imaging. Proc SPIE 4620:79–84
19. Ruedas-Rama MJ, Orte A, Hall EAH, Alvarez-Pez JM, Talavera EM (2011) Effect of surface modification on semiconductor nanocrystal fluorescence lifetime. ChemPhysChem 12 (5):919–929. doi:10.1002/cphc.201000935
20. Orte A, Alvarez-Pez JM, Ruedas-Rama MJ (2013) Fluorescence lifetime imaging microscopy for the detection of intracellular pH with quantum dot nanosensors. ACS Nano 7 (7):6387–6395. doi:10.1021/nn402581q
21. Baggaley E, Gill MR, Green NH, Turton D, Sazanovich IV, Botchway SW, Smythe C, Haycock JW, Weinstein JA, Thomas JA (2014) Dinuclear ruthenium(II) complexes as two-photon, time-resolved emission microscopy probes for cellular DNA. Angew Chem Int Ed 53:3367–3371. doi:10.1002/anie.201309427
22. Chen L-C, Lloyd WR III, Chang C-W, Sud D, Mycek M-A (2013) Chapter 20 – fluorescence lifetime imaging microscopy for quantitative biological imaging. In: Greenfield S, David EW (eds) Methods in cell biology, vol 114. Academic, pp 457–488. doi:http://dx.doi.org/10.1016/B978-0-12-407761-4.00020-8
23. Tantama M, Hung YP, Yellen G (2011) Imaging intracellular pH in live cells with a genetically encoded red fluorescent protein sensor. J Am Chem Soc 133(26):10034–10037. doi:10.1021/ja202902d
24. Sagolla K, Löhmannsröben H-G, Hille C (2013) Time-resolved fluorescence microscopy for quantitative Ca^{2+} imaging in living cells. Anal Bioanal Chem 405(26):8525–8537. doi:10.1007/s00216-013-7290-6
25. Sanders R, Draaijer A, Gerritsen HC, Houpt PM, Levine YK (1995) Quantitative pH imaging in cells using confocal fluorescence lifetime imaging microscopy. Anal Biochem 227 (2):302–308. doi:http://dx.doi.org/10.1006/abio.1995.1285
26. Hille C, Berg M, Bressel L, Munzke D, Primus P, Löhmannsröben H-G, Dosche C (2008) Time-domain fluorescence lifetime imaging for intracellular pH sensing in living tissues. Anal Bioanal Chem 391(5):1871–1879. doi:10.1007/s00216-008-2147-0
27. Lin H-J, Herman P, Kang JS, Lakowicz JR (2001) Fluorescence lifetime characterization of novel low-pH probes. Anal Biochem 294(2):118–125. doi:http://dx.doi.org/10.1006/abio.2001.5155
28. Hanson KM, Behne MJ, Barry NP, Mauro TM, Gratton E, Clegg RM (2002) Two-photon fluorescence lifetime imaging of the skin stratum corneum pH gradient. Biophys J 83 (3):1682–1690. doi:http://dx.doi.org/10.1016/S0006-3495(02)73936-2
29. Kuimova MK, Yahioglu G, Levitt JA, Suhling K (2008) Molecular rotor measures viscosity of live cells via fluorescence lifetime imaging. J Am Chem Soc 130(21):6672–6673. doi:10.1021/ja800570d
30. Loison P, Hosny NA, Gervais P, Champion D, Kuimova MK, Perrier-Cornet J-M (2013) Direct investigation of viscosity of an atypical inner membrane of Bacillus spores: a molecular rotor/FLIM study. Biochim Biophys Acta 1828(11):2436–2443. doi:http://dx.doi.org/10.1016/j.bbamem.2013.06.028
31. van Manen H-J, Verkuijlen P, Wittendorp P, Subramaniam V, van den Berg TK, Roos D, Otto C (2008) Refractive index sensing of green fluorescent proteins in living cells using fluorescence lifetime imaging microscopy. Biophys J 94(8):L67–L69. doi:http://dx.doi.org/10.1529/biophysj.107.127837
32. Andrews LM, Jones MR, Digman MA, Gratton E (2013) Detecting Pyronin Y labeled RNA transcripts in live cell microenvironments by phasor-FLIM analysis. Methods Appl Fluoresc 1(1):015001. doi:10.1088/2050-6120/1/1/015001

33. Tseng T-Y, Chien C-H, Chu J-F, Huang W-C, Lin M-Y, Chang C-C, Chang T-C (2013) Fluorescent probe for visualizing guanine-quadruplex DNA by fluorescence lifetime imaging microscopy. J Biomed Opt 18(10):101309
34. Botchway SW, Parker AW, Bisby RH, Crisostomo AG (2008) Real-time cellular uptake of serotonin using fluorescence lifetime imaging with two-photon excitation. Microsc Res Tech 71(4):267–273. doi:10.1002/jemt.20548
35. Wang H-W, Chen C-T, Guo H-W, Yu J-S, Wei Y-H, Gukassyan V, Kao F-J (2008) Differentiation of apoptosis from necrosis by dynamic changes of reduced nicotinamide adenine dinucleotide fluorescence lifetime in live cells. J Biomed Opt 13(5):054011
36. Gerritsen HC, Sanders R, Draaijer A, Ince C, Levine YK (1997) Fluorescence lifetime imaging of oxygen in living cells. J Fluoresc 7(1):11–15. doi:10.1007/bf02764572
37. Sud D, Zhong W, Beer DG, Mycek M-A (2006) Time-resolved optical imaging provides a molecular snapshot of altered metabolic function in living human cancer cell models. Opt Express 14(10):4412–4426. doi:10.1364/oe.14.004412
38. Sud D, Mycek M-A (2009) Calibration and validation of an optical sensor for intracellular oxygen measurements. J Biomed Opt 14(2):020506
39. Fercher A, O'Riordan TC, Zhdanov AV, Dmitriev RI, Papkovsky DB (2010) Imaging of cellular oxygen and analysis of metabolic responses of mammalian cells. Methods Mol Biol 591:257–273. doi:10.1007/978-1-60761-404-3_16
40. Beck GR, Zerler B, Moran E (2000) Phosphate is a specific signal for induction of osteopontin gene expression. Proc Natl Acad Sci U S A 97:8352–8357
41. Förster T (1949) Fluoreszenzspektrum und Wasserstoffionenkonzentration. Naturwissenschaften 36:186–187
42. Weller A (1961) Fast reactions of excited molecules. Prog React Kinet 1:189–214
43. Tolbert LM, Solntsev KM (2002) Excited-state proton transfer: from constrained systems to "super" photoacids to superfast proton transfer. Acc Chem Res 35:19–27
44. Agmon N (2005) Elementary steps in excited-state proton transfer. J Phys Chem A 109:13–35
45. Yguerabide J, Talavera EM, Alvarez-Pez JM, Quintero B (1994) Steady-state fluorescence method for evaluating excited state proton reactions: application to fluorescein. Photochem Photobiol 60:435–441
46. Alvarez-Pez JM, Ballesteros L, Talavera E, Yguerabide J (2001) Fluorescein excited-state proton exchange reactions: nanosecond emission kinetics and correlation with steady-state fluorescence intensity. J Phys Chem A 105:6320–6332
47. Crovetto L, Orte A, Talavera EM, Alvarez-Pez JM, Cotlet M, Thielemans J, De Schryver FC, Boens N (2004) Global compartmental analysis of the excited-state reaction between fluorescein and (±)-N-acetyl aspartic acid. J Phys Chem B 108:6082–6092
48. Boens N, Basaric N, Novikov E, Crovetto L, Orte A, Talavera EM, Alvarez-Pez JM (2004) Identifiability of the model of the intermolecular excited-state proton exchange reaction in the presence of pH buffer. J Phys Chem A 108(40):8180–8189. doi:10.1021/jp0402941
49. Orte A, Crovetto L, Talavera EM, Boens N, Alvarez-Pez JM (2005) Absorption and emission study of 2′,7′-difluorofluorescein and its excited-state buffer-mediated proton exchange reactions. J Phys Chem A 109:734–747. doi:10.1021/jp046786v
50. Orte A, Bermejo R, Talavera EM, Crovetto L, Alvarez-Pez JM (2005) 2′,7′-Difluorofluorescein excited-state proton reactions: correlation between time-resolved emission and steady-state fluorescence intensity. J Phys Chem A 109:2840–2846. doi:10.1021/jp044681m
51. Paredes JM, Orte A, Crovetto L, Alvarez-Pez JM, Rios R, Ruedas-Rama MJ, Talavera EM (2010) Similarity between the kinetic parameters of the buffer-mediated proton exchange reaction of a xanthenic derivative in its ground- and excited-state. Phys Chem Chem Phys 12:323–327. doi:10.1039/b917333c
52. Paredes JM, Crovetto L, Orte A, Alvarez-Pez JM, Talavera EM (2011) Influence of the solvent on the ground- and excited-state buffer-mediated proton-transfer reactions of a xanthenic dye. Phys Chem Chem Phys 13(4):1685–1694

53. Urano Y, Kamiya M, Kanda K, Ueno T, Hirose K, Nagano T (2005) Evolution of fluorescein as a platform for finely tunable fluorescence probes. J Am Chem Soc 127(13):4888–4894. doi:10.1021/ja043919h
54. Crovetto L, Paredes JM, Rios R, Talavera EM, Alvarez-Pez JM (2007) Photophysics of a xanthenic derivative dye useful as an 'on/off' fluorescence probe. J Phys Chem A 111 (51):13311–13320. doi:10.1021/jp077249o
55. Paredes JM, Crovetto L, Rios R, Orte A, Alvarez-Pez JM, Talavera EM (2009) Tuned lifetime, at the ensemble and single molecule level, of a xanthenic fluorescent dye by means of a buffer-mediated excited-state proton exchange reaction. Phys Chem Chem Phys 11(26):5400–5407
56. Paredes JM, Giron MD, Ruedas-Rama MJ, Orte A, Crovetto L, Talavera EM, Salto R, Alvarez-Pez JM (2013) Real-time phosphate sensing in living cells using fluorescence lifetime imaging microscopy (FLIM). J Phys Chem B 117(27):8143–8149. doi:10.1021/jp405041c
57. Giron MD, Havel CM, Watson JA (1999) Mevalonate-mediated suppression of 3-hydroxy-3-methylglutaryl coenzyme A reductase function in alpha-toxin-perforated cells. Proc Natl Acad Sci U S A 91:6398–6402
58. Sudo H, Kodama H, Amagi Y, Yamamoto S, Kasai S (1983) In vitro differentiation and calcification in a new clonal osteogenic cell line derived from newborn mouse calvaria. J Cell Biol 96:191–198
59. Suzuki A, Ghayor C, Guicheux J, Magne D, Quillard S, Kakita A, Ono Y, Miura Y, Oiso Y, Itoh M, Caverzasio J (2006) Enhanced expression of the inorganic phosphate transporter Pit-1 is involved in BMP-2-induced matrix mineralization in osteoblast-like cells. J Bone Miner Res 21:674–683
60. Martínez-Peragón A, Miguel D, Jurado R, Justicia J, Alvarez-Pez JM, Cuerva JM, Crovetto L (2014) Synthesis and photophysics of a new family of fluorescent 9-alkyl substituted xanthenones. Chem Eur J 20:447–455
61. Yaron P, Holt B, Short P, Lösche M, Islam M, Dahl K (2011) Single wall carbon nanotubes enter cells by endocytosis and not membrane penetration. J Nanobiotechnol 9(1):45. doi:10.1186/1477-3155-9-45
62. Hu Z, Pantoş GD, Kuganathan N, Arrowsmith RL, Jacobs RMJ, Kociok-Köhn G, O'Byrne J, Jurkschat K, Burgos P, Tyrrell RM, Botchway SW, Sanders JKM, Pascu SI (2012) Interactions between amino acid-tagged naphthalenediimide and single walled carbon nanotubes for the design and construction of new bioimaging probes. Adv Funct Mater 22(3):503–518. doi:10.1002/adfm.201101932
63. Zhang Y, Birch DJS, Chen Y (2011) Two-photon excited surface plasmon enhanced energy transfer between DAPI and gold nanoparticles: opportunities in intra-cellular imaging and sensing. Appl Phys Lett 99(10). doi:http://dx.doi.org/10.1063/1.3633066
64. Okabe K, Inada N, Gota C, Harada Y, Funatsu T, Uchiyama S (2012) Intracellular temperature mapping with a fluorescent polymeric thermometer and fluorescence lifetime imaging microscopy. Nat Commun 3:705. doi:10.1038/ncomms1714
65. Resch-Genger U, Grabolle M, Cavaliere-Jaricot S, Nitschke R, Nann T (2008) Quantum dots versus organic dyes as fluorescent labels. Nat Methods 5(9):763–775. doi:10.1038/nmeth.1248
66. Ruedas-Rama MJ, Orte A, Hall EAH, Alvarez-Pez JM, Talavera EM (2012) A chloride ion nanosensor for time-resolved fluorimetry and fluorescence lifetime imaging. Analyst 137:1500–1508
67. Dahan M, Laurence T, Pinaud F, Chemla DS, Alivisatos AP, Sauer M, Weiss S (2001) Time-gated biological imaging by use of colloidal quantum dots. Opt Lett 26(11):825–827. doi:10.1364/ol.26.000825
68. Giraud G, Schulze H, Bachmann T, Campbell C, Mount A, Ghazal P, Khondoker M, Ross A, Ember S, Ciani I, Tlili C, Walton A, Terry J, Crain J (2009) Fluorescence lifetime imaging of quantum dot labeled DNA microarrays. Int J Mol Sci 10(4):1930–1941

69. Pai RK, Cotlet M (2011) Highly stable, water-soluble, intrinsic fluorescent hybrid scaffolds for imaging and biosensing. J Phys Chem C 115(5):1674–1681. doi:10.1021/jp109589h
70. Yaghini E, Giuntini F, Eggleston IM, Suhling K, Seifalian AM, MacRobert AJ (2014) Fluorescence lifetime imaging and FRET-induced intracellular redistribution of Tat-conjugated quantum dot nanoparticles through interaction with a phthalocyanine photosensitiser. Small 10(4):782–792. doi:10.1002/smll.201301459
71. Ruedas-Rama MJ, Orte A, Hall EAH, Alvarez-Pez JM, Talavera EM (2011) Quantum dot photoluminescence lifetime-based pH nanosensor. Chem Commun 47(10):2898–2900. doi:10.1039/c0cc05252c
72. Liu Y-S, Sun Y, Vernier PT, Liang C-H, Chong SYC, Gundersen MA (2007) pH-sensitive photoluminescence of CdSe/ZnSe/ZnS quantum dots in human ovarian cancer cells. J Phys Chem C 111(7):2872–2878. doi:10.1021/jp0654718
73. Wang X, Boschetti C, Ruedas-Rama MJ, Tunnacliffe A, Hall EAH (2010) Ratiometric pH-dot ANSors. Analyst 135(7):1585–1591. doi:10.1039/b922751b
74. Despa S, Steels P, Ameloot M (2000) Fluorescence lifetime microscopy of the sodium indicator sodium-binding benzofuran isophthalate in HeLa cells. Anal Biochem 280 (2):227–241. doi:http://dx.doi.org/10.1006/abio.2000.4505
75. Edelhoch H, Brand L, Wilchek M (1967) Fluorescence studies with tryptophyl peptides. Biochemistry 6(2):547–559. doi:10.1021/bi00854a024
76. Stryer L, Haugland RP (1967) Energy transfer: a spectroscopic ruler. Proc Natl Acad Sci U S A 58(2):719–726
77. Stryer L (1978) Fluorescence energy transfer as a spectroscopic ruler. Annu Rev Biochem 47:819–846
78. Joo C, Balci H, Ishitsuka Y, Buranachai C, Ha T (2008) Advances in single-molecule fluorescence methods for molecular biology. Annu Rev Biochem 77:51–76. doi:10.1146/annurev.biochem.77.070606.101543
79. Kapanidis AN, Strick T (2009) Biology, one molecule at a time. Trends Biochem Sci 34 (5):234–243
80. Orte A, Clarke RW, Klenerman D (2011) Single-molecule fluorescence coincidence spectroscopy and its application to resonance energy transfer. ChemPhysChem 12(3):491–499. doi:10.1002/cphc.201000636
81. Ruedas-Rama MJ, Alvarez-Pez JM, Orte A (2013) Solving single biomolecules by advanced FRET-based single-molecule fluorescence techniques. Biophys Rev Lett 08(03n04):161–190. doi:10.1142/S1793048013300041
82. Wallrabe H, Periasamy A (2005) Imaging protein molecules using FRET and FLIM microscopy. Curr Opin Biotechnol 16(1):19–27. doi:http://dx.doi.org/10.1016/j.copbio.2004.12.002
83. Borst JW, Visser AJWG (2010) Fluorescence lifetime imaging microscopy in life sciences. Meas Sci Technol 21(10):102002
84. Becker W (2012) Fluorescence lifetime imaging – techniques and applications. J Microsc 247 (2):119–136. doi:10.1111/j.1365-2818.2012.03618.x
85. Sun Y, Day RN, Periasamy A (2011) Investigating protein–protein interactions in living cells using fluorescence lifetime imaging microscopy. Nat Protoc 6(9):1324–1340
86. Broussard JA, Rappaz B, Webb DJ, Brown CM (2013) Fluorescence resonance energy transfer microscopy as demonstrated by measuring the activation of the serine/threonine kinase Akt. Nat Protoc 8(2):265–281
87. Chen Y, Mills JD, Periasamy A (2003) Protein localization in living cells and tissues using FRET and FLIM. Differentiation 71(9–10):528–541. doi:http://dx.doi.org/10.1111/j.1432-0436.2003.07109007.x
88. Russinova E, Borst J-W, Kwaaitaal M, Caño-Delgado A, Yin Y, Chory J, de Vries SC (2004) Heterodimerization and endocytosis of Arabidopsis brassinosteroid receptors BRI1 and AtSERK3 (BAK1). Plant Cell 16(12):3216–3229. doi:10.1105/tpc.104.025387
89. Peter M, Ameer-Beg SM, Hughes MKY, Keppler MD, Prag S, Marsh M, Vojnovic B, Ng T (2005) Multiphoton-FLIM quantification of the EGFP-mRFP1 FRET pair for localization of

membrane receptor-kinase interactions. Biophys J 88(2):1224–1237. doi:http://dx.doi.org/10.1529/biophysj.104.050153
90. Bayle V, Nussaume L, Bhat RA (2008) Combination of novel green fluorescent protein mutant TSapphire and DsRed variant mOrange to set up a versatile in planta FRET–FLIM assay. Plant Physiol 148(1):51–60. doi:10.1104/pp. 108.117358
91. Liu Q, Leber B, Andrews DW (2012) Interactions of pro-apoptotic BH3 proteins with anti-apoptotic Bcl-2 family proteins measured in live MCF-7 cells using FLIM FRET. Cell Cycle 11(19):3536–3542
92. Zelazny E, Borst JW, Muylaert M, Batoko H, Hemminga MA, Chaumont F (2007) FRET imaging in living maize cells reveals that plasma membrane aquaporins interact to regulate their subcellular localization. Proc Natl Acad Sci U S A 104(30):12359–12364. doi:10.1073/pnas.0701180104
93. Jose M, Nair DK, Altrock WD, Dresbach T, Gundelfinger ED, Zuschratter W (2008) Investigating interactions mediated by the presynaptic protein bassoon in living cells by Foerster's resonance energy transfer and fluorescence lifetime imaging microscopy. Biophys J 94:1483–1496
94. Guzmán C, Šolman M, Ligabue A, Blaževitš O, Andrade DM, Reymond L, Eggeling C, Abankwa D (2014) The efficacy of Raf kinase recruitment to the GTPase H-ras depends on H-ras membrane conformer specific nanoclustering. J Biol Chem. doi:10.1074/jbc.M113.537001
95. Castro BM, Fedorov A, Hornillos V, Delgado J, Acuña AU, Mollinedo F, Prieto M (2013) Edelfosine and miltefosine effects on lipid raft properties: membrane biophysics in cell death by antitumor lipids. J Phys Chem B 117(26):7929–7940. doi:10.1021/jp401407d
96. Carillo MA, Bennet M, Faivre D (2013) Interaction of proteins associated with the magnetosome assembly in magnetotactic bacteria as revealed by two-hybrid two-photon excitation fluorescence lifetime imaging microscopy Förster resonance energy transfer. J Phys Chem B 117(47):14642–14648. doi:10.1021/jp4086987
97. Scolari S, Engel S, Krebs N, Plazzo AP, De Almeida RFM, Prieto M, Veit M, Herrmann A (2009) Lateral distribution of the transmembrane domain of influenza virus hemagglutinin revealed by time-resolved fluorescence imaging. J Biol Chem 284(23):15708–15716. doi:10.1074/jbc.M900437200
98. Batisse J, Guerrero SX, Bernacchi S, Richert L, Godet J, Goldschmidt V, Mély Y, Marquet R, de Rocquigny H, Paillart J-C (2013) APOBEC3G impairs the multimerization of the HIV-1 Vif protein in living cells. J Virol 87(11):6492–6506. doi:10.1128/jvi.03494-12
99. Berezovska O, Ramdya P, Skoch J, Wolfe MS, Bacskai BJ, Hyman BT (2003) Amyloid precursor protein associates with a nicastrin-dependent docking site on the presenilin 1–γ-secretase complex in cells demonstrated by fluorescence lifetime imaging. J Neurosci 23(11):4560–4566
100. Bacskai BJ, Skoch J, Hickey GA, Allen R, Hyman BT (2003) Fluorescence resonance energy transfer determinations using multiphoton fluorescence lifetime imaging microscopy to characterize amyloid-beta plaques. J Biomed Opt 8(3):368–375
101. Tavares E, Macedo JA, Paulo PMR, Tavares C, Lopes C, Melo EP (2014) Live-cell FRET imaging reveals clustering of the prion protein at the cell surface induced by infectious prions. Biochim Biophys Acta 1842:981–991
102. Esposito A, Gralle M, Dani MAC, Lange D, Wouters FS (2008) pHlameleons: a family of FRET-based protein sensors for quantitative pH imaging. Biochemistry 47(49):13115–13126. doi:10.1021/bi8009482
103. Jose M, Nair DK, Reissner C, Hartig R, Zuschratter W (2007) Photophysics of Clomeleon by FLIM: discriminating excited state reactions along neuronal development. Biophys J 92(6):2237–2254. doi:http://dx.doi.org/10.1529/biophysj.106.092841
104. Palmer AE, Qin Y, Park JG, McCombs JE (2011) Design and application of genetically encoded biosensors. Trends Biotechnol 29(3):144–152. doi:http://dx.doi.org/10.1016/j.tibtech.2010.12.004

105. Laine R, Stuckey DW, Manning H, Warren SC, Kennedy G, Carling D, Dunsby C, Sardini A, French PMW (2012) Fluorescence lifetime readouts of troponin-C-based calcium FRET sensors: a quantitative comparison of CFP and mTFP1 as donor fluorophores. PLoS One 7 (11):e49200
106. Markova O, Mukhtarov M, Real E, Jacob Y, Bregestovski P (2008) Genetically encoded chloride indicator with improved sensitivity. J Neurosci Methods 170(1):67–76. doi:http://dx.doi.org/10.1016/j.jneumeth.2007.12.016
107. Grimley JS, Li L, Wang W, Wen L, Beese LS, Hellinga HW, Augustine GJ (2013) Visualization of synaptic inhibition with an optogenetic sensor developed by cell-free protein engineering automation. J Neurosci 33(41):16297–16309. doi:10.1523/jneurosci.4616-11.2013
108. Thestrup T, Litzlbauer J, Bartholomaus I, Mues M, Russo L, Dana H, Kovalchuk Y, Liang Y, Kalamakis G, Laukat Y, Becker S, Witte G, Geiger A, Allen T, Rome LC, Chen T-W, Kim DS, Garaschuk O, Griesinger C, Griesbeck O (2014) Optimized ratiometric calcium sensors for functional in vivo imaging of neurons and T lymphocytes. Nat Methods 11(2):175–182. doi:10.1038/nmeth.2773
109. Munsie L, Caron N, Atwal RS, Marsden I, Wild EJ, Bamburg JR, Tabrizi SJ, Truant R (2011) Mutant huntingtin causes defective actin remodeling during stress: defining a new role for transglutaminase 2 in neurodegenerative disease. Hum Mol Genet 20(10):1937–1951. doi:10.1093/hmg/ddr075
110. Caron NS, Munsie LN, Keillor JW, Truant R (2012) Using FLIM-FRET to measure conformational changes of transglutaminase type 2 in live cells. PLoS One 7(8):e44159
111. Harvey CD, Ehrhardt AG, Cellurale C, Zhong H, Yasuda R, Davis RJ, Svoboda K (2008) A genetically encoded fluorescent sensor of ERK activity. Proc Natl Acad Sci U S A 105 (49):19264–19269. doi:10.1073/pnas.0804598105
112. Yasuda R, Harvey CD, Zhong H, Sobczyk A, van Aelst L, Svoboda K (2006) Supersensitive Ras activation in dendrites and spines revealed by two-photon fluorescence lifetime imaging. Nat Neurosci 9(2):283–291
113. Oliveira AF, Yasuda R (2013) An improved Ras sensor for highly sensitive and quantitative FRET–FLIM imaging. PLoS One 8(1):e52874
114. Ganesan S, Ameer-beg SM, Ng TTC, Vojnovic B, Wouters FS (2006) A dark yellow fluorescent protein (YFP)-based resonance energy-accepting chromoprotein (REACh) for Förster resonance energy transfer with GFP. Proc Natl Acad Sci U S A 103(11):4089–4094. doi:10.1073/pnas.0509922103
115. Murakoshi H, Lee S-J, Yasuda R (2008) Highly sensitive and quantitative FRET–FLIM imaging in single dendritic spines using improved non-radiative YFP. Brain Cell Biol 36 (1–4):31–42. doi:10.1007/s11068-008-9024-9
116. Duncan RR, Bergmann A, Cousin MA, Apps DK, Shipston MJ (2004) Multi-dimensional time-correlated single photon counting (TCSPC) fluorescence lifetime imaging microscopy (FLIM) to detect FRET in cells. J Microsc 215(1):1–12. doi:10.1111/j.0022-2720.2004.01343.x
117. Becker W, Bergmann A, Hink MA, König K, Benndorf K, Biskup C (2004) Fluorescence lifetime imaging by time-correlated single-photon counting. Microsc Res Tech 63(1):58–66. doi:10.1002/jemt.10421
118. Millington M, Grindlay GJ, Altenbach K, Neely RK, Kolch W, Benčina M, Read ND, Jones AC, Dryden DTF, Magennis SW (2007) High-precision FLIM–FRET in fixed and living cells reveals heterogeneity in a simple CFP–YFP fusion protein. Biophys Chem 127(3):155–164. doi:http://dx.doi.org/10.1016/j.bpc.2007.01.008
119. Becker W, Bergmann A, Biskup C (2007) Multi-spectral fluorescence lifetime imaging by TCSPC. Microsc Res Tech 70:403–409
120. Xu L, Wang L, Zhang Z, Huang Z-L (2013) A feasible add-on upgrade on a commercial two-photon FLIM microscope for optimal FLIM–FRET imaging of CFP–YFP pairs. J Fluoresc 23(3):543–549. doi:10.1007/s10895-013-1188-8

121. Grecco HE, Roda-Navarro P, Verveer PJ (2009) Global analysis of time correlated single photon counting FRET–FLIM data. Opt Express 17(8):6493–6508. doi:10.1364/oe.17.006493
122. Laptenok S, Snellenburg J, Bücherl C, Konrad K, Borst J (2014) Global analysis of FRET–FLIM data in live plant cells. In: Engelborghs Y, Visser AJWG (eds) Fluorescence spectroscopy and microscopy, vol 1076. Methods in molecular biology. Humana, pp 481–502. doi:10.1007/978-1-62703-649-8_21
123. Adbul Rahim NA, Pelet S, Kamm RD, So PTC (2012) Methodological considerations for global analysis of cellular FLIM/FRET measurements. J Biomed Opt 17(2):0260131–02601313
124. Warren SC, Margineanu A, Alibhai D, Kelly DJ, Talbot C, Alexandrov Y, Munro I, Katan M, Dunsby C, French PMW (2013) Rapid global fitting of large fluorescence lifetime imaging microscopy datasets. PLoS One 8(8):e70687
125. Laptenok SP, Borst JW, Mullen KM, van Stokkum IHM, Visser AJWG, van Amerongen H (2010) Global analysis of Förster resonance energy transfer in live cells measured by fluorescence lifetime imaging microscopy exploiting the rise time of acceptor fluorescence. Phys Chem Chem Phys 12(27):7593–7602. doi:10.1039/b919700a
126. Wagnieres GA, Star WM, Wilson BC (1998) In vivo fluorescence spectroscopy and imaging for oncological applications. Photochem Photobiol 68(5):603–632. doi:10.1111/j.1751-1097.1998.tb02521.x
127. König K, Ehlers A, Stracke F, Riemann I (2006) In vivo drug screening in human skin using femtosecond laser multiphoton tomography. Skin Pharmacol Appl Skin Physiol 19:78–88
128. Elson D, Requejo-Isidro J, Munro I, Reavell F, Siegel J, Suhling K, Tadrous P, Benninger R, Lanigan P, McGinty J, Talbot C, Treanor B, Webb S, Sandison A, Wallace A, Davis D, Lever J, Neil M, Phillips D, Stamp G, French P (2004) Time-domain fluorescence lifetime imaging applied to biological tissue. Photochem Photobiol Sci 3(8):795–801. doi:10.1039/b316456j
129. Salmon J-M, Kohen E, Viallet P, Hirschberg JG, Wouters AW, Kohen C, Thorell B (1982) Microspectrofluorometric approach to the study of free/bound NAD(P)H ratio as metabolic indicator in various cell types. Photochem Photobiol 36(5):585–593. doi:10.1111/j.1751-1097.1982.tb04420.x
130. Koretsky AP, Katz LA, Balaban RS (1987) Determination of pyridine nucleotide fluorescence from the perfused heart using an internal standard. Am J Physiol 253(4):H856–H862
131. Scott TG, Spencer RD, Leonard NJ, Weber GJ (1970) Synthetic spectroscopic models related to coenzymes and base pairs. V. Emission properties of NADH. Studies of fluorescence lifetimes and quantum efficiencies of NADH, AcPyADH, [reduced acetylpyridineadenine dinucleotide] and simplified synthetic models. J Am Chem Soc 92:687–695
132. Lakowicz JR, Szmacinski H, Nowaczyk K, Johnson ML (1992) Fluorescence lifetime imaging of free and protein-bound NADH. Proc Natl Acad Sci U S A 89(4):1271–1275
133. Lee KCB, Siegel J, Webb SED, Lévêque-Fort S, Cole MJ, Jones R, Dowling K, Lever MJ, French PMW (2001) Application of the stretched exponential function to fluorescence lifetime imaging. Biophys J 81(3):1265–1274
134. Papour A, Taylor Z, Sherman A, Sanchez D, Lucey G, Liau L, Stafsudd O, Yong W, Grundfest W (2013) Optical imaging for brain tissue characterization using relative fluorescence lifetime imaging. J Biomed Opt 18(6):060504. doi:10.1117/1.JBO.18.6.060504
135. Li D, Zheng W, Qu JY (2009) Two-photon autofluorescence microscopy of multicolor excitation. Opt Lett 34(2):202–204. doi:10.1364/ol.34.000202
136. Ehlers A, Riemann I, Stark M, König K (2007) Multiphoton fluorescence lifetime imaging of human hair. Microsc Res Tech 70(2):154–161. doi:10.1002/jemt.20395
137. Nie Z, An R, Hayward JE, Farrell TJ, Fang Q (2013) Hyperspectral fluorescence lifetime imaging for optical biopsy. J Biomed Opt 18(9):096001
138. Seidenari S, Arginelli F, Dunsby C, French PMW, König K, Magnoni C, Talbot C, Ponti G (2013) Multiphoton laser tomography and fluorescence lifetime imaging of melanoma:

morphologic features and quantitative data for sensitive and specific non-invasive diagnostics. PLoS One 8(7):e70682
139. Siegel J, Elson DS, Webb SED, Lee KCB, Vlandas A, Gambaruto GL, Lévêque-Fort S, Lever MJ, Tadrous PJ, Stamp GWH, Wallace AL, Sandison A, Watson TF, Alvarez F, French PMW (2003) Studying biological tissue with fluorescence lifetime imaging: microscopy, endoscopy, and complex decay profiles. Appl Opt 42(16):2995–3004. doi:10.1364/ao.42.002995
140. Markvicheva KN, Bilan DS, Mishina NM, Gorokhovatsky AY, Vinokurov LM, Lukyanov S, Belousov VV (2011) A genetically encoded sensor for H_2O_2 with expanded dynamic range. Bioorg Med Chem 19(3):1079–1084. doi:http://dx.doi.org/10.1016/j.bmc.2010.07.014
141. Bilan DS, Pase L, Joosen L, Gorokhovatsky AY, Ermakova YG, Gadella TWJ, Grabher C, Schultz C, Lukyanov S, Belousov VV (2012) HyPer-3: a genetically encoded H_2O_2 probe with improved performance for ratiometric and fluorescence lifetime imaging. ACS Chem Biol 8(3):535–542. doi:10.1021/cb300625g
142. Ackroyd R, Kelty C, Brown N, Reed M (2001) The history of photodetection and photodynamic therapy. Photochem Photobiol 74(5):656–669. doi:10.1562/0031-8655(2001)0740656thopap2.0.co2
143. Cubeddu R, Comelli D, D'Andrea C, Taroni P, Valentini G (2002) Time-resolved fluorescence imaging in biology and medicine. J Phys D Appl Phys 35(9):R61
144. Galletly NP, McGinty J, Dunsby C, Teixeira F, Requejo-Isidro J, Munro I, Elson DS, Neil MAA, Chu AC, French PMW, Stamp GW (2008) Fluorescence lifetime imaging distinguishes basal cell carcinoma from surrounding uninvolved skin. Br J Dermatol 159(1):152–161. doi:10.1111/j.1365-2133.2008.08577.x
145. Kaneko H, Putzier I, Frings S, Kaupp UB, Gensch T (2004) Chloride accumulation in mammalian olfactory sensory neurons. J Neurosci 24:7931–7938
146. Hötzer B, Ivanov R, Brumbarova T, Bauer P, Jung G (2012) Visualization of Cu^{2+} uptake and release in plant cells by fluorescence lifetime imaging microscopy. FEBS J 279(3):410–419. doi:10.1111/j.1742-4658.2011.08434.x
147. McLoskey D, Campbell D, Allison A, Hungerford G (2011) Fast time-correlated single-photon counting fluorescence lifetime acquisition using a 100 MHz semiconductor excitation source. Meas Sci Technol 22(6):067001
148. Ghioni M, Gulinatti A, Rech I, Zappa F, Cova S (2007) Progress in silicon single-photon avalanche diodes. IEEE J Quantum Electron 47:151–159
149. Michalet X, Colyer RA, Scalia G, Ingargiola A, Lin R, Millaud JE, Weiss S, Siegmund OHW, Tremsin AS, Vallerga JV, Cheng A, Levi M, Aharoni D, Arisaka K, Villa F, Guerrieri F, Panzeri F, Rech I, Gulinatti A, Zappa F, Ghioni M, Cova S (2013) Development of new photon-counting detectors for single-molecule fluorescence microscopy. Philos Trans R Soc B 368(1611). doi:10.1098/rstb.2012.0035
150. Köllner M, Wolfrum J (1992) How many photons are necessary for fluorescence-lifetime measurements? Chem Phys Lett 200(1–2):199–204. doi:http://dx.doi.org/10.1016/0009-2614(92)87068-Z
151. Maus M, Cotlet M, Hofkens J, Gensch T, De Schryver FC, Schaffer J, Seidel CAM (2001) An experimental comparison of the maximum likelihood estimation and nonlinear least-squares fluorescence lifetime analysis of single molecules. Anal Chem 73(9):2078–2086. doi:10.1021/ac000877g
152. Tremsin AS, Siegmund OHW, Vallerga JV, Raffanti R, Weiss S, Michalet X (2009) High speed multichannel charge sensitive data acquisition system with self-triggered event timing. IEEE Trans Nucl Sci 56(3):1148–1152. doi:10.1109/tns.2009.2015302
153. Colyer RA, Lee C, Gratton E (2008) A novel fluorescence lifetime imaging system that optimizes photon efficiency. Microsc Res Tech 71(3):201–213. doi:10.1002/jemt.20540
154. Colyer RA, Siegmund OHW, Tremsin AS, Vallerga JV, Weiss S, Michalet X (2012) Phasor imaging with a widefield photon-counting detector. J Biomed Opt 17(1):016008

155. Spriet C, Trinel D, Waharte F, Deslee D, Vandenbunder B, Barbillat J, Héliot L (2007) Correlated fluorescence lifetime and spectral measurements in living cells. Microsc Res Tech 70(2):85–94. doi:10.1002/jemt.20385
156. Owen DM, Auksorius E, Manning HB, Talbot CB, de Beule PAA, Dunsby C, Neil MAA, French PMW (2007) Excitation-resolved hyperspectral fluorescence lifetime imaging using a UV-extended supercontinuum source. Opt Lett 32(23):3408–3410. doi:10.1364/ol.32.003408
157. Turgeman L, Fixler D (2013) The influence of dead time related distortions on live cell fluorescence lifetime imaging (FLIM) experiments. J Biophotonics. doi:10.1002/jbio.201300018
158. Turgeman L, Fixler D (2013) Photon efficiency optimization in time-correlated single photon counting technique for fluorescence lifetime imaging systems. IEEE Trans Biomed Eng 60 (6):1571–1579. doi:10.1109/tbme.2013.2238671
159. Laptenok S, Mullen KM, Borst JW, van Stokkum IHM, Apanasovich VV, Visser AJWG (2007) Fluorescence lifetime imaging microscopy (FLIM) data analysis with TIMP. J Stat Soft 18:1–20
160. Padilla-Parra S, Audugé N, Coppey-Moisan M, Tramier M (2008) Quantitative FRET analysis by fast acquisition time domain FLIM at high spatial resolution in living cells. Biophys J 95(6):2976–2988. doi:http://dx.doi.org/10.1529/biophysj.108.131276
161. Hu D, Sarder P, Ronhovde P, Orthaus S, Achilefu S, Nussinov Z (2014) Automatic segmentation of fluorescence lifetime microscopy images of cells using multiresolution community detection—a first study. J Microsc 253(1):54–64. doi:10.1111/jmi.12097
162. Leray A, Padilla-Parra S, Roul J, Héliot L, Tramier M (2013) Spatio-temporal quantification of FRET in living cells by fast time-domain FLIM: a comparative study of non-fitting methods. PLoS One 8(7):e69335
163. Digman MA, Caiolfa VR, Zamai M, Gratton E (2008) The phasor approach to fluorescence lifetime imaging analysis. Biophys J 94(2):L14–L16. doi:http://dx.doi.org/10.1529/biophysj.107.120154
164. Stringari C, Cinquin A, Cinquin O, Digman MA, Donovan PJ, Gratton E (2011) Phasor approach to fluorescence lifetime microscopy distinguishes different metabolic states of germ cells in a live tissue. Proc Natl Acad Sci U S A 108(33):13582–13587. doi:10.1073/pnas.1108161108
165. Torno K, Wright B, Jones M, Digman M, Gratton E, Phillips M (2013) Real-time analysis of metabolic activity within Lactobacillus acidophilus by phasor fluorescence lifetime imaging microscopy of NADH. Curr Microbiol 66(4):365–367. doi:10.1007/s00284-012-0285-2
166. Battisti A, Digman MA, Gratton E, Storti B, Beltram F, Bizzarri R (2012) Intracellular pH measurements made simple by fluorescent protein probes and the phasor approach to fluorescence lifetime imaging. Chem Commun 48(42):5127–5129. doi:10.1039/c2cc30373f
167. Hinde E, Digman MA, Welch C, Hahn KM, Gratton E (2012) Biosensor Förster resonance energy transfer detection by the phasor approach to fluorescence lifetime imaging microscopy. Microsc Res Tech 75(3):271–281. doi:10.1002/jemt.21054
168. Hinde E, Digman MA, Hahn KM, Gratton E (2013) Millisecond spatiotemporal dynamics of FRET biosensors by the pair correlation function and the phasor approach to FLIM. Proc Natl Acad Sci U S A 110(1):135–140. doi:10.1073/pnas.1211882110

Multiple-Pulse Pumping with Time-Gated Detection for Enhanced Fluorescence Imaging in Cells and Tissue

Rafal Fudala, Ryan M. Rich, Joe Kimball, Ignacy Gryczynski, Sangram Raut, Julian Borejdo, Dorota L. Stankowska, Raghu R. Krishnamoorthy, Karol Gryczynski, Badri P. Maliwal, and Zygmunt Gryczynski

Abstract Fluorescence-based sensing and imaging experiments are constrained by the background signal generated on a sample. A main contribution to the background, besides direct scattering of excitation and Raman scattering of the solvent, comes from sample autofluorescence and additives used for sample preparation. Such unwanted signals from endogenous chromophores and fixatives typically are broad and spectrally overlap with the probe signal; thus becoming a major limitation for sensitive detection and quantitative imaging. Since the fluorescence lifetimes of the majority of naturally occurring chromophores are relatively short, long-lived fluorophores allow for background discrimination by time-gated detection. Unfortunately, the brightness of long-lived, red-emitting fluorescent probes is inherently very low, consequently limiting many applications. Recently we reported a simple new approach with bursts of closely spaced laser excitation pulses for excitation (multi-pulse excitation) that allows for many-fold increase in the intensity of a long-lived probe over the background signal. This technology can be easily implemented for biomedical diagnostics and imaging to significantly enhance the signal of long-lived probes over the background. In this report, we

R. Fudala, R.M. Rich, I. Gryczynski, S. Raut, J. Borejdo, D.L. Stankowska, R.R. Krishnamoorthy, K. Gryczynski, and B.P. Maliwal
Department of Cell Biology and Immunology, Center for Fluorescence Technologies and Nanomedicine, University of North Texas Health Science Center, Fort Worth, TX 76107, USA

J. Kimball
Department of Physics and Astronomy, Texas Christian University, TCU Box 298840, Fort Worth, TX 76129, USA

Z. Gryczynski (✉)
Department of Cell Biology and Immunology, Center for Fluorescence Technologies and Nanomedicine, University of North Texas Health Science Center, Fort Worth, TX 76107, USA

Department of Physics and Astronomy, Texas Christian University, TCU Box 298840, Fort Worth, TX 76129, USA
e-mail: zgryczynski@tcu.edu

P. Kapusta et al. (eds.), *Advanced Photon Counting: Applications, Methods, Instrumentation*, Springer Ser Fluoresc (2015) 15: 225–240, DOI 10.1007/4243_2014_68,

are discussing an example of the Ruthenium-based dye tris(2,2′-bipyridyl) dichlororuthenium(II) hexahydrate (Ru) (Sigma–Aldrich) (~2% quantum yield and ~350 ns fluorescence lifetime) that when used with the multi-pulse approach and time-gated detection allows for high quality imaging that can easily be enhanced two orders of magnitude as compared to the normal approach (imaging with typical fluorescence microscopy).

Keywords Long lifetime probe · Multi-pulse excitation · Time-gated detection

Contents

1 Introduction 226
2 Theoretical Model 228
2.1 Time-Gated Detection 228
2.2 Multi-Pulse Approach 230
3 Experiment 235
3.1 Instrumentation 235
3.2 Preparation of Ruthenium Labeled IgG 236
3.3 Animals 236
3.4 Histology, Paraffin Sections 236
4 Results and Discussion 237
References 238

1 Introduction

As detection sensitivity reaches the single molecule level, we realize that the main limiting factor for many practical applications is the background generated in the sample. Most biological samples contain a small level of naturally occurring chromophores (from tryptophan, NADH, flavins, to porphyrin byproducts) as well as many impurities incorporated during necessary steps of sample preparation. Typically, the background signal covers a broad wavelength range and only fades in the far red spectral range. As a result, for many years researchers tried to develop probes emitting in the near infra-red (NIR) spectral range [1–7]. Typically the brightness of endogenous components is low, but the overwhelming abundance of them makes their contribution to the observed signal in tissue and cells significant. It is very difficult to reduce the contribution from autofluorescence without altering properties of the biological system [8–12] and typically the only choice is to increase the concentration of the dye to a level at which the fluorescence of the probe dominates the overall signal. However, when searching for low abundance biological markers, this is not easy and frequently impossible. Physiologically acceptable levels of the probe should thus be low, requiring an increased excitation intensity that in turn also increases the background.

Long efforts focused on the search for high brightness and red-emitting probes stimulated many innovative chemistry approaches and led to the development of many novel probes [13–18]. In effect many bright (high extinction coefficient and high quantum yield) fluorophores have been recently introduced that allowed for very sensitive imaging and single molecule studies. Unfortunately, such bright fluorophores inherently exhibit short fluorescence lifetimes and their emission overlaps easily with background components.

Notable progress in detection sensitivity has been promised by introducing long-lived fluorophores and time-gated detection [19–21]. Switching on the detector a short time after the excitation pulse significantly improves the signal-to-background ratio; especially when using long-lived, microsecond probes which allow for excellent suppression of the sample background and detection at a very low (practically zero) background level. The major limitations of such microsecond probes are low photon flux and extended detection time severely limiting the speed of imaging or in some cases even preventing the detection of kinetics of fast processes occurring in the sample.

Potential advantages of time-gated detection stimulated development of fluorescent probes with fluorescence lifetimes in the range of a few hundred nanoseconds. As an example probes based on metal–ligand complexes (MLC) have been developed, and probes like the Ruthenium-based dye Tris(2,2′-bipyridyl)dichlororuthenium(II) hexahydrate) offer over 300 ns fluorescence lifetime and very large Stoke's shift [13, 22]. Also, some new quantum dots exhibit emissive lifetimes in the range of 50–100 ns and have been successfully used in the imaging field [23, 24]. Lifetimes in the order of 100–500 ns are sufficiently long to comfortably apply time-gated detection to discriminate against the most common background signals and in the same time allowing for use in commercially available pulsed laser systems with a reasonable scanning time.

Recently we successfully used a metal–ligand probe with a 370 ns fluorescence lifetime for ocular tissue imaging using multi-pulse excitation technology [12], demonstrating a significant signal-to-background improvement. By using 10–20 pulses we were able to increase the signal-to-background ratio almost an order of magnitude. We now realize that by combining multi-pulse excitation and time-gated detection, we can easily increase the signal-to-background ratio over 100-fold with the initial probe signal significantly higher as compared to traditional single pulse excitation, i.e., a probe-to-background signal ratio that in a traditional experiments can only be achieved using a 100 times brighter probe. As extensive efforts to develop bright, long-lived red-emitting probes have only limited successes this new approach presents a great opportunity to utilize existing long-lived probes for biomedical diagnostics and imaging. In this chapter we present the theoretical model and experimental data demonstrating that low brightness, long-lived probes can present signals comparable to high brightness probes while yielding much better signal-to-background ratio.

2 Theoretical Model

2.1 Time-Gated Detection

Metal–ligand probes and many quantum dots offer long (over 100 ns) fluorescence lifetimes but rather low brightness (small extinction coefficient and low quantum yield) [13, 22–24]. Such long-lived probes present great potential only if efficient signals can be obtained over the majority of typical background components from tissue and cells with much shorter fluorescent lifetimes (i.e., below 10 ns) [25].

Time-gated detection has been successfully used to increase the ratio between signals of long-lived probes and a short-lived fluorescence background. To discuss the benefits of time-gated detection, we will consider a probe with fluorescence lifetime of 350 ns and the background with an average fluorescence lifetime of 10 ns; which is an overestimate of fluorescence lifetimes for typical tissue or cell backgrounds [25]. In an ideal detection system the ratio of the signal from the long-lived probe to the short-lived background will increase as the start time of the gate increases. For simplicity we assume that the initial steady-state intensity of the background and the probe are identical. In other words, the signal from the probe and signal from the background are equal when we do not use the gate. Typically such large background contribution would disqualify imaging or sensing experiment. Figure 1a shows time-dependent intensity decays for the probe and background. The relative initial intensities are adjusted so the integrated intensities over time (steady-state intensities) are equal. Since the probe's fluorescence lifetime is much longer, its time-dependent peak intensity is much lower and in the figure we also present the probe's intensity decay multiplied by 20. Figure 1b presents a bar representation of the relative signals from the probe and background when intensity is collected immediately after each excitation pulse (no gate applied). Figure 1c presents the relative signals from the probe and background when intensity is collected 20 ns after each excitation pulse (as marked in Fig. 1a). For the 20 ns delay the total signal of the probe decreases less than 5% but the background decreases almost 87%; resulting in a dramatic difference between the useful signal of the probe and the background. As the initial signal of the probe was only 50% of the total signal, detected after 20 ns it constitutes almost 88% of the total signal. In such a time-gated approach, both the signal of the probe and background are decreasing with the only advantage that the signal of the background decays much faster. The short-lived signal of the background quickly decays to values close to zero and the ratio of signals for the long-lived probe to the short-lived background increases exponentially. Obviously when time-gated detection is used the signal-to-background ratio will depend on the gate time delay, and theoretically for longer time delays one may achieve very high values of the ratio. However, one has to remember that in such a case the limiting factor becomes the dark signal for the detection system and how precisely we can measure a decreasing signal over the dark counts. In practice this will strongly depend on the detection system that is used. For the purpose of our simulation we arbitrarily assume that the cumulative (integrated) signals from probe and background have equal initial steady-state

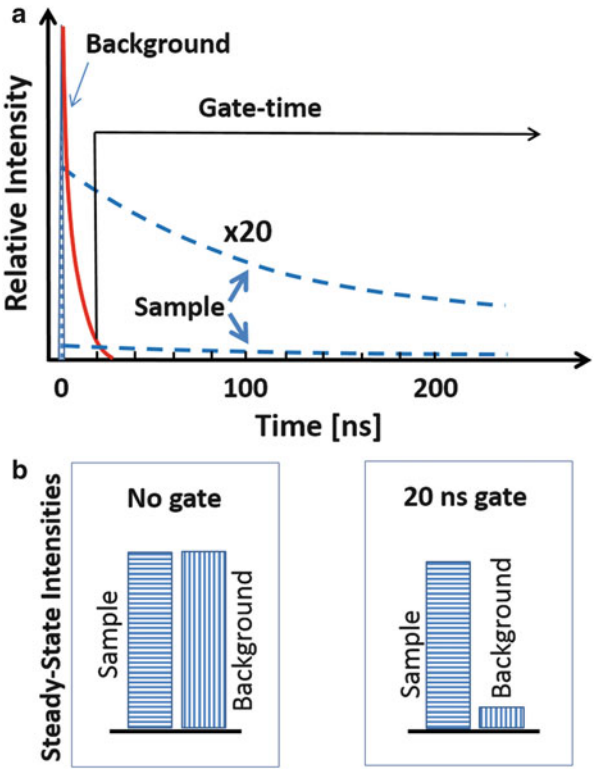

Fig. 1 (**a**) Time-dependent intensity decay for long-lived fluorophore sample (*dashed line*) and short-lived background (*solid line*) after pulse excitation. (**b**) Relative steady-state intensity contribution for the sample and background emissions collected immediately after pulse excitation. (**c**) Relative steady-state intensity contribution for the sample and background emissions collected with 20 ns time delay after pulse excitation (20 ns time-gate)

intensities and each is ten times larger than the detector dark count level. To find the optimal time-gate we consider the signal-to-noise ratio as:

$$R_{\mathrm{gt}} = \frac{\mathrm{Ip}_{\mathrm{gt}}}{\mathrm{Ib}_{\mathrm{gt}} + \mathrm{Id}_{\mathrm{gt}}},$$

where $\mathrm{Ip}_{\mathrm{gt}}$, $\mathrm{Ib}_{\mathrm{gt}}$, and $\mathrm{Id}_{\mathrm{gt}}$ are steady-state intensities measured starting with time-gate delay (gt) for probe, background, and dark current defined as follow:

$$\mathrm{Ip}_{\mathrm{gt}} = \int_{\mathrm{gt}}^{T} \mathrm{Ip}(t)dt; \quad \mathrm{Ib}_{\mathrm{gt}} = \int_{\mathrm{gt}}^{T} Ib(t)dt; \quad \mathrm{Id}_{\mathrm{gt}} = \int_{\mathrm{gt}}^{T} \mathrm{Id}(t)dt,$$

where gt is the opening time for the gate and T is the time separation between two consecutive pulses ($T = 1/\mathrm{RR}$). Figure 2 shows the dependence of the signal-to-background ratio as a function of gate opening time. At the initial time $\mathrm{gt} = 0$ (no gate) the signal from sample and background are equal and the dark counts are 10%, 20%, and 50% of sample counts, respectively. As the gate time increases the ratio quickly improves in favor of the probe signal. The ratio reaches a maximum at about 60 ns delay time for 10% of dark reading and then slowly decreases.

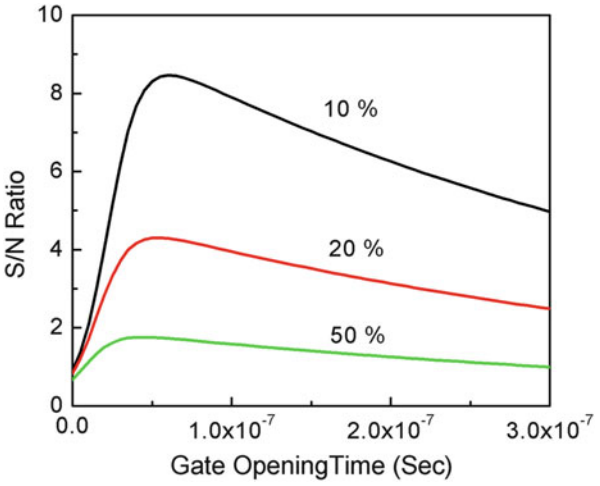

Fig. 2 Ratio of total intensities (sample-to-background) as function of time-gate delay assuming the dark signal to be of 10%, 20%, and 50% of initial signals of sample. The signals from sample and background are assumed to be equal for no gate (time-gate equal zero)

Through this approach, it is possible to optimize the opening time for the gate to maximize the ratio for any fluorescence lifetime of the probe and the background. Both the delay time for gate opening and the maximum ratio (signal-to-background) enhancement strongly depend on the dark current contribution. For our example the maximum ratio enhancement is about 8.5-fold. However, if the dark detector reading is five times higher than assumed, the maximum enhancement will be only 1.75 and if it is 5 times smaller than assumed it increases to over 40. It is clear that in real experiments where the signals are small (i.e., not much larger than background) the achievable enhancement generated by time-gating is limited. With low brightness, long-lived MLCs this is a common problem, especially when efficient labeling is not possible or the access of long-lived probe alters physiological conditions making it impossible to increase the concentration of the probe.

2.2 Multi-Pulse Approach

We recently introduced a new approach based on a burst of pulses which allows for a significant increase of initial signal of the long-lived probe over a short-lived background [12, 26]. It is important to comprehend the concept of a multi-pulse experiment. In a typical time-resolved system we use a pulsed excitation and collect the intensity decay over time. We collect the entire time-trace including the excitation pulse and use a reconvolution analysis to resolve the pulse and intensity decays [27]. If the fluorescence lifetime is much longer than the excitation pulse duration we can only consider the intensity decay without pulse reconvolution analysis using the so-called tail-fitting approach. In fact, in most systems it is easy to start data collection with any time delay after the triggering pulse. For the probe that has a 350 ns fluorescence lifetime, to completely decay between two

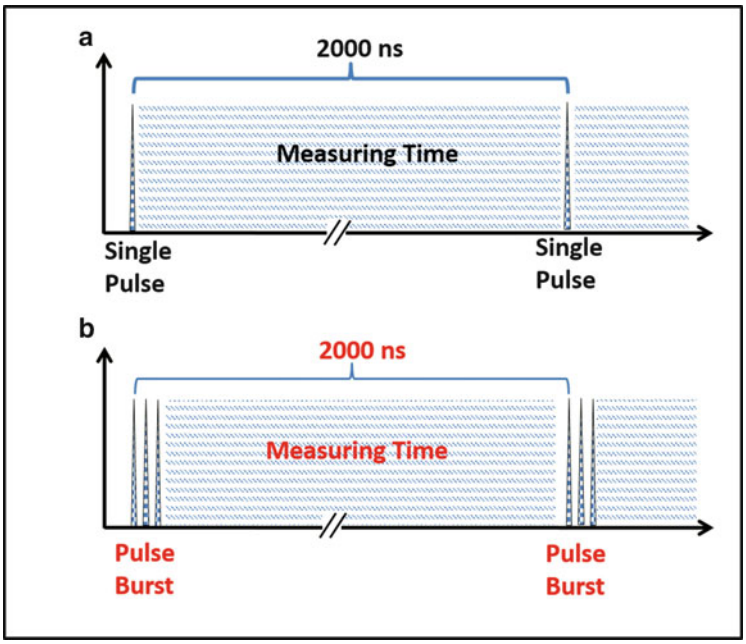

Fig. 3 Concept for detection with single pulse (*top*) and burst of pulses (*bottom*)

consecutive pulses we should use low-repetition rate (RR), typically 500 kHz or below, which results in a pulse-to-pulse separation of 2,000 ns. In such cases, the pulse shape and duration are considered negligible since most typical sources will have pulses shorter than 1 ns. Let us now consider excitation with a burst of short, picosecond pulses that have a high repetition rate. A typical commercial laser diode can work with a repetition rate of 80 MHz, resulting in a 12.5 ns pulse-to-pulse separation. It is also easy to lower the repetition rate or shoot a few pulses and then have the system rest for a fixed time like 2 μs. In this case we are creating a burst of pulses with a repetition rate of 500 kHz. Each burst can have any desired number of pulses that have a much higher internal repetition rate. The concept is schematically shown in Fig. 3. The top represents a single pulse experiment with a pulse repetition rate of 500 kHz where data are collected between pulses. The bottom shows the burst of 3 pulses with a high internal repetition rate 80 MHz repeated within the low 500 kHz burst repetition rate. The data are collected between the last pulse and the first pulse of the incoming burst. The duration of the burst is very small (37.5 ns) compared to the burst separation (2,000 ns).

It is important to realize the fundamental differences between an excitation with a single δ-pulse, a broad pulse, and an excitation with a burst of δ-pulses. For instance, a burst of 3 pulses with an internal repetition rate of 80 MHz will take 37.5 ns. Similarly we can use one broad 37.5 ns excitation pulse that excites the same number of molecules. The concept is schematically presented in Fig. 4. The number of excited long-lived molecules increases during the pulse duration reaching to the number of molecules excited by the one short pulse. When we

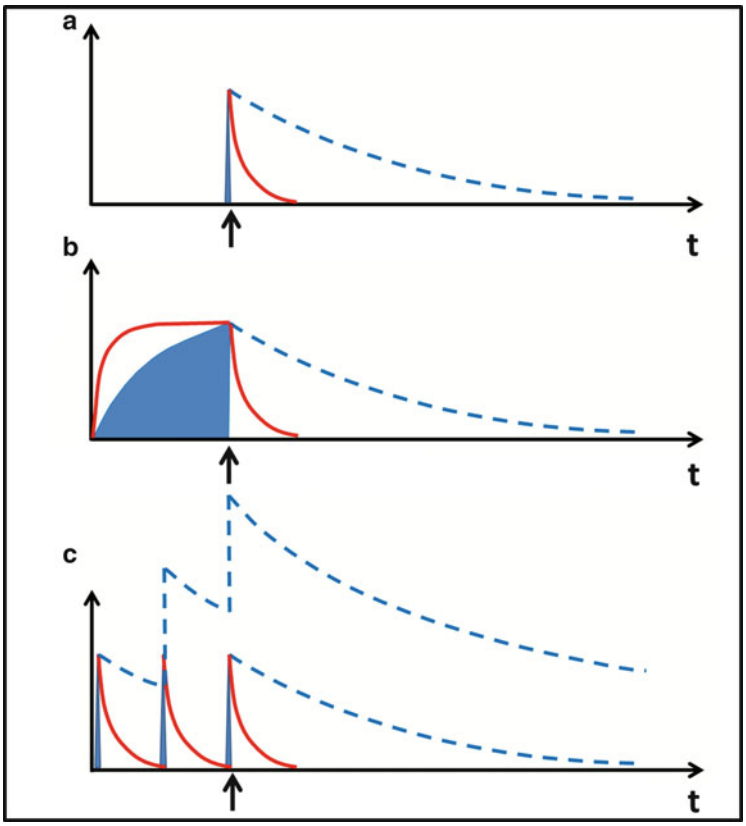

Fig. 4 Concept representing intensity decay signals with single pulse (**a**), a broad 37.5 ns pulse (**b**), and burst of 3 pulses with internal repetition rate 80 MHz spaced over 37.5 ns (**c**). The *arrow marks* the point for starting detection (37.5 ns)

measure the steady-state intensity, the relative intensities will depend on number of molecules excited in a single pulse, broad pulse, and a burst of 3 pulses. If we adjust the pulse intensities so that the number of photons in a single pulse, 3 pulse burst, and one broad 37.5 ns pulse are the same, the measured steady-state intensities will be the same in all cases. When we collect data for the entire time and do pulse reconvolution, the result will be the same steady-state intensity for a single pulse, one broad pulse, and a burst of pulses independently of the fluorescence lifetime of the probe. This is because the intensity decay is a property of the probe and does not depend on the excitation pulse profile. However if we start our data collection at a time 37.5 ns as marked by the arrow (the end of the last pulse in the burst or the end of broad pulse) we will get completely different results when we compare signals from a long lifetime (much longer than the pulse separation in the burst) and one from a short lifetime (shorter than the pulse separation in the burst). The total number of excited molecules with a single pulse, a broad pulse, and a burst of pulses will be constant for each configuration (we assume we work much below saturation

conditions). However, for the burst of 3 pulses the number of excited long-lived molecules remaining in the excited state after the last pulse in the burst will be much greater. The number of long-lived molecules in the excited state increases from pulse-to-pulse in the burst (only few molecules decay between pulses) while the number of excited molecules with a short lifetime decays quickly and will be the same after each pulse (short-lived molecules completely decay to the ground state between two consecutive pulses). Starting the measurement after the last pulse creates a favorable situation for long-lived molecules. In other words, with each of 3 pulses we excited the same number of short-lived molecules and long-lived molecules but most of the short-lived ones decayed before the next pulse, resulting in a relative increased number of excited long-lived molecules.

For the majority of sensing and imaging experiments, the number of molecules excited by a single pulse is much smaller than the total number of available chromophores in the excitation volume. In this case, the number of excited molecules after n consecutive excitation pulses in the burst can be described by [12, 27]:

$$N(\tau, n, \mathrm{RR}) = N_\mathrm{e} \frac{1 - e^{-n/\tau \cdot \mathrm{RR}}}{1 - e^{-1/\tau \cdot \mathrm{RR}}},$$

where τ is the fluorescence lifetime, RR is the repetition rate in the pulse burst, and N_e is the number of molecules excited with the single pulse. For low-repetition rates as compared to the fluorescence lifetime ($\mathrm{RR} \ll 1/\tau$) after each pulse, the number of excited molecules is constant (all fluorophores decay after each pulse) and equal to N_e. As the repetition rate increases, not all the fluorophores decay to the ground state. Each pulse adds new molecules to the excited state, which leads to the apparent increase of the observed fluorescence signal. Figure 5 shows the number of molecules in the excited state that have different fluorescence lifetimes for a RR

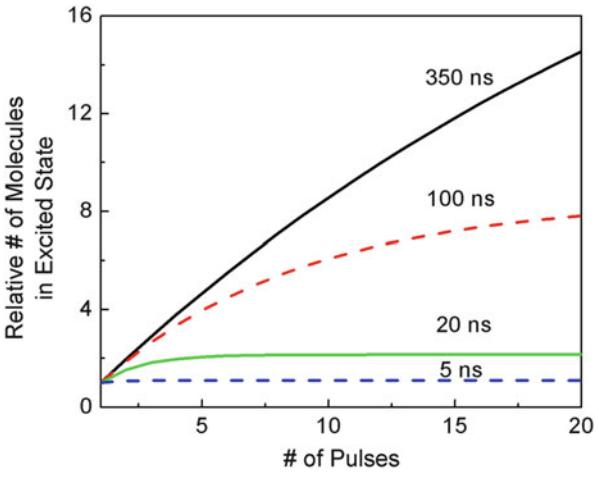

Fig. 5 Relative number of molecules in the excited state as a function of number of pulses in the burst. The internal repetition rate in the burst is 80 MHz

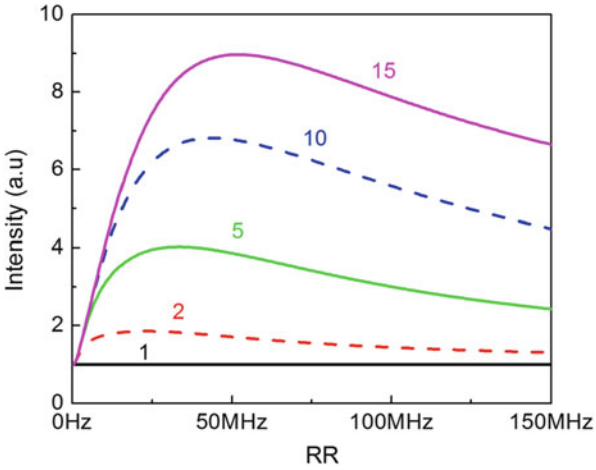

Fig. 6 Ratio of intensities of the probe (350 ns) and the background (10 ns) as function of burst internal repetition rate for a different number of pulses in the bursts

of 80 MHz after each consecutive pulse (up to 20 pulses in the burst). For short fluorescence lifetimes, molecules decay after each pulse and the number of molecules in the excited state after each pulse is constant. As the fluorescence lifetime increases we can observe an increase of molecules in the excited state after each consecutive pulse, reaching an equilibrium (the number of excited molecules is equal to the number of decaying molecules between two consecutive pulses). For long fluorescence lifetimes (longer than 200 ns) the increase is practically linear for 10 pulses with repetition rates in the burst larger than 20 MHz.

Since the number of molecules in the excited state depends on the fluorescence lifetime and the repetition rate in the burst, it is valuable to consider the ratio of the signal from the sample (350 ns fluorescence lifetime) to the signal of the background (10 ns) as a function of the number of pulses and the repetition rate in the burst [12, 26]. Figure 6 presents the ratio of intensities of the probe (350 ns) to the background (10 ns) as a function of the burst internal repetition rate for a different number of pulses in the bursts. For a single pulse, the ratio is 1 since we assumed that the steady-state intensities for the sample and background are identical. For an increasing number of pulses in the burst a clear maximum can be observed. Already for 2 pulses in the burst spaced by about 25 ns (~40 MHz apparent repetition rate), the signal of the probe almost doubles, and for 10 pulses in the burst with repetition rate ~40 MHz, the signal from the probe is ~7 times higher than the background.

From this simulation it is clear that just by using bursts of 5–10 pulses, we can improve the signal-to-background ratio four to seven times. Such a dramatic improvement will have a profound effect on image resolution and quality as presented in [12]. We also realize that it will be very beneficial to use time-gated detection with multi-pulse excitation in a similar fashion as earlier described for single pulse experiments. We consider the previous case of the probe with a fluorescence lifetime of 350 ns and a background with average fluorescence lifetime of 10 ns. Both signals have identical steady-state intensities. The dark current

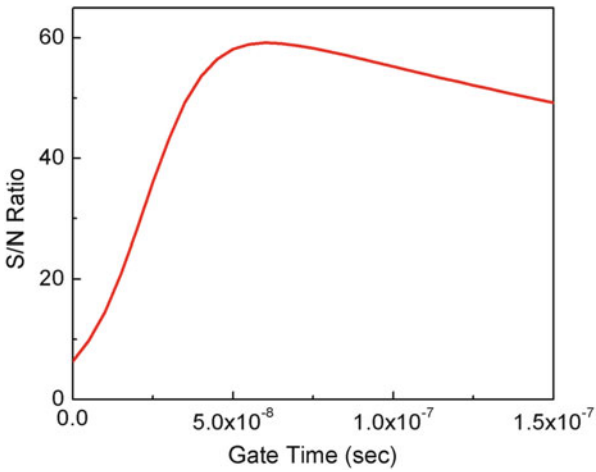

Fig. 7 Signal-to-background ratio for 350 ns sample and 10 ns background as a function of the gate delay time for 10 pulses in the burst

is 10% of each initial signal (probe or background). In a single pulse experiment, a time-gate of about 60 ns improves the signal-to-background ratio about eightfold. Using 10-pulse bursts our initial signal of the probe increases about seven times. Figure 7 shows the signal-to-background ratio as a function of the gate delay time. For 60 ns time delay for the gate the signal-to-background ratio improves almost 60-fold. This is a magnificent improvement of image quality. For our simulation we started with rather poor initial conditions, and by using smaller dark current (or relatively higher probe intensity) the improvement can be dramatic – much greater than 2 orders of magnitude.

3 Experiment

3.1 Instrumentation

Laser excitation was provided by a pulsed laser diode (LDH-P-C470B) emitting 470 nm light and driven by a PDL 828 "Sepia II" driver. This driver was operated at 40 MHz and configured so that the pulse train consisted of bursts of laser pulses with 40 MHz RR and followed by a series of blank "pulses." In the case of conventional, single pulse excitation, one pulse from the 470 nm diode laser was followed by 124 blank pulses, exciting the sample with an *effective* repetition rate of 320 kHz. For the case of excitation by a burst of n pulses, the burst would be followed by 125-n blank pulses, so that the total pulse train remained 125 pulses long, or 3.125 μs in length. Because the base oscillator operated at 40 MHz, there were 25 ns between each excitation pulse. In order to differentiate the advantageous pumping of long-lived dyes from the increased intensity that simply results from increased repetition rate of the excitation source, only the fluorescence following

the final excitation pulse was analyzed. For example, when 10 pulses were used, the final pulse arrived 250 ns after the synchronization pulse from the laser driver. So only photons arriving between 251 ns and the end of the synchronization period at 2,100 ns were analyzed. The *effective* synchronization period was therefore 1,849 ns, and this was kept constant for all excitation schemes. However, the *effective* synchronization period was shifted to start at the peak of the last pulse in the excitation burst.

Measurements were performed on a MicroTime 200 time-resolved, confocal microscope by PicoQuant. The excitation and emission light was focused by a 60× 1.2 NA Olympus objective in an Olympus IX71 microscope, and the emission light was filtered by a 488 long wave pass filter before passing through a 50 μm pinhole. Detection was made by a hybrid photomultiplier assembly. The resolution of the time correlated single photon counting (TCSPC) module was set to 512 ps/bin in order to facilitate the detection of the long-lived Ruthenium dye, producing a measurement window around 1.2 μs in length. All data analysis was performed using the SymPhoTime software, version 5.3.2. All experimental equipment and the SymPhoTime software were provided by PicoQuant, GmbH as part of the MicroTime 200 system.

3.2 Preparation of Ruthenium Labeled IgG

Donkey anti-mouse IgG (amIgG) was mixed with a freshly prepared 100 mmol L^{-1} bicarbonate solution (0.1–0.4 mL), and to this was added a small volume of Bis (2,2′-bipyridine)-4,40-dicarboxybipyridine-ruthenium di(*N*-succinimidyl ester) bis (hexafluorophosphate) (active Ru dye) (Sigma–Aldrich) in DMF (less than 5% by volume). After 18 h of gentle shaking, excess free dye was separated from the labeled amIgG by passing over a Sephadex G-25 desalting column (GE Electric, USA).

3.3 Animals

All animal-related procedures were approved by the Institutional Animal Care and Use Committee (IACUC) of the UNTHSC and are in compliance with the ARVO Statement for the Use of Animals in Ophthalmic and Vision Research.

3.4 Histology, Paraffin Sections

Retired breeder Brown Norway rats (Rattus Norvegicus) were sacrificed with an overdose of pentabarbitol, after which the eyes were enucleated, immersion fixed in

4% phosphate-buffered formalin, and processed for paraffin embedding. Paraffin sagittal retinal sections through the optic nerve head (5 mm thick) were cut and deparaffinated in xylene (Fisher Scientific, NJ, USA), re-hydrated using a descending series of ethanol washes, and processed for immunohistochemical staining. The deparafinized and re-hydrated retinal sections were blocked with 5% Donkey serum and 5% BSA in PBS, and then treated with primary antibody: mouse anti-tubulin III antibody (Sigma–Aldrich) diluted 1:500 and incubated overnight at 4°C. Secondary incubation for 1 h was carried out with a 1:1,000 (1 μg/mL) dilution of the secondary antibody donkey anti-mouse IgG conjugated with Ru fluorophore. Next the samples were analyzed on the MicroTime 200 time-resolved, confocal microscope by PicoQuant.

4 Results and Discussion

To demonstrate how multi-pulse excitation with time-gated detection works, we selected ocular tissue samples for which autofluorescence is a significant problem. We used rat retinal tissue samples stained with Ru-labeled IgG to detect the β-tubulin III. We performed immunostaining of rat retinal ganglion cells (RGCs) using the RGC specific marker β-tubulin III. Apart from being a RGC marker, β-tubulin III contributes to microtubule stability in neuronal somas and axons, by playing an important role in axonal structure [28]. Moreover, β-tubulin III plays a crucial role in axon guidance and maintenance [29].

The labeling with Ru-labeled IgG is sufficient, but the sample brightness is limited and the background contribution is significant. Figure 8 (top-down) presents the results obtained with single pulse excitation, and 5 and 20 pulses burst excitation. The internal repetition rate in the burst was 40 MHz, which we theoretically predicted would be optimal for enhancement, and the external repetition rate for bursts was 300 kHz. The single pulse experiment made with a 300 kHz repetition rate (top left corner frame) presents a rather dim image, and when the gate is applied (top frames to the right) we can see contours of labeled structures. The lower frames show the experiments with 5 and 20 pulses in the burst, respectively. Already 5 pulses results in a significant brightness increase and 20 pulses produce excellent image quality. Application of time gates of 10, 50, and 100 ns highly increases image quality, clearly showing the labeled structures without background contribution. Inspection of the images also shows that 50–100 ns is the optimal time delay for the gate resulting in clear high intensity images. In conclusion, we have demonstrated a method by which the substantial contributions of background fluorescence can be significantly reduced in imaging and confocal microscopy. The time-gated multi-pulse method with long-lived Ru probes gives excellent results and can be used for tissue samples in which autofluorescence is especially strong. The method does not require long collection times or heavy labeling, thus making it ideal for high-resolution, laser scanning, confocal microscopy. Detailed analysis of such images may lead to fully quantitative measurements of labeling

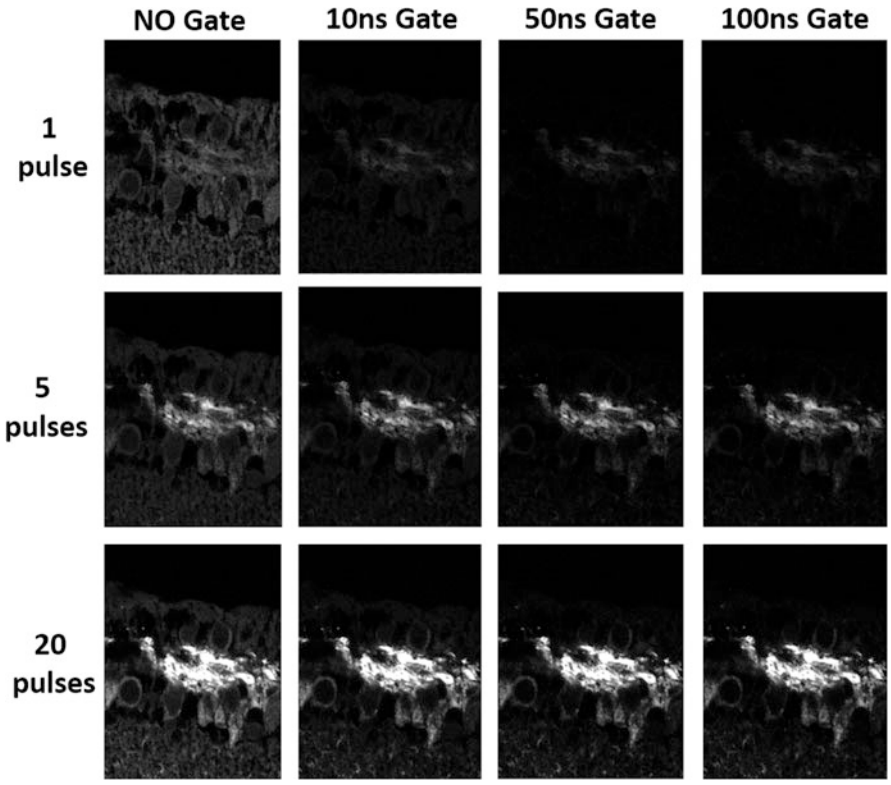

Fig. 8 Fluorescence intensity images of Ru-labeled IgG detecting the β-tubulin III in the rat retinal tissue with single, 10, and 20 pulses in the burst (*top-down*) and time delay for gate opening 0, 10, 50, and 100 ns

efficiency that can be used to detect a variety of transient cellular processes or disease stages.

Acknowledgements This work was supported by the National Institutes of Health (USA): NIH-5R01 EB012003 and NIH-R21EB017985-01A1 (Z.G), and NSF-CBET 1264608 (I.G).

References

1. Lakowicz JR (2006) Principles of fluorescence spectroscopy, 3rd edn. Springer, New York
2. Valeur B, Berberan-Santos M (2012) Molecular fluorescence: principles and applications, 2nd edn. Wiley-VCH, Weinheim
3. Jameson DM (2014) Introduction to fluorescence. CRC/Taylor and Francis Group, Boca Raton
4. Haugland RB (1996) Handbook of fluorescent probes. Molecular Probes Inc., Eugene
5. Nolting DD, Gore JC, Pham W (2011) Near-infrared dyes: probe development and applications in optical molecular imaging. Curr Org Synth 8:521–534

6. Fischer GM, Isomaki-Krondahl M, Gottker-Schnetmann I et al (2009) Pyrrolopyrrole cyanine dyes: a new class of near-infrared dyes and fluorophores. Chem Eur J 15:4857–4864
7. Achilefu S (2010) The insatiable quest for near-infrared fluorescent probes for molecular imaging. Angew Chem Int Ed 49:9816–9818
8. Schnell SA, Staines WA, Wessendorf MW (1999) Reduction of lipofuscin-like autofluorescence in fluorescently labeled tissue. J Histochem Cytochem 47:719–730
9. Clancy B, Cauller L (1998) Reduction of background autofluorescence in brain sections following immersion in sodium borohydride. J Neurosci Methods 8:97–102
10. Cowen T, Haven AJ, Burnstock G (1985) Pontamine sky blue: a counterstain for background autofluorescence in fluorescence and immunofluorescence histochemistry. Histochemistry 82:205–208
11. Schneckenburger H, Wagner M, Weber P et al (2004) Autofluorescence lifetime imaging of cultivated cells using a UV picosecond laser diode. J Fluoresc 14:649–654
12. Rich RM, Gryczynski I, Fudala R et al (2013) Multiple-pulse pumping for enhanced fluorescence detection and molecular imaging in tissue. Methods 66(2):292–298
13. Damas JN, DeGraff BA (1991) Design and applications of highly luminescent transition metal complexes. Anal Chem 17:829–837
14. Laursen BW, Krebs FC (2001) Synthesis, structure, and properties of azatriangulenium salts. Chem Eur J 7:1773–1783
15. Maliwal BP, Fudala R, Raut S et al (2013) Long-lived bright red emitting azaoxotriangulenium fluorophores. PLoS One 8(5):e63043
16. Kelloff GJ, Krohn KA, Larson SM et al (2005) The progress and promise of molecular imaging probes in oncologic drug development. Clin Cancer Res 11:7967–7985
17. Jaffer FA, Weissleder R (2005) Molecular imaging in the clinical arena. JAMA 293:855–862
18. Achilefu S (ed) (2010) Concept and strategies for molecular imaging. Chem Rev 110:2575–2755
19. Cubeddu R, Ramponi R, Taroni P et al (1990) Time-gated fluorescence spectroscopy of porphyrin derivatives incorporated into cells. J Photochem Photobiol B 6:39–48
20. Periasamy A, Siadat-Pajouh M, Wodnicki P, Wang XF, Herman B (1995) Time-gated fluorescence microscopy in clinical imaging. Micros Anal (March):33–35
21. Dahan M, Laurence T, Pinaud F (2001) Time-gated biological imaging by use of colloidal quantum dots. Opt Lett 26:825–827
22. Terpetschnig E, Szmacinski H, Malak H et al (1995) Metal–ligand complexes as new class of long-lived fluorophores for protein hydrodynamics. Biophys J 68:342–350
23. Resch-Genger U, Grabolle M, Cavaliere-Jaricot S et al (2008) Quantum dots versus organic dyes as fluorescent labels. Nat Methods 5(9):763–775
24. Seo J-T, Raut S, Abdel-Fattah M et al (2013) Time-resolved and temperature-dependent photoluminescence of ternary and quaternary nanocrystals of CuInS2 with ZnS capping and cation exchange. J Appl Phys 114:094310
25. Rich RM, Stankowska DL, Maliwal BP et al (2013) Elimination of autofluorescence background from fluorescence tissue images by use of time-gated detection and the AzaDiOxaTriAngulenium (ADOTA) fluorophore. Anal Bioanal Chem 405:2065–2075
26. Shumilov D, Rich RM, Gryczynski I et al (2014) Generating multiple-pulse bursts for enhanced fluorescence detection. Methods Appl Fluoresc 2:024009
27. Gryczynski I, Luchowski R, Bharill S et al (2009) Nonlinear curve-fitting methods for time-resolved data analysis. Chapter 12. FLIM microscopy in biology and medicine (Hardcover) by Ammasi Periasamy (ed), Robert M. Clegg (ed)
28. Niwa S, Takahashi H, Hirokawa N (2013) β-Tubulin mutations that cause severe neuropathies disrupt axonal transport. EMBO J 32:1352–1364
29. Tischfield MA, Baris HN, Wu C et al (2010) Human TUBB3 mutations perturb microtubule dynamics, kinesin interactions, and axon guidance. Cell 140:74–87

Pattern-Based Linear Unmixing for Efficient and Reliable Analysis of Multicomponent TCSPC Data

Ingo Gregor and Matthias Patting

Abstract A method for a reliable quantitative analysis of fluorescence lifetime imaging microscopy (FLIM) data is presented. It is based on the linear unmixing of the intensity decay on the basis of selected reference patterns. This approach allows to use decays that are not mono-exponential without increasing the complexity of the analysis. This is a major benefit when working with labeled biomolecules or using autofluorescent cellular chromophores.

The method can be used intuitively and is fast. Furthermore, based on the reference patterns and the amount of recorded photons, one can easily determine confidence levels of the obtained results. We demonstrate that for a decomposition to three patterns of common chromophores, one achieves a standard deviation of better than 10% for as few as 1,000 photons per pixel, where the total amplitude of such a signal will show an error of 3% due to shot noise. Indeed, the accuracy of the results is very close to a maximum-likelihood estimator that defines the absolute limit for this kind of problem.

Keywords Fluorescence lifetime imaging microscopy (FLIM) • Linear unmixing • Spectrally resolved imaging • Time-resolved imaging • Time-correlated single-photon counting (TCSPC)

I. Gregor (✉)
Third Institute of Physics, Georg-August-University, Göttingen, Germany
e-mail: ingo.gregor@phys.uni-goettingen.de

M. Patting
PicoQuant GmbH, Berlin, Germany
e-mail: patting@picoquant.com

P. Kapusta et al. (eds.), *Advanced Photon Counting: Applications, Methods, Instrumentation*, Springer Ser Fluoresc (2015) 15: 241–264, DOI 10.1007/4243_2014_70,

Contents

1 Introduction 242
2 Theory 243
2.1 Statement of the Problem 243
3 Description of the Algorithm 244
3.1 Preparation of the Raw Data 244
3.2 Optimization and Data Preparation for Pattern Analysis 245
4 Figures of Merit 246
4.1 Validation 246
4.2 Error Analysis 247
4.3 Limits of the Method 247
5 Comparison to Other Methods 248
5.1 Comparison to a Maximum-Likelihood Estimator 249
5.2 Comparison to Nonnegative Least Squares 249
5.3 Comparison to Phasor Analysis 249
6 Application to FLIM 252
6.1 Choosing the Pattern 252
6.2 Moments in Time 253
6.3 Decay Diversity Map 254
6.4 Exponential Fitting Versus Pattern Analysis 256
6.5 Dealing with Mixed Signals 257
6.6 Post-processing 259
7 Extension to Spectrally Resolved FLIM 260
8 Conclusion 262
References 262

1 Introduction

The fluorescence lifetime is a well-known and widely used reporter for the physical or chemical state of a fluorescent molecule. Common examples are the oxidation state of NAD/NADH$^+$ or FAD/FADH$^+$; the water accessibility of tryptophan, calcium, or chloride concentration; and the proximity of acceptor molecules in FRET constructs. All these parameters provide a key to answer important problems in biological or medical research or diagnostics. Fluorescence lifetime imaging microscopy (FLIM) can visualize these processes with subcellular resolution and high temporal dynamics [1–4]. Therefore, FLIM has become a valuable method in biophysical and biochemical research. However, despite of its superior capabilities, the method has not yet become a routine tool in biological or clinical research, but is still considered to require expert knowledge. The technologies and instrumentation to record the data with high accuracy and resolution have evolved considerably since the introduction of the method in the 1990s. Yet, the applicability did not keep the pace. One reason may lie in the instrument costs, but more importantly, it is just not straightforward to interpret the data in a general and appropriate way.

The usual way to process and analyze FLIM images is firstly to calculate the average fluorescence lifetime per pixel, i.e., the average arrival time of the fluorescence photons after the excitation pulse. This data can be taken as a basis to select pixels of similar kind (regions of interest, ROI) in order to gather sufficient data to

fit an exponential decay model to the photon data. This procedure requires supervision by a trained scientist in order to select meaningful ROIs and judge the quality of the fit. The introduction of the phasor approach [5–7] for the analysis of FLIM images has been a valuable progress to make the analysis more intuitive and to give a quick insight into the data. However, this method has also not yet been able to find widespread application as a standard tool for biomedical research.

The approach that we describe here aims to deliver an intuitive and yet quantitative method to analyze FLIM data based on TCSPC recordings in a general way. The concept is relatively simple. The algorithm looks for the best linear combination of a selection of fixed decay patterns that represents the actual pixel data. However, the method does not give a suggestion as to which and how many patterns should be included in the analysis. This is not a problem since in the vast majority of the practical cases, the number of labeled species is known. The necessary patterns can be obtained and tested in appropriate control samples.

2 Theory

In this section we describe the basic idea underlying the method and the necessary mathematical framework in order to obtain a good-enough solution of the presented problem.

2.1 Statement of the Problem

Fluorescence typically decays within nanoseconds. The temporal decay is characteristic for a fluorophore in a defined environment. If one tries to measure the fluorescence decay of a homogeneous sample of only one type of fluorophore using repetitive short pulse excitation, one obtains the convolution of the instrument response function (IRF) and the decay behavior. The normalized measured function gives the probability density function $p(t)\,dt$, describing how many photons per time interval dt are expected from the fluorophore. We refer to this function as the pattern of the fluorophore.

Measuring a sample containing multiple fluorophores, the measurement will yield a superposition $I(t)\,dt$ of individual patterns [8]:

$$I(t)\,dt = \sum_i n_i p_i\,dt, \tag{1}$$

where n_i denotes the amount of fluorophore i. In a pixel-wise sampled measurement of an inhomogeneous specimen, a typical task is finding the respective n_i in each pixel. An analogous quest occurs in a spectrally resolved measurement, where the $p_i(\lambda)\,d\lambda$ would resemble the spectral detection probabilities. What looks mathematically trivial becomes numerically extremely challenging. The most important

obstacles are: (a) The patterns decay exponentially; therefore, they are self-similar and it is not practicable to find even nearly orthogonal coordinates. (b) The Poissonian statistics of photon emission leads to highest relative noise where the most significant differences between patterns are found and prevents successful application of algorithms based on finding least squares. (c) All meaningful values of the variables in (1) are constrained to positive numbers leading to problems when applying classical matrix factorization methods. Here, we describe an approach that allows quantitative discrimination with high reliability.

3 Description of the Algorithm

3.1 Preparation of the Raw Data

Typically, TCSPC instruments sample the fluorescence decay on a linear timescale using a bin width of a few picoseconds. For photon numbers in the order of 1,000 per pixel, the raw data typically will have more bins than photons. For a quantitative evaluation, this is rather unfortunate. Therefore, we conduct several steps to convert the raw data into a consistent format. In the first step, the TCSPC data is binned into bins of width 32 ps. This resolution will provide sufficient information for the decay analysis as the width of the IRF is usually in the order of 50 ps to 100 ps due to the detector timing uncertainties.

Second, the data is shifted such that the center of gravity of the IRF falls into the 33rd bin (about 1 ns). This step is crucial if the data is to be analyzed using pattern functions that were obtained from separate experiments. The timing variation in the synchronization between the laser source and the TCSPC electronics will lead to a shift of the exact position of the IRF in time. If one does not compensate for this, the analysis will lose accuracy.

An optional final step is to re-bin to a multiple-tau scale:

$$\tau_j = \delta \begin{cases} 1 & \mid \quad j < 33, \\ 2^{\lfloor j-33 \rfloor / 8} & \mid \quad \text{else}, \end{cases} \tag{2}$$

with the base resolution of $\delta = 32$ ps. This follows the rationale that the amplitude of decay components with a time constant of $k \sim 1/\tau_j$ will have dropped down to $<0.1\%$ after $t \sim 8\,\tau_j$. Therefore, this data representation conserves most of the original information but reduces the amount of memory by a factor of 5 to 10, depending on the repetition frequency and the base resolution of the instrument. A second benefit of this binning is the substantial reduction of photon noise in the time bins distant to the excitation pulse. For bins with low photon numbers, the sensitivity of the discriminator [see (4)] is low; therefore, the binning can help to improve the convergence of the algorithm to find the minimum of (4).

This processing of the data has to be done only once after the recording of the data. It is necessary to have a good estimate of the temporal center of gravity of the

IRF. It should be always measured in addition to the decay measurement of the sample of interest, if possible. If there is no possibility to do so, one alternatively can compute an appropriate estimate of this function using the algorithms described in the literature (e.g., [9]). For the purposes of the method described here, they usually work reasonably well.

3.2 Optimization and Data Preparation for Pattern Analysis

In order to perform a fast and reliable computation of the fractional intensities, we process the preconditioned data depending on the selection of patterns $P_i(\tau)\,d\tau$ that all have the same data representation as the recorded pixel data. The goal of further reducing the size of the data (i.e., the number of time bins) is primarily to reduce the noise and secondly to speed up the evaluation. Noise reduction is a crucial point in the analysis of data where the noise is dependent on the signal itself rather than defined by the sampling bandwidth. However, this is an optional step and the method will also work just using the raw data that has been shifted in time, accordingly.

In this second step, the data is binned a second time depending on the patterns chosen for the analysis. The strategy to obtain the new bins is as follows: First we define a vector k with the elements $k = \{1, 17, 33, k_4, \ldots, k_l\}$. Starting with $m = 4$ and bin $b = 34$, we determine the order of the patterns for bin b in terms of amplitude. We set $k_m = b$ and subsequently $m = m + 1$, if any change in the sequence of the three biggest amplitudes compared to the sequence in $b' = b - 1$ is found. We repeat this step for every b until we reach the last bin $b = b_{\text{end}}$. The last element of k is given by the index of the last bin of the patterns $k_l = b_{\text{end}} + 1$.

Using the vector k, we obtain the compact representation $T_i(m)\,dm$ of the pattern $P_i(\tau)\,d\tau$ as

$$T_i(m)\,dm = \sum_{\tau=k_m}^{k_{m+1}-1} P_i(\tau)\,d\tau \text{ with } m \in \{1, 2, \ldots, l-1\}. \tag{3}$$

Data recorded in different spectral channels or after different excitation pulses (pulsed interleaved excitation (PIE) experiments) is processed identically.

The remaining task is to solve (1) for n_i any pixel. The numerical solution of this problem is found by minimizing the Kullback–Leibler discrepancy Δ_{KL} [10]:

$$\Delta_{\text{KL}} = \sum_b \tilde{I} - \hat{I} + \hat{I}\left(\ln \hat{I} - \ln \tilde{I}\right), \tag{4}$$

where the $\tilde{I}$ represents the measured decay and $\hat{I}$ represents the approximation that was obtained by

$$\hat{I} = T\hat{n}\,. \tag{5}$$

One can easily show that the minimum of (4) is equivalent with the maximum likelihood for data showing a Poissonian noise figure. An efficient algorithm using multiplicative update rules to find a positively defined solution to this problem has been described by Lee and Seung [11] and has been successfully applied to similar problems [12, 13]. In short terms, the algorithm starts from a suitably chosen (positively confined) starting vector $\hat{n}_0$ and determines the local gradient. The step-size is chosen such that the increment of the coordinate vector can be expressed as a multiplication with a positively constrained scaling vector $\gamma : \hat{n}_{i+1} = \gamma \hat{n}_i$.

4 Figures of Merit

4.1 Validation

A quantitative and experimental validation of the method was done by measuring homogeneous solutions of mixtures of labeled secondary antibodies in different compositions. We selected the fluorescent labels *Cy3*, *TRITC*, and *Texas Red*. The decay patterns of the individual probes are shown in Fig. 1. The stock solutions of the respective conjugate were diluted to have approximately the same concentration. Then, defined amounts of each conjugate were mixed together to form a sample solution. A droplet of the final sample solution was placed on top of a coverslip and a FLIM image of this solution was recorded using a two-photon microscope (Olympus FV1000 equipped with a Coherent Chameleon and PicoQuant TCSPC upgrade[1]) in a single detection channel (λ_{em} = 500 nm to 540 nm). The resulting images were analyzed using the described method, and the obtained amplitudes for each component were analyzed. As volume errors in pipetting such small amounts of liquids can be substantial, the data was first analyzed globally, i.e. all photons of the image were added together in order to obtain a highly accurate ratio of the respective dyes. In a next step, the data was analyzed pixel-wise and the distribution of the obtained dye ratios was determined.

Of course, the three pure samples do not show the same molecular brightness. However, the analysis is based on patterns that are normalized to unit area. In order to obtain the correct amounts, one has to divide the amplitudes by the respective molecular brightness.

[1] http://www.picoquant.com/products/category/fluorescence-microscopes/lsm-upgrade-kit-compact-flim-and-fcs-upgrade-kit-for-lsms

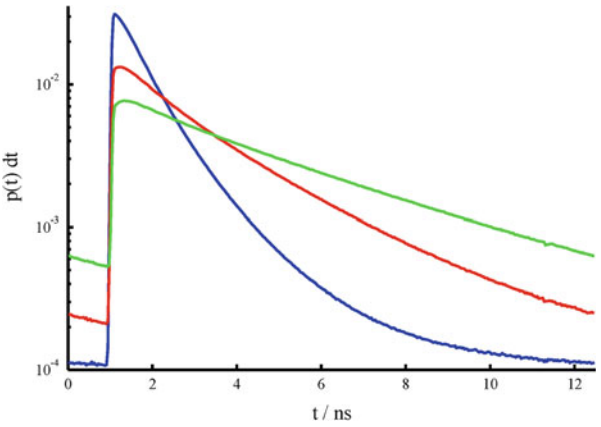

Fig. 1 Fluorescence decay patterns of three different probes labeled with *Cy3* (*blue*), *TRITC* (*red*), and *Texas Red* (*green*), respectively. The decays are not mono-exponential and show average lifetimes of 1.12 ns, 2.30 ns, and 3.36 ns

4.2 Error Analysis

The reliability of the described algorithm depends on many parameters in a highly nonlinear way. Therefore, it is not possible to give an analytical expression for the error of the method. The main parameters that can be influenced by the experimentalist are the number of photons collected (integration time) and the shape of the patterns to be separated (choice of dyes). Based on this we did a simulation study, where we added varying amounts of three experimentally determined patterns, and simulated a number ($N = 400$) of resulting pixel decays for six amounts of total photons $ph_{\text{tot}} = 200, 400, 800, 1,600, 2,400,$ and $3,600$. With this given data set, we used the described method to determine the relative amplitudes n_i of the dyes in each pixel. The first point to show is that the algorithm has no bias. This can be seen from the error of the mean values of the obtained amplitudes. Even for quite low photon numbers, the deviation from the correct value is very small.

The second point is the variance of the result. Due to the Poissonian nature of photon statistics, it is evident that even for these "controlled mixtures," we have to expect a standard deviation of the amplitude of each pattern as $\sqrt{n_i ph_{\text{tot}}}$. The standard deviation of the simulation results are taken as confidence levels. To obtain an overview of the results, one can plot the results as maps that show the confidence level of a given ratio for a given photon number. The results show (see Fig. 2) that the accuracy is excellent even for total photon numbers as low as 1,000.

4.3 Limits of the Method

The conclusion of the previous sections is that the method is able to determine the amplitudes of up to three components with very good accuracy and for realistic numbers of photons. An extension to four components without including additional

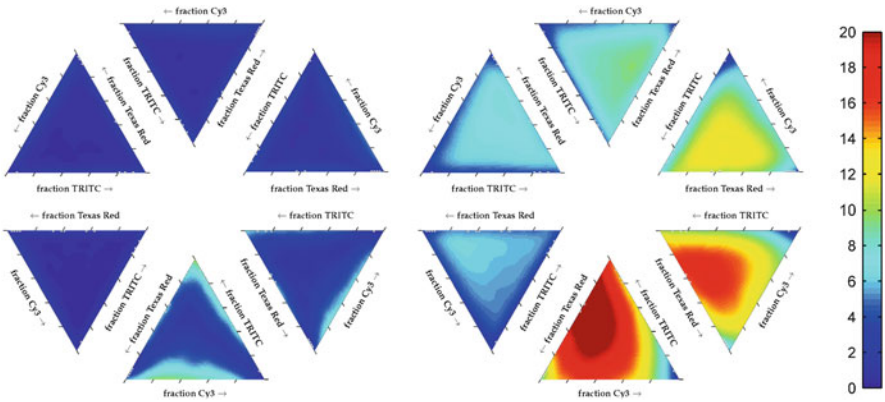

Fig. 2 Error of the mean amplitude (*left*) and the standard deviation of the amplitude of *Texas Red* in mixtures containing *Cy3*, *TRITC*, and *Texas Red*. The photon numbers in the simulations are 200, 400, 800, 1,600, 2,400, and 3,600 (starting from *bottom* and going *counterclockwise*). The *color bar* shows the respective values as percentage of the total number of photons per pixel

information such as a second color channel or excitation wavelength appears to be too demanding in terms of photon numbers to be a realistic option. The reason is that certain linear combinations of two patterns can closely match the pattern of an intermediate fluorescence lifetime. However, we will show in Sect. 7 how additional spectral information can be used to extend the described limit.

A second important limit lies in the fact that the algorithm in principle will not leave photons "unassigned" even if the chosen patterns are not able to describe the decay of the data. For example, consider to analyze the amplitudes of a specimen stained with, e.g., *Cy3*, *Texas Red*, and *TRITC* using only two patterns representing the decays of *Cy3* and *Texas Red*. The algorithm will split practically all photons between the two chosen patterns, because the discrepancy can be minimized to a great extent using the wrong pattern. Therefore, it is really necessary to provide a full set of patterns that represent all the expected components in the specimen.

5 Comparison to Other Methods

In this section we want to compare the performance of the presented method to other methods in order to judge the applicability and accuracy. The comparison does not involve explicit fitting of the obtained decays because here the number of parameters depends strongly on the peculiarities of the decays. Instead, we take into account only methods that are based on a linear decomposition involving the very same reference patterns. Examples of the errors are shown exemplarily for one component only.

5.1 Comparison to a Maximum-Likelihood Estimator

It has been shown [14] that the best possible criterion to analyze the data sets involved in this study is maximum likelihood. However, there is no straightforward way to find the absolute optimum of this criterion. Any algorithm based on gradient search is prone to end up in a local optimum. In order to judge the results of our method, we created a full set of test patterns representing each possible composition with a resolution for n_i of 0.5% for each number of photons. For each pixel we determined the test pattern, which gave the maximum-likelihood value with the data. This determines the global optimum of the available supporting points and prevents the analysis from errors arising from local maxima. However, the chosen grid will always have a finite resolution which limits the maximum precision.

The overall comparison with pattern matching for all three components reveals that the maximum-likelihood estimator gives slightly better results, as expected. This means that the used algorithm works quite reliably, but in some cases, the absolute minimum is not reached. However, the computational effort to directly determine the full maximum-likelihood function is much higher than for all the other methods. For the analysis of two or three components, it may be still feasible to implement this. When the analysis is to be extended to four or even more components, this will not be possible.

5.2 Comparison to Nonnegative Least Squares

A fast and successful algorithm to solve matrix factorization problems with positively defined amplitudes is the NNLS algorithm as introduced by Lawson and Hanson [15]. Since least squares minimizations do not converge to the true minimum when the data error is not Gaussian, we expect this algorithm to be less efficient.

The results (see Fig. 3c and d) show the expected outcome. However, despite the reduced quality, the results are still quite acceptable considering the speed and efficiency of the algorithm resulting in low computational cost.

5.3 Comparison to Phasor Analysis

There are much faster ways to describe the characteristics of TCSPC data. The phasor approach as introduced by Gratton and others [5–7] is such a measure. A phasor is the representation of a vector by its modulus and phase angle. The phasor analysis of a TCSPC histogram computes the Cartesian coordinates of the phasor by cosine and sine summation of the histogram $I(k)$:

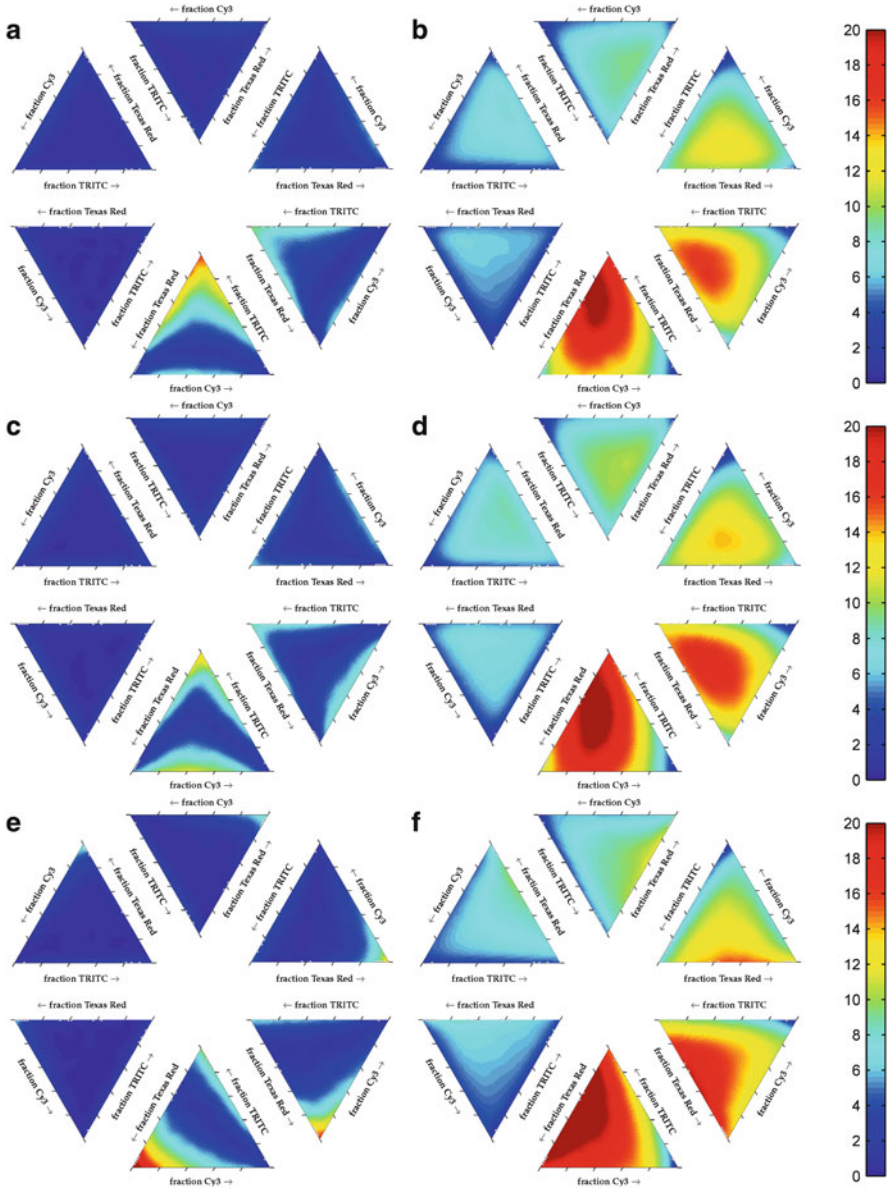

Fig. 3 Error (**a**, **c**, and **e**) of the mean amplitude and the standard deviation of the amplitude (**b**, **d**, and **f**) of *Texas Red* in mixtures containing *Cy3*, *TRITC*, and *Texas Red* obtained by a maximum-likelihood estimator (**a**, **b**), nonnegative least squares (**c**, **d**), and phasor analysis (**e**, **f**). The photon numbers in the simulations are 200, 400, 800, 1,600, 2,400, and 3,600 (starting from *bottom* and going *counterclockwise*, respectively). The *color bar* shows the respective values as percentage of the total number of photons per pixel

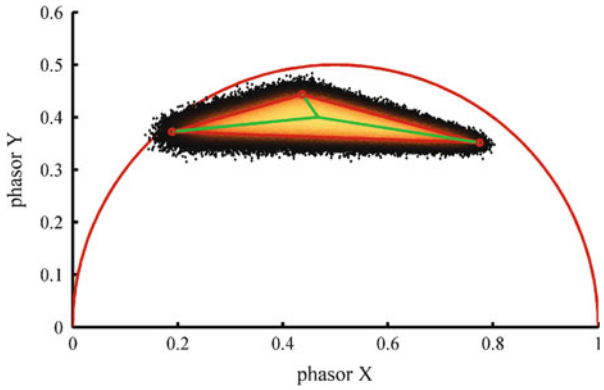

Fig. 4 Phasor plot of mixtures of *Cy3*, *TRITC*, and *Texas Red* computed for simulated pixels having 1,600 photons. *Red circles* indicate the phasor coordinates of the pure components. The composition of the mixture can be obtained by the relative areas of the triangles formed by the phasor coordinates of two pure components and the mixture value as indicated by the *green lines*, respectively

$$g = \frac{1}{N}\sum_{k=1}^{k_{\max}} I(k)\cos\left(2\pi f_{\text{rep}}(k-\delta)\right), \tag{6}$$

$$s = \frac{1}{N}\sum_{k=1}^{k_{\max}} I(k)\sin\left(2\pi f_{\text{rep}}(k-\delta)\right). \tag{7}$$

Here, k is the bin index of the TCSPC histogram, N the total number of photons, f_{rep} the repetition frequency of the laser, and δ a correction accounting for the center of gravity of the IRF. It can be easily shown that the phasor of a mixture equals the linear combination of its components. Therefore, the phasor analysis in itself bears the capability to extract information about the sample composition.

The difficulty in the phasor analysis for three components lies in the fact that the pure components show phasor values close to the unit circle indicated in red in Fig. 4. This can lead to quite extreme aspect ratios of the resulting triangle that is formed by the phasor coordinates of the pure components, resulting in a pronounced inaccuracy of one component.

The results of the phasor analysis are shown in Fig. 3e and f. The accuracy is slightly worse than the nonnegative least squares. The computational costs are even less than for the other methods. An extension to more components is not a problem, in principle. However, due to the special distribution of the pure components in the parameter space, they will not always form a convex polygon for $n > 3$. In this case a general analysis is not possible. Also, it is not straightforward to combine the phasor analysis with additional spectral information.

6 Application to FLIM

The main application of the method depicted here is the quantitative analysis of FLIM images in order to extract the fractional contributions of the respective dye for every pixel of the image. This approach is particularly useful if one is looking for molecules that are either localized in small spotlike areas, for example, focal adhesions, or if the molecules of interest do only appear co-localized with other molecules. In these cases the analysis based on regions of interest is not possible. Here, the pattern analysis can reveal quantitative results.

Pattern analysis of FLIM images extracts the fractional contributions of multiple dyes with ease. Even the most simple approach separates the relative concentration maps of up to three dyes without the need for additional spectral information if the decay behavior of the dyes is sufficiently different.

This decay behavior, the pattern of the dye, merely serves as a fingerprint. Unlike multi-exponential fitting, the complexity of the decay of each contributing dye has no impact on the complexity of the analysis: Only the amplitude of the pattern in each pixel has to be estimated—a single parameter compared to at least two parameters (amplitude and lifetime) for a single exponential decay.

Reduction of complexity is beneficial especially for dark image regions suffering from low signal to noise. In an image pixel with only some hundreds of photons, it is nearly impossible to apply the four-exponential model that would be needed to separate two double-exponential dyes, whereas the contributions of two patterns can still be distinguished with good accuracy.

6.1 Choosing the Pattern

A fundamental problem of all the methods covered here is how to find or choose the set of patterns for the analysis. Fully blind methods such as independent or principal component analysis (ICA/PCA) try to find a complete set of components within the set of data that has to be analyzed. For the specific case of exponential decay patterns, these methods usually fail. Here, we need to manually choose the set of pattern for the analysis. For most of the given situations, this is more or less straightforward, as the samples are stained with a distinct set of labels. In these cases one can obtain the patterns from singly labeled control samples.

However, there are cases where singly labeled control samples are not readily available. This is the case for autofluorescent or intrinsic cellular chromophores like $NAD/NADH^+$, $FAD/FADH^+$, or tryptophan. In these cases, or in general whenever there is no predefined set of patterns available, one has to extract the patterns from the data itself.

If the image contains large, simply connected areas exposing only a single dye, these areas can be selected as a region of interest yielding the dye's pattern. However, if the patterns are not at least partly separated, or if their spatial

distribution is complex, manual selection of a region of interest is impossible or at least impracticable.

A convenient and useful approach is to plot key values of the pixels as two-dimensional scatterplots or correlograms. Parameters can be the average lifetime vs. the reduced second moment of the TCSPC histogram but also the phasor values of the pixel. Separable dyes appear as accumulation points within these scatterplots or maxima within the correlograms.

Once a complete set of patterns is available, pattern decomposition of an image is straightforward and fast. However, in some cases finding this set of patterns can be considerably more complex than applying a multi-exponential fit.

6.2 Moments in Time

Although any characteristic figure of a decay curve would be sufficient to distinguish dyes, it is often desirable to work with parameters that are easy to interpret. It is well established that the statistical moments can be used to extract the lifetimes of a multi-exponential model [16]. However, especially in dark image regions, the number of photons in a single pixel is too small to extract multiple lifetimes.

The (normalized) first moment of the decay curve $I(t)$ extracts the average arrival time of a photon with respect to the preceding excitation pulse. It can be interpreted as the average lifetime τ_{Av} of the fluorophore:

$$m_1 = \frac{\int_0^\infty t I(t)\,dt}{\int_0^\infty I(t)\,dt} = \tau_{\mathrm{Av}}. \tag{8}$$

The second moment is given by

$$m_2 = \frac{\int_0^\infty t^2 I(t)\,dt}{\int_0^\infty I(t)\,dt}. \tag{9}$$

To facilitate interpretation of the second moment, let the decay be expressed as a lifetime distribution:

$$I(t) = \int \frac{\alpha(\tau)}{\tau}\,\mathrm{e}^{-t/\tau}\,d\tau, \tag{10}$$

where

$$\int \alpha(\tau)\, d\tau = 1. \tag{11}$$

Then the second moment transforms into

$$m_2 = \int \tau^2\, \alpha(\tau)\, d\tau = \left[\int (\tau - \tau_{\mathrm{Av}})^2\, \alpha(\tau)\, d\tau + \tau_{\mathrm{Av}}^2 \right] = \left(\sigma_\tau^2 + \tau_{\mathrm{Av}}^2\right), \tag{12}$$

where

$$\sigma_\tau^2 = \int (\tau - \tau_{\mathrm{Av}})^2\, \alpha(\tau)\, d\tau. \tag{13}$$

σ_τ is the width of the lifetime distribution $\alpha(\tau)$. Therefore, a natural choice for intuitive parameters describing the decay is

$$\tau_{\mathrm{Av}} = m_1, \tag{14}$$

$$\sigma_\tau = \sqrt{m_2 - m_1^2}. \tag{15}$$

For a mono-exponential decay, σ_τ identically vanishes. In intuitive terms we could call σ_τ the "multi-exponentiality" of the decay.

6.3 Decay Diversity Map

Figure 5 shows the intensity image and a false-color image of the average fluorescence lifetime τ_{av}. From such a figure alone, it is hard to identify the fluorescent species that are present in the sample. A scatterplot or correlogram of τ_{Av} against σ_τ (named *decay diversity map*) not only helps us to separate fluorescent species, it also tells us how complex the decay of a given pixel is. Whenever the maxima in the decay diversity map are as pronounced as in Fig. 6, patterns can be generated by selecting regions of interest in the decay diversity map and integrating over the image pixels that contribute to the regions of interest.

Figure 7 shows the patterns that were extracted from the pixels of regions 1, 2, and 3 in the decay diversity map. The black line represents a fit of the three patterns to the overall decay as obtained by summation of all pixels. Note that all three patterns show heavily multi-exponential behavior. A multi-exponential analysis would have to include at least six exponentials to model this situation appropriately.

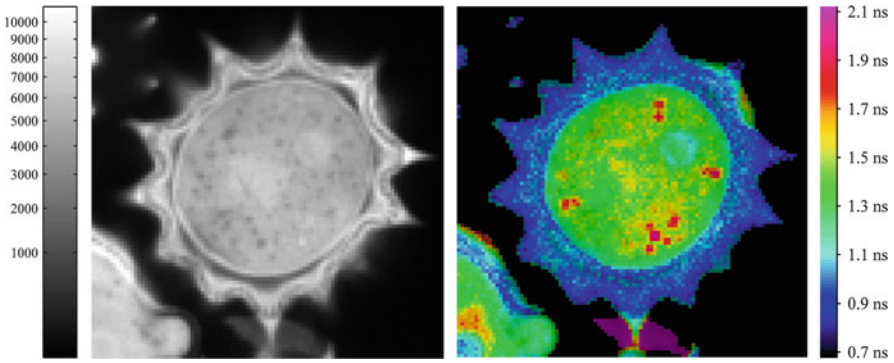

Fig. 5 Intensity image (*left*) and false-color image of the average lifetime (*right*) of a daisy pollen cell (autofluorescence)

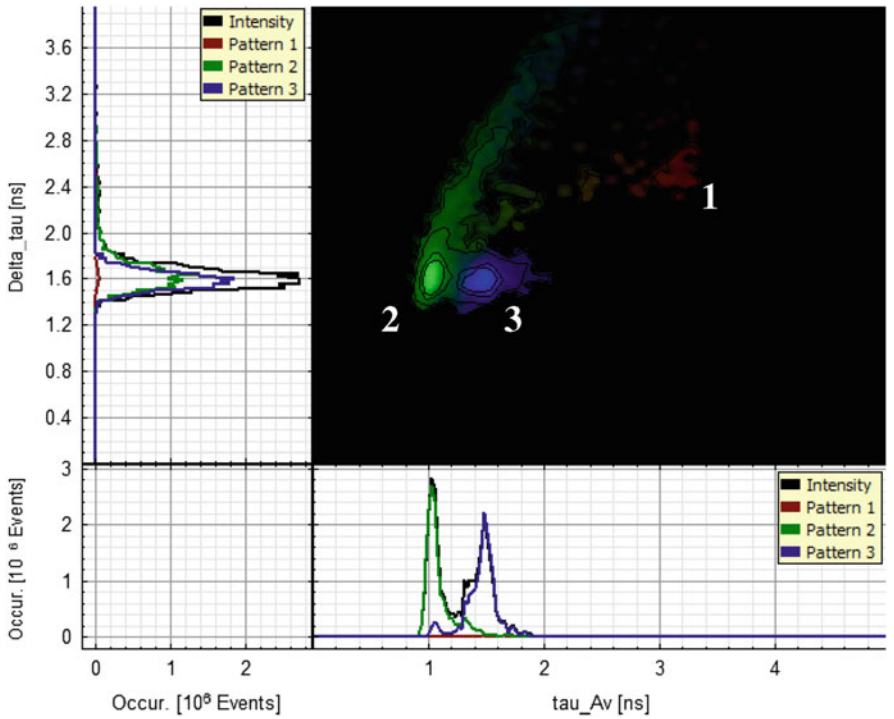

Fig. 6 Decay diversity map of the daisy pollen cell shown in Fig. 5. Three maxima show the presence of three independent species. The two species at 1.0 ns and 1.5 ns dominate the image, but a third species can be found at 3.0 ns. Note that all species behave multi-exponentially. Filaments between the maxima show intermixing; the comet-like tail of the dye at 1.0 ns originates from background effects

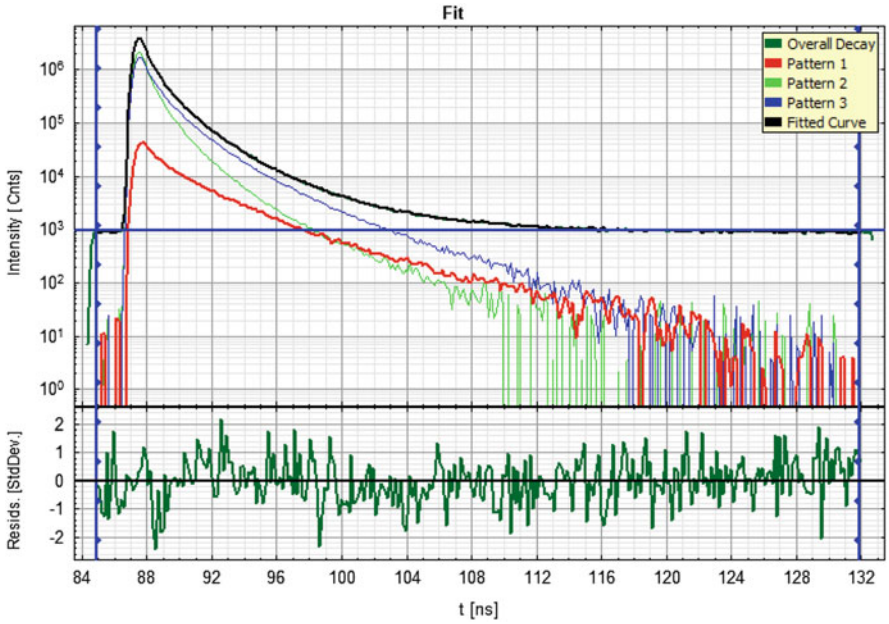

Fig. 7 Extracted decay patterns (*red*, *green*, and *blue lines*) of a daisy pollen cell fluorescence. *Dark green lines* show the overall decay as obtained by summation of all pixels (*top*) and the residuals of a fit of the three patterns to this decay (*bottom*). The *black line* of the fit is undiscernible from the data

6.4 Exponential Fitting Versus Pattern Analysis

Figure 8 shows a comparison of an exponential fit (using four fixed lifetimes) with a three-pattern analysis. The intensities of the three lifetimes which show the best contrast are compared to the pre-factors of the patterns. While the results are qualitatively similar, the separation of contributions is much better for the pattern analysis: While for the exponential fit, there is intermixing between the exponentials (seen as magenta and cyan colors), the contributions of the patterns mostly do not mix, as visible by "pure" green, blue, and red colors. Also, the noise level is visibly reduced for the pattern analysis.

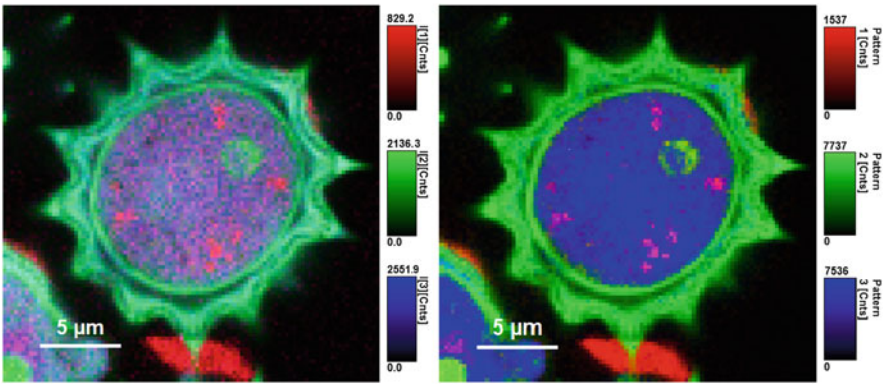

Fig. 8 Comparison of a four-exponential fit (*left*) with a pattern analysis (*right*)

As the results of Fig. 8 are derived from the same image discussed in Fig. 7, it is evident where the shortcomings of the multi-exponential approach originate. Because all involved species behave heavily multi-exponentially, several or even all of the exponentials will be associated with more than one species: Unless the separation of the lifetimes is unusually extreme, it is impossible to resolve six exponentials in a decay curve, not even in the overall decay from all image pixels. Thus, if all three species behave multi-exponentially, some of their lifetimes are shared or at least appear to be shared within the resolution limits of the method.

In conclusion, the more complex the decay behavior of the fluorescent species is, the more that pattern analysis will become our only chance of extracting useful information.

6.5 *Dealing with Mixed Signals*

Data points forming arcs in the decay diversity map (e.g., the arc connecting the red and the green maxima in Fig. 6) indicate intermixing of fluorophores. In the following, we will derive the trajectory connecting two intermixing species.

Let the decays $I^A(t)$ and $I^B(t)$ of two fluorophores be defined according to (16):

$$I(t) = I^A(t) + I^B(t) = \int a\frac{\alpha(\tau)}{\tau}\,\mathrm{e}^{-t/\tau} + b\frac{\beta(\tau)}{\tau}\,\mathrm{e}^{-t/\tau}\,d\tau, \tag{16}$$

$$\int \alpha(\tau)\,\mathrm{d}\tau = \int \beta(\tau)\,d\tau = 1, \tag{17}$$

$$a + b = 1. \tag{18}$$

For the average lifetime and the width of the lifetime distribution follows:

$$\tau_{\mathrm{Av}} = a\,\tau_{\mathrm{Av}}^{A} + b\,\tau_{\mathrm{Av}}^{B} = a\,\tau_{\mathrm{Av}}^{A} + (1-a)\,\tau_{\mathrm{Av}}^{B}, \tag{19}$$

$$\sigma_{\tau}^{2} + \tau_{\mathrm{Av}}^{2} = a\,{m_2}^{A} + b\,{m_2}^{B} = a\,{m_2}^{A} + (1-a)\,{m_2}^{B}. \tag{20}$$

Substitution of (19) into (20) in order to eliminate a yields

$$\sigma_{\tau}^{2} + \tau_{\mathrm{Av}}^{2} - \tau_{\mathrm{Av}}\,\frac{\sigma_{\tau}^{A^2} - \sigma_{\tau}^{B^2} + \tau_{\mathrm{Av}}^{A^2} - \tau_{\mathrm{Av}}^{B^2}}{\tau_{\mathrm{Av}}^{A} - \tau_{\mathrm{Av}}^{B}} = \frac{\tau_{\mathrm{Av}}^{A}\sigma_{\tau}^{B^2} - \tau_{\mathrm{Av}}^{B}\sigma_{\tau}^{A^2}}{\tau_{\mathrm{Av}}^{A} - \tau_{\mathrm{Av}}^{B}} - \tau_{\mathrm{Av}}^{A}\tau_{\mathrm{Av}}^{B}, \tag{21}$$

which can be written as

$$\sigma_{\tau}^{2} + \left(\tau_{\mathrm{Av}}^{2} - C\right) = R^{2}\,. \tag{22}$$

Here, we have introduced the abbreviations R and C as

$$C = \frac{1}{2}\frac{\sigma_{\tau}^{A^2} - \sigma_{\tau}^{B^2} + \tau_{\mathrm{Av}}^{A^2} - \tau_{\mathrm{Av}}^{B^2}}{\tau_{\mathrm{Av}}^{A} - \tau_{\mathrm{Av}}^{B}}, \tag{23}$$

$$R^{2} = \frac{\tau_{\mathrm{Av}}^{A}\sigma_{\tau}^{B^2} - \tau_{\mathrm{Av}}^{B}\sigma_{\tau}^{A^2}}{\tau_{\mathrm{Av}}^{A} - \tau_{\mathrm{Av}}^{B}} - \tau_{\mathrm{Av}}^{A}\,\tau_{\mathrm{Av}}^{B} + C^{2}. \tag{24}$$

Thus, it is evident that the filament that connects the maxima of the pure species in the decay diversity map is a circular arc with its center point on the τ_{Av} axis. Figure 9 illustrates the situation for the decay diversity map of the previous example.

In the special case where $\sigma_{\tau}^{A} = \sigma_{\tau}^{B} = \sigma_{\tau}^{AB}$, it follows:

$$C = \frac{\tau_{\mathrm{Av}}^{A} + \tau_{\mathrm{Av}}^{B}}{2}, \tag{25}$$

$$R^{2} = \sigma_{\tau}^{AB^2} + \frac{1}{4}\left(\tau_{\mathrm{Av}}^{A} - \tau_{\mathrm{Av}}^{B}\right)^{2}. \tag{26}$$

For two mono-exponential species with $\sigma_{\tau}^{AB} = 0$, the arc becomes a half circle with its center right between the lifetimes of the pure species. When intermixing occurs, the patterns for the pure species can always be found at the extreme points along the average lifetime direction, even if there is no pronounced maximum at these places.

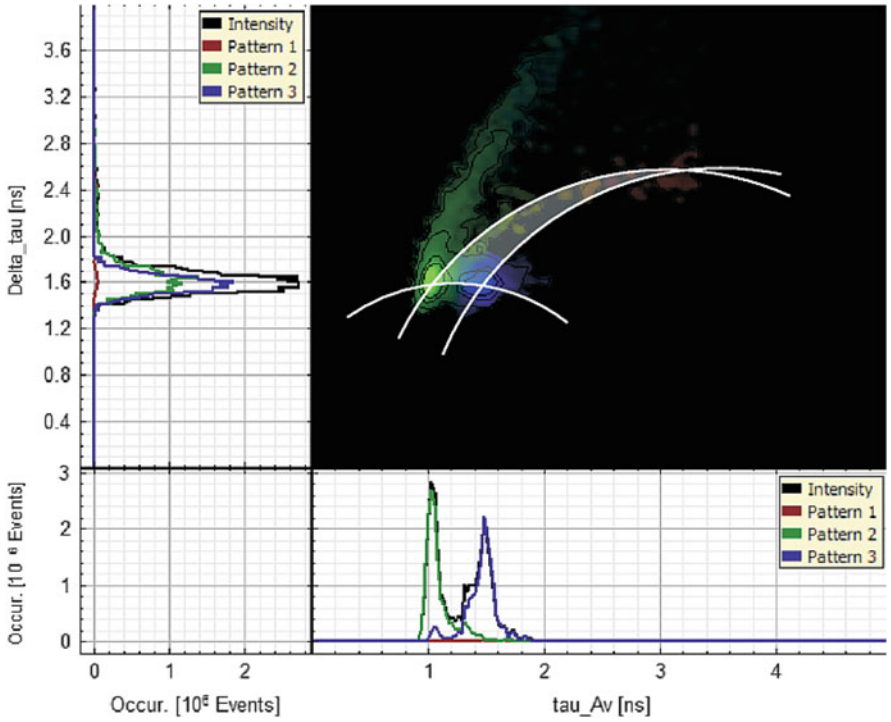

Fig. 9 Decay diversity map of a daisy pollen cell (autofluorescence). The three circular arcs connecting each pair of species limit the region in which image pixels can be found, which expose a mixture of the pure species. In this particular example, intermixing of the *red* species with the *green* species contributes visibly to the image intensity

6.6 Post-processing

In many studies analyzing the quantities of certain components in, for example, certain subcellular structures, one can easily enhance the accuracy of the analysis. After a first pixel-wise mapping of the components, one can specifically select pixels of similar content ratio or using other selection rules. The raw data of such a defined set of pixels can be summed up to form a super-pixel with a multifold increased number of photons. This can be analyzed using the very same algorithm (or any other method) to give a result of even better accuracy.

7 Extension to Spectrally Resolved FLIM

One major advantage of the described algorithm is that it can be easily generalized for the analysis of spectrally resolved data, data that was recorded using interleaved excitation using different laser lines, and other possible excitation and detection schemes such as polarization-sensitive data. Such multidimensional patterns can be used in the very same way as the simple TCSPC histograms. Taking full advantage of the spectral and temporal characteristics of a fluorescent probe dramatically improved the accuracy of the decomposition. In a single-channel measurement, the unmixing of three probes is somewhat the limit of the method in terms of an acceptable accuracy. In a spectrally resolved measurement, one can decompose up to five probes that are spectrally similar. Two examples for such a separation are shown in Fig. 11.

The spectral and temporal characteristics of the five patterns that were used to analyze the data presented in the lower part of Fig. 11 are shown in Fig. 10. One finds that the spectra of these labels are overlapping widely, thus preventing an unmixing based on the pure spectral information. However, in combination with the temporal decay, a separation of the different species can be achieved. For the analysis only, data after a single excitation pulse (488 nm or 640 nm, respectively) was used. Remarkably, the fluorophore in three of the four patterns used for the analysis in Fig. 11b was Atto 488. The changes in its spectral and temporal properties due to conjugation to different molecules are sufficient to provide a clear separation. The data was recorded using a modified time-resolved confocal fluorescence microscope (MicroTime 200, PicoQuant GmbH) equipped with a spectrograph and a 32-channel multi-anode PMT (H7260-20, Hamamatsu Photonics Deutschland GmbH) was used. Each detection channel had a spectral width of about 9.4 nm. Custom-built cooling and routing electronics were used to record

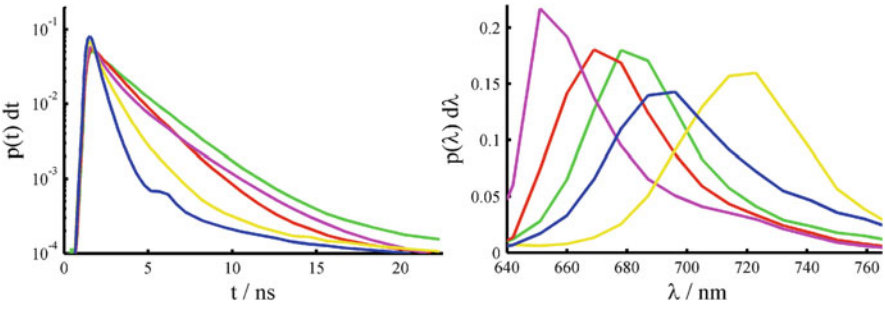

Fig. 10 Temporal (*left*) and spectral (*right*) characteristics of the five fluorescent probes after excitation with a 640 nm laser pulse. Data was obtained from separate nonoverlapping stainings. *Red*, antitubulin directly stained with Alexa 647; *green*, Phalloidin-Atto 655; *blue*, DNA intercalator DRAQ5; *yellow*, anti-giantin stained with Alexa 700 s antibody; and *magenta*, anti-fibrillarin stained with Alexa 633 s antibody (Data courtesy of T. Niehörster, A. Löschberger, and M. Sauer, Institute of Biotechnology and Biophysics, Julius Maximilian University, Würzburg, Germany)

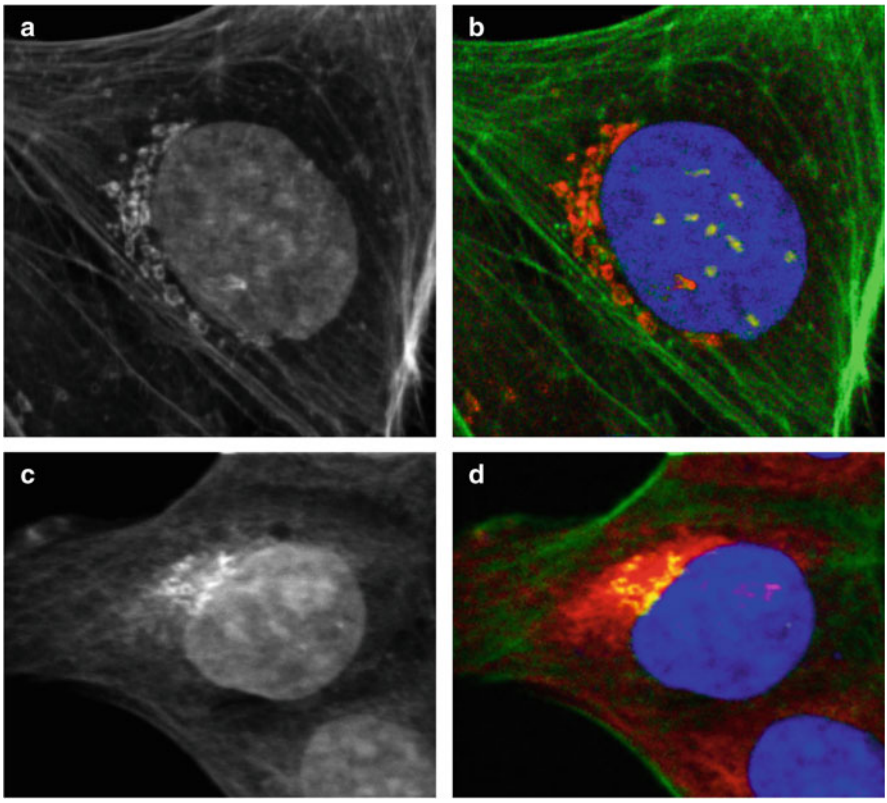

Fig. 11 Intensity images (**a** and **c**) and pattern-resolved composite images (**b** and **d**) of U2OS cells (Mowiol fixation). (**b**) Patterns correspond to *red* anti-giantin stained with Atto 488 s antibody; *green* Phalloidin-Atto 488; *blue* DNA marked with EdU coupled to Atto 488 azide; and *yellow* anti-fibrillarin stained with Alexa 488 s antibody. (**d**) Patterns correspond to *red* antitubulin directly stained with Alexa 647; *green* Phalloidin-Atto 655; *blue* DNA intercalator DRAQ5; *yellow* anti-giantin stained with Alexa 700 s antibody; and *magenta* anti-fibrillarin stained with Alexa 633 s antibody (Data courtesy of T. Niehörster, A. Löschberger, and M. Sauer, Institute of Biotechnology and Biophysics, Julius Maximilian University, Würzburg, Germany)

TCSPC data individually from each detection channel. For the spectrally resolved FLIM (sFLIM) analysis of the recorded signals, typically 10–12 channels covering the fluorescence emission spectrum of the dyes were used.

Applying an extended excitation scheme using pulsed interleaved excitation with laser pulses of different wavelengths, one can easily extend this method to separate many more dyes, e.g., three dyes excited in the blue (450 nm), three dyes excited in the green (530 nm), and another three dyes excited in the red (640 nm) spectral range.

8 Conclusion

In this chapter a new concept of analyzing FLIM data is presented. The method was shown to work accurately and fast and can be used intuitively. With a set of fixed fluorescence decay patterns, one can quantitatively analyze large data sets. This feature reduces much of the workload and necessary expertise that still is required to analyze such data in the classical way. Therefore, this approach can provide a great leap toward a fully automated analysis. While working in the same way for unmixing spectrally resolved data, the full power of the method is gained by using spectrally resolved decay patterns. We estimate that a simultaneous analysis of up to ten labels in a sample should be feasible. Also the application of this method for analyzing FLIM-FRET data should provide a reliable and fast way to obtain quantitative results from cellular FRET studies. Large amounts of recorded data of (s)FLIM experiments can be processed automatically. This opens up the perspective for conducting much more comprehensive studies using FLIM as a standard tool.

Acknowledgments The authors thank Jörg Enderlein, Fred Wouters, Gertrude Bunt, and Benedikt Krämer for valuable discussions. The funding of the German Federal Ministry for Education and Research (BMBF) is gratefully acknowledged.

References

1. Harvey CD, Yasuda R, Zhong H, Svoboda K (2008) The spread of Ras activity triggered by activation of a single dendritic spine. Science 321(5885):136–140
2. Verveer PJ, Wouters FS, Reynolds AR, Bastiaens PIH (2000) Quantitative imaging of lateral ErbB1 receptor signal propagation in the plasma membrane. Science 290:1567–1570
3. Wouters FS, Bastiaens PIH (1999) Fluorescence lifetime imaging of receptor tyrosine kinase activity in cells. Curr Biol 9(19):1127–1130
4. Yasuda R (2006) Imaging spatiotemporal dynamics of neuronal signaling using fluorescence resonance energy transfer and fluorescence lifetime imaging microscopy. Curr Opin Neurobiol 16(5):551–561
5. Clayton AHA, Hanley QS, Verveer PJ (2004) Graphical representation and multicomponent analysis of single-frequency fluorescence lifetime imaging microscopy data. J Microsc 213 (1):1–5
6. Digman MA, Caiolfa VR, Zamai M, Gratton E (2008) The phasor approach to fluorescence lifetime imaging analysis. Biophys J 94(2):L14–L16
7. Redford GI, Clegg RM (2005) Polar plot representation for frequency-domain analysis of fluorescence lifetimes. J Fluoresc 15(5):805–815
8. Lakowicz JR (2006) Principles of fluorescence spectroscopy, 3rd edn. Springer, New York
9. Walther KA, Papke B, Sinn MB, Michel K, Kinkhabwala A (2011) Precise measurement of protein interacting fractions with fluorescence lifetime imaging microscopy. Mol Biosyst 7 (2):322–336
10. Kullback S, Leibler RA (1951) On information and sufficiency. Ann Math Stat 22(1):79–86

11. Lee DD, Seung HS (2000) Algorithms for non-negative matrix factorization. In: Leen TK, Dietterich TG, Tresp V (eds) Advances in neuronal image processing systems 13. MIT, Cambridge, pp 556–562
12. Neher RA, Neher E (2004) Applying spectral fingerprinting to the analysis of FRET images. Microsc Res Tech 64(2):185–195
13. Neher RA, Neher E (2004) Optimizing imaging parameters for the separation of multiple labels in a fluorescence image. J Microsc 213:46–62
14. Enderlein J, Sauer M (2001) Optimal algorithm for single-molecule identification with time-correlated single-photon counting. J Phys Chem A 105(1):48–53
15. Lawson CL, Hanson RJ (1974) Solving least squares problems. Prentice Hall, Englewood Cliffs
16. Isenberg I, Dyson RD (1969) The analysis of fluorescence decay by a method of moments. Biophys J 9:1337–1350

Metal-Induced Energy Transfer

Narain Karedla, Daja Ruhlandt, Anna M. Chizhik, Jörg Enderlein, and Alexey I. Chizhik

Abstract This chapter presents an overview of the recently introduced concept of metal-induced energy transfer and two of its applications. We discuss the basic principle of the method and its application to the mapping of the membrane of a living cell and to the single-molecule axial localization with 2–3 nm accuracy.

Keywords Energy transfer · Fluorescence lifetime imaging · Fluorophore–metal interaction · Plasmonics

Contents

1 Introduction 266
2 Theory 267
3 The MIET-GUI Software 269
4 Live-Cell Nanoscopy Using Metal-Induced Energy Transfer 270
5 Influence of Photon Statistics on Axial Resolution 276
6 Resolving Nanometer Axial Distances at the Single-Molecule Level 277
7 Conclusion 279
References 280

N. Karedla, D. Ruhlandt, A.M. Chizhik, J. Enderlein (✉), and A.I. Chizhik (✉)
III. Institute of Physics, Georg August University, Friedrich-Hund-Platz 1, 37077 Göttingen, Germany
e-mail: jenderl@gwdg.de; alexey.chizhik@phys.uni-goettingen.de

P. Kapusta et al. (eds.), *Advanced Photon Counting: Applications, Methods, Instrumentation*, Springer Ser Fluoresc (2015) 15: 265–282, DOI 10.1007/4243_2014_77,

1 Introduction

The field of super-resolution microscopy has seen a tremendous development over the last two decades and has opened up new advances for the application of fluorescence microscopy in the life sciences. However, each of the existing methods is either technically challenging and requires high light excitation intensities at the limit of what is tolerable for live-cell imaging or is rather slow and requires specialized labels and environmental conditions, which are not always compatible with live-cell microscopy. Moreover, the majority of these methods suffer from one common problem: their axial resolution is by roughly one order of magnitude worse than their lateral resolution.

In this chapter, we present a new fluorescence-based method, which employs the energy transfer from an optically excited donor molecule to a thin metal film and which allows for achieving an axial localization of a fluorophore with 1 nm accuracy. This goes far beyond the diffraction limit of light microscopy and surpasses in accuracy all known light-based techniques for enhancing the axial resolution.

It has long been known that placing a fluorescent molecule in the vicinity of a metal quenches its fluorescence emission and decreases its fluorescence lifetime. This was first predicted by Edward Purcell in a seminal short note in 1946 [1]. From a physics point of view, the mechanism behind this phenomenon is similar to that of FRET [2]: energy from the excited molecule is transferred, via electromagnetic coupling, into plasmons of the metal, where energy is either dissipated or reradiated as light. This fluorophore–metal interaction was extensively studied in the 1970s and 1980s [3], and a quantitative theory was developed on the basis of semiclassical quantum optics [4, 5]. The achieved quantitative agreement between experimental measurement and theoretical prediction was excellent.

Here, we will show that the metal-induced energy transfer (abbreviated later as MIET) can be used to localize fluorescent molecules along one dimension with nanometer accuracy [6, 7]. A first proof-of-principle study was given in [8], but the general idea has found little attention at that time. The core idea is that MIET accelerates the return of excited fluorescent molecules to their ground state, which manifests itself as a shortening of their fluorescence lifetime [9–11]. Owing to the fact that the energy transfer rate is dependent on the distance of a molecule from the metal layer, the fluorescence lifetime can be directly converted into a distance value (Fig. 1). The theoretical basis for the success of this conversion is the perfect quantitative understanding of MIET [12]. It is important to emphasize that the energy transfer from the molecule to the metal is dominated by the interaction of the molecule's near-field with the metal and is thus a thoroughly near-field effect, similar to FRET. However, due to the planar geometry of the metal film, which acts as the acceptor, the distance dependency of the energy transfer efficiency is much weaker than the sixth power of the distance, which leads to a monotonous relation between lifetime and distance over a size range between zero and 100–200 nm above the surface. One of the key advantages of this method is that

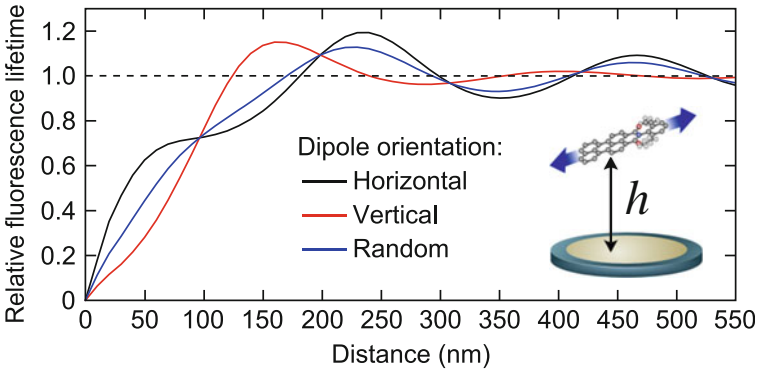

Fig. 1 Calculated dependence of fluorophore lifetime on its axial position over the metal film. Curves are calculated for an emission wavelength of 650 nm and a gold film thickness of 20 nm deposited on the glass cover slide

it does not require any hardware modification to a conventional fluorescence lifetime imaging microscope (FLIM), thus preserving its full lateral resolution. The technical simplicity of MIET and its compatibility with live-cell imaging make it applicable for a broad range of studies.

In this chapter, we will describe the details of the technique and discuss its advantages, limitations, and future perspectives for combining it with other super-resolution methods for enhancing the in-plane resolution. We will also present its application for live-cell imaging and single-molecule axial localization studies.

2 Theory

For evaluating MIET measurements, one has to model the emission properties of a fluorescing molecule above a metallized surface. The geometry of the modeled situation is shown in Fig. 2. Let us consider the emission of a single molecule with orientation angles (α, β), where β denotes the inclination towards the vertical axis and α the angle around that axis. The molecule is assumed to be an electric dipole emitter. Then, the electric field amplitude of its emission into direction (θ, ϕ) is given by the general formula

$$E_{\mathrm{em}} = e_p\left[A_\perp \cos\beta + A_P^c \sin\beta \cos\left(\phi - \alpha\right)\right] + e_s A_P^s \sin\beta \sin\left(\phi - \alpha\right),$$

where $A_\perp, A_P^c$, and A_P^s are functions of emission angle θ but not of α, β, or ϕ. Explicit expressions for $A_\perp, A_P^c$, and A_P^s can be found in a standard way by expanding the

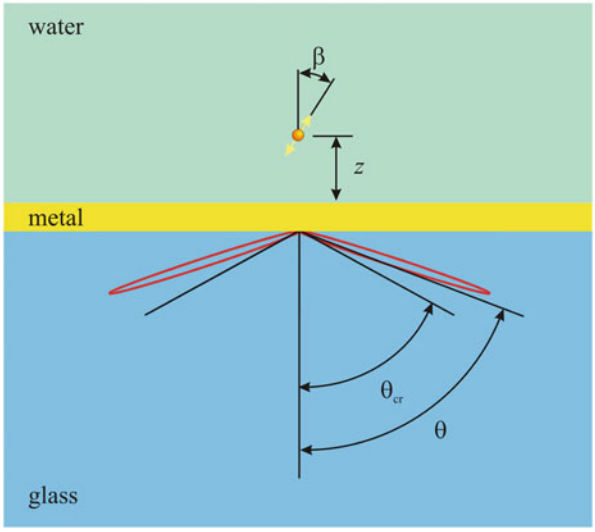

Fig. 2 Geometry of MIET: A fluorescing molecule is placed above of a thin metal film deposited on glass. Fluorescence detection is done with a high-N.A. objective from the glass side. Fluorescence excitation is performed by the same objective from the glass side. In the figure, a single molecule (electric dipole emitter) is placed at a distance z from the metal surface. Its orientation is described by the angle β between its dipole axis and the vertical axis (optical axis). The angular distribution of radiation into the glass is depicted as a *red curve* and is a function of angle θ. The critical angle θ_{cr} of total internal reflection between glass and water is also shown

electric field of the dipole emission into a plane wave superposition and tracing each plane wave component through the planar structures using Fresnel's relations; for details, see [12–15]. It is important to note that the functions $A_{\perp}, A_P^c$, and A_P^s depend also on wavelength.

Knowing the electric field amplitude of the emission into a given direction (θ, ϕ), one can then derive the total power of emission as

$$S_{\text{total}}(\beta, \alpha) \propto B_{\perp} \cos^2\beta + B_P \sin^2\beta$$

with weight factors $B_{\perp}$ and B_P that take into account also the absorption of emitted energy in the metal layer; for details of their calculation, see [12]. Knowing the total emission power S_{total}, one can then calculate the lifetime of the molecule by

$$\frac{\tau}{\tau_0} = \frac{S_0}{\phi S_{\text{total}} + 1 - \phi},$$

where ϕ is the quantum yield, τ_0 the free lifetime, and S_0 the total emission power of the emitter in free space (sample space).

For finally calculating the actual lifetime–distance curve, one has to average the result over all possible molecular orientations (assuming that there is no preferred

molecular orientation in the sample) and also the emission spectrum of the emitter (using the free-space emission spectrum as weight function). The complex-valued refractive indices of the metal layer as a function of wavelength are either taken from publications or have to be measured with ellipsometry.

3 The MIET-GUI Software

We have developed a dedicated Matlab-based MIET-GUI for evaluating measured MIET data. The MIET-GUI is a graphical user interface designed for many different types of data evaluation, including the conversion of the raw FLIM data into a MIET image. The software can be downloaded via the link www.joerg-enderlein.de/MIET/MIETGUI.zip. The MIET-GUI accepts .ht3-files generated by the time-correlated single-photon counting (TCSPC) hardware HydraHarp of PicoQuant GmbH (Berlin) http://www.picoquant.com/products/category/tcspc-and-time-tagging-modules/hydraharp-400-multichannel-picosecond-event-timer-tcspc-module. Accessed 30 Oct 2014, from which it calculates the lifetime and intensity of single pixels, elliptical regions of interest (ROI), or the patterns generated by scanning the excitation light over single dipole emitters. These lifetimes are converted into height information via the MIET lifetime versus height calibration curve.

As a first step, the user has to choose the general type of evaluation, pixel by pixel or one of the more elaborate ROI/pattern techniques. In the pixel by pixel mode, the TCSPC histogram of each pixel with more than 25 photons is assembled. The shape of these histograms can be described by a steep rise followed by a peak and then an exponential decay. By setting a cutoff after which the curve is purely exponential and calculating the mean arrival time of the photons after this cutoff, one gets the lifetime value for this pixel. In the ROI mode, the user specifies an elliptical region of interest believed to belong to molecules with the same lifetime. The photons from all pixels within the ROI are collected into a single histogram, which is less prone to noise problems than histograms for single pixels. For this reason, the histogram can be fitted with either mono- or multi-exponential decay curves, thus finding the lifetime of the molecules in the ROI. The most sophisticated mode is the pattern matching mode. Here, the user has to specify the parameters of the excitation light such as the wavelength, the polarization mode of the laser, the numerical aperture of the objective, and the defocusing of the objective. From these parameters, the patterns generated by scanning the excitation beam over molecules with different angular orientations can be calculated. The intensity image obtained by integrating the TCSPC data over time is now fitted with the simulated patterns to determine the position and orientation of each single dipole emitter. The photons from all the pixels assigned to a molecule's pattern are grouped into a single histogram and fitted as in the ROI mode.

In the second step, the lifetime information is converted into height information. To this end, the user has to specify the emission wavelength, the quantum yield, and the excited state lifetime of the emitters as well as the thicknesses and complex

refractive indices of all materials in the sample (e.g., metal-coated glass cover slides, buffer solutions, etc.). As described above, this data can be used to calculate the observed lifetime as a function of the dipole's height above the interface and its angle with the optical axis. In the pixel-by-pixel evaluation mode, nothing is known about the particle's orientation, so a random orientation is assumed and the calibration curve calculated accordingly. In the pattern matching mode, the particle's orientation is known and the correct curve is used for the evaluation. If the emission spectrum of the fluorescent probe is known, the calibration curves obtained for all wavelengths that are able to pass the optical filters are calculated and averaged according to the spectrum. A complication arises from the fact that the lifetime versus height curve oscillates, meaning that some lifetime values cannot be matched unambiguously to a height value. The first possibility for dealing with this problem is to crop the calibration curve at the largest unique value and to mark all longer lifetimes as "not a number" in the height image. If some prior knowledge about the sample states that no height values larger than the value corresponding to the first peak in the calibration curve can exist, it is possible to crop the calibration curve at this peak. The height information gained through this progress can then be visualized or used for further analysis.

4 Live-Cell Nanoscopy Using Metal-Induced Energy Transfer

We demonstrate the applicability of MIET for live-cell imaging by mapping the basal membrane of living cells with nanometer accuracy. Knowledge of the precise cell–substrate distance as a function of time and location with unprecedented resolution provides a new means to quantify cellular adhesion and locomotion, as is required for a deeper understanding of fundamental biological processes such as cell differentiation, tumor metastasis, and cell migration.

As a biological model system, we chose three adherent cell lines: MDA-MB-231 human mammary gland adenocarcinoma cells and A549 human lung carcinoma cells, which are able to form metastasis in *in vivo* models, and MDCK II from canine kidney tissue as a benign epithelial cell line. Figure 3 illustrates the experimental setup, which comprises a conventional confocal microscope equipped with an objective lens (numerical aperture, 1.49), a pulsed excitation light source (20 MHz repetition rate, 50 ps pulse width, wavelength range 450–800 nm, 1 mW average power per nm; Fianium), and a time-correlated single-photon counting (TCSPC) module (HydraHarp, PicoQuant). The only additional requirement for MIET, when compared to conventional FLIM, is the presence of a thin semitransparent 20 nm gold film deposited on the glass cover slide supporting the sample.

The cells were stained with a membrane-staining fluorophore (CellMask Deep Red plasma membrane stain, Invitrogen), which emits photons in the deep red region of the visible spectrum. Using fluorescence interference contrast (FLIC)

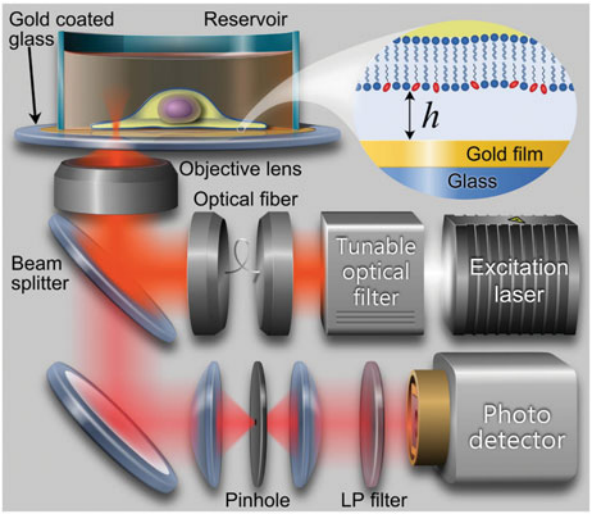

Fig. 3 Scheme of the experimental setup for live-cell imaging LP - long pass

microscopy, it has been shown that the average distance of the basal membrane from the substrate typically varies between 20 and 100 nm depending on cell type [17], which is far below the diffraction-limited axial resolution of a confocal microscope. To keep the cells in physiological conditions, the microscope was equipped with an incubator, which kept the temperature constant at 37°C. The cells were grown directly on a gold-coated glass substrate. FLIM images were acquired every 5 min with a field of view of $70 \times 70\ \mu m^2$ (175×175 scan positions). As the apical cell membrane is at least 500 nm away from the substrate, only dye molecules within the basal membrane were efficiently excited and detected. Further experimental details can be found in [6].

Figure 4a, b presents examples of the collected fluorescence intensity and lifetime images of the basal membrane of MDA-MB-231 cells, respectively. Because the variation of the fluorescence intensity is not only dependent on the metal-induced quenching, but also on the homogeneity of labelling, we exclusively used the lifetime information for reconstructing a three-dimensional map of the basal membrane. Computation of the local height of the basal membrane above the gold film was accomplished by using the theoretically calculated dependence of the fluorescence lifetime on the distance of a fluorophore from the metal film (Fig. 1).

The model takes into account all the details of the optical properties of the glass/gold substrate (thickness- and wavelength-dependent complex-valued refractive index of the metal film; refractive index of the cover slide), as well as the photophysics of the used dye (emission spectrum, dye orientation with respect to the substrate).

The dye orientation within the cell membrane was checked by defocused imaging [18] and was found to be random without any preferential orientation. The distance–lifetime dependence, as calculated for the experimental conditions used in our experiment, is shown in Fig. 1.

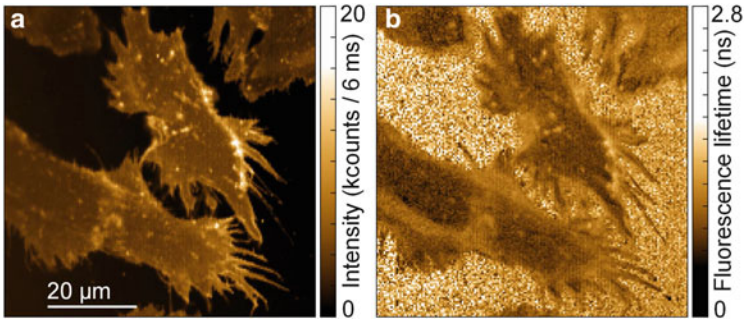

Fig. 4 Fluorescence lifetime imaging. Simultaneously acquired fluorescence intensity (**a**) and lifetime (**b**) images of the basal membrane of living MDA-MB-231 cells grown on a gold-covered glass substrate, acquired with a standard confocal microscope

Whereas the three-dimensional reconstruction of the membrane profile is recalculated solely from the lifetime image of the sample, the intensity distribution is used for discriminating, in the lifetime images, the membrane fluorescence against the background. Regions with no cells are difficult to identify from the lifetime images alone, as the lifetime values become exceedingly scattered at low signal-to-noise ratios. We eliminated such patches by removing areas where the fluorescence intensity did not exceed the background level. Finally, to ensure that the membrane stain had not diffused inside the cell during the experiment, we carried out FLIM imaging of the intracellular compartments, which did not yield any detectable fluorescence signal.

Figure 5a presents a three-dimensional reconstruction of the basal membrane of MDA-MB-231 cells calculated from the lifetime images shown in Fig. 4. The local cell–substrate distance varies between 50 and 100 nm, whereby at the edges, the cells exhibit a higher distance from the surface. The average cell–substrate distance is in very good agreement with the recently reported results of Wegener and colleagues, who reported 27 nm for MDCK II and 87 nm for NIH 3T3 fibroblasts [19]. Differences in cell–substrate distance for different cell types can occur due to variations in adhesion strength and in the secretion of extracellular matrix (ECM) proteins by the cells themselves. To follow the temporal dynamics of the cell–substrate distance, we recorded a time-lapse series of fluorescence lifetime and intensity images at 5 min intervals. The three-dimensional maps allow the cell motion to be followed over time with 200 nm lateral (as defined by the confocal microscope) and 3 nm axial resolution (see Sect. 5).

Although the cell–substrate distance at each lateral position changes over time, the average distance remains the same over the full measurement time. We found that the tumor cells display a larger cell–substrate distance in the periphery compared to the center, where they firmly adhere to the gold surface. A comparison of the three cell lines (MDA-MB-231, A549, and MDCK II) with respect to the average distance of the basal membrane from the gold surface, as well as, for

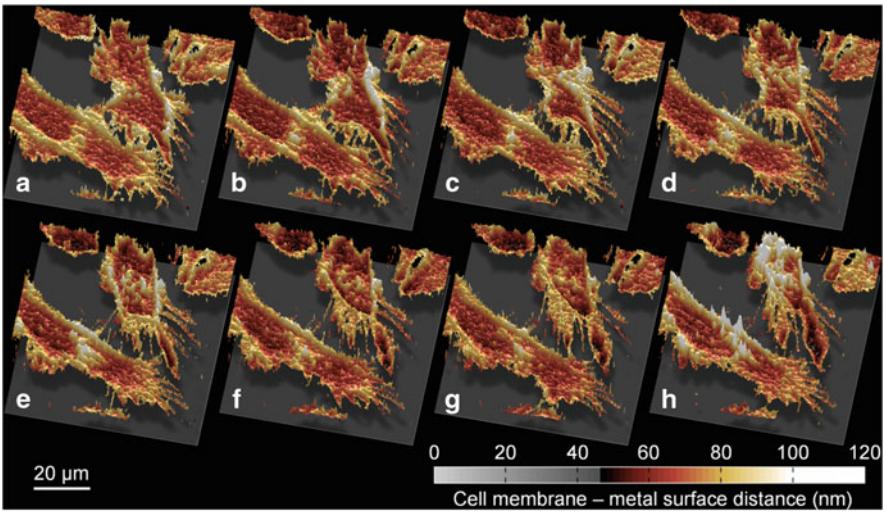

Fig. 5 Three-dimensional reconstruction of the basal membrane. Three-dimensional profiles computed from fluorescence lifetime images recorded over 40 min. Acquisition time of one image is 90 s of MDA-MB-231 cells

example, MIET images, is provided in Fig. 6. We found excellent agreement with data obtained previously using FLIC microscopy, which showed that MDCK II cells are extremely close to the surface (near 27 nm) [18]. Note that MDCK II cells are benign epithelial cells, whereas the other cell lines are cancerous and show a higher invasiveness/motility. This might be inferred from the higher cell–substrate distances of 54 ± 8 nm (MDA-MB-231) and 67 ± 7 nm (A549).

We also monitored the spread of single MDCK II cells by visualizing the various stages of adhesion from initial contact to the formation of lamellipodia. Generally, the spreading process of adherent cells can be divided into three distinct temporal phases. The first phase is characterized by the formation of initial bonds between adhesion molecules and molecules of the ECM. This process of tethering is followed by the second phase, which comprises the initial cell spreading, which is driven by actin polymerization that forces the cell surface area to increase by drawing membrane from a reservoir of folded regions and blebs. The third phase encompasses recruitment of additional plasma membrane from the internally stored membrane buffer and extension of lamellipodia to occupy a larger area. By using MIET imaging, we could monitor the individual phases by visualizing the cell–substrate distance as a function of time (Figs. 7 and 8). The MIET imaging shows that the initial contact of the cell is characterized by concentric areas, with alternating distance from the surface. The occupied area increases with time and, eventually, lamellipodia occur at the border of the cells that have close contact with the gold surface.

To estimate the resolution of the recorded images, we calculated the standard deviation of cell–substrate distance. For the acquired series of images, the

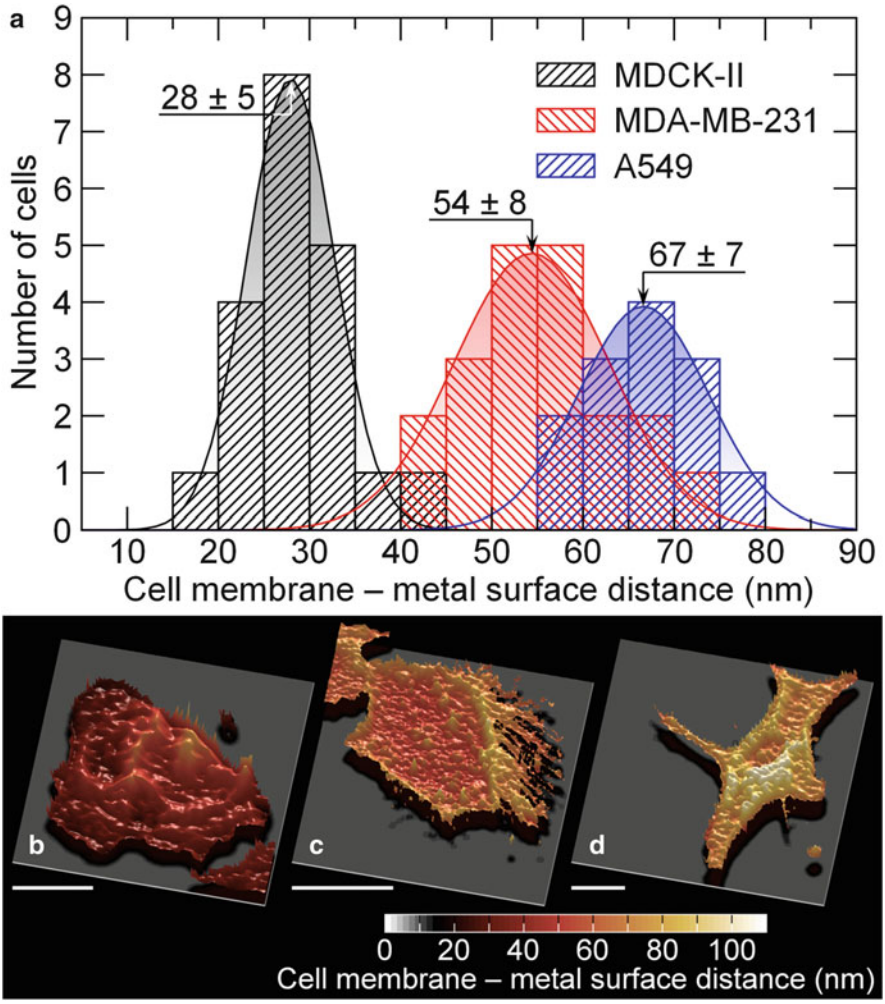

Fig. 6 Comparison of three cell lines. (**a**) Average distance of basal membrane from the gold surface for MDA-MB-231, A549, and MDCK II cell lines. *Solid curves* show the fit to the experimental data with a Gaussian function. (**b**–**d**) Exemplary three-dimensional reconstructions of the basal membrane of the MDCK II (**b**), MDA-MB-231 (**c**), and A549 (**d**) cells. Scale bars, 20 mm. For a better comparison, all images are normalized to the same scale

resolution of the axial distance (determined with MIET) varies between 3 nm (at nearly 10×10^3–15×10^3 counts per pixel) and 4 nm (at nearly 5×10^3–10×10^3 counts per pixel), depending on the local signal-to-noise ratio. This substantially exceeds the precision of most existing techniques currently used for axial imaging. To prevent fast photobleaching of the sample, we used a moderate excitation power (~100–300 W/cm^2) and acquisition time. However, as the

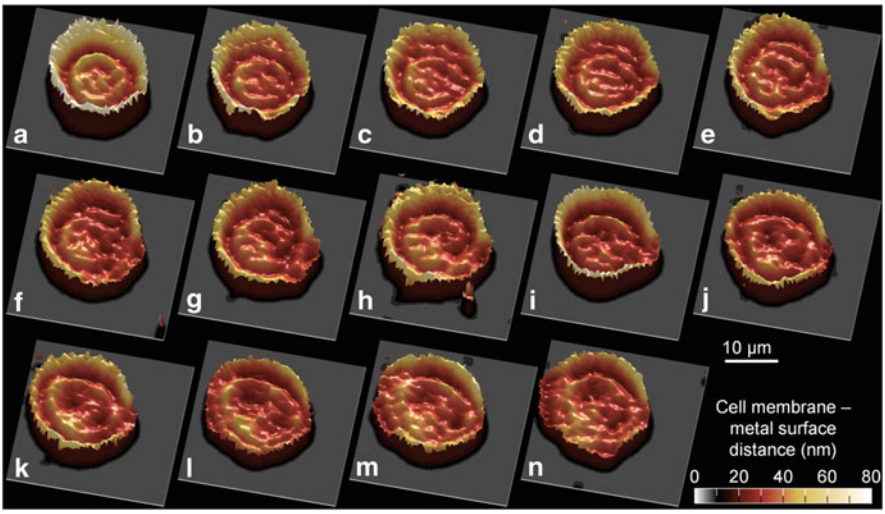

Fig. 7 Time-elapsed MIET images recorded in 3 min time intervals showing the early stages of cell (MDCK II) spreading on gold. Initially, concentric rings of strong and weaker adhesion (judged by cell–substrate distance) are visible. A *darker color* refers to lower cell–substrate distance. At later stages (**k**–**n**), first lamellipodia are formed that exhibit a low cell–substrate distance

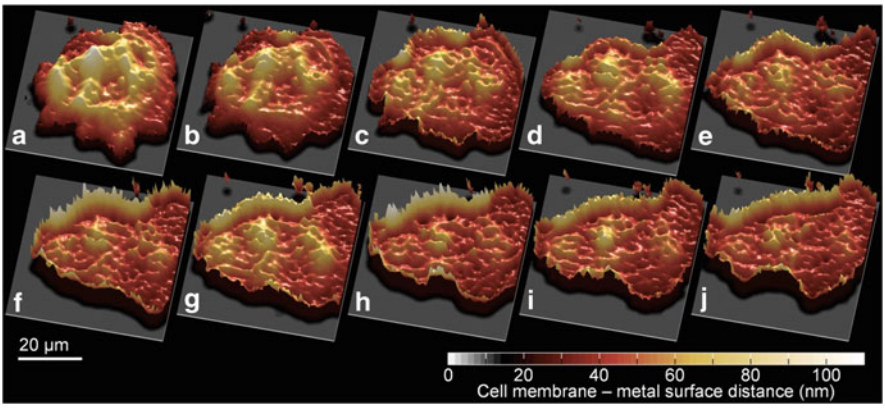

Fig. 8 Time-elapsed MIET images recorded in 5 min time intervals showing the late stages of cell (MDCK II) spreading on gold. The cell forms tightly attached protrusions/lamellipodia away from the center of the cell. The cell occupies a larger area with time and presses down more closely. A *darker color* refers to lower cell–substrate distance

resolution is determined by the signal-to-noise ratio of the recorded fluorescence decay curves, a further increase in precision can be achieved by collecting more fluorescence signal using longer acquisition time or higher excitation laser power.

5 Influence of Photon Statistics on Axial Resolution

To study the influence of the photon statistics on axial resolution of MIET, we recorded fluorescence lifetime images of the test sample, schematically shown in the inset of Fig. 9(i). A glass cover slide was coated with 20 nm gold film and 50 nm SiO_2. On the surface of a dielectric spacer, a thin polymer film doped with CellMask Deep Red molecules with random orientation was deposited. On top of the polymer layer, a droplet of optical glue was placed, which has a refractive index equal to that of glass. As a result, the test sample represents a typical configuration of the cell membrane in close proximity to the gold film.

We recorded FLIM images of the same area of the sample at different count numbers from 30 down to 1 kcounts per pixel by subsequent bleaching of the dye. Typical cross sections through the fluorescence lifetime images recorded at 1, 10, 20, and 30 kcounts per pixel are shown in Fig. 9(a)–(d), respectively. Using the distance–lifetime dependence as modeled for the current experimental conditions, the FLIM images were recalculated into the dye-to-metal film distance profiles (Fig. 9(e)–(h), respectively). To estimate the resolution of the recorded images, we calculated a standard deviation of the height values obtained within each of the images. Open circles in Fig. 9(i) show the experimentally obtained values of the standard deviation. From the Poissonian statistics of single-photon counting, one expects that the accuracy of determining a mean fluorescence lifetime value scales with the square root of the number of detected photons. Correspondingly, we expect to see a roughly similar dependence of the accuracy of determined height values on the number of detected photons, which is excellently verified by the fit of an inverse square root function of the count number to the data (solid curve).

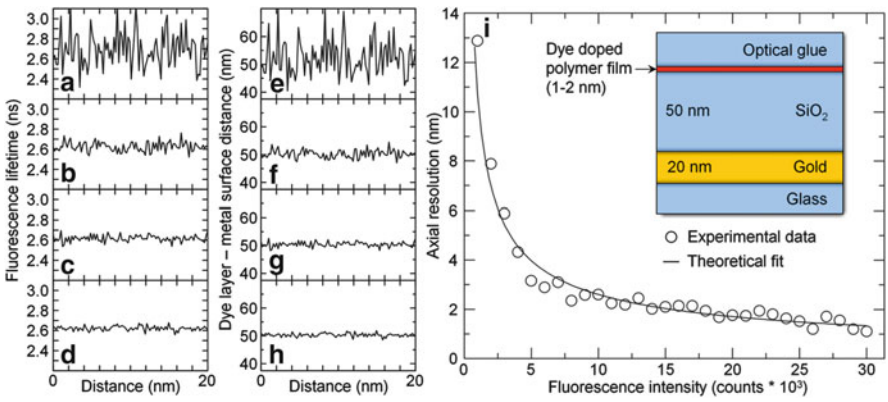

Fig. 9 (*a*)–(*d*) Cross sections through the fluorescence lifetime images recorded at the same sample area at count numbers of 1, 10, 20, and 30 kcounts per pixel, respectively. (*e*)–(*h*) Dye layer-to-metal film distance profiles recalculated from the images (*a*)–(*d*), respectively. *i*) Resolution of the axial localization of a fluorophore calculated as a standard deviation at different count numbers. *Open circles* – experimental data; *solid curve* – theoretical fit. *Inset* shows a schematic of the test sample

6 Resolving Nanometer Axial Distances at the Single-Molecule Level

Herein, we present the first experiments with MIET for localizing single molecules axially from a surface. The presented data show that single-molecule MIET (smMIET) indeed has the capacity of measuring distances of individual molecules from a surface with nanometer accuracy. We measure the fluorescence lifetime of individual dye molecules deposited on a dielectric spacer as a function of a spacer thickness. Figure 10 shows four images of single dye molecules deposited on a silicon oxide layer (20, 30, 40, and 50 nm thick) above a thin metal film (2 nm titanium, 10 nm gold) on a glass cover slide. The image was taken by using a standard confocal laser scanning microscope. The shown area is $30 \times 30\ \mu m^2$. The background that can be seen on the image is due to the spectrally broad photoluminescence from the gold. However, the photoluminescence lifetime of a smooth gold surface is less than 2 ps, which does not affect the result of the measurement. For each spacer thickness, we calculated the distribution of single-molecule lifetimes, as shown in Fig. 11. The obtained lifetime values are (0.50 ± 0.06), (0.81 ± 0.07), (1.19 ± 0.08), and (1.50 ± 0.08) ns for 20, 30, 40, and 50 nm spacer thicknesses, respectively.

Figure 12 shows the calculated fluorescence lifetime values along with curves of the lifetime modulation for purely horizontally and purely vertically oriented dipoles. The shaded area in between these two curves indicates the possible lifetime values for dipoles with polar orientations in between the two extremes. From the fit, we found that the observed lifetime–distance behavior is best described if it is assumed that almost all molecules are horizontally oriented, which is confirmed by defocused imaging.

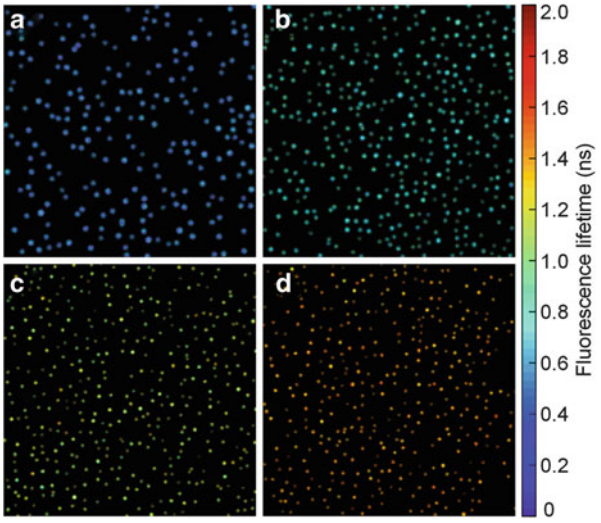

Fig. 10 Lifetime images for (**a**) 20, (**b**) 30, (**c**) 40, and (**d**) 50 nm SiO_2 spacer thicknesses for the identified single-molecule pixels. The *color bar* shows the color index for lifetime values in nanoseconds. Each image is $30 \times 30\ \mu m^2$

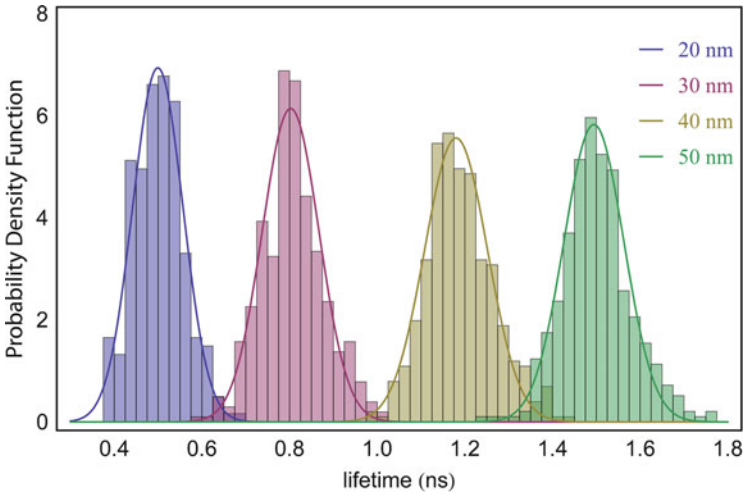

Fig. 11 Lifetime distributions for the four samples with 20, 30, 40, and 50 nm SiO_2 spacers between the metal film and the deposited molecules

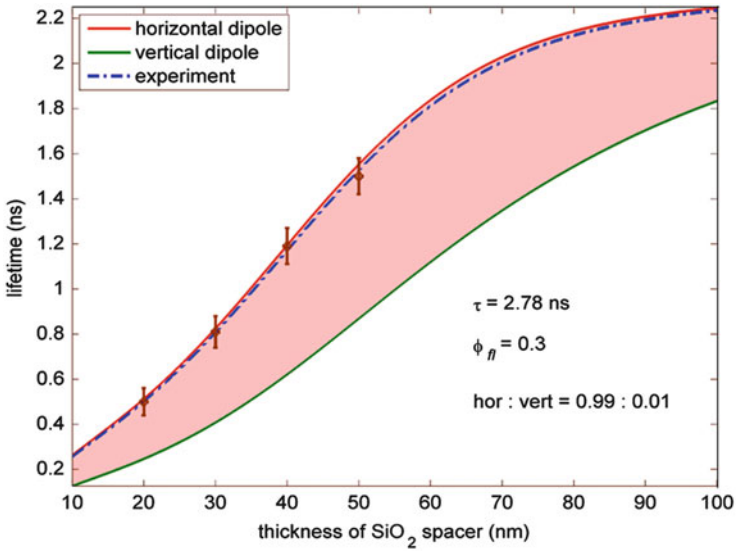

Fig. 12 Fitting of experimental lifetime values. The unperturbed lifetime τ_0 obtained as a fit parameter is 2.78 ns, which is in good agreement with the lifetime of Atto655 measured in air on glass

The standard deviation for the observed single-molecule lifetime values is less than 0.1 ns, which corresponds to an axial localization accuracy of less than 2.5 nm for horizontal dipoles. A further reduction in the spread of the lifetime distribution can be achieved by increasing the number of collected photons per molecule, for

example, by preventing photobleaching by using suitable oxygen-scavenging protocols [19]. In our current experiment, we detected on average 369, 767, 1.002, and 1.031 photons per identified molecule for spacer thickness values of 20, 30, 40, and 50 nm, respectively. In our current measurement scheme, the fundamental limitation is that we have no means of measuring the orientation (polar angle) of the molecule simultaneously with the intensity and lifetime. As can be seen from Fig. 12, the relation between distance and lifetime is strongly orientation dependent, and to use smMIET for nanometer-precise distance measurements of single molecules, one will need to know both the lifetime and the orientation. There are several options to achieve this, including defocused imaging [17, 20], scanning with radially polarized light [21] or detecting separately subcritical and supercritical fluorescence emission [22]. However, all these methods require significant extensions and/or modifications of a conventional confocal laser scanning microscope, and future investigations must be made to determine which of these methods is the most robust and efficient in terms of extracted information per detected photon.

7 Conclusion

Although we have focused on the application of MIET to the mapping of the membrane of a living cell and the single-molecule axial localization, which shows its versatility, relative technical simplicity, and its applicability for life science, the potential scope of applications of MIET is much greater. The size range over which MIET works nicely bridges (and complements) the realm of conventional FRET and all the recently developed super-resolution imaging techniques. Although MIET has to rely on a perfect theoretical understanding of the fluorophore–metal interaction, which is certainly more involved than that of FRET, this is no serious obstacle in the current age of powerful desktop computers. In contrast to FRET, the infamous orientation-factor problem is greatly relaxed because one has to know only the relative orientation of one species of fluorescent molecules with respect to the planar metal film. Moreover, in contrast to FRET, one needs to label only one site of a sample with one species of fluorophore, instead of double labelling with a donor and acceptor. MIET is exceedingly simple to set up, and neither requires modification of the FLIM system nor preparation of complex sample substrates. Coating glass cover slides with a thin metal film is the only prerequisite of the technique. Thus, the technical simplicity of MIET will allow its application in a wide range of studies where nanometer resolution is required.

Combining MIET with ideas from super-resolution microscopy techniques based on photoswitching and high-precision localization of single molecules will enable the resolution of intermolecular and intramolecular distances with nanometer precision. The first step on that way is application of MIET for single-molecule imaging, which was shown here. Already with our non-optimized (in terms of photobleaching) measurements, we could estimate a positional accuracy of better than 2.5 nm. Although smMIET achieves this resolution only along one single axis,

this method will open new fascinating possibilities for structural biology. For example, for determining the intramolecular distance between two fluorescent labels in a macromolecule, one can envision using smMIET to measure the absolute distance values of both labels for a large number of macromolecules immobilized on a surface. One could then apply a statistical analysis of the acquired distance histograms to obtain the absolute distance between the labels.

References

1. Purcell EM (1946) Proceedings of the american physical society. Phys Rev 69(11–12):674
2. Förster TH (1948) Zwischenmolekulare energiewanderung und fluoreszenz. Ann Phys 437:55–75
3. Drexhage KH (1974) Interaction of light with monomolecular dye layers, chap IV. In: Wolf E (ed) Progress in optics. Elsevier, Amsterdam, pp 163–232
4. Lukosz W, Kunz RE (1977) Light emission by magnetic and electric dipoles close to a plane interface. I Total radiated power. J Opt Soc Am 67(12):1607–1615
5. Chance RR, Prock A, Silbey R (2007) Molecular fluorescence and energy transfer near interfaces. In: Prigogine I, Rice SA (eds) Advances in chemical physics. Wiley, New York, pp 1–65
6. Chizhik AI et al (2014) Metal-induced energy transfer for live cell nanoscopy. Nat Photonics 8 (2):124–127
7. Karedla N et al (2014) Single-molecule metal-induced energy transfer (smMIET): resolving nanometer distances at the single-molecule level. ChemPhysChem 15(4):705–711
8. Colyer RA, Lee C, Gratton E (2008) A novel fluorescence lifetime imaging system that optimizes photon efficiency. Microsc Res Tech 71(3):201–213
9. Chizhik AI et al (2011) Probing the radiative transition of single molecules with a tunable microresonator. Nano Lett 11(4):1700–1703
10. Chizhik AI, Gregor I, Enderlein J (2013) Quantum yield measurement in a multicolor chromophore solution using a nanocavity. Nano Lett 13(3):1348–1351
11. Chizhik AI et al (2012) Electrodynamic coupling of electric dipole emitters to a fluctuating mode density within a nanocavity. Phys Rev Lett 108(16):163002
12. Enderlein J (1999) Single-molecule fluorescence near a metal layer. Chem Phys 247(1):1–9
13. Enderlein J, Ruckstuhl T, Seeger S (1999) Highly efficient optical detection of surface-generated fluorescence. Appl Opt 38(4):724–732
14. Enderlein J, Ruckstuhl T (2005) The efficiency of surface-plasmon coupled emission for sensitive fluorescence detection. Opt Express 13(22):8855–8865
15. Enderlein J (2000) A theoretical investigation of single-molecule fluorescence detection on thin metallic layers. Biophys J 78(4):2151–2158
16. Braun D, Fromherz P (1998) Fluorescence interferometry of neuronal cell adhesion on microstructured silicon. Phys Rev Lett 81(23):5241–5244
17. Patra D, Gregor I, Enderlein J (2004) Image analysis of defocused single-molecule images for three-dimensional molecule orientation studies. J Phys Chem A 108(33):6836–6841
18. Heitmann V, Reiß B, Wegener J (2007) The quartz crystal microbalance in cell biology: basics and applications. In: Steinem C, Janshoff A (eds) Piezoelectric sensors. Springer, Berlin, pp 303–338
19. Vogelsang J et al (2008) A reducing and oxidizing system minimizes photobleaching and blinking of fluorescent dyes. Angew Chem Int Ed 47(29):5465–5469

20. Böhmer M, Enderlein J (2003) Orientation imaging of single molecules by wide-field epifluorescence microscopy. J Opt Soc Am B 20(3):554–559
21. Chizhik AI et al (2011) Excitation isotropy of single CdSe/ZnS nanocrystals. Nano Lett 11 (3):1131–1135
22. Hohlbein J, Hübner CG (2008) Three-dimensional orientation determination of the emission dipoles of single molecules: the shot-noise limit. J Chem Phys 129(9):094703

The Importance of Photon Arrival Times in STED Microscopy

Giuseppe Vicidomini, Ivàn Coto Hernàndez, Alberto Diaspro, Silvia Galiani, and Christian Eggeling

Abstract Lens-based or far-field fluorescence microscopy is a very popular technique for investigating the living cell. However, the spatial resolution of its standard versions is limited to about 200 nm due to diffraction, impeding the imaging of molecular assemblies at smaller scales. The turn of the twenty-first century has witnessed the advent of far-field fluorescence super-resolution microscopy or nanoscopy, a fluorescence microscopy featuring a spatial resolution down to molecular scales. STED microscopy was the first of such nanoscopy techniques, but was for a long time considered as a very complex technique, hard to apply in everyday biological research. Based on developments in label and laser technology, recent years have however seen major improvements of the STED nanoscopy approach, one of which is gated continuous-wave STED (gCW-STED) microscopy. gCW-STED microscopy reduces complexity by combining STED laser operating in CW with pulsed excitation and time-gated photon detection. Here, we describe the physical principles of gCW-STED, formulate the theoretical framework which characterizes its main benefits and limitations, as well as show experimental data.

Keywords Confocal · FCS · gCW-STED · Point-spread function · Stimulated emission depletion

G. Vicidomini
Nanophysics, Istituto Italiano di Tecnologia, Via Morego 30, 16163 Genoa, Italy

I. Coto Hernàndez and A. Diaspro
Nanophysics, Istituto Italiano di Tecnologia, Via Morego 30, 16163 Genoa, Italy

Department of Physics, University of Genoa, Via Dodecaneso 33, 16146 Genoa, Italy

S. Galiani and C. Eggeling (✉)
MRC Human Immunology Unit, Weatherall Institute of Molecular Medicine, Radcliffe Department of Molecular Medicine, University of Oxford, OX3 9DS Oxford, UK
e-mail: christian.eggeling@rdm.ox.ac.uk

P. Kapusta et al. (eds.), *Advanced Photon Counting: Applications, Methods, Instrumentation*, Springer Ser Fluoresc (2015) 15: 283–302, DOI 10.1007/4243_2014_73,

Contents

1 Introduction 284
2 Principle of Gated CW-STED Microscopy 288
2.1 Theory 290
3 Results 294
4 Conclusions and Discussions 296
References 299

1 Introduction

It is of historical interest that the fluorescence microscope was a by-product of the search for increasing spatial resolution in the light microscope [1, 2]. In 1873 Abbe [3] demonstrated that diffraction limits the spatial resolution of a far-field light microscope: A far-field light microscope is using lenses and focused light to observe samples placed >μm away from any optical element, i.e., allowing non-invasive and intra-cellular studies. However, using focused light comes with the price of diffraction of light, meaning that with a far-field microscope one cannot discern objects any closer together than a distance $d = \lambda/(2n\sin\alpha)$ given by the numerical aperture of the microscope's objective lens ($n\sin\alpha$, with refractive index n of the embedding medium and α the focusing angle) and the wavelength λ of the light used. Inspired by Abbe's results, that shorter wavelengths of light lead to higher spatial resolution, August Köhler built the first ultraviolet (UV) transmission microscope in 1904. In his experiments, Köhler noted that some biological structures emitted auto-fluorescence upon illumination with UV light. While the auto-fluorescence was a major problem for setting up the initial UV microscope experiments (since it reduced the specimen's contrast in the final image), Köhler immediately realized the potential of fluorescence to map specific structures in biological samples. A few years later (1908), Köhler together with Henry Siedentopf demonstrated the first fluorescence microscope [4].

Since the invention of fluorescence microscopy, advances in instruments, technologies, fluorescent probe synthesis, and labeling techniques have contributed to its continuing widespread utility. At the beginning of the 1990s, a modern far-field florescence microscope was a turn-key instrument, able to provide excellent contrast, single protein specificity, single-molecule sensitivity, and minimal specimen perturbation. But Abbe's resolution limit was still entirely in place. In this context, it is also important to remember that the Abbe's resolution limit applies only to light that propagates for a distance substantially larger than its wavelength (i.e., in the far-field). Therefore, as predicted by Edward Hutchinson Synge in 1928 and demonstrated in the 1980s', a fluorescence microscope with a spatial resolution well below the Abbe's resolution limit can be obtained by placing the illumination and/or detection within tens of nanometer to the sample (i.e., in the near-field) [5, 6]. However, this particular architecture limits the use of near-field microscopy to cellular surface structures and cell interiors are out of reach.

As with many other leaps in science, the breaking of the diffraction resolution limit in far-field fluorescence microscopy has not been due to gradual improvements from persisted technological progress: In the early 1990s new viable physical concepts for overcoming the diffraction barrier set of a quest that has led to readily applicable and widely accessible fluorescence microscopes with sub-diffraction resolution ($\ll d$) [7, 8]. These microscopes are usually called far-field super-resolution techniques or optical nanoscopy techniques [9–11].

Unique to all the current super-resolution microscopy techniques is that they overcome the diffraction limit by precluding the simultaneous signaling (in general) of adjacent ($<d$) molecules and thereby recording them sequentially in time and/or space [12–14]. Here, inhibition of signaling, i.e., fluorescence emission is realized by optically driving the labels between states of different fluorescence emission characteristics, such as a bright on- and a dark off-state. Under this scope individual nanoscopy methods differ from each other by the molecular mechanism by which the signal is precluded and by whether the transfer between states is driven at (1) targeted coordinates in space or (2) random molecular positions. Stimulated emission depletion (STED) microscopy is the most representative method among the targeted coordinate techniques and also the first far-field nanoscopy method [7, 9, 13, 15, 16].

In a STED microscope, stimulated emission (SE) is the optically driven molecular mechanism by which fluorescent labels are driven between an on- and off-state and (spontaneous) fluorescence signal is precluded. Specifically, a second laser, the STED laser, is added to the microscope's fluorescence excitation laser to drive excited (fluorescent on-state) molecules into their dark ground off-state (Fig. 1). Thereby, the STED laser features one or more intensity zeroes and thus controls the coordinates where molecules contribute to the overall signal. In the most representative STED microscopy implementation, a regular Gaussian excitation laser beam is co-aligned with a doughnut-shaped STED beam that features a nearly "zero-intensity" point and a wavelength in the red edge of the emission spectrum of the fluorescence labels (Fig. 1). Under these conditions, the STED beam transiently de-excites and thus inhibits fluorescence emission of all molecules in the focal laser spots except those located in or at the closest proximity of the "zero-intensity" point. Most importantly, increasing the STED intensity above a certain threshold drives essentially all molecules to their off-state and confines the region in which on-state population and thus fluorescence emission is still allowed (the effective fluorescence or observation spot) (Fig. 1). Scanning the two co-aligned beams across the sample and collecting only the spontaneous emission (stimulated signal is discarded by appropriate spectral filters) yields images whose spatial resolution is given by the size of the effective fluorescence spot. Theoretically, the size of the effective fluorescence spot can be decreased to infinitesimal dimensions (and thus the spatial resolution increased to "infinity") by increasing the intensity of the STED beam. Practically, possible photodamage and phototoxic effects limit the amount of STED laser light that can be focused on the sample, and thereby the ultimate resolution of a STED microscope.

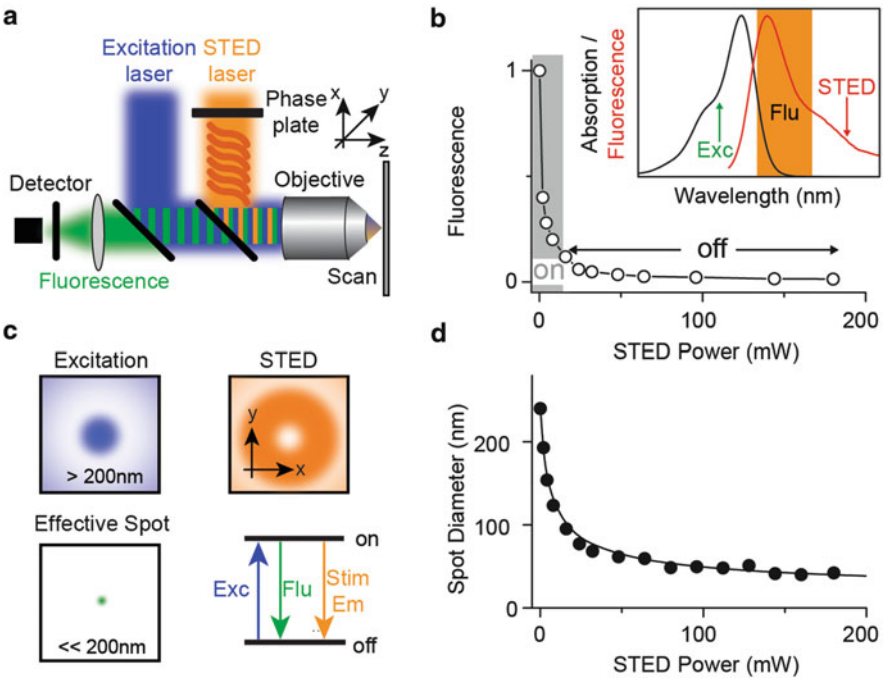

Fig. 1 Principle of STED microscopy. (**a**) Schematic drawing of the setup of a STED microscope with the microscope objective which focuses the excitation laser (*blue*) and the STED laser (*orange*), and collects the fluorescence signal (*green*) for detection, a phase plate in the STED beam, and a three-dimensional (*x*, *y*, *z*) scanning device for moving the sample relative to the laser light. (**b**) In STED, the registered spontaneous fluorescence is inhibited by stimulated emission induced by the STED laser. The amount of spontaneous fluorescence decreases with increasing STED laser power and is basically switched off when driving the laser power above a certain threshold. (*Inset*) The wavelength of the STED laser (*red arrow*) is chosen at the red edge of the fluorophores' fluorescence emission spectrum (*red*), while spontaneous fluorescence, which is excited by the excitation laser with a wavelength (Exc, *green arrow*) in the absorption spectrum of the fluorophore (*black*), is selectively detected (Flu, *orange*). (**c**) The excitation laser renders an ordinary diffraction limited focal spot (*blue*), while the STED laser passes through a phase plate that realizes a focal intensity distribution with a local zero such as a doughnut-like pattern (*orange*), creating an effective excitation volume with dimensions of much below the diffraction limit (*green*). (*Lower right panel*) When electrons are excited (Exc), the STED laser inhibits spontaneous emission of fluorescence photons (Flu) by de-exciting the excited state (*on*-state) to the ground state (*off*-state) via stimulated emission (Stim Em). Increasing the power of the STED laser over a certain threshold effectively precludes the occupation of the excited on-state and thus spontaneous emission of fluorescence photons. (**d**) Sub-diffraction volumes to which the occupation of the excited state and hence fluorescence emission is restricted are created by driving the STED laser intensity up, and the volume's size (or spot diameter) decreases with increasing STED laser power

Although, STED microscopy was developed in 1994 [7] and was first experimentally demonstrated in 1999/2000 [17, 18], its practical implementation has only gained substantial momentum over the last few years [9, 14, 15, 19]: The initial STED systems provided outstanding spatial resolution, but they were rather

complex and cost-intensive. As a consequence, the dissemination of STED microscopy was hampered. Since conventional fluorescent molecules have an excited-state lifetime τ_{S1} of 1–10 ns and a SE cross-section of ~10^{-17} cm^2, only STED beam intensities I_{STED} of several hundred MW/cm^2 provide SE rates k_{STED} much greater than the spontaneous emission rates $k_{S1} = 1/\tau_{S1}$, and thereby efficient inhibition of spontaneous fluorescence. To keep the time-averaged power P_{STED} low, such intensities were most conveniently realized by using costly pulsed mode-locker laser system, whose pulses need synchronization and time-alignment with the excitation counterpart: the STED beam pulse must arrive virtually simultaneously of a few picoseconds after the excitation pulse (all-pulsed STED implementation) [18, 19]. Further, the femtosecond STED beam pulses originating from the mode-locked laser system had to be stretched to 100–300 ps to minimize non-linear photodamage effects [20, 21] and direct excitation (one- or two-photons) from the STED beam [22, 23]. Although such pulse preparations were routinely prepared in conventional laser spectroscopy, they introduced a large complexity for non-expert STED microscopy users, and required diligent operations and maintenances [19]. Complexity and costs were further increased when extending STED microscopy to the green/orange wavelength spectrum (e.g., for using GFP, Alexa488, or similar fluorescence labels). This extension required conversion of the STED laser pulses to the 600–650 nm wavelength range by non-linear optics [24]. Consequently, to make STED microscopy amenable to a wider community, there was a strong demand for alternative lasers sources, suitable to implement STED microscopes at lower cost and complexity.

The introduction of stable, powerful, and turn-key super-continuum lasers made the sophisticated pulse preparation of the first STED implementations obsolete. Indeed, the very same super-continuum source provides already synchronized STED and excitation beams [25–27]. However, current commercial super-continuum sources do not produce light of sufficient intensity to induce effective SE below 630 nm. Vice versa, a light source, generating a comb spectrum via stimulated Raman scattering within a fiber was shown to produce light suitable for STED imaging at multiple wavelengths red-shifted from 532 nm [28]. Fiber-based lasers are easy to maintain, but semiconductor laser technology promises even greater robustness and cost-efficiency due to the lower complexity. By giving up the wavelength tunability, efficient STED microscopy implementations have also been obtained using smaller and less complex pulsed STED laser sources [29–31].

A fundamental step towards the reduction of complexity and cost of STED microscopy was to demonstrate that pulsed lasers are not strictly mandatory: a STED microscope based on lasers running in continuous wave (CW) can also be implemented [32]. STED microscopy with CW laser makes any laser pulse preparation redundant, strongly reduces the costs, and improves the versatility of the technique: Almost any wavelength can be covered by a CW laser [33–35]. However, the resolution performance of a CW-STED system lags behind that of a pulsed STED system [22].

A remedy to this situation is to use a pulsed excitation beam, a STED beam running in CW, and time-gated photon detection [36, 37]. This implementation

[denoted gated CW-STED (gCW-STED) or gated STED (gSTED)] still avoids laser pulse preparation, but obtains a similar performance as the pulsed STED implementation. In this chapter, we describe the physical principles of the gCW-STED implementation, formulate the theoretical framework which characterizes its main benefits and limitations, and show experimental data.

2 Principle of Gated CW-STED Microscopy

The main reason for the poorer spatial resolution of the CW-STED microscope (with respect to the pulsed STED microscope) is the low peak intensity provided by the STED beam operating in CW. Unlike in the pulsed STED implementation, where all the photons (of the STED pulse) act instantaneously after the fluorescent label's (or fluorophore's) excitation event (i.e., the population of its on-state), in the CW-STED implementation the photons are spread over the whole excited-state lifetime of the fluorophore. As a consequence, the STED intensity instantaneously acting on the excited-state is typically lower, and so is the instantaneous probability for de-excitation to the ground off-state (i.e., the rate of SE k_{STED} is lower). This results in a non-negligible part of the fluorophores still emitting fluorescence because they have not been exposed to enough stimulating photons. Such fluorescence is particularly prevalent at the slopes of the doughnut zero-intensity point where the STED beam intensity is lower thus decreasing the fluorescence spatial confinement and reducing the spatial resolution [38].

In other words, the inhibition of fluorescence by SE strongly depends on the number of stimulating photons to which the fluorophore is exposed while residing in the excited-state. If the fluorescence photons are collected only after a time $>T_{\mathrm{g}}$ of the fluorophores' excitation, it ensures that the collected fluorescence photons stems from fluorophores which have resided in the excited-state for at least a time $>T_{\mathrm{g}}$ and have thereby been exposed to stimulating photons for at least the same amount of time. As a result, mainly the fluorescence emission of those fluorophores is recorded, that are exposed to rather low levels of STED light, i.e., which are at or close to the zero-intensity center, thus further confining the effective spot size (Fig. 2). Practically, it is necessary to know the time at which the fluorophores are excited, which is realized by using a pulsed excitation laser that triggers the excitation and synchronizes the photon detection: The fluorophores are excited all at the same time, and time-gated photon detection allows to discard early fluorescence photons ($<T_{\mathrm{g}}$) (Fig. 2a). As a result, the ability to force fluorophores to their ground off-state for a given STED laser power P_{STED}, also called the fluorescence depletion curve, is substantially optimized (Fig. 2b). In particular, the longer the delay T_{g} between the excitation and the detection of fluorescence photons, the more it is ensured that fluorescence photons are recorded mainly from fluorophores located in the doughnut center where the STED beam intensity is "zero."

A different explanation to the principle governing the gCW-STED implementation relies on the STED light induced change of the fluorophore's excited-state

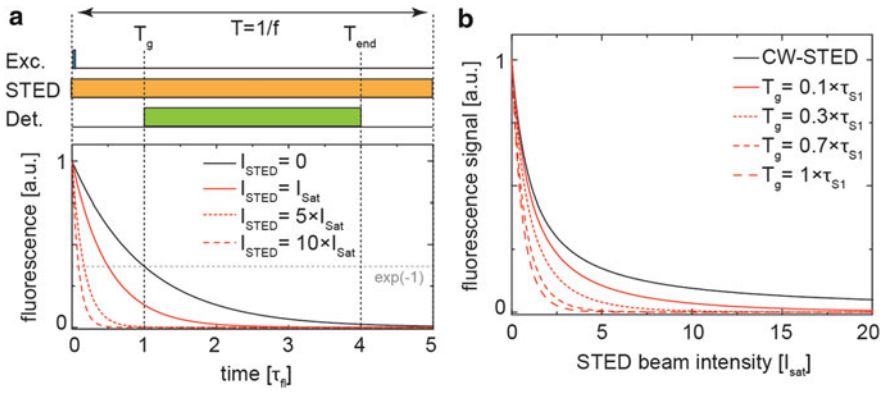

Fig. 2 Laser timing in gCW-STED and detected fluorescence signal. (**a**) (*Upper panel*) Sketch of experimental time sequence of excitation laser pulse (Exc), CW STED laser illumination (STED, *orange*), and gated detection window (Det., *green*) with pulse repetition rate f and inter-pulse distance T of the excitation laser, and start T_g and end time T_{end} of the gated detection (relative to the excitation pulse). (*Lower panel*) Theoretical time-evolution of the probability of emitting fluorescence photons [Eq. (2), time axis in units of τ_{S1}] following an excitation event at time 0 in the absence ($I_{STED} = 0$, *black*) and presence ($I_{STED} = 1, 5, 10 \times I_{sat}$, *red* as labeled) of CW STED light. (**b**) Calculated depletion curve of the gCW-STED microscope [Eq. (4)]: detected fluorescence signal as function of the STED laser intensity (in units of I_{sat}) for increasing delay time T_g (in units of fluorescence lifetime τ_{S1}). In the CW-STED implementation the photon-arrival time information is discarded and the whole signal is registered

lifetime. SE shortens the average time a fluorophore spends in the excited-state; that is, its effective excited-state lifetime τ varies inversely with the de-excitation rate of SE, i.e., also with the intensity of the STED laser. Consequently, the effective excited-state lifetime τ of a fluorophore changes according to its position within the doughnut-shaped pattern. In particular, the effective excited-state lifetime τ is lowest in the doughnut crest and highest in the doughnut center (Fig. 3b). By collecting the fluorescent photons after a time delay T_g from the excitation events it is possible to reject photons emitted by fluorophores with a short excited-state lifetime, located in the periphery of the excitation spot, and highlight photons emitted by fluorophores with a long excited-state lifetime, located close to the "zero-intensity point." As a result, the effective area from which the fluorescence signal is registered is further confined (Fig. 3c, d).

Theoretically, this area can be tuned to infinitely small sizes by infinitely delaying the detection. Practically, the loss of signal, which is intrinsic to the time-gated detection, introduces an upper limit on the time delay T_g [37, 38].

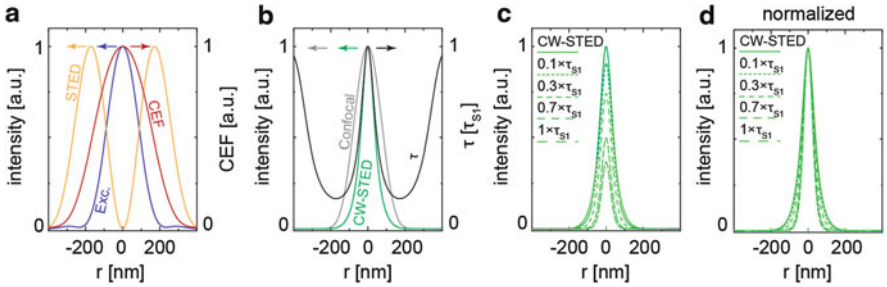

Fig. 3 Effective observation spot in gCW-STED microscopy. (**a**) Calculated radial r focal intensity profile of the excitation beam (Exc., *blue*), the STED beam (STED, *orange*), and the radial distribution of the collection efficiency function (CEF, *red*; namely the projection of the confocal pinhole into the specimen space). (**b**) Calculated focal intensity radial profile of the effective observation spot or E-PSF of the confocal microscope (*gray*) and CW-STED microscope when the intensity at the doughnut crest I^{m}_{STED} is five times greater than the saturation intensity I_{sat} (*green*), together with the calculated excited-state lifetime τ profile (*black*). (**c**, **d**) Calculated radial intensity profile of the un-normalized (**c**) and normalized (**d**) E-PSF of the gCW-STED microscope for different delay-times T_g (in units of τ_{S1}). Focal intensity calculations for the excitation beam $h_{exc}(r)$, the STED beam $I_{STED}(r)$ as well as the collection efficiency $h_{det}(r)$ were carried out for a 1.4 NA oil immersion lens, an excitation wavelength of 488 nm, a STED wavelength of 577 nm, an emission wavelength of 520 nm, and a back projected pinhole radius of 250 nm. All calculations are based on Fourier theory [39]

2.1 Theory

In the following, we present a theoretical model that describes the effect of the time-gated photon detection in a STED microscope based on a pulsed excitation laser and a STED laser running in CW [38]. We start describing the temporal evolution of the probability of emitting fluorescence photons under SE and derive an expression for the inhibition of the spontaneously emitted fluorescence photons by SE and time-gated detection as a function of the intensity I_{STED} of the STED beam. Finally, we present an expression for the effective spot or point-spread-function (E-PSF) of the gCW-STED microscope.

We make several assumptions: (1) The electronic level system of the fluorophores is described by a simple two-level model consisting of a ground S_0 (off) and a first excited electronic state S_1 (on); dark states (such as the triplet state) and vibrational sub-states are neglected. (2) Possible excitation from $S_0 - S_1$ by the STED laser is neglected. (3) The fluorophores are initially in their S_1 state due to an instantaneously assumed excitation pulse. We also assume that the time period $T = 1/f$ between two pulses (with f being the pulse repetition frequency) is substantially longer than the excited-state lifetime τ_{S1} of the fluorophores, i.e., all fluorophores have relaxed to S_0 before the arrival of the next excitation pulse; hence, the conditions at the beginning of every excitation cycle are the same. (4) The spontaneous de-excitation $S_1 \rightarrow S_0$ takes place with a rate constant $k_{S1} = 1/\tau_{S1}$, and fluorescence photons are emitted with a quantum yield q_{fl}, i.e.,

with a rate $k_{fl} = k_{S1} q_{fl}$. (5) The rate of stimulated photon emission during the STED beam action is given by $k_{STED} = \sigma^{\sim}_{STED} I^{*}_{STED}$ with $\sigma^{\sim}_{STED} = \sigma_{STED} \lambda_{STED}/(\hbar c)$ being the SE cross-section σ_{STED} divided by the photon energy $\hbar c/\lambda_{STED}$ (λ_{STED} is the wavelength of the STED laser, $hc = 1.99 \times 10^{-25}$ J m is the product of Planck's constant and the velocity of light), and I^{*}_{STED} defines the transient (instantaneous) STED intensity. In the case of CW illumination the transient STED intensity I^{*}_{STED} is equal to the time-average STED intensity I_{STED}, i.e., $I_{STED} = I^{*}_{STED}$. (6) We define a saturation intensity I_{sat} as the STED intensity at which $k_{S1} = k_{STED}$, i.e., $I_{sat} = k_{S1}/\sigma^{\sim}_{STED}$ revealing a transient saturation factor $\varsigma = I_{STED}/I_{sat} = k_{STED}/k_{S1}$. (7) The STED beam is intensity noise-free and circular polarized; potential bias in the ability to inhibit fluorescence emission by SE due to fluctuations of the STED beam intensity [35] and by fluorophore orientations [39] is neglected.

The probability of emitting fluorescence photons (or further on more simply the fluorescence signal) is proportional to the relative population P_{S1} of the first excited-state S_1, whose change over time t can be expressed by the rate equation

$$dP_{S1}/dt = -k_{S1} P_{S1} - k_{STED} P_{S1}, \tag{1}$$

with $P_{S1}(0) = 1$. Consequently, the fluorescence emission rate at time t after the excitation pulse is (with $k_{STED} = \varsigma \cdot k_{S1}$)

$$F(t, I_{STED}) = k_{S1}\, q_{fl} \exp(-(k_{S1} + k_{STED})t) = k_{S1}\, q_{fl} \exp(-(1+\varsigma) k_{S1} t). \tag{2}$$

It is clear that in the presence of the STED beam the excited-state lifetime $\tau = 1/(k_{S1} + k_{STED})$ is shortened with increasing I_{STED} ($\varsigma = I_{STED}/I_{sat}$).

From Eq. (2) we can calculate the normalized probability that an excited fluorophore contributes to the measured signal as a function of the STED beam intensity I_{STED} and the time delay T_g, i.e., the fluorescence depletion curve $\eta(I_{STED}, T_g)$ of the gCW-STED microscope

$$\eta\left(I_{STED}, T_g\right) = \int_{T_g}^{T} F(t, I_{STED}) dt \Big/ \int_{T_g}^{T} F(t, 0) dt. \tag{3}$$

Solving Eq. (3) under the above assumption one obtains

$$\begin{aligned} \eta\left(I_{STED}, T_g\right) &= \exp\left(-\sigma^{\sim}_{STED} I_{STED} T_g\right) \times k_{S1} / \left(k_{S1} + \sigma^{\sim}_{STED} I_{STED}\right) \\ &= \exp\left(-\varsigma \times T_g/\tau_{S1}\right) \times 1/(1+\varsigma) \end{aligned} \tag{4}$$

In the absence of time gating ($T_g = 0$), Eq. (4) represents the depletion curve of the classical CW-STED implementation. Introducing the time-gated detection $T_g > 0$ strongly improves the probability of inhibiting fluorescence emission from the fluorophore, which is essential for obtaining an improvement in spatial resolution. Note, that with the time-gated detection an improved inhibition of emitting fluorescence photons can already be achieved by increasing the time gating T_g, i.e.,

without increasing the intensity of the STED beam further (Fig. 2). However, note that without any STED light ($\varsigma = 0$), there is no depletion ($\eta = 1$), and the time gating has no effect on the depletion.

To understand the relation to and differences from the pulsed STED implementation, it is also crucial to note that Eq. (4) consists of two parts. The first exponential term is reminiscent of the depletion curve of the all-pulsed STED implementation, with T_g replacing the pulse-width of the STED beam. The second term $(1/(1+\varsigma))$ is equivalent to the depletion curve for the all CW-STED implementation. In other words, Eq. (4) reveals that depletion of fluorescence emission by SE follows an exponential decay until T_g (as for the all-pulsed STED scheme), and fluorescence emitted from fluorophores still present in the excited state after time T_g is depleted as in the classical CW-STED implementation.

Given the depletion curve [Eq. (4)] one can now compute the effective point-spread-function (E-SPF) of the gCW-STED approach. The E-PSF of a STED microscope describes the region in which fluorophores are still able to contribute to the measured fluorescence signal. More specifically, it gives the normalized probability with which fluorophores at a given distance r from the focal center are still able to (1) spontaneously emit fluorescence photons and (2) contribute to the measured signal. While the first depends on the intensity profile of the excitation laser and the spatial dependency of fluorescence inhibition by the STED laser, the latter involves the detection or (photon) collection efficiency of the microscope (given by optical elements such as the confocal pinhole or filters). Consequently, the E-PSF of the gCW-STED microscope $h(r)$ is expressed as the product of the probability to excite the fluorophore (the intensity profile of the focused excitation laser) $h_{exc}(r)$, the collection efficiency probability $h_{det}(r)$, and the depletion probability $\eta(I_{STED}(r), T_g)$ [Eq. (4)]. Note, that the product $h_c(r) = h_{exc}(r)h_{det}(r)$ represents the PSF of the conventional confocal microscope without a STED laser.

A simple analytical description of the E-PSF can be derived by approximating the confocal PSF with a Gaussian distribution $h_c(r) = \exp(4\ln 2 r^2/{d_c}^2)$ with a full-width-at-half-maximum (FWHM) diameter d_c, and the doughnut-shaped intensity profile of the STED laser with a parabola $I_{STED}(r) \approx 4I^m_{STED}a^2r^2$, where I^m_{STED} is the intensity at the doughnut crest, and a is a constant that depends on the shape of the doughnut minimum.

$$\begin{aligned} h(r) &= h_c(r) \times \eta\big(I_{STED}(r),\ T_g\big) \\ &= \exp\big(-T_g/\tau_{S1}\big) \times h_c(r) \times \big(1 + 4ar^2 I^m_{STED}/I_{sat}\big)^{-1} \\ &\quad \times \exp\big(-4ar^2 I^m_{STED}/I_{sat} T_g/\tau_{S1}\big). \end{aligned} \tag{5}$$

The spatial r dependency of Eq. (5) includes the confocal PSF $h_c(r)$, a Lorentzian term $(1 + 4ar^2 I^m_{STED}/I_{sat})^{-1}$ linked to the SE process, and a Gaussian term linked to the time-gated detection $\exp(-4ar^2 I^m_{STED}/I_{sat} T_g/\tau_{S1})$. By replacing the Lorentzian term with a Gaussian term [37, 38] the FWHM diameter d_{STED} of the E-PSF reads [37, 38]

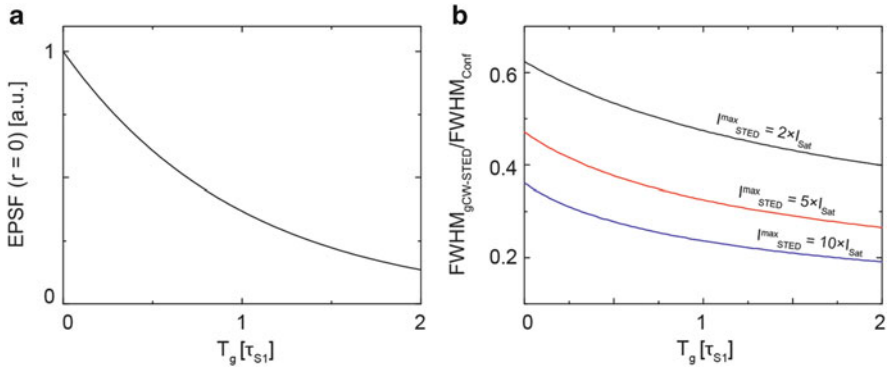

Fig. 4 Characteristic dependencies of the E-PSF properties for the gCW-STED microscope. (**a**) Calculated amplitude of the E-PSF as a function of the delay time T_g (in units of τ_{S1}). (**b**) Calculated relative reduction of the FWHM of the E-PSF, with respect to the confocal counterpart, as a function of the delay time T_g (in units of τ_{S1}) for three different STED intensities as labelled. Same parameters of Fig. 3

$$d_{\mathrm{STED}}\left(I_{\mathrm{STED}}, T_g\right) = d_c / \sqrt{1 + {d_c}^2 a^2 I_{\mathrm{STED}}^m / I_{\mathrm{sat}}\left(1 + T_g/(\tau_{S1} ln 2)\right)}. \qquad (6)$$

Consequently, d_{STED} decreases both with increasing STED intensity I_{STED} as well as with the time gating position T_g (Fig. 4b). In addition to the reduction of the FWHM diameter d_{STED} of the E-PSF, also the pedestal (which is characteristic for the CW-STED E-PSF, $T_g = 0$) is significantly reduced with time gating (Fig. 2d). This is the fundamental improvement in imaging contrast and thus effective spatial resolution over (ungated) CW-STED.

As we have pointed out before [38], the improvement in effective spatial resolution due to the time gating can also be explained in spatial frequency space, where in principle the appearance of large spatial frequencies in the Fourier transform of the E-PSF indicates higher effective spatial resolution. Rather than creating higher spatial frequencies (as is the case with increasing the STED laser intensity), the time gating process damps lower frequencies and thus amplifies the fraction of already existing larger spatial frequencies.

It is important to keep in mind, that the time gating ($T_g > 0$) not only reduces the FWHM and pedestal of the E-PSF, but also the amplitude of the E-PSF, i.e., $h(0) = \exp(-T_g/\tau_{S1})$ [Eq. (5) and Fig. 4]. Thus, it is necessary to balance the choice of the time delay T_g against the reduction in signal. Reduction of the signal usually results in a degradation of the signal-to-noise/background ratio (SNR and SBR), and thus in a potential degradation of the effective resolution, as will be pointed out later on.

3 Results

The performance of the gCW-STED microscope is well demonstrated by imaging sub-diffraction sized fluorescence beads (40 nm in diameter). Figure 5 shows, in a tabular form, images obtained with different combinations of STED laser power P_{STED} (i.e., STED laser intensities I_{STED}) and delays T_{g} of the time-gated detection. From the size of the imaged beads, one can estimate the effective spatial resolution. As predicted by theory [see Eq. (6)], the effective spatial resolution improves with increasing P_{STED} (from top to bottom), but more importantly with increasing time delay T_{g} (left to right). In addition to the decreased spot size of the imaged beads, one can also observe a reduced blur in the images of the beads with increasing T_{g}, as also pointed out in the theory by the reduction of the E-PSF's pedestal.

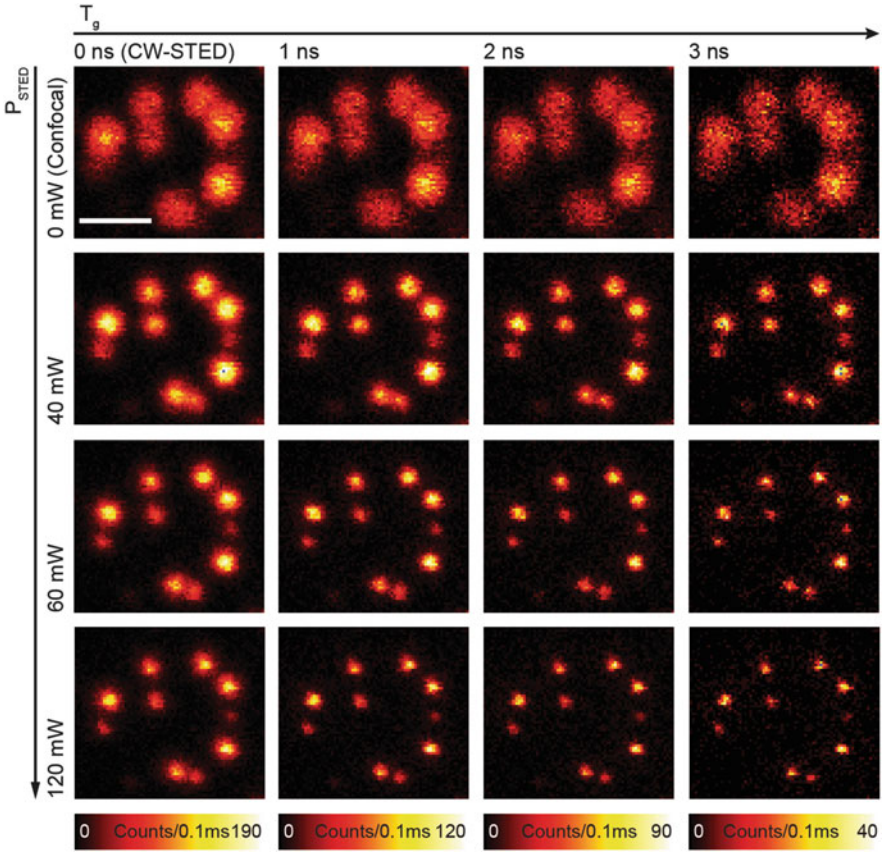

Fig. 5 Effective resolution tuning for gCW-STED microscopy. gCW-STED imaging of 40 nm fluorescent beads for different STED beam powers P_{STED} (*rows*) and different delay-times T_{g} (*columns*). Excitation: 488/6 nm, $f = 80$ MHz, $P_{\mathrm{exc}} = 20$ µW; STED: 577 nm. Scale bar 1 µm. Figure is modified, with permission, from reference [41]

Notably, in the classical CW-STED implementation ($T_g = 0$ ns) the effective spatial resolution substantially improves only at comparatively large STED powers $P_{STED} > 120$ mW. In contrast, with time gating ($T_g > 0$ ns) a similar effective spatial resolution is already obtained with threefold lower STED laser powers $P_{STED} > 40$ mW. As also pointed out in theory, the effective spatial resolution is not improved by time gating in the confocal case, i.e., without STED light, $P_{STED} = 0$ mW. Figure 5 thus clearly points out the major benefits of the gCW-STED implementation over the classical CW-STED microscope: Reduction of the E-PSF's pedestal or image blur and requirement of substantially lower STED laser powers.

The potential to obtain sub-diffraction resolution at moderate STED beam power is very attractive for live-cell imaging. Indeed, reducing the CW-STED laser power and still obtaining an improved spatial resolution greatly reduces the photodamage and phototoxic stress on the sample. Figure 6a compares classical CW-STED and gCW-STED microscopy images of a living PtK2 cell with keratin filaments tagged with the yellow fluorescent protein Citrine. In addition, Fig. 6b compares similar images of a fixed Ptk2 cell with vimentin filaments immunolabeled with the organic dye Alexa Fluor 488. Following the increase in effective resolution and the suppression of the E-PSF's pedestal (or image blur), as provided by the time-gated detection, the gCW-STED microscopy images are clearly superior in contrast and detail. More importantly, these improvements were obtained at moderate STED intensity ($P_{STED} = 200$ mW at 592 nm). A similar spatial resolution on a similar sample was obtained in the classical CW-STED modality with threefold larger STED laser powers ($P_{STED} > 600$ mW at 592 nm) [42]. Note, that we have in these applications chosen a moderate time gate ($T_g = 1.5$ ns). Much larger time gates would have reduced the overall signal too much, resulting in rather bad SNR of the images [38].

Recently, it has been demonstrated that the STED laser power can be further reduced ($P_{STED} = 70$–90 mW) if a laser with a lower noise level is used (such as a 577 nm OPSL vs a 592 nm fiber laser) [35, 41]. This level of STED laser power is comparable to the average power used by the more complex all-pulsed STED implementations (with 80 MHz pulse repetition rates).

Time-gated detection also opens new perspectives for combining STED microscopy with fluorescence-correlation-spectroscopy (FCS) [37]. Before the introduction of time gating this combination was only possible using an all-pulsed STED system [43]: The pedestal of the E-PSF of the classical CW-STED microscope deteriorates the FCS performance too much [22, 37].

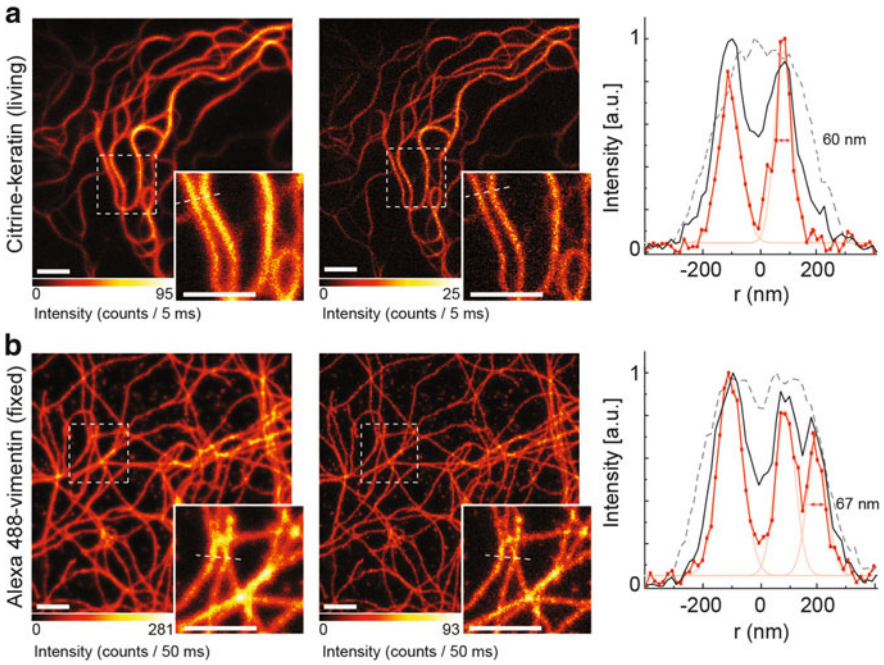

Fig. 6 gCW-STED microscopy and cellular imaging. (**a**) Keratin fused to the fluorescent protein citrine in a living PtK2 cell and (**b**) vimentin filaments in a fixed PtK2 cell labeled by immunocytochemistry with the organic dye Alexa Fluor 488. Shown are CW-STED (*left panels*) and gCW-STED (*middle panels*) recordings, (*insets*) magnified views of the marked (*dotted squares*) areas (renormalized in signal intensity), as well as (*right panels*) normalized intensity (arbitrary units; *a.u.*) profiles along the *dashed lines* in the *insets* for confocal (*dashed gray*), CW-STED (*black*), and gCW-STED (*red*) with Gaussian fits (*red shallow*) to the peaks of the gCW-STED recordings, indicating the disclosure of structures less than 67 nm in diameter. Scale bars, 1 μm. Excitation: 485 nm, $f = 80$ MHz and $P_{exc} = 11$ μW; STED: 592 nm and $P_{STED} = 200$ mW; gated detection: $T_g = 1.5$ ns and $\Delta T = T_{end} - T_g = 8$ ns. Figure is modified, with permission, from reference [37]

4 Conclusions and Discussions

Although, in the past, the instrumentation for STED microscopy was perceived to be too complex and costly, recent advances have demonstrated its ease of implementation by simplifying the original experimental design. The so-called CW-STED implementation is probably the most straightforward version, since it uses a STED laser operating in CW. This CW modus does not require any temporal synchronization of excitation and STED lasers as well as pulse optimization of the STED laser. However, the spatial resolution and image contrast of the CW modality lacks behind that of the pulsed STED implementation. Gated CW-STED overcomes this limitation without increasing complexity. In particular, a classical CW-STED can be updated to a gated version by simply substituting the excitation source with a

pulsed laser and filtering the registered fluorescence photons relative to the excitation pulse using additional hardware and/or software post-processing [37, 41, 44]. While the pulsed and the gCW-STED implementations employ comparable time-averaged STED laser intensities, the gCW-STED approach strongly reduces the peak intensity. The latter reduction is often important for minimizing both phototoxicity and photodamage of the fluorescent labels, since these effects usually scale non-linearly with the intensity [45].

Theoretically, time-gated detection can continuously increase the effective spatial resolution of a gCW-STED microscope. However, time gating also introduces a concomitant decrease in overall signal, which imposes an upper limit on the choice of time gate position T_g. In the presence of background, long T_g can induce a strong reduction of the SNR and SBR, which cancels out the benefits of the time gating and, in the worst case, reduces the effective resolution. Intuitively, this degradation can be compensated for by increasing the intensity of the excitation laser; however, this option is again limited by an increase in photodamaging effects, and by the saturation of the fluorescence emission [45].

An obvious way of optimizing the SNR of gCW-STED experiments is by maximizing the detection efficiency of the microscope setup, as done by using photon detectors with high-quantum efficiency and low dead times [46] as well as dead-time free photon-counting electronics [47]. Within this context, further important characteristics of the photon detectors and photon-counting electronics are by Bülter et al. [46] and by Wahl et al. [47]: (1) high temporal resolution, i.e., low temporal jitter, since such jitter results in the unwanted detection of early-emitted fluorescence photons, slipping through the gated detection, and thus a reduction of the effective spatial resolution and image contrast; (2) low shift of the instrument response function (IRF) with changing photon count rates, since a shift in the IRF requires also a shift of the absolute gating positions, which is impractical; (3) low dark-count rate and low afterpulsing probabilities.

Removal of background is another obvious choice for recovering the SBR and restoring the benefits of the time-gated detection. A potential source of background in STED microscopy is spontaneous fluorescence signal induced by the STED beam itself. While the stimulating and stimulated light can be spectrally rejected from the detected signal, spontaneous fluorescence emission induced by unwanted $S_0{-}S_1$ excitation by the strong STED laser illumination (anti-Stokes emission) is spectrally identical to the fluorescent signal evoked by the excitation laser, and can thus not straightforwardly be rejected. Anti-Stokes emission by the STED light usually only occurs when choosing a wavelength of the STED light close to the emission maximum of a fluorescent label, where the cross-section of SE is large, but also that of the absorption becomes larger again. The anti-Stokes signal mainly shows up at the doughnut crest, and thus contributes to the detected signal and final image (together with the (non-inhibited) fluorescence emission from the doughnut center). If the anti-Stokes signal becomes comparable to the signal emitted from the doughnut center, the contrast of the image is reduced and the improvement in spatial resolution without effect. This situation most likely happens when using large T_g, since the amount of the desired fluorescence signal decays exponentially

with T_g, while the anti-Stokes emission background decreases linearly with T_g [38]. Red-shifting the wavelength of the STED laser, where the absorption cross-section of the fluorophore is practically zero, obviously reduces anti-Stokes fluorescence emission, but the concomitant decrease in SE cross-section demands the use of larger STED laser intensities. Different temporal characteristics of the excitation and STED laser offer a way to separate fluorescence contributions from both lasers using, for example, a lock-in (synchronous) detection scheme [23, 48]. Here, the gCW-STED modality brings along a straightforward realization, since the temporal characteristics are significantly different for the pulsed excitation and the CW operating STED lasers. Fluorescence signal that is uncorrelated to the excitation pulses can straightforwardly be filtered out using a lock-in detection scheme in a time-correlated-single-photon-counting (TCSPC) measurement mode [49], which is anyway usually applied in a gCW-STED microscope [37, 41, 50].

Image deconvolution [51] is a common way of increasing the SNR of specifically STED microscope images. Due to the non-linear dependence of the fluorescence signal on the intensity of the STED laser, the microscope can potentially transmit all spatial frequencies of the sample. This theoretically band-unlimited nature of the STED microscope offers a new perspective for image deconvolution algorithms, whose aims, in this context, are the recovery of spatial frequencies in the microscope images otherwise hidden by noise [52].

We conclude this chapter by discussing a strategy to further reduce photodamage in a gCW-STED microscope. It has been demonstrated that a prominent photodamage pathway of the fluorescence labels is via long-lived dark states such as the triplet state (which are populated after excitation to S_1). Fluorophores residing in their dark states may be, with large probability, elevated to higher excited electronic states by absorption of additional (STED beam) light, from where photodamage or photobleaching reactions are highly efficient [53], so-called non-linear photobleaching [44, 54]. By implementing an all-pulsed STED microscopy modality with low-repetition rates, lower than the typical few-μs long lifetime of a fluorophore's triplet state in aqueous environment, the population of fluorophores in their dark triplet state can be reduced for the arrival of subsequent laser pulses, since the triplet state has enough time to relax to the ground state before it is exposed to the successive STED pulse. As a consequence, the probability of non-linear photobleaching is strongly reduced. Such implementation has been denoted triplet relaxation (T-REX) STED microscopy [55]. For example, 250 kHz instead of 80 MHz pulse repetition has been employed, corresponding to 4 μs instead of 12.5 ns inter-pulse delay times, respectively. Since gCW-STED relies on a STED beam operating in CW, this approach cannot straightforwardly be used. A T-Rex effect similar to reducing the laser repetition rate can be achieved by fast beam-scanning [54], also when using STED beam operating in CW [42]. One can also reduce the probability of non-linear photobleaching by shutting down the STED laser at times longer than the fluorescence lifetime τ_{S1} of the fluorophores in the doughnut center, i.e., at times when most of the spontaneous fluorescence has decayed. STED light at these late time points ($\gg\tau_{S1}$ after the excitation pulse) will not act on molecules in the S_1 state, as desired, but rather on fluorophores

populating longer-lived dark states, i.e., will introduce non-linear photobleaching. In the case of an usual 80 MHz pulsed excitation and a 3 ns excited-state lifetime, the STED laser should thus be switched off in the interval between 6 and 12.5 ns after the excitation pulse, which requires a fast modulation of the laser light such as by a synchronized acoustic or electro optical modulator. Unfortunately, this again increases complexity of the gCW-STED setup, but still leaves the ability of working at relatively low peak laser intensities, at least when compared to the current all-pulsed implementations. Such considerations suggest the use of long ($>$1 ns) STED laser pulses in the all-pulsed STED modality (instead of the often applied 100–300 ps), in combination with a time-gated photon detection triggered to the end of the STED pulses [31]: The time-gated photon detection maintains the efficiency of the SE process, while still using strongly lowered peak laser intensities, and reducing costs compared to costly mode-locked laser.

This chapter has given an overview on the basic principle, limitations as well as potentials of the gCW-STED microscope modality. As pointed out, it not only optimizes setup complexity and costs, improves effective spatial resolution and image contrast at rather low CW laser intensities, but also leaves open many spectroscopy possibilities for further improving the STED modality, including its combination with FCS. With commercial turn-key (gCW-)STED setups around and more technological and methodological advancements anticipated, the impact of STED microscopy in biomedical research is expected to significantly increase over the next years.

References

1. Masters BR (2010) The development of fluorescence microscopy. Wiley, Chichester
2. Cella Zanacchi F, Bianchini P, Vicidomini G (2014) Fluorescence microscopy in the spotlight. Microsc Res Tech 77(7):479–482
3. Abbe E (1873) Beiträge zur theorie des mikroskops und der mikroskopischen wahrnehmung. Archiv für Mikroskopische Anatomie 9:413–468
4. Rost FWD (1995) Fluorescence microscopy, vol 2. Cambridge University Press, Cambridge
5. Pohl DW, Denk W, Lanz M (1984) Optical stethoscopy: image recording with resolution lambda/20. Appl Phys Lett 44:651–653
6. Mivelle M, Van Zanten TS, Manzo C, Garcia-Parajo MF (2014) Nanophotonic approaches for nanoscale imaging and single-molecule detection at ultrahigh concentrations. Microsc Res Tech 77(7):537–545
7. Hell SW, Wichmann J (1994) Breaking the diffraction resolution limit by stimulated emission: stimulated-emission-depletion fluorescence microscopy. Opt Lett 19(11):780–782
8. Hell SW, Kroug M (1995) Ground-state depletion fluorescence microscopy, a concept for breaking the diffraction resolution limit. Appl Phys B 60:495–497
9. Hell SW (2009) Microscopy and its focal switch. Nat Methods 6(1):24–32
10. Diaspro A (ed) (2009) Nanoscopy and multidimensional optical fluorescence microscopy. Chapman & Hall, New York
11. Huang B, Babcock H, Zhuang X (2010) Breaking the diffraction barrier: super-resolution imaging of cells. Cell 143(7):1047–1058

12. Hell SW, Jakobs S, Kastrup L (2003) Imaging and writing at the nanoscale with focused visible light through saturable optical transitions. Appl Phys A Mater Sci Process 77(7):859–860
13. Hell SW (2007) Far-field optical nanoscopy. Science 316(5828):1153–1158
14. Eggeling C, Heilemann M (2014) Editorial overview: molecular imaging. Curr Opin Chem Biol 20:v–vii
15. Eggeling C, Willig KI, Barrantes FJ (2013) STED microscopy of living cells: new frontiers in membrane and neurobiology. J Neurochem 126(2):203–212
16. Blom H, Widengren J (2014) STED microscopy: towards broadened use and scope of applications. Curr Opin Chem Biol 20:127–133
17. Klar TA, Hell SW (1999) Subdiffraction resolution in far-field fluorescence microscopy. Opt Lett 24(14):954–956
18. Klar TA, Jakobs S, Dyba M, Egner A, Hell SW (2000) Fluorescence microscopy with diffraction resolution barrier broken by stimulated emission. Proc Natl Acad Sci U S A 97 (15):8206–8210
19. Clausen MP, Galiani S, Bernardino de la Serna J, Fritzsche M, Chojnacki J, Gehmlich K, Lagerholm BC, Eggeling C (2013) Pathways to optical STED microscopy. NanoBioImaging 1 (1):1–12
20. Dyba M, Hell SW (2003) Photostability of a fluorescent marker under pulsed excited-state depletion through stimulated emission. Appl Optics 42(25):5123–5129
21. J-i H, Fron E, Dedecker P, Janssen KPF, Li C, Müllen K, Harke B, Bückers J, Hell SW, Hofkens J (2010) Spectroscopic rationale for efficient stimulated-emission depletion microscopy fluorophores. J Am Chem Soc 132(14):5021–5023
22. Leutenegger M, Eggeling C, Hell SW (2010) Analytical description of STED microscopy performance. Opt Express 18(25):26417–26429
23. Vicidomini G, Moneron G, Eggeling C, Rittweger E, Hell SW (2012) STED with wavelengths closer to the emission maximum. Opt Express 20(5):5225–5236
24. Willig KI, Rizzoli SO, Westphal V, Jahn R, Hell SW (2006) STED microscopy reveals that synaptotagmin remains clustered after synaptic vesicle exocytosis. Nature 440(7086):935–939
25. Wildanger D, Rittweger E, Kastrup L, Hell SW (2008) STED microscopy with a supercontinuum laser source. Opt Express 16(13):9614–9621
26. Bückers J, Wildanger D, Vicidomini G, Kastrup L, Hell SW (2011) Simultaneous multi-lifetime multi-color STED imaging for colocalization analyses. Opt Express 19(4):3130–3143
27. Galiani S, Harke B, Vicidomini G, Lignani G, Benfenati F, Diaspro A, Bianchini P (2012) Strategies to maximize the performance of a STED microscope. Opt Express 20(7):7362–7374
28. Rankin BR, Hell SW (2009) STED microscopy with a MHz pulsed stimulated-Raman-scattering source. Opt Express 17(18):15679–15684
29. Rittweger E, Han KY, Irvine SE, Eggeling C, Hell SW (2009) STED microscopy reveals crystal colour centres with nanometric resolution. Nat Photonics 3:144–147
30. Schrof S, Staudt T, Rittweger E, Wittenmayer N, Dresbach T, Engelhardt J, Hell SW (2011) STED nanoscopy with mass-produced laser diodes. Opt Express 19(9):8066–8072
31. Göttfert F, Wurm CA, Mueller V, Berning S, Cordes VC, Honigmann A, Hell SW (2013) Coaligned dual-channel STED nanoscopy and molecular diffusion analysis at 20 nm resolution. Biophys J 105:L01–L03
32. Willig KI, Harke B, Medda R, Hell SW (2007) STED microscopy with continuous wave beams. Nat Methods 4(11):915–918
33. Honigmann A, Eggeling C, Schulze M, Lepert A (2012) Super-resolution STED microscopy advances with yellow CW OPSL. Laser Focus World 48(1):75–79
34. Honigmann A, Mueller V, Fernando UP, Eggeling C, Sperling J (2013) Simplifying STED microscopy of photostable red-emitting labels. Laser + Potonik 5:40–42
35. Coto Hernàndez I, d'Amora M, Diaspro A, Vicidomini G (2014) Influence of laser intensity noise on gated CW-STED microscopy. Laser Phys Lett 11(9):095603
36. Moffitt JR, Osseforth C, Michaelis J (2011) Time-gating improves the spatial resolution of STED microscopy. Opt Express 19(5):4242

37. Vicidomini G, Moneron G, Han KY, Westphal V, Ta H, Reuss M, Engelhardt J, Eggeling C, Hell SW (2011) Sharper low-power STED nanoscopy by time gating. Nat Methods 8 (7):571–573
38. Vicidomini G, Schönle A, Ta H, Han KY, Moneron G, Eggeling C, Hell SW (2013) STED nanoscopy with time-gated detection: theoretical and experimental aspects. PLoS One 8(1): e54421
39. Leutenegger M, Rao R, Leitgeb RA, Lasser T (2006) Fast focus field calculations. Opt Express 14(23):11277–11291
40. Westphal V, Hell SW (2005) Nanoscale resolution in the focal plane of an optical microscope. Phys Rev Lett 94:143903
41. Vicidomini G, Coto Hernández I, d'Amora M, Cella Zanacchi F, Bianchini P, Diaspro A (2014) Gated CW-STED microscopy: a versatile tool for biological nanometer scale investigation. Methods 66(2):124–130
42. Moneron G, Medda R, Hein B, Giske A, Westphal V, Hell SW (2010) Fast STED microscopy with continuous wave fiber lasers. Opt Express 18(2):1302–1309
43. Eggeling C, Ringemann C, Medda R, Schwarzmann G, Sandhoff K, Polyakova S, Belov VN, Hein B, von Middendorff C, Schonle A, Hell SW (2009) Direct observation of the nanoscale dynamics of membrane lipids in a living cell. Nature 457(7233):1159–1162
44. Westin L, Reuss M, Lindskog M, Aperia A, Brismar H (2014) Nanoscopic spine localization of Norbin, an mGluR5 accessory protein. BMC Neurosci 15(1):45
45. Eggeling C, Widengren J, Rigler R, Seidel CAM (1998) Photobleaching of fluorescent dyes under conditions used for single-molecule detection: evidence of two-step photolysis. Anal Chem 70:2651–2659
46. Bülter A (2014) Single-photon counting detectors for the visible range between 300 and 1,000 nm. Springer Ser Fluoresc. doi:10.1007/4243_2014_63
47. Wahl M (2014) Modern TCSPC electronics: principles and acquisition modes. Springer Ser Fluoresc. doi:10.1007/4243_2014_62
48. Ronzitti E, Harke B, Diaspro A (2013) Frequency dependent detection in a STED microscope using modulated excitation light. Opt Express 21(1):210–219
49. Coto Hernàndez I, Peres C, Cella Zanacchi F, d'Amora M, Christodoulou S, Bianchini P, Diaspro A, Vicidomini G (2014) A new filtering technique for removing anti-stokes emission background in gated CW-STED microscopy. J Biophotonics 7(6):376–380
50. Wang Y, Kuang C, Gu Z, Xu Y, Li S, Hao X, Liu X (2013) Time-gated stimulated emission depletion nanoscopy. Opt Eng 52(9):093107
51. Bertero M, Boccacci P, Desiderá G, Vicidomini G (2009) Image deblurring with Poisson data: from cells to galaxies. Inverse Probl 25(12):123006
52. Zanella R, Zanghirati G, Cavicchioli R, Zanni L, Boccacci P, Bertero M, Vicidomini G (2013) Towards real-time image deconvolution: application to confocal and STED microscopy. Sci Rep 3:2523
53. Donnert G, Eggeling C, Hell SW (2007) Major signal increase in fluorescence microscopy through dark-state relaxation. Nat Methods 4(1):81–86
54. Donnert G, Eggeling C, Hell SW (2009) Triplet-relaxation microscopy with bunched pulsed excitation. Photochem Photobiol 8:481–485
55. Donnert G, Keller J, Medda R, Andrei MA, Rizzoli SO, Lührmann R, Jahn R, Eggeling C, Hell SW (2006) Macromolecular-scale resolution in biological fluorescence microscopy. Proc Natl Acad Sci 103(31):11440–11445

Single-Color Centers in Diamond as Single-Photon Sources and Quantum Sensors

Boris Naydenov and Fedor Jelezko

Abstract Single quantum systems in the solid state have a potential application for quantum information processing. Among these, color defects in diamond seem to be the most promising ones, as they can operate at ambient conditions. In this chapter the optical and spin properties of the widely investigated nitrogen-vacancy (NV) and silicon-vacancy (SiV) centers in diamonds will be reviewed. We will present the latest experiments showing their application as single-photon sources, qubits, and sensitive magnetic field sensors with nanometer spatial resolution.

Keywords Diamond • NV centers • Single-photon sources • Single-spin detection • SiV centers

Contents

1 Optical Properties of Color Centers in Diamond 304
2 Long Coherence Time (T_2) of Single Spins in Ultrapure Diamond Material: Application to Nanoscale Sensing 305
3 Active Control of Decoherence 307
4 Engineering Defects by Ion Implantation 308
5 Toward Scalable Quantum Registers: Coherent Control of Single Nuclear Spins 310
6 Experimental Realization of Quantum Entanglement Between Engineered Defects and Elements of Quantum Memory 311
7 Coupling to Photons: Spin–Photon Interface and Single-Photon Sources 313
References 316

B. Naydenov and F. Jelezko (✉)
University of Ulm, Institute for Quantum Optics, Albert-Einstein-Allee 11, 89081 Ulm, Germany
e-mail: fedor.jelezko@uni-ulm.de

P. Kapusta et al. (eds.), *Advanced Photon Counting: Applications, Methods, Instrumentation*, Springer Ser Fluoresc (2015) 15: 303–318, DOI 10.1007/4243_2014_78,

1 Optical Properties of Color Centers in Diamond

The nitrogen-vacancy center (shortly NV) is one of the more than 500 known color defects in diamond [1], and it became very popular in the last decade due to its unique physical properties. NV centers can be created in high-purity diamond, using two methods – through nitrogen ion implantation and annealing and by introducing nitrogen gas during the chemical vapor deposition (CVD) diamond growth. Each NV center consists of a nitrogen atom substituting a carbon atom in the diamond crystal lattice and a vacancy in one of the nearest neighbor sites. The NV electronic ground and excited states are spin triplets each having three spin sublevels, $m_S = 0$ and ± 1. In the absence of external fields, the $m_S = 0$ state is separated from $m_S = \pm 1$ by a 2.87 GHz zero-field splitting in the ground state and 1.4 GHz in the excited state. There is an optical transition between these two states with a zero-phonon line (ZPL) at 637. The first amazing feature of this color center is that the fluorescence of a single NV can be detected. This has been demonstrated in anti-bunching (see [2]) in a Hanburry Brown and Twiss experimental setup equipped with efficient avalanche photodiodes (APD, see chapter by Bülter et al. [3]) as detectors [4]. Single optically active quantum systems can find a wide application as single-photon source for quantum cryptography protocols, and actually the first commercial devices based on NV are already available on the market.[1]

However, the ability to observe single NVs is not the feature that makes these defects unique; there are other color centers in diamond which can also be detected at the single level – for example, TR12 [5], SiV [6], NE8 [7], and many more. It is a fact that the NV electronic spin state can be efficiently prepared, manipulated, and measured with optical and microwave excitation at room temperature [8, 9]. Moreover, they show long-lived spin coherence lifetimes ($T_2 > 1$ ms, see below) at room temperature for ultrapure, ^{12}C-enriched diamond [10]. The optical detection of the spin state works the following way. Illumination with green laser light excites both the $m_S = 0$ and 1 spin states into the excited state, followed by a red fluorescence on timescales ~10 ns back to the same spin state with >95% probability for $m_S = 0$ and ~50% probability for $m_S = 1$. The electronic excited state with $m_S = 1$ can also decay with probability ~50% to the $m_S = 0$ state via non-radiative, non-spin-preserving transitions through metastable electronic states. This process of spin state-dependent fluorescence and decay allows both initialization of the NV electronic spin into the $m_S = 0$ state (optical polarization within ~1 μs) and measurement of the relative population in the $m_S = 0$ and 1 ground spin states via green excitation and red fluorescence intensity measurements (over timescales <1 μs). Once initialized (polarized) via optical pumping, the NV electronic spin state can be manipulated with microwave fields using standard electron spin resonance (ESR) methods. For example, using the appropriate ESR pulse sequences (e.g., free induction decay, Hahn echo, CPMG, etc.) and detecting the NV spin state-dependent fluorescence,

[1] For more information visit http://qcvictoria.com/.

one can detect very low external magnetic fields. Variations on this idea are applicable to measurements of DC, AC, and fluctuating (incoherent) magnetic fields. NV-diamond magnetometry has been proposed [11] and experimentally demonstrated [12, 13], showing that a single NV center in room temperature diamond can provide magnetic field sensitivity approaching 1 $nT/Hz^{1/2}$. Additionally the application of super-resolution optical imaging, scanning AFM, magnetic field gradient, and nanoparticle techniques to NV-diamond magnetometry has been shown, realizing spatial resolution of a few nm for magnetic field sources external to the diamond sample and single nuclear spin (^{13}C) sensing within the diamond crystal.

2 Long Coherence Time (T_2) of Single Spins in Ultrapure Diamond Material: Application to Nanoscale Sensing

Diamond provides a unique platform for quantum information processing in solids owing to the ability to generate optically active spins in a nuclear spin-free lattice. It has been shown that coherence time of electron spins associated with NV defects is solely limited by interaction with the nuclear spin bath in a diamond crystal with very low concentration of paramagnetic impurities. The next step was to extend this coherence time by isotopically engineering the diamond lattice (making diamond containing solely ^{12}C isotope). There were several experimental challenges related to this goal. Commercially available sources of ^{12}C carbon usually contain other impurities (e.g., nitrogen at ppm level, silicon, and others). During the CVD process of diamond growth, these impurities are incorporated into the crystal lattice, thus introducing paramagnetic defects. Such a contamination of the diamond can pose problems related to fluorescence background (preventing detection of single NV defects) and decrease of the coherence time. Nevertheless, with a careful control of the growth parameters, synthetic diamond via CVD process with concentration of parasitic impurities below few parts per billion (ppb) level can be produced. Furthermore, such ultrapure isotopically purified ^{12}C diamond can be synthesized on the surface of other materials (heteroepitaxial growth). Figure 1 (left) shows a confocal microscopy image of such polycrystalline diamond sample with single NV defects visible. Figure 1 shows the measurement of a spin echo (Hahn echo) of single NV center in this diamond. Echo decay time of single electron spin at room temperature approaches 2 ms [14] (comparable with previously reported coherence time for monocrystalline material) [10].

Hahn echo allows detecting coherence lifetimes pure from experimental artifacts like low-frequency magnetic noise in the laboratory and temperature variations which would affect the Zeeman shifts of the spin levels and the zero-field spin-level splitting of NV defects, respectively. Note that other decoupling techniques have been established for active control of the spin coherence (see below). However, all these decoupling and echo methods also refocus unknown magnetic or electric

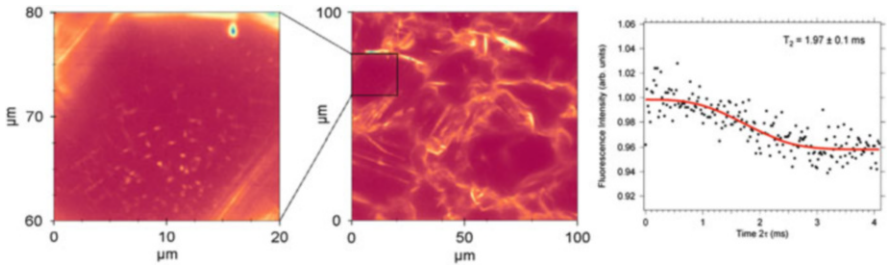

Fig. 1 Confocal image of NV centers in polycrystalline isotopically pure ^{12}C diamond (*left*). Hahn echo decay of a single electron spin (*right*)

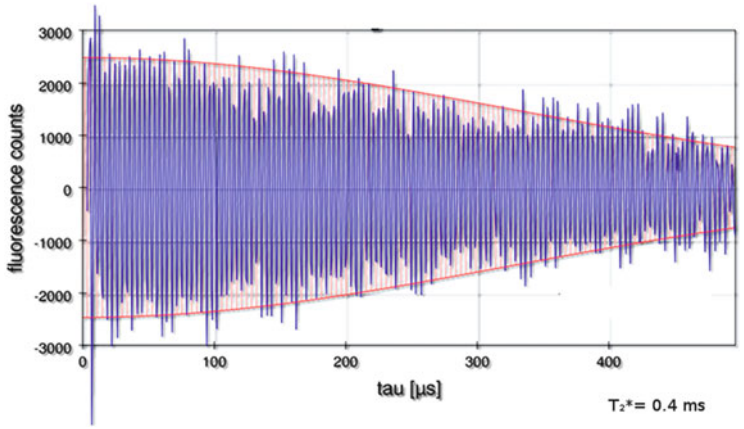

Fig. 2 Free induction decay of a single electron spin in isotopically enriched ^{12}C diamond

fields or temperature drifts which one wants to measure. For this reason, the inhomogeneities in the samples have to be eliminated. The quality of the diamonds can then be determined by measuring the phase memory time using Ramsey sequence or free induction decay (FID) which is sensitive to static or slowly varying fields and temperatures. Such measurements were realized in a magnetically shielded setup built at the University of Stuttgart. Experimental data shown in Fig. 2 demonstrates that coherence time of a single electron spin is approaching ms timescale even without refocusing pulses (longest coherence time reported for any solid state system). Based on this new degree of inhomogeneously broadened spin coherence time, new measurement schemes have been designed specialized for measuring either fields or temperature while being insensitive to the respective other one. Hence magnetic field measurements can be performed which are insensitive to temperature drifts, and temperature can be estimated without being affected by fluctuating magnetic fields [15].

3 Active Control of Decoherence

The loss of coherence is one of the main obstacles for the implementation of quantum information processing, and not all the problems associated with the spin bath can be solved by material science improvement. It was realized a long time ago that active driving of quantum systems provides the possibility to decouple them from environmental noise. The most famous example of this technique is the Hahn echo. In order to reach higher degrees of control, several protocols have been established allowing to reach coherence times approaching the limit imposed by relaxation of the spin state due to coupling to phonons (milliseconds). The next decoupling protocol has been developed in the early days of NMR by Carr-Purcell [16] and later improved by Meiboom and Gill [17]. This pulse sequence is an extension of the Hahn echo idea, by adding many π pulses to flip the spin to be measured. The constant flipping leads to decoupling of the spins from the surrounding spin bath. An example of such decoupling protocol implemented with NVs is shown in Fig. 3 [18].

The efficiency of the dynamic decoupling schemes, which have been introduced to address this problem, is itself limited by the fluctuations in the driving fields which will also introduce noise. This is a big challenge, both experimentally and theoretically, but it has been solved by developing and realizing the concept of concatenated continuous dynamic decoupling. This method can overcome not only the external noise but also fluctuations in driving fields that implement the decoupling sequences and thus holds the potential for achieving relaxation-limited coherence times. The major idea behind this scheme is the use of the first driving

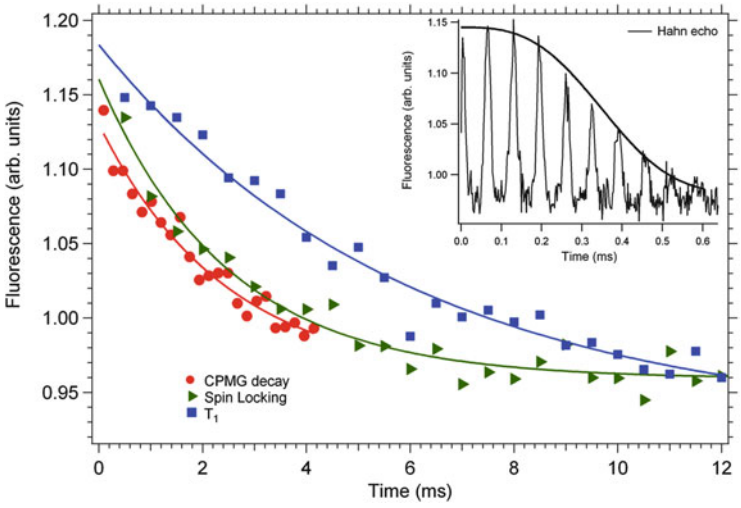

Fig. 3 Experimental data. Hahn echo decay (inset, $T_2 = 0.39 \pm 0.16$ ms), CPMG (*red markers*, $T_2 = 2.44 \pm 0.44$ ms), spin locking (*green markers*, $T_2 = 2.47 \pm 0.27$ ms), and spin lattice relaxation (*blue*, $T_1 = 5.93 \pm 0.7$ ms). The *blue*, *red*, and *green curves* are fits to the data

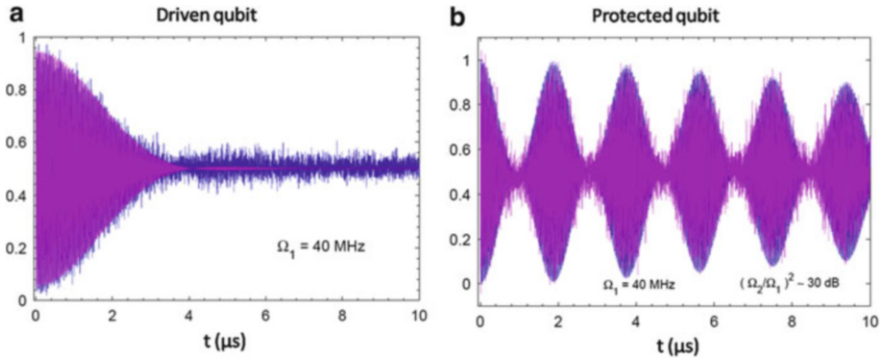

Fig. 4 (**a**) Coherently driven oscillations of NV center with a single microwave field (Rabi oscillations). The *blue curve* is the experimental data, and the purple one is the fitting with a Gaussian decay envelope. The decay of coherence is related to fluctuation of the driving field. (**b**) Persistent Rabi oscillations by adding a second-order driving field

field allowing to suppress environmentally induced decoherence and the second weak field which suppresses noise induced by the first field [19]. Figure 4 demonstrates the efficiency of this scheme. If one wants to couple two or more NV centers and preserving entanglement between them, optimal control techniques have been developed in order to *combine quantum gate synthesis with decoupling* the system from fast relaxing modes. This will be of importance to fully exploit subspaces of slow decoherence, no matter whether they are used as quantum memories or as registers for active computation.

The proposed scheme can be applied to a wide variety of other physical systems including trapped atoms and ions and quantum dots and may be combined with other challenges for quantum technologies such as quantum sensing.

4 Engineering Defects by Ion Implantation

In order to create scalable arrays of quantum registers, it is crucial to be able to produce defects with high yield and high positioning accuracy. An essential requirement here is the strength of dipole–dipole coupling which needs to be stronger than the decoherence rates. Previously magnetic coupling between two single defects was demonstrated, but decoherence of the individual NV spins in this case was too strong, and it was impossible to realize coherent quantum gates (although classical NOT gate was demonstrated for single spins [20]).

Several new ways have been established for optimizing the engineering of NV centers by ion implantation [21–24]. In order to increase the yield of creation of NV spins, color centers were generated with relatively high energy (MeV).

When compared to low energy (keV) implantation, this regime leads to an increased number of vacancies created in close proximity to NV centers, leading

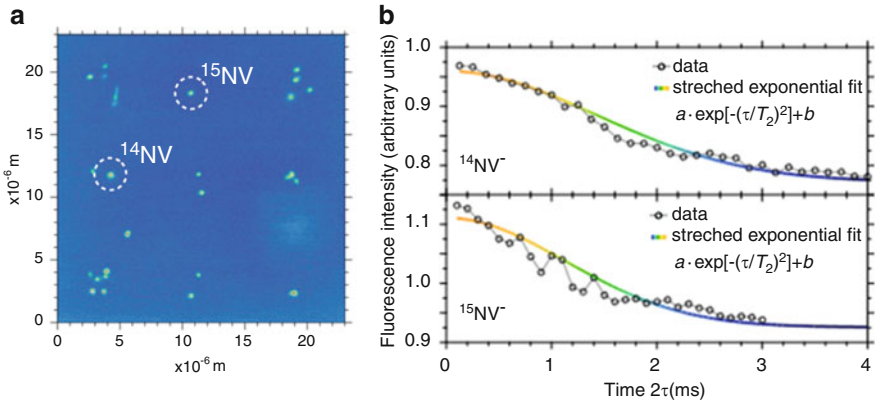

Fig. 5 Confocal image showing the pattern of implanted centers (^{15}NV). Owing to diffusion of vacancies, NV centers associated with native nitrogen incorporated into diamond during growth are also created (^{14}NV). B. Hahn echo decay for "native" (^{14}NV) and implanted (^{15}NV) color centers

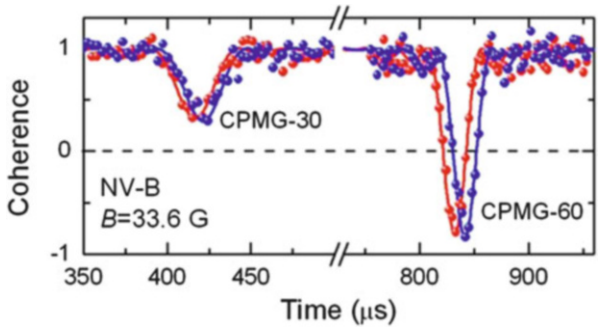

Fig. 6 CPMG measurement showing sharp peaks associated with flip-flops between the electron spin and a distant ^{13}C nucleus

to a higher production yield. Spatial confinement of defects was realized by focusing the ion beam or implantation through nanoapertures. Big effort was directed to eliminate unwanted impurities created close to NV during implantation process (vacancy aggregates). Such defects are stable at annealing temperatures that were previously used to produce NVs (1,100 K), and it has been proven by using ensemble EPR methods in the group of Prof. Isoya at the University of Tsukuba that they are the major obstacle for achieving long coherence time of implanted NV centers. Annealing at higher temperatures (1,300 K) was shown to be a successful tool to increase the phase memory time. Figure 5 shows coherence time measurements for implanted (^{15}NV, NV centers containing rare ^{15}N isotope) and native NV in the isotopically pure crystals. There is a significant improvement in the coherence time compared to the usual annealing procedure (Fig. 6).

5 Toward Scalable Quantum Registers: Coherent Control of Single Nuclear Spins

Optical readout of single NV centers provides unique opportunity to detect coupling to close nuclear spins. Unfortunately this coupling spoils some of the advantages of the nuclear spins. Although their coherence lifetime usually exceeds seconds at room temperature, the presence of the NV center electron spin induces flips on the ms range or even faster. Nevertheless, it is possible to decouple the most prominent nuclear spin, namely, the one of the nitrogen atom, from these flip-flops extending its lifetime close to a second. Even under optical illumination, which is necessary for spin state readout, spin population is preserved allowing for quantum non-demolition measurements on that nuclear spin [25]. This was the first demonstration for a solid state spin. Using this new measurement technique, the measurement speed for sensing applications can be increased up to 400 times. In addition a new insight into the NV center was gained using this nuclear spin as a probe for hidden states that were not accessible before [26]. Moreover, the high fidelity of the quantum non-demolition measurement (QND) of the nitrogen nuclear spin enabled the violation of temporal Bell inequalities rendering this system really quantum mechanical. Further increase is possible by the implementation of bit-flip error correction methods. As further weakly coupled nuclear spins are involved here, robust control techniques have been applied for a high-fidelity control.

As opposed to close nuclear spins, further apart ones are much weakly coupled and very often are hidden within the homogeneous broadening of the EPR resonances. However, such distant nuclear spins were shown to be very useful as a resource (e.g., as additional qubits with long-living quantum memory). Although a successful realization of decoupling protocols was realized by several groups previously, one of the important questions needed to be answered is: is it possible to combine decoupling while keeping the coupling to qubit of interest active? It is indeed possible to realize decoupling of single NV centers from the bath and keep the coupling to a particular nuclear spin visible. A CPMG echo-assisted method allows one to measure and control single ^{13}C nuclear spins situated as far as 3 nm away from the NV [27].

Such electron–nuclear quantum register might be interesting for realizing long-range coupling between nuclear spins via electron spins as a bus (notably such idea was proposed a long time ago in context of bulk spin-based quantum information protocols [28]). The main idea behind this quantum bus approach can be understood as follows. Since the nuclear spin at each site (bearing a qubit) is able to “see” its local electron spin partner via the hyperfine interaction, it follows that if the electron spins at neighboring sites can interact sufficiently strongly, then the two nuclei will be able to communicate indirectly through their electron brothers. While the idea is simple, it turns out to be more complex than one might imagine. A detailed analysis [29] shows that such an electron-mediated interaction between nuclei at adjacent NV sites will be far too weak to be useful. It can be estimated that even quite closely neighboring sites, 10 nanometers (nm) apart, will have an

effective nuclear–nuclear coupling strength of only 0.1 Hz – requiring several seconds to achieve a useful exchange of information. This is impractical, since nuclear spins suffer dephasing (losing any stored qubit) in less than a second.

Recently developed dynamic decoupling schemes combined with the quantum bus approach provide the solution of this hard problem. Theoretical analysis predicts that when the spins are resonantly driven by externally applied electromagnetic fields, the effective strength of the interaction increases dramatically [29] as these fields not only protect against decoherence but also suppress a destructive interference of excitation pathways that is responsible for the very low coupling rates in the undriven scheme. In essence, they introduce a new energy scale into the system, replacing the effect of the crystal field splitting (which acts to suppress the effective nuclear–nuclear coupling) with the Rabi frequencies of the driven spins – a parameter that is under experimental control. Remarkably, with a suitable choice for this parameter, the coupling between nuclei is enhanced a thousand times, becoming entirely practicable as a channel to exchange quantum information. As an added bonus, the act of driving the spins serves to protect the quantum state from the decohering effects of the surroundings. The effect is equivalent to "dynamic decoupling" described in 1.2 in which a spin that is periodically inverted at a frequency faster than the local magnetic field fluctuations acquires an average zero phase. These recent results of driving spins (based on analytical schemes fighting dephasing errors) can be extended by combining them with optimal control methods, thus allowing for other sources of noise to be compensated for at the same time.

6 Experimental Realization of Quantum Entanglement Between Engineered Defects and Elements of Quantum Memory

Experimental realization of entanglement between electron spins and long-living quantum memory allowing to protect entanglement against decoherence has been recently demonstrated [30]. The key point allowing to achieve this goal was the implantation of single defect centers with high spatial resolution and high coherence time of the implanted defects. To generate strongly coupled defect pairs with high probability and at the same time optimum decoherence properties, nitrogen ions with kinetic energies of 1 MeV, corresponding to an implantation depth of 1 μm, have been implanted using a mica nanoaperture mask [31] (hole diameter 20 nm) creating NV pairs at distances less than 20 nm with a success rate of 2%. Figure 7 shows the schematics and results of the experiment.

As it is visible in Fig. 7d, coupling of two single spins as weak as 4 kHz is clearly resolvable. The coupling strength allows the realization of high fidelity of quantum gate and the generation of entanglement between the two spins. The lifetime of the entangled states can be significantly prolonged by mapping the state of

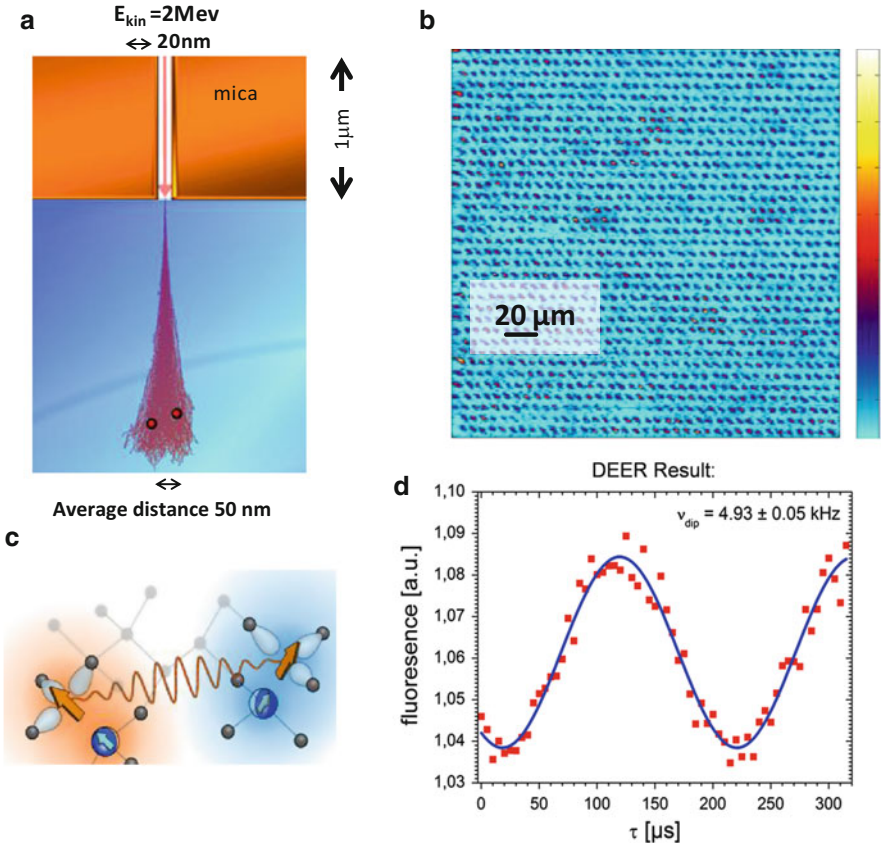

Fig. 7 Coupled NV center spins. (**a**) Schematics of the NV pair implantation. (**b**) Fluorescence image of an array containing NV pairs. (**c**) Scheme showing a pair of dipolar coupled defects. (**d**) Double electron–electron resonance experiment on the NV pair. The oscillation is a direct measure of the coupling frequency $\nu_{\mathrm{dip}} = 4.93 \pm 0.05$ kHz

electron spins into the state of the ^{15}N nuclear spins; see Fig. 8. As these nuclear spins are not interacting on their coherence lifetime of a few seconds, this is the first demonstration of deterministic remote entanglement of two solid state qubits. The tomography of the entangled state of these two-spin qutrits has been measured. This pair of NV centers is an ideal test candidate for the new decoupling methods introduced above like continuous driving. Furthermore, robust control techniques taking into account all peculiarities of the full spin Hamiltonian offer an additional gain both in fidelity and speed with respect to establishing quantum entanglement between remote nuclear spins.

The experiments reveal a fidelity of the entangled state of about 0.67, although the theoretically expected (after considering this particular NV pair) value was about 0.85. It turned out that the limiting factor was the fidelity of the quantum gates (radio frequency and microwave pulses) used for the preparation of the

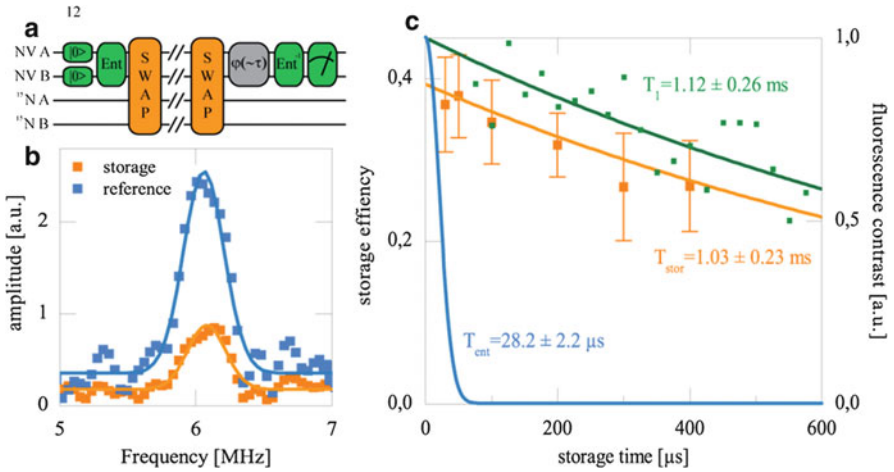

Fig. 8 (**a**) Quantum circuits diagram used for the creation of the entanglement and for the transfer to the nuclear spins. (**b**) Fourier transform of the entanglement signal showing a reference measurement (without storage in the nuclear spins, *blue*) and the single of swapping the entanglement (*orange*). (**c**) Lifetime of the entangled state without saving (*blue*) and after saving and retrieving from the nuclear spins (*orange*). The *green curve* shows the electron spin relaxation time which is limiting the lifetime of the entanglement

entanglement. This problem was solved by applying optimal control theory to design the RF and MW pulses for maximum fidelity. Using this approach, the fidelity could be increased up to the theoretical limit – 0.824 [32].

7 Coupling to Photons: Spin–Photon Interface and Single-Photon Sources

Large-scale entanglement between the quantum registers described above can be realized via an optical channel. Spin selective optical transitions of NV centers provide the possibility to generate entanglement probabilistically via interference of emitted photons. Such schemes rely on the indistinguishability of photons; therefore, fluorescence emission needs to satisfy the so-called "transform-limited" criteria (broadening of the optical lines needs to be within the limit imposed solely by relaxation of the excited states). Dynamic spectral line jumps often appear in CVD and even more in high pressure and high temperature (HPHT) crystals, thus limiting this application. In addition, large static strain distorts the spin and the angular momentum Hamiltonian into an unfavorable parameter range, which needs to be avoided. The spectral jumps and the static disorder can be reduced in low-strain high-quality HPHT crystals, and the static inhomogeneity of NV centers can be reduced down to an unprecedented range of only a few GHz (see Fig. 9).

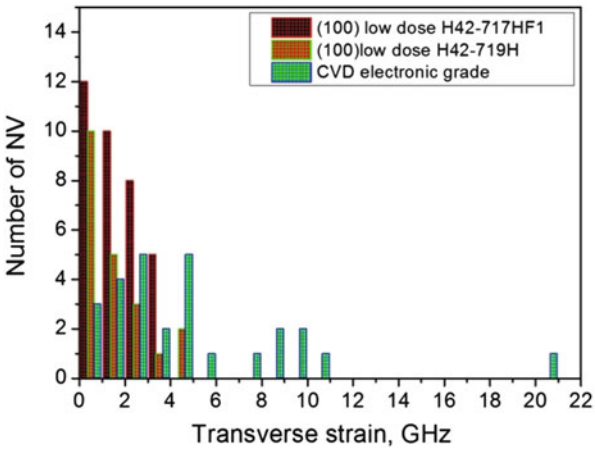

Fig. 9 Histogram of static disorder (transverse strain) in the new HPHT diamond material from Tsukuba ((100) low-dose samples) compared to the best CVD material commercially available from Element Six company

Success rates of probabilistic entanglement generation schemes rely on the effective collection of the emitted photons. The collection efficiency can be significantly increased by engineering nano-optics elements (like solid immersion lenses) in diamond [33]. Further improvement can be achieved by using color centers with strong zero-phonon line (for NV centers narrowband emission accounts for 4% of total emission rate). The silicon-vacancy (SiV) centers are very promising candidates for this purpose. Although a lot of work needs to be done for the detailed understanding of the energy level scheme, it has been already reported that single SiV centers can be detected on the single site level [34].

The SiV center has narrow emission centered at 738 nm, with more than half of the integrated fluorescence intensity lying within a 2 nm spectral window (Fig. 10), making much more suitable as a photon source for integration into photonic devices. It is possible to achieve on-demand production of bright SiV centers (inset in Fig. 10) having identical properties for incorporation into photonic structures. Investigations on single emitters have demonstrated that it is an ideal dipole with high polarization contrast and a fluorescence lifetime of 1 ns.

The first demonstration of coupling to a photonic device has been achieved by manufacturing solid immersion lenses (SIL) in diamond containing SiV centers (Fig. 10b). Centers located near the focal point of the SIL have enhanced brightness due to more efficient coupling of the fluorescence out of the diamond (Fig. 10b). As a result photon collection can be increased by nearly an order of magnitude [35]. Additionally, critical technology steps toward fabrication of plasmonics elements [36], and diamond photonic crystal cavities have been also demonstrated [37].

Single-photon emission from individual quantum systems was demonstrated for single molecules [38]. Color centers in diamond offer the possibility of continuous room temperature operation for single-photon light sources owing to their unlimited photostability under ambient conditions. Note that not only NV centers (for which single-photon emission was demonstrated more than a decade ago [39]) but also

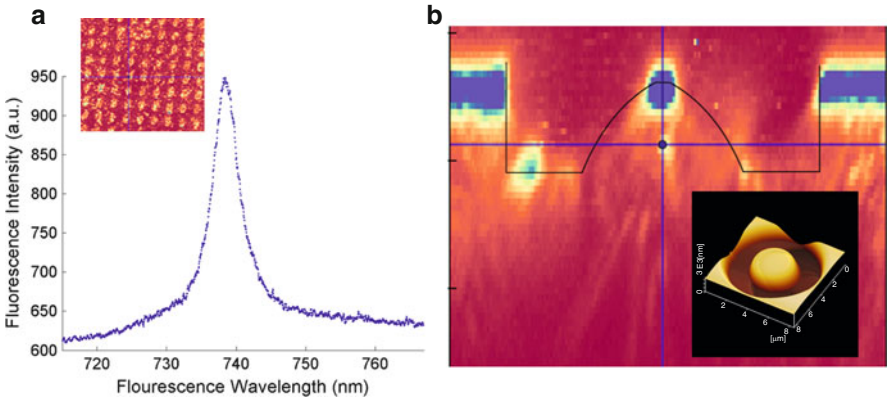

Fig. 10 Fluorescence spectrum of the SiV center in diamond. The fluorescence is sharply peaked with a zero-phonon line centered at 738 nm and a full width at half maximum of 2 nm. The *inset* shows an array of single SIV centers created by deterministic ion implantation (Prof. Shinada, AIST). (**b**) Coupling of SiV centers to a solid immersion lens manufactured in the diamond substrate. A cross-sectional confocal image shows enhanced brightness of SiV centers located at the focus of the SIL. *Black lines* have been drawn to outline the SIL structure for clarity. The *inset* shows AFM picture of SIL polished by laser-assisted ion etching (polishing has been performed by the group of Prof. Yatsui, University of Tokyo)

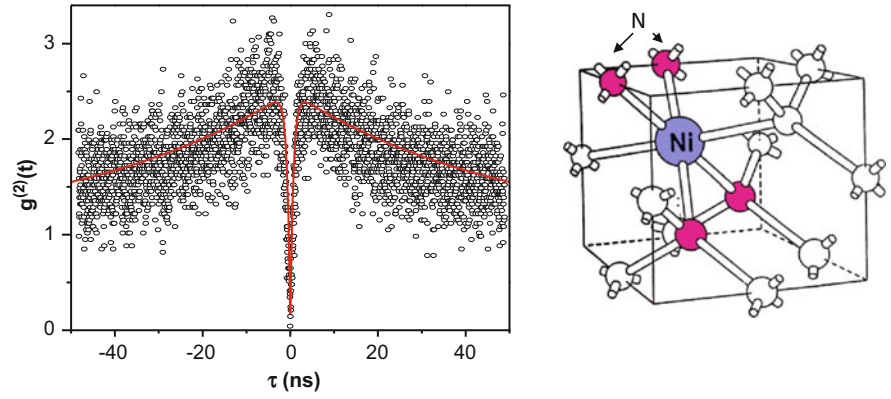

Fig. 11 Fluorescence intensity autocorrelation function of single NE8 defect in diamond

other optically active defects can be used for this purpose. Several color centers show narrow and strong zero-phonon line at room temperature. Figure 11 shows fluorescence intensity autocorrelation function of single nickel–nitrogen complex in diamond. When low-temperature operation is possible, single defects can also be considered as a source of transform-limited photons [40]. The unique spectral homogeneity of SiV center and its strong zero-phonon line emission [41] allowed to demonstrate non-classical interference of photons from two quantum emitters recently [42].

References

1. Zaitsev AM (2001) Optical properties of diamond: a data handbook. Springer, New York
2. Ahlrichs A, Sprenger B, Benson O (2014) Photon counting and timing in quantum optics experiments. Springer Ser Fluoresc. doi:10.1007/4243_2014_69
3. Bülter A (2014) Single-photon counting detectors for the visible range between 300 nm and 1000 nm. In: Kapusta P et al. (eds) Advanced photon counting: applications, methods, instrumentation. Springer series on fluorescence. Springer. doi:10.1007/4243_2014_63
4. Kurtsiefer C, Mayer S, Zarda P, Weinfurter H (2000) Phys Rev Lett 85:290
5. Naydenov B, Kolesov R, Batalov A, Meijer J, Pezzagna S, Rogalla D, Jelezko F, Wrachtrup J (2009) Engineering single photon emitters by ion implantation in diamond. Appl Phys Lett 95: 181109. doi:10.1063/1.3257976
6. Neu E, Agio M, Becher C (2012) Photophysics of single silicon vacancy centers in diamond: implications for single photon emission. Opt Express 20:19956–19971
7. Gaebel T, Popa I, Gruber A, Domhan M, Jelezko F, Wrachtrup J (2004) Stable single-photon source in the near infrared. New J Phys 6:98. doi:10.1088/1367-2630/6/1/098
8. Gruber A, Drabenstedt A, Tietz C, Fleury L, Wrachtrup J, von Borczyskowski C (1997) Scanning confocal optical microscopy and magnetic resonance on single defect centers. Science 276:2012–2014
9. Jelezko F, Gaebel T, Popa I, Gruber A, Wrachtrup J (2004) Observation of coherent oscillations in a single electron spin. Phys Rev Lett 92:076401
10. Balasubramanian G, Neumann P, Twitchen D, Markham M, Kolesov R, Mizuochi N, Isoya J, Achard J, Beck J, Tissler J, Jacques V, Hemmer PR, Jelezko F, Wrachtrup J (2009) Ultralong spin coherence time in isotopically engineered diamond. Nat Mater 8:383–387. doi:10.1038/Nmat2420
11. Taylor JM, Cappellaro P, Childress L, Jiang L, Budker D, Hemmer PR, Yacoby A, Walsworth R, Lukin MD (2008) High-sensitivity diamond magnetometer with nanoscale resolution. Nat Phys 4:810
12. Maze JR, Stanwix PL, Hodges JS, Hong S, Taylor JM, Cappellaro P, Jiang L, Gurudev Dutt MV, Togan E, Zibrov AS, Yacoby A, Walsworth RL, Lukin MD (2008) Nanoscale magnetic sensing with an individual electronic spin in diamond. Nature 455:644
13. Balasubramanian G, Chan IY, Kolesov R, Al-Hmoud M, Tisler J, Shin C, Kim C, Wojcik A, Hemmer PR, Krueger A, Hanke T, Leitenstorfer A, Bratschitsch R, Jelezko F, Wrachtrup J (2008) Nanoscale imaging magnetometry with diamond spins under ambient conditions. Nature 455:648-U646. doi:10.1038/Nature07278
14. Jahnke KD, Naydenov B, Teraji T, Koizumi S, Umeda T, Isoya J, Jelezko F (2012) Long coherence time of spin qubits in [sup 12]C enriched polycrystalline chemical vapor deposition diamond. Appl Phys Lett 101:012405
15. Neumann P, Jakobi I, Dolde F, Burk C, Reuter R, Waldherr G, Honert J, Wolf T, Brunner A, Shim JH, Suter D, Sumiya H, Isoya J, Wrachtrup J (2013) Nano Lett 13:2738
16. Carr HY, Purcell EM (1956) Phys Rev 94:630
17. Meiboom S, Gill D (1958) Rev Sci Instrum 29:688
18. Naydenov B, Dolde F, Hall LT, Shin C, Fedder H, Hollenberg LCL, Jelezko F, Wrachtrup J (2011) Dynamical decoupling of a single-electron spin at room temperature. Phys Rev B 83: 081201
19. Cai J, Naydenov B, Pfeier R, McGuinness LP, Jahnke KD, Jelezko F, Plenio MB, Retzker A (2012) Robust dynamical decoupling with concatenated continuous driving. arXiv 1111.0930v2
20. Neumann P, Kolesov R, Naydenov B, Beck J, Rempp F, Steiner M, Jacques V, Balasubramanian G, Markham ML, Twitchen DJ, Pezzagna S, Meijer J, Twamley J, Jelezko F, Wrachtrup J (2010) Quantum register based on coupled electron spins in a room-temperature solid. Nat Phys 6:249–253. doi:10.1038/Nphys1536

21. Naydenov B, Richter V, Beck J, Steiner M, Neumann P, Balasubramanian G, Achard J, Jelezko F, Wrachtrup J, Kalish R (2010) Enhanced generation of single optically active spins in diamond by ion implantation. Appl Phys Lett 96:163108
22. Pezzagna S, Wildanger D, Mazarov P, Wieck AD, Sarov Y, Rangelow I, Naydenov B, Jelezko F, Hell SW, Meijer J (2010) Nanoscale engineering and optical addressing of single spins in diamond. Small 6:2117. doi:10.1002/smll.201000902
23. Pezzagna S, Naydenov B, Jelezko F, Wrachtrup J, Meijer J (2010) Creation efficiency of nitrogen-vacancy centres in diamond. New J Phys 12:065017. doi:10.1088/1367-2630/12/6/065017
24. Naydenov B, Reinhard F, Lämmle A, Richter V, Kalish R, D'Haenens-Hohansson UFS, Newton M, Jelezko F, Wrachtrup J (2010) Increasing the coherence time of single electron spins in diamond by high temperature annealing. Appl Phys Lett 97:242511
25. Neumann P, Beck J, Steiner M, Rempp F, Fedder H, Hemmer PR, Wrachtrup J, Jelezko F (2010) Single-shot readout of a single nuclear spin. Science 329:542
26. Waldherr G, Beck J, Steiner M, Neumann P, Gali A, Frauenheim T, Jelezko F, Wrachtrup J (2011) Dark states of single nitrogen-vacancy centers in diamond unraveled by single shot NMR. Phys Rev Lett 106:157601
27. Fedder H, Zhao N, Honert J, Schmid B, Klas M, Isoya J, Markham M, Twitchen D, Jelezko F, Liu PR-B, Wrachtrup PJ (2012) Sensing single remote nuclear spins. Nat Nanotechnol 7:657–662. doi:10.1038/NNANO.2012.1152
28. Mehring M, Mende J (2006) Spin-bus concept of spin quantum computing. Phys Rev A 73:052303. doi:10.1103/Physreva.73.052303
29. Bermudez A, Jelezko F, Plenio MB, Retzker A (2011) Electron-mediated nuclear-spin interactions between distant nitrogen-vacancy centers. Phys Rev Lett 107:150503. doi:10.1103/Physrevlett.107.150503
30. Dolde F, Jakobi I, Naydenov B, Zhao N, Pezzagna S, Trautmann C, Meijer J, Neumann P, Jelezko F, Wrachtrup J (2013) Room-temperature entanglement between single defect spins in diamond. Nat Phys 9:139–143
31. Pezzagna S, Rogalla D, Becker HW, Jakobi I, Dolde F, Naydenov B, Wrachtrup J, Jelezko F, Trautmann C, Meijer J (2011) Creation of colour centres in diamond by collimated ion-implantation through nano-channels in mica. Phys Stat Solid 208:2017–2022. doi:10.1002/pssa.201100455
32. Dolde F, Bergholm V, Wang Y, Jakobi I, Naydenov B, Pezzagna S, Meijer J, Jelezko F, Neumann P, Schulte-Herbruggen T, Biamonte J, Wrachtrup J (2014) Nat Commun 5:3371
33. Siyushev P, Kaiser F, Jacques V, Gerhardt I, Bischof S, Fedder H, Dodson J, Markham M, Twitchen D, Jelezko F, Wrachtrup J (2010) Monolithic diamond optics for single photon detection. Appl Phys Lett 97:241902,241902. doi:10.1063/1.3519849
34. Rogers LJ, Jahnke KD, Marseglia L, Müller C, Naydenov B, Schauffert H, Kranz C, Teraji T, Isoya J, McGuinness LP, Jelezko F (2013) arXiv:1310.3804
35. Marseglia L, Hadden JP, Stanley-Clarke AC, Harrison JP, Patton B, Ho YLD, Naydenov B, Jelezko F, Meijer J, Dolan PR, Smith JM, Rarity JG, O'Brien JL (2011) Nanofabricated solid immersion lenses registered to single emitters in diamond. Appl Phys Lett 98:133107. doi:10.1063/1.3573870
36. Chi YZ, Chen GX, Jelezko F, Wu E, Zeng HP (2011) Enhanced photoluminescence of single-photon emitters in nanodiamonds on a gold film. IEEE Photon Tech Lett 23:374–376. doi:10.1109/Lpt.2011.2106488
37. Bayn I, Meyler B, Lahav A, Salzman J, Kalish R, Fairchild BA, Prawer S, Barth M, Benson O, Wolf T, Siyushev P, Jelezko F, Wrachtrup J (2011) Processing of photonic crystal nanocavity for quantum information in diamond. Diamond Relat Mater 20:937–943. doi:10.1016/j.diamond.2011.05.002
38. Brunel C, Lounis B, Tamarat P, Orrit M (1999) Triggered source of single photons based on controlled single molecule fluorescence. Phys Rev Lett 83:2722–2725. doi:10.1103/PhysRevLett.83.2722

39. Kurtsiefer C, Dross O, Voigt D, Ekstrom CR, Pfau T, Mlynek J (1997) Observation of correlated atom-photon pairs on the single-particle level. Phys Rev A 55:R2539–R2542
40. Batalov A, Zierl C, Gaebel T, Neumann P, Chan IY, Balasubramanian G, Hemmer PR, Jelezko F, Wrachtrup J (2008) Temporal coherence of photons emitted by single nitrogen-vacancy defect centers in diamond using optical Rabi-oscillations. Phys Rev Lett 100:077401. doi:10.1103/Physrevlett.100.077401
41. Neu E, Fischer M, Gsell S, Schreck M, Becher C (2011) Fluorescence and polarization spectroscopy of single silicon vacancy centers in heteroepitaxial nanodiamonds on iridium. Phys Rev B 84:205211. doi:10.1103/Physrevb.84.205211
42. Sipahigil A, Jahnke KD, Rogers LJ, Teraji T, Isoya J, Zibrov AS, Jelezko F, Lukin MD (2014) Indistinguishable photons from separated silicon-vacancy centers in diamond. Phys Rev Lett 113:113602. doi:10.1103/Physrevlett.113.113602

Photon Counting and Timing in Quantum Optics Experiments

Andreas Ahlrichs, Benjamin Sprenger, and Oliver Benson

Abstract In this chapter we briefly review present implementations of single-photon and photon-pair sources. After providing the basic fundamentals of nonclassical light, the role of photon detection to characterize these sources is highlighted. Then, we motivate why ongoing experiments heading at the realization of more complex quantum optical devices make very high demands on detectors and detection electronics. First, results towards quantum repeater architectures and hybrid quantum systems are discussed. Finally, we outline future prospects of all-optical quantum technologies.

Keywords Entangled photons · Quantum information · Quantum key distribution · Quantum optics · Single-photon source

Contents

1 Introduction 320
1.1 Classical and Quantum States of Light 320
1.2 Wave–Particle Duality 322
1.3 Detecting Photons 322
2 Single-Photon Sources 324
2.1 Principles of Photon Generation 324
2.2 Strategies for Light Collection 326
2.3 Integrated Sources 328
3 Heralded Photons and Photon Pair Sources 330
3.1 Principle of Heralding 330
3.2 Entangled Photon Pairs 332
3.3 Optical Parametric Oscillator as Photon Pair Source 333
3.4 Characterization of Cavity-Enhanced SPDC by Photon Counting 334

A. Ahlrichs, B. Sprenger, and O. Benson (✉)
Humboldt-Universität zu Berlin, Berlin, Germany
e-mail: oliver.benson@physik.hu-berlin.de

P. Kapusta et al. (eds.), *Advanced Photon Counting: Applications, Methods, Instrumentation*, Springer Ser Fluoresc (2015) 15: 319–342, DOI 10.1007/4243_2014_69,

4 Complex Counting Tasks in Quantum Optics 335
4.1 Quantum Repeaters: Long-Distance Transfer of Entanglement 335
4.2 Hybrid Quantum Systems 336
5 Future Prospects 338
References 340

1 Introduction

The suggestion of the particle nature of electromagnetic radiation by Einstein in 1905 [1] marks a breakthrough of our understanding of light. Remarkably, Einstein himself considered his suggestion of the existence of light quanta as his most revolutionary idea. Knowing light as an electromagnetic wave, it is no surprise that Einstein's postulate was heavily doubted. Already in 1909 Taylor [2] performed a double-slit experiment with highly attenuated light looking for interference fringes which are the ultimate fingerprint of a wave. The intensity of a light source was attenuated so much that on average only one photon at a time passed by the slit. After long averaging the expected double-slit interference pattern appeared. The existence of both particle and wave aspects was only understood later after a quantum theory of light was available. Today we know that it is impossible to show the quantum character of light with a first-order interference experiment. Such experiments, also the double-slit experiment, measure amplitude correlations. It is, however, the intensity correlation, where the particle character of light appears. For this reason photon counting is the major technique to study the quantum nature of light.

In the remaining section we will introduce some fundamentals of quantized light and photon detection. Then, in the following sections we will review several approaches how to generate and detect single photons (Sect. 2) and photon pairs (Sect. 3) before we outline recent more complex quantum optics experiments (Sect. 4). We concentrate on solid-state systems. Finally, we conclude our chapter with a short summary and outlook (Sect. 5).

1.1 Classical and Quantum States of Light

Glauber introduced the normalized first- and second-order correlation functions $g^{(1)}(\tau)$ and $g^{(2)}(\tau)$ as discussed in Loudon's book [3]:

$$g^{(1)}(\tau) = \frac{\langle E^+(t)E(t+\tau)\rangle}{\sqrt{\left\langle |E^+(t)|^2 \right\rangle \left\langle |E(t+\tau)|^2 \right\rangle}},$$

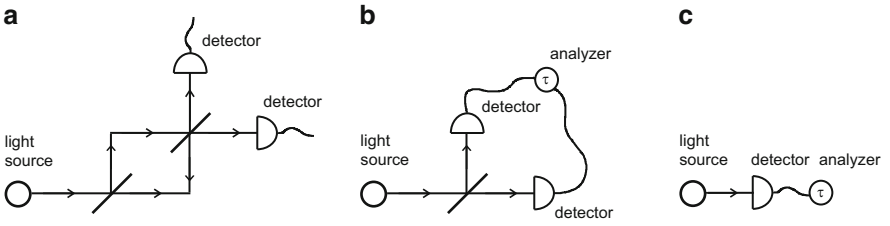

Fig. 1 (**a**) Schematic of a Mach–Zehnder interferometer to measure amplitude correlations. (**b**) A Hanbury Brown–Twiss setup to measure intensity correlations. (**c**) Most fundamental setup to measure photon statistics

$$g^{(2)}(\tau) = \frac{\langle E^+(t)E^+(t+\tau)E(t+\tau)E(t)\rangle}{\sqrt{\left\langle |E^+(t)|^2\right\rangle \left\langle |E(t+\tau)|^2\right\rangle}}.$$

E^+ and E denote field operators and the brackets indicate time averaging. $g^{(1)}(\tau)$ correlates the phase, i.e., complex amplitudes at time t and $t+\tau$, respectively. It can be measured in an interference experiment, e.g., using a Mach–Zehnder interferometer (Fig. 1a). $g^{(2)}(\tau)$ correlates intensities and is derived in a setup suggested by Hanbury Brown and Twiss (HBT) [4] (Fig. 1b). One has to note that the HBT setup was first introduced to measure classical correlations of light from distant stars. $g^{(2)}(\tau)$ can be interpreted in terms of photon statistics: if a photon is detected at time t what is the probability to detect another one at time $t+\tau$? The role of the beam splitter is often misinterpreted as a device that splits photons. However, it is only needed to overcome the finite dead time of single-photon counters which is often larger than the characteristic photon correlation time. In a recent experiment, Steudle et al. [5] have shown that the nonclassical character of light can easily be demonstrated with one single-photon detector only. They used light from a single-photon source (see Sect. 2) and a superconducting single-photon detector with a dead time of only a few nanoseconds. The setup, illustrated schematically in Fig. 1c, is the most fundamental one to test the nonclassicality of light.

In quantum optics one typically distinguishes three different states of light: light from a thermal source, where photons tend to 'bunch' together, light from a classical source like a laser far above threshold where photon statistics follow Poisson statistics, and finally light in a Fock state. Only the latter state has to be described by a quantum theory of light. Light in a Fock state is emitted from quantum light sources that contain a discrete number of excitations. A specific example is a single-photon source (see next section), where photons come one after the other, i.e., they are anti-bunched. The corresponding $g^{(2)}(\tau)$ functions for the three cases are sketched in Fig. 2a together with a measured photon correlation of fluorescence light emitted from a single quantum dot (Fig. 2b).

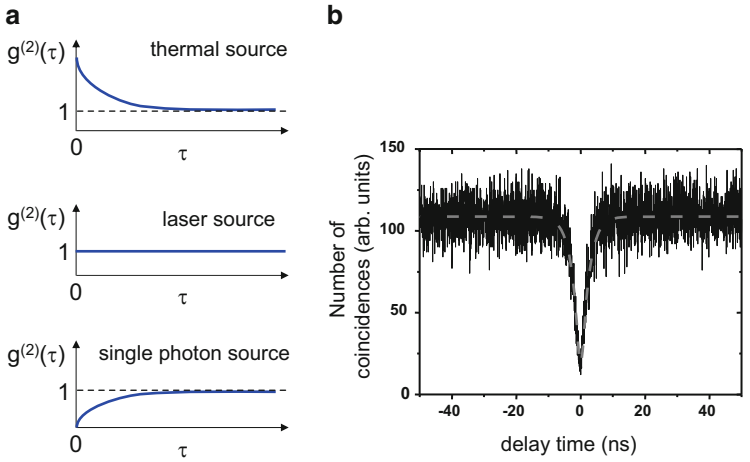

Fig. 2 (**a**) Normalized $g^{(2)}$ functions for three different states of light. (**b**) Measured second-order photon correlation function of fluorescence light from a single-photon source (here a single semiconductor quantum dot [6])

1.2 Wave–Particle Duality

Both the wave and the particle character can be measured in one experimental setup. For example, Aichele et al. [7] performed photon correlation measurements between the two outputs of a Mach–Zehnder interferometer (similar as sketched in Fig. 1a) while one interferometer arm was changed. The light source was a single-photon source based on a single quantum dot. Whereas the detected signal in each arm was modulated as expected from the Mach–Zehnder interference fringes, the correlation between the two outputs always showed anti-bunching, i.e., a typical particle property of light. In another experiment, already in 1997, Hoffges et al. [8] analyzed light that was resonantly scattered from a single trapped ion. Both anti-bunching and phase stability of the scattered photons were shown. This again highlights the appearance of both the nonclassical particle and classical wave nature of light in one experiment. We will discuss resonant scattering again in the following section.

1.3 Detecting Photons

Statistical analysis of light is only possible with detectors that are capable of detecting the fundamentally lowest energy of one $\hbar\omega$. Depending on the required efficiency, bandwidth, wavelength range, as well as energy resolving capability, different photon detectors are used. We briefly review [9, 10] four types of detectors in the following.

- *Photomultiplier tubes* (PMTs) are based on the photoelectric effect, i.e., the emission of an electron from a cathode caused by absorption of a photon. The emitted electron is multiplied by a cascade of secondary electron emission generated in a series of electrodes after the photodiode, producing a macroscopic voltage pulse. PMTs cover a spectral range of 115–1,700 nm, but with large differences in performance. In the visible, quantum efficiencies of 40% can be achieved at low dark count rates of 100 Hz and a temporal jitter of 300 ps using GaAsP photocathodes [10]. At 1,550 nm, however, the performance of PMTs is relatively poor. Quantum efficiencies of a few percent can be found at a dark count rate of 200 kHz, which results in a very low sensitivity.
- The configuration of *avalanche photodiodes* (APDs) is similar to a p-i-n-diode. For single-photon counting the APD is operated in reverse bias above the breakdown voltage (Geiger mode). The absorption of a photon in the intrinsic layer creates an electron–hole pair. Carriers are then multiplied due to impact ionization. The most commonly used material is silicon where quantum efficiencies up to 70% (at 700 nm) and a very low dark count rate below 100 Hz can be achieved. However, the spectral range is limited to wavelengths up to 1,100 nm by the band gap in silicon. For detection of photons at the telecommunication wavelengths at 1,300 nm and 1,500 nm, other materials, e.g., InGaAs, have to be used. Such APDs have a much poorer performance regarding quantum efficiency (around 20%), dark counts (1–20 kHz), and dead times (typically ~100 ns).
- *Superconducting transition edge sensors* (TESs) are bolometers that consist of a superconducting material operated very close to the critical temperature, where small changes in temperature result in a large change in resistance. A photon can be detected through the small increase in temperature in the material where it is absorbed. TESs provide photon number resolution capability [11] and quantum efficiencies of over 90% in the near infrared [12]. However, the disadvantage of this detector type is that it has to be operated at temperatures as low as 100 mK. For some applications the comparatively long dead time of typically 1 μs might be inconvenient, although faster detectors with below 200 ns dead time have been reported.
- The operation principle of *nanowire superconducting single-photon detectors* (NSSPDs) [10] is similar to the one of TESs. The fact that absorption of a photon can disrupt superconductivity is exploited. NSSPDs are operated well below the superconductor's critical temperature (at liquid helium temperature), but close to its critical current. They cover a broad spectral range at reasonable quantum efficiencies, low dark count rates, and short dead times.

Whereas radiometry of low-intensity light relies mostly on TESs [13], photon detection in quantum optics is mostly done with silicon APDs. The limitation of Si APDs to detect photons only with wavelengths shorter than about 1 μm used to be a minor issue since most of the nonclassical light sources, such as single atoms, ions, molecules, or semiconductor quantum dots, emitted in the near infrared to the visible. However, when transmitting quantum information over large distances

via optical fiber networks, wavelengths in the telecom bands are required. Also, complex quantum information tasks using photons, such as quantum repeaters or quantum logic elements (Sect. 4), require efficient multiphoton detection. Very high efficiency, ultralow dark count rates, and photon number resolving capability are urgently needed. For this reason superconducting single-photon detectors are becoming more and more relevant. For more details on single-photon detectors, see also the chapters by Buelter [14] and Buller et al. [15].

Photon counting can be applied to classical light as well, but it is indispensable to characterize nonclassical light sources, like the ones introduced in the following section.

2 Single-Photon Sources

2.1 Principles of Photon Generation

A photon is a single excitation of an electromagnetic field mode. A generation of a single excitation is straightforward in a fermionic system where the Pauli principle applies. Therefore, quantum systems with discrete electronic states and predominantly radiative relaxation, such as atoms, ions, molecules, quantum dots, or color defects in crystals, are potential single-photon sources.

Figure 3 shows three different approaches to realize single-photon sources based on single quantum emitters. The simplest approach (Fig. 3a) is to pump a single quantum emitter incoherently and to wait until a single photon is emitted. This approach provides the photon emission event within a short time interval given by the inverse of the relaxation rate into the excited state and the spontaneous emission time. In this sense it is *on demand*. However, the process is still probabilistic and has its limitations in particular with respect to the indistinguishability of the emitted photons [16]. A coherently driven Raman transition in a single three-level system strongly coupled to a high-Q cavity (Fig. 3b) provides a superior approach. This scheme realizes a coherently pumped single-photon source that does not involve coupling to reservoirs other than the one into which single photons are emitted [16, 17]. Pulse shaping and a high degree of indistinguishability can be obtained. Finally, Fig. 3c sketches direct resonant scattering. Although this method was demonstrated already by Hoffges et al. [8] with trapped ions in 1997, it took more than 10 years to learn how to separate the single-photon signal from the strong pump light in a solid-state system [18, 19].

In the previous section in Fig. 2b, we already showed a measurement of single photons from an incoherently pumped single quantum dot (approach a) in Fig. 3. In the following Fig. 4 we show a result from He et al. [20] where single photons were generated by resonant scattering (approach c) in Fig. 3. The degree of indistinguishability, which is crucial for applications in all-optical quantum information [21], was quantified by observing two-photon interference at a beam splitter in a

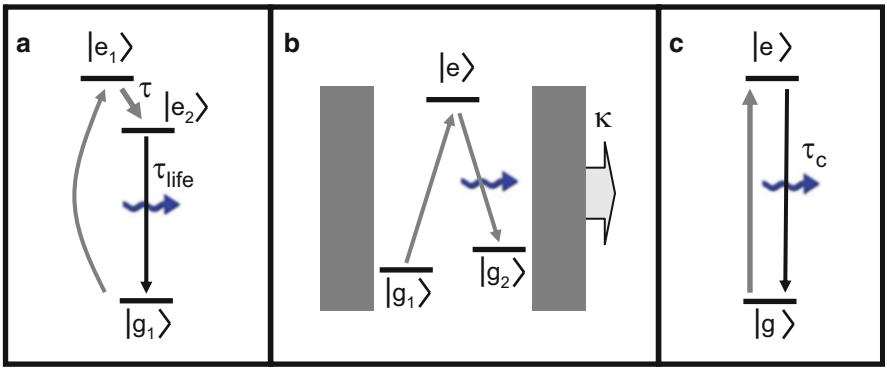

Fig. 3 Three different approaches of single-photon generation from single quantum systems. (**a**) Incoherent excitation of a single quantum emitter modeled as three-level system. After excitation to a higher excited state, there is a fast relaxation within the relaxation time τ followed by a spontaneous emission within the time τ_{life}. (**b**) A three-level emitter coherently driven by two Raman pulses. One is a classical laser pulse, the other one is the vacuum field of a cavity which is strongly coupled to the emitter. Photons are finally released from the cavity with the cavity's decay rate κ. (**c**) Schematic of resonant scattering by driving a two-level system with a coherent laser pulse. Scattering can be understood classically, yet the single-photon character is "imprinted" through the quantum character of the single emitter. The scattered photons have the same coherence properties as the pump laser

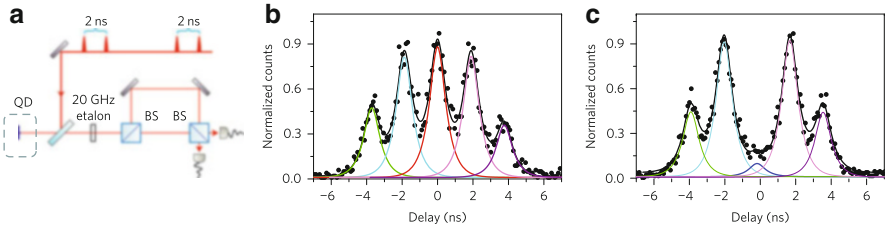

Fig. 4 Hong–Ou–Mandel-type interference experiment between two photons subsequently scattered from a single quantum dot [20]. (**a**) Two unbalanced Mach–Zehnder interferometers with a path-length difference of 2 ns are used both in the excitation arm (not shown) and in the two-photon interference. (**b**, **c**) The central cluster of the histogram of two-photon detection events with a relative delay time. In (**b**) and (**c**), the two input photons are prepared in cross and parallel polarizations, respectively. The fitting function for each peak is the convolution of a double exponential decay (exciton decay response) with a Gaussian (single-photon detector time response). Owing to the limited time response, the five peaks have finite overlaps. The disappearance of the central peak in (**c**) is a clear signature of destructive quantum interference of two indistinguishable photons

Hong–Ou–Mandel experiment [22]: if the two photons simultaneously impinge onto a 50/50 beam splitter from two different input ports, they will always exit the beam splitter through the same output port. This coalescence of photons can easily be verified with single-photon detectors at the two output ports of the beam splitter and measuring the coincidence rate of events where the two photons are

split up. The coincidence rate drops to zero for perfectly indistinguishable photons (see disappearance of the central peak in Fig. 4c) and reaches a value corresponding to 50% of the events for perfectly distinguishable photons.

Besides excellent control of the photon's temporal and spatial wave packet, also its frequency locking to the excitation was shown, proving the coherent nature of the generation process.

2.2 Strategies for Light Collection

In general, spontaneous emission from single-photon sources such as atoms, color defect centers in crystals, or quantum dots occurs into a random direction. Various possibilities exist to either collect as much of the full solid angle of the emission or to enhance the emission into specific optical modes. Strategies for efficient light collection will be discussed in the rest of this section.

In 1946 Purcell proposed that the spontaneous emission rate can be enhanced when an emitter is placed in a resonant cavity, which is commonly referred to as the *Purcell Effect* [23]. The Purcell factor defines the enhancement as

$$F_{\mathrm{P}} = \frac{3}{4\pi^2} \cdot \left(\frac{\lambda}{n}\right)^3 \cdot \left(\frac{Q}{V}\right), \tag{1}$$

where λ is the wavelength, n is the refractive index, Q is the quality factor of the cavity, and V is the mode volume. The two free parameters that can be used to maximize the Purcell factor are thus a large quality factor and a small mode volume of the cavity.

After first pioneering experiments with trapped $^{40}Ca^{+}$ ions [24, 25], recent developments have focused on solid-state single-photon sources, such as nitrogen-vacancy (NV) defect centers in diamond, or semiconductor quantum dots. Defect centers have discrete electronic energy states and can thus be used as stable single-photon sources [26], even at room temperature. Single defect centers can be isolated in nanodiamonds, which can be characterized and then placed in almost any desired location, by employing micropositioners or an atomic force microscope [27].

In order to exploit the Purcell effect for enhancing photon emission, photonic crystal cavities have several advantages [28]. Their compact size allows extremely small mode volumes, combined with ultrahigh quality factors. Since room temperature emission from NV centers is spectrally broad, an enhancement of the collection of single photons from the narrow zero-phonon line (ZPL) is desirable.

Figure 5 shows a nanodiamond with a single NV defect center positioned on a two-dimensional photonic crystal cavity [29]. Here, the evanescent field of the NV center and the photonic crystal cavity overlap. The cavity is tuned into resonance

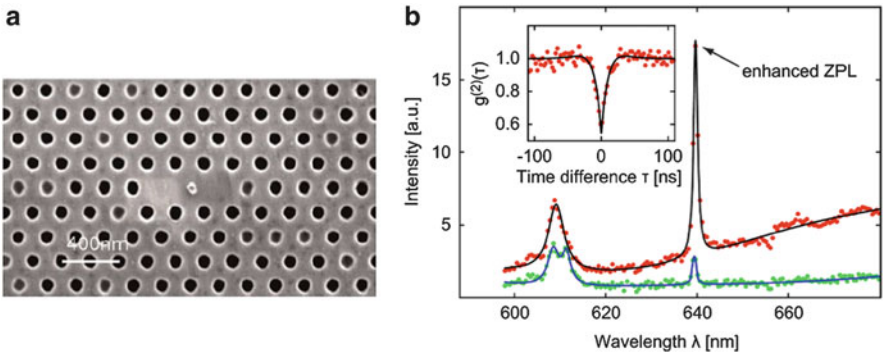

Fig. 5 (**a**) Scanning electron micrograph of a two-dimensional GaP photonic crystal with an L3 defect cavity in the center [29]. A nanodiamond with a single NV center is placed in the center of the cavity and couples to the light field. (**b**) *Lower dots*: Normalized spectrum of intrinsic cavity fluorescence without nanodiamond. The peak around 640 nm is the fundamental mode tuned to the ZPL of the NV center. The peaks around 610 nm stem from higher-order modes. *Upper dots*: Normalized fluorescence spectrum with nanodiamond showing an increase of the ZPL emission in the cavity mode. *Solid curves* are fits to the data. *Inset*: Autocorrelation measurement of fluorescence from the nanodiamond. The anti-bunching dip proves the single-photon character

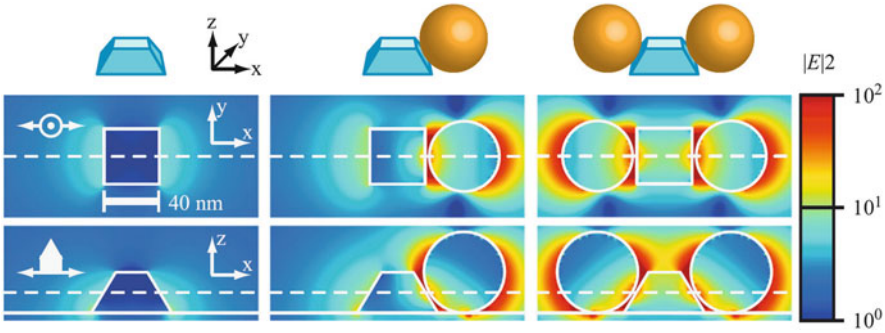

Fig. 6 The schematic of the experimental configuration shows a nanodiamond without plasmonic enhancement and then as it couples to a single or two gold nanoparticles. The numerical simulation shows the electric field intensity using a logarithmic color scale [30]. Field enhancement at so-called hot spots is clearly visible

with the single-photon emission by local laser heating. A drastic enhancement of emission into the ZPL by a factor of 12.1 was observed.

A radically different approach to single-photon emission enhancement and collection is the use of plasmonic structures as *optical nanoantennas*. Highly localized electromagnetic fields enhance both the excitation, as well as the radiative and non-radiative decay rates. Figure 6 shows a schematic of an experiment, where an NV center in a nanodiamond was sandwiched in between two small gold spheres acting as a plasmonic antenna [30]. The radiative decay rate of a single NV center

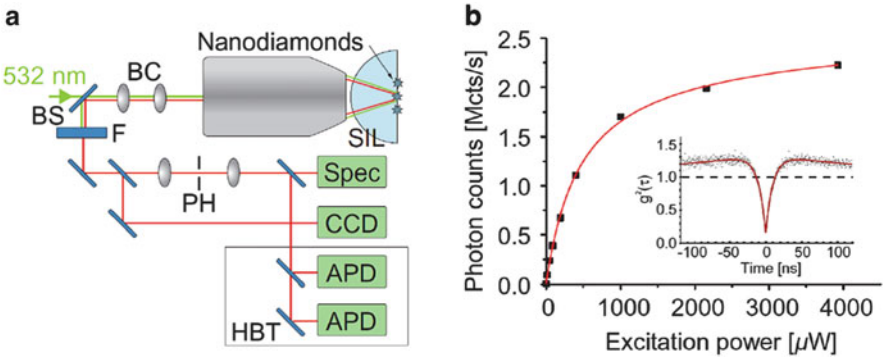

Fig. 7 Enhanced photon collection via a solid immersion lens (SIL). (**a**) Nanodiamonds containing single NV centers are spin coated on the flat facet of the SIL. Both the 532 nm excitation light and the emitted photons are coupled using the same microscope objective. BC, BS, F, PH, HBT, and APD stand for beam control, beam splitter, filter, pinhole, Hanbury Brown and Twiss setup, and avalanche photodiode, respectively [31]. (**b**) Single-photon count rate of a single NV center as a function of the pump power. The *inset* shows a measurement of the second-order correlation function

could be enhanced by nearly an order of magnitude, which corresponds to the same enhancement in the single-photon rate.

Another method of preventing the single-photon emission from spreading over a 4π solid angle is placing an emitter close to a dielectric interface with a higher index material. This sort of structure functions as a dielectric antenna, in which the emission preferentially couples into the higher index material. One example of this is the light collection from NV centers using a *solid immersion lens* (SIL) [31]. A schematic of the setup is shown in Fig. 7a. Nanodiamonds were spin coated on the flat surface of such a lens. Collection efficiencies of 4.2% and single-photon count rates exceeding 2 million counts per second (see Fig. 7b) were achieved. Both excitation and emission collection were performed using the same microscope objective.

Various types of single emitters can be coupled in a similar way, and further tailoring of the dielectric antenna by layering and precise alignment of the emitter's dipole axis have led to light collection efficiencies of 96% and beyond, using either single molecules or semiconductor nanocrystals [32, 33].

The different light collections strategies can be applied to any single-photon emitter in the solid-state or condensed phase.

2.3 *Integrated Sources*

Quantum technologies such as quantum communication or computing make high demands also on the practical properties of single-photon sources: ideally, they should operate without maintenance for thousands of hours providing a high rate of

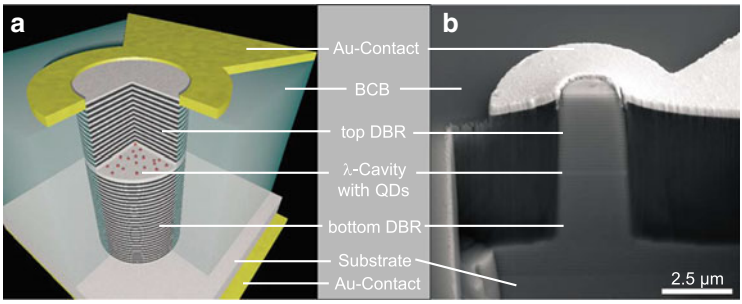

Fig. 8 (**a**) A schematic of quantum dots in the micropillar cavity. (**b**) Scanning electron micrograph of a cut pillar with gold contact and a diameter of 2.5 µm [36]

photons even at room temperature. Electrical pumping, efficient coupling of emitted photons to optical waveguides or fibers, and integration on an electro-optical chip would be extremely useful as well. Current technologies allow at least a few of these criteria to be met.

The most direct approach is to put single quantum emitters directly onto optical waveguides or optical fibers. This is possible with single molecules, colloidal quantum dots, or NV centers in diamond via spin coating or more advanced positioning techniques. For example, an optical fiber can be tapered down to sub-micrometer thickness. Then, the evanescent field of the guided mode is large at the fiber's surface and can overlap with deposited emitters. Such a nanofiber can be fabricated from regular optical fibers by heating and pulling it in a controlled manner. A nanodiamond attached to a nanofiber can be excited using a perpendicular focused laser beam, and the single-photon emission can be collected through the fiber [34]. Alternatively, an NV center can be placed directly on the facet of an optical fiber [35].

An even higher level of integration was obtained with semiconductor quantum dots, where charge carriers are confined in all three spatial dimensions. In a quantum dot, an electron–hole pair can form an exciton, which emits one photon after radiative recombination. Optical excitation of carriers using a focused laser is common, but recently progress has been made in electrical excitation, which paves the way to more integrated sources. Heindel et al. [36] embedded quantum dots in pillar structures with dielectric mirrors to enhance directional coupling from the surface and placed gold contacts at the top and bottom for electrical excitation as shown in Fig. 8.

Pioneering work on the so-called single-photon light-emitting diode was performed by Yuan et al. in 2002, where electrical pumping of a single quantum dot within the intrinsic region of a p–i–n junction was demonstrated with single-photon emission [37]. More recently, InAsP material has been used to fabricate nanowire light-emitting diodes operating in the telecommunication band [38].

The concept of single-photon-emitting diodes can also be applied to other material systems. Mizuochi et al. demonstrated a p-i-n structure using diamond films, and electrically excited carriers in nitrogen-vacancy centers, and thereby

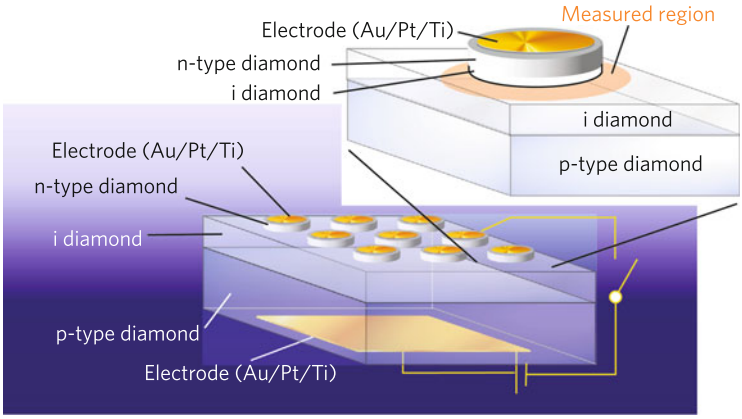

Fig. 9 Schematic of a nitrogen vacancy in diamond-based single-photon source, consisting of a p–i–n junction in diamond layers, with nitrogen-vacancy centers in the intrinsic region [39]. Emission of single photons is around the perimeter of the round electrode in the vertical direction

produced a continuous stream of single photons [39]. Figure 9 shows a schematic of the three diamond layers and the electrodes attached to the top and bottom to induce carriers in the nitrogen-vacancy centers. As compared to a quantum dot device, a diamond-based source does not require cryogenic temperatures, making it advantageous for integration into quantum devices. On the other hand, the wavelength of about 640 nm only allows local use of photons. Telecommunication range photons would be required for long-distance transfer.

In principle, the technology to fabricate reliable single-photon sources has been demonstrated, and first commercial single-photon sources are available. However, a crucial step for further applications in quantum information processing is the capability to generate a well-defined number $N > 1$ of *indistinguishable* photons with near unity probability. For $N > 2$ this remains a challenge, but pairs of indistinguishable photons can be realized as will be discussed in the following section.

3 Heralded Photons and Photon Pair Sources

3.1 Principle of Heralding

Quantum correlations allow for the application of heralding and remote preparation of quantum states. The detection of one excitation, e.g., a photon, *heralds* the presence of another excitation if they are quantum mechanically correlated. Figure 10 illustrates two examples.

In Fig. 10a heralding is utilized to generate a single excitation of a specific state in an ensemble of identical atoms [40]. A Raman process in a three-level atom

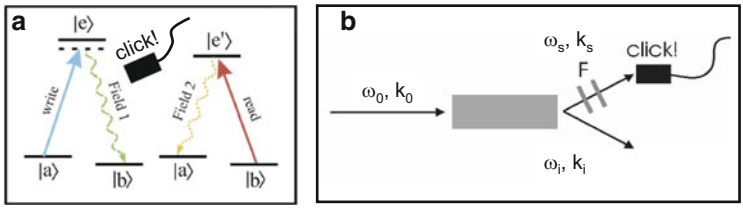

Fig. 10 Schematic of heralding to generate single photons. (**a**) Heralded single-photon generation from an atomic ensemble using Raman transitions. Detection of a single scattered photon from Field 1 heralds a single excitation in state $|b\rangle$ in one of the atoms of the ensemble. By shining in the read pulse, only this single excitation can be converted into a scattered single photon. (**b**) In a parametric process, photon pairs are generated. Detection of one photon with frequency ω_s (through filters F) in direction k_s heralds the presence of a single photon with frequency ω_i in direction k_i

(initially in a state $|a\rangle$) is utilized. First, a weak write pulse probabilistically excites a virtual transition from states $|a\rangle$ to $|e\rangle$, followed by Raman scattering from $|e\rangle$ to a lower ground state $|b\rangle$. When one photon from this transition is detected, one knows that a coherent transfer from $|a\rangle$ to $|b\rangle$ has occurred. The detected photon hence functions as a *herald* for a single excitation generated in the atomic ensemble. A read pulse is then fired into the ensemble, resonant with $|b\rangle \rightarrow |e'\rangle$, which is a lower excited state. The timing of this read pulse can be selected to produce the $|e'\rangle \rightarrow |a\rangle$ photon at a defined time.

The most prominent example for heralding is utilized in single-photon generation from spontaneous parametric down-conversion (SPDC) in nonlinear crystals (see Fig. 10b). In a medium with an optical $\chi^{(2)}$-nonlinearity, one photon of a pump beam can spontaneously decay into a pair of photons under energy and momentum conversation. This process has its classical counterpart in three-wave mixing.

In heralded single-photon sources, the two photons of a pair are generated simultaneously into two distinct optical modes (often called the *signal* and the *idler* mode). Photon pair generation itself is a stochastic process. In each of the two arms, there is a thermal photon statistics. However, the quantum mechanical correlation guarantees that whenever a photon is detected in the idler mode, the probability to find the corresponding photon in the signal is one. Detection of one photon *heralds* the other one.

One distinguishes three types of SPCD depending on the polarization of the three fields. In Type 0 all three fields have the same polarization, while in type I signal and idler are both polarized orthogonally to the pump. In type II signal and idler photons have orthogonal polarization. While energy conservation offers the opportunity to generate signal and idler photons at a wide range of frequencies, momentum conservation (also called phase matching) can only be achieved by carefully selecting a nonlinear medium with suitable refractive indices for the desired process.

Due to the stochastic nature of the process, the simultaneous generation of more than one pair of photons cannot be excluded. In each of the two arms, one always

obtains thermal photon statistics. Although the probability to generate two pairs of photons simultaneously can be made arbitrarily small by reducing the pump power, this drastically reduces the single pair production rate. For practical application as a heralded photon source, a compromise between single pair production rate and two-pair admixture always has to be found. The heralding rate can in principle be greatly improved by using photon number resolving detectors in the heralding arm and by combining the output of multiple SPDC sources with optical switches [41].

There are several shortcomings in experiments which reduce the fidelity of the desired single-photon state. Detector dark counts or stray light can produce false heralding events when no corresponding signal photon is present. Losses in either the idler or the signal channel reduces the heralding efficiency of the source and thus the attainable rate with which experiments can be performed. When using single-photon detectors without photon number resolution in the heralding arm, multi-pair events cannot be distinguished from the desired single-pair events in the heralding process.

3.2 Entangled Photon Pairs

Due to their simultaneous creation, the photons from one pair can be highly correlated in various degrees of freedom. These correlations can be utilized to build sources of entangled photons. While most experimental realizations of entangled photons are based on entanglement in polarization [42, 43], it is also possible to generate photons with entanglement in momentum and position [44], time and energy [45], or different time bins [46]. Even sources of *heralded* entangled photon pairs based on SPDC can be built [47].

Besides violating Bell inequalities, many important experimental demonstrations in the field of quantum information processing (like quantum teleportation [48] or entanglement swapping [49]) could be performed for the first time using SPDC-based sources of entangled photons.

Generally speaking, an entangled state is a superposition of a two- or multiparticle state that cannot be factorized as single-particle states. In other words, if a process can prepare two (or more) quantum objects in two different configurations, then the resulting state is often an entangled state. This is most apparent in a cascaded decay, which in fact was the first source for entangled photons [50]. Figure 11a shows a schematic of a cascaded decay of a biexciton state, i.e., a state formed by two electrons and two holes in a quantum dot. There are two possible cascades which lead to emission of two orthogonally polarized photons. Since it is impossible to distinguish between the two decay paths, an entangled state is generated [52]. Entanglement has to be proven by reconstructing the quantum state's density matrix through photon correlation measurements (see Fig. 11b). Exploiting the possibility of electrical excitation of quantum dots even an entangled photon-pair emitting diode was realized [53].

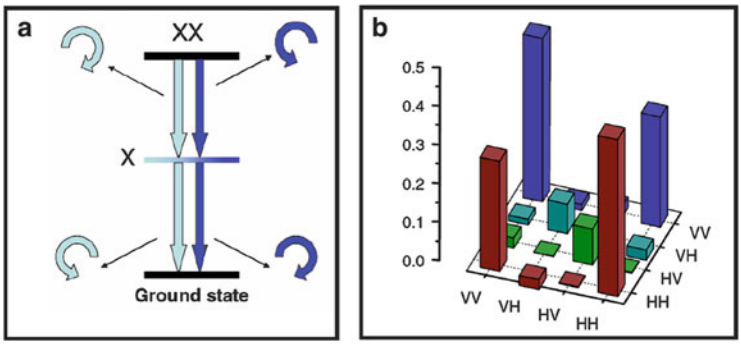

Fig. 11 (**a**) Schematic of a cascaded decay of a biexciton state in a quantum dot. XX and X denote the biexciton state (two electron–hole pairs) and the exciton state (one electron–hole pair), respectively. *Curved arrows* denote the circular polarizations of the emitted photons. (**b**) Reconstructed real part of the density matrix of the photon-pair state emitted from a biexciton decay in a single quantum dot [51]. Entanglement is indicated by pronounced off-diagonal elements

3.3 Optical Parametric Oscillator as Photon Pair Source

Many experiments in quantum optics require the generation of single or entangled photons with a small bandwidth (MHz to GHz regime) in a well-defined single spatial mode. Both of these requirements are hard to fulfill with SPDC and bulk crystals, since the created photons are intrinsically broadband (100 GHz to THz) and are emitted into multimode cones. Spatial and spectral filtering would be possible in principle but would drastically reduce the brightness of the source.

One solution to obtain small bandwidth, single-mode photons is to use the configuration of an optical parametric oscillator (OPO) [54] which is pumped far below the threshold (see Fig. 12). These kinds of setups are often called cavity-enhanced SPDC sources. In the OPO configuration the nonlinear crystal is placed inside an optical cavity. The down-converted photons can only be emitted into the spectral and spatial modes of the cavity. With a high finesse cavity, the coherence length of the generated photons can be increased by several orders of magnitude [56]. Due to the increased effective interaction length of the nonlinear medium, the photon-pair generation rate is also increased. Since the down-converted photons are generated into the transverse fundamental mode of the cavity, they can be coupled into a single-mode optical fiber with high efficiency.

Since the down-conversion bandwidth is often much larger than the free spectral range of the cavity, the photons are emitted into multiple frequency modes. To obtain single-frequency mode operation, additional frequency filtering is necessary [57]. If the generation of signal and idler photons with degenerate frequency is required in a type II configuration, an additional compensation crystal can be added to the cavity [58]. With this additional crystal the path-length differences of the two

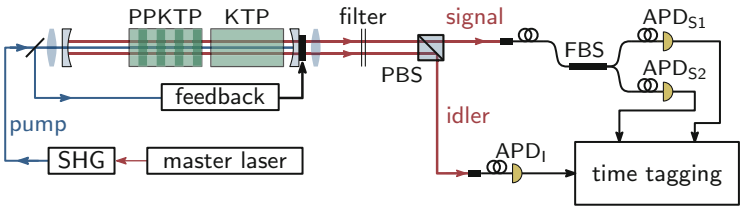

Fig. 12 Setup for charactreization of cavity-enhanced SPDC in an optical parametric oscillator (OPO) [55]. Photon pairs are generated inside a PPKTP crystal located inside a linear cavity. The cavity length is stabilized to a resonance of the pump laser, which is produced by second harmonic generation (SHG). After spectral filtering signal and idler photons are separated at a polarizing beam splitter (PBS) and coupled into single-mode fibers. Signal photons are split by a 50/50 fiber beam splitter (FBS). Three avalanche photodiodes (APD) are used to detect photons. Their arrival times are measured with time-correlated single-photon electronics in time-tagging mode

orthogonal polarizations inside the cavity can be compensated, allowing for the simultaneous resonance of both polarizations at the same frequency.

3.4 Characterization of Cavity-Enhanced SPDC by Photon Counting

Heralded single-photon emission of an SPDC source is characterized by the conditioned second-order autocorrelation function $g_{ssi}^{(2)}(\tau)$, which evaluates the fidelity of the heralded single photon [55]. The function $g_{ssi}^{(2)}(0)$ can be interpreted as follows: if a photon is detected in the idler mode i, then the probability to find two photons at a time in the signal mode s is suppressed. This is equivalent to assuming that a single-photon state in mode s was prepared remotely. Only for sources with a low $g_{ssi}^{(2)}(0)$ value, the probability to emit multiple pairs simultaneously is low. Figure 13a shows a measurement with the setup depicted in Fig. 12.

Another important parameter is the degree of indistinguishability of the two emitted photons. It can be measured via two-photon interference in a Hong–Ou–Mandel experiment as discussed in detail in Sect. 2. As pointed out, two indistinguishable photons impinging from two sides on a 50/50 beam splitter should coalesce, and the coincidence rate measured between the two outputs of the splitter should drop to zero. Figure 13b shows such a measurement of the two photons from a cavity-enhanced SPDC source as sketched in Fig. 12. An excellent degree of indistinguishability is observed.

At the end of this section, we would like to point out that besides high efficiency and good time resolution of single-photon detectors, photon number resolving capability would be an enormous benefit, both for heralding and for full characterization of multiphoton sources.

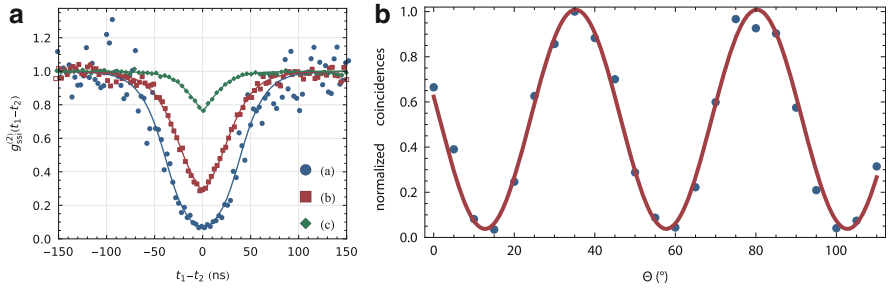

Fig. 13 (**a**) Measured (*symbols*) conditioned autocorrelation function $g_{ssi}^{(2)}(t_1 - t_2)$ for the three different pump powers ($P^{(a)}_{\text{pump}} = 0.8$ mW, $P^{(b)}_{\text{pump}} = 4$ mW, and $P^{(c)}_{\text{pump}} = 13$ mW) [55]. A binning of 4.5 ns is chosen. As a guide to the eye, a fit (*lines*) to a theoretical model is added. (**b**) Detected coincidence counts after a beam splitter as a function of the relative angle between the linear polarization of the photons. A minimum is detected when both photons impinge with the same polarization on the beam splitter, i.e., when they are indistinguishable

4 Complex Counting Tasks in Quantum Optics

In the previous section we saw that even the rather simple task of characterizing a heralded photon source or a photon-pair source requires analysis of correlations between three detection events. A much more demanding challenge is to realize quantum optical logic elements for quantum information processing. In such devices the number of required photon counters scales dramatically for three reasons:

1. Optical quantum bits are encoded in photons and a final readout is a detection of a photon state.
2. The required nonlinearity in quantum logic elements based on photons is induced by photon interference together with photon detection [21].
3. Any signal to characterize, control, or stabilize the active elements of a quantum photonic device is very weak, often on the level of few photons, and requires single-photon detectors.

In the following we discuss two examples of recently performed experiments addressing more complex tasks in quantum technology than just realizing photon sources.

4.1 Quantum Repeaters: Long-Distance Transfer of Entanglement

The most advanced quantum technology is secure information exchange using quantum key distribution (QKD) [59]. Bits are encoded in photons and the 'fragility' of the quantum state provides unconditional security against eavesdropping.

However, the transmission of single photons is always subject to inevitable photon loss (due to absorption or scattering), which limits the achievable quantum communication distance over optical fibers to approximately 100 km even at telecommunication wavelengths. To overcome this severe limitation, Briegel et al. [60] proposed the concept of a quantum repeater [61]. The idea of a quantum repeater is not to directly transmit quantum information with single photons, but instead distribute entanglement over a quantum network. Once the first and the last node of such a network are entangled, the quantum information can be transmitted by quantum teleportation. The distribution of entanglement is done by consecutive entanglement swapping. At each node a quantum repeater produces pairs of entangled photons. Then, entanglement swapping is performed between adjacent nodes until the first and the last node of the network are entangled. Since standard fiber optical links between adjacent nodes are used, the entanglement swapping steps cannot be deterministic due to photon losses. Therefore, additional quantum memories at each quantum repeater node are needed, which store the quantum information until entanglement swapping with the next node was performed successfully. The fidelity of the transmitted entangled state can be increased by multiplexing the quantum network and by performing entanglement distillation [62].

The realization of two entangled nodes is a first key experiment to realizing a quantum repeater. Due to their long coherence time, trapped ions or atoms are a possible system, but the experimental effort is huge [63]. In 2013 Bernien et al. [64] demonstrated for the first time a heralded entanglement between two solid-state quantum bits separated by 3 m. Figure 14 shows a schematic of the complex experiment. The electron spins in two NV centers in diamond were utilized. They have a long coherence time and can be manipulated as well as read out by microwave and optical fields, respectively. Radiative emission from the centers generates two photons each entangled with its resident electron spin. The photons are sent to a beam splitter. A coincidence in the two outputs of the beam splitter finally heralds entanglement between the two spins.

The experiment required excellent stability and suppression of dark counts of the four involved avalanche photodiode detectors since there was only one entanglement event every 10 min, and data acquisition was done for about 160 h.

4.2 Hybrid Quantum Systems

A quantum repeater consists of photon-pair sources, transmission lines, and quantum storage devices. These different parts are subject to conflicting requirements, e.g., telecom wavelength of photons for transmission, but a visible wavelength for more efficient detection. The situation is even more challenging for assembling the different parts of a quantum computer: main processor, memory, readout and initialization unit, interfaces, etc. It is expected that these different parts have to be realized in different physical systems. This motivates the novel research field of

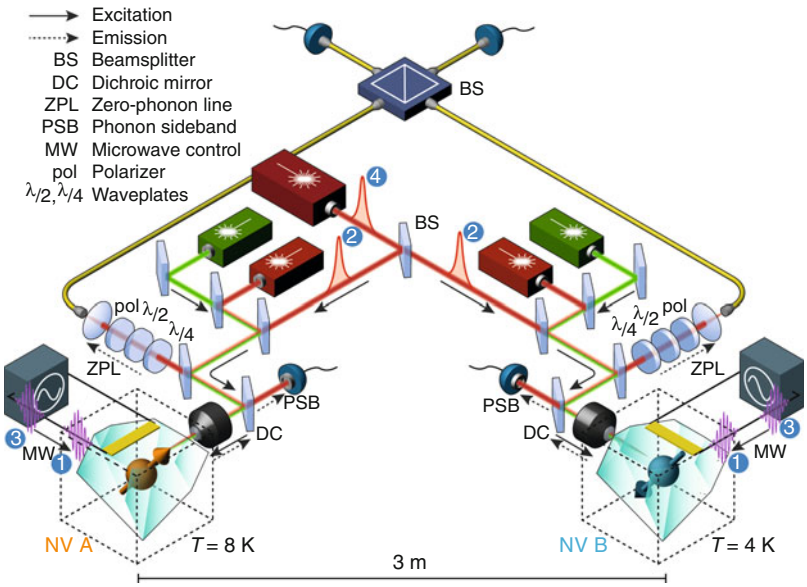

Fig. 14 Experimental setup for generating long-distance entanglement between two solid-state spin qubits [64]. Each nitrogen-vacancy (NV) center resides in a synthetic ultrapure diamond. The two diamonds are located in two independent low-temperature confocal microscope setups separated by 3 m. The NV centers can be individually excited resonantly by red lasers and off-resonantly by a green laser. The emission (*dashed arrows*) is spectrally separated into an off-resonant part (phonon sideband, PSB) and a resonant part (zero-phonon line, ZPL). The PSB emission is used for independent single-shot readout of the spin qubits. The ZPL photons from the two NV centers are overlapped on a fiber-coupled beam splitter. Microwave pulses for spin control are applied via on-chip microwave striplines

hybrid quantum systems. The only way to transfer quantum information between dissimilar physical systems is to use photons as quantum transducer.

A particularly demanding task in hybrid quantum systems is to bring together, e.g., entangle, solid-state systems, which are characterized by fast decay processes (in the GHz regime) and short coherence times with atomic systems, which are almost perfectly isolated from the environment, but have electronic transitions with optical linewidths in the MHz regime. First steps towards entanglement between systems in the condensed phase and atomic ensembles were demonstrated by Akopian et al. [65] and by Siyushev et al. [66]. Photons from a single GaAs quantum dot and a single dibenzanthanthrene (DBATT) molecule, respectively, were filtered and tuned to an electronic transition of a rubidium and a sodium cell, respectively. Tuning over an atomic resonance demonstrated precise spectroscopy with a single-photon source. As an evidence of a coherent interaction of the photons with the atomic ensembles, slowing down of single-photon pulses was shown as well.

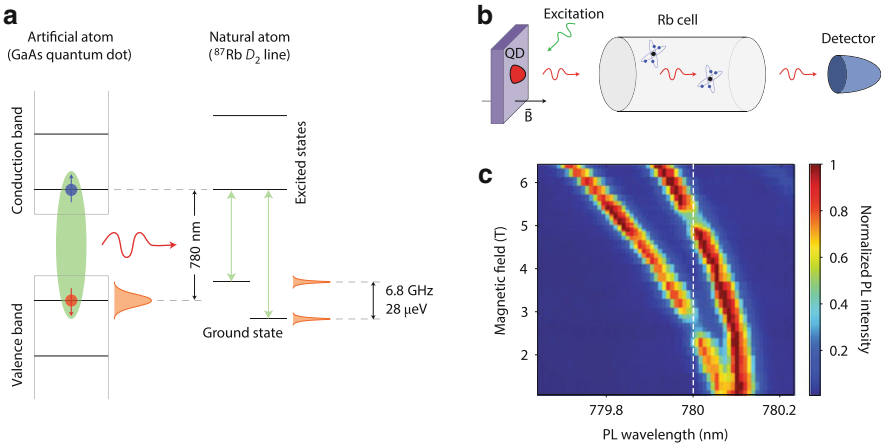

Fig. 15 Concept of coupling a quantum dot and an atomic ensemble. (**a**) Energy level diagrams in a quantum dot and a rubidium atom. The *blue circle* represents an electron, the *red circle* a hole, and the *arrows* their spin projections. The hyperfine splitting of the ^{87}Rb D2 ground state is 28 μeV. Relevant, Fourier-limited optical transitions in quantum dots and rubidium are shown in *green* and are represented by *orange* Lorentzians. (**b**) Schematics of the experiment. An optically excited quantum dot (QD) emits single photons, which propagate through the cell with a warm rubidium vapor before detection. (**c**) Photoluminescence (PL) spectra of a quantum dot emission under tuning with an increasing magnetic field. The quantum dot was excited with a 532 nm continuous-wave laser. A cell with a rubidium vapor at 120°C was placed in front of the detector. *Dashed line* corresponds to the ^{87}Rb D2 transitions. Each branch of the Zeeman-split emission is tuned to the D2 transitions and is partially absorbed by the vapor

Figure 15 outlines the concept of the experiment performed by Akopian et al. [65].

Aside from establishing a quantum hybrid system, tuning of single-photon sources in condensed phase to an atomic frequency standard is an important way to overcome their inevitable spectral inhomogeneity. Here one has to face the difficulty of using the absorption of a single-photon stream as a feedback signal. Only a fraction of the total single-photon flux on the order of 10.000–100.000 photons per second is available to generate such a signal.

5 Future Prospects

A strong motivation for many experiments in quantum optics is *quantum information processing*. First steps towards a commercial quantum technology have been taken, in particular with respect to secure information exchange. Inevitably photons have to be used to transfer quantum information over larger distances, but also small quantum computational tasks can be performed all optically. The maturity of single-photon sources and single-photon detectors renders an optical quantum

technology very attractive. If, however, clock cycles comparable to classical information processing systems are envisioned, then bandwidths and timing jitter of single-photon detectors and single-photon sources have to be improved. Further unresolved issues are still the lack of fast photon number resolving detectors with high efficiency and efficient detection in the near infrared above a wavelength of 1 μm. Nanowire superconducting detectors have become more widely used, in particular in quantum optics labs where their required cryogenic environment is not a critical issue. Their ultralow dark count level was mandatory for experiments looking for rare photon coincidence events. The ease of their integration on chip may also be a major advantage for more complex multiphoton counting tasks.

Assembling quantum optical devices from dissimilar physical systems is the key goal in research with *hybrid quantum systems*. If the interaction between these systems is mediated via photons, then a tuning and matching of absorption and emission spectra, as well as of photon wave packets, is required. Additionally, with the exception of isolated atoms, all quantum emitters suffer from an inhomogeneous distribution of their emission wavelength. We have outlined in the previous section how locking to frequency standards may overcome this problem. Here a key task is to generate a continuous feedback signal from (perhaps only a few) detection events. More generally speaking, fast algorithms have to be developed that evaluate a discrete set of events in order to estimate the most likely reason for a deviation from an optimum performance of a multiparameter system. For example, a feedback signal to maintain the indistinguishability of two photons would be the two-photon coincidence rate after a beam splitter in a Hong–Ou–Mandel configuration. Auxiliary optical signals like the absorption of a probe beam which can be utilized as feedback to lock single emitters as well [67] are also very faint signals. They may require single-photon detectors as well. Finally, hybrid quantum systems will very likely involve dissimilar detectors providing different electronic signals. This makes high demands on the counting electronics.

The level of integration in the first proof-of-principle experiments aiming at an optical quantum technology is still low. Often only passive optical elements, like waveguides, beam splitters, or filters, are fabricated on chip. Single-photon sources and detectors are connected via free space beams or optical fibers. A key goal for an *all-integrated quantum electro-optic technology* would be to integrate sources, passive elements, as well as the detectors on a single chip. It is however unlikely that a unified fabrication technology for all these components can be developed. More promising ways in short to midterm will have to exploit micro-packaging techniques. Such an approach could also be attractive to merge integrated classical and quantum optical technology on a unique platform.

Acknowledgments This work was supported by the DFG (SFB 787) and by the BMBF (project Q.com-H).

References

1. Einstein A (1905) Ann Phys 17:132
2. Taylor GI (1909) Proc Camb Philos Soc 15:114
3. Loudon R (1973) The quantum theory of light. Oxford University Press, Oxford
4. Hanbury Brown R, Twiss RQ (1956) Nature 177:27
5. Steudle G, Schietinger S, Höckel D, Dorenbos SN, Zadeh IE, Zwiller V, Benson O (2012) Phys Rev A 86:053814
6. Zwiller V, Aichele T, Seifert W, Persson J, Benson O (2003) Appl Phys Lett 82:1509
7. Zwiller V, Aichele T, Benson O (2004) Phys Rev B 69:165307
8. Hoffges JT, Baldauf HW, Lange W, Walther H (1997) J Mod Opt 44:1999
9. Steudle G (2012) Dissertation, Humboldt-University Berlin
10. Hadfield RH (2009) Nat Photonics 3:696
11. Miller AJ, Nam SW, Martinis JM, Sergienko AV (2003) Appl Phys Lett 83:791
12. Lita AE, Miller AJ, Nam SW (2008) Opt Express 16:3032
13. Hoyt CC, Foukal PV (1991) Metrologia 28:163
14. Bülter A (2014) Springer Ser Fluoresc. doi:10.1007/4243_2014_63
15. Buller GS, Collins RJ (2014) Springer Ser Fluoresc. doi:10.1007/4243_2014_64
16. Kiraz A, Atatüre M, Imamoglu A (2004) Phys Rev A 69:032305
17. Kuhn A, Hennrich M, Rempe G (2002) Phys Rev Lett 89:067901
18. Flagg EB, Muller A, Robertson JW, Founta S, Deppe DG, Xiao M, Ma W, Salamo GJ, Shih CK (2009) Nat Phys 5:203
19. Vamivakas AN, Zhao Y, Lu CY, Atatüre M (2009) Nat Phys 5:198
20. He YM, He Y, Wei YJ, Wu D, Atatüre M, Schneider C, Höfling S, Kamp M, Lu CY, Pan JW (2013) Nat Nanotechnol 8:213
21. Knill E, Laflamme R, Milburn GJ (2001) Nature 409:46
22. Hong CK, Ou ZY, Mandel L (1987) Phys Rev Lett 59:2044
23. Purcell EM (1946) Phys Rev 69:681
24. Keller M, Lange B, Hayasaka K, Lange W, Walther H (2004) Nature 431:1075
25. Barros HG, Stute A, Northup TE, Russo C, Schmidt PO, Blatt R (2009) New J Phys 11:103004
26. Kurtsiefer C, Mayer S, Zarda P, Weinfurter H (2000) Phys Rev Lett 85:290
27. Schell AW, Kewes G, Schröder T, Wolters J, Aichele T, Benson O (2011) Rev Sci Instrum 82:073709
28. Wolters J, Kewes G, Schell AW, Nüsse N, Schoengen M, Löchel B, Hanke T, Bratschitsch R, Leitenstorfer A, Aichele T, Benson O (2012) Phys Status Solidi B 249:918
29. Wolters J, Schell AW, Kewes G, Nüsse N, Schoengen M, Döscher H, Hannappel T, Löchel B, Barth M, Benson O (2010) Appl Phys Lett 97:141108
30. Schietinger S, Aichele T, Wang H, Nann T, Benson O (2010) Nano Lett 10:134
31. Schröder T, Gädeke F, Banholzer MJ, Benson O (2011) New J Phys 13:055017
32. Lee KG, Chen XW, Eghlidi H, Kukura P, Lettow R, Renn A, Sandoghdar V, Götzinger S (2011) Nat Photonics 5:166
33. Chen X-W, Götzinger S, Sandoghdar V (2011) Opt Lett 36:3545
34. Schröder T, Fujiwara M, Noda T, Zhao HQ, Benson O, Takeuchi S (2012) Opt Express 20:10490
35. Schröder T, Schell AW, Kewes G, Aichele T, Benson O (2011) Nano Lett 11:198
36. Heindel T, Schneider C, Lermer M, Kwon SH, Braun T, Reitzenstein S, Höfling S, Kamp M, Forchel A (2010) Appl Phys Lett 96:011107
37. Yuan Z, Kardynal BE, Stevenson RM, Shields AJ, Lobo CJ, Cooper K, Beattie NS, Ritchie DA, Pepper M (2002) Science 295:102
38. Minot ED, Kelkensberg F, van Kouwen M, van Dam JA, Kouwenhoven LP, Zwiller V, Borgström MT, Wunnicke O, Verheijen MA, Bakkers EPAM (2007) Nano Lett 7:367
39. Mizuochi N, Makino T, Kato H, Takeuchi D, Ogura M, Okushi H, Nothaft M, Neumann P, Gali A, Jelezko F, Wrachtrup J, Yamasaki S (2012) Nat Photonics 6:299

40. Chou CW, Polyakov SV, Kuzmich A, Kimble HJ (2004) Phys Rev Lett 92:213601
41. Christ A, Silberhorn C (2012) Phys Rev A 85:023829
42. Shih YH, Alley CO (1988) Phys Rev Lett 61:2921
43. Ou ZY, Mandel L (1988) Phys Rev Lett 61:50
44. Howell JC, Bennink RS, Bentley SJ, Boyd RW (2004) Phys Rev Lett 92:210403
45. Brendel J, Mohler E, Martienssen W (1992) Europhys Lett 20:575
46. Brendel J, Gisin N, Tittel W, Zbinden H (1999) Phys Rev Lett 82:2594
47. Barz S, Cronenberg G, Zeilinger A, Walther P (2010) Nat Photonics 4:553
48. Bouwmeester D, Pan JW, Mattle K, Eibl M, Weinfurter H, Zeilinger A (1997) Nature 390:575
49. Pan JW, Bouwmeester D, Weinfurter H, Zeilinger A (1998) Phys Rev Lett 80:3891
50. Aspect A, Dalibard J, Roger G (1982) Phys Rev Lett 49:1804
51. Young RJ, Stevenson RM, Atkinson P, Cooper K, Ritchie DA, Shields AJ (2006) New J Phys 8:29
52. Benson O, Santori C, Pelton M, Yamamoto Y (2000) Phys Rev Lett 84:2513
53. Salter CL, Stevenson RM, Farrer I, Nicoll CA, Ritchie DA, Shields AJ (2010) Nature 465:594
54. Ou ZY, Lu YJ (1999) Phys Rev Lett 83:2556
55. Wahl M, Röhlicke T, Rahn HJ, Erdmann R, Kell G, Ahlrichs A, Kernbach M, Schell AW, Benson O (2013) Rev Sci Instrum 84:043102
56. Scholz M, Koch L, Benson O (2009) Phys Rev Lett 102:063603
57. Scholz M, Koch L, Ullmann R, Benson O (2009) Appl Phys Lett 94:201105
58. Kuklewicz CE, Wong FNC, Shapiro JH (2006) Phys Rev Lett 97:223601
59. Gisin N, Thew R (2007) Nat Photonics 1:165
60. Briegel HJ, Dür W, Cirac JI, Zoller P (1998) Phys Rev Lett 81:5932
61. Duan LM, Lukin MD, Cirac JI, Zoller P (2001) Nature 414:413
62. Bratzik S, Abruzzo S, Kampermann H, Bruß D (2013) Phys Rev A 87:062335
63. Hofmann J, Krug M, Ortegel N, Gérard L, Weber M, Rosenfeld W, Weinfurter H (2012) Science 337:72
64. Bernien H, Hensen B, Pfaff W, Koolstra G, Blok MS, Robledo L, Taminiau TH, Markham M, Twitchen DJ, Childress L, Hanson R (2013) Nature 497:86
65. Akopian N, Wang L, Rastelli A, Schmidt OG, Zwiller V (2011) Nat Photonics 5:230
66. Siyushev P, Stein G, Wrachtrup J, Gerhardt I (2014) Nature 509:66
67. Prechtel JH, Kuhlmann AV, Houel J, Greuter L, Ludwig A, Reuter D, Wieck AD, Warburton RJ (2013) Phys Rev X 3:041006

Photon Counting in Diffuse Optical Imaging

Dirk Grosenick

Abstract The high sensitivity and the picosecond time resolution of time-correlated single photon counting have led to the application of this technique for diffuse optical imaging of biological tissue in vivo in the near-infrared spectral range. In this chapter the fundamentals of photon propagation in biological tissue and the concept of the distribution of times of flight of scattered photons are briefly discussed. Then the main features of time-resolved, frequency-domain, and continuous-wave techniques are compared. An overview is given on the application of time-correlated single photon counting for investigations on human breast tissue, on the brain, and on muscle tissue. In the second part, experimental approaches and clinical studies on the detection and characterization of breast tumors based on oxy- and deoxyhemoglobin concentrations are considered in more detail. The application of time-resolved measurements to monitor breast tumor degeneration by neoadjuvant chemotherapy is discussed. Finally, fluorescence mammography with the contrast agent indocyanine green is considered as a tool to improve differentiation between malignant and benign breast lesions.

Keywords Breast cancer · Diffuse optical imaging · Fluorescence imaging · Near-infrared spectroscopy · Tissue optical properties

Contents

1 Introduction 344
2 Diffuse Light Propagation in Tissue 345
3 Time-Resolved, Frequency-Domain and Continuous-Wave Techniques 347

D. Grosenick (✉)
Physikalisch-Technische Bundesanstalt (PTB), Berlin, Germany
e-mail: dirk.grosenick@ptb.de

P. Kapusta et al. (eds.), *Advanced Photon Counting: Applications, Methods, Instrumentation*, Springer Ser Fluoresc (2015) 15: 343–366, DOI 10.1007/4243_2014_74,

4 Application of Photon Counting in Diffuse Optical Imaging and Spectroscopy 349
4.1 Overview 349
4.2 Optical Mammography 350
4.3 Monitoring of Neoadjuvant Chemotherapy Response 356
4.4 Fluorescence Optical Mammography 357
5 Conclusions 361
References 362

1 Introduction

In the near-infrared spectral range the absorption of biological tissue in vivo is mainly determined by oxygenated and deoxygenated hemoglobin, water, and lipids. As first reported by Jöbsis [1], absorption in this wavelength range is weak and the light can penetrate deeply into the tissue. This finding offers the possibility of imaging the spatial distribution of hemoglobin and the other absorbers in the tissue in vivo. However, optical imaging in the near-infrared is hampered by the strong scattering of light. Each boundary in the tissue at the cellular level influences the propagation direction of the photons by refraction or reflection. Basic investigations have shown that on the macroscopic scale photon propagation in tissue can be approximately described as a diffusion process [2]. Accordingly, near-infrared imaging of biological tissue on the centimeter scale is called diffuse optical imaging. Since measurements at several wavelengths are required to separate the concentrations of oxy- and deoxyhemoglobin, the termini diffuse optical spectroscopy or near-infrared spectroscopy of tissue is used as well.

The possibility of characterizing the spatial distribution of oxy- and deoxyhemoglobin has led to several applications of diffuse optical imaging. The main applications are investigations on lesions of the female breast [3], investigations on brain tissue [4, 5], and investigations on muscle tissue [6]. Furthermore, during the past few years the number of applications in monitoring the somatic oxygenation status in preterm infants has been growing [7]. Besides the investigation of the hemoglobin concentration in tissue, diffuse optical imaging can also be used to detect fluorescent markers with excitation and emission wavelengths in the near infrared [8]. This possibility is extensively exploited in the characterization of newly developed markers for molecular imaging in small animal models.

In order to derive the local concentration of oxy- and deoxyhemoglobin or the concentration of a fluorescent marker one has to apply a suitable measurement technique together with an appropriate model to analyze the diffusely transmitted or reflected light [9, 10]. One main requirement is to separate the contribution of scattering from that of absorption or fluorescence to the measured light signals. According to the temporal characteristics of the laser radiation used for diffuse optical imaging, the measurement techniques can be divided into continuous-wave (CW) methods, time-domain techniques, and frequency-domain techniques [10]. Hereby, time-domain techniques yield the most comprehensive information

about the tissue [9]. The corresponding method of choice for light detection is time-correlated single photon counting [11]. It combines high sensitivity and high dynamic range with the required picosecond time resolution.

2 Diffuse Light Propagation in Tissue

When a photon enters biological tissue, its path inside the tissue can be understood as a series of small straight lines interrupted by changes in the propagation direction due to refraction or reflection at internal tissue structures (Fig. 1). Typical mean free path lengths in tissue are about 100 µm. Along its way, the photon can be absorbed, e.g., by a hemoglobin molecule. In the case of a fluorescent molecule, the absorption process could result in emission of a fluorescence photon which then propagates in a manner similar to the originally injected photon. In particular, it could be absorbed by hemoglobin, too. Photons which are not absorbed will leave the tissue somewhere. Due to the large number of scattering events, the photon could exit the tissue even in reflection. The time of exit depends on the total path length and the speed of light in the tissue.

A second photon will follow a different path through the tissue, since it does not exactly enter the tissue at the same point and at the same time. As a result, when considering injection of a picosecond laser pulse into the tissue the individual (non-absorbed) laser photons will exit the tissue at different locations at different times. By placing a detection fiber at a selected position on the tissue surface one can measure a broadened light pulse which represents the distribution of times of

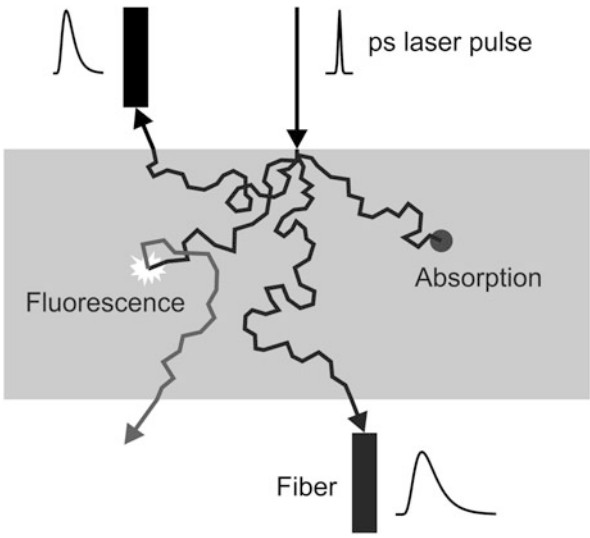

Fig. 1 Photon propagation in tissue and principle of time-resolved detection of diffusely transmitted or reflected light for a slab-like tissue structure

flight of the diffusely scattered photons at this position. Similarly, with a suitable fluorescence bandpass the distribution of times of arrival of fluorescence photons at the detector position can be measured.

The times of flight of the detected laser or fluorescence photons depend on the scattering and absorption properties of the tissue. The scattering properties are described by the scattering coefficient μ_s which is the inverse of the mean free path length between two scattering events and by the anisotropy factor g which is the mean cosine value of the photon scattering angle. Typical values for biological tissue are $\mu_s = 100\ \text{cm}^{-1}$ and $g = 0.9$. The latter value means that the photon scattering angle in tissue is small, i.e., the scattering in tissue is forward directed. The absorption properties of the tissue are described by the absorption coefficient μ_a, which is the inverse of the mean distance the photon travels before absorption happens. For breast tissue the absorption coefficient is around $0.04\ \text{cm}^{-1}$; for brain tissue the average absorption coefficient amounts to about $0.1\ \text{cm}^{-1}$. In the case of highly vascularized organs such as muscle tissue, the absorption can even be higher. When the distance between the point of light injection and the detector position amounts to a few centimeters the mean time of flight of the detected photons is typically a few nanoseconds. In this time range, time-correlated single photon counting is the mean of choice for detecting the distribution of times of flight.

The propagation of light through the tissue can be modeled by Monte Carlo simulations [12]. In this approach the propagation of single photons through the tissue is tracked as drawn in Fig. 1, i.e., the photon path is constructed from a sequence of (1) free movement to the next scattering event and (2) the change of the direction due to this event. Furthermore, the probability of the photon to be absorbed during propagation is taken into account. Typically, the three tissue parameters μ_s, g, and μ_a are sufficient to describe the propagation. Monte Carlo simulations are time-consuming, in particular for tissue dimensions on the centimeter scale.

The radiative transfer equation is another model of light propagation in tissue. When tissue absorption μ_a is small compared to tissue scattering μ_s, the photon diffusion equation as an approximation of the radiative transfer equation can be applied to calculate photon flux densities at positions which are sufficiently far away from the photon source [2]. In this approximation, the diffusely scattering medium is described by the absorption coefficient μ_a and the reduced scattering coefficient $\mu_s' = \mu_s(1 - g)$. Analytical solutions of the diffusion equation are available for several geometries of homogeneous media that can be used to mimic tissue such as the semi-infinite medium, the infinitely extended slab or the infinitely extended cylinder. Furthermore, a few cases of heterogeneous media such as a spherical or cylindrical object in a homogeneous medium or layered structures can be handled. Numerical methods such as finite-element or finite-difference methods permit the description of arbitrary geometries on voxel-based medium properties.

3 Time-Resolved, Frequency-Domain and Continuous-Wave Techniques

The detection of the distribution of times of flight (DTOF) of photons by time-correlated single photon counting is a well-known method to derive the absorption coefficient μ_a and the reduced scattering coefficient μ_s' of a homogeneous medium with planar boundaries from diffuse reflection or transmission measurements. To this end, a picosecond or femtosecond laser [13] is employed as a light source (Fig. 2). The optical properties are derived by using the analytical solution of the photon diffusion equation for the homogeneous semi-infinite medium or the homogeneous infinite slab to analyze the measured distribution of times of flight. With a source-detector distance of typically 2–6 cm the full width at half maximum of the detected light pulse is in the order of one to several nanoseconds.

According to this half-width, the Fourier spectrum of the measured light pulse contains frequencies up to a few GHz. Instead of using an ultrashort light pulse for the measurement, one can equivalently employ a set of measurements with an amplitude modulated laser covering the required frequency range from 0 to a sufficiently large value of the cut-off frequency. This approach is of particular interest for applying diode lasers which can be easily modulated by the driving current. By detecting the frequency-dependent damping of the modulation amplitude (demodulation) as well as the corresponding phase shifts, this frequency-domain technique provides about the same information as the time-resolved approach. In several investigations a much simpler frequency-domain setup was used with only one modulation frequency of about 100 MHz (Fig. 2). Such a measurement yields the minimum information required to derive both the absorption and the reduced scattering coefficient of the homogeneous medium.

The third experimental method used in diffuse optical imaging is the CW technique in which the damping of a time-independent laser signal due to the tissue

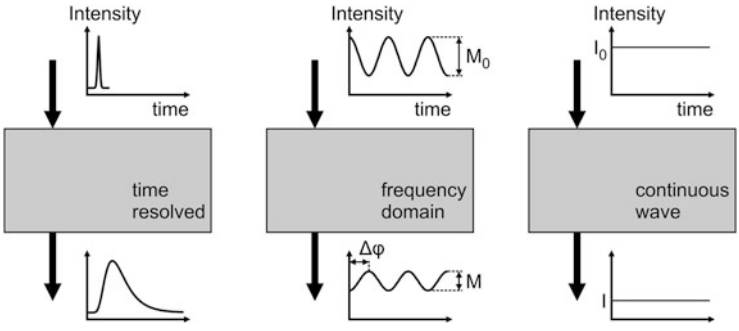

Fig. 2 Principle of time-resolved, frequency-domain (single modulation frequency), and CW light detection

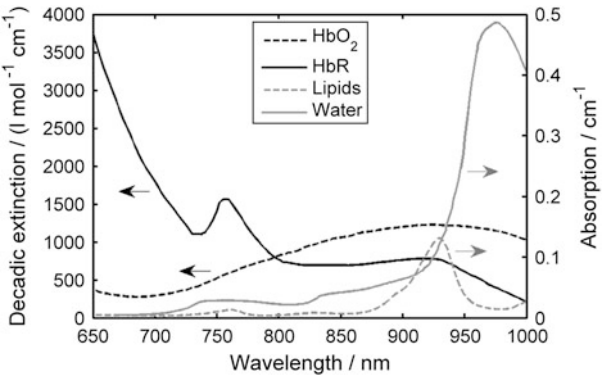

Fig. 3 Molar decadic extinction coefficients of oxy- and deoxyhemoglobin [14], and absorption coefficients of pure water [15] and lipids [16] in the near-infrared spectral range

is measured (Fig. 2). From this type of investigation one can derive only the tissue attenuation coefficient which depends on both μ_s' and μ_a.

In order to derive the tissue oxy- and deoxyhemoglobin concentrations, time-resolved or frequency-domain measurements have to be performed for at least two optical wavelengths. Typically, one of the wavelengths is chosen between 650 and 750 nm where the absorption of deoxyhemoglobin is dominant (Fig. 3), and the other between 780 and 830 nm where the absorption of both substances is similar. When the other tissue absorbers (water, lipids) in the near-infrared are of interest, too, then additional wavelengths sensitive to these substances are required. As illustrated in Fig. 3, lipids show significant absorption around 925 nm, and water has a strong peak around 975 nm.

The relationship between the measured absorption coefficients μ_a at the selected wavelengths λ_k and the underlying tissue absorber concentrations is given by:

$$\begin{aligned}\mu_a(\lambda_k) = &[\varepsilon_{HbR}(\lambda_k)c_{HbR} + \varepsilon_{HbO_2}(\lambda_k)c_{HbO_2}] \cdot \ln(10) \\ &+\mu_{a,H_2O}(\lambda_k)\kappa_{H_2O} + \mu_{a,lip}(\lambda_k)\kappa_{lip}\end{aligned} \quad (1)$$

Here, c_{HbR} and c_{HbO_2} are the tissue concentrations of deoxy- and oxyhemoglobin, respectively. The contributions of water and lipids to the total tissue absorption are described by their volume fractions κ_{H_2O} and κ_{lip}. The symbols ε_{HbR} and ε_{HbO_2} denote the molar decadic absorption coefficients of deoxy- and oxyhemoglobin, and the quantities μ_{a,H_2O} and $\mu_{a,lip}$ are the absorption coefficients of pure water and pure lipids. The latter four quantities are the substance-specific properties plotted in Fig. 3.

4 Application of Photon Counting in Diffuse Optical Imaging and Spectroscopy

4.1 Overview

The time-resolved technique is more complex and more expensive than CW or frequency-domain instrumentation. Therefore, it cannot compete against the other techniques in the development of cheap and portable instrumentation for near-infrared imaging and spectroscopy. Accordingly, the time-resolved technique has preferably been used in research studies, in particular when quantification of tissue optical properties was of main interest. Main fields of application have been the detection and characterization of breast tumors [17, 18] and functional imaging of the brain [9, 19]. Furthermore, the time-resolved technique was applied to functional imaging on muscle [6]. Figure 4 shows the basic measurement geometries applied on these organs.

The main task in optical breast imaging is to either detect or characterize a lesion. Breast tissue has very low absorption in the near-infrared spectral range. Therefore, investigations can be performed in transmission geometry with the breast being positioned between two transparent plates combined with fiber scanning for imaging (Fig. 4a) [20, 21]. Alternatively, a tomographic arrangement of light sources and detection fibers can be used (Fig. 4b) [22].

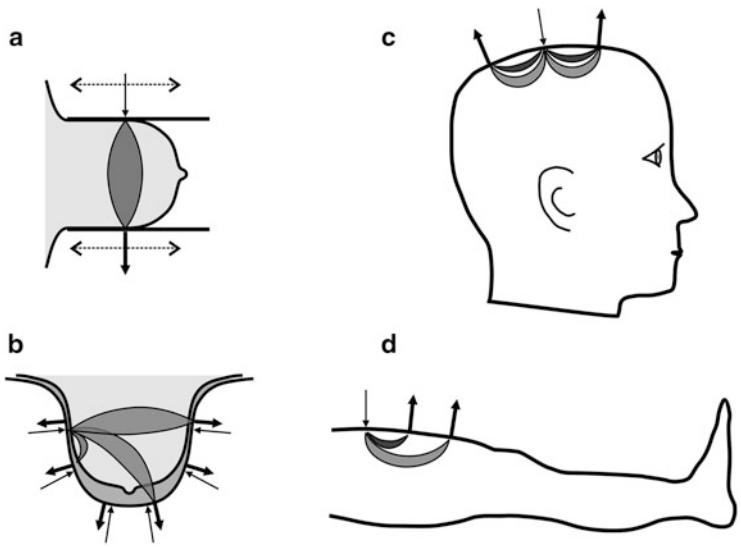

Fig. 4 Examples of measurement geometries. The banana-like shapes (photon bananas) illustrate the sampled volumes for selected source-detector combinations. (**a**) Breast tissue in transmission, (**b**) Breast tissue in a cup-like hemisphere filled with coupling fluid, (**c**) brain with photon bananas for early photons (*dark gray*) and late photons (*light gray*), (**d**) femoral muscle tissue

In functional imaging of the brain local changes of oxy- and deoxyhemoglobin concentrations caused by stimulation have to be recorded [5]. Brain tissue has higher absorption than breast tissue. In the case of neonates, a fully tomographic set of sources and detectors can be used since the small head can be transilluminated with a sufficient signal-to-noise ratio [4]. However, measurements on adults are restricted to the reflection geometry. Typically, a set of fixed source and detector fibers is employed on top of the region of interest with source-detector distances of 3–5 cm to gain access to the gray matter through the superficial layers. As illustrated in Fig. 4c, the depth sensitivity can be increased by looking at photons with long times of flight, since photons with short times of flight could not reach deeper regions before returning to the detector [23, 24]. Here the picosecond temporal resolution achievable with photon counting methods is superior to CW or single modulation frequency techniques. Recently, a non-contact scanning approach was presented for the brain in which the light detection is accomplished at the source position by suppressing the large number of photons with short times of flight by utilizing a single photon avalanche diode with a special gating technique [25, 26]. In the few studies on muscle with time-domain photon counting techniques [27–29], reflectance spectrometers with several detector positions have been used (Fig. 4d).

In the following sections we will focus on the application of photon counting for investigations on breast tissue and tumors. We illustrate methods to determine the optical properties of healthy tissue and tumors, and we discuss the detection and characterization of lesions based on oxy- and deoxyhemoglobin and on fluorescent measurements using indocyanine green (ICG) as a contrast agent.

4.2 Optical Mammography

Investigations on optical mammography started in the 1990s. Originally, the research aimed at developing optical imaging as a tool to detect carcinomas and to distinguish them from benign lesions. The basic idea of this approach was that carcinomas should show an increased concentration of total hemoglobin due to neovascularization and a decreased oxygen saturation due to an increased metabolism compared to both healthy tissue and benign lesions. Accordingly, several attempts were undertaken to determine the optical properties of healthy breast tissue and of both malignant and benign breast lesions. Hereby, the time-resolved technique has played a central role. During the past few years, the focus has shifted to exploiting the capability of measuring oxy- and deoxyhemoglobin for monitoring the response of patients with large breast carcinomas to neoadjuvant chemotherapy.

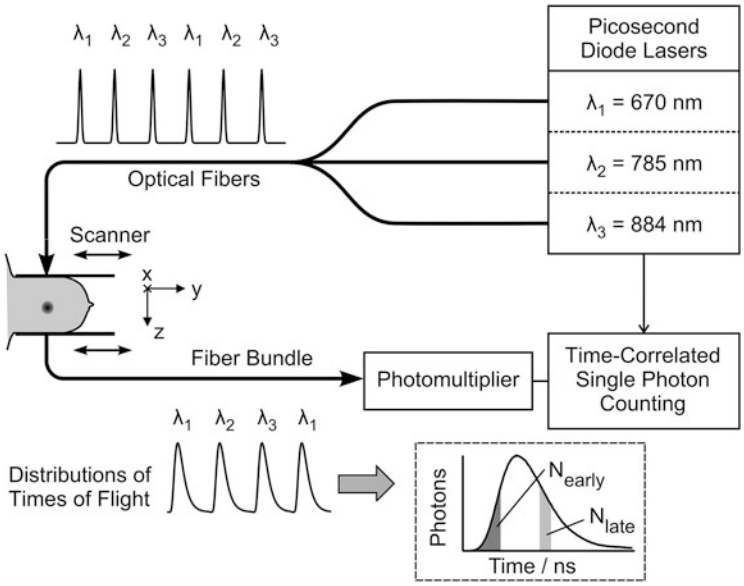

Fig. 5 Block diagram of the first generation PTB optical mammograph [31]

4.2.1 Time-resolved Breast Scanners

The first time-resolved optical mammograph was developed at the Physikalisch-Technische Bundesanstalt (PTB) Berlin [30]. In this device, parallel-plate geometry was used with the breast being slightly compressed between two glass plates. Figure 5 shows a schematic diagram of this instrument in its final configuration with three picosecond diode lasers emitting at 670, 785, and 884 nm [31]. Each laser emitted its pulses with a repetition rate of 24 MHz. Since the pulse trains at the second and third wavelength were shifted in time by about 13 and 26 ns with respect to the first one, the wavelengths could be easily separated as illustrated in Fig. 5.

The breast under investigation was scanned by moving the source fiber and the detection fiber bundle depicted in Fig. 5 in tandem in a meander-like way across the breast. At each scan position the three distributions of times of flight were measured with a collection time of 150 ms. With a typical overall photon count rate of 600 kHz a total of about 3×10^4 photons was obtained per distribution of times of flight at each wavelength. This signal intensity is a compromise between a sufficient signal-to-noise ratio and the time needed for a full scan of the breast. With a step size of 2.5 mm, a full scan of the breast was completed after about 3–10 min, depending on the breast size. When the scanner approached the edges of the breast the photon count rate strongly increased due to the decreasing breast thickness. This feature was used to determine the turning points of the meander-like scan.

A similar device was built by Politecnico di Milano in Italy. This instrument was finally equipped with seven optical wavelengths in order to determine not only oxy- and deoxyhemoglobin concentrations, but additionally the water and fat content of the tissue [32].

4.2.2 Optical Mammograms and Tissue Optical Properties

Due to the constant thickness of the breast in the slab-like geometry, optical mammograms displaying either absorption or scattering contrast can be easily generated by displaying photon counts derived from a late or from an early time window of the measured distributions of times of flight (indicated as N_{early} and N_{late} in Fig. 5) [30]. Maps of the hemoglobin concentration and the blood oxygen saturation values can be obtained by analyzing the tissue optical properties for the various wavelengths at each scan position with the model of the homogeneous slab [20].

Figure 6 shows an example of a fit result for a distribution of times of flight recorded in vivo. The fit interval starts at the 20% level of the pulse amplitude on the rising edge and stops at the 5% level of the trailing edge. Generally, the first part of the rising edge is excluded in the time-domain analysis of the optical properties by the diffusion model, since deviations between the experiment and diffusion theory are expected here due to limitations of the diffusion model. As fit parameters the absorption coefficient, the reduced scattering coefficient, and an additional time shift between theory and the experiment are used. An amplitude scaling factor is omitted by exploiting the integral below the experimental and theoretical curve for scaling. Before scaling, the theoretical pulse is convolved with the instrument response function. The absorption and reduced scattering coefficients obtained by the homogeneous model are average values over the volume sampled by the particular source-detector combination as illustrated in Fig. 6 (right). This volume can be estimated from photon measurement density functions [33] or photon bananas [34].

Having estimated the optical properties at each scan position, the maps of total hemoglobin concentration and blood oxygen saturation in the tissue can be derived from the absorption coefficients by solving the set of linear equations defined by Eq. (1). Figure 7 displays several types of optical mammograms obtained by these methods for a patient with a carcinoma. The best contrast is obtained in the left mammogram displaying normalized photons counts of a late time window [17] at 670 nm. The other quantities show the tumor, too, but contrast is only moderate. Furthermore, blood vessels and a high absorption at the position of the nipple can be seen.

With the exception of the late time window map, all mammograms shown in Fig. 7 have been corrected for edge effects caused by the decreased breast thickness. In the correction algorithms the mean time of flight of the detected photons at the various scan positions is used as a relative measure for breast thickness, i.e., temporal resolution plays an important role in the correction [30]. From the optical

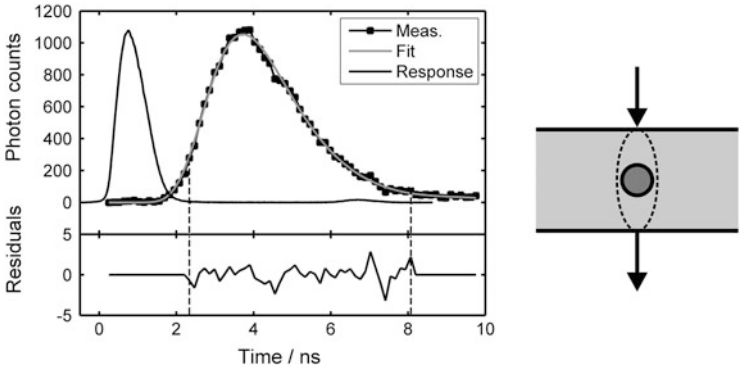

Fig. 6 *Left*: Measured and fitted distribution of times of flight for an arbitrary scan position of a 7.1 cm thick breast using the model of the homogeneous slab. The left pulse is the measured instrument response function. *Right*: Illustration of the volume sampled by the homogeneous model (*dashed line*) in relation to the true tumor size

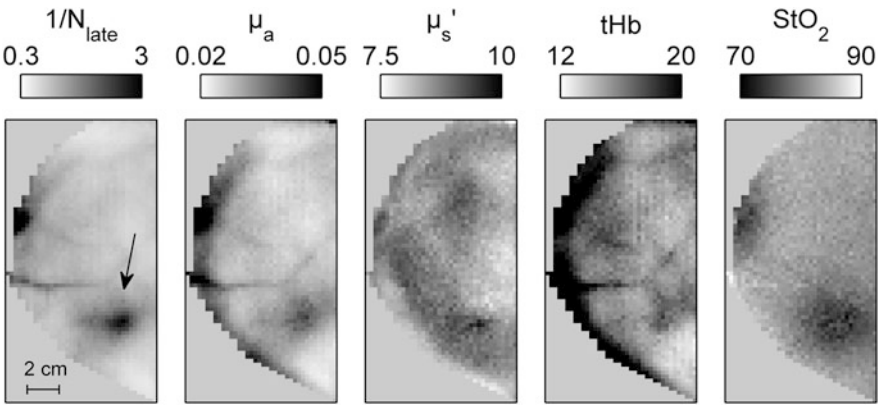

Fig. 7 Optical mammograms (craniocaudal view) of a patient with an invasive ductal carcinoma indicated by the *arrow*. From left to right: reciprocal normalized photon counts in a late time window of the distributions of times of flight (670 nm), absorption coefficient μ_a (670 nm) in cm^{-1}, reduced scattering coefficient μ_x'(670 nm) in cm^{-1}, total hemoglobin concentration tHb in μmol/l, and blood oxygen saturation StO_2 in percent. Optical properties, hemoglobin concentration, and oxygen saturation have been derived with the model of the homogeneous slab

properties and physiological parameters obtained in this way, one can derive average properties for healthy breast tissue. Table 1 summarizes results obtained from a clinical study with the first generation PTB time-domain optical mammograph and compares them with the optical properties of carcinomas derived in the next subsection [35].

Table 1 Total hemoglobin concentration c_{HbT}, blood oxygen saturation StO_2, and optical properties of healthy breast tissue and of carcinomas obtained by time-resolved measurements on 87 patients [35]

Quantity	Wavelength	Number of cases	Healthy tissue	Carcinomas	Ratio
c_{HbT} (μmol/l)		87	17.3 ± 6.2	53 ± 32	3.1
StO_2 (%)		87	74 ± 7	72 ± 14	0.97
μ_a (cm^{-1})	670 nm	87	0.036 ± 0.008	0.110 ± 0.066	2.5
	785 nm	87	0.039 ± 0.011	0.100 ± 0.060	2.2
	884 nm	22	0.059 ± 0.016	0.124 ± 0.089	1.7
μ_s' (cm^{-1})	670 nm	87	10.5 ± 1.3	13.5 ± 4.7	1.2
	785 nm	87	9.5 ± 1.4	11.6 ± 3.9	1.2
	884 nm	22	8.0 ± 1.0	9.1 ± 1.9	1.1

4.2.3 Tumor Optical Properties from Heterogeneous Tissue Models

The optical properties at the tumor position in Fig. 7 represent average values over the sampled tissue volume at this position, i.e., they account for the tumor as well as for the over- and underlying healthy tissue. More realistic values of the tumor optical properties have been obtained by using heterogeneous models for data analysis. Perturbation models are limited to small differences between tumor and healthy tissue optical properties [36]. A well-suited model without such limitations is the solution of the diffusion equation for a homogeneous slab with a spherical inhomogeneity [35]. In order to apply heterogeneous models to analyze the data of a breast scan one should use prior knowledge about the size of the lesion. This information can be estimated either from the extension of the lesion in optical mammograms or from clinical modalities such as X-ray or MR mammography or histopathology. In the latter cases one has to be careful, since the origin of contrast in the optical images is different from that of the clinical modalities. Besides the size of the lesion it is of advantage to know its 3D location for the analysis. The two-dimensional optical mammograms in Fig. 7 yield only the x-y position. The z position can be obtained by measurements with a lateral offset of the detection fiber in Fig. 5 with respect to the source fiber [37].

Table 1 summarizes the results for tumor optical properties and physiological parameters from the abovementioned clinical study with the PTB optical mammograph obtained by the heterogeneous sphere model. The data show that carcinomas have on average an approximately threefold total hemoglobin concentration compared to the surrounding healthy tissue which confirms the original assumption that carcinomas should be visible in optical mammography due to neovascularization. In contrast, the expected overall decrease in the blood oxygen saturation in carcinomas due to an increased metabolism could not be confirmed. A detailed analysis shows that carcinomas with high vascularization have more or less about the same oxygen saturation as the healthy tissue of the same breast, whereas carcinomas with only a slight increase in the hemoglobin concentration are typically characterized by decreased oxygen saturation [35].

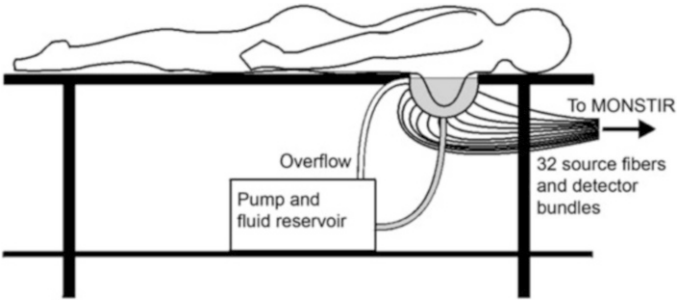

Fig. 8 Tomographic optical mammograph with fluid-coupled patient interface (Reprinted with permission of Optical Society of America from [22])

In summary, one main result of the studies on optical properties of carcinomas in the breast by time-resolved measurements is that carcinomas can be recognized in optical mammograms by their increased hemoglobin concentration. However, also benign lesions, in particular mastopathic alterations, show a larger hemoglobin concentration making their differentiation from carcinomas difficult. Consequently, the specificity of optical mammography was found to be insufficient for breast tumor screening [3, 31].

4.2.4 Tomographic Optical Breast Imaging

The possible directions of breast transillumination in the slab-like geometry are limited to paraxial axes in transmission and to measurements in reflection. To obtain a fully three-dimensional data set several research groups have built optical mammographs for investigating the freely hanging breast with circular arrangements of fixed source and detection fibers. One of these systems, the optical mammograph at University College of London (UCL), is based on time-correlated single photon counting [22]. This system uses 32 detection channels which is the largest number of parallel channels for time-resolved detection realized so far. Originally it was developed for investigations on the human brain [38]. Figure 8 shows a drawing of the interface for breast imaging. The patient is lying in the prone position on a bed with one breast hanging freely in a hemispherical cup filled with a scattering fluid. This fluid is made of Intralipid and an absorbing dye. 32 source fibers and 32 detection fibers are arranged around the cup which has a diameter of 160 mm and a height of 85 mm, respectively. A fiber laser is used, emitting pulses about 2 ps in duration at 780 and 815 nm.

Measurements are done by sequentially using each of the 32 source positions and recording the distributions of times of flight for all detector channels in parallel with an exposure time of 10 s. For the largest source-detector distance a photon count rate between 50 and 100 photons per second is reached typically. This little signal shows that the advantage of 3D tomographic imaging is paid for by a tissue thickness (including coupling fluid) of up to 16 cm compared to typically 6.5 cm

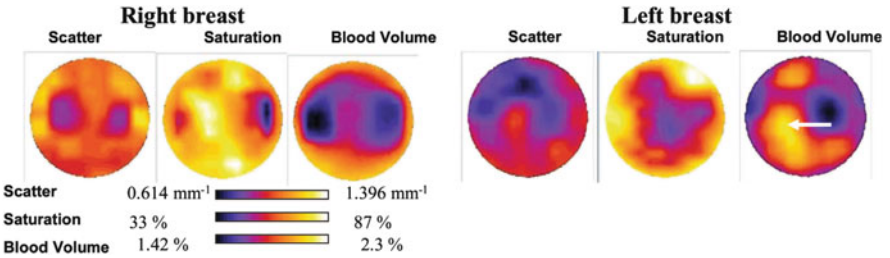

Fig. 9 Reduced scattering coefficients, oxygen saturation, and blood volume images from a 45-year-old woman. The position of the carcinoma in the left breast is indicated by the *arrow* (Reprinted with permission of Optical Society of America from [22])

of tissue thickness in the slab-like scanners which strongly affects the signal-to-noise ratio.

In order to create three-dimensional images of the optical properties of the breast, a reconstruction algorithm is used with the total intensities and the first moments of the measured distributions of times of flight as input parameters. Hereby, the differences in optical properties between the breast and the cup filled with only the scattering fluid are reconstructed. From the absorption coefficients total hemoglobin concentration and oxygen saturation are derived. Figure 9 shows an example of images for a patient with a carcinoma which was visible in the X-ray mammogram as an ill-defined 15 mm diameter mass. As indicated by the arrow, the carcinoma shows contrast in the blood volume image which can be converted to tissue total hemoglobin concentrations by multiplication with a value of 2 mmol/l.

The UCL optical tomograph was used for a clinical study on 38 patients. The results are in accordance with those of the larger studies performed with the breast scanners as summarized at the end of the preceding subsection.

4.3 Monitoring of Neoadjuvant Chemotherapy Response

Due to its insufficient specificity and due to its poor spatial resolution, diffuse optical imaging of the breast does not seem to be suitable for the detection of carcinomas and for their differentiation from benign alterations. However, the possibility of measuring local hemoglobin concentrations makes diffuse optical imaging interesting for monitoring the reduction of tumor size during neoadjuvant chemotherapy [39]. This therapy is used for large breast tumors prior to surgery to reduce their size in order to allow breast conserving surgery. In order to assess the response of a patient to the therapy as early as possible, suitable methods are required. Since diffuse optical imaging is safe, it can be repeatedly applied to study the degeneration of the carcinoma. Starting in 2003, several investigations were performed with frequency-domain devices [40–42]. Since the time-domain technique provides the most comprehensive information about diffuse photon

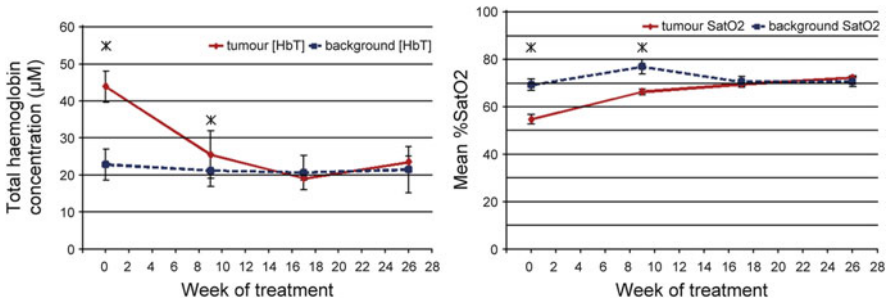

Fig. 10 Mean and standard deviation of the tumor ROI and the healthy background tissue during neoadjuvant chemotherapy. *Left*: total hemoglobin concentration, *Right*: oxygen saturation (Reprinted with permission of Adenine Press (www.tcrt.org) from [43])

propagation it should be well suited or even be advantageous for such monitoring studies where the focus is on reliable determination of tumor optical properties.

The first application of the time-resolved photon counting technique was carried out by UCL using the optical tomograph introduced in Sect. 4.2.4. In a study on four patients investigations were performed immediately before the therapy, at the end of the therapy, and ones or twice during the therapy The duration of the therapies ranged between 14 and 26 weeks. By using the experimental and reconstruction methods described in Sect. 4.2.4, total hemoglobin concentration and oxygen saturation were determined for the carcinomas and for the background tissue. Generally, the background values were found to be almost constant over time. In three of the four cases, the large hemoglobin concentration of the carcinoma decreased to the background level until the end of therapy. For all patients a response in the oxygen saturation was seen, with an increase or decrease of this quantity towards the background level. Figure 10 shows an example of the time courses. The results of the study show that diffuse optical imaging of the breast is capable of monitoring long-term changes in the breast caused by neoadjuvant chemotherapy [43].

4.4 Fluorescence Optical Mammography

A promising way to differentiate malignant from benign lesions in the breast is the application of a contrast agent that behaves differently for both groups of lesions. In diffuse optical imaging such a contrast agent can be detected either by its absorption or by its fluorescence emission [8]. When absorption imaging is used the specific contribution of the contrast agent has to be detected versus the large background signal arising from the inhomogeneous tissue absorption. Fluorescence detection has the advantage of much less background signal because of the small tissue autofluorescence in the near infrared, but signals are smaller due to the quantum yield of the contrast agent. So far, two near-infrared contrast agents have been

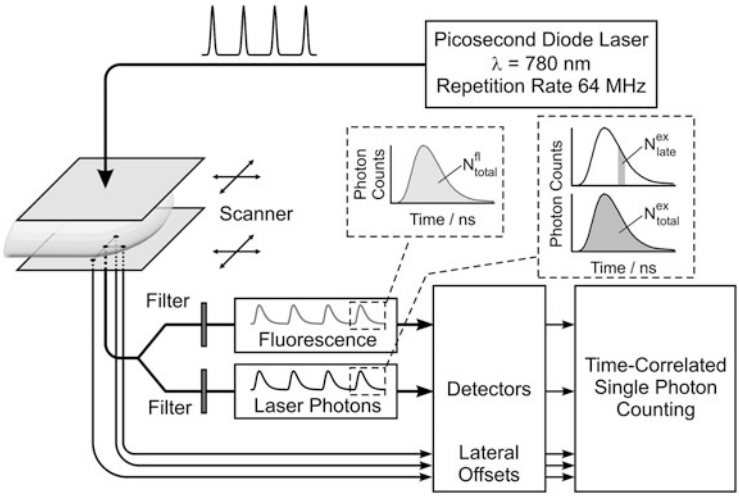

Fig. 11 Block diagram of the PTB fluorescence mammograph [49]

investigated for fluorescence imaging of breast tumors on humans in vivo. The first one is ICG [44, 45]. This near-infrared dye is widely used in clinical routine for studying microcirculation in ophthalmology, for cardiac output monitoring, and to test the liver function [8]. The second dye is omocianine, an indocyanine derivative which has not yet been approved for clinical routine [46, 47]. Both dyes are unspecific dyes, i.e., they do not bind to ligands which are specific for the disease. There have been many attempts made to develop targeting probes for the detection of breast cancer. However, at present these probes are still in preclinical research.

The most promising results on the differentiation of malignant and benign breast lesions in humans have been obtained with ICG [45, 48]. The corresponding clinical study was performed with the second generation optical mammograph of the PTB. This time-resolved instrument is capable of detecting the fluorescence of ICG [49]. Figure 11 shows the block diagram of the device which is a parallel-plate scanning instrument with a slight compression of the breast.

The device is equipped with a ps diode laser (780 nm) for fluorescence excitation of ICG. It contains eight detection channels for time-correlated single photon counting. Four detection fiber bundles are used to record data in transmission. One of the bundles collects the light on-axis to the source fiber, and the other bundles have lateral offsets. In addition, three fiber bundles are used at fixed distances from the source for measurements in reflection. The on-axis transmission fiber bundle is bifurcated to permit simultaneous detection of the DTOF of photons at the excitation wavelength and of the times of arrival of the fluorescence photons. The other six bundles can be used to detect either the excitation wavelength or the fluorescence. The information obtained by the off-axis detection channels permits creating three-dimensional images of the breast by tomosynthesis [49]. Alternatively, a 3D reconstruction based on the diffusion approximation of photon

transport can be made with these data. The instrument also offers an absorption mode to investigate the breast in transmission and reflection at four near-infrared wavelengths.

It is known that the ICG molecules immediately bind to lipoproteins in the blood serum after intravenous injection. At higher concentrations they also bind to albumin [50]. In humans with normal liver function ICG is washed out from the blood usually within 5 to 10 min. The washout characteristic shows a second decay time of about 1 h which becomes longer with increasing dye concentration. Previous studies on patients with ICG focused on detecting the pharmacokinetics in the breast within typically 10 min using a bolus injection. Hereby, the decay of the ICG concentration in the blood can be monitored by measuring the total absorption of the laser radiation which is the combination of the time-independent intrinsic tissue absorption and the absorption of ICG. Such studies were performed with CW or time-resolved techniques [51, 52]. In particular, the first generation PTB optical mammograph with its photon counting technology was used to record the washout kinetics in this way [31].

The clinical study performed with the PTB fluorescence mammograph differed in two main aspects from the previous approaches [48]. First, ICG was injected by a combination of a bolus and an infusion of about 20 min duration instead of the simple bolus to enlarge the interaction time between the ICG and the tissue. Second, a measurement of the ICG concentration in the tissue was made about 25 min after the end of the dye injection [45]. The main idea behind this protocol was to search for extravasated ICG molecules, i.e., for molecules which have left the blood vessels in the breast resulting in an enrichment in the tumor. Figure 12 illustrates the features of optical images obtained at different times during the investigation for a carcinoma and for a fibroadenoma as an example of a benign lesion. The data refer to the on-axis transmission and fluorescence channels of the mammograph.

In the first case in Fig. 12, the optical mammogram at 797 nm recorded prior to injection of the contrast agent exhibits the carcinoma with high contrast due to its enlarged hemoglobin content caused by neovascularization. The contrast at 660 nm (not shown here) is even larger, which indicates a decreased oxygen saturation in that case. For the patient with a fibroadenoma, increased absorption (here at 780 nm) can be recognized in the suspicious area. Furthermore, for both patients other parts of the breasts exhibit contrast mainly due to blood vessels.

The next two mammograms (Figs. 12b, c) show the transmission in the late time window (absorption image) and the fluorescence during the infusion period. In the absorption images, the two lesions and the blood vessels can be seen with high contrast. This contrast comes from the intrinsic absorption by hemoglobin and from the overlaid absorption of ICG circulating through the vessels. According to this situation, the time of measurement is called the vascular phase of the investigation. The fluorescence images in Fig. 12c are ratio images displaying the ratio of the raw fluorescence signal and the (time-integrated) transmission signal at 780 nm. Without such normalization the fluorescence images show the combined effect of fluorescence emission and the subsequent absorption by hemoglobin. As a result, the increased fluorescence emission at the tumor position is reduced by the

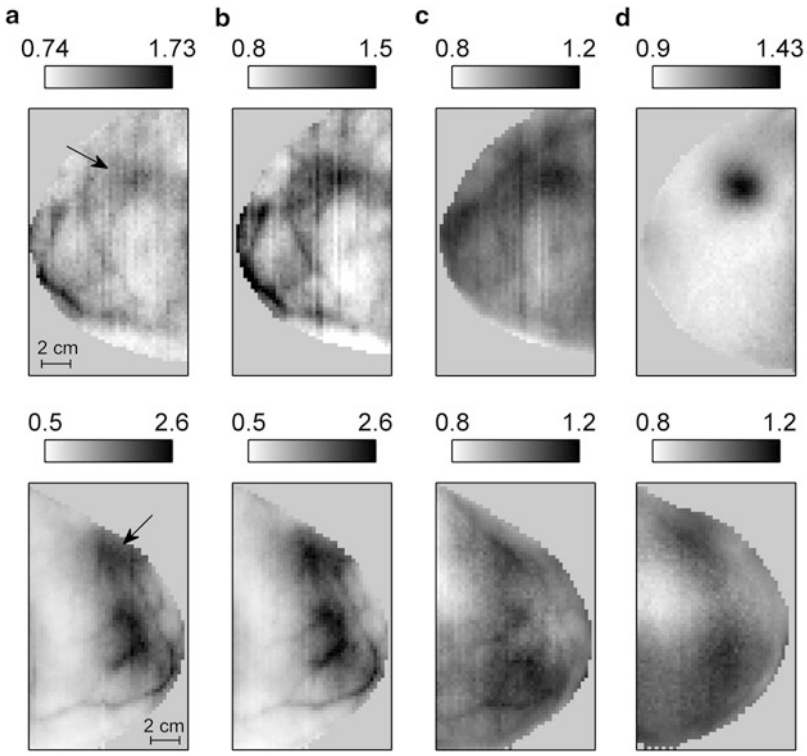

Fig. 12 Optical mammograms (craniocaudal views) of a patient with an invasive ductal carcinoma in the right breast (*top row*) and a patient with a fibroadenoma in the left breast (*bottom row*); (**a**) transmission mammogram at 797 nm (*top row*) and 780 nm (*bottom row*) before injection of the contrast agent (reciprocal normalized photon counts in a late time window), (**b**) transmission mammograms (780 nm) of the vascular phase, (**c**) fluorescence ratio mammograms of the vascular phase, (**d**) fluorescence ratio mammograms of the extravascular phase. The lesions are indicated by the *arrows*

increased light absorption in the tumor which can even cancel out the contrast [45]. The fluorescence ratio images in Fig. 12c show essentially the same structures as the absorption images since the dye is contained in the blood vessels during the vascular phase.

The images in Fig. 12d display the fluorescence ratio mammograms during the so-called extravascular phase, i.e., at a time when ICG has been washed out from the blood vessels through the liver. At this time the small amount of dye becomes visible that has left the blood vessels during circulation. The high contrast at the position of the carcinoma indicates a substantial enrichment of ICG in this malignant lesion. For the fibroadenoma the fluorescence ratio image of the extravascular phase looks similar to that of the vascular phase, apart from the vanished vessel structures. The contrast in the extravascular image is unchanged here which means that the dye could not leave the vessels in the lesion.

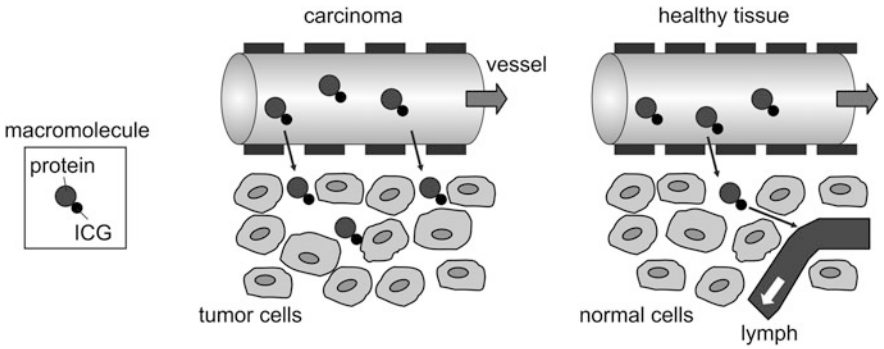

Fig. 13 Principle of extravasation and retention of macromolecules in carcinomas (*left*) and the corresponding situation in healthy tissue and benign lesions (*right*)

The different behavior of the carcinoma and the fibroadenoma can be explained with the enhanced permeability and retention effect [53] which is illustrated in Fig. 13. Since ICG binds to lipoproteins and to albumin the dye acts as a label for macromolecules. The vessels in carcinomas have a higher permeability than those in the other tissue regions, and the labeled macromolecules can move to the interstitial space. The lymphatic system in carcinomas is impaired. That is why the extravasated molecules and the ICG labels can stay here for a long time. These features provide the possibility of detecting the extravasated ICG molecules after washout of the dye from the vessels through the liver.

In the clinical study with the PTB fluorescence mammograph 20 patients with suspicious lesions were investigated. The results show that imaging the extravasation of macromolecules labeled with ICG is a promising way to differentiate malignant from benign breast lesions [48].

5 Conclusions

Investigations with time-resolved photon counting techniques have shown the potential of this method to characterize tissue optical properties and physiological parameters and to monitor hemodynamics during interventions on breast tissue, on the brain, and on muscle tissue. Due to the relatively high costs of the equipment including picosecond laser sources and detectors, the photon counting techniques are not as widely used in diffuse optical imaging and spectroscopy as frequency-domain or CW methods. In particular, the number of detection channels that can be realized in parallel is limited for these reasons. However, time-resolved photon counting methods provide the most comprehensive information on diffuse light propagation in tissue in combination with a high signal-to-noise ratio. The temporal resolution fits well to the demands in diffuse optical imaging of tissue. Accordingly, these methods are best suited for deriving absolute values of tissue optical

properties, hemoglobin concentration, and blood oxygen saturation with high accuracy. Furthermore, the high sensitivity makes them to ideal candidates in detecting fluorescence from small amounts of disease specific contrast agents in tissue. With these capabilities time-resolved photon counting methods are of fundamental importance in the development of optical imaging methods for diagnostics and therapy.

References

1. Jöbsis F (1977) Noninvasive, infrared monitoring of cerebral and myocardial oxygen sufficiency and circulatory parameters. Science 198:1264–1267
2. Ishimaru A (1989) Diffusion of light in turbid material. Appl Optics 28:2210–2215. doi:10.1364/AO.28.002210
3. Leff DR, Warren OJ, Enfield LC, Gibson AP, Athanasiou T, Patten DK, Hebden JC, Yang GZ, Darzi A (2008) Diffuse optical imaging of the healthy and diseased breast: a systematic review. Breast Cancer Res Treat 108:9–22. doi:10.1007/s10549-007-9582-z
4. Lloyd-Fox S, Blasi A, Elwell CE (2010) Illuminating the developing brain: the past, present and future of functional near infrared spectroscopy. Neurosci Biobehav Rev 34:269–284. doi:10.1016/j.neubiorev.2009.07.008
5. Ghosh A, Elwell CE, Smith M (2012) Review article: cerebral near-infrared spectroscopy in adults: a work in progress. Anesth Analg 115:1373–1383. doi:10.1213/ANE.0b013e31826dd6a6
6. Contini D, Zucchelli L, Spinelli L, Caffini M, Re R, Pifferi A, Cubeddu R, Torricelli A (2012) Review: brain and muscle near infrared spectroscopy/imaging techniques. J Near Infrared Spectrosc 20:15. doi:10.1255/jnirs.977
7. Mittnacht AJC (2010) Near infrared spectroscopy in children at high risk of low perfusion. Curr Opin Anaesthesiol 23:342–347. doi:10.1097/ACO.0b013e3283393936
8. Grosenick D, Wabnitz H, Ebert B (2012) Review: recent advances in contrast-enhanced near infrared diffuse optical imaging of diseases using indocyanine green. J Near Infrared Spectrosc 20:203. doi:10.1255/jnirs.964
9. Gibson AP, Hebden JC, Arridge SR (2005) Recent advances in diffuse optical imaging. Phys Med Biol 50:R1–R43. doi:10.1088/0031-9155/50/4/R01
10. Durduran T, Choe R, Baker WB, Yodh AG (2010) Diffuse optics for tissue monitoring and tomography. Rep Prog Phys 73:076701. doi:10.1088/0034-4885/73/7/076701
11. Wahl M (2014) Modern TCSPC electronics: principles and acquisition modes. Springer Ser Fluoresc. doi:10.1007/4243_2014_62
12. Alerstam E, Svensson T, Andersson-Engels S (2008) Parallel computing with graphics processing units for high-speed Monte Carlo simulation of photon migration. J Biomed Opt 13:060504. doi:10.1117/1.3041496
13. Lauritsen K, Riecke S, Bülter A, Schönau T (2014) Modern pulsed diode laser sources for time-correlated photon counting. Springer Ser Fluoresc. doi:10.1007/4243_2014_76
14. Prahl SA. Tabulated molar extinction coefficient for hemoglobin in water. http://omlc.ogi.edu/spectra/hemoglobin/summary.html
15. Kou L, Labrie D, Chylek P (1993) Refractive indices of water and ice in the 0.65- to 2.5 μm spectral range. Appl Optics 32:3531–3540
16. Van Veen RLP, Sterenborg HJCM, Pifferi A, Torricelli A, Chikoidze E, Cubeddu R (2005) Determination of visible near-IR absorption coefficients of mammalian fat using time- and spatially resolved diffuse reflectance and transmission spectroscopy. J Biomed Opt 10:054004. doi:10.1117/1.2085149

17. Grosenick D, Moesta KT, Möller M, Mucke J, Wabnitz H, Gebauer B, Stroszczynski C, Wassermann B, Schlag PM, Rinneberg H (2005) Time-domain scanning optical mammography: I. Recording and assessment of mammograms of 154 patients. Phys Med Biol 50:2429–2449. doi:10.1088/0031-9155/50/11/001
18. Taroni P, Torricelli A, Spinelli L, Pifferi A, Arpaia F, Danesini G, Cubeddu R (2005) Time-resolved optical mammography between 637 and 985 nm: clinical study on the detection and identification of breast lesions. Phys Med Biol 50:2469–2488. doi:10.1088/0031-9155/50/11/003
19. Torricelli A, Contini D, Pifferi A, Caffini M, Re R, Zucchelli L, Spinelli L (2014) Time domain functional NIRS imaging for human brain mapping. Neuroimage 85(Pt 1):28–50. doi:10.1016/j.neuroimage.2013.05.106
20. Grosenick D, Moesta KT, Wabnitz H, Mucke J, Stroszczynski C, Macdonald R, Schlag PM, Rinneberg H (2003) Time-domain optical mammography: initial clinical results on detection and characterization of breast tumors. Appl Optics 42:3170–3186
21. Taroni P, Danesini G, Torricelli A, Pifferi A, Spinelli L, Cubeddu R (2004) Clinical trial of time-resolved scanning optical mammography at 4 wavelengths between 683 and 975 nm. J Biomed Opt 9:464–473. doi:10.1117/1.1695561
22. Enfield LC, Gibson AP, Everdell NL, Delpy DT, Schweiger M, Arridge SR, Richardson C, Keshtgar M, Douek M, Hebden JC (2007) Three-dimensional time-resolved optical mammography of the uncompressed breast. Appl Optics 46:3628–3638
23. Liebert A, Wabnitz H, Steinbrink J, Obrig H, Möller M, Macdonald R, Villringer A, Rinneberg H (2004) Time-resolved multidistance near-infrared spectroscopy of the adult head: intracerebral and extracerebral absorption changes from moments of distribution of times of flight of photons. Appl Optics 43:3037–3047
24. Zucchelli L, Contini D, Re R, Torricelli A, Spinelli L (2013) Method for the discrimination of superficial and deep absorption variations by time domain fNIRS. Biomed Opt Express 4:2893–2910. doi:10.1364/BOE.4.002893
25. Mazurenka M, Di Sieno L, Boso G, Contini D, Pifferi A, Mora AD, Tosi A, Wabnitz H, Macdonald R (2013) Non-contact in vivo diffuse optical imaging using a time-gated scanning system. Biomed Opt Express 4:2257–2268. doi:10.1364/BOE.4.002257
26. Bülter A (2014) Single-photon counting detectors for the visible range between 300 and 1,000 nm. Springer Ser Fluoresc. doi:10.1007/4243_2014_63
27. Torricelli A, Quaresima V, Pifferi A, Biscotti G, Spinelli L, Taroni P, Ferrari M, Cubeddu R (2004) Mapping of calf muscle oxygenation and haemoglobin content during dynamic plantar flexion exercise by multi-channel time-resolved near-infrared spectroscopy. Phys Med Biol 49:685–699. doi:10.1088/0031-9155/49/5/003
28. Yamada E, Kusaka T, Arima N, Isobe K, Yamamoto T, Itoh S (2008) Relationship between muscle oxygenation and electromyography activity during sustained isometric contraction. Clin Physiol Funct Imaging 28:216–221. doi:10.1111/j.1475-097X.2008.00798.x
29. Ferrante S, Contini D, Spinelli L, Pedrocchi A, Torricelli A, Molteni F, Ferrigno G, Cubeddu R (2009) Monitoring muscle metabolic indexes by time-domain near-infrared spectroscopy during knee flex-extension induced by functional electrical stimulation. J Biomed Opt 14:044011. doi:10.1117/1.3183802
30. Grosenick D, Wabnitz H, Rinneberg H, Moesta KT, Schlag PM (1999) Development of a time-domain optical mammograph and first in vivo applications. Appl Optics 38:2927–2943
31. Rinneberg H, Grosenick D, Moesta KT, Wabnitz H, Mucke J, Wübbeler G, Macdonald R, Schlag PM (2008) Detection and characterization of breast tumours by time-domain scanning optical mammography. Opto Electron Rev 16:147–162. doi:10.2478/s11772-008-0004-5
32. Taroni P, Pifferi A, Salvagnini E, Spinelli L, Torricelli A, Cubeddu R (2009) Seven-wavelength time-resolved optical mammography extending beyond 1000 nm for breast collagen quantification. Opt Express 17:15932–15946
33. Arridge SR (1995) Photon-measurement density functions. Part I: Analytical forms. Appl Optics 34:7395–7409

34. Feng SC, Zeng F-A, Chance B (1995) Photon migration in the presence of a single defect: a perturbation analysis. Appl Optics 34:3826–3837
35. Grosenick D, Wabnitz H, Moesta KT, Mucke J, Schlag PM, Rinneberg H (2005) Time-domain scanning optical mammography: II. Optical properties and tissue parameters of 87 carcinomas. Phys Med Biol 50:2451–2468. doi:10.1088/0031-9155/50/11/002
36. Grosenick D, Kummrow A, Macdonald R, Schlag PM, Rinneberg H (2007) Evaluation of higher-order time-domain perturbation theory of photon diffusion on breast-equivalent phantoms and optical mammograms. Phys Rev E 76:061908. doi:10.1103/PhysRevE.76.061908
37. Grosenick D, Wabnitz H, Moesta KT, Mucke J, Möller M, Stroszczynski C, Stößel J, Wassermann B, Schlag PM, Rinneberg H (2004) Concentration and oxygen saturation of haemoglobin of 50 breast tumours determined by time-domain optical mammography. Phys Med Biol 49:1165–1181. doi:10.1088/0031-9155/49/7/006
38. Schmidt F, Fry M, Hillman EMC (2000) A 32-channel time-resolved instrument for medical optical tomography. Rev Sci Instrum 71:256–265
39. Cerussi AE, Hsiang D, Shah N, Mehta R, Durkin A, Butler JA, Tromberg BJ (2007) Predicting response to breast cancer neoadjuvant chemotherapy using diffuse optical spectroscopy. Proc Natl Acad Sci U S A 104:4014–4019. doi:10.1073/pnas.0611058104
40. Jakubowski DB, Cerussi AE, Bevilacqua F, Shah N, Hsiang D, Butler JA, Tromberg BJ (2004) Monitoring neoadjuvant chemotherapy in breast cancer using quantitative diffuse optical spectroscopy: a case study. J Biomed Opt 9:230–238. doi:10.1117/1.1629681
41. Choe R, Corlu A, Lee K, Durduran T, Konecky SD, Grosicka-Koptyra M, Arridge SR, Czerniecki BJ, Fraker DL, DeMichele A, Chance B, Rosen MA, Yodh AG (2005) Diffuse optical tomography of breast cancer during neoadjuvant chemotherapy: a case study with comparison to MRI. Med Phys 32:1128–1139
42. Jiang S, Pogue BW, Carpenter CM, Poplack SP, Wells WA, Kogel CA, Forero JA, Muffly LS, Schwartz GN, Paulsen KD, Kaufman PA (2009) Evaluation of breast tumor response to neoadjuvant chemotherapy with tomographic diffuse optical spectroscopy: case studies of tumor region-of-interest changes. Radiology 252:551–560
43. Enfield LC, Cantanhede G, Westbroek D, Douek M, Purushotham AD, Hebden JC, Gibson AP (2011) Monitoring the response to primary medical therapy for breast cancer using three-dimensional time-resolved optical mammography. Technol Cancer Res Treat 10:533–547
44. Corlu A, Choe R, Durduran T, Rosen MA, Schweiger M, Arridge SR, Schnall MD, Yodh AG (2007) Three-dimensional in vivo fluorescence diffuse optical tomography of breast cancer in humans. Opt Express 15:6696–6716
45. Hagen A, Grosenick D, Macdonald R, Rinneberg H, Burock S, Warnick P, Poellinger A, Schlag PM (2009) Late-fluorescence mammography assesses tumor capillary permeability and differentiates malignant from benign lesions. Opt Express 17:17016–17033
46. Van de Ven S, Wiethoff A, Nielsen T, Brendel B, van der Voort M, Nachabe R, Van der Mark M, Van Beek M, Bakker L, Fels L, Elias S, Luijten P, Mali W (2010) A novel fluorescent imaging agent for diffuse optical tomography of the breast: first clinical experience in patients. Mol Imaging Biol 12:343–348. doi:10.1007/s11307-009-0269-1
47. Poellinger A, Persigehl T, Mahler M, Bahner M, Ponder SL, Diekmann F, Bremer C, Moesta KT, Dye F (2011) Near-infrared imaging of the breast using omocianine as a fluorescent dye: results of a placebo-controlled, clinical, multicenter trial. Invest Radiol 46:697–704. doi:10.1097/RLI.0b013e318229ff25
48. Poellinger A, Burock S, Grosenick D, Hagen A, Lüdemann L, Diekmann F, Engelken F, Macdonald R, Rinneberg H, Schlag PM (2011) Breast cancer: early-and late-fluorescence near-infrared imaging with indocyanine green—a preliminary study. Radiology 258:409–416
49. Grosenick D, Hagen A, Steinkellner O, Poellinger A, Burock S, Schlag PM, Rinneberg H, Macdonald R (2011) A multichannel time-domain scanning fluorescence mammograph: performance assessment and first in vivo results. Rev Sci Instrum 82:024302. doi:10.1063/1.3543820

50. Yoneya S, Saito T, Komatsu Y, Koyama I, Takahashi K, Duvoll-Young J (1998) Binding properties of indocyanine green in human blood. Invest Ophthalmol Vis Sci 39:1286–1290
51. Ntziachristos V, Yodh AG, Schnall M, Chance B (2000) Concurrent MRI and diffuse optical tomography of breast after indocyanine green enhancement. Proc Natl Acad Sci U S A 97:2767–2772. doi:10.1073/pnas.040570597
52. Intes X, Ripoll J, Chen Y, Nioka S, Yodh AG (2003) In vivo continuous-wave optical breast imaging enhanced with indocyanine green. Med Phys 30:1039. doi:10.1118/1.1573791
53. Maeda H, Wu J, Sawa T, Matsumura Y, Hori K (2000) Tumor vascular permeability and the EPR effect in macromolecular therapeutics: a review. J Control Release 65:271–284

Index

A
Acoustic optical tunable filters (AOTF), 84
Afterpulsing, 24, 28, 32, 95
Alternating laser excitation (ALEX), 129, 130
Amyloid precursor protein (APP), 206
Analog-to-digital converter (ADC), 4
Antibunching, 159
Apolipoprotein A-I, 173
Application-specific integrated circuit (ASIC), 50
Atto-488, 96, 152, 154, 260
Atto-532, 142
Atto-633, 184
Atto-647N, 182
Atto-655, 97, 139, 260, 278
Autofluorescence, 192, 208, 225, 237, 357
Avalanche photodiodes (APD), 33, 49, 323
Axial resolution, 276

B
Biological macromolecules, 111
Bis(2,2′-bipyridine)-4,4-dicarboxybipyridine-ruthenium di(N-succinimidyl ester) bis (hexafluorophosphate), 236
Bis-(2-carboxyethyl)-5-(and-6)-carboxyfluorescein (BCECF), 193
Bleaching step analysis (BS), 178
Bragg-reflector (DBR) laser, 77
Breast tissue, cancer imaging, 343, 349
Burst-integrated fluorescence lifetime (BIFL), 12, 112

C
Cancer/carcinomas, breast, 208, 343
Cell–substrate distance, 270
Chromophores, natural, 226
Clomeleon, 206
Coincidence correlation/analysis, 1, 159
Confocal laser scanning microscopy (CLSM), 145
Confocal microscopy, 283
Constant fraction discriminator (CFD), 4
Correlation, 91
Counting by photon statistics (CoPS), 159, 177
Cross-correlation raster image correlation spectroscopy (ccRICS), 129
CW-STED, 288
Cy5, 106
Cy5-DNA-Ag, 99
Cyan fluorescent protein (CFP), 206
Cyano-substituted polyphenylene vinylene (CN-PPV), 168

D
Dark counts, 24, 28, 32, 97
Decay diversity map, 254
Decoherence, 307
Delay-locked loop (DLL), 6
Deoxyhemoglobin, 344
Detection efficiency, 24, 27, 31, 37
Detectors, 24
Diamond, 303
Dibenzanthanthrene (DBATT), 337

P. Kapusta et al. (eds.), *Advanced Photon Counting: Applications, Methods, Instrumentation*, Springer Ser Fluoresc (2015) 15: 367–370, DOI 10.1007/4243_2015,

Differential nonlinearity (DNL), 5
Diffuse optical imaging, 343
Diode lasers, 73
Distribution of times of flight (DTOF), 347
DNA, Cy5, 172
  dynamics, 123
  Origami, 181
Dynamic light scattering (DLS), 7

E
Energy transfer, 265
Entangled photons, 319
ERK, 207
Excited-state proton-transfer (ESPT), 197
Extravasation, 361

F
Fabry-Pérot (FP) resonator, 74
Far-field fluorescence microscopy, 283
Fiber beam splitter (FBS), 334
Fibroadenoma, 359
Field-programmable gate arrays (FPGA), 11
FIFO mode, 12
Fluorescence correlation spectroscopy (FCS), 7, 89, 111, 283
  dual-focus, 89, 100
  filtered (fFCS), 8
  lifetime-weighted, 114
Fluorescence fluctuation spectroscopy (FFS), 145
Fluorescence imaging, 343
Fluorescence intensity and lifetime distribution analysis (FILDA), 112
Fluorescence lifetime, 2, 72, 111
Fluorescence lifetime correlation spectroscopy (FLCS), 8, 89, 93
  two-dimensional (2D FLCS), 111, 116
Fluorescence lifetime imaging microscopy (FLIM), 191, 241, 265
Fluorescence optical mammography, 357
Fluorescent proteins (FPs), 191, 206
Fluorophore–metal interaction, 265
Förster resonance energy transfer (FRET), 76, 133, 191, 205
Four-wave mixing (FWM), 82
Free induction decay (FID), 306
Frequency conversion, 76

G
Gain switching, 71, 74
Gated continuous-wave STED (gCW-STED) microscopy, 283
Global compartment analysis (GCA), 197
Green fluorescent protein (GFP), 196
GTPase, 207

H
Hanbury Brown and Twiss interferometer, 159
Hemoglobin, 344
Heralding, 330
High density lipoprotein (HDL), 173
Hong–Ou–Mandel-type interference, 325
Hybrid PMTs, 23, 32
Hybrid quantum systems, 336, 339
5-Hydroxytriptophan, 196

I
IgG, 236
Image correlation spectroscopy (ICS), 145
Indocyanine green (ICG), 350
Infrared, 43
InGaAs/InP, 47
Instrument response function (IRF), 125, 243
Ion implantation, 308

L
Lasers, 71
  excitation pulses, 72
LEDs, pulsed, 71
  sub-nanosecond, 80
Lifetime imaging, 191
Light, collection, 326
  quantum states, 320
Linear unmixing, 241
Live-cell imaging, MIET, 270
Long lifetime probes, 225

M
Mach–Zehnder interferometer, 321
Mammography, 350
Master oscillator-power amplifier (MOPA), 77
Maximum-likelihood estimator, 249
Mercaptopropionic-acid-capped QD nanoparticles (QD-MPAs), 202
Mercury, 57
Metal-induced energy transfer, 265
Metal–ligand probes, 228
Methoxy-5-methylphenyl-6-hydroxy-3H-xanthen-3-one, 199
MFD-PIE, 129
Microchannel plate photomultipliers tubes (MCP-PMT/MCP), 23, 30
Microchip laser, 83

Microsecond dynamics, 111
Molecule detection function (MDF), 92, 100
Multiparameter fluorescence detection (MFD), 129, 132
Multi-pulse excitation, 225, 230
Multiple-pulse pumping, 225

N
NAD(P)H, 208
Nanodiamonds, 168, 328
Nanoparticles, sensors, 201
Nanowires, superconducting, 43, 58
  single-photon detectors (NSSPDs), 323
NbN, 60
Near-infrared spectroscopy, 343
Neoadjuvant chemotherapy, 356
Nitrogen-vacancy (NV) centers, 303
Noise-equivalent power (NEP), 45
Noninvasive tissue imaging, 191
Nonnegative least squares (NNLS), 249
Number and brightness analysis (N&B), 129, 153

O
Omocianine, 358
Ophthalmology, 358
Optical breast imaging, 349
Optical nanoantennas, 327
Optical parametric oscillator (OPO), 333
Optical time-domain reflectometery (OTDR), 44
Oxyhemoglobin, 344

P
Periodically poled lithium niobate (PPLN), 62, 79
Periodically poled potassium titanyl phosphate (PPKTP), 79
Phase-locked loop (PLL), 6
Phase matching, 331
Phasor method, 212, 249
Photomultiplier tubes (PMTs), 23, 25, 46, 323
Photonic crystal fibers (PCF), 82
Photons, antibunching, 159, 162
  arrival times, 283
  correlations, 159
  counting, 319, 343
  generation, 324
  increasing, 143
  interval analysis, 125
  pairs, entangled, 332
Photosensitizers, 202, 209
Phycoerythrin (PE), 168
Picosecond timing, 1
PIE-FI, 129
Plasmonics, 265
Point-spread function, 283
Polarizing beam splitter (PBS), 334
PPKTP. *See* Periodically poled potassium titanyl phosphate (PPKTP)
PPLN. *See* Periodically poled lithium niobate (PPLN)
Preselin, 206
Protorphyrin IX, 209
Pulsed diode lasers, 71
Pulsed interleaved excitation (PIE), 104, 129
Pulsed LEDs, 71
Purcell effect, 326
Pyronin Y, 196

Q
Quantum dots, 55, 191, 202, 228, 329
Quantum efficiency, 24
Quantum information processing, 319, 338
Quantum key distribution (QKD), 319, 335
Quantum memory, 311
Quantum non-demolition measurement (QND), 310
Quantum optics, 319
Quantum repeaters, 335

R
Raman scattering, 225
Ramsey sequence, 306
Rare-earth-doped fiber amplifiers, 78
Raster image correlation spectroscopy (RICS), 146
Raster lifetime image correlation spectroscopy (RLICS), 129, 151
Resonators, 73

S
Scattering, 97
Self-differencing circuits, 52
Self-phase modulation (SPM), 82
Semiconductor lasers, 73
Semiconductor optical amplifiers (SOA), 78
Sensitivity, 24
Serotonin, 196
Silicon/silicon germanium (Si/SiGe), 53

Silicon-vacancy (SiV) centers, 303, 314
Sine gating, 51
Single detector cross-correlation, 99
Single molecules, 89
  fluorescence spectroscopy (SMFS), 159
Single-pair Förster resonance energy transfer (spFRET), 129
Single-photon avalanche diodes (SPADs), 23, 35, 43, 47, 95
Single-photon counting, 1, 23, 43
Single-photon light-emitting diode, 329
Single-photon sources, 303, 319, 324
Single-photon timing (SPT), 191
Single quantum emitters, 324
Single-spin detection, 303
SNAFL-1, 196
SNAP proteins, 185
Solid immersion lenses (SIL), 314, 327
Spatio-temporal image correlation spectroscopy (STICS), 145
Spectrally resolved imaging, 241
Spectroscopy, 89
Spin–photon interface, 313
Spontaneous parametric down-conversion (SPDC), 331
STED microscopy/nanoscopy, 283
  continuous wave (CW-STED), 288
  gated (gSTED), 288
Stimulated emission depletion, 283
SuperClomeleon probe, 207
Superconducting quantum interference device (SQUID) array, 58
Superconducting transition edge sensors (TESs), 56, 323
Superconductors, 56
Supercontinuum generation, 82
Supercontinuum lasers, 71

T
Texas Red, 246
Time-correlated single-photon counting (TCSPC), 1, 71, 93, 129, 159, 162, 241
  time-tagged, 9, 111
Time-gated detection, 225, 228
Time-solved imaging, 241
Time tagging, 1
Time-to-amplitude converter (TAC), 4
Time-to-digital converters (TDCs), 1, 5
Timing resolution, 24, 29, 32, 38
Tissues, cancer, 208
  diffuse light propagation, 345
  FLIM, 208
  optical properties, 208, 343
T3 mode, 12
Tokyo Green (TG) dyes, 198
Transglutaminase type 2, 207
Transition edge sensor, 43
Transition edge sensor (TES), superconducting, 57
Transit time spread (TTS), 4, 29
Tris(2,2′-bipyridyl)dichlororuthenium (II) hexahydrate (Ru), 225, 227
Tryptophan, fluorescence, 209, 242
Tumors, optical properties, 354
Tungsten, 57
Two-dimensional fluorescence lifetime correlation spectroscopy (2D FLCS), 111

U
Upconversion, 61

W
Wavelength division multiplexer (WDM), 78
Wave–particle duality, 322
WSi, 60

X
Xanthene dyes, 191

Y
Yellow fluorescent protein (YFP), 206, 209

Z
Zero-phonon line (ZPL), 304, 314, 326, 337